Modelling diffuse groundwater recharge in Irish karst

PHILIP SCHULER

A thesis submitted for the degree of Doctor of Philosophy to the University of Dublin, Trinity College

2020

Department of Civil, Structural and Environmental Engineering
University of Dublin
Trinity College
Dublin

Declaration

I declare that this thesis has not been submitted as an exercise for a degree at this or any other university and it is entirely my own work.

I agree to deposit this thesis in the University's open access institutional repository or allow the Library to do so on my behalf, subject to Irish Copyright Legislation and Trinity College Library conditions of use and acknowledgement.

Philip Schuler

Summary

Karst aquifers are highly heterogeneous, usually described by a 'duality of recharge and flow' or triple porosities and associated ranges of recharge and flow dynamics comprising laminar (diffuse) and partly or fully turbulent groundwater flow. Such heterogeneity challenges the management related to karst aquifers, including landuse management mitigating contaminant input and transfer (i.e. source protection, etc.), or understanding and mitigating groundwater flooding. Hence, the development of numerical models for karst aquifers is crucial with regard to improving the understanding of flow and transport dynamics, as well as providing decision support systems that can incorporate climate change scenarios.

The aim of this research, carried out between 2015 and 2019, is to characterise diffuse recharge and flow components of three distinct autogenic karst aquifers (1. Ballindine spring, a low lying catchment in interaction with a river; 2. Bell Harbour, a coastal-upland catchment impacted by the tide and discharging as submarine and intertidal groundwater discharge; and 3. Manorhamilton spring, an upland-lowland catchment) as basis and part of the development of semi-distributed hydraulic pipe network models using the urban drainage software InfoWorks ICM. The research question and objectives comprised: 1.) developing an hydrogeological understanding and conceptual site model (CSM) of each study site; 2.) applying a suitable set of statistical and hydrochemical (time series) analyses to distinguish between recharge and flow components; and 3.) numerically simulate these recharge and flow components in pipe network models, and by doing so, evaluate 1.) and 2.).

Several extensive **hydrogeological field investigations** had to be carried out in order to improve the conceptual understanding of each catchment as well as to delineate the groundwater catchment areas, including continuously automated monitoring of hydroclimatic parameters as well as 'spot' field investigations.
Three different types of **artificial tracer tests** were applied: 1.) 'classical' artificial tracer tests using fluorescent dyes carried out between terrestrial injection sites (e.g. swallow holes) and spring outlets; 2.) single borehole dilution tests (SBDTs) using the conservative tracer $NaCl$ and deionized water; and 3.) tracing submarine groundwater discharge (SGD) using fluorescent dyes injected into terrestrial sites while monitoring is carried onboard of a vessel using a field fluorometer submerged in the sea sampling 'mobile' in transects.
The characterisation of the study sites was further facilitated by **using continuously and automated observed basic hydroclimatic variables** such as rainfall, water levels, spring discharge and electrical conductivity (EC) over a period of at least one (hydrological) year. The availability of long-term EC time series of the outlet of Bell Harbour Bay allowed the estimation of submarine and intertidal groundwater discharge (SiGD) into Bell Harbour Bay using a pollution flushing model for well-mixed tidal embayments.

The analysis of recharge and flow components and the development of the hydraulic pipe models was based on – and carried out hand in hand with - **Conceptual Site models (CSM)** for each study site: groundwater flow in the **Bell Harbour** catchment is very complex, integrating deep and shallow flow discharging into the sea with a clear seasonal pattern of 'low-flow' vs. 'high-flow'. The catchment of **Ballindine spring** was delineated along the River Robe, which is believed to be a losing stream impacting on the aquifer. **Manorhamilton spring** is a 'contact type' spring, largely controlled by the regional structural pattern, the dip of the formations and the topography.

A combination of **time series analysis**, including **uni- and bivariate statistical methods**, **frequency, noise and multi-resolution analysis** (discrete and continuous wavelet transform, cross wavelet transform, wavelet coherence) was applied to support the development of CSMs, but mainly to characterise and quantify different **flow components**: a concentrated, an intermediate and a **low-flow component (LFC)**. The innovative approach of combining **frequency analysis (i.e. Fourier transform)** with **noise analysis** lead to the interpretation of different recharge and flow components towards 3 generic components. The LFC was conceptualised as the component that sustains the lowest discharge of a spring as part of an overall diffuse recharge and flow signal established by using digital recursive filter.

The identified recharge and flow components were incorporated into the developed CSMs and finally numerically simulated in the pipe network models. The 3 different recharge and flow components were numerically represented in InfoWorks ICM using the soil store and groundwater store of the Ground Infiltration Module (GIM), a rainfall-runoff routing method as well as different discrete flows through pipes, using permeable pipes to simulate Darcian flow and open pipes to model both pressurised and open channel turbulent flows using the Saint-Venant equations to allow the modelling of time transient effects.

In all three catchment models, the simulated discharges match relatively well the observed or estimated reference discharges as indicated by different performance indicators. Further, the frequency spectra of the simulated discharges match well the spectra of the observed time series, which suggests that the different recharge and flow components were realistically represented in the model. These findings are supported by the well simulated recessions of the individual components, including partly the LFC. **The identified recharge and flow components – where reliably detected - as well as the final discharge of the study sites could successfully be modelled using InfoWorks**. The conceptual understanding according to which different recharge and flow components integrate towards a spring outlet discharge is the sum of different recharge and flow components has proven to be adequate, at least in a numerical sense, which is largely based on the combination of a triangular recharge function, linear reservoirs as well as laminar, turbulent and open-channel pipe flow dynamics.

Finally, this thesis concludes that the methods adopted are well suited to study relatively unknown and complex karst aquifer systems, and that InfoWorks ICM is able numerically to represent individual recharge and flow components.

Acknowledgements

I wish to express my sincerest thanks to Laurence Gill for giving me the opportunity to develop this piece of research under his supervision. The confidence I felt was enlightening and motivating, not only for writing paragraphs and running model simulations, but also for the countless times spent in the field to installing, collecting and fixing samplers, rowing out into Bell Harbour Bay, sneaking into turloughs, abseiling into Poll Gonzo and camping on Turlough Hill.

Within the past three to four years, Léa Duran and Paul Johnston were very important sources of knowledge and experience. To both I am very grateful.

In 2009, a four-days field trip along the Vienna Aqueducts led by Christian Maslo opened my eyes for karst and groundwater. Since then, Armin Margane, Ramon Brentführer, Thomas Himmelsberger, Charlotte Wilczok and Jean Abi-Rizk thankfully shared - amongst other things - their rational and profound way of thinking when it comes to karst hydrogeology, research and work-life.

During the period of carrying out this research, many people have directly and indirectly supported me, namely Maurice Brodbeck, Colin Bunce, Kirsty Callaghan, Èlia Cantoni, Mary Curley, David Drew, Natalie Duncan, Eoin Dunne, John Gallagher, Moritz Helmes, Mark Gilligan, Michael Grimes, David Mc Aulay, Ted McCormack, Gerard Mc Granaghan, Malte Janßen, Coran Kelly, Hilde Koch, Denis Korflür, Paul Königer, Monica Lee, Anthony Mannix, Bruce Misstear, Dave Morgan, Patrick Morrissey, Kevin Ryan, Fabi Schloz, Pierre-André Schnegg, Leonard Stöckl, Katie Tedd, Patrick Veale, John Walsh, Daniel Wearen.

One major key I have been using to decipher various codes in my life is firstly the ‘education’ I received from my older siblings Gusche and Toni, and secondly the trust to follow my instincts - which both of my parents Angie and Uli conveyed to me in their own way.

And finally, it is the source of joy, optimism and indefinite confidence that I feel every day by my beloved wife Sara and our little daughter Magali, providing a home wherever we are, which is so important for my being and making.

Abbreviations

ACF	autocorrelation function
BFI	baseflow index
BGR	Bundesanstalt für Geowissenschaften und Rohstoffe (*Federal Institute for Geoscience and Natural Resources*)
BOEC	Burren Outdoor and Education Centre
CSO	combined sewer overflow
CSM	conceptual site model
CWT	continuous wavelet transforms
Co.	County
XWT	cross wavelet transforms
CCF	cross-correlation function
A	cross-sectional area
db	Daubechies (wavelet)
d	day
D	detail
2H	deuterium
Ø	diameter
DEM	digital elevation model
Q	discharge
DCN	Discrete Conduit Network
DWT	discrete wavelet transforms
DOC	dissolved organic carbon
DOM	dissolved organic matter
EC	electrical conductivity
EMMA	end member mixing analysis
EPA	Environmental Protection Agency
ET	evapotranspiration
FFT	fast Fourier Transform
f	friction factor
GSI	Geological Survey Ireland
GMWL	Global Meteoric Water Line
GPS	global positioning system
GIM	Ground Infiltration Module
GWR	groundwater recharge
Q_{Gi}	groundwater store inflow
GWS	Group Water Scheme
Hz	hertz
h	hour
K	hydraulic conductivity
IS	injection site
ICM	Integrated Catchment Modelling
IAEA	International Atomic Energy Agency
ITM	Irish Transverse Mercator
Jan	January (*all months abbreviated using the first 3 letters*)
KGE	Kling-Gupta efficiency
l	litre
LFC	low-flow component
masl	m above sea level
mbsl	m below sea level
MI	Marine Institute
MRC	master recession curve
MWL	Meteoric Water Line

min	minute
MRA	multi-resolution analysis
nm	nanometre
NSE	Nash-Sutcliffe efficiency
OS	observation site
18O	oxygen-18
ppb	parts per billion
P	rainfall (precipitation)
a	recession coefficient
k	recession constant
RH	relative humidity
RMSE	root mean square error
R	runoff
s	second
SRTM	Shuttle Radar Topography Mission
SBDT	single borehole dilution test
S	smooth (or residual)
SCS	Soil Conservation Service
Q_{ri}	soil store inflow
β	spectral exponent
SWMM	Storm Water Management Model
SC	sub-catchment
SiGD	submarine and intertidal groundwater discharge
SGD	submarine groundwater discharge
T	temperature
T_c	time of concentration
T_p	time of peak flow
TDS	total dissolved solids
TON	Total organic nitrate
T_b	total runoff time
TBC	tracer break-through curve
TCD	Trinity College Dublin
TCMA	two component mixing analysis
UK	United Kingdom
USGS	United States Geological Survey
VSMOW	Vienna Standard Mean Ocean Water
VCC	volume conservation criteria
WTC	wavelet coherence

Table of Contents

Walk in the Sky – Sara Makdessi, 2015

1. General Introduction

1.1. Overview

Karstified carbonate aquifers – or 'karst aquifers' - exist on all continents in the world, their discharge constitutes the largest springs. Moreover, an estimated 25% of the global population receives drinking water that originates from karstified carbonate aquifers (Ford and Williams, 2007). Approx. 22% of the European land surface is characterised by the presence of carbonate rocks (Chen, et al., 2017) presumably karstified to a large extent with such carbonate groundwater resources providing an important contribution to the European population's drinking water supply. For example, the capital of Austria, Vienna, is almost exclusively supplied by carbonate spring water via a 330 km long-distance carrier (Rihas, 2010). In Ireland, Carboniferous limestone aquifers provide the majority of groundwater supplies (Drew, 2018).

Karstified carbonate aquifers are highly heterogeneous geological formations which are characterised by multi-scale temporal and spatial hydrological behaviour. Karst aquifers are usually described in terms of two or three distinct types of porosity models: matrix, fracture and conduit permeabilities (White and White, 2005). Multiple permeabilities relate to different fluid flow dynamics within such systems. This is usually summarised as fast conduit flow vs. slow matrix/fracture flow, described by the "duality of karst aquifers" in relation to infiltration, flow and discharge (Kiraly, et al., 1995). Accordingly, the availability of quantitative information about these different flow processes is crucial as it is ultimately linked to the appropriate management and protection of karst groundwater.

A major challenge in the quantitative analysis of karst aquifers is the combined dynamics of these different permeabilities, which build up the architecture of properties of such an aquifer. The intrinsic properties of an aquifer constitute a unique signature that drives infiltration, flow and discharge over space and time. Information about these processes and aquifer properties can be studied using time-amplitude signals, e.g. a karst spring hydrograph, which describes the hydrodynamic response observed at the spring outlet to an input signal (e.g. rainfall). A given discharge response measured at a spring characterises the rainfall signature as well as the global structure of the drained aquifer. Following a rain event, each hydrograph shows a unique recession response. Such recession describes exponential courses following the principles of emptying nonlinear reservoirs (Chang, et al., 2015) or much more commonly applied linear reservoirs (Maillet, 1905). Accordingly, the different components of permeability making up a karst aquifer can be conceptualised as distinct reservoirs.
Drainage of a specific conceptual reservoir that resembles the slow-flow component occurring within the fissured matrix porosity is normally referred to as baseflow. A baseflow component can be established using recession analysis. Such an approach is based on the principle of fitting a

series of exponential curves onto the entire recession of a karst hydrograph resembling the different permeabilities in the karst aquifer (Forkasiewicz and Paloc, 1967). Today, the separation of karst spring recession into a slow-flow baseflow component and fast flowing flood components is widely accepted.

Different methods for separation or decomposition of the baseflow component from the total hydrograph or only recession are available ranging between numerical approaches such as digital recursive filtering (Chapman, 1999) and numerical baseflow separation (Kovács, et al., 2005; Kovács and Perrochet, 2008; Kovács, et al., 2015) or chemical approaches such as two component mixing analysis (TCMA) or end-member mixing analysis (EMMA) using for example stable isotopes (^{18}O, ^{2}H) (Fritz, et al., 1976; Laudon and Slaymaker, 1997). Further, signal analysis in the form of multiresolution analysis (MRA) (Torrence and Compo, 1998; Labat, et al., 2000b) may evolve as a potential method for baseflow separation.

Complementary to the approaches of baseflow separation, numerical groundwater modelling can be applied in order to infer information about - and simulate - different groundwater flow dynamics, including the slow-flow component. Different modelling approaches exist ranging between global (lumped) and fully distributed approaches. The models and/or the interpretation of their results are all challenged by the heterogeneity of karst aquifers.
In the Irish context, semi-distributed pipe network models have been proven to excel well in the context of karst aquifers with a high proportion of fast-flow components in the conduit permeability domain. Yet, until now, the fissured matrix permeability and its slow-flow components was not sufficiently represented in terms of linking such flow components to a measured of quantified contribution.

The purpose of this research is therefore to identify and study the slow-flow dynamics in three Irish karst aquifers (Ballindine, Bell Harbour and Manorhamilton) by means of baseflow separation using a combination of different techniques. A set of different methods is applied to separate the baseflow component of karst springs, which is considered to be representative for diffusely infiltrating rainfall and slow-flow components originating from the low permeability domain. The resulting baseflow time series have then been specifically used as reference for a semi-distributed numerical pipe network modelling approach using InfoWorks ICM alongside the heretofore more resolved fast-flow component originating from the conduit domain.

1.2. Aims and objectives

The aim of the research is to investigate three separate karst aquifers in Ireland in order to characterise their diffuse recharge and slow-flow components which can then be used to develop more

realistic numerical models of these aquifers. For example, such models can then be used to make predictions as to the aquifer response due to climate change, develop engineering solutions to potential flooding predictions or to evaluate contaminant transport and landuse options.

The project objectives are to:

1. Provide a hydrogeological assessment of each catchment: quantify its discharge and representative rainfall over at least one hydrological year, establish water balances, delineate the catchment boundaries, assess flow dynamics and develop conceptual site models (CSM) as basis for a profound hydrogeological understanding as basis for any recharge-discharge assessments;
2. Differentiate between slow (diffuse) and fast (concentrated) recharge and flow into and within a karst network using both chemical (isotopic and trace element water quality) and numerical and statistical approaches towards spring hydrograph separation, and quantify the flow and response times of diffusely recharged flow;
3. Develop numerical (pipe network) models of the three karst aquifers that allow to distinguish different flow components as a result of the intrinsic heterogeneity of the aquifer and the CSM.

The numerical modelling approach is based on the principles applied in the lowland karst area of south Galway in the west of Ireland which accurately simulates the temporal flooding dynamics of the turloughs on the network (Gill, et al., 2013a). This modelling approach has worked well with respect to the groundwater – surface water interactions (water levels in the ephemeral lakes known as ‘turloughs’) but it is recognised that it is limited as to the accuracy of the representation of the diffuse autogenic recharge into the network. Such autogenic recharge is of significant interest particularly with regard to contaminant transport and attenuation across such catchments.
Hence, this research investigates three different karst networks all with autogenic recharge, but each with different characteristics found in the Irish context: a lowland karst aquifer (Ballindine, County (Co.) Mayo); a upland-lowland karst aquifer (Manorhamilton, Co. Leitrim); and a complex coastal-upland karst aquifer (Bell Harbour, Co. Clare).
This research focusses on characterising diffuse - but also concentrated - recharge and flow through the karst system in these three different aquifers by applying different investigative techniques. The investigative techniques involve both chemical (stable isotopes and ions) and statistical and numerical methods, such as hydrograph separation techniques, time series analysis Including uni- and bivariate methods, Fourier analysis coupled with noise analysis and multi-resolution analysis (MRA).
Water quality sampling was required in order to analyse for isotopic fractionation techniques using the stable isotopes oxygen-18 (18O) and deuterium (2H) as well as using anions, such as silica.

In addition, numerical analysis of the spring hydrographs of Ballindine and Manorhamilton, which represent the global aquifer response, are used to differentiate the fast aquifer and spring response following rain events as opposed to the slower more diffuse response.

This research trials different numerical techniques such as discrete wavelet techniques and noise analysis (Schroeder, 1991; Beier and Hardy, 1996; Fournillon, 2012) to investigate the inherent non-linear, non-stationery natural hydrological processes in such a karst system.

1.3. Thesis layout

The three study sites differ significantly from each other. Ballindine and Manorhamilton constitute terrestrial inland karst catchments with more or less well-defined discharge locations. In turn, the catchment of Bell Harbour is a coastal terrestrial-marine aquifer that is impacted by the sea and its tide, and it is drained via multiple intertidal and submarine outlets. Within this project, much research had to be conducted to understand the system of Bell Harbour to a level that is necessary for recharge-discharge analyses. In fact, the amount of work put into Bell Harbour significantly exceeds respective workload for Ballindine and Manorhamilton.
Further, some different approaches were applied in Bell Harbour as opposed to the other two sites. These circumstances were acknowledged in the structure of this work. Accordingly, at first, results are presented and compared between Ballindine and Manorhamilton. Conclusions from that are then used and applied on the catchment of Bell Harbour, which is presented at last.

The thesis is structured as follows: The conceptual understanding of karst aquifers underlying this research is summarised within ‘State of the Art Review’. Further, this chapter presents the literature on different methods related to hydrograph separation, numerical and chemical characterisation of karst aquifers and groundwater flow modelling.
Chapter ‘Study Sites’ introduces the three karst systems, including their delineated catchment boundaries resulting from this research. Chapter ‘Materials and Methods’ presents the primary and secondary data that was used in this study, sampling and lab analysis, as well as the main statistical and numerical methods for hydrograph separation and groundwater modelling, tracer testing, and quantifying of submarine and intertidal groundwater discharge (SiGD) applied in Bell Harbour.
Chapter ‘Catchment Studies’ presents the process of delineating the catchment boundaries of Ballindine and Manorhamilton using water balances, reservoir modelling and artificial tracer tests. Further, the average recession, namely the master recession curve (MRC) is used to characterise both aquifers with regard to recharge, flow and discharge. Both systems are then numerically and statistically evaluated using their spring discharge time series (‘Time Series Analysis’). The evaluation of time series then leads to the identification of continuous time series of flow components, including a low-flow component (LFC). The results of this Chapter are then used as reference for groundwater

flow modelling using InfoWorks ICM® (version 7.0.5., Innovyze Ltd., Wallingford, UK) presented in Chapter ‘Groundwater Modelling using InfoWorks ICM’, finalising the analyses on Ballindine and Manorhamilton.

Finally, Chapter ‘Bell Harbour’ presents all results achieved for the coastal system of Bell Harbour. In a similar way to the Ballindine and Manorhamilton catchments, the studies that have informed the understanding of the global functioning of the system, as well delineation of the catchment boundaries, are first presented. Bell Harbour has proven to be a complex multi-level coastal karst aquifer, which had to be examined extensively using a high resolution hydrometeorological monitoring network along with discrete sampling and tracer testing. The synthesis of results was applied on a numerical model, which in turn yields additional information on groundwater flow dynamics.

Chapter ‘Conclusions’ highlights the main results within the overall context of this thesis. And finally, Chapter ‘9.2. Recommendations’ rounds up this work along with recommendations for future research.

2. State of the Art Review

2.1. Overview of karst systems

The term ‘karst’ can be tracked back to pre-Indoeuropean origins. In the context of karst hydrogeology, the more recent origin in Slovenia is of relevance where the word ‘kar(r)a’ underwent the evolution via ‘kars’ to ‘kras’, which means stoney, barren ground (Ford and Williams, 2007). Ultimately, karst describes a landscape that is developed on especially soluble rocks such as limestone, marble, and gypsum. In the introduction of their seminal publication, Ford and Williams (2007) highlight the two key aspects of karst landscapes, i.e. a) the groundwater/hydrogeology domain, and b) the karst landscape/geomorphology domain, both above and below the surface. It is important to note, especially for this study, that an absence of features above the ground doesn’t imply an absence of features below the ground.

The existence of karst and karst features is ultimately linked to the geological structure providing the framework for preferential dissolution, and to the underlying lithology and mineralogy that allows for the development of karst, i.e. ‘karstification’, caused by the process of chemical solution of rocks. In Ireland, karst features are documented in >80% of the limestone outcrops indicating widespread karstification (Drew, et al., 1996). Karstification is related to the presence of ‘karst minerals’ belonging to three classes, i.e. carbonate minerals (e.g. calcite, dolomite), sulphate minerals (gypsum, anhydrite), and halide minerals (halite) (Goldscheider and Andreo, 2007). Of most importance and relevance to this study is the group of carbonate minerals, which are composed of the carbonate anion (CO_3^{2-}). The most important karst mineral is calcite ($CaCO_3$), which - if predominantly present - forms limestone, i.e. a carbonate rock. Another relevant karst mineral is dolomite, which forms dolostone or dolomite. Dolomite is an anhydrous carbonate mineral composed of calcium magnesium carbonate ($CaMg(CO_3)_2$).
Carbonate rocks are all types of sedimentary or metamorphic rocks with >50% carbonate minerals in weight (Ford and Williams, 2007; Goldscheider and Andreo, 2007). Depending on the percentage of calcite or dolomite, as well as impurities, carbonate rocks may be classified according to Figure 2.1.

In Ireland, the majority of karstified carbonates originates from the Lower Carboniferous (Mississippian: Tournaisian and Viséan) consisting of limestones. Sedimentation of early Carboniferous rocks occurred in the context of a marine transgression progressing northwards and a change from global greenhouse conditions during the Tournaisian towards global icehouse conditions during the Asbian. By the Viséan, Ireland had turned into a shallow water carbonate shelf surrounding deeper water basins. Within nutrient rich oceans, the carbonate production with depth is more uniform, whereas during the colder periods, carbonate production decreased significantly <10 m (Sevastopulo and Wyse Jackson, 2009; Davies, et al., 2012).

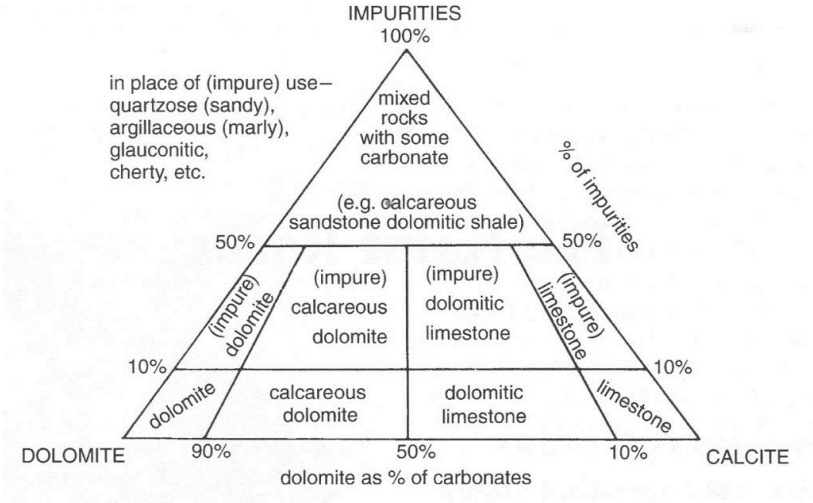

Figure 2.1: Bulk compositional classification of carbonate rocks (Ford and Williams, 2007).

Carbonates are considered to have a ‘primary porosity’ that describes all pore space present immediately after final deposition, and a ‘secondary porosity’ and ‘tertiary porosity’ that are created after final deposition (Choquette and Pray, 1970; Teutsch and Sauter, 1991). The effective porosity of carbonates is of major importance as it directly influences the permeability, i.e. hydraulic conductivity, of rocks, hence, enabling flow and storage of groundwater. More precisely, it is the effective porosity, i.e. the interconnected pore space (excluding only localised openings) that must be considered as only this proportion of the overall bulk porosity allows free gravity flow of groundwater (Kresic, 2007). Newly deposited carbonates have a porosity of 40-70%, but this drops to a few percent as the rock consolidates over time (Choquette and Pray, 1970).

Many of the important changes in sedimentary carbonates and their pore systems occur near the surface, either very early in burial history or at later stage in relation to erosion and uplift (Choquette and Pray, 1970). Tectonics and mechanical stress often impact on the rock matrix, which is visible today as subvertical fractures such as joints or veins. Joints may be stratabound with regular spacing forming the characteristic geometrical fracture networks of grykes and clints on the outcrop surface. Joints are relatively shallow and may be limited to limestone mechanical units. In turn, veins, which developed in deeper depths across strata, are therefore non-stratabound and are scale-independent (Gillespie, et al., 2001).
The network of joints, faults, bedding planes and veins provides the pathways for hierarchical dissolution of secondary porosity fissures creating tertiary porosity where fissures, i.e. fractures, became enlarged by dissolution (Teutsch and Sauter, 1991; Worthington, et al., 2000). For example, mineralised veins can constitute preferential pathways for dissolution along them (Appleton, 1989; Bunce, 2010).

The dissolution of carbonates differs between rocks. Limestones are generally more karstifiable than dolostone whereas the karstifiability of a rock decreases with increasing impurity caused by clay content, for example. Other impurities that impact on the chemistry of groundwater may be related to mineralisation, including for example sulphate (SO_4^{2-}) that is derived from the slow oxidation of pyrite (FeS_2) (Tooth and Fairchild, 2003).

The dissolution (or karstification) of carbonate rock is described by the process of acid dissolution, a sequence of reactions. Eqn. 2.1 describes the reaction of limestone in water, i.e. the dissociation, which in fact is small for limestone in pure water. However, in presence of a free proton H^+, the sequence of reactions Eqn. 2.1 and Eqn. 2.2 become active,

$$CaCO_3 \Leftrightarrow Ca^{2+} + CO_3^{2-} \qquad \text{Eqn. 2.1}$$

$$Ca^{2+} + CO_3^{2-} + H^+ \Leftrightarrow Ca^{2+} + HCO_3^- \qquad \text{Eqn. 2.2}$$

CO_3^{2-} becomes hydrated to form soluble bicarbonate HCO_3^-. The process depends on the saturation of given minerals in the solution as well as the availability of CO_2 which forms carbonic acid. The concentration of carbonic acid is affected by different factors, such as microbial activity in the soil which in turn depends on the soil temperature (Tooth and Fairchild, 2003). Yet, more importantly, the rate of limestone dissolution is four orders higher in turbulent flow compared to laminar flow (Dreybrodt, 2004), enabling speleogenesis to progress.
Within the saturated zone, with increasing vertical depth, the saturation of HCO_3^- generally increases and the rate of dissolution decreases. This phenomenon results in the potential presence of a highly karstified or weathered upper zone of a karst aquifer, i.e. subcutaneous zone, or 'epikarst' (Mangin, 1975) of high permeability (Figure 2.2) usually diminishing exponentially with depth over typically 3 to 10 meters (Ford and Williams, 2007). However, in Ireland, if present, the epikarst may be limited to a depth of only 1 m (Williams, 2008).

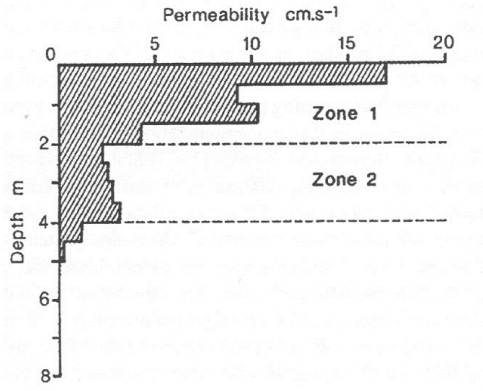

Figure 2.2: Variation of permeability in depth (Ford and Williams, 2007).

The ‘epikarst’ has been conceptualised as a sub-system of the karst aquifer largely influencing the recharge dynamics of the aquifer (Figure 2.3) (Kiraly, et al., 1995; Bakalowicz, 2004). Below the upper weathered zone or epikarst, a karst aquifer is commonly conceptualised by a hierarchical network of flow paths in the form of a matrix embedded in a network of fissures, fractures and conduits enlarged by dissolution and flow kinetics (Figure 2.5).

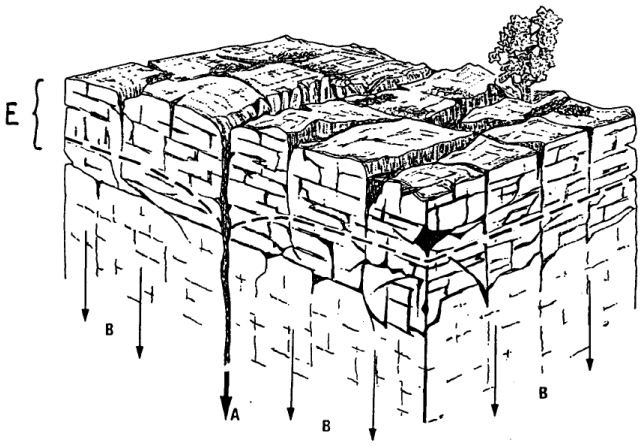

Figure 2.3: Schematic of the epikarst (E) with concentrated (A) and diffuse (B) infiltration (Mangin, 1975; Kiraly, et al., 1995).

Conduits, fractures and the matrix have distinct properties and functioning within carbonate aquifers. In a comprehensive review on carbonate aquifers, Worthington, et al. (2000) conclude that the permeability structure following dissolutionally enlarged networks applies to all unconfined carbonate aquifers (dolostone, limestone and chalk) irrespectively of the deposition age. The authors provide average hydraulic properties of the three different permeabilities, which previously had more commonly been stated for aquifers or strata as a whole. Generally, the matrix accounts for the largest share of porosity and the highest proportion of groundwater storage with the lowest hydraulic conductivities and lowest proportion of overall groundwater flow. Conversely, conduits account for the largest proportion of groundwater flow related to the highest hydraulic conductivities, low proportions of storage and very low porosities. The fracture domain is somewhat between the conduit and matrix domain, with a low proportion of groundwater flow, moderate hydraulic conductivities, low proportions of storage and low porosity. For example, Worthington, et al. (2000) provide an average porosity, proportion of storage, hydraulic conductivity and proportion of flow for the three permeabilities for the prominent limestone system of the Mammoth cave area of Mississippian age (Table 2.1).
It becomes evident that the matrix and its porous structure has a negligible influence on groundwater flow in the exemplified limestone aquifer (as opposed to chalk). Yet, many (groundwater flow modelling) studies related to limestone aquifers refer to a ‘matrix domain’ and groundwater flow related to the matrix permeability (Geyer, et al., 2008a; Reimann, et al., 2011; Doummar, et al.,

2012), which may cause confusion from a geological point of view. However, all these referred authors consider the matrix domain as ‘fissured’ or ‘fractured’ (porous) matrix domain, abbreviated as ‘matrix domain’. Hence, the term ‘matrix’ incorporates some level of secondary porosity, i.e. (narrow) fissures/fractures.

Table 2.1: Average hydraulic properties of the matrix, fractures and conduits of the Mammoth Cave limestone aquifer (Worthington, et al., 2000).

Property	Matrix	Fracture	Conduit
Porosity [%]	2.4	0.03	0.06
Proportion of storage [%]	96.4	1.2	2.4
Hydraulic conductivity [m/s]	2×10^{-11}	1×10^{-5}	3×10^{-3}
Proportion of flow [%]	0.00	0.3	99.7

Mature karst systems include different porosities and permeabilities ranging between the primary porosity of the matrix and larger conduits (Figure 2.4). Most commonly, permeabilities are expressed as a) matrix (µm to mm opening), b) fractures (10 µm to 10 mm) and c) conduits (>10 mm) (Ghasemizadeh, et al., 2012).

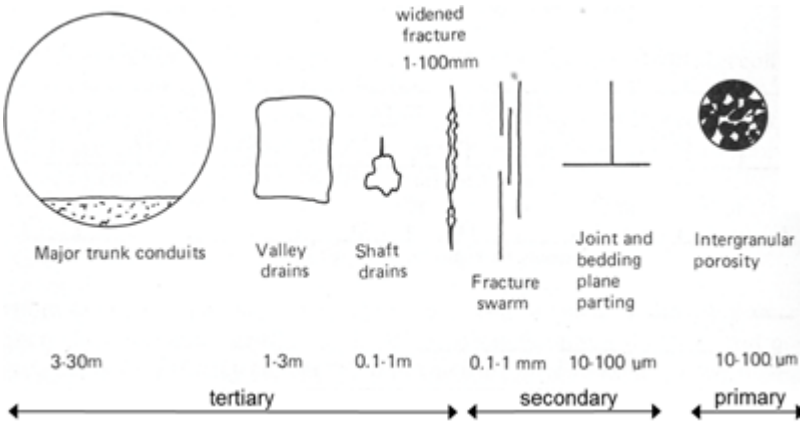

Figure 2.4: Types pf porosities in carbonate aquifers with geometrical dimensions, modified after White (1988).

Referring to the abovementioned characteristics, a karst aquifer may be defined according to Huntoon (1995) as “an aquifer containing soluble rocks with a permeability structure dominated by interconnected conduits dissolved from the host rock which are organized to facilitate the circulation of fluid on the downgradient direction wherein the permeability structure evolved as a consequence of dissolution by fluid”. Furthermore, to refer to the introduction of this section, a karst aquifer differs from a karst landscape by being saturated whereas a karst landscape may be unsaturated. A conceptual model of a karst aquifer is illustrated in Figure 2.5.

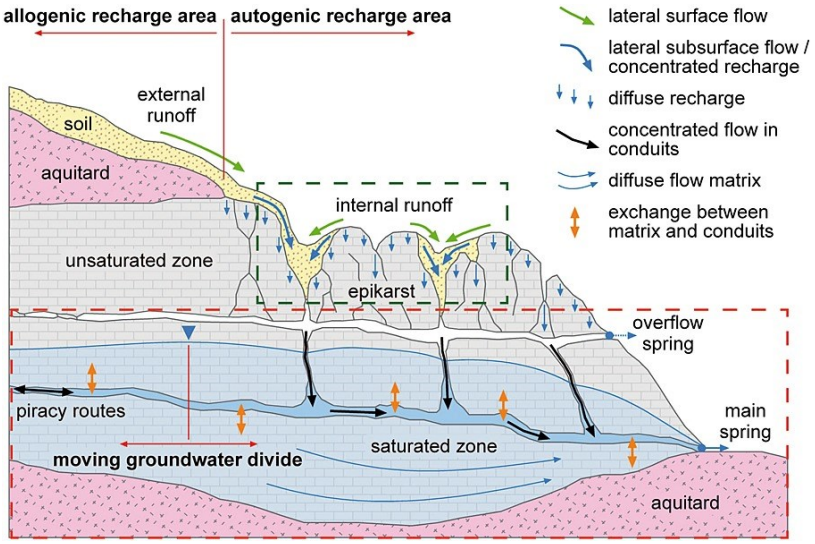

Figure 2.5: Conceptual model of a karst system including diffuse recharge and concentrated recharge into the conduits (Hartmann, et al., 2014a).

2.2. Hydrogeology of karst systems

2.2.1. Groundwater

Freeze and Cherry (1979) refer to groundwater as subsurface water that occurs beneath the water table in soils and geologic formations that are fully saturated. This definition relates groundwater to the saturated, i.e. phreatic, zone, and it further implies the existence of a water table, whose existence has been subject to controversial discussion in the context of karst aquifers. White (1988) argued that the nature of a water table in karst needs to be considered. This nature is dynamic, and therefore, in certain areas, the water table may just be very irregular, yet present. However, a water table refers to an unconfined aquifer in which water freely moves under gravity forming the piezometric surface (Ford and Williams, 2007). There, the pressure head at the water table equals the atmospheric pressure. In turn, within confined systems, the pressure head may exceed the water table. The imaginary surface of interpolated pressure heads is called the ‘potentiometric surface’. Essentially, the potentiometric surface may differ from the piezometric surface (Siegel, 2008). To better understand the differences between water table and piezometric surface, Figure 2.6 illustrates the dynamics of a piezometric surface in relation to the different permeabilities (conduit and surrounding bedrock/matrix) in a karst aquifer. During periods of low flow (or baseflow, Figure 2.6a), a karst conduit receives inflow, and the potentiometric surface coincides locally with a quasi-water table within this conduit. The water table of the saturated zone may be on the same level as the water table within the conduit, but it also may be above or below the level in the conduit. During periods of flood, this conduit becomes saturated and pressurized and the head above the conduit rises beyond the water table within the conduit (see Figure 2.6b).

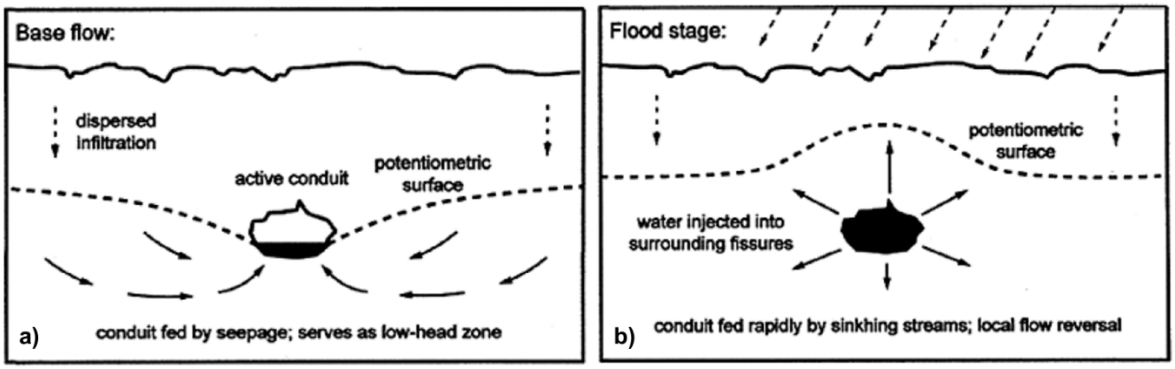

Figure 2.6: Change of the piezometric surface according to the change in the drainage regime between a) baseflow and b) flood conditions (Gunn, 2004).

Within the context of the Water Framework Directive (WFD) of the European Union (EU), groundwater is defined as “all water which is below the surface of the ground in the saturation zone and in direct contact with the ground or subsoil” (EPA, 2006). This definition does not consider the existence or concept of a water table. In fact, the majority of karstified limestone aquifers in Ireland are considered as ‘low lying’ cropping out <100 m above sea level (masl) (Drew, 2008). These areas are characterised by a very shallow unsaturated zone and seasonal groundwater flooding via turloughs (Naughton, et al., 2012). Turloughs are described as topographic depressions in karst which are intermittently flooded on an annual cycle via groundwater sources and have substrate and/or ecological communities characteristic of wetlands (EPA, 2004).
Turlough water levels constitute a visible potentiometric surface of the aquifer rather than a piezometric surface. Therefore, in the context of low lying topography and a shallow unsaturated zone, the notation of a potentiometric surface rather than a piezometric surface or water table is favourable working on the scale of an entire aquifer. Accordingly, the definition of groundwater by EPA (2006) is extended to account for the heterogeneities in karst, where ‘groundwater is all water below the surface in the ground in the saturated zone and in direct contact with the ground or subsoil forming a potentiometric surface over the aquifer unit’.

2.2.2. Groundwater recharge

Because of the heterogeneity of karst aquifers constituted by different permeabilities (White, 1988), karst groundwater recharge occurs on different scales. Groundwater recharge may be described as the “entry into the saturated zone of water made available at the water table surface, together with the associated flow away from the water table within the saturated zone” (Freeze and Cherry, 1979) or as “the downward flow of water reaching the water table, forming an addition to the groundwater reservoir” (Lerner, et al. (1990) in Fitzsimons and Misstear (2006)). Both definitions imply the existence of a water table surface which, as just discussed, may be inaccurate in this context. Therefore, it seems more plausible to describe recharge as the downward flow of water reaching the saturated zone.

Recharge to an aquifer can originate from the karst area itself (autogenic) or from adjacent non-karst areas (allogenic) (Goldscheider, et al., 2007). Further, two types of recharge can be distinguished, a) direct (vertical infiltration of precipitation where it falls on the ground) and b) indirect (infiltration following runoff) (Misstear and Brown, 2007).

The role of groundwater recharge on the evolution of caves and conduits is displayed in Figure 2.7, distinguishing between concentrated recharge (via depressions), diffuse and hypogenic with respect to different types of pre-solutional porosity. Of relevance for this study is concentrated recharge via swallow holes into bedding partings and fractures and diffuse recharge through sandstone into bedding partings and fractures. Even though none of the study sites in this research project receive allogenic recharge from sandstone at present (see 'Study Sites'), allogenic recharge may have been the case in the past explaining the current hierarchy of dissolution pathways.

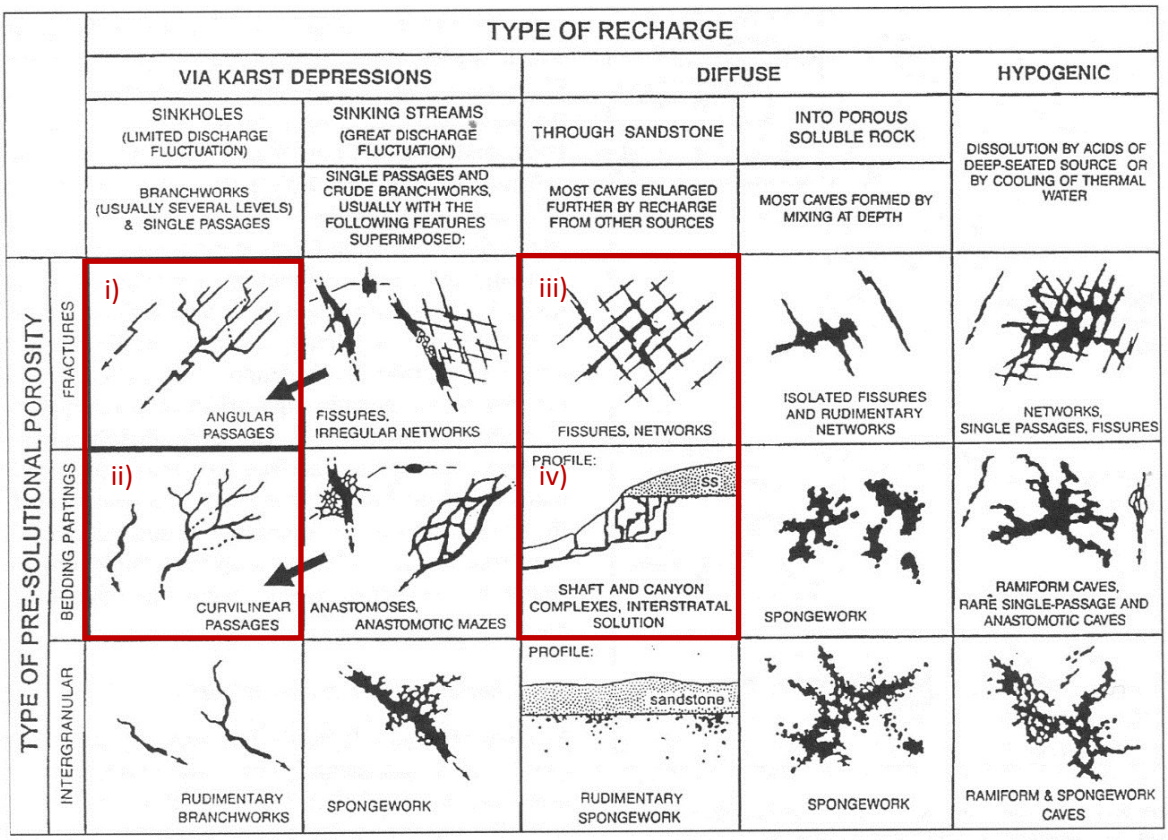

Figure 2.7: Relationship between geomorphology and groundwater recharge. Modified after Ford and Williams (2007).

Karst aquifers have been largely conceptualised as two component systems, distinguishing between concentrated flow and recharge vs. diffuse flow and recharge (Atkinson, 1977). Concentrated or direct recharge occurs usually very rapidly and highly localised into the conduit system. In turn, diffuse groundwater recharge occurs over an entire catchment area entering the low permeability fissured matrix blocks rather slowly (Geyer, et al., 2008b). In fact, diffuse groundwater

recharge follows the hierarchical network of flow paths enlarged by dissolution, as it is shown in Figure 2.7iv, eventually discharging into conduits and drained by springs. Depending on the evolution of the karst system, diffusely recharged groundwater will travel through different sized openings, from small fissures towards conduits. Accordingly, diffuse groundwater recharge will experience different flow dynamics, i.e. laminar through to fully turbulent flow. This conceptual understanding is illustrated as part of the overall functioning of a karst aquifer in Figure 2.5.

Additional complexity is associated with the epikarst and its role in the recharge process. The epikarst may form a perched and shallow - potentially saturated - unit from where water infiltration is concentrated or via diffuse flow paths, depending on the magnitude of recharge, saturation of the epikarst with relatively short residence times and piston-like functioning (Perrin, et al., 2003; Aquilina, et al., 2006). The first reference to epikarst in the Irish context was provided by Daly (1997). The presence of an epikarst layer that acts like a reservoir may be subject to debate at a site-specific level as epikarst is not ubiquitous. The epikarst simply may not have formed or it may have been scoured off by glacial processes eroding off the weathered zone. As a result, such weathered zone may be limited to 1 m depth, as exemplified in the Burren, western Ireland (Williams, 2008). Since much of Ireland was impacted by glacial erosion in the past, the vertical depth, and hence the role of the epikarst in recharge processes may be considered as limited.
Further complexity in recharge processes is added by considering the soil layer and its properties, including different flow routes, namely slow matrix flow (a) and rapid macropore flow (b, c) (Figure 2.8). Such different permeabilities are related to the conceptual dual porosity properties of soils, for example in the case of a clay-dominated glacial till (Tooth and Fairchild, 2003), which is very common in Ireland. Rapid flow occurs through cracks and macropores, also called bypass flow (or preferential flow paths). For example, bypass flow may occur in periods of soil moisture deficit (Rushton and Ward, 1979). In turn, micropores exhibit the large storage capacity, e.g. in till, providing constant delivery of matrix flow. Groundwater recharge originating from slow matrix flow is associated with the baseflow sustaining the low flow, and generally with a slow groundwater flow dynamic (Tooth and Fairchild, 2003).

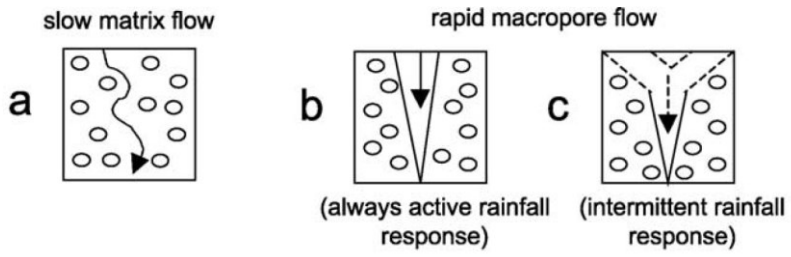

Figure 2.8: Different types of flow dynamics within a soil layer above a limestone aquifer. Modified after Tooth and Fairchild (2003).

The quantification of groundwater recharge is very difficult as it is not directly measurable. Indirect methods for quantifying recharge rely on chemical measurements (e.g. tracers) and/or physical measurements (e.g. water content, water table fluctuation) (Ireson and Butler, 2013). The use of water table fluctuations, however, is based on the premise of an existing water table, which may be the case in certain carbonates, such as chalk, but which is considered not necessarily to be the case in karstified limestone. Further, hydrochemical approaches or water budget estimations tend to require lots of site-specific parameters. While there are numerous studies on groundwater recharge, e.g. in the chalk of the UK, based on the premise of a groundwater table (Mathias, et al., 2006; Van den Daele, et al., 2007; Ireson, et al., 2009), the contrary is the case for limestone aquifers in Ireland or indeed other comparable shallow and low lying limestone aquifers more internationally on which this research could refer to.

However, importantly, groundwater recharge impacts on the shape and magnitude of groundwater discharge in time. This is perhaps the most fundamental premise for this research, as it allows recharge to be approached from the 'discharge perspective'. With the beginning of effective recharge during an event impacting on the phreatic zone, spring discharge increases – the spring hydrograph rises. At the time of maximum recharge an inflection point can be identified on the rising limb of the spring hydrograph (Figure 2.9i). Another inflection point occurs at the end of the recharge event on the falling limb (Figure 2.9ii). The falling limb can be sub-divided into different recession components, such as the flood recession and the baseflow recession (Kovács, et al., 2005; Geyer, et al., 2008b). Hence, analysis of the falling hydrograph, i.e. recession analysis, allows conclusions to be drawn with respect of the recharge event (Mangin, 1975). This understanding allows conclusions to be drawn on groundwater recharge dynamics from the analysis of spring hydrographs, which again forms the underlying principle of this study.

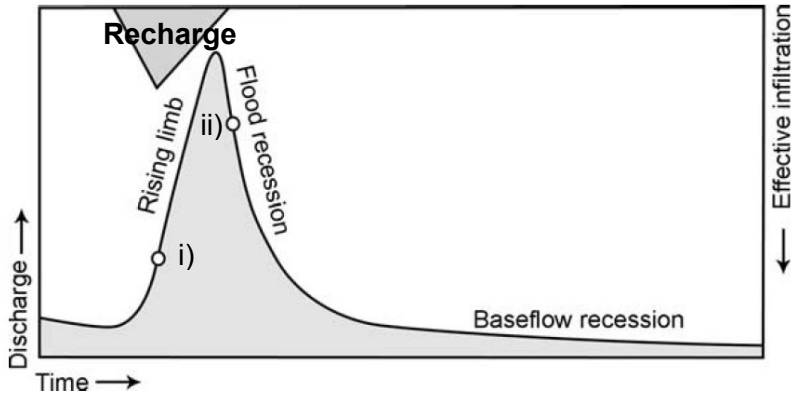

Figure 2.9: Typical spring hydrograph as response to recharge with inflection points for the time of maximum recharge (i) and for the end of the recharge event (ii). Modified after Kovács, et al. (2005).

The relevance of the epikarst influencing recharge volumes of the low permeability domain and consequently impacting the baseflow of spring hydrographs of a heterogeneous aquifer was numerically justified by Kiraly, et al. (1995). In fact, the epikarst may be conceptualised as a storage reservoir that drains as a baseflow component, or as a quick-flow component. The characteristic of the drainage may depend on the saturation of the epikarst with relatively short residence times and piston-like functioning (Perrin, et al., 2003; Aquilina, et al., 2006). Accordingly, the epikarst may be interpreted as a perched aquifer, and where present, its drainage may influence the spring hydrograph and its chemograph.

2.2.3. Groundwater flow

Groundwater flow is a physical process along a gradient where the potential may be defined as a "physical quantity, capable of measurement at every point in a flow system, whose properties are such that flow always occurs from regions in which the quantity has higher values to those in which it has lower, regardless of the direction in space" (Hubbert, 1940). Different potential gradients impact on the motion of groundwater, such as a temperature gradient, electrical gradient, chemical gradient and a hydraulic head gradient. The consideration of multiple potentials in the quantification of groundwater flow is called 'coupled flow'. However, within the saturated zone of an aquifer, groundwater flow may be fully described by hydraulic head (elevation + pressure components) and hydraulic conductivity (Freeze and Cherry, 1979).
Accordingly, in a porous, isotropic and homogeneous medium, groundwater flow in the saturated zone can be approximated by linearity and Darcy's law (Darcy, 1856) where,

$$u = -K\frac{dh}{dl} = \frac{Q}{A} \qquad \text{Eqn. 2.3}$$

with the specific discharge u, the hydraulic conductivity K, the hydraulic gradient dh/dl, discharge Q and the cross-sectional area of the granular medium A. Darcy's law (or rather, empirical study) describes a linear relationship between u and dh/dl and laminar flow, in which conceptually water molecules move in parallel to the direction of flow. There is an upper and lower limit for the validity of this linear relationship, of which the upper limit is of relevance in karst hydrogeology. At high flow rates, Darcy's law is not valid anymore. A threshold that distinguishes between laminar flow and the application of Darcy's law and non-laminar or turbulent flow at higher velocities is given by the dimensionless Reynolds number R_e. In fact, R_e describes the state of flow given as,

$$R_e = \frac{\rho u d}{\mu} \qquad \text{Eqn. 2.4}$$

with the fluid density ρ, the fluid velocity u, the viscosity μ and d, which is the length dimension of the porous medium or pore dimension or mean grain diameter or some function of the square root

of the permeability k. The transition between laminar and turbulent flow is expressed by the critical Reynolds number N_{Re} that depends on the hydraulic properties of the fluid and the pore space. For porous media, the generally accepted range of laminar flow applies to R_e in the range between 1 to 10 (Zeng and Grigg, 2006) (Figure 2.10). Above N_{Re}, flow is fully turbulent in porous media (Freeze and Cherry, 1979; Giese, et al., 2018).

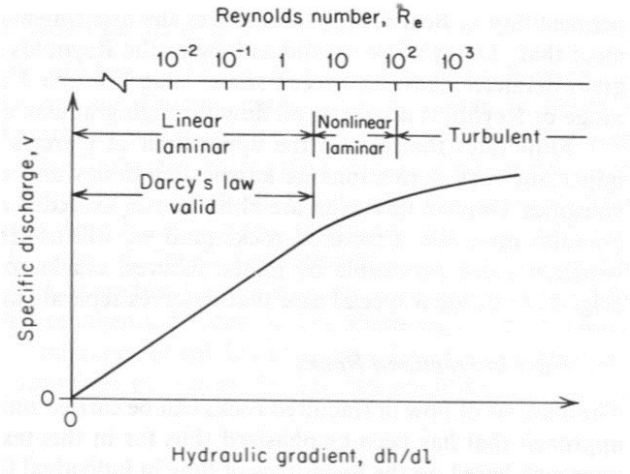

Figure 2.10: Range of validity of Darcy's law (Freeze and Cherry, 1979).

However, karst aquifers cannot be approached by the assumption or simplification of acting like a 'porous, isotropic and homogeneous medium'. Instead, karst is a medium of preferential flow paths, including conduits, which are similar to pipes. In pipes, laminar flow usually applies to R_e <2,000 (Mays, 2011) while turbulent flow is considered to start at N_{Re} of 500 to 2,000, where N_{Re} being site-specific with regard to each karst system or sub-system (Giese, et al., 2018). The change of flow regimes is transitional.

Laminar flow through pipes, which may be realistic representations of conduits, may be approached by Poiseuille's law or with the Hagen-Poiseuille equation as,

$$Q = \frac{\pi d^4 \rho g}{128 \mu} \times \frac{dh}{dl} \qquad \text{Eqn. 2.5}$$

with the gravitational acceleration g, and the fluid density ρ and viscosity μ (Ford and Williams, 2007).

Turbulent flow through pipes may be approached by the Darcy-Weisbach equation where,

$$Q = \left(\frac{2dga^2}{f}\right)^{1/2} \times \left(\frac{dh}{dl}\right)^{1/2} \quad \text{Eqn. 2.6}$$

with the friction factor f (Ford and Williams, 2007) defined according to the Darcy-Weisbach friction law,

$$\tau = \frac{f\rho_f}{8} \times v^2 \quad \text{Eqn. 2.7}$$

with the shear stress τ, the density of fresh water ρ_f and the mean velocity through a pipe v. Another way to estimate the friction factor f is to apply the Colebrook-White equation (Colebrook and White, 1937). Different forms of the Colebrook-White equation exist, e.g.

$$\frac{1}{\sqrt{f}} = -2\ \log_{10}\frac{\varepsilon}{3.71D} + \frac{2.51}{R_e\sqrt{f}} \quad \text{Eqn. 2.8}$$

with the absolute roughness coefficient ε and the inner pipe diameter or hydraulic radius D (Rollmann and Spindler, 2015). Hence, the Colebrook-White equation relates the friction factor, the Reynolds number, pipe roughness and the inside pipe diameter. In karst conduits, f may range between 0.1 and 340 (Jeannin, 2001).

While the abovementioned flow types through porous medium and fractures/fissures and pipes may be valid for saturated conditions and specific geometries, there often is also unsaturated open-channel flow occurring in karst aquifers. Conduits that drain fractures, fissures and the matrix may be not fully saturated in periods of recessions following recharge events (Figure 2.6). Shallow water flow as occurring in under-pressurized conduits influenced by the atmosphere is generally approached by using the Saint-Venant equations of conservation of mass and momentum unsteady open channel flow (Gill, et al., 2013a),

$$\frac{\delta A}{\delta t} + \frac{\delta Q}{\delta x} = 0 \quad \text{Eqn. 2.9}$$

$$\frac{\delta Q}{\delta t} + \frac{\delta}{\delta x}\left(\frac{Q^2}{A}\right) + gA\left(\cos\theta\frac{\delta y}{\delta x} - S_0 + \frac{Q|Q|}{K^2}\right) = 0 \quad \text{Eqn. 2.10}$$

with the discharge Q [m^3/s], the cross-sectional area A [m^2], the acceleration due to gravity g [m/s^2], the angle of bed to horizontal (°) θ, the bed slope S_0 and the conveyance K. The conveyance may then be based on the Colebrook-White expression.

The type of groundwater flow occurring depends on the geometries of openings, which is related to the type of porosity and aquifer characteristics, ranging between laminar flow and turbulent flow. Table 2.2 gives an overview of types of groundwater flow grouped according to the porosity. Laminar flow is commonly called diffuse groundwater flow, which is assigned to the low-permeability domain of primary and secondary porosity (fissures/fractures created by tectonics). Accordingly, in the context of this study, diffuse groundwater flow is related to laminar flow and a specific geometry or size of the opening within the aquifer in which such flow occurs. In turn, turbulent and concentrated flow is assigned to the high-permeability domain of strictly tertiary porosity (dissolutionally enlarged).

Table 2.2: Aquifer properties for different porosities. Modified after White (1988).

Attribute	**Porosity**		
	Primary	**Fissure/fracture**	**Conduit**
Physical situation	Intergranular pores, isolated joints and bedding plane partings	Concentrations of joints and fractures, bedding plane partings	Open channels and conduits of various sizes and shapes
Homogeneity	Usually isotropic	Usually anisotropic (may be statistically isotropic over larger volumes)	Usually highly anisotropic
Flow regime	Diffuse and laminar, Darcy flow	Diffuse and laminar, may deviate from Darcy flow	Concentrated and turbulent, non-Darcy flow
Water table	Well-defined water table surface	Irregular surface	May be above or below adjacent water table
Response to short-term events	Slow	Moderate	Rapid

Depending on the evolutional state of a karst aquifer, the system may be composed of different proportions of porosities with a higher proportion of low-permeability domain for immature aquifers and a higher proportion of dissolutionally enlarged fissures/fractures and conduits for mature aquifers. The proportions of such geometrical openings (Figure 2.11a) impacts on the overall proportions of flow regimes (Figure 2.11b) and therefore on the overall hydraulic response of the aquifer to a recharge event.

Groundwater flow components grouped according to porosities (Table 2.2) show distinct flow and discharge dynamics. Their contribution of flow and discharge can be conceptually approached by the drainage of individual reservoirs that may be associated with different physical dimensions (Figure 2.12).

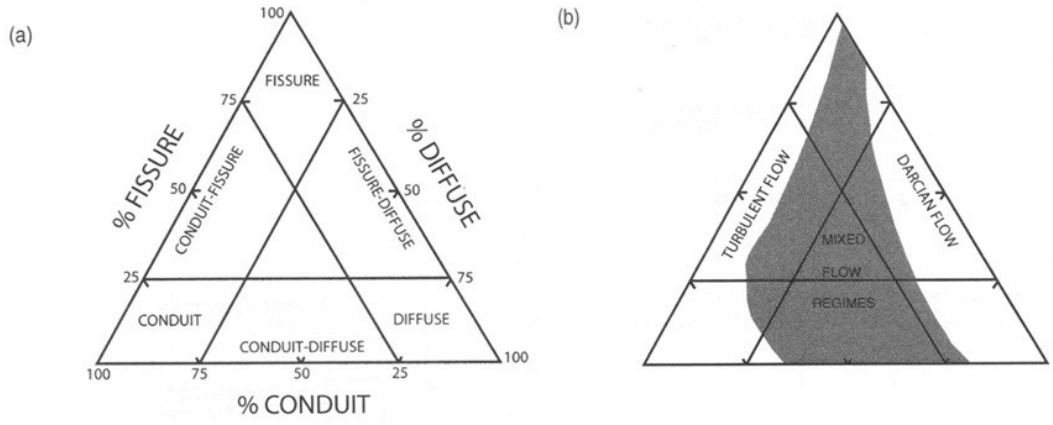

Figure 2.11: Classification of karst aquifers (a) and related groundwater flow regimes (b) (Ford and Williams, 2007).

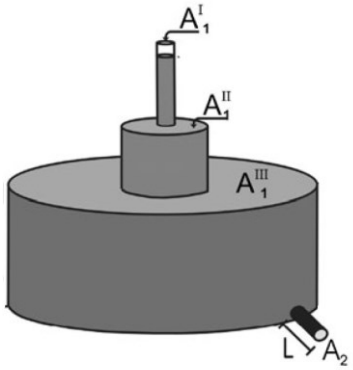

Figure 2.12: Discharge of different domains (A'_1, A''_1, A'''_1). Modified after Fiorillo (2011).

2.2.4. Groundwater discharge

Groundwater discharge may be defined as the "removal of water from the saturated zone across the water table surface together with associated flow toward the water table within the saturated zone" (Freeze and Cherry, 1979). Once more, the definition implies the existence of a water table, which may not be the case in karstified limestones. Irrespective of the existence of a water table, groundwater discharge is considered as the drainage or removal of water from the saturated zone and potentially epikarst at outlets called springs, which are subject to topographic and/or structural control (Ford and Williams, 2007). Ford and Williams (2007) classify springs according to 1. freely draining, 2. dammed, and 3. confined (see Figure 2.13). Freely draining discharge often occurs in shallow karst, which may be entirely or predominantly saturated. Dammed discharge is the most common type and the result of barriers in the underground, e.g. lithology, faults, glacio-fluvial deposits, or sea water that is denser than the discharged groundwater. The latter one is relevant for the functioning of intertidal groundwater discharge and submarine groundwater discharge (SGD) (see section '2.2.6. Submarine and intertidal groundwater discharge (SiGD)').

Confined springs are impacted by impervious formations and/or fault planes, which may lead to artesian conditions where groundwater is under positive pressure high enough that the piezometric potential reaches the ground surface.
Groundwater discharge is linked to recharge and flow processes. Hence, the analysis of spring discharge, and in particular its recession, highlights information on recharge and flow. For example, a rapid recession of a spring hydrograph indicates limited storage of the aquifer (Friederich and Smart, 1982).

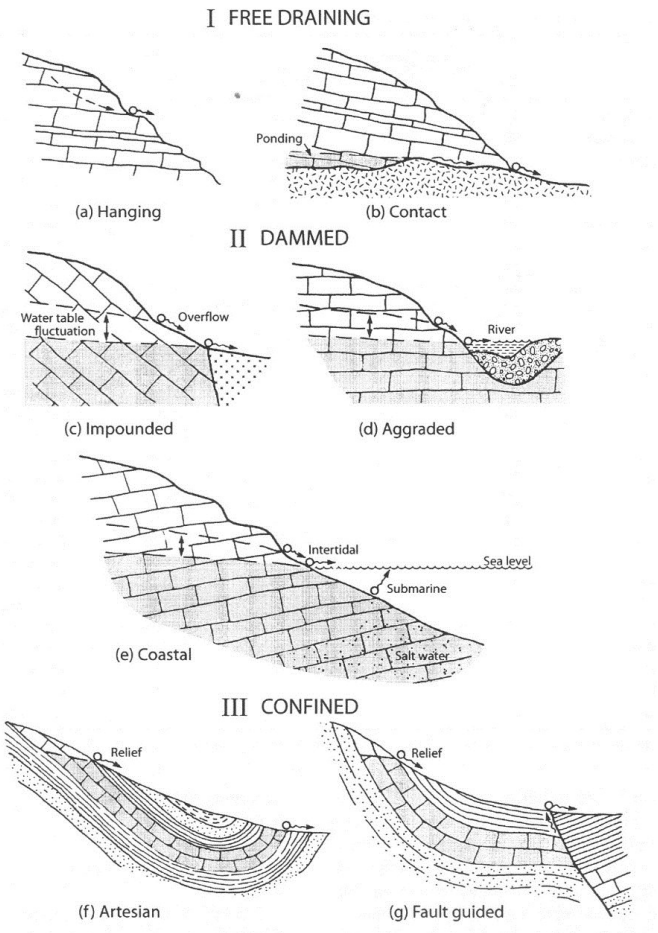

Figure 2.13: Type of karst springs (Ford and Williams, 2007).

2.2.5. Baseflow

The number of terminologies used by hydrologists or engineers applied to baseflow indicates the variety of different interests associated with it, using expressions such as ‘ground-water flow‘, ‘low flow‘, ‘percolation flow‘, ‘under-run‘, ‘seepage flow‘ or ‘sustained flow‘, all of them relating to stream hydrology (Hall, 1968). In fact baseflow may be referred to as the contribution to a stream system from water in the ground above or below groundwater level (Barnes, 1939), being the result of a slow response to long-term changes in the regional groundwater flow system (Freeze and Cherry,

1979) and characterised by a low-frequency phenomenon (Spongberg, 2000). An important aspect is the notation of a long-term change, hence originating from delayed sources (Hall, 1968).
Baseflow is one element that contributes to the shape of a stream hydrograph. Faster responding contributions were referred to as ‘surface flow’ (Barnes, 1939), ‘overland flow‘ and ‘sub-surface storm flow’ (Freeze and Cherry, 1979), ‘interflow’ and ‘direct runoff’ (Hall, 1968), or ‘overland flow’ and ‘interflow’ (Hiscock, 2014), for example. Accordingly, a stream hydrograph can be sub-divided into a baseflow component and other superimposed components. The contribution of baseflow to a stream ranges between a maximum (fully saturated basin) and a minimum (lowest recorded water-table configuration) (Freeze and Cherry, 1979).
The shape of a baseflow hydrograph may exhibit sharp rises, but there is always a very conspicuous time-lag between the storm input and the baseflow response (Barnes, 1939), with the general agreement that the shape of the recession follows an exponential decline (Maillet, 1905), valid for periods of no recharge (Hiscock, 2014). However, the baseflow component may also be approximated by the combination of linear or linear and non-linear curves (Hall, 1968).
The concept of a delayed, low-flow groundwater-fed baseflow component of the total stream hydrograph applies similarly to karst spring hydrographs, which are sustained by discharge of diffuse (slow) flow into the conduits (White, 1988). In fact, Forkasiewicz and Paloc (1967) were the first authors that decomposed a karst spring hydrograph into three different superimposed components, each representing a different conceptual flow draining the aquifer. During the recession of a karst spring, once the level of ‘pure baseflow’ is reached, the discharge can be linked to the drainage of the phreatic zone without any recharge or influence of rainfall occurring (Mangin, 1975). In drawing explicit parallels to surface hydrology, Atkinson (1977) interpreted the baseflow component of karst springs as the contribution from the narrow fissures, as opposed to the quick-flow assigned to the conduit domain. Since then, in the context of karst spring hydrography, the baseflow component has been interpreted as contribution from the low-permeability domain (Geyer, et al., 2008a), which justifies recession analysis in the context of coupled karst groundwater recharge, flow and discharge studies.
In this study, the baseflow component is referred to as the delayed response and low-flow component stored in the fissure openings a karst aquifer. During baseflow conditions, such low-flow component is drained into domains of larger permeability within the aquifer, e.g. into a conduit as illustrated in Figure 2.6.
In this study the term ‘baseflow’ is replaced by the term ‘low-flow’ to avoid confusion with surface water hydrology. Depending on the level of karstification of the aquifer, this low flow component (LFC) resembles the drainage of a part or of the entire low-permeability fissured matrix domain, which can be approximated by an exponential component following Maillet (1905). A recession that can be represented by three exponential components indicates symmetric block shape (Kovács and Perrochet, 2008) where the lowest component (LFC) is the most damped one.

2.2.6. Submarine and intertidal groundwater discharge (SiGD)

Groundwater discharge from coastal aquifers is grouped as intertidal discharge and/or SGD (Figure 2.13), where the combination of flows is summarised as submarine and intertidal groundwater discharge (SiGD).

Taniguchi, et al. (2002) pointed out the ambiguity of 'older' SGD definitions in which the consideration of re-circulated seawater wasn't always clearly considered. For that reason, the same authors defined SGD as the sum of submarine fresh groundwater discharge and recirculated saline groundwater discharge, or, alternatively simply as the "mass transfer of groundwater across the sea floor" (Zekt͡ser, et al., 2007).

In Ireland, SGD has been known from ancient times, mainly associated with karstic limestones (Zekt͡ser, et al., 2007). Important submarine and intertidal springs are known to drain the Gort Lowlands at Kinvara, or the northern and western part of the Burren Plateau. Further, the bay of Bell Harbour receives discharges from submarine and intertidal springs; the intertidal springs commonly emerge from enlarged joints, successively higher outlets becoming operative with higher flows (Drew, 1990). While many locations of intertidal springs are known, the discharge locations of purely SGD off the shore are more difficult to locate. SGD is presumably linked to lower sea levels during the Pleistocene (Drew, 1990). For example, the link between present SGD and formerly lower sea level during which the today's SGD locations formed the principal outlet of an aquifer are well documented for the Mediterranean region where stacked karstic drainage networks have developed resulting from changes in the sea level that have occurred since the end of the Miocene (Fleury, et al., 2007a).

The quantification of SiGD is difficult because their outlet cannot be physically captured / monitored as in the case of onshore springs. Therefore, for measuring or estimating SiGD of coastal aquifers, alternative (i.e. indirect methods) must be applied, such as:

a) measuring the seepage flow rate using seepage meters (Carr and Winter, 1980; Corbett, et al., 2003) or multi-level onshore piezometers (Freeze and Cherry, 1979; Taniguchi and Fukuo, 1996);
b) applying mass-balance approaches using natural geochemical tracers such as electrical conductivity (EC), short-lived radium isotopes, i.e. ^{222}Ra, ^{223}Ra, ^{224}Ra, ^{226}Ra, or oxygen-18 (δ18O) and deuterium (δ2H) (Moore, 2006; Peterson, et al., 2008; Santos, et al., 2008; Cave and Henry, 2011; Lee, et al., 2012; Null, et al., 2014; Knee, et al., 2016);
c) applying water balance approaches based on upon the contributing catchment (Sekulic and Vertacnik, 1996; Smith and Nield, 2003);
d) using hydrograph separation techniques to quantify the groundwater contribution of surface water streams and extrapolating this contribution to the coastal shore (Zekt͡ser, et al., 2007);

e) using numerical modelling (Thompson, et al., 2007; McCormack, et al., 2014; Taniguchi, et al., 2015); or
f) applying thermal imaging from remote sensing (Johnson, et al., 2008; Wilson and Rocha, 2012; Tamborski, et al., 2015).

While methods a) to e) can be considered as quantitative, method f) will only yield a purely qualitative result.

The abovementioned methods, however, all have limitations. Manual seepage meters in coastal environments are very labour intensive while the use of piezometric data (from multi-level nests), requires estimates of the aquifer hydraulic conductivity to calculate the groundwater discharge. The latter method implies practically a homogeneous lithological medium and Darcian flow – which is not the case in the context of karst, as discussed previously.
Distributed numerical modelling requires data on the spatial and temporal variation of boundary conditions, which is very difficult to obtain in reality (Taniguchi, et al., 2003).
Furthermore, most groundwater flow models are based on the assumption of constant fluid density, which may not be the case in coastal environments where the interface between fresh and saline groundwater is highly dispersed. In most coastal aquifers, this is, however, not the case (Zektser, et al., 2007).
The extraction of the baseflow component of streamflow hydrographs can only be applied to catchments that are drained by surface water and therefore generally not particularly suitable for karst catchments.
The use of remote sensing data seems to be limited to a qualitative SGD estimation, rather than a quantitative one, by estimating the temperature variations (Taniguchi, et al., 2003) or the salinity (Elachi and Van Zyl, 2006) on the sea water surface.

In Ireland, several studies have assessed the dynamics of local intertidal and submarine springs. Cave and Henry (2009) used a tidal prism model to estimate the SGD in Kinvara Bay. Between November 2006 and June 2007, the average discharge was estimated at 22 m^3/s, with maximum records reaching 200 m^3/s. Following this work, Cave and Henry (2011) quantified SiGD for the southern Galway Bay in order to estimate the nutrients output. The authors applied the water balance method, coupled with an approach similar as the tidal prism model to estimate the SiGD during an ebb tide, achieving similar results as Cave and Henry (2009) for Kinvara Bay. In turn, significantly lower SiGD estimates for Kinvara Bay were derived by McCormack, et al. (2014). The authors coupled a pipe network model (Gill, et al., 2013a) with salinity records from three different locations in the bay. Groundwater discharge was then calculated by modelling the dynamic behaviour of a freshwater wedge in the bay. The total mean discharge from both Kinvara springs was determined to range between 11.9 and 12.3 m^3/s.

Using the same approach of Cave and Henry (2009), Perriquet, et al. (2012) and Perriquet (2014) calculated a water balance for the catchment of Bell Harbour by estimating an upper limit (Eqn. 2.11) and lower limit (Eqn. 2.12) of SiGD by,

$$Q = 1 - (S_{HW} - S_{LW})/33.5 \times (H_{HW} - H_{LW}) \times \text{surface area} \quad \text{Eqn. 2.11}$$

$$Q = 1 - (S_{HW} - S_{LW})/\text{max. salinity flood tide} \times (H_{HW} - H_{LW}) \times \text{surface area} \quad \text{Eqn. 2.12}$$

with the average of salinity $S_{HW} - S_{LW}$ and the difference of height between high tide and low tide $H_{HW} - H_{LW}$. The authors used electrical conductivity (EC) records collected from one sampler located in the middle of the bay at 1 m below sea level (mbsl). For the periods 02 Dec 2011 to 24 Jun 2011, 28 Mar 2012 to 07 Dec 2012 and 23 Dec 2012 to 28 Aug 2013, Perriquet (2014) estimated a mean SiGD of 4.9, 4.45 and 4.05 m^3/s, respectively.

2.2.7. Quantifying groundwater flow dynamics in a well or borehole

Boreholes or wells can be used to infer local information on groundwater flow dynamics.
Different methods have been applied to study groundwater flow velocities within boreholes including high sensitivity impeller flow meters, electromagnetic flow meters and heat-pulse flow meters (Molz, et al., 1989; Molz, et al., 1994; Paillet, 2004; Busse, et al., 2016). However, deployment of the previously mentioned technologies depends on different conditions. For example, as summarised by Stowell (2013), all the above methods, with the exception of the heat-pulse flow meter, can be applied to cases where the vertical flow velocity exceeds 4 m/min. Another way of evaluating groundwater flow velocities in boreholes is done using distributed temperature sensing using optical fibre cables (Read, et al., 2014). A more simple approach in assessing groundwater flow directions and zones of inflow and outflow is by the use of single borehole dilution tests (SBDT) (Maurice, 2009).
Further, due to the physical size of the instrumentation, certain minimum radii for boreholes must be available in order to fit the instruments into. To overcome this obstacle, SBDT is a suitable low-cost method that can be applied on narrow-diameter boreholes. Essentially, the equipment needed for SBDT encompasses a probe measuring depth and conductivity and a hose to inject the tracer into the borehole (Maurice, et al., 2011). Because of the simplicity and affordability of the method, SBDT can easily be conducted in almost any open boreholes. In addition to flow direction and mean flow velocities during the test, SBDT have the advantage to yield information on flowing features, i.e. locations of inflow, outflow or cross-flow.

2.3. Numerical characterisation of groundwater dynamics

2.3.1. Time series analysis

Time series analysis in the context of karst hydrogeology aims to characterise and quantify the hydrological functioning of aquifers. Hydroclimatic time series analysis and associated modelling may be considered as stochastic processes. Accordingly, a hydrologic time series or signal can be split into (or artificially built up by) a) the independent random noise component, b) the stochastic dependence, c) the periodicity and d) the trend (Yevjevich, 1993). Dependence describes the persistence of the time series, while periodicity is related to astronomical cycles and a trend is related to a natural or artificial change that can be expressed by a linear or non-linear model (Machiwal and Jha, 2006). The differentiation of different components present within a time series is of major importance to this research, as they may be associated with different dynamics of water movement through the aquifer.

A karst aquifer is conceptualised to act as a filter that transforms the input signal (e.g. random rainfall) towards an outlet (spring). The way the signal is transformed can be associated with a time dimension, e.g. short, medium or long-term (Mathevet, et al., 2004). For example, Bailly-Comte, et al. (2011) distinguish between a long-term (>30 days (d)), medium term (<10 d) and short-term (<6 hours (h)) response. In general, the input-output approach using long-term series of rainfall, spring discharge, etc. yields valuable information on the aquifer, and is therefore a favourable approach given the complexity and heterogeneity of karst (Mathevet, et al., 2004).

A way to systematically assess the relationship between rainfall, infiltration into and storage within the aquifer on one side, and a karst spring recession on the other side, was established by Mangin (1975) and further extended by El-Hakim and Bakalowicz (2007). The method characterises karst aquifers using two parameters, a) the infiltration delay i (describing the infiltration conditions, i.e. slow vs. fast) and b) the regulating power k (describing the mean residence time of groundwater in the phreatic zone).

The method divides the recession into two parts, a) the upper part representing the effect of recharge on spring discharge impacted rainfall, and b) the 'pure' baseflow or low-flow which corresponds to the drainage of the phreatic zone not impacted by rainfall. Accordingly, the average daily spring discharge Q [m^3/s], namely its recession, is approached by the sum of two functions,

$$Q = \psi(\mathrm{t}) + \varphi(\mathrm{t}) \qquad \text{Eqn. 2.13}$$

with the infiltration function $\psi(\mathrm{t})$ and the baseflow recession $\varphi(\mathrm{t})$, the latter one following Maillet's law. The infiltration function is valid for the recession section between the start of the falling hydrograph and the beginning of pure baseflow, and it is approached by the homographic function,

$$\psi(\mathrm{t}) = q_0 \frac{(1-\eta t)}{(1+\varepsilon t)} \qquad \text{Eqn. 2.14}$$

with the initial infiltration flow rate q_0 [m³/s], the infiltration velocity η [d⁻¹] and the flow heterogeneity ε [d⁻¹].

The method estimates the dynamic storage in the phreatic zone V_d [m³] by integrating the baseflow function from the flood peak time t_0,

$$V_d = \mathrm{c}\frac{Q_{R0}}{a} \qquad \text{Eqn. 2.15}$$

with the baseflow discharge Q_{R0} [m³/s] at t_0, c = 86,400, and the recession coefficient a [d⁻¹]. The regulating power of the karst aquifer on spring discharge depends on $Max(V_d)$ and expressed through the regulating power k that is given by,

$$\mathrm{k} = \frac{Max(V_d)}{V_{trans}} \qquad \text{Eqn. 2.16}$$

with the mean annual volume flowing through the phreatic zone V_{trans} [m³]. $Max(V_d)$ represents the maximum volume of storage at the beginning of the recession period. It is an estimate of the storage extent, which is lower than the total volume stored in the saturated zone (Marsaud, 1997; El-Hakim and Bakalowicz, 2007). The infiltration delay i ranges between 0 and 1 where fast infiltration tends towards i = 0 and slow infiltration tends towards i = 1 given by,

$$\mathrm{i} = \frac{1-2\eta}{1+2\varepsilon} \qquad \text{Eqn. 2.17}$$

with the infiltration rate η and the heterogeneity of infiltration ε. The parameters k and i are then used to classify karst springs following five groups (Figure 2.14).

The delay of response and regulating power of an aquifer may also expressed in terms of a 'memory effect', where slow systems with a high regulating power show a larger memory effect compared with systems of rapid infiltration and low regulating power. Based on the principles of such memory effect, Mangin (1984) applied correlogram and variance spectral density on rainfall and spring discharge time series to characterise their storages and how they are filled and emptied, gaining insights into the karstification of the aquifers.

Correlation and spectral methods may involve univariate and cross-spectral analysis. Univariate analysis characterises the individual structure of the time series with the autocorrelation function (time domain) and the spectral density function (frequency domain), as well as the cross-correlation function (time domain) and cross-amplitude, phase, coherence and gain functions (frequency domain) (Padilla and Pulido-Bosch, 1995).

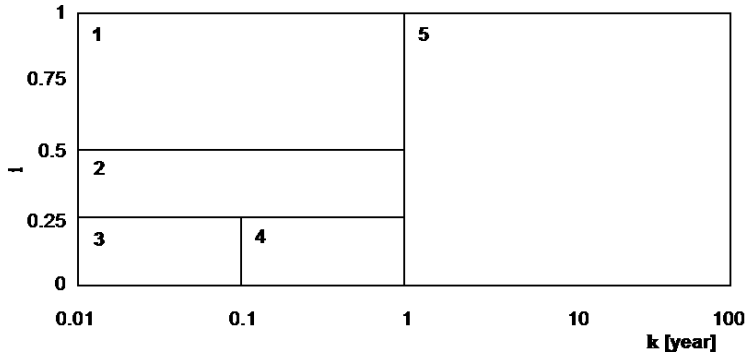

Figure 2.14: Classification of karst aquifers following Mangin (1975); El-Hakim and Bakalowicz (2007): 1.) complex karst systems largely extended and made up of several sub-systems; 2.) aquifers with a conduit system that is more developed in the upper parts in the catchment than close to the spring; 3.) intensively karstified systems with a well-developed conduit system directly connected to the spring; 4.) aquifers with a well karstified infiltration zone and extended conduit network ending into a flooded phreatic zone; and 5.) aquifers with a deep phreatic zone partly or totally confined under low permeable sediments with a complex drainage structure responsible for very long, multiannual or secular residence times.

2.3.2. Autocorrelation

Autocorrelation is a form of univariate analysis that characterises the individual structure of the time series in the time domain (Larocque, et al., 1998). Autocorrelation describes the time series' persistence, which is the tendency for the magnitude of an event to be dependent on the magnitude of the previous event. Accordingly, persistence is present if data in the time series are dependent on each other (Machiwal and Jha, 2006). The autocorrelation function (ACF) of a time series represents the linear dependence of an event on the remainder of the same time series: each time series is correlated to itself for increasing lag times in order to characterise the duration of the influence of an event on subsequent measurements (Massei, et al., 2006).
Persistence is also referred to as the memory effect of the system. Non-persistence is referred to as randomness defined as independence of the data in a time series, as opposed to persistence, which describes dependence of the data to each other (Machiwal and Jha, 2006). Detection of persistence using autocorrelation has been used extensively in hydrology by several researchers including Mangin (1984), Padilla and Pulido-Bosch (1995) and Jemcov and Petrič (2010), all referring to Box and Jenkins (1976), to identify two or three distinct memory effects. These memory effects were interpreted as different storage systems releasing different flow components (fast and slow) within the aquifer. For example, Jemcov and Petrič (2010) interpreted the change in slopes of the recessing of the autocorrelation coefficient (ACC) as an indication of the duality of a karst aquifer.

The ACF of a stochastic process is based on the premise of stationarity. Stationary time series can be described by its mean, variance and autocorrelation function, or equivalently by its mean,

variance and spectral density function. The stationarity assumption implies that the joint probability distribution $p(z_{t1}, z_{t2})$ is the same for all times t_1, t_2 being constant interval apart. Following on, the quality of this joint distribution can be inferred by plotting pairs of values (z_t, z_{t+k}) of the time series, separated by a constant $lag\ k$ (Box and Jenkins, 1976).
A finite time series with N observations has the autocorrelation r_k at the lag k,

$$r_k = \frac{c_k}{c_0} \qquad \text{Eqn. 2.18}$$

with the autocovariance function,

$$c_k = \frac{1}{N}\sum_{t=1}^{N-k}(z_t - \bar{z}) + (z_{t+k} - \bar{z}), k = 0, 1, 2, \ldots \qquad \text{Eqn. 2.19}$$

and the variance function,

$$c_0 = \frac{\sum_{t=1}^{N}(z_t - \bar{z})^2}{N} \qquad \text{Eqn. 2.20}$$

with the mean $\bar{z}$ of the time series.

Since the introduction of autocorrelation in karst hydrology, a value r_k = 0.2 has been widely used to distinguish a memory effect from white noise (Mangin, 1984). White noise describes random data because white light is composed of light with the same amplitude for all its frequencies (Beier and Hardy (1996). This distinction seems to be convenient, as it provides a value for comparison between studies. However, in fact, any value can be used, such as a significance level of 0.05 (Jemcov and Petrič, 2010).

Autocorrelation is a good measure of a system's memory effect revealing information on the extent as to which the aquifer acts as a filter measured by linearity of the time series. Accordingly, the pattern of the ACF may reveal important global characteristics of the draining aquifer (Figure 2.15, Table 2.3). For example, changes in the recession of the ACF were interpreted as distinct flow components (Panagopoulos and Lambrakis, 2006; Jemcov and Petrič, 2010).
While autocorrelation is a method frequently applied on characterising karst spring hydrographs, the method is stationary (invariant in time) and linear. Hence, both characteristics impose limitations on the analysis, since time series are time-variant and karstic systems are highly heterogenous and non-linear (Labat, et al., 2000a), which must be kept in mind.

An alternative way of using the autocorrelation function is as goodness-of-fit indicator comparing measured versus simulated time series (Labat, et al., 2000a).

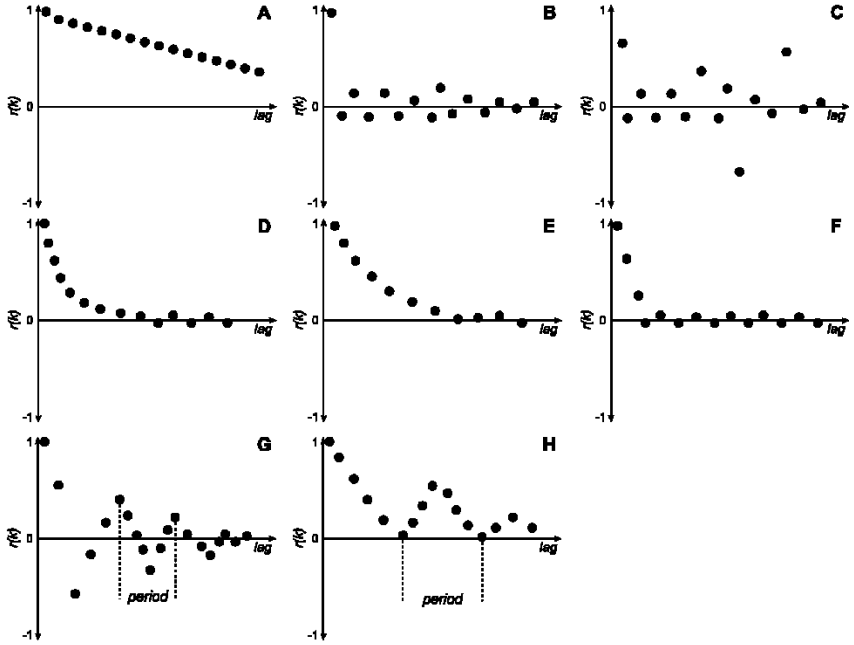

Figure 2.15: Different forms of autocorrelation plots. Modified after Fournillon (2012).

Table 2.3: Relationship between pattern and its meaning in correlograms (Fournillon, 2012).

Form	Meaning	Type (Figure 2.15)
r_k never reaches 0	Non-stationary series	A
Max. correlation at k = 0, else r_k = 0	White noise	B
r_k = 0 except few values	Series type 'moving average', no memory effect	C
Exponential decline until r_k = 0	Series type 'autoregressive', memory effect depends on speed of decline	D, E
First lags different to 0, else r_k = 0	Series type 'autoregressive' and then 'moving average'	F
Peaks of r_k in regular intervals	Series with a seasonal component	G, H
Alternations of positive and negative values towards r_k = 0	Series type 'autoregressive' with a seasonal component	G

2.3.3. Cross-correlation

In karst hydrogeology, cross-correlation has been used by several authors to characterise input-output relationships (Padilla and Pulido-Bosch, 1995; Angelini, 1997; Larocque, et al., 1998; Labat, et al., 2000a; Mathevet, et al., 2004; Massei, et al., 2006).

Cross-correlation measures the strength of the linear relationship between time series, not any causality per se. The method is based on the assumption that time series are regarded as bivariate

stochastic processes that are stationary (Box and Jenkins, 1976). The latter one means that the processes x_t and y_t have constant means μ_x and μ_y and constant variances σ_x^2 and σ_y^2.
For a discrete number of n pairs of values (x_1, y_1), (x_2, y_2), ... (x_n, y_n) it is shown that the cross-covariance $c_{xy}(k)$ at lag k is estimated by,

$$c_{xy}(k) = \begin{cases} \frac{1}{n}\sum_{t=1}^{n-k}(x_t - \bar{x})(y_{t+k} - \bar{y}), k = 0, 1, 2, \dots \\ \frac{1}{n}\sum_{t=1}^{n+k}(y_t - \bar{y})(x_{t-k} - \bar{x}), k = 0, -1, -2, \dots \end{cases} \quad \text{Eqn. 2.21}$$

where $\bar{x}, \bar{y}$ are the means of series x and y, respectively.
The cross-correlation $r_{xy}(k)$ at lag k is estimated by,

$$r_{xy}(k) = \frac{c_{xy}(k)}{s_x s_y}, k = 0, \pm 1, \pm 2, \pm \dots \quad \text{Eqn. 2.22}$$

with the standard deviation s_x and s_y of series x and y, respectively (Box and Jenkins, 1976). The cross-correlation may become negative, e.g. if an increase in x causes a decrease in y, or if other variables are involved in explaining y (Jukić and Denić-Jukić, 2015).
Cross-correlation can be used to establish impulse-response functions of systems without pre-whitening the signal, if it can be considered as white noise, i.e. no visible memory effect (Massei, et al., 2006).

Similar to the autocorrelation function, Labat, et al. (2000a) discussed the shortcomings of a linear time-invariant rainfall–runoff CCF in reconstructing the temporal structure of relatively infrequent flow events, such as local maxima (floods) and local minima (low-water periods). The authors argued that more realistic models for such hydrological basins will have to include non-linear and non-stationary aspects, given the heterogeneity (different degrees of karstification) and non-linearity of karst systems. Correlation analyses cannot fully take into account this temporal variability; hence, autocorrelation and cross-correlation shall be considered as one method to quantify average dynamics, ideally complemented by non-linear methods.

2.3.4. Spectral analysis

Spectral analysis evaluates a signal in terms of its spectrum of frequencies or related quantities such as energies. The frequency domain is useful for data manipulation or detecting average periodicities or dominant oscillations, for example. This could not necessarily be done using time domain data, as certain characteristics may be buried in noise (Chiaudani, et al., 2017). The decomposition

of an observed time-amplitude signal, such as spring discharge, into its frequencies (spectra), is done using the Fourier Transform.
Over the last decades, Fourier analysis has been much applied in karst hydrology, often in combination with cross-correlation and/or autocorrelation analysis to evaluate the time delay between rainfall events and the response of springs (Labat, et al., 2000a; Massei, et al., 2006; Bailly-Comte, et al., 2011), or to characterise the intrinsic structure of karst aquifers linked to frequency components of spring hydrographs and chemographs (Mathevet, et al., 2004; Massei, et al., 2007; Fournillon, 2012). These studies suggest that drainage of flow components associated with different karst aquifer heterogeneities correspond to distinctive frequencies.

Fourier analysis is spectrum analysis as it operates on the wave shapes of a given signal. The method was established by the French administrator, historian, and mathematician Jean Baptiste Joseph Fourier (1768 to 1830). It allows the transformation of physically realizable time-domain waveforms to the frequency domain, and vice versa, as very well documented in Ramirez (1985), for example. The idea goes back to the principle that any waveform is described by the time and amplitude relationship, which is conventionally plotted on x and y axes like a simple time series plot, as well as by the frequency and amplitude relationship, which is plotted on the z and y axes, and which may be less familiar. A waveform, such as the thick non-sinusoidal waveform on the upper part in Figure 2.16 is composed by different sinusoidal waves, here with the frequency F_0 and $2F_0$ plotted in thinner lines. Figure 2.16 combines a time-domain with a frequency-domain, where multiple time-plane projections (dotted lines) are summed up to the thick line. In fact, any observed time series is a combination of sinusoidal functions each one representing the multiple periodical nature of the phenomena (Chiaudani, et al., 2017).

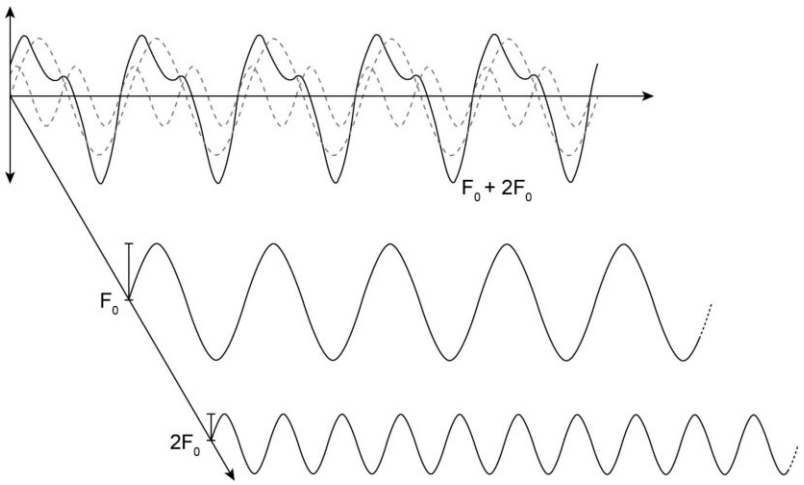

Figure 2.16: Composing a non-sinusoidal waveform by summing sinusoids. Modified after Ramirez (1985).

Given that certain conditions (Dirichlet conditions: for a real-valued, periodic function f is equal to the sum of its Fourier series at each point where f is continuous) hold true, a nonperiodic, i.e. indefinite, waveform $x(f)$ can be transformed from a function of time to a function of frequency using the Fourier transform,

$$X(f) = \int_{-\infty}^{\infty} x(t) e^{-j2\pi ft} dt \qquad \text{Eqn. 2.23}$$

where $X(f)$ is referred to as the Fourier transform of $x(t)$, with the continuous frequency variable f. In the same way, the frequency domain function $X(f)$ can be inverse transformed back to the time domain function x(t) using,

$$x(t) = \int_{-\infty}^{\infty} X(f) e^{j2\pi ft} df \qquad \text{Eqn. 2.24}$$

The transform is linear. Any component added in the time domain is a component added in the frequency domain. Thus, given the functions $x(t)$ and $y(t)$, and their transforms $X(f)$ and $Y(f)$, then $x(t) +$ y(t) transforms to $X(f) +$ Y(f).

The abovementioned integrals refer to indefinite time series, and so they cannot be applied on sampled definite time series. To overcome this problem, an approximation is used, the discrete Fourier Transform (DFT), which applies a window on the discrete values that are sampled over a finite interval, and which is commonly stated as,

$$X_d(k) = \sum_{n=0}^{N-1} x(n) e^{-j2\pi kn/N} \qquad \text{Eqn. 2.25}$$

and the inverse DFT as,

$$x(n) = \frac{1}{N} \sum_{k=0}^{N-1} X_d(k) e^{j2\pi kn/N} \qquad \text{Eqn. 2.26}$$

with the Fourier coefficient X_d, the number of samples N, the time sample index n with $n = 0, 1, 2, \dots, N-1$, the index for the computed set of discrete frequency components k with $k = 0, 1, 2, \dots, N-1$, and the symbol of complex notation indicating the imaginary part of a complex quantity j where $j = \sqrt{-1}$.

Summing up the Fourier coefficients X_d for all values of n at each k is a heavy computing task applying the DFT. To make this process feasible, an algorithm for computing the DFT was developed by Cooley and Tukey (1965), namely the Fast Fourier Transform (FFT), which yields exactly the same results as the DFT, just in a very short computing time.

The Fourier transform a correlation function yields a power spectrum, and the Fourier transform of an autocorrelation function is generally referred to as auto spectrum or power spectral density (PSD) (Ramirez, 1985).
Hence, the amplitude spectrum of the ACF (energy spectrum) describes in the frequency domain what the ACF describes in the time domain (Mangin, 1984; Massei, et al., 2006). This fact relates to the Wiener-Khinchin theorem, which again relates the Fourier Transform of the function $x(t)$ to the ACF, resulting in the PSD of $x(t)$. The PSD shows generally a power law decay if related to a stochastic signal.
A spectral density function $P(f)$ can be characterised by the spectral exponent β and the Fourier Transform f where,

$$P(f) \propto f^{-\beta} \qquad \text{Eqn. 2.27}$$

so that the spectral density P is given by,

$$P = C\ (1/f^{-\beta}) \qquad \text{Eqn. 2.28}$$

with the constant of proportionality C. In fact, Eqn. 2.28 can be written as $\log(P) = \log(C) - \beta \log(f)$, which shows that β can be approached by a linear regression in a spectral log-log plot as exemplified in Figure 2.17.

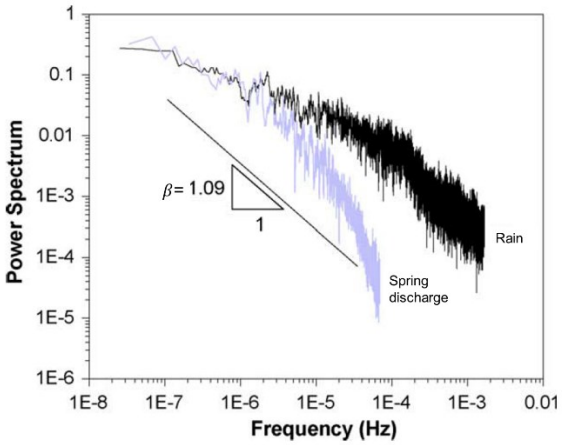

Figure 2.17: Power spectrum of rainfall and spring discharge and associated spectral coefficient. Modified after Majone, et al. (2004).

Further, β is related to the Hurst exponent H by $-\beta = 2H - 1$, $-\beta = -2H + 1$ respectively (Figure 2.18). H describes the persistence of a statistical phenomenon (Schroeder, 1991) and is related to the long-term memory of natural systems and their observed time series (as opposed to random series) as Herold Edwin Hurst (Hurst, 1951) defined in the framework of designing the Aswan High dam in Egypt. In fact, it was Mandelbrot and Wallis (1968) who introduced the nomenclature of the 'Hurst exponent'.

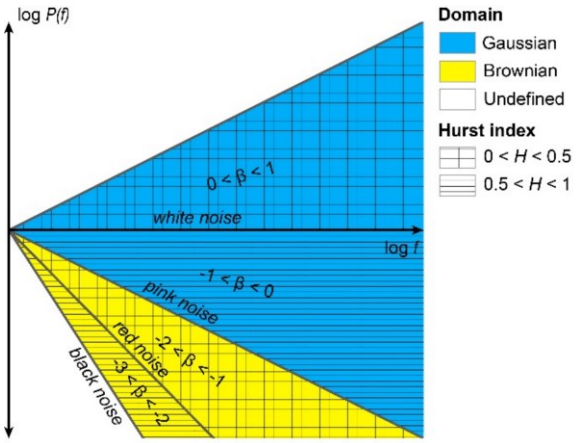

Figure 2.18: Slopes of spectral densities and associated spectral exponents β and Hurst exponents H for typical power law decays. Modified after Beier and Hardy (1996).

Mathevet, et al. (2004) and Fournillon (2012) were probably the first authors who analysed the spectra of karst spring hydrographs and chemographs using the spectral exponent β, and further associated β to the noise type classification of Beier and Hardy (1996) and referring to Schroeder (1991) who assigned a colour-code to the noise, i.e. squared magnitude of the Fourier Transform, related to ranges of β where (Beier and Hardy (1996) in Fournillon (2012); Schroeder (1991); Mathevet, et al. (2004)):

- -1 < β < 1 is noise in the Gaussian domain: both variables are stochastic and independent from each other, the noise contains no information; $-\beta = 2H - 1$:
  - β = 0 is white noise: the power spectrum is independent of frequency, no information in the spectrum, $H = -0.5$;
  - β = 1 is pink noise: also called $1/f$ noise, describing ubiquitous natural phenomena on a large scale in time and space, present in many time series.

The colour classification for the region of β < -1 is not consistent in the literature. The classification below is a synthesis of Fournillon (2012) and Mathevet, et al. (2004):

- -3 < β < -1 is noise in the Brownian domain, $-\beta = -2H + 1$:
  - -2 < β < -1 corresponds to anti-persistent Brownian noise with poor correlation between variables;

- β = -2 is red noise (or brown noise following Schroeder (1991)) where the data pairs are independent from each other but following a statistical law, Brownian motion;
- -3 < β < -2 corresponds to persistent Brownian noise with a memory effect and high correlation between variables;

- β < -3 is black noise: wide-spread occurring signal that is not stochastic and structured, and the signal may represent exceptional events and catastrophes like floods and droughts.

An important aspect is that the power spectra are homogeneous over the range of frequencies (Schroeder, 1991).

The analysis of different spectral exponents β may infer information on the underlying dynamics present in the frequency domain, namely if the frequency ranges associated with individual βs are stochastic or not, and if they may be linked to physically meaningful systematics. For example, pink and red noise may be associated with low frequencies related to seasonal or monthly patterns.

Fournillon (2012) identified between one and three β coefficients (β_1, β_2, β_3) for the water level spectra of his analysed springs by fitting a linear regression onto frequency ranges in a log-log plot. As important as his approach is, the interpretation of β_1 to β_3 remains somehow descriptive, without really linking the coefficients to the drainage regime of the aquifers. This important analysis was then provided by Duran (2015) who linked frequency patterns of simulation results of a KarstMod reservoir model to frequency patterns of observed time series.
The spectra could be sub-divided into distinct segments characterised by an individual spectral exponent β. There, the low frequency domain (β_1) was related to the fissured matrix domain (simulated by a 'matrix reservoir'), while a medium frequency domain (β_2) was related to the discharge of the epikarst (simulated by an 'epikarst reservoir'). Importantly, it was shown that the change of slopes coincides with a change in the discharge dynamics. Further, the work suggests that components of 'internal discharges' or flow components may be artificially re-produced by combining frequency components that were previously decomposed using the Fourier Transform.
One limitation of this approach is the identification of 'frequency ranges' onto which a linear regression is fitted on to yield the representative coefficient β – i.e. where should frequency ranges to be cut-off from neighbouring frequency ranges? Fournillon (2012) and Duran (2015) have subjectively sub-divided the log-log frequency plot into segments that can be characterised by a single slope. A more objective approach separating distinct frequency intervals was provided by Dufoyer, et al. (2018) who detects change points using the non-parametric Pettitt test. The resulting frequency intervals are called a) low, b) Intermediate and c) high frequency components resembling a) diffuse recharge and very slow flow through the matrix, b) all aquifer parts that can deform the input signal and c) highly transmissive zones that do not smooth the input signal. By doing so, the method is more objective. Interestingly, until present, no author has combined an objective approach

separating frequency components by e.g. using the Pettit test and change of slopes along with noise analysis.

2.3.5. Wavelet analysis

Wavelets offer a powerful method to overcome the limitation of Fourier transform related to the loss of time information in the frequency domain. Instead, wavelets provide information in both time and frequency domains.
An abundant amount of literature is available introducing the wavelet method, such as Percival and Walden (2000) or Walker (1999). The application of wavelets in karst hydrogeology dates back to Labat, et al. (2000b) who applied wavelet transform to interpret the temporal structures of the response of a karstic basin to rainfall, by separating the fast response (karstic network draining) and a slower response (diffuse infiltration) within the signal.

A wavelet is a mathematical object than can be used then to extract information from a signal using different methods: for example the continuous wavelet transform (CWT) providing a complete time-scale representation of localised and transient phenomena at different timescales, or the discrete wavelet transform (DWT) allowing to split the time series into timescale domains (Mathevet, et al., 2004). Essentially, a wavelet provides a localised analysis of a function in terms of changes in averages over various scales (Percival and Walden, 2000). The wavelet cuts up data into different frequency components to then study each component with a resolution matched to its scale providing a tool for time-frequency localisation (Daubechies, 1992). The DWT is able to separate different levels of frequencies of a signal in time allowing the signal to be re-built using all or different levels again.

The first wavelet originated from geophysical signal analysis and is known today as the Morlet or Gabor wavelet. Since then, wavelets were commonly used in the field of imagery and audio signals, such as audio or image denoising, signal compression, object detection in images, image enhancement, image recognition, speech recognition, or in the field of medicine such as diagnosing heart troubles.
The simplest type of wavelets in discrete form is the Haar wavelet, or if related to a mathematical operation, the Haar transform. Figure 2.19 shows a 10-level Haar multiresolution analysis (MRA) for a signal of $N = 2^{10}$ values and therefore 10 possible levels of MRA. The first signal (Figure 2.19a, top) shows A^{10} an average of all 2^{10} values of signal f repeated 2^{10} times. Below A^{9} is displayed, which equals A^{10} plus the details in D^{10}. By successively adding details, the full signal is constructed (Figure 2.19b, bottom).

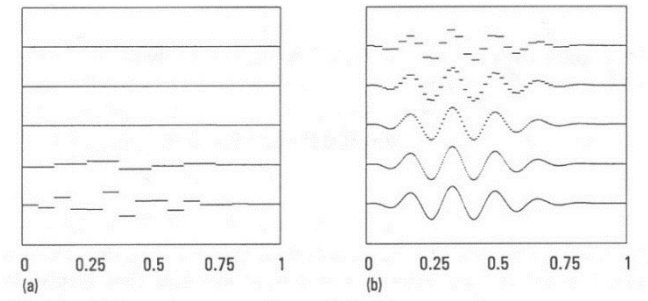

Figure 2.19: Haar MRA of the ten averaged signals A^{10} (top in a) to A^{1} (bottom in b) (Walker, 1999).

Of much relevance to hydrological applications are the Daubechies (db) wavelet transforms, which are similar to the Haar transform as described above, yet, they differ in the definition of a) the scaling signals and b) wavelets. The db4 wavelet provides a very good localisation in time. Complementary to Figure 2.19, Figure 2.20 shows the same signal, but as it can be seen, the db4 transformation converges more quickly towards the original signal, and also, the patchy appearance of the Haar transform does not appear in the db4, making the db4 superior to the Haar transform (Walker, 1999).

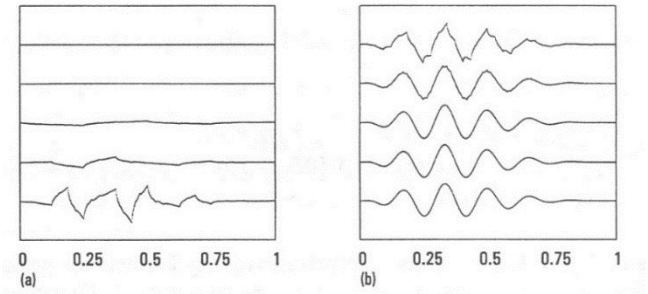

Figure 2.20: db4 MRA of the ten averaged signals A^{10} (top in a) to A^{1} (bottom in b) (Walker, 1999).

Any form of the discrete wavelet transform starts from the basic formula (Eqn. 2.29) (Daubechies, 1992),

$$T_{m,n}^{wav}(f) = a_0^{-m/2} \int dt\, f(t)\, \psi(a_0^{-m} t - n b_0) \qquad \text{Eqn. 2.29}$$

with the dilation and translation parameters a and b, assuming that $\int dt\ \psi(t) = 0$.

In turn, the basic formula of the continuous wavelet transform is given by Eqn. 2.30 (Daubechies, 1992),

$$(T^{wav} f)(a, b) = |a|^{1/2} \int dt\, f(t)\, \psi\left(\frac{t-b}{a}\right) \qquad \text{Eqn. 2.30}$$

assuming that $\int dt\ \psi(t) = 0$.

The CWT of different time series can be used to examine if they are linked to some extent. Given two signals X and Y with the wavelet transform $W_n^X(s)$ and $W_n^Y(s)$, a cross-wavelet spectrum $W_n^{XY}(s)$ can be calculated using $W_n^{XY}(s) = W_n^X(s)W_n^{Y^*}(s)$ where $W_n^{Y^*}$ is the complex conjugate of $W_n^Y(s)$. The cross-wavelet power is given as $|W_n^{XY}(s)|$. Confidence levels of a cross-wavelet power can be derived using the square root of the product of two chi-square distributions (Torrence and Compo, 1998). The cross-wavelet spectrum or cross wavelet transform (XWT) can be interpreted as the local relative phase between X and Y in time and frequency space illustrating common powers, yet, no cause-effect relationships. Cause-effect relationships can be assessed by evaluating the cross wavelet phase angle using the circular mean of a set of the angles and the confidence interval of the phase difference (Grinsted, et al., 2004). The difference in phase is then plotted in an angle between 0 and 360º into the XWT plot. Two sine waves are in phase, if their phase difference is 0º, and completely out of phase if their phase difference is 180º. For example, an opposing signal such as the El Niño – Southern Oscillation pattern shows a 180º out of phase pattern (Torrence and Webster, 1999). Regions of common high powers in the XWT plot, which further show a consistent phase relationship , i.e. 'phase locked', or that change progressively and smoothly suggest causality between the time series (Grinsted, et al., 2004). Phase arrows pointing to the right means the signals are 'in-phase', pointing to the left means 'anti-phase', pointing down means variable x leading variable y by 90º, and pointing up means variable y leading variable x by 90º.
While the XWT shows regions of common power, the wavelet coherence (WTC) is a measure of the localised correlation coefficient between the two time series in time-frequency space. WTC is defined as the square of the cross-spectrum normalised by the individual power spectra to range between 0 and 1 (Torrence and Compo, 1998). WTC indicates how coherent the XWT is in time frequency space, and it can be thought of as a localised correlation coefficient in time frequency space (Grinsted, et al., 2004).

Wavelets are relatively innovative in karst hydrogeology. Labat, et al. (2000b) was the first author who applied CWT and DWT for the analysis on karst aquifers identifying a fast and a slow-flow component in discharge. Amongst others, the authors applied the Daubechies (db) 4, db12, and db20. Since then, also Charlier, et al. (2015) and Massei, et al. (2006) combined the use of correlation and spectral analysis along with wavelet analysis. Both studies reveal the structure in the rainfall, which was recovered in the output signals, while this structure was not detected by correlation and spectral analyses. With more relevance to the decomposition of different components on karst hydrographs, Massei, et al. (2006) managed to separate fast-flow (high frequency, <3 d) and slow-flow (low frequency, >10 d) components using wavelet analysis, demonstrating the usefulness of applying the method on time series to reveal information of the different dynamics of discharges from a karst aquifer.

Gill, et al. (2013b) combined the use of CWT and DWT to characterise surface water-groundwater interactions in a low lying karst system.
XWT and WTC was applied in the context of rainfall-discharge analysis for the karst spring of Fuenmayor (Chinarro, et al., 2010). As to be expected, rainfall correlates well with discharge in time and frequency. Yet, a zone of very low coherence was interpreted as soil/epikarst storage, which mitigates the influence of the rainfall signal onto the discharge signal. This result is interesting, as it provides an example for the use of XWT/WTC in characterising the conceptual functioning of a karst aquifer.

2.4. Chemical characterisation of groundwater dynamics

Various natural (environmental) and artificial tracers can be used to derive information on the aquifer properties and flow and transport dynamics in the vadose and phreatic zone.

2.4.1. Environmental tracers

In relation to hydrology, environmental tracers can be defined as the "properties or constituents of water that have not been induced as a result of an intended experiment and which provide qualitative or quantitative information about the hydrological system" (Leibundgut, et al., 2009). Environmental tracers integrate over space and time, making them very useful for the understanding of dynamics in a system.
Environmental tracers have been applied to a) assign the origin of water and water constituents; b) investigate hydrological processes (different flow components in systems or water balances); c) determine quantitatively flow components (e.g. for the separation of hydrographs); and d) evaluate residence times (Leibundgut, et al., 2009).
Further, the use of environmental tracers along the application of artificial tracers can improve the results of tracer studies in hydrology.

The most common environmental tracers used are specific electrical conductivity (EC) and temperature due to their relatively easy measurement, but also major ions (Na^+, Mg^{2+}, Ca^{2+}, K^+, Cl^-, SO_4^{2-}, HCO_3^-), silicon dioxide (silica, SiO_2), and different stable (non-radioactive) and unstable (radioactive) isotopes are applied. Isotopic concentrations can be useful for the determination of ages of analysed waters. In turn, hydrochemical concentrations (ions, EC) are the result of interactions of water with organic and inorganic material during the recharge and flow processes in the vadose and phreatic zone, accordingly, these tracers provide rather information on the source areas rather than on the age (Uhlenbrook, et al., 2002).

2.4.1.1. Geochemical source tracers

As an example, Grasso and Jeannin (2002) presented a method to measure the diffuse flow component and to infer information about the structure of the karst system by simultaneous analysis of chemical and hydraulic response, establishing a functional relationship of chemical (concentration) and hydraulic (flow). The concentration of discharge is equal to the relationship between the dissolved limestone mass flux and the volumetric flux of discharge, using total dissolved solids (TDS) as a proxy for dissolved carbonate. For simplicity, the study assumes that the variation of dissolved carbonate is a result of changing velocity while solution concentration, saturation concentration, rock/water contact surface are constant. During a cycle of increased flow rate/recession, two phases characterize the hydraulic behaviour of karst systems, the piston flow phase (PF) and the chemically-based recession flow (CBRF). While analysis of the PF is difficult, during the CBRF the processes of dissolution, dilution and convective transport should be at any point in equilibrium with the average flow velocity. During this phase, the relationship between the concentration and the flow rate yields the parameter α that reflects the relative importance of dilution and dissolution, and which is primarily dependent on the average geometric dimensions of the karst network. Hence, this approach exemplifies the use of geochemical data for the study of the structure of karst networks.

Further, for the analysis of rock-water interaction, silica is a useful tracer because its concentration in rainfall is very small, potentially below the detection limit. Silica reaches equilibrium within a few minutes in which silica-free water has been in contact with the matrix, so it is assumed that any new recharge has silica concentrations equal to zero (as opposed to previously recharged groundwater, potentially corresponding to the baseflow component). Therefore, silica functions as a flow path tracer as its concentration depends on the availability of the mineral in the rock, similar to electrical conductivity, while stable isotopes act as a geographical source tracer following the fractionation process (Laudon and Slaymaker, 1997).

2.4.1.2. Isotopic tracer

The origin of tracer hydrology using stable isotopes dates back to the publications by Friedman (1953) and Epstein and Mayeda (1953) (Aggarwal, et al., 2012), and today the use of environmental isotopes is a standard investigative tool in hydrology (Kendall and McDonnell, 1998). Application of isotopes includes the identification of the sources of waters and solutes, determination of water flow paths, determination of weathering reactions, assessment of biologic cycling of nutrients within the ecosystem, and testing flow paths, water-budget, and geochemical models. Water isotope hydrology focusses on the oxygen isotopes ^{16}O, ^{17}O, ^{18}O and hydrogen isotopes ^{1}H, ^{2}H, ^{3}H, as they are water molecule constituents that behave conservative in most low-temperature environments. Other elements for which stable isotopes and radioisotopes are used include carbon, nitrogen and sulphur (Kendall, et al., 2014).

Isotopic data are generally reported according to the Vienna Standard Mean Ocean Water (VSMOW) defined as an international standard for isotopic abundance rations by the International Atomic Energy Agency (IAEA) referring to Baertschi (1976) and Hagemann, et al. (1970) as,

$$\left(\frac{^{18}O}{^{16}O}\right)_{VSMOW} = 2005.2 \pm 0.45 \times 10^{-6} \quad \text{Eqn. 2.31}$$

$$\left(\frac{^{2}H}{^{1}H}\right)_{VSMOW} = 155.76 \pm 0.05 \times 10^{-6} \quad \text{Eqn. 2.32}$$

The isotopic abundance ratio of any given sample R_{sample} is then referred to the VSMOW $\mathrm{R}_{standard}$ as the difference between the sample and the standard as,

$$\delta = \frac{R_{sample} - R_{standard}}{R_{standard}} \quad \text{Eqn. 2.33}$$

where positive values indicate an enrichment of ^{18}O or ^{2}H compared to the standard and a negative value indicates the depletion of heavier isotopes in the sample (Leibundgut, et al., 2009). Isotope compositions are reported in the usual δ-scale in parts per thousand (‰).

The Global Network of Isotopes in Precipitation (GNIP) (IAEA/WMO, 2016) provides a globally distributed time series of deuterium (2H), oxygen-18 (18O) and tritium (3H). The isotopic compositions of precipitation are aligned along what is referred to as a Meteoric Water Line (MWL) for which a global average is called the Global Meteoric Water Line (GMWL) that yields (UNESCO/IAEA, 2001a),

$$^{2}\delta = 8\ ^{18}\delta + 10‰ \quad \text{Eqn. 2.34}$$

where according to UNESCO/IAEA (2001b),

$$^{2}\delta = (^{2}H/^{1}H)_{A} / (^{2}H/^{1}H)_{r} - 1 \quad \text{Eqn. 2.35}$$

and,

$$^{18}\delta = (^{18}O/^{16}O)_{A} / (^{18}O/^{16}O)_{r} - 1 \quad \text{Eqn. 2.36}$$

of the isotope sample A, and the reference sample r,

$$\delta_{A/r} = \frac{R_A}{R_r} - 1 \ \ (\cdot 10^3‰) \qquad \text{Eqn. 2.37}$$

with the isotope ratio R, e.g. $^2R = {}^2H/{}^1H$ and $^{18}R = {}^{18}O/{}^{16}O$.

Stable isotopes have been used to quantify recharge and flow dynamics in karst aquifers. Perrin, et al. (2003) investigated the dynamic behaviour of an epikarst system of the Milandre karst aquifer that receives mainly diffuse recharge, using 2H and 18O time series from rainfall, spring discharge and underground streams. The results show that the epikarst separates flow into baseflow and quick-flow, while above a recharge threshold, part of the water bypasses the epikarst. Further, the epikarst sub-system appears to act as the important groundwater storage element of the karst system. These findings correspond to Aquilina, et al. (2006) who quantified the water storage and transfer in the epikarst during high discharge events using Cl^- and Br^- ions and 18O and 2H isotopes of spring and rain samples.
The exchange and mixing between a saturated conduit and the surrounding matrix was estimated by Binet, et al. (2017) using 18O and 2H of rainfall, water samples of a losing stream and groundwater samples, coupled with a groundwater flow model (FEFLOW). The results provide field evidence of the existence of steady state exchanges that are controlled by the ratio between discharge at the boundaries governed by river water dynamics and the conduit discharge capacity governed by the conduit morphology.
Research carried out along a lowland karst conduit network in western Ireland which exhibits frequent groundwater–surface water interaction, showed that the concentrations of 18O fluctuates seasonally as well as event-based, with complex interactions of rainfall, stream flow and turlough storages. The fluctuation of the streams and turloughs is higher than for groundwater (McCormack, 2014; Gill, et al., 2015).

In addition to stable isotopes, radioactive isotopes have also been applied. Einsiedl (2005) used long-term records of radioactive 3H along with chemical tracers to demonstrate the low storage capacity of a soil-epikarst system compared to the rock matrix porosity and fissures of a karst aquifer. Schubert, et al. (2014) used 18O and 2H, along with a radioactive isotope of radon (Rn-222) and radioactive isotopes of radium (Ra-224, Ra-223, Ra-228, Ra-226 with half-lives of 3.82 d, and 3.7 d, 11.4 d, 5.57 y and 1,600 y) to investigate SGD of a Mediterranean karst aquifer. The authors concluded that the use of 18O, 2H and Rn-222, along with salinity is the most useful set of parameters to estimate the fraction of groundwater discharge into the sea. Ra isotope samples, however, were not of use presumably due to a poorly developed subterranean estuary inhibiting significant radium mobilization from the aquifer matrix; hence, Rn-222 is considered as the most robust environmental tracer for SGD.

2.4.2. Artificial tracer hydrology

Artificial tracer tests are common methods in karst hydrogeology (Benischke, et al., 2007) to study conduit network parameters (Geyer, et al., 2007; Luhmann, et al., 2012), the transportation characteristics of potential contaminants (Flynn and Sinreich, 2010), or to generally establish hydraulic connections and estimating transit times (Lauber and Goldscheider, 2014; Margane, et al., 2018) and delineate groundwater protection zones (Goldscheider, 2010).
Artificial tracers are commonly applied to study the pathways between discrete injection sites (e.g. swallow holes) and sampling sites (e.g. springs, rivers) (Figure 2.21). By measuring the input flux of tracer at the injection site and flux at the output location (spring), the total recovery of tracer can be estimated, and hypothesis about additional flow paths can be made. Such quantitative analysis accounts for the varying concentration of tracer in time, and is therefore based on continuous sampling using a field fluorometer, e.g. Schnegg (2002). Alternatively, a qualitative tracer test, which only informs whether the tracer was recovered or not, can be done using activated charcoal (Smart and Simpson, 2002).

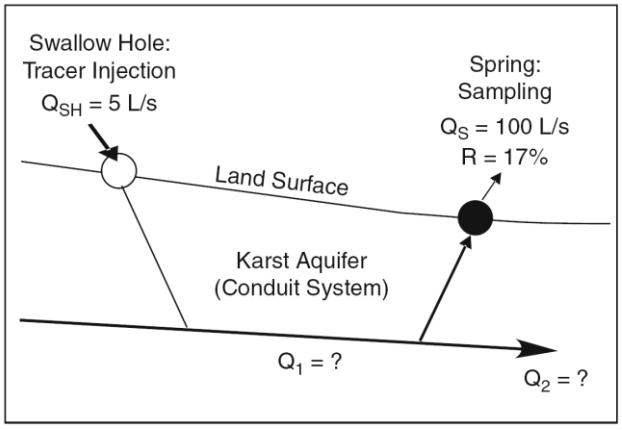

Figure 2.21: Conceptual understanding of a tracer study between a swallow hole and spring (Goldscheider, 2010).

Various types of artificial tracers have been applied. Fluorescent dyes are commonly used, such as uranine (sodium fluorescein), rhodamines or optical brightener, as are physico/chemical tracers such as chloride and temperature (Luhmann, et al., 2012) or particulate bacteriophages (Sinreich and Flynn, 2006; Maurice, et al., 2010). Detailed summaries on dye tracers can be found in Flury and Wai (2003); Runkel (2015).
The usefulness of a tracer depends on different factors (Kaess (1998) in Trček and Zojer (2010)):

- A physical and chemical structure should let the tracer travel in such a manner that allows the hydraulic parameter to be measured accurately; hence, it should be chemically stable and not be sorbed to aquifer materials or lost by filtration or any process of degradation;
- the tracer needs to be detectable in at levels of high dilution; and
- the tracer must be non-toxic, and its use should be economic.

Conservative, i.e. non-reactive, tracers are favourable to obtain break-through curves that fully mimic the behaviour of the traced water (Sinreich and Flynn, 2006).
The estimation of the tracer mass recovered in tests has been subject to many empirical assessments. For example, Leibundgut, et al. (2009) list more than 33 methods to quantify the tracer mass recovery, but the usefulness of these approaches is arguable as they usually result in a wide range of estimated tracer masses.
While there have been concerns related to the use of rhodamine WT/B (Behrens, et al., 2001), according to Flury and Wai (2003) the toxicologic impact of artificial tracers is related to their reaction with natural occurring compounds or water treatment agents (e.g. to react with nitrite to form diethylnitrosamine), which should, however, not pose any hazard under "customary dye use" (although it remains unclear what is meant by 'customary').
Sampling of fluorescent dyes follows the principle of excitation of a water sample and measuring the ensuing emission intensity. Fluorescence is the ability of chemical compounds to emit an activating light impulse as longer-wave radiation over a range; tracers with small fluorescent emission ranges are most suitable for groundwater tracing to clearly identify the fluorescent substance in water. The intensity of fluorescence varies between tracers, and it is largest for uranine making it - amongst other reasons - the most suitable tracer with a relative fluorescence of 100 and a detection limit of 0.001 mg/m^3, compared to a relative fluorescence of 9.5 and 10% (relative to the fluorescence of uranine) and a detection limit of 0.02 mg/m^3 for rhodamine WT. The fluorescence of a substance depends on the pH – an acid environment causes a drop of fluorescence and also it affects the sorption affinity of a tracer, which is of major importance. The higher the pH, the lower the sorption. Rhodamine WT is fairly insensitive to pH variations with its full fluorescent intensity between pH 5 and 9, whereas uranine is very sensitive to pH variations with gradual decrease of intensity < pH of 9.
Solubility is another important aspect as it necessitates a given volume of water to dilute a solid dye. Solubility is 300 g/l for uranine compared to 3 to 20 g/l for rhodamines.
Fluorescent tracers are subject to photolytic decay, which makes them less suitable for surface water tracing than for groundwater tracing (where for obvious reasons photolytic decay is not considered as a problem).
Of major importance is the sorption behaviour of tracers, with the general rule that states the higher the solubility in water, the lower the sorption capacity of the substance, with the exception of Amidorhodamine G (Leibundgut, et al., 2009). Rhodamine WT consists of two isomers with different sorption properties and different emission spectra, limiting its effectiveness as groundwater tracer and determining its non-conservative behaviour (Sutton, et al., 2001; Vasudevan, et al., 2001). Its sorption behaviour is described as moderate (Field, 2002) making rhodamine WT not suitable for quantitative analysis and should preferably be applied in low pH environments or across short distances (Leibundgut, et al., 2009).
In turn, sodium fluorescein has a very low sorption tendency (Field, 2002), yet, sorption is strong at low pH (Benischke, et al., 2007), making it a very good tracer outside of humic soils or acid aquatic

environments with low pH (Leibundgut, et al., 2009) where it can be considered to be conservative (Geyer, et al., 2007).
Excitation and emission maxima are 491 and 516 nm for uranine and 561 and 586 nm for rhodamine WT.

There is an abundant number of studies related to artificial tracer tests as per the example depicted in Figure 2.21, where injection and sampling is carried out in terrestrial catchments. Interestingly, to the knowledge of the author, there hasn't been any tracer method yet developed or tested that focusses on tracing SGD or SiGD in order to trace injection points of a coastal aquifer to discharge locations in the marine. This seems to be surprising given the rising interest in coastal karst aquifers and related discharge flux on the one hand (Burnett, et al., 2006; Fleury, et al., 2007a) and the vast applications of artificial tracer tests on the other hand.

2.5. Hydrograph analysis and low-flow separation

A hydrograph describes a discharge or level (head) amplitude of a river, stream, well/borehole, spring, etc. in time. A hydrograph consists of a rising limb as a result of a recharge event and a recession once the recharge event recesses/terminates. While the shape of the rising limb is subject to the characteristics of the recharge (e.g. rain) event itself, the recession reflects the drainage characteristics and global properties of the aquifer in case of a spring (Kovács, et al., 2005) or on the local aquifer properties in case of well head hydrograph (Kovács, et al., 2015). The recession is considered as the more stable part of a hydrograph as opposed to the rising limb (Fiorillo, 2014). Accordingly, hydrograph analysis focusses on the study of recession curves. For such a study, the recession chosen for analysis should not be impacted by subsequent rainfall events that would disturb the course of the recession. However, due to potentially frequent rain events in a given study area, this may not be possible. A way to overcome this problem is to establish a master recession curve (MRC) (Forkasiewicz and Paloc, 1967). A MRC is an average recession representative for a specific hydrograph, and it is constructed by summing up multiple recession segments of a hydrograph that are not impacted by rainfall. Once individual recession segments are extracted, a site-specific MRC is established by fitting the parts along the x-axis (time) to create a smooth recession curve characteristic for the site.
The stable recession limb starts after an inflection point Q_0 when the recharge event terminates, as illustrated in Figure 2.22. Generally, analysing the recession rate of karst spring hydrographs is conducted on semi-logarithmic plots where different values of slope are interpreted as different conditions of flow, summarised in Fiorillo (2014).

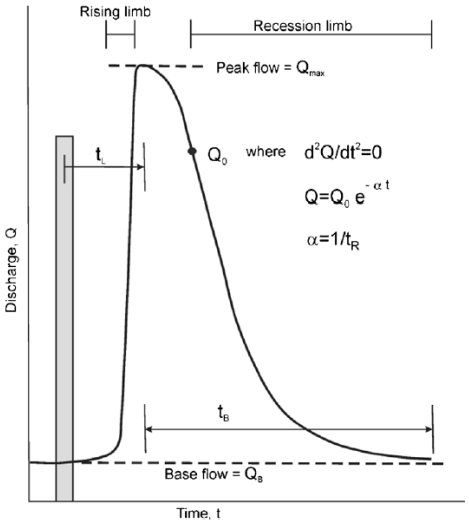

Figure 2.22: Sections of a spring hydrograph triggered by a storm event; t_L is the length of time between the storm pulse and the peak in the discharge hydrograph, t_B is the time to return to base flow, α is the recession coefficient, t_R = 1/α = response time (Fiorillo, 2014).

Karst hydrograph analysis is largely applied on spring hydrographs (e.g. Padilla, et al. (1994)) as opposed to well or borehole hydrographs. In fact, the approach is linked to the concept of multiple (dual or triple) porosities of the aquifer and the association of different discharge flow components to the different porosities, with different flow regimes from diffuse Darcian flow to fully turbulent flow in the conduits (Atkinson, 1977). These different flow components constitute different parts or segments of a recession.

The different flow components that contribute to the overall hydrograph each show different characteristic frequencies: while the baseflow or slow-flow component is associated with low frequencies, the quick-flow component or direct runoff is associated with high frequencies (Eckhardt, 2005). From this understanding, it seems to be plausible to separate 'continuous flow components', including a baseflow component, from the total hydrograph in order to establish a continuous time series of a characteristic flow component.
To separate a baseflow signal from the total discharge hydrograph in time (which is usually applied on streams in surface hydrology), different methods can be used such as a) chemical hydrograph separation using e.g. stable isotopes and/or major ions (Fritz, et al., 1976; Lakey and Krothe, 1996; Katz, et al., 1997; Winston and Criss, 2004; Katz, 2005) and b) mathematical or numerical separation techniques such as recursive digital filtering based on the low frequency of the slow-flow component (Chapman, 1999) or separation techniques based on recession analysis (Maillet, 1905). It should be noted that all methods yield estimates that can vary substantially.
A problem that arises using frequencies for the separation of flow components is the fact that the single frequencies associated with flow components are not separated from each other but rather overlap with each other. Therefore, perfect separation is not possible due to the overlapping

frequency domain of both signals (Spongberg, 2000). Further, different approaches for baseflow separation yield different results. In fact, to the knowledge of the author, there hasn't been yet any study that directly links a separated baseflow component to a conceptualised physical dimension of the aquifer. Therefore, the interpretation of any separated baseflow is limited to a conceptual understanding. Accordingly, it seems favourable to apply a range of different methods for baseflow separation in order to benefit from different approaches.

2.5.1. Spring hydrography

The use of spring hydrograph recession analysis is standard in hydrology and hydrogeology. The earliest mathematical characterisation of the long-term baseflow recession of spring discharge vs. time was conducted by Maillet (1905), assuming that the spring recession can be approached by an exponential function of the volume held in storage in a reservoir that is drained. Accordingly,

$$Q_{(t)} = Q_0 e^{-kt} \qquad \text{Eqn. 2.38}$$

where $Q_{(t)}$ is the discharge [L^3T^{-1}] at time *t*, Q_0 is the initial discharge [L^3T^{-1}] at time *0*, and k is the recession constant [T^{-1}]. Over the past, the recession constant has been expressed mostly as k or a, so care must be taken when dealing with different references that apply both of them.
Eqn. 2.38 is that of a linear reservoir adequately for describing the baseflow recession of karst systems (Kovács and Perrochet, 2008) where the discharge $Q_{(t)}$ is at any time proportional to the water stored in the reservoir $V_{(t)}$ and k,

$$Q_{(t)} = k \cdot V_{(t)} \qquad \text{Eqn. 2.39}$$

The shape of the exponential recession is controlled by the intrinsic properties of the aquifer expressed by the recession constant k (or α). In turn, the recession constant itself is subject to studies as it allows conclusions to be drawn about the intrinsic properties of the system. Drogue (1972) applied a statistical approach to estimate the decrease of discharge of karst springs, using 100 studied hydrographs where,

$$Q_{(t)} = \frac{Q_0}{(1 + \alpha \cdot t)^n} \qquad \text{Eqn. 2.40}$$

with n having the values $\frac{1}{2}, \frac{3}{2}, 2$ according to the difference in initial and final discharges, with $n = \frac{3}{2}$ as the most representative. Further, the author introduces the coefficient $\beta = \alpha \cdot Q_0^{-1/n}$ that is related to the characteristics of the spring and its recharge basin. It may be written as,

$$\beta = f\left(\frac{K}{E \cdot R \cdot S}\right) \qquad \text{Eqn. 2.41}$$

where K is the permeability of the karst, E is the moisture condition of the karst and of the soil due to precipitation prior to discharge, R is the karst area and S is the storage coefficient of the karst. Bonacci (1993) linked the recession coefficient to the storage and transportation characteristics of a karst aquifer by sub-dividing the hydrograph recession into quasi-stationary segments. Within a segment, a linear reservoir with one value of the linear reservoir coefficient j is introduced to relate the observed discharge records to the modelled records. Yet, the procedure is not based on real physical aquifer properties.
Both approaches are mainly empiric, leaving α or β without an analytical solution or a precise physical meaning.

Perhaps the earliest work linking α to meaningful aquifer characteristics was done by Rorabaugh (1964) who estimated groundwater discharge from an aquifer with uniform, homogeneous, and isotropic characteristics based on heat-flow theory, as well as by Berkaloff (1966) to establish an approach to estimate the recession coefficient as,

$$\alpha = \frac{\pi^2 T}{4SL^2} \qquad \text{Eqn. 2.42}$$

with the transmissivity T [L^2T^{-1}], the width of the aquifer L [L] and the storativity S [-].

According to Kovács, et al. (2005), Eqn. 2.42 considers the recession process as exclusively dependent on the hydraulic parameters of the low-permeability matrix, as it was established in the context of a uniform, homogeneous, and isotropic medium. In fact, α is only valid for the baseflow component without considering the heterogeneity of karst aquifers that results in slow-flow components and fast-flow components (Atkinson, 1977).

The first study combining the approach of establishing physical meaningful recession coefficients along with findings on the existence of multiple flow components in a karst spring recession based on Forkasiewicz and Paloc (1967) was provided by Kovács, et al. (2005) who quantitatively characterized the connection between the hydraulic and geometric properties of karst aquifers and their global response, integrating the influence of the conduit network on the recession coefficient. The authors manifested the concept of the ‘duality of groundwater flow’ by providing recession coefficients for two different flow domains, i.e. the conduit-influenced flow regime (CIFR) and the matrix-restrained flow regime (MRFR).
The MRFR is valid for mature karst systems. During the baseflow recession the hydraulic parameters of karst conduits do not influence the drainage of the low-permeability matrix. The drainage

process is influenced by the size and hydraulic parameters of the low-permeability blocks alone. The recession coefficient can be estimated by Eqn. 2.43 and Eqn. 2.44,

$$\alpha = \frac{2\pi^2 T}{SL^2} \qquad \text{Eqn. 2.43}$$

with the 2D block area L^2, or by,

$$\alpha = \frac{2\pi^2 T_m f^2}{S_m} \qquad \text{Eqn. 2.44}$$

with the transmissivity T_m of the matrix medium [L^2T^{-1}], the conduit frequency (number of conduits per unit length) f and the matrix storativity S_m [-].

The CIFR is valid for the baseflow recession of early karst systems and fissured systems. The recession process depends on the hydraulic parameters and the size of the low-permeability blocks, conduit conductivity and the total extent of the aquifer.
The recession coefficient can be estimated by,

$$\alpha = \frac{2}{3}\frac{K_c \cdot f}{S_m \cdot A} \qquad \text{Eqn. 2.45}$$

with the conduit conductance K_c [L^3T^{-1}], the conduit frequency f [L^{-1}], and the block area A. The threshold frequency dividing MRFR (Eqn. 2.44) and CIFR (Eqn. 2.45) is given by,

$$f^* \approx \frac{K_c}{3\pi^2 T_m A} \qquad \text{Eqn. 2.46}$$

Kovács and Perrochet (2008) presented a combined analytical–numerical study for the characterization of spring hydrographs for estimating the hydraulic and geometric parameters of karst aquifers. Numerical simulations suggest that the concave recession segment of any arbitrary karst spring hydrograph can be decomposed into multiple exponential segments for different flow components,

$$\alpha_1 = 2\frac{\pi^2 T}{SL^2}, \alpha_2 = 10\frac{\pi^2 T}{SL^2}, \alpha_3 = 26\frac{\pi^2 T}{SL^2} \qquad \text{Eqn. 2.47}$$

with the baseflow recession coefficient α_1, the intermediate recession coefficient α_2, and the flood recession coefficient α_3, assuming symmetric block shape. Deviation of the recession coefficients of Eqn. 2.47 on spring hydrograph segments may indicate block asymmetry.

Aquifer parameters can be simply estimated from the baseflow recession coefficient (Eqn. 2.43),

$$\alpha_b = \frac{\pi^2 T}{S}\left(\frac{1}{L_x^2} + \frac{1}{L_y^2}\right) \qquad \text{Eqn. 2.48}$$

with the block sizes L_x and L_y in the x and y directions. Significant discrepancies in the proportion between the recession coefficients of different hydrograph segments may indicate block asymmetry and/or variations of block shape or block size over the catchment area.

The decomposition of the total recession into different (exponential) components has been conceptualised as a representation of distinct flow components. These findings are very important in karst hydrogeology and beyond. For example, the hydrogeological approach outlined above has also been adopted in surface hydrology, decomposing stream runoff into several contributing components (Holko, et al., 2013).

2.5.2. Well/borehole hydrography

The use of well hydrographs for the study of aquifer parameters has been less studied in comparison to spring hydrographs. However, the principles behind spring hydrography apply in a similar way also to well hydrography.

Perhaps the first major work linking the quantitative findings on discharge hydrograph analysis with water level hydrographs considering the heterogeneity of karst aquifers was done by Moore (1992), combining streamflow and well hydrograph analysis to demonstrate the contribution of groundwater to the late streamflow recession component where,

$$\ln\left(\frac{Y_1}{Y_2}\right) / \left(\frac{t_2}{t_1}\right) = \lambda = \ln\left(\frac{Q_1}{Q_2}\right) / \left(\frac{t_2}{t_1}\right) \qquad \text{Eqn. 2.49}$$

with the water level Y_x, the streamflow Q_x at time t_x and the slope λ of the straight-line segment (in a semi-logarithmic plot) in the unit of inverse time. Eqn. 2.49 shows that, for hydrographs, discharge Q can equally expressed as head Y. Further, the authors estimate specific yield S_y and transmissivity T for different flow components that vary with head using the relationship between streamflow recession and storage depletion using,

$$S_y = \frac{Q_t}{\lambda A Y_t} \qquad \text{Eqn. 2.50}$$

$$T_0 = S_y Y_0 \lambda a_0 / I \qquad \text{Eqn. 2.51}$$

with the drainage area A, the water level at peak discharge Y_0 and the average distance from a drainage divide to the stream at peak discharge a_0 and the hydraulic gradient I.

The work of Moore (1992) is relevant as it provided the basis for more detailed quantitative analysis of karst well hydrographs based on the principles of straight-line segments occurring on semi-logarithmic plots, further developed by Shevenell (1996) and Powers and Shevenell (2000). The authors combine the method of Moore (1992) for estimating specific yields (S_y) and continuum transmissivities (T) using head time series of karst aquifers together with findings of Forkasiewicz and Paloc (1967) (although not referring directly to their publications). Again, the three types of storage, i.e. conduit, fracture, and fissured matrix can be approximated by straight lines on a semi-logarithmic plot – if conduits exist, recessions with only one straight line represent drainage from the low transmissivity fissured matrix, while segments with ≥2 segments represent drainage from the higher T and lower S_y domain (fractures/conduits) and the low T and high S_y domain (fissured matrix).

Based on the spring hydrograph analytical methods for parameter estimation (Rorabaugh, 1964; Berkaloff, 1966; Kovács, et al., 2005; Kovács and Perrochet, 2008) and spring hydrograph analytical methods for the estimation of conduit network geometry (Kovács, et al., 2005; Kovács and Perrochet, 2008), Kovács, et al. (2015) introduced a well hydrograph analytical tool for parameter estimation in karst aquifers of MRFR. Such well hydrograph analysis provides information on local hydraulic and geometric properties of individual matrix blocks and in certain cases on the deep unkarstified aquifer zone.

Similarly to Kovács and Perrochet (2008), three recession coefficients contribute exponential components to the hydrograph, in this case for individual block properties, yielding,

$$\alpha_1 = \frac{\pi^2 T}{S}\left(\frac{1}{L_x^2} + \frac{1}{L_y^2}\right), \qquad \text{Eqn. 2.52}$$

$$\alpha_2 = \frac{\pi^2 T}{S}\left(\frac{1}{L_x^2} + \frac{9}{L_y^2}\right) for\ L_y > L_x;\ \alpha_2 = \frac{\pi^2 T}{S}\left(\frac{9}{L_x^2} + \frac{1}{L_y^2}\right) for\ L_y < L_x \qquad \text{Eqn. 2.53}$$

$$\alpha_3 = \frac{\pi^2 T}{S}\left(\frac{1}{L_x^2} + \frac{25}{L_y^2}\right) for\ L_y > L_x;\ \alpha_3 = \frac{\pi^2 T}{S}\left(\frac{25}{L_x^2} + \frac{1}{L_y^2}\right) for\ L_y < L_x \qquad \text{Eqn. 2.54}$$

Information on the average block properties within a catchment are expressed by,

$$\alpha_1 = 2\frac{\pi^2 T}{SL^2}, \alpha_2 = 10\frac{\pi^2 T}{SL^2}, \alpha_3 = 18\frac{\pi^2 T}{SL^2} \qquad \text{Eqn. 2.55}$$

with the baseflow recession coefficient α_1, the intermediate recession coefficient α_2, and the flood recession coefficient α_3.

In the absence of spring hydrographs, well or borehole hydrographs may be a favourable approach to characterise individual segments of well/borehole recessions to characterise at least domains of the vicinity of the well/borehole. A challenge though is the necessity of hydraulic data/information (T, S_y) that may be not available and/or difficult to acquire, e.g. through a pumping test.

2.5.3. Digital/recursive filtering

The previous section has outlined methods to be applied on individual recessions or a MRC. Often, it is necessary to analyse or separate a continuous signal from a hydrograph, which can be achieved by applying 'filtering'. Filtering is based on the principle of the separation of two signals with different frequencies (Holko, et al., 2013). Two types of filtering exist, namely a) digital, i.e. automated, and b) analogue, i.e. graphical. The graphical method is inconvenient to deploy on longer time series due to the required workload, which led to the development of specific numerical or digital algorithms to separate the baseflow signal in hydrological studies (Chapman, 1999). In fact, digital filters are recursive as they reuse the output from a previous time step in generating the output of the current or next time step. Digital filtering is perhaps the most common tool for separating low-frequency slow-flow components from a total hydrograph, keeping in mind that there is no unique definition of baseflow (Miljević, et al., 2013). One definition for the separation of baseflow using recursive digital filter approaches may be to distinguish between the rapidly occurring discharge components and the slowly changing discharge originating from interflow and groundwater applying mathematical procedures, which perform the separation using a set of separation parameters (Rimmer and Hartmann, 2014).

Many software packages and methods are available that separate the slow-flow component from the total stream hydrograph in an automated way, such as the fixed-interval, sliding-interval, and local minimum HYSEP methods (USGS, Sloto and Crouse (1996)), the baseflow index (BFI) (UK Institute of Hydrology/ Centre for Ecology & Hydrology, Gustard, et al. (1992)), PART (USGS, Rutledge (1998)), BFLOW (Arnold and Allen, 1999) or Eckhardt (2005). All of these methods include different numbers of parameters that must be fitted. According to the comparison between one-, two- and three-parameter algorithms, two-parameter algorithms yield more consistent and plausible results (Chapman, 1999).

A one-parameter exponential smoothing algorithm to separate quick-flow (surface runoff) from slow-flow (baseflow) from a stream hydrograph was provided by Chapman and Maxwell (1996); Chapman (1999) who estimate the baseflow Q_b at time i as a weighted average of the direct runoff Q_d, and the baseflow component at the previous time step as,

$$Q_b(i) = kQ_b(i-1) + (1-k)Q_d(i) \qquad \text{Eqn. 2.56}$$

with the recession constant during periods of no direct runoff k. Removing the direct runoff component Q_d leaves the baseflow component Q_b as,

$$Q_b(i) = \frac{k}{2-k}Q_b(i-1) + \frac{1-k}{2-k}Q(i) \qquad \text{Eqn. 2.57}$$

with the total flow Q, and $Q_b(i) \leq Q(i)$.

The underlying premise to estimate Q_b as a weighted average of Q_d is problematic because the flow components' contribution to total discharge varies in time.

Based on the linear reservoir assumption that the outflow from an aquifer is proportional to its storage, Eckhardt (2005) suggests a two-parameter algorithm to separate a hydrograph into baseflow and direct runoff. Baseflow is considered as discharge from groundwater storage associated with the low frequency spectrum of a hydrograph. Thus, the proposed method is based on the principle by identifying the baseflow component by low-pass filtering of the hydrograph according to,

$$b_k = \frac{(1-BFI_{max})ab_{k-1} + (1-a)BFI_{max}y_k}{1-aBFI_{max}} \qquad \text{Eqn. 2.58}$$

with baseflow b_k, the time step k, the filter parameter a, the maximum baseflow index, i.e. the ratio of baseflow to stream flow BFI_{max} (<1) and the total stream flow y.
The parameter a may be derived from the hydrograph applying Maillet's law where the filter parameter $a = \exp(-k)$ (Eqn. 2.58). BFI_{max} is adjusted subjectively based on the catchment's hydrogeology with respective values suggested based on empirical studies for perennial streams in porous and hard rock aquifers. No validation of the method was done in the context of a karst system. The problem of subjectively defining BFI_{max} was tackled by Collischonn and Fan (2013) who proposed a method to estimate BFI_{max} based entirely on discharge records and the application of a backwards running filter. The method was empirically derived based on records from 15 river gauging stations draining porous or hard rock aquifers with the equation,

$$BFI_{max} = \frac{\sum_{i=1}^{N} b'_i}{\sum_{i=1}^{N} y_i} \qquad \text{Eqn. 2.59}$$

with the maximum of baseflow b' originating from a backwards running baseflow hydrograph with an assumed parameter a.

Eckhardt (2008) considers his method to be hydrologically more plausible than others while the method is considered as one of the most important contributions in the context of recursive filtering (Collischonn and Fan, 2013). Yet, it seems that the Eckhardt method yields (at least partly) relatively high estimates of baseflow according to others (Miljević, et al., 2013; Indarto, et al., 2016).

Digital filtering or computerized baseflow separation has widely been applied in surface hydrology on stream runoff time series to distinguish between a fast and slow response, and to a lesser extent on karst spring hydrology. However, arguably special forms of the two-parameter filter may be well applied in groundwater fed streams as they recess exponentially (Rimmer and Hartmann, 2014).
For example, Duran (2015) separated the baseflow of a karst system using - amongst others - the method of Eckhardt (2005) to analyse the performance of a reservoir model and its baseflow contribution. The results show that the model achieves the best results calibrated against the results of the Eckhardt method, indicating the reasonability of the Eckhardt method in conjunction with karst groundwater flow modelling.
Rimmer and Salingar (2006) used the Eckhardt filter to separate the baseflow from streams in the karstic region of the Hermon Mountain. The authors infer a from the ratio between each daily streamflow and the streamflow of the preceding day, while BFI_{max} is estimated via trial-and-error. This limitation was tackled by Rimmer and Hartmann (2014) who present an algorithm to optimise BFI_{max} (Eqn. 2.58) (here listed as β) based on measured hydrochemistry applying a complete mixing model for the baseflow (Q_{Bj}) and quick-flow (Q_{Sj}), and minimizing the value of the root-mean-squared error $E(\beta)$ given by,

$$E(\beta) = \left[\sum_{j=1}^{j=n} [\, C_{obsj} - C_{sepj}(\beta)]^2\right]^{1/2} \qquad \text{Eqn. 2.60}$$

and

$$C_{sepj}(\beta) = \frac{C_{\boldsymbol{B}} \times Q_{\boldsymbol{B_j}}(\beta) + C_{\boldsymbol{S}} \times Q_{\boldsymbol{S_j}}(\beta)}{Q_{\boldsymbol{j}}} \qquad \text{Eqn. 2.61}$$

with the j times measured concentration C_{obsj} in streamflow, and the stream flow concentration function $C_{sepj}(\beta)$, which is described by the separated baseflow component Q_{Bj} and the separated quick-flow component Q_{Sj}, their sum Q_j, as well as their attributed constant concentrations C_B and C_S. Thus, the estimation of BFI_{max}/β becomes more comprehensible. The method was applied on karst spring and stream records using different parameters (SO_4^{2-}, total suspended solids). The results show different optimised BFI_{max}/β values for the same parameters, which is related to the fact that the separation procedure of two flow components is physically not unique. Rather, the resulting separation depends on the nature of the tested parameter and its behaviour. Therefore, the

authors argue that baseflow separation should not be reduced to a pure distinction between e.g. groundwater and surface water.

There are many different digital filters available that can be used for baseflow separation. However, the Eckhardt filter has only two parameters to be fitted (and has previously been applied in the context of karst hydrograph analysis. Therefore, this filter seems to be the most favourable one.

2.5.4. Two-component and end-member mixing analysis

Baseflow separation using geochemistry is based on the premise that variations of solute concentrations depend on the composition of different sources (Laudon and Slaymaker, 1997) or reservoirs/flow components, relating discharge to chemistry. It was introduced by Pinder and Jones (1969) separating a groundwater component from total stream runoff using major ions and silica according to the mass balance equation,

$$Q_t C_t = Q_S C_S + Q_P C_P \qquad \text{Eqn. 2.62}$$

with the discharge Q and its concentration C, and the components T for total, S for storm, and P for pre-storm.
This approach is referred to as two-component mixing analysis (TCMA) assuming complete mixing between independent, distinct and conservative tracers (Leibundgut, et al., 2009). Earliest approaches on hydrograph separation date back to Mook and Groeneveld (1974) using 18O, and Fritz, et al. (1976) using 18O and 2H along with major ions (Na^+, Ca^{2+}, Mg^{2+}) concentrations and EC. Assuming constant concentrations of 18O and 2H in rainfall, Fritz, et al. (1976) distinguish quantitatively between pre-event water or baseflow (groundwater component) and the event water or flood (rainfall) component of short-term rain events, based on the premise that a) groundwater contributions have a uniform stable isotope composition; and b) isotopic composition of rainfall contributing to the runoff event must be significantly different to the composition of groundwater. Further, as summarised in Leibundgut, et al. (2009), c) boundaries must be considered and d) it is assumed that there is no other flow components (e.g. soil water) contributing to the mass balance of the tracer. If a), b), c) and d) hold true, then,

$$Q_T = Q_S + Q_R \qquad \text{Eqn. 2.63}$$

$$Q_T \, \delta_T = Q_S \, \delta_S + Q_R \, \delta_R \qquad \text{Eqn. 2.64}$$

with the streamflow Q, the isotopic content δ of 2H or 18O, stream water at the gauging station T, pre-storm water component of the streamflow S, and the storm water component of the streamflow R. Combining Eqn. 2.63 and Eqn. 2.64 yields,

$$Q_R = Q_T \frac{\delta_T - \delta_S}{\delta_R - \delta_S} \quad \text{Eqn. 2.65}$$

that can be used to separate a hydrograph into its storm and pre-storm components, where the pre-storm component may be considered as baseflow, or, into rain component and groundwater component.

Stable isotopes are generally regarded as conservative tracers, while ions and EC are considered as non-conservative tracer due to their ongoing reaction when in contact with rock (Uhlenbrook, et al., 2002). Therefore, it seems more appropriate to use stable isotopes for TCMA as opposed to other geochemical tracers, such as EC.

Akram, et al. (2013) applied the two-component mixing model to quantify the baseflow contribution (in % of total flow) for surface waters in Pakistan using the average isotopic data (18O) of groundwater and surface water in high flow and low flow different periods. Pellerin, et al. (2008) applied two-component mixing analysis using silica, 2H and EC to separate event water from pre-event water for 19 events. EC was considered as inexpensive, high-frequency tracer for hydrograph separation which can be measured continuously.

The assumption of two mixing reservoirs is a major simplification, which may not be enough to represent recharge and multiple flow components. The differentiation of reservoirs may go beyond a groundwater contribution as opposed to a storm contribution, to include multiple reservoirs, e.g. soil, epikarst, etc. At the same time, different reservoirs (e.g. soil) show a different isotopic composition compared to the phreatic zone and may also vary internally. In case of considering multiple flow components (e.g. soil water or surface runoff, etc.) Eqn. 2.63 and Eqn. 2.64 must be extended to account for additional contributing end members in the end-member mixing analysis (EMMA) to yield,

$$Q_t = Q_1 + Q_2 + Q_3 + \cdots + Q_n \quad \text{Eqn. 2.66}$$

$$C_t Q_t = C_1 Q_1 + C_2 Q_2 + C_3 Q_3 + \cdots + C_n Q_n \quad \text{Eqn. 2.67}$$

with the total streamflow Q_t, the particular runoff component Q_n, and the particular isotopic concentration C_n (Klaus and McDonnell, 2013).

For the application of a three-component mass balance approach, either one of the flow components must be known or an additional tracer must be used, as different tracers may describe different end-members. For example, chloride is suitable to differentiate between the end-member pre-event water and event water, while silicate may characterise the activation of different flow paths in the catchment (Klaus and McDonnell, 2013). For example, for the separation of the pre-event water into groundwater (baseflow) and soil water, Laudon and Slaymaker (1997) used 2H, 18O, EC and

silica, while Wels, et al. (1991) used silica and magnesium in addition to 2H to split spring discharge into surface flow and subsurface flow.
The studies highlight the importance of integrating different storage reservoirs and tracers to improve the separation of the pre-event (baseflow) component. This is very relevant for the separation of the baseflow of karst hydrographs, as it can be expected that different reservoirs play an important role in modifying the input signal towards the output.

Complications in EMMA arise if the isotopic composition of rain (i.e. input) varies in a high temporal resolution. Differences in time and space in the isotopic signal of rainfall during events are related to temperature of condensation, origin of air mass vapour, evaporation and isotopic exchange between falling raindrops and surrounding water. These processes can all cause substantial variations (McDonnell, et al., 1990; Fischer, et al., 2017; Koeniger, et al., 2017). Based on a weighted mean value of the concentration of 2H at different rain sampling locations, McDonnell, et al. (1990) present an incremental intensity mean that includes a weighting according to rainfall intensity, accounting for higher runoff caused by higher rainfall intensity to yield,

$$\delta \mathrm{D} = \frac{\sum_{i=1}^{n} Pi\delta_P}{\sum_{i=1}^{n} Pi} \qquad \text{Eqn. 2.68}$$

with the isotopic input signal $\delta \mathrm{D}$, the average rainfall intensity [mm/h] during the sampling increment Pi, and the fractionally collected rainfall δ_P.

Uncertainty estimations related to isotopic based hydrograph separation was applied by Genereux (1998) who introduced a Gaussian error propagation approach that is considered to be 'state of the art' (McDonnell, et al., 1990). The method is applicable for two- and three component-based tracer hydrograph separation techniques. For the two-component analysis, the uncertainty of the fraction 1 (of 2 fractions) in streamflow W_{f1} is defined as,

$$W_{f1} = \left\{ \left[\frac{C_2 - C_S}{(C_2 - C_1)^2} W_{f1} \right]^2 + \left[\frac{C_S - C_1}{(C_2 - C_1)^2} W_{C2} \right]^2 + \left[\frac{-1}{(C_2 - C_1)} W_{Cs} \right]^2 \right\}^{\frac{1}{2}} \qquad \text{Eqn. 2.69}$$

with the tracer concentrations C_1 and C_2, the stream water S, and the fraction f of total stream flow due to a component ($f_1 + f_2 = 1$).

Based on the premise that the baseflow or groundwater component of a karst spring hydrograph resembles the low permeability 'fissured matrix' storage or diffuse groundwater flow component, isotopic separation techniques coupled with major ions time series analysis, as introduced by Fritz, et al. (1976), may be a promising approach for baseflow separation of karst spring hydrographs/

chemographs. Nevertheless, the method has some limitations in the context of karst spring hydrograph separation. TCMA yields only one groundwater component and so it cannot distinguish between flow components. Therefore, additional reservoirs (end members) would be necessary to account for additional flow components. Yet, the use of such additional reservoirs may be difficult as to which samples to use for representation.
Further, the method tends to yield relatively large baseflow components, as already stated by Fritz, et al. (1976) and seen in Laudon and Slaymaker (1997); Pellerin, et al. (2008). Such high baseflow components, exceeding 50% of the total hydrograph, may be valid for certain surface waters, but are more questionable for karstified aquifers.
Further, in reality, the storage volume of an aquifer and its different permeability domains is physically limited. However, EMMA and TCMA apply a relative contribution of baseflow onto the total observed hydrograph, without considering any physical limitation in storage of the system.

2.6. Groundwater flow modelling

With the beginning of the 20th century, research in karst hydrogeology shifted towards a quantitative approach considering the temporal aspect in groundwater flow and transport referring to the laws postulated by Darcy (1856), Hagen (1839) and Poiseuille (1846) (Sauter, et al., 2006). Yet, early karst groundwater flow models followed relatively recent, dating back to Kiraly (1975) or Mangin (1975). In these modelling approaches, a matrix domain is connected to the main conduit system, draining the aquifer.
The representation of a heterogenous karst aquifer in a (conceptual) numerical environment is considered very challenging, including assigning continuous hydraulic parameters to that model. Another difficulty arises choosing the appropriate modelling approach, and further, transferring modelling results then to the real physical environment, bearing in mind uncertainties due to simplifying assumptions in the modelling process. Generally, two fundamentally different flow modelling approaches can be distinguished, a) global models (lumped parameter models) and b) distributed models (Kovács and Sauter, 2007).

2.6.1. Global (lumped) parameter models

Global or lumped models are based on deconvolution or a simple transfer function (Fleury, et al., 2007b), which transforms the input signal (usually rainfall) into an output signal (typically spring discharge). Depending on the available information, global or lumped models can further be distinguished between ‘grey box’ models and ‘black box’ models.
Grey box models often form a cascade of more or less complex reservoirs. This modelling approach provides semi-quantitative relationships between the global response and hydraulic parameters and geometric aquifers properties. Therefore, the modelling approach is linked to physically meaningful (hydraulic) parameters. Different flow dynamics are resembled by specific reservoirs to

account for e.g. fast and slow-flow components. Such model may be based on spring hydrograph decomposition (recession analysis), e.g. Kovács, et al. (2005); Kovács and Perrochet (2008).
While in a grey system a part of the information is clearly understood and part is obscure (Hao, et al., 2006), a black box represents a completely unknown system, not linked to physically meaningful hydraulic parameters. Black box models relate the global response to recharge using mathematical operators that cannot be directly related to physical phenomena. This approach may be based on using univariate methods (auto-correlation, spectral analysis) and bivariate methods (cross-correlation, cross-spectral analysis) (Kovács and Sauter, 2007).

Labat, et al. (2000a) estimated linear black box rainfall–runoff relationships for karstic systems located in the Pyrenees Mountains considering rainfall and spring discharge as two autocorrelated and cross-correlated stochastic processes. The models show that karstic circulation models based on linear and stationary laws are unable to account for the complexity of the behaviour of these aquifers, especially at small sampling intervals and for extreme events.
Wagner, et al. (2013) tested the applicability of a lumped parameter rainfall-runoff model (N-A-Modell GR2M) to represent karst spring hydrographs of the Lurbach system using monthly data of 11 years' time series. The modelled spring hydrograph matched the observed hydrograph well over a period of 7 years, but for the next four years the model parameters had to be changed in order to match modelled and observed hydrographs. The reason for this was interpreted as changing hydrological conditions, i.e. inter-catchment flow over the last 4 years' period.
While the previous two models do not account for the different flow components within a karst aquifer, Denić-Jukić and Jukić (2003) integrated a diffuse groundwater flow component as distinguished from the fast-flow component. The authors introduced the composite transfer function (CTF) in a black box approach estimating discharge time series of the Jadro spring in a rainfall-runoff model. The CTF simulates discharges by two transfer functions adapted for the quick-flow and the slow-flow component (Figure 2.23): a nonparametric transfer function modelling the quick-flow and a parametric transfer function responsible for the slow-flow (diffuse) component.

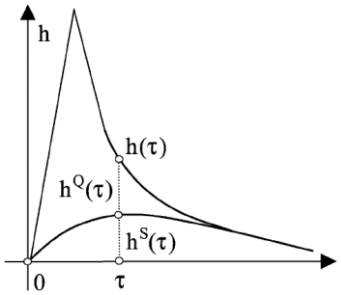

Figure 2.23: Elements of the composite transfer function modelling a fast-flow component $h^Q(\tau)$ and a slow-flow component $h^S(\tau)$ (Denić-Jukić and Jukić, 2003).

Transfer functions were used by Fleury (2005) modelling long-term discharge time series of different karst springs in the Mediterranean using a reservoir model built in Vensim. The model structure considers a soil reservoir from where water infiltrates towards a smaller slow flow reservoir for the diffuse groundwater flow and a larger reservoir for concentrated and fast groundwater flow. Both combined components then constitute the overall spring hydrograph. The results were used to relate the development of the karst network to the functioning of the aquifers.
The importance of considering an additional reservoir for the diffuse groundwater flow component for the correct representation of the dynamics of the system was demonstrated by Tritz, et al. (2011). The authors further developed the rainfall-discharge reservoir model for the Durzon spring (Fleury, 2005), considering a non-linear, hysteretic discharge law accounting for the variations of connectivity in the soil/epikarst zone. A threshold-based discharge law was applied accounting for the time variability of the active catchment area via losses to secondary springs.
Following Fleury (2005), Fleury, et al. (2007b) integrated recession coefficients obtained from hydrograph analysis for the Vaucluse Spring, transforming the previous model towards a grey system. The improved model is able to quantify the volumes of slow (diffuse) and quick discharges. The modelling results achieved by the authors were successfully reproduced by Mazzilli, et al. (2017) using the modelling platform KarstMod. KarstMod allows the structure of conceptual lumped models of karst systems to be reproduced and can be used as a straightforward analysis tool to evaluate internal discharges of karst aquifers as part of the overall aquifer dynamics (Duran, 2015; Kazakis, et al., 2018).

Jukić and Denić-Jukić (2009) presented a conceptual rainfall–runoff model for time-variant Jadro spring catchment for the estimation of the groundwater balance and identification, quantification and characterization of non-conservative and time-variant components in the groundwater balance. The model distinguishes between 1) a soil cover and epikarst production store, 2) an epikarst routing store, and 3) reservoirs representing fissures, fractures, vertical shafts producing respective flows. The recession coefficient of the spring's master recession curve was integrated in modelling the baseflow component.
Based on a single event, Geyer, et al. (2008a) employed a simple two-serial reservoir model to estimate the inflow into the conduit system of the Gallus spring karst aquifer which consists of the sum of direct recharge and flow from the fissured matrix blocks into the conduit system (Figure 2.24). The approach utilises the first time derivative of the spring hydrograph and the recession coefficient of the conduit system for the determination of this function.

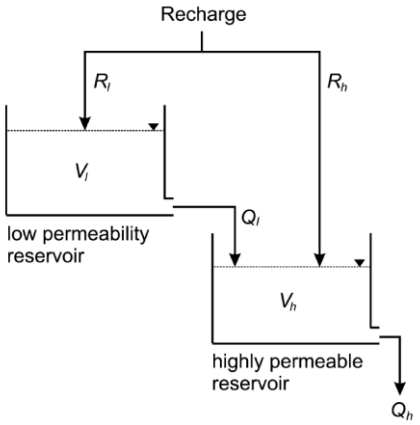

Figure 2.24: Two-reservoir model for the simulation of the hydraulic behaviour of karst aquifer: diffuse recharge into the low permeability domain (R_l), concentrated recharge into the high permeability domain (conduits) (R_h), flow from the low permeability domain into the high permeability domain (Q_l), and groundwater discharge (Q_h) (Geyer, et al., 2008b).

Another grey box approach previously mentioned was followed by Kovács, et al. (2005) and Kovács and Perrochet (2008) estimating recession coefficients based on hydraulic and geometric parameters of the given aquifer. The authors differentiate between two states of karst aquifers characterised either by a conduit-influenced flow regime (CIFR) of early systems or by a matrix-restrained flow regime (MRFR) of mature karst systems.

Lumped models are not spatially distributed, which simplifies this approach. Yet, examples of how to account for the spatial heterogeneity of recharge was accounted for in the VarKarst model (Hartmann, et al., 2014b) or in the LuKARS model (Bittner, et al., 2018). LuKARS was developed to investigate the impact of quarrying on a karst aquifer. The model approach consists of a non-linear threshold function applied on different 'hydrotopes' (recharge area with distinct vegetation, soil type and soil thickness). On the other hand, VarKarst considers the spatial variability of a) soil and epikarst depths, b) fractions of concentrated and diffuse recharge to the phreatic zone, c) epikarst hydrodynamics, and d) groundwater hydrodynamics.

Depending on the chosen approach, lumped models have the capability to account for different flow dynamics and even spatial catchment characteristics. These models can distinguish between fast-flow and slow-flow by assigning one reservoir each of the respective flow component. The different signals from the reservoirs may then transformed into spring discharge using e.g. CTFs. Further, grey box models can incorporate mean aquifer hydraulic properties that were previously established using spring hydrographs.
Reservoir models can be considered as very useful tools. The examples of Wagner, et al. (2013) or Duran (2015) show that they can be used to better understand the underlying principles of a karst system, including seasonal variations of flows. Also, the structure of a reservoir model reveals

insights into the functioning of a karst system. Further, such models can be used to fill gaps in field data time series.

2.6.2. Distributed flow models

Distributed groundwater flow models discretise the aquifer into homogeneous sub-units and describe groundwater flow by differential equations. Amongst others, the combination of diffuse and conduit flow regimes that makes the numerical distributed modelling of karst aquifers very challenging (Meyer, et al., 2008).
The two numerical methods most frequently used to solve differential equations are the Finite Difference Method (FDM) and the Finite Element Method (FEM) (Botha and Bakkes, 1984; Kovács and Sauter, 2007). An overview on the two principles is given for example by Wang (1995).
The type of groundwater flow and its ruling equations is determined by, 1) hydraulic conditions of the aquifer, 2) space, and 3) time. Equations describing confined groundwater flow are less complex because the cross-sectional area of flow at any given location in the aquifer remains constant, regardless of time. In turn, groundwater flow within an unconfined aquifer is more complex because of varying recharge conditions that cause a changing water table and changing thickness of the saturated zone (Kresic, 2009).

The principal formula representing transient groundwater flow in saturated medium is the classical diffusivity equation derived from Darcy's law (momentum conservation) and the continuity equation (mass conservation),

$$S\frac{\delta H}{\delta t} = \nabla \cdot (K \nabla H) + i \qquad \text{Eqn. 2.70}$$

with the storage coefficient S [L^{-1}], the hydraulic conductivity K [LT^{-1}], the hydraulic head H [L], the time t [T] and the source term i [T^{-1}]. The source term considers the volume of water added per unit time and volume (as opposed to sink term).

Distributed karst groundwater flow models include two principal concepts: the discrete concept considers flow within individual fractures or conduits while the continuum concept considers heterogeneities through effective model parameters and their spatial distribution. Different approaches can be summarised as: 1) Discrete Fracture Network (DFN), 2) Discrete Conduit Network (DCN), 3) Equivalent Porous Medium (EPM), 4) Double Continuum (DC) and 5) Combined Discrete-Continuum (Hybrid) (CDC) (Teutsch and Sauter, 1991; Kovács and Sauter, 2007) (see Figure 2.25).

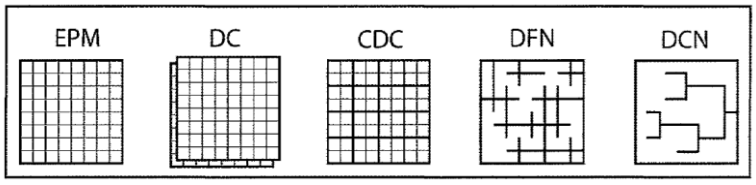

Figure 2.25: Classification of distributed karst modelling approaches (Kovács and Sauter, 2007).

The FEM has been applied in water resources groundwater flow modelling since the 1960s. The method derives its power from the fact that it uses a very general technique for the evaluation of spatial gradients in any direction at any point within the flow domain (Narasimhan and Witherspoon, 1982). The first application of the FEM for karst groundwater flow modelling presumably dates back to 1973 and relates to the Areuse basin (Kiraly, 1998). By using a 3-D finite element model, Kiraly, et al. (1995) confirmed that the proportion of the infiltration drained by the epikarst greatly influences the general shape of the spring hydrograph and its baseflow component. By doing so, the model suggests that the epikarst enhances concentrated infiltration so that diffuse groundwater recharge is short-circuited.
A common software for modelling groundwater flow and transport using the FEM is the Finite Element subsurface FLOW system (FEFLOW) (DHI-WASY, 2012). FEFLOW was applied by Dafny, et al. (2010) in the groundwater basin of Yarqon-Taninim to quantify the flow regime, the groundwater mass balance and the aquifer hydraulic properties. The karst system includes phreatic and confined parts, shallow and deep sub-aquifers, stratified and relatively-homogeneous sub-basins, saline and fresh water bodies, as well as stagnant and fast-flowing groundwater regions. However, there is no distinction between concentrated flow and diffuse flow, instead, hydraulic conductivities are homogeneously applied to single regions.
A distinction between concentrated flow and diffuse flow was made in the context of modelling groundwater flow in the conduit-dominated Santa Fe river basin and the Woodville Karst Plain in northern Florida using FEFLOW (Meyer, et al., 2008). Conduit flow paths were simulated by using the 1D discrete feature elements that were mixed with the porous matrix elements for diffuse groundwater flow. The matrix system was sub-divided into four different conductivity zones.

Early groundwater flow models based on the FDM date back to Rushton and Wedderburn (1973), Trescott and Larson (1976) or Teutsch (1989).
Since 1984, MODFLOW has probably been the most common software used to solve the equations of the FDM for groundwater flow, with MODFLOW-2005 being the latest version (Harbaugh, 2005).
Based on tracer tests and time series analysis using autocorrelation and cross-correlation from single events, Mayaud, et al. (2014) used a single-continuum FDM (MODFLOW) and its wetting capability package to model intermittent catchment overflow between two springs of the Lurbach system. Two parallel lines of high hydraulic conductivity representing the fast-flow were embedded in a

low permeability matrix. The results suggest that the single-continuum approach is weak in reproducing turbulent conduit flow. For this reason, Mayaud (2014) integrated non-linear flow using the Forchheimer equation.

The Conduit Flow Process (CFP) package for MODFLOW-2005 allows simulating turbulent groundwater flow conditions by, 1) coupling the traditional groundwater flow equation with formulations for a discrete network of cylindrical pipes (Mode 1), 2) inserting a high-conductivity flow layer that can switch between laminar and turbulent flow (Mode 2), or 3) simultaneously coupling a discrete pipe network while inserting a high-conductivity flow layer that can switch between laminar and turbulent flow (Mode 3) (Shoemaker, et al., 2008). Example studies using the CFP can be found in Gallegos, et al. (2013) or Hill, et al. (2010).

Reimann, et al. (2011) simulated laminar and turbulent flow using a single-continuum model, i.e. conduit-type flow in continuum cells (CTFC) (Figure 2.26). The authors used the enhanced single-continuum model to investigate the significance of turbulent flow on the dynamic behaviour of karst springs. The results are compared to a hybrid model in which a conduit is embedded into a low permeability fractured porous matrix. This demonstrated that the dual-porosity flow components of karstic aquifers can be simulated within a single continuum where karst conduits are represented by highly conductive model cells. CTFC successfully simulates spring discharge of a conduit system embedded within a fractured porous medium matrix.

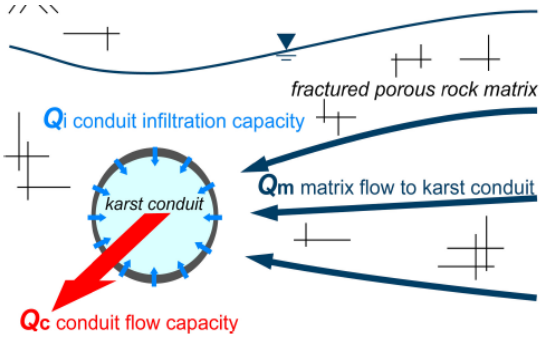

Figure 2.26: Karst conduit embedded in the matrix (Reimann, et al., 2011).

Doummar, et al. (2012) estimated groundwater flow dynamics and spring discharge of the karst catchment of the Gallus spring using the FDM in MIKE SHE (DHI, 2007) for a period of 10 years. The highly conductive zone (representing conduits) and the fissured matrix are represented by individual continua.

In karstic regions, groundwater-surface water exchange plays an important role, especially in low lying catchments as they exist in Ireland. Sutton, et al. (2015) applied an EPM approach using a two-dimensional (2D) transient groundwater flow model (MODFLOW) to quantify the exchange between the Suwannee River and the karstic upper Floridan aquifer. Rivers are represented using MODFLOW's River Package, which calculates the volumetric exchange of river water and

groundwater as a function of the head difference between the water table and the specified river stage, as well as the conductance of the river bed sediments.
The most recent attempt to realistically represent the conduit domain embedded in a matrix flow domain was provided through MODFLOW Unstructured Grid (USG) Combined Linear Network (CLN). The CLN approach allows integration of a vectorised conduit independently of the unstructured grid (cell) (Panday, 2017).

Diffuse groundwater flow within FD models is usually incorporated by own continua of low conductivity cells that may be in exchange with a neighbouring high conductivity cells representing a conduit. An exception is the above mentioned CTFC approach in which turbulent flow and diffuse flow are combined within a single continuum, or the USG CLN approach that allows integrating vectorised conduits to be integrated into the grid domain.

Discrete conduit networks (DCNs) differ to the abovementioned approaches in a way that DCNs solve groundwater flow equations along discretely defined networks of conduits and pipes rather than in a continuum domain.
An early approach similar to the DCN method was applied by Thrailkill (1974) modelling the Sinkhole Plain aquifer in Kentucky. Groundwater flow in the rectangular grid of pipes is modelled either as laminar and or turbulent. Differences between the two flow domains are too small to allow the mode of flow in the aquifer to be distinguished using observational data.
A steady-state discrete conduit network model for the Hölloch cave was developed by Jeannin (2001) combining observed heads, discharge rates, conduit sizes and conduit lengths. The model only represents the conduit flow domain without a diffuse flow component. The Louis formula is used to calculate head losses in those conduits and turbulent flow in the conduits is related to the Darcy-Weisbach equation. In a network of conduits with loops enclosed one into another, two Kirchhoff equations must be solved additionally, forming altogether a non-linear system that was solved iteratively. As a result, flow velocity and discharge in some conduits do not increase linearly with the total discharge flowing through the system. The model suggests that storage effects (in matrix and in conduits) are of minor importance. The use of the Louis formula was justified by Jeannin and Maréchal (1995) who reviewed applied formulae that are used to model the head loss in relation to groundwater flow in karst conduits. For flow in the vadose zone, the Strickler formula underestimates the loss of head because it takes into account only friction losses. For the phreatic zone, head losses are less important, yet, the Louis formula gives correct values for the case study.
Gill (2010) and Gill, et al. (2013a) used the urban drainage software InfoWorks CS (Figure 2.27) to model the conduit dominated karst catchment and turloughs of the Gort Lowlands in the west of Ireland.

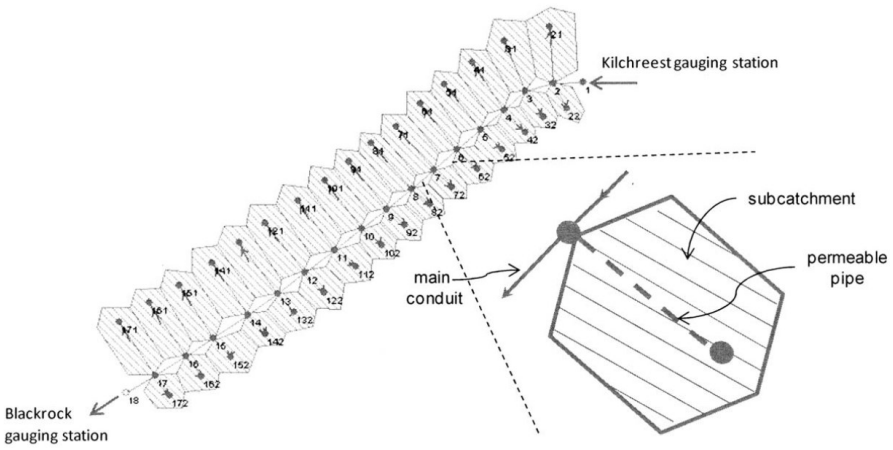

Figure 2.27: InfoWorks CS model outline: sub-catchments draining diffusely via GIM into a central conduit (Gill, et al., 2013a).

The pipe model resembles the course of major conduits and losing streams that connect a series of turloughs considering open channel and pressurized flow hydraulic conditions. The governing model equations are the Saint-Venant equations of conservation of mass and momentum while the conveyance function was based on the Colebrook-White equation. Diffuse groundwater recharge and Darcian flow through the epikarst via the matrix and fracture flow was considered using a combination of the Ground Infiltration Module (GIM) and a network of permeable pipes. However, this model was never calibrated against estimated flow components or even observed discharge.

Using this model outline and applying the same principles, McCormack (2014) and McCormack, et al. (2014) quantified the nutrient dynamics through the karst network and estimate SGD into Kinvara Bay.

Based on the aforementioned principle, Chen and Goldscheider (2014) applied a conduit model using the sewer system Storm Water Management Model (SWMM) to simulate highly variable flow in a folded alpine karst aquifer system. The model integrates coupled reservoirs representing a lumped system of recharge, storage and transfer of water in the epikarst and the unsaturated zone. Groundwater flow in the vadose zone is modelled as slow-flow and fast-flow. The unsteady flow in the conduits is solved using the Saint Venant equations. Friction slope for non-pressurized conduits is calculated using Manning's equation while the Darcy–Weisbach equation computes the friction loss for conduits with pressurized flow.

Until present, diffuse groundwater recharge in DCN models has been incorporated using either reservoirs that acts as, for example, an epikarst storage with certain drainage specifications, or using permeable conduits modelling laminar groundwater flow. The latter one has also been used to model slow-flow in the vadose zone.

Pipe network models have been proven to be an adequate tool in the context of Irish karst aquifers with their specifications of incorporating turloughs, surface water-groundwater interactions, partly low lying topography and exposure to coastal zones and the sea. To achieve the objectives of this research, InfoWorks is used to further improve modelling techniques towards incorporating diffuse recharge and flow components. For example, different recharge zones could be accounted for in the GIM, similarly to the approach taken by Bittner, et al. (2018).

2.7 Conceptual elements of an Irish karst aquifer

The abovementioned literature resources related to karst aquifers were synthesised to provide a conceptual model of a karst aquifer typical for Ireland (Figure 2.28).

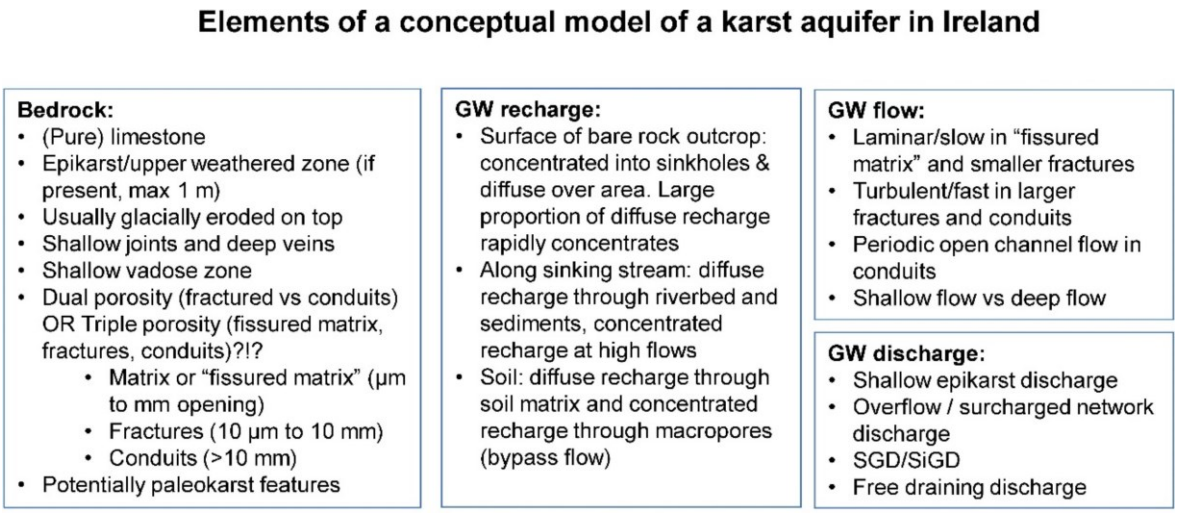

Figure 2.28: Elements related to a conceptual model for a karst aquifer in Ireland (GW = groundwater).

3. Study Sites

The research was carried out at three study sites located in different regions of Ireland. This chapter presents the three catchments of Ballindine, Manorhamilton and Bell Harbour, including the delineated catchment boundaries of all sites. Catchment delineation for each site is a result of this study to be presented in the Chapters 'Catchment Studies' and 'Bell Harbour'.

3.1. Ballindine

3.1.1. Study area

Ballindine spring is located in the south-east of the Co. Mayo (Figure 3.1). The spring discharge is continuously monitored by the EPA. In the past, the spring was used for public water supply, but today, the spring is disconnected from any water supply.

The spring is described as an overflow discharge type with the spring capture illustrated in Figure 3.2. Accordingly, discharge emerges from conduits starting at 48.8 masl where overflow into a small reservoir occurs. The discharging conduit is likely to be connected to the regional Claremorris fault, which seems to constitute a flow barrier and path for preferential dissolution not only impacting on sub-surface conduits but potentially also on the course of major streams, such as the River Robe (Figure 3.4).

The spring catchment is considered as a lowland type with altitudes ranging between 48.7 masl at the EPA gauging at the spring in the south-west and up to approx. 65 masl in the north-east. The topography of the catchment is very flat and land use comprises a western fraction of the town of Ballindine, individual housing and pasture or grassland.

There is a relatively dense network of streams and artificial drainage channels in the area. It must be assumed that these artificial surface water features interact with underlying aquifers. In fact, these drainage channels are conceptualised as additional outflow from the delineated catchment, yet, the quantity is unknown, and is very difficult to estimate.

The Robe River is the main stream that flows north-south on the northern side of the catchment. The discharge of Ballindine spring flows into the Robe River adding approx. 1% to the total stream flow. The confluence is measured at the station Christina S BR. (53.6847ºN, -8.9930ºW) at 44.2 masl (Figure 3.1).

The catchment shows moderate karstification on the land surface or topography. In fact, there is no exposed bedrock, except at parts along the bed of the River Robe. There are no known karst features except topographic depressions that may indicate dissolution of the bedrock below.

Figure 3.3 shows the soil associations as delineated by Teagasc and Cranfield-University (2014) in 1:250,000 summarised in Table 3.1. Almost the entire catchment and surrounding area is covered by soil association '1030a' which is described by "luvisols, surface water gleys and stagnic brown earths on drift with siliceous stones, with inclusions of groundwater gleys" (Creamer, et al., 2014).

Luvisols are soils with clay-enriched sub-soils. The clay content is higher in the sub-soil than in the topsoil. The parent material includes unconsolidated materials such as glacial till (IUSS, 2015). Brown earth soils are described as relatively young or soils with limited profile development (Creamer, et al., 2014). Gleysols are affected by underwater conditions resulting in reducing conditions (IUSS, 2015). Hence, gleysols indicate a very shallow unsaturated zone, if at all present.

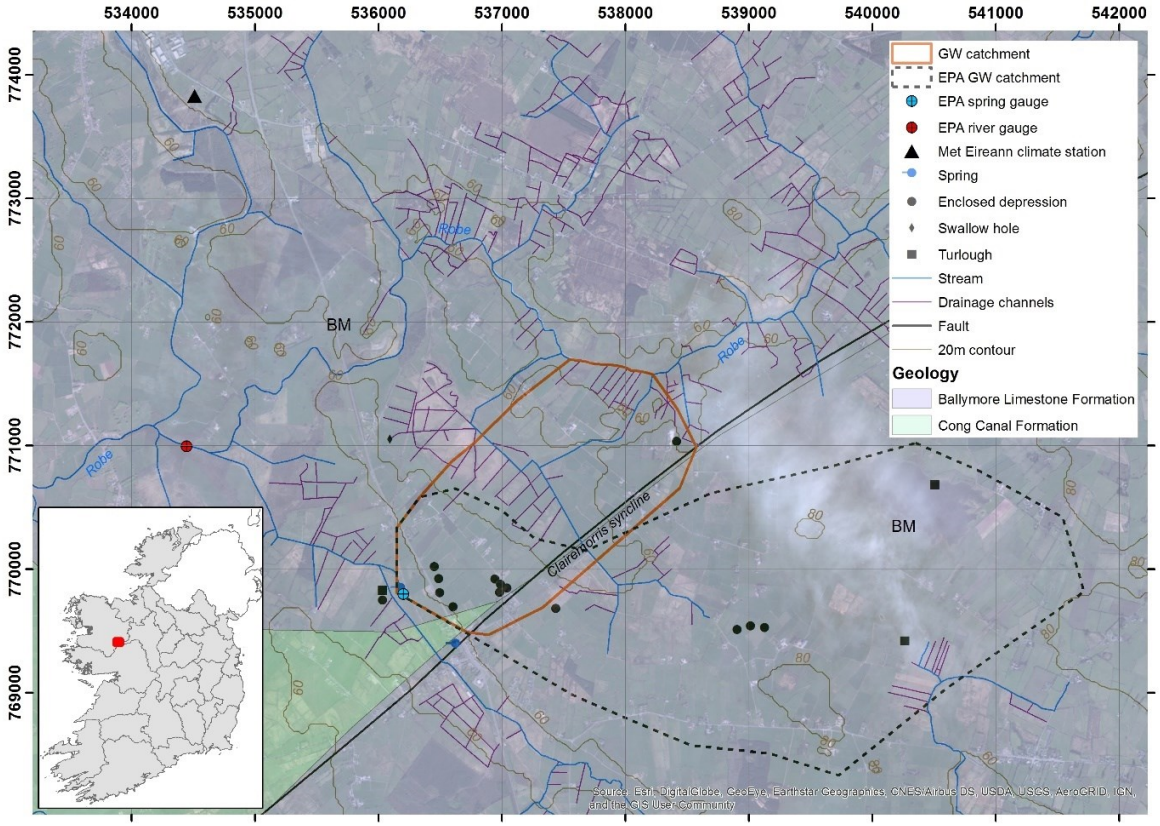

Figure 3.1: Geology of the Ballindine groundwater catchment and location of the MetEireann climate station Claremorris.

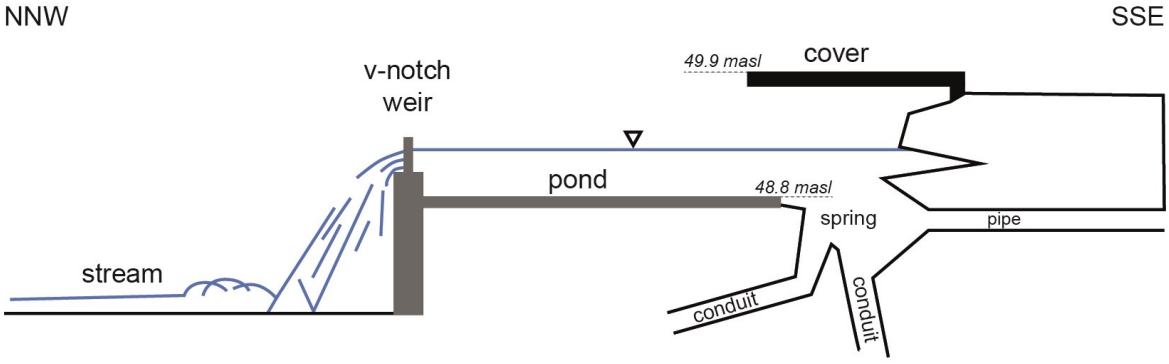

Figure 3.2: Schematic of Ballindine spring, illustrated after Price (1999).

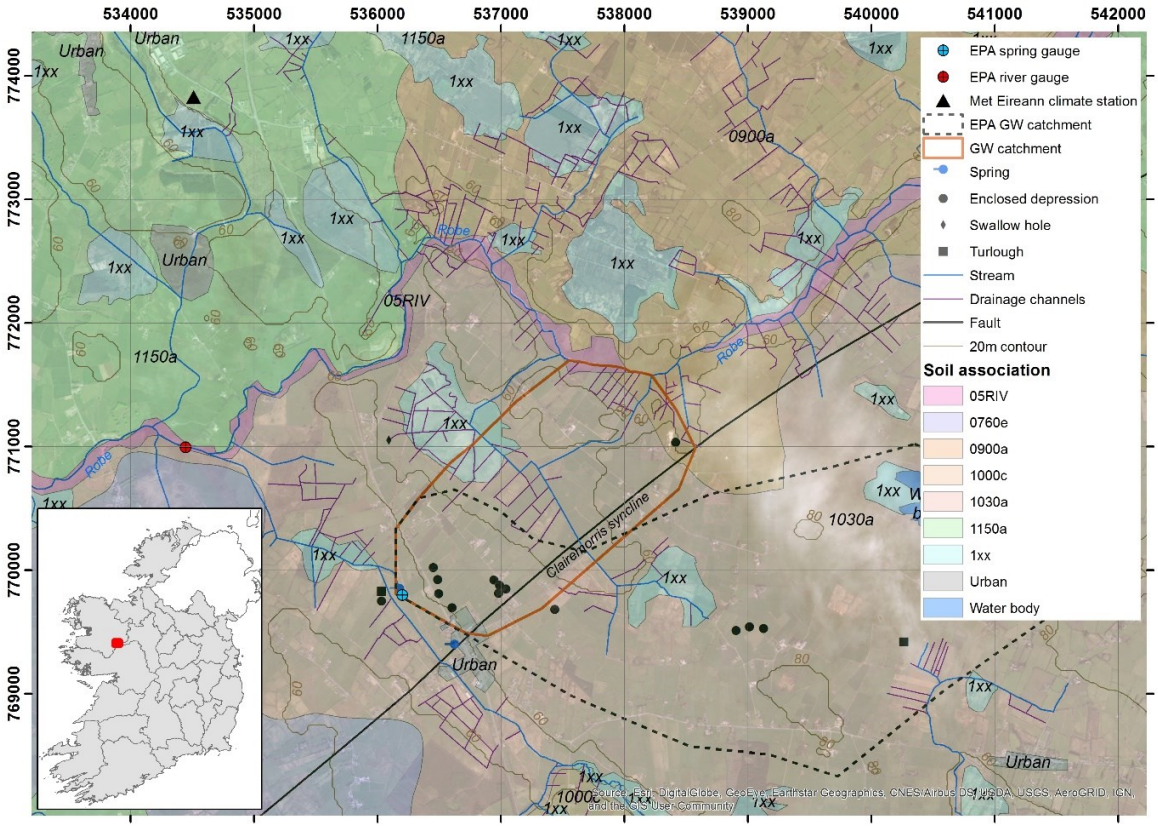

Figure 3.3: Soil cover in the area of Ballindine spring. For description of soil associations see Table 3.1.

Table 3.1: Description of soil associations occurring in the area of Ballindine spring (Creamer, et al., 2014).

Soil association	Description
05RIV	Alluvial and drained alluvial soils on river floodplain with base rich and medium to coarse textures
0760e	Humic surface water gleys and humic groundwater gleys, on drift with limestones, and peat
0900a	Brown podzolic soils with groundwater gleys on drift with siliceous stones and inclusions of podzols and brown earths
1000c	Luvisols associated to histic and humic groundwater gleys and calcareous brown earths, on drift with limestones and basin peat
1030a	Luvisols, surface water gleys and stagnic brown earths on drift with siliceous stones, with inclusions of groundwater gleys
1150a	Calcareous brown earths, brown earths and luvisols on calcareous gravels and on drift limestones, inclusions of rendzinas
1xx	Peat
Urban	Paved surfaces
Water body	Surface water

In the absence of any known swallow holes that would be locations for concentrated infiltration and given the ubiquitous soil cover, it must be assumed that all or almost all rainfall infiltrates diffusely.

As a result of this work (see Chapter '5.1. Ballindine'), it was concluded that the River Robe seems to exhibit a hydraulic influence onto the hydrograph of Ballindine spring. Hence, the previously established catchment boundaries delineated by the EPA assuming a size of 8.92 km^2 and crossing the Claremorris fault (EPA, 2011a) were rejected, and instead the catchment was delineated as illustrated in Figure 3.1 covering approx. 3.3 km^2. Accordingly, surface water-groundwater interaction is assumed to influence the aquifer of Ballindine along a stretch approx. 5.5 to 6.2 km upstream the gauging station Christina S BR. where the river bed of the Robe is elevated between 54.1 and 54.8 masl.

3.1.2. Geology and structure

There are no known boreholes inside of the catchment, and the area has only been geologically mapped to a very low level of detail. In fact, there is very little biostratigraphical information, which makes the dating uncertain, and further, the area is covered by thick drift which, together poses a challenge on mapping. Geological information covering the area originates from reconnaissance and compilation of open file mineral exploration data, summarised in Long (2005). Accordingly, the entire area is underlain by Viséan limestones that originated between the Brigantian and Chadian. According to the 1:50,000 geological bedrock information 'Bedrock 50k Northeastern block' of the Geological Survey Ireland (GSI), the area is underlain more specifically by the Ballymore Limestone Formation, which consists of dark fine-grained limestone and shale, and the younger Cong Canal Formation that is described as a thick-bedded pure limestone. The thickness of the limestones may reach several hundred meters.

Close to Ballindine spring, the less-defined southeast-dipping half-graben Claremorris syncline/fault is present (Figure 3.4).

The southern side of the Claremorris fault is constituted by the Slieve Dart fault, which runs approx. 8 km in parallel. Displacement of the lithological units across the fault is assumed, presumably acting as a flow barrier. It seems that the regional pattern of streams, including the River Robe and its tributaries, is influenced by the structural pattern (Figure 3.4).

Figure 3.1 shows the presence of many enclosed depressions within and around the catchment, but there are no known mapped swallow holes within the catchment.

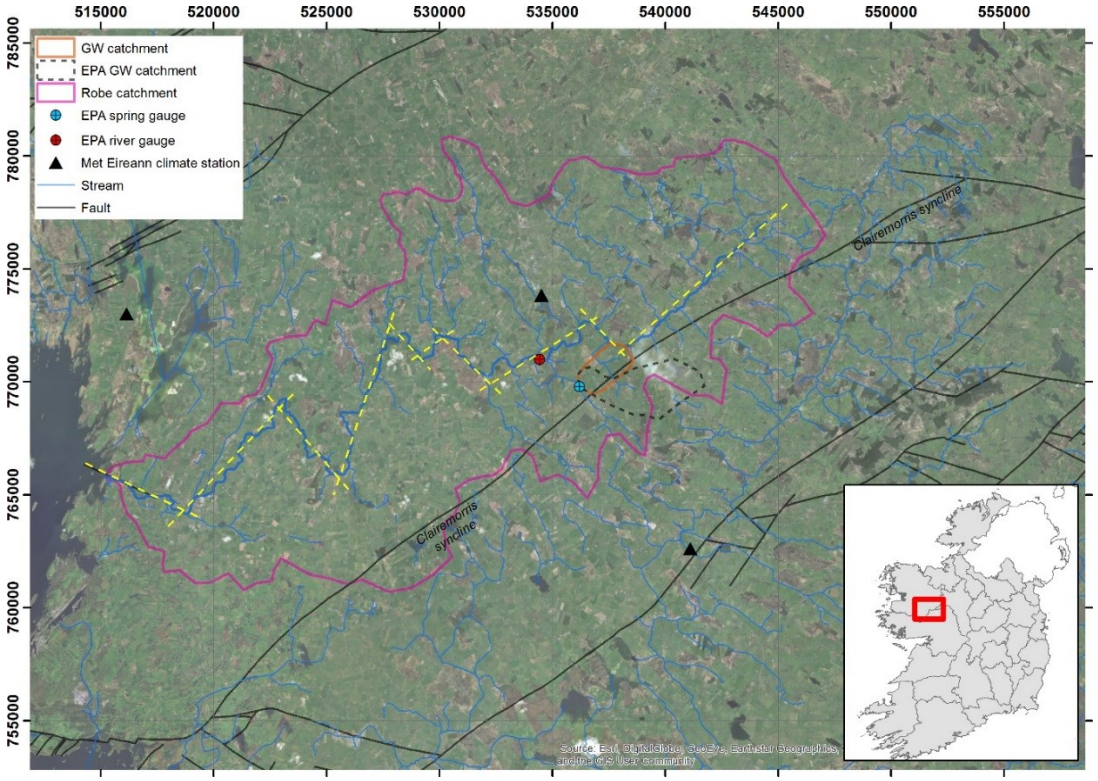

Figure 3.4: Delineated groundwater catchment of Ballindine spring in the context of the Robe River catchment and the Claremorris fault. The yellow dashed line highlights the structural pattern of the course of the River Robe.

3.1.3. Hydrogeology

Apart from spring discharge monitoring, no known continuous and systematic groundwater observation has been carried out within the catchment or close to its vicinity and so the hydrogeology remains fairly uncertain until today. It is assumed that the location of the spring is fault related, hence, that the Claremorris fault promoted groundwater flow circulation along it.

Further, the true extent of the catchment boundaries is difficult to delineate. The existence of numerous streams and channels complicates the understanding of the hydrogeology, as it must be assumed that groundwater-surface water interaction occurs along them.

The aquifer of Ballindine spring is constituted by the undifferentiated Viséan limestones (VIS), which is classified as conduit-dominated regional important aquifer (Rkc) (GSI, 2016) with a mean bulk transmissivity >500 m^2/d (Kelly, et al., 2015). Based on annual average groundwater level variations, the storativity (confined) and specific yield (drainable porosity, unconfined) for karstic aquifers in Ireland (incl. Rkc) is estimated at 1.1×10^{-4} and 1.4×10^{-2} respectively.

Bulk groundwater recharge is estimated to be 300 mm/year (EPA, 2011a). All recharge is autogenic. According to the GSI groundwater recharge map (Hunter Williams, et al., 2013), recharge coefficients [%] in the catchment range between 0 and 85 (Figure 3.5). Groundwater flow was

generally assumed to be from the east to the west (Price, 1999; EPA, 2011a) and yet, this would mean that groundwater crosses the Claremorris fault, which doesn't seem to be a favourable assumption.

In general, much of the recharge, flow and discharge dynamics of the study area relate to a relatively shallow zone at the top of the (potentially) deep aquifer, namely between 65 masl at the maximum land elevation within the catchment, >54.1 masl at the river bed where presumably river flow exfiltrates into the aquifer towards Ballindine spring, and 48.8 masl at Ballindine spring. Yet, deeper groundwater flow in the area is known to exists (e.g. at the Irishtown Group Water Scheme). Further, deeper groundwater flow may occur along the Claremorris fault towards Lough Mask and Lough Corrib, which is located 21 km west/southwest of Ballindine spring.

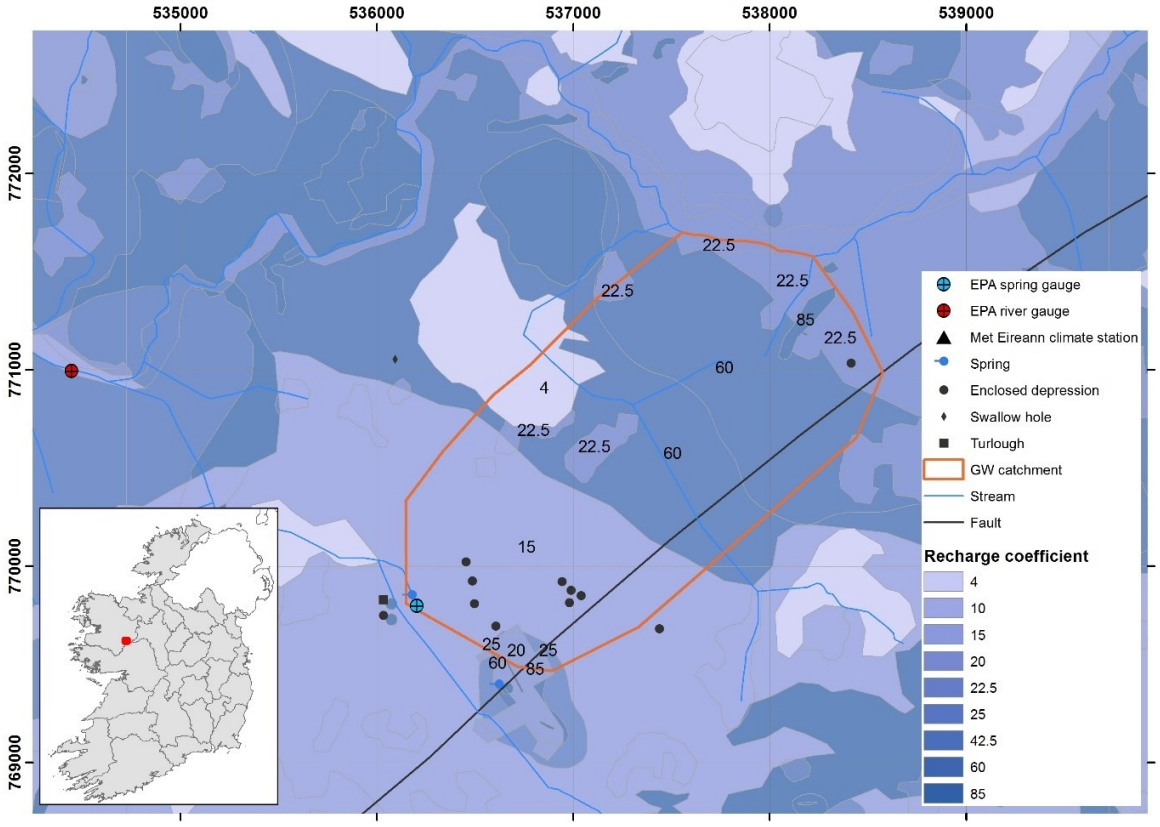

Figure 3.5: Groundwater recharge coefficients in the area of Ballindine spring.

A large proportion of the catchment is covered by low permeability subsoils with poor drainage characteristics. Accordingly, the overall bulk recharge coefficient is estimated at 38% of total rainfall (Table 3.2).

Table 3.2: Areal contribution of recharge coefficients and weighted recharge coefficient for the entire catchment.

Recharge coefficient [%]	Land cover	Area [km^2]	Percentage [%]
4	Peat	0.15	4.46
15	Low permeability subsoil	1.09	33.46
20	Made ground	0.04	1.14
22.5	Moderate permeability subsoil and overlain by poorly drained gley soil / low permeability subsoil	0.35	10.73
25	Peat	0.01	0.40
60	Moderate permeability subsoil overlain by poorly drained gley soil or well drained soil	1.59	48.88
85	Sand & gravels subsoil overlain by well drained soil / bare rock	0.03	0.94
38	**Weighted average / total**	**3.25**	**100.00**

3.2. Manorhamilton

Unlike the Ballindine catchment, there is a reasonable understanding of the catchment of Manorhamilton as a result of previous studies conducted as well as the site investigations undertaken in this research.

3.2.1. Study area

The groundwater catchment of Manorhamilton spring is located in the 'Yeats Country' in the north of Ireland, Co. Leitrim (Figure 3.6).

The spring catchment is considered as an upland-lowland type with altitudes ranging between 112 masl at the EPA gauging station at the spring in the east as high as approx. 343 masl at Mt Leean (392 masl) in the west. The topography of the catchment is shaped by rounded or hummocky hills with grassland, covering largely chert-free forms of limestones occurring as mudbanks (MacDermot, 1996).

The catchment is highly karstified including many swallow holes as well as minor springs within the catchment. Based on tracer tests, it appears that minor springs may act as rather shallow epikarst springs, as it was interpreted to be the case with the 'minor spring' in Figure 3.7.

Initially, the boundaries of the catchment were delineated according to topography and geology with an estimated size of 1.95 km^2 provided by (EPA, 2011b). Tracer tests conducted within the framework of this research suggest that the catchment boundaries cover an area of approx. 2.4 km^2. Further, reservoir modelling and water balances suggest that the catchment covers an area of 3.3 to 4.3 km^2. Finally, a size of 3.6 km^2 was applied in this study.

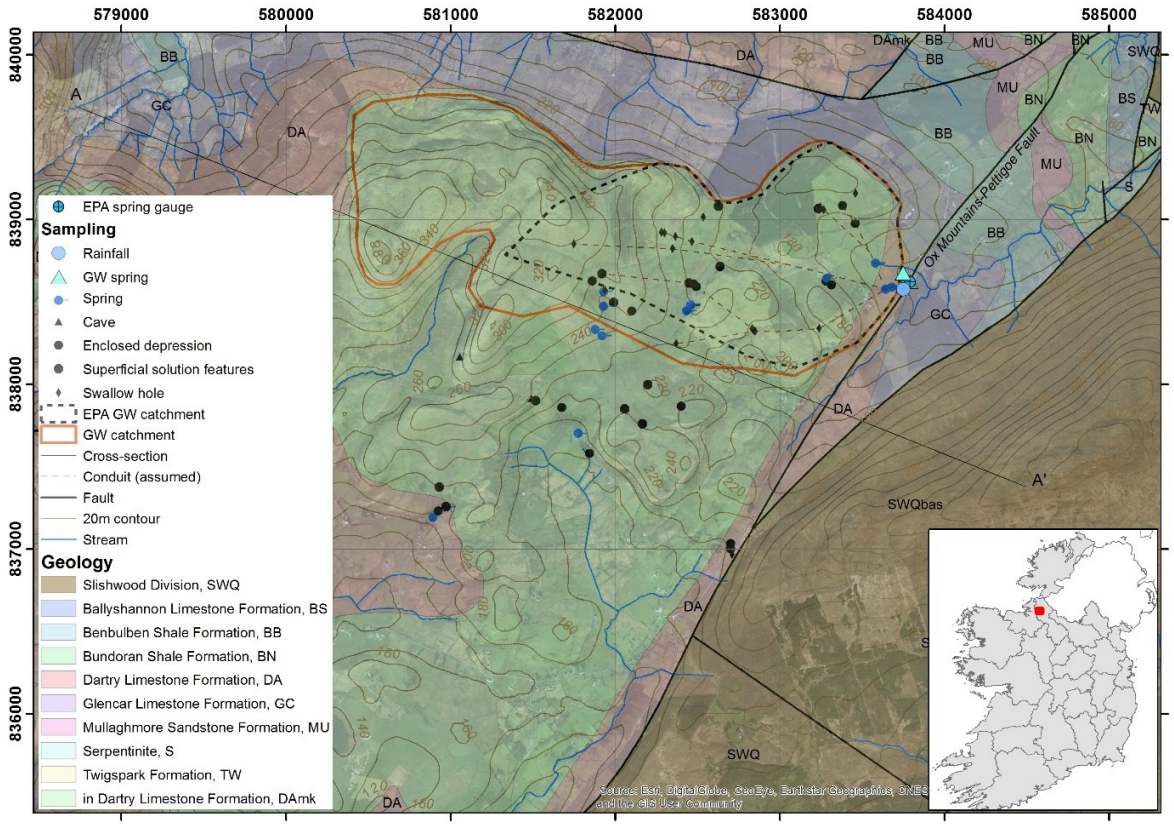

Figure 3.6: Geology and sampling locations in the groundwater catchment of Manorhamilton (3.6 km^2).

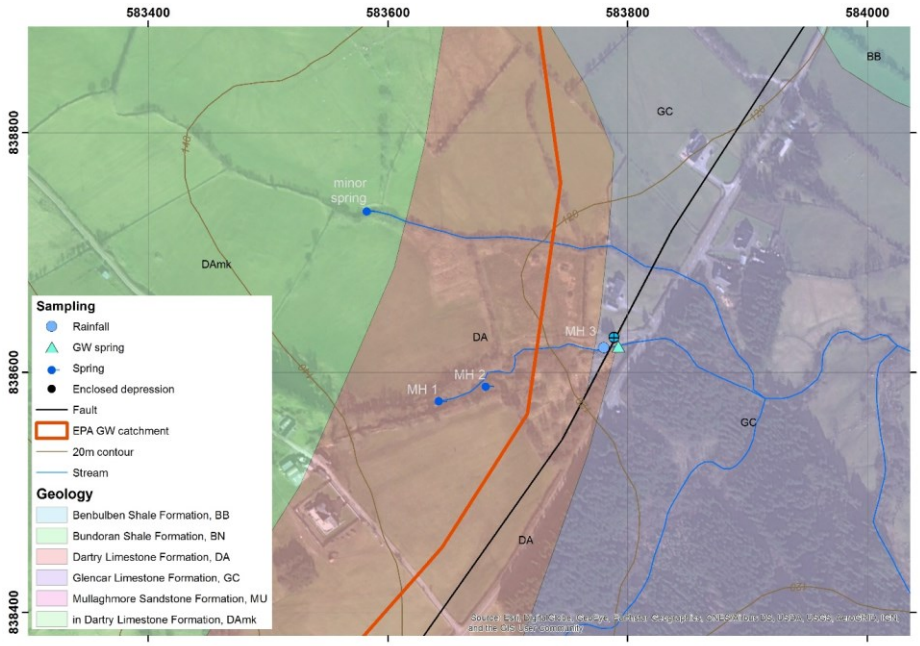

Figure 3.7: Location of the EPA gauging station (MH3), the two springs of Manorhamilton (MH1 and MH2) and a minor spring.

Figure 3.8 shows the soil associations as delineated by Teagasc and Cranfield-University (2014) in 1:250,000. The three associations describing the cover are ‘peat’, ‘rock’ and “rendzinas and decalcified lithosols on outcropping limestone, luvisols and brown earth associated with limestone bedrock and peat“. The thickness of soil cover ranges from absent where bare rock crops out to relatively shallow (~<1 m) in the lower parts of the catchments.

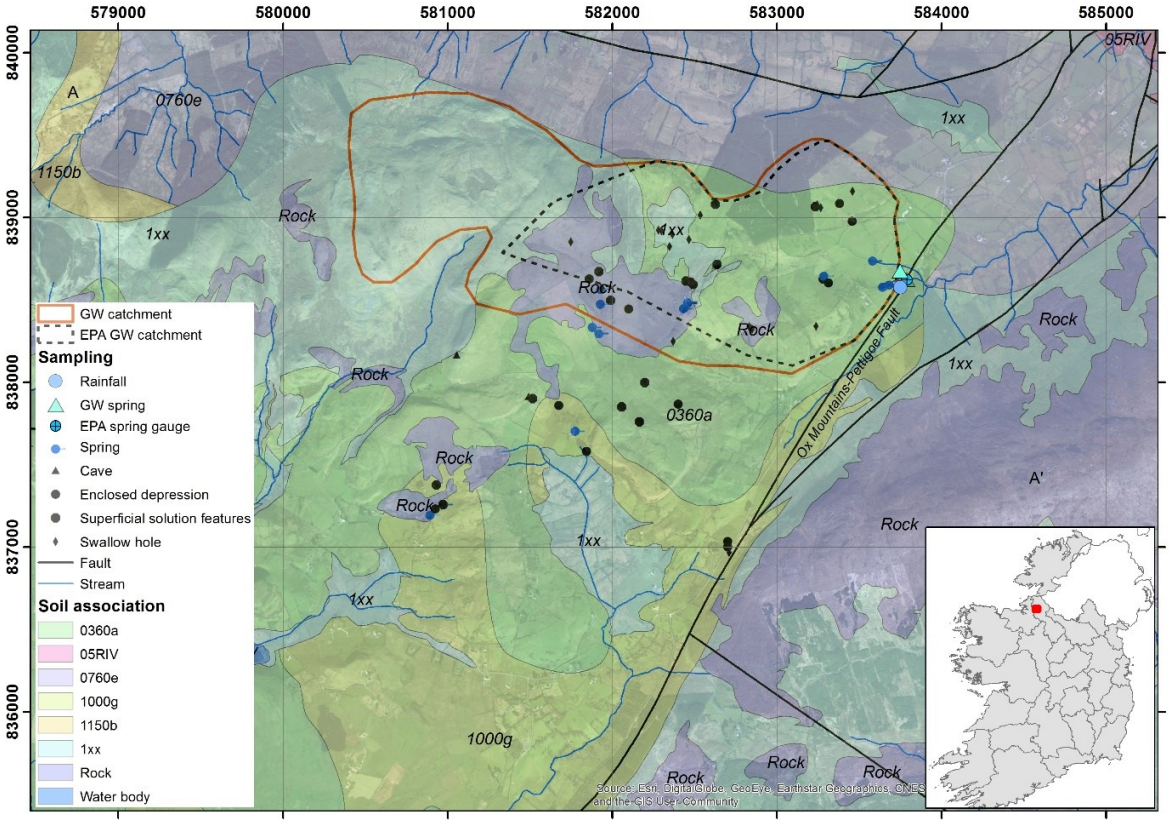

Figure 3.8: Soil cover in the area of Manorhamilton spring. For description of soil associations see Table 3.3.

Table 3.3: Description of soil associations occurring in the area of Manorhamilton spring (Creamer, et al., 2014).

Soil association	Description	Cover	
		km²	%
0360a	Rendzinas and decalcified lithosols on outcropping limestone, luvisols and brown earth associated with limestone bedrock and Peat	1.32	37.0
05RIV	Alluvial and drained alluvial soils on river floodplain with base rich and medium to coarse textures		-
0760e	Humic surface water gleys and humic groundwater gleys, on drift with limestones, and peat	0.14	4.0
1000g	Heavier textures in the soils of this association. Association with luvisols, groundwater gleys and calcareous brown earths, on drift with limestones		-

1150b	Calcareous brown earths and luvisols associated with rendzinas and decalcified lithosols, on limestones bedrock		-
1xx	Peat	1.49	42.0
Rock	Rock outcrop	0.60	17.0
Water body	Surface water		-

In the past, Manorhamilton spring was used for public water supply. In fact, there are two springs, which are both captured, and the confluence has been monitored by the EPA. The major discharge (called MH1) occurs at 122 masl and the minor discharge (MH2) is discharged at 118 masl (Figure 3.7). The monitoring station (MH3) is located at 112 masl. The linear distance between MH3 and MH2 is 45 m, and between MH2 and MH3 the linear distance is 113 m. Discrete analysis for d18O and d2H of MH1 and MH2 (Figure 3.9) show that the values of measured parameters can be considered to be the same for both springs, which suggests that they drain the same aquifer. Therefore, throughout this work, analyses are referred to MH3 as Manorhamilton, including the contribution from MH1 and MH2.

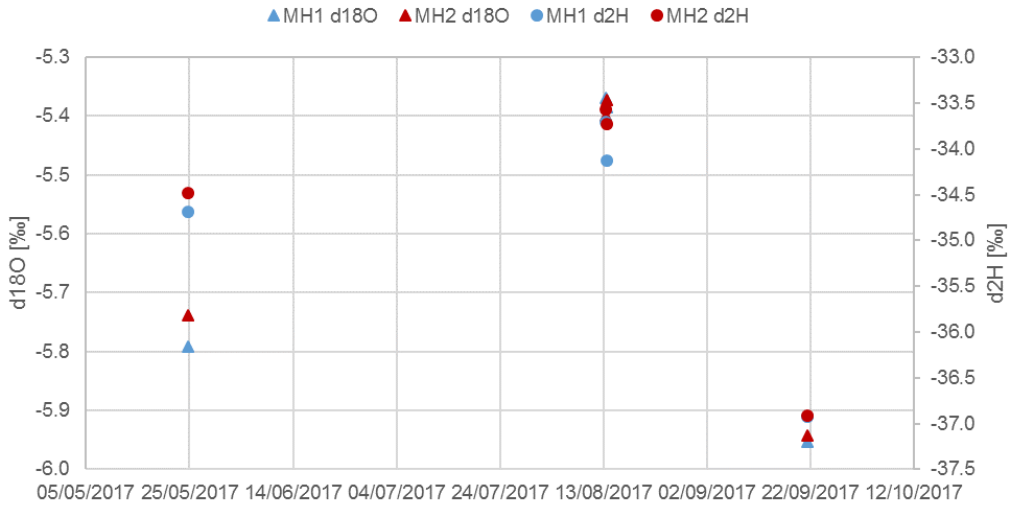

Figure 3.9: d18O and d2H [‰] of four groundwater samples of MH1 and MH2.

3.2.2. Geology and structure

There are no known boreholes within or close to the catchment.

The catchment, as well as the region of Sligo-Leitrim was glaciated by ice of different domes during the last ice age, with ice flow generally from the southeast to the northwest. At the maximum extent of glaciation, the thickness of the ice sheet was estimated to be 650 m. The movement of the ice sheet caused the bedrock to become ice-moulded and ice-polished, as well as transporting erratics. Further, existing valleys were shaped into classic straight U-shaped glaciated valleys, such as the ‘Glencar valley’ adjacent in the north to the catchment. Drumlins are indicators for ice flow extending in parallel in the direction of ice flow.

The entire catchment is underlain by Carboniferous limestones, i.e. the 'Upper Limestones' originating from a period of shelf sedimentation with local development of mudbank limestones of Holkerian and Asbian age, namely the Dartry formation (DA), and specifically Mudbank Limestones (mk) to from the in Dartry Limestone formation (DAmk) (Figure 3.6).
The dominant facies of the Dartry Limestone formation is a massive to thick-bedded, mostly very fine-grained and dark wackestone, with bedding by bands of nodules of irregular chert, sometimes forming 50% of the rock.
Mudbanks occur within the Dartry Formation at its base in contact with the Glencar Limestone formation. This is the case in the study area, which can be regarded as the base of the Dartry formation.
Within the Mudbank Limestones (mk), two facies are present, i.e. a) a 'core' bank facies, and b) a 'detrital' facies. The core facies occupies the massive-bedded, geometrical core of the banks and the thick-bedded and often steeply-dipping bank margins. The core consists of lime mudstone with filled-in cavities seldom longer than 5 cm. The detrital facies occurs as draping cover beds and as horizontal peripheral beds consisting mainly of coarse, well-bedded crinoidal calcarenites. The thickness of the Mudbank Limestones ranges between a couple of meters and 120 m or more. The dip of the formation is gently towards south-south/southwest (Figure 3.10).
In the east and north, the catchment is bounded by the Glencar Limestone formation (GC), which may reach 150 m in thickness. The formation contains impure limestone beds, and alternations of calcareous shales and limestones ranging between argillaceous calcisiltites to very fine calcarenites. Individual composite limestone beds are present, ranging between 10 and 20 cm thickness with an upper and lower subdivision of dolomitic laminated limestones.

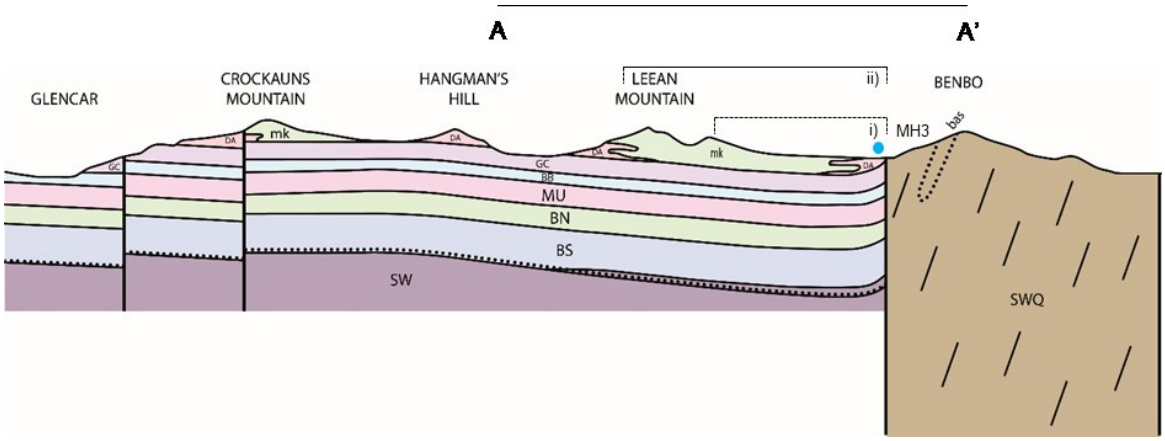

Figure 3.10: NWW-SEE (left to right) geological cross-section A-A', vertical scale 1.67 times horizontal scale. Modified after MacDermot (1996) illustrated in Figure 3.6, including catchment boundaries according to EPA (2011b) (i) and catchment boundaries as delineated in this study (ii).

The regional geology is very variable including many faults. The overall pattern of faulting is a sinsitral northeast – southwest shear couple with roughly north-northeast – south-southwest sinistral synthetic strike slip faults and northwest – southeast dextral antithetic strike slip faults. Major

northeast-southwest faults represent reactivation of pre-Carboniferous lines of weakness and syn-depositional faults controlled the generation of transtensional basins, for example the North Ox Mountains Fault (NOMF).
The catchment is bound to the east by the Ox Mountains-Pettigoe Fault (OMPF) and fine-grained granoblastic psammitic paragneiss (SWQ) of Proterozoic age (Figure 3.10) (MacDermot, 1996). Figure 3.6 shows the presence of many karst dissolution features such as depressions and swallow holes, the latter ones verified in the field.

3.2.3. Hydrogeology

There are no known wells in the catchment or in close vicinity.
The aquifer of Manorhamilton springs is constituted by the Dartry limestone formation (DAmk) which sits on top of the low-permeable Glencar Limestone formation (GC), both dipping gently to the south, south southwest (Figure 3.10). In the wider context, the occurrence of the springs of Manorhamilton is related to the presence of the OMPF, while locally the discharge location is attributed to the contact between the Dartry formation and the Glencar formation.
As a result of tracer tests, swallow holes have proven to rapidly concentrate water towards the saturated zone and spring outlet. Groundwater flow was proven to follow more or less the topography and dip, i.e. from north/northwest to south/southeast.
According to the GSI classification, the aquifer is classified as conduit-dominated regional important aquifer (Rkc) (GSI, 2016) with a mean bulk transmissivity >500 m^2/d (Kelly, et al., 2015). Accordingly, groundwater flow follows a hierarchical network of larger and large conduits approaching the spring. This general description was confirmed by tracer tests in the catchment.
Again, based on annual average groundwater level variations, storativity (confined) and specific yield (unconfined) for karstic aquifers in Ireland (incl. Rkc) is estimated at 1.1×10^{-4} and 1.4×10^{-2} respectively.

Bulk groundwater recharge is estimated to be 400 mm/year (EPA, 2011b), all of which is autogenic. According to the GSI groundwater recharge map (Hunter Williams, et al., 2013), recharge coefficients [%] in the catchment comprise 22.5, 60, and 85 (Figure 3.11). Groundwater recharge is concentrated at point locations (swallow holes) and diffuse over the catchment.
17.5% of the catchment has been assigned a recharge coefficient of 22.5 related to peat or till overlain by poorly drained gley soil (Table 3.4). 13.6% of the catchment is covered by till overlain by well drained soil resulting in a recharge coefficient of 60. 69.0% of the catchment is covered by outcropping rock, resulting in a high recharge coefficient of 85. Altogether, applying a weighted average, the bulk recharge is estimated at 71% of rainfall.

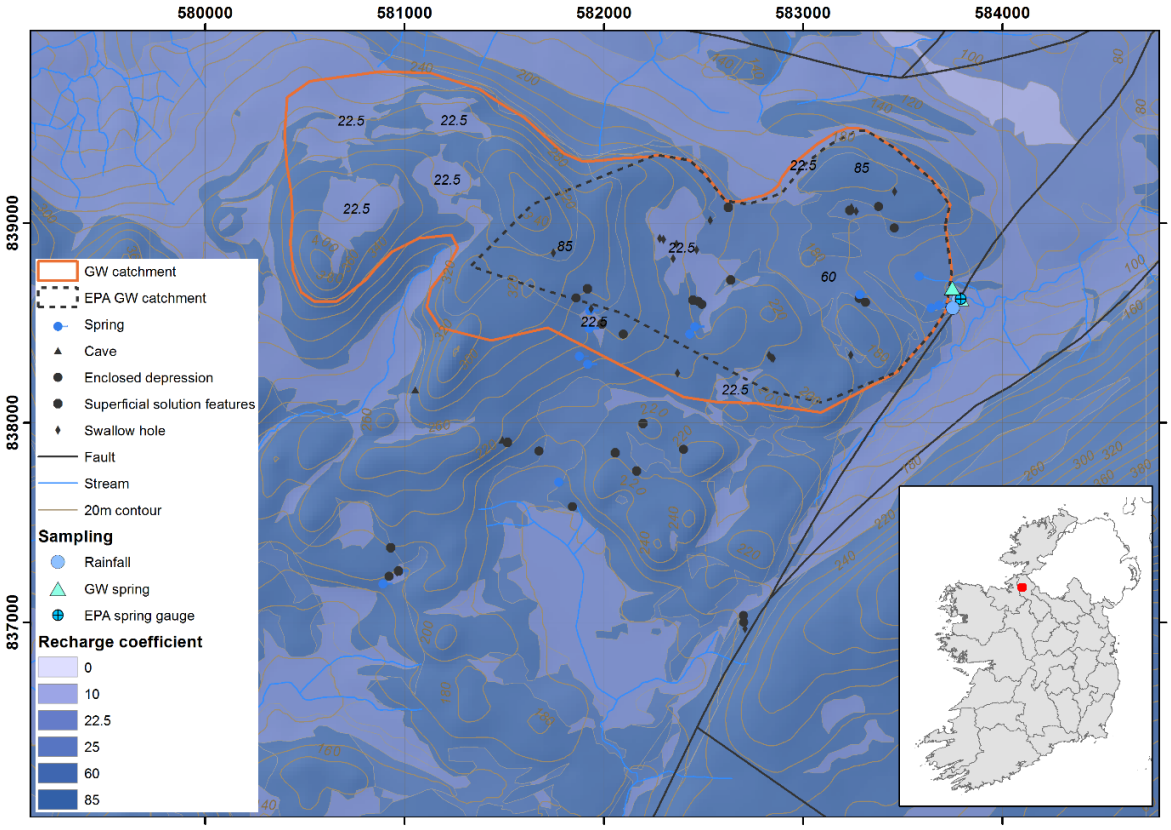

Figure 3.11: Groundwater recharge coefficients in the area of Manorhamilton spring.

Table 3.4: Areal contribution of recharge coefficients and weighted recharge coefficient for the entire catchment.

Recharge coefficient [%]	Land cover	Area [km²]	Percentage [%]
22.5	Till overlain by poorly drained gley soil / peat	0.6	17.47
60	Till overlain by well drained soil	0.5	13.58
85	Bare rock	2.5	68.95
71	**Weighted average / total**	**3.6**	**100.0**

3.3. Bell Harbour

The karst system of Bell Harbour is the catchment that has received the most investigation during these studies which was essential given its proven complexity.

3.3.1. Study area

The groundwater catchment of Bell Harbour (Figure 3.12) forms the north-eastern part of the limestone Burren Plateau located in the west of Ireland. The limestone massive of the Burren, including the upland catchment of Bell Harbour, is described as a temperate glaciokarst landscape, which has been subject to repeated glaciation during the Pleistocene showing features typical of

glaciation such as ice-plucked crags, scoured rock surfaces, limestone pavements and erratic boulders (Simms, 2014). Today's morphology of the catchment and the bay may partly be the result from glacial erosion of the last ice advance whose direction is pretty much parallel to the bay (Drew, 1990).

The catchment was progressively delineated throughout this research, considering previous tracer tests conducted in the region (Drew, 2003) as well as using a set of methods, including water balances, artificial tracer tests, numerical modelling and estimating SiGD over more than two years. While the eastern and western boundaries are constituted by sharp escarpments and the northern boundary intersects with the shore, the extent of the catchment to the south is more uncertain. Prior to this work, no artificial tracer injected in the southern part of the catchment was recovered in Bell Harbour Bay. The average catchment size is defined to cover an area of 50 km^2 based on the topographical extent and previous studies (Perriquet, et al., 2014; McCormack, et al., 2017), but as indicated by Bunce and Drew (2017), it may extend more towards the south. As a result of this work, the underground river in Poll Gonzo (PG, Figure 3.12) was traced to Galway Bay (Schuler, et al., 2018b), hence, the southern boundary was moved south of PG to cover an area of 55.6 km^2. In addition, it is believed that the polje-like feature Carron adds at least seasonally contribution towards flow to the north, adding an area of 5.5 km^2 to the south.

The catchment is intersected by multiple valleys, with elevations ranging between sea level in the north and up to 320 masl at Slievecarran in the east. Along the slopes the bare outcrop is uncovered showing high degrees of karstification. Due to the high degree of karstification, surface water features are limited to short reaches of ephemeral streams, drainage from adjacent non-carbonate rocks and turloughs (Drew, 1990). Within the catchment there are two turloughs (Figure 3.12), a) Luirk (T2) in the Lower Burren formation and b) Gortboyheen (T1) within the Maumcaha formation. The topography divides the catchment into outcrop as opposed to areas covered by soil bare. Within the valleys, relatively deep soil cover (up to 1 to 2 m) on outcrops of the limestone unit is attributed to Holocene weathering forming nowadays an erosion-resistant clay-rich soil (Moles and Moles, 2002). Figure 3.13 shows the soil associations as delineated by Teagasc and Cranfield-University (2014) in 1:250,000. The descriptions of the all soil associations are given in Table 3.5. Further, the absolute sizes and relative proportions of soil associations occurring within the delineated catchment of Bell Harbour (without the Carron sub-catchment) are listed.

The proportion between bare rock and soil cover was quantified as 64:36. The 36% of soil cover is made up by three soil associations: a) 'Rendzinas and decalcified lithosols' (0360a) in the south, b) 'luvisols associated with surface water gleys' (1000a) in the west, and c) 'calcareous brown earths, brown earths and luvisols' (1150c) in the north.

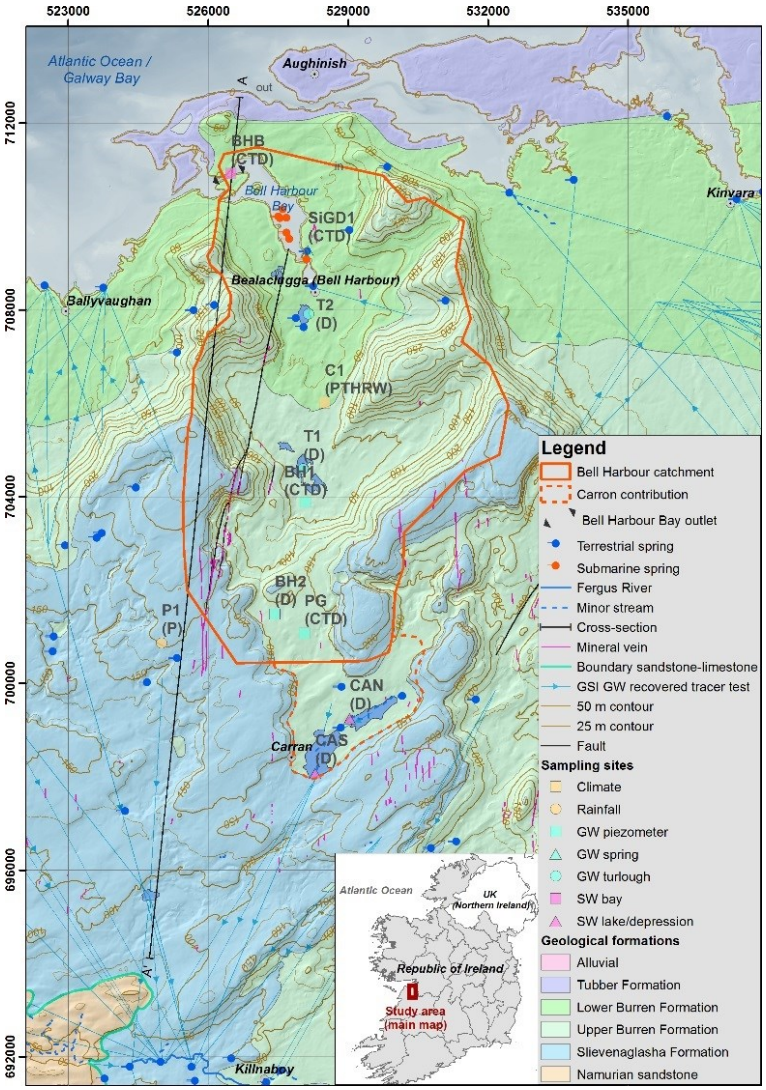

Figure 3.12: Geology and sampling locations in the groundwater catchment of Bell Harbour.

Table 3.5: Description of soil associations occurring in the area of Bell Harbour (Creamer, et al., 2014).

Soil association	Description	Cover	
		km²	%
1xx	Peat		-
0360a	Rendzinas and decalcified lithosols on outcropping limestone, luvisols and brown earth associated with limestone bedrock and peat	9.14	17.00
05LAK	Alluvial and drained alluvial soils of fine textures and base rich		-
0760c	Surface-water gley and luvisols in clayey lowlands on drift with limestones with inclusions of calcareous brown earth		-
1000a	Luvisols associated with surface-water gleys, stagnic brown earths and calcareous brown earths, on drift with limestones	1.62	3.00
1150c	Calcareous brown earths, brown earths and luvisols on drift with limestones, associated with rendzinas and decalcified lithosols on limestones bedrock and peat	8.37	15.56
Island	Island		-

Rock	Rock outcrop	34.54	64.22
Tidal marsh	Tidal marsh		-
Water body	Surface water	0.12	0.22

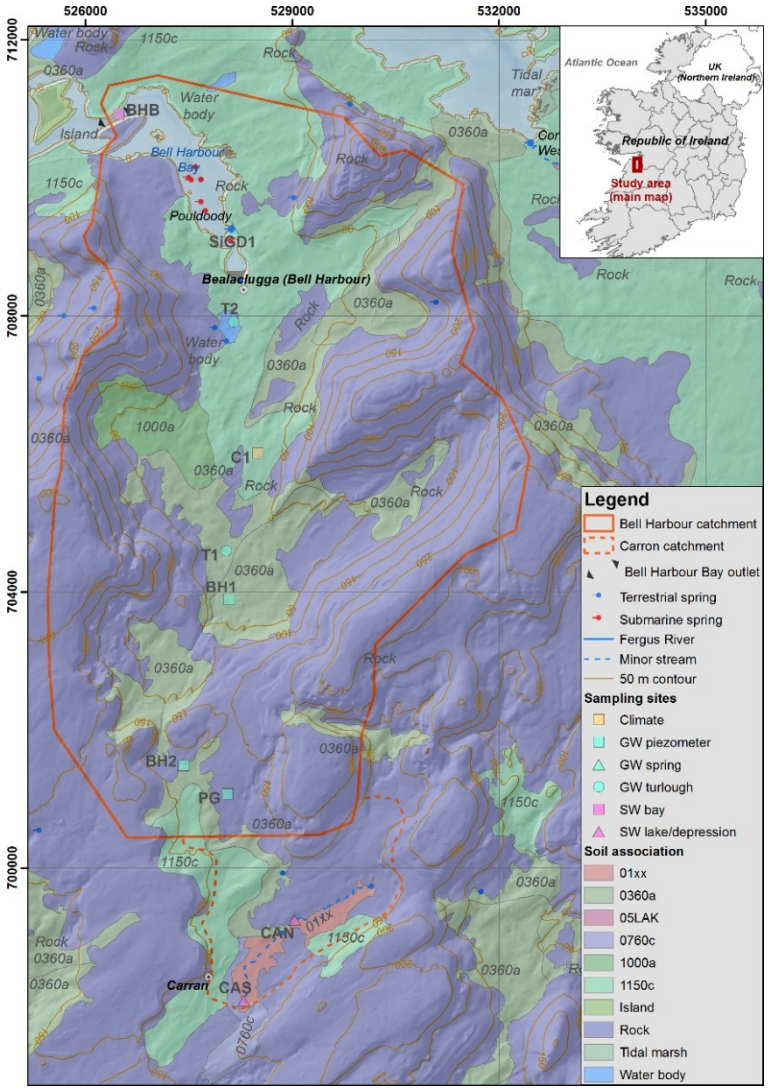

Figure 3.13: Soil cover in the area of the Bell Harbour catchment. For description of soil associations see Table 3.3.

3.3.2. Geology and structure

The entire catchment is underlain by Lower Carboniferous well-bedded and pure limestones ranging between the Tubber formation (early Viséan), the Lower Burren and Upper Burren formation (mid-Viséan, Asbian), and the Slievenaglasha formation (late Viséan, Birgantian). The Tubber formation is approx. 300 m thick and characterised by medium-grey, crinoidal calcarenites with shaly partings at some level and several cherty horizons, while the top, including the Finavarra member, is usually dolomitic (Pracht, et al., 2004). The Lower Burren formation reaches approx. 160 m encompassing the Black Head member and the Fanore member consisting of grey and medium to

thick bedded limestones. A dolomite horizon separates the Lower Burren formation from the Upper Burren formation above (Gallagher, et al., 2006), reaching approx. 230 m thick and includes the Maumcaha, Lower Aillwee and Upper Aillwee members. The Maumcaha member consists of pale-grey, massive limestones forming a distinctive, evenly sloped facet in the landscape, where its top can be distinguished from the overlying Aillwee member by a paleokarst horizon. MacDermot, et al. (2003) separate between a Lower and Upper Aillwee member. The Aillwee member consists of pale grey massive limestone that show a prominent terraced, well-bedded morphology in the landscape (Gallagher, et al., 2006). It contains clay wayboards, interpreted as palaeosols, which rest on irregular limestone surfaces considered to be palaeokarsts (Pracht, et al., 2015). The top of the Aillwee member is marked by paleokarst horizons. The total thickness of limestones reaches >510 meters underneath which it is supposed lies Galway Granite, although boreholes have has not penetrated deep enough so far to confirm this. The dip of the strata is uniformly to the south, ranging between 2 and 3 degrees (Figure 3.14).

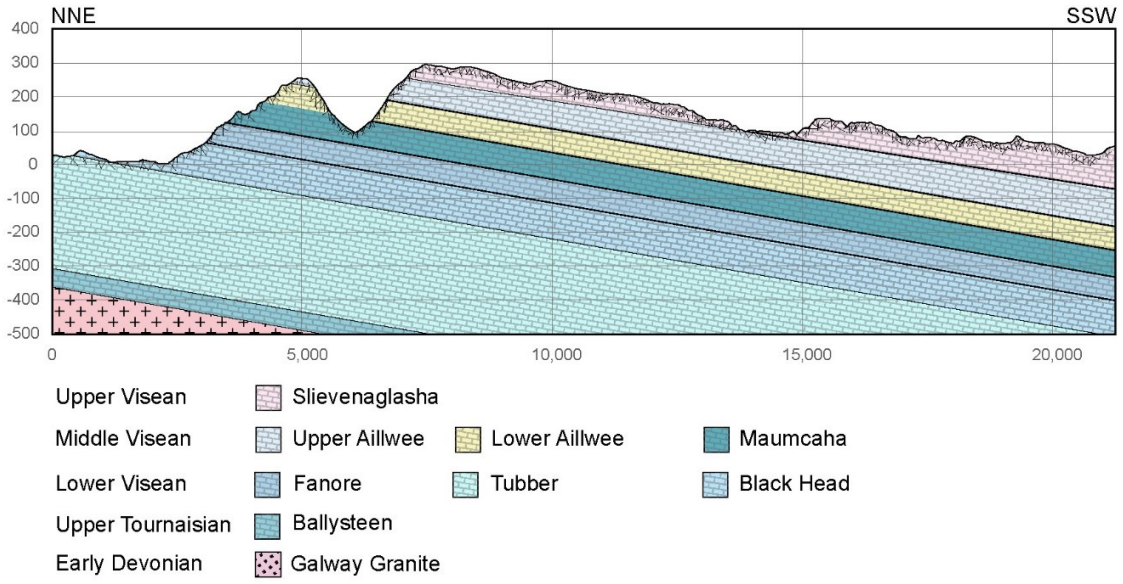

Figure 3.14: Geological cross-section (A-A', Figure 3.12) through the catchment of Bell Harbour.

In the Burren, very few structural features are present or visible from the surface. Deformation of Carboniferous rocks in Ireland are largely attributed to the Variscan orogeny, during which period a north-north/northwest oriented compression caused broader and more gentle faults and folding in the north, i.e. in the Burren (Graham, 2009). One of two faults in the Burren is MacDermot's fault in the western part of the study area striking into north-northeast sub-parallel to the Fergus Shear Zone with a slight (<200 m) sinistral displacement of members of the Burren and Slievenaglasha formation (Pracht, et al., 2004). Joints strike northwest-southeast and east-west and the age of joint formation is post-Variscan. The Variscan contractional deformation caused the formation of veins, which are lateral continuous and vertical consistent across bedding discontinuities (Gillespie, et al.,

2001). Horizontal persistency of veins along strikes reaches over 7 km, interconnecting caves (Mac Sharry, 2006). Increased veining was recorded up to depths of 204 to 228 mbsl in the deep borehole drilled by the GSI at location BH1 (Figure 3.12).

3.3.3. Hydrogeology

The hydrogeology of the catchment is largely influenced by erosion during the recent glacial advances as well as limestone dissolution. The groundwater flow is conduit dominated from south to north, i.e. updip, as in the neighbouring catchment of Ballyvaughan in the west, and the main groundwater discharge from the catchment was believed to occur via submarine springs and terrestrial intertidal springs into Bell Harbour Bay (Figure 3.12) (Perriquet, et al., 2012; McCormack, et al., 2017). The discharge regime of the catchment is quite complex: a minor share drains intermittent as shallow submarine and intertidal groundwater discharge at the intertidal Pouldoody spring at -0.1 masl. The major share of the catchment is drained via SGD into Galway Bay (Schuler, et al., 2018a). Questions remain as to what extent the shallow discharge regime fluctuates in time and is connected to the deeper discharge regime.

The south-north discharge pattern towards the bay allows for the possibility that preferential solution of the limestones would have taken place in the dominant south-north joints in the zone where fresh and saline water mix to produce subsaturated waters (Drew, 1990). Minor and seasonal groundwater discharge occurs along the escarpment of the Aillwee member where clay wayboards prevent vertical percolation but instead favour lateral flow above. However, clay wayboards are not continuous laterally and can be locally intersected by vertically continuous dissolved mineral veins (Mac Sharry, 2006) resulting both locally in possible deep percolation. One example of the impact of veins on the hydrogeology is the formation of the Poll Gonzo cave, along a dissolved vein that was explored between its top at 116 masl and the water table at 31 masl (Bunce, 2010). Within the cave, laterally inflowing groundwater from the south rapidly travels downwards, and potentially further to the north into Galway Bay (Bunce and Drew, 2017).
The combination of the structural pattern and extensive erosion and dissolution caused the formation of conduits; the limestones of the Burren are classified as Rkc (GSI, 2016).
A shallow conduit following south-north within the valley was detected by geophysical methods by McCormack, et al. (2017). The conduit is supposed to connect the two turloughs in the valley, Gortboyheen (T1) and Luirk (T2), allowing the turloughs rapidly to fill following persistent periods of rain, and empty again in a longer-lasting way.
Zones of deep karstification and high densities of perpendicular fractures were found in the deep borehole (BH1) at depths between 93 and 110 mbgl corresponding approximately to the sea level of the most recent ice age (McCormack, et al., 2017).
The only mapped fault in the catchment, Mac Dermott's fault, shows indications of being hydraulically active, rather than acting as a flow barrier (O'Connell, et al., 2012).

According to the GSI groundwater recharge map (Hunter Williams, et al., 2013), recharge coefficients [%] in the catchment comprise 60 and 85 (Figure 3.15). Low recharge coefficients of 0 and 22.5 only apply to small-scale depressions, turloughs and Bell Harbour Bay. More than 96% of catchment is subject to recharge coefficients 60 or 85 (Table 3.6). Overall, the bulk recharge can be estimated to be at 74%.

Only a very small share of the catchment is estimated to be subject to low groundwater recharge. This highlights the very fast recharge dynamics in the catchment.

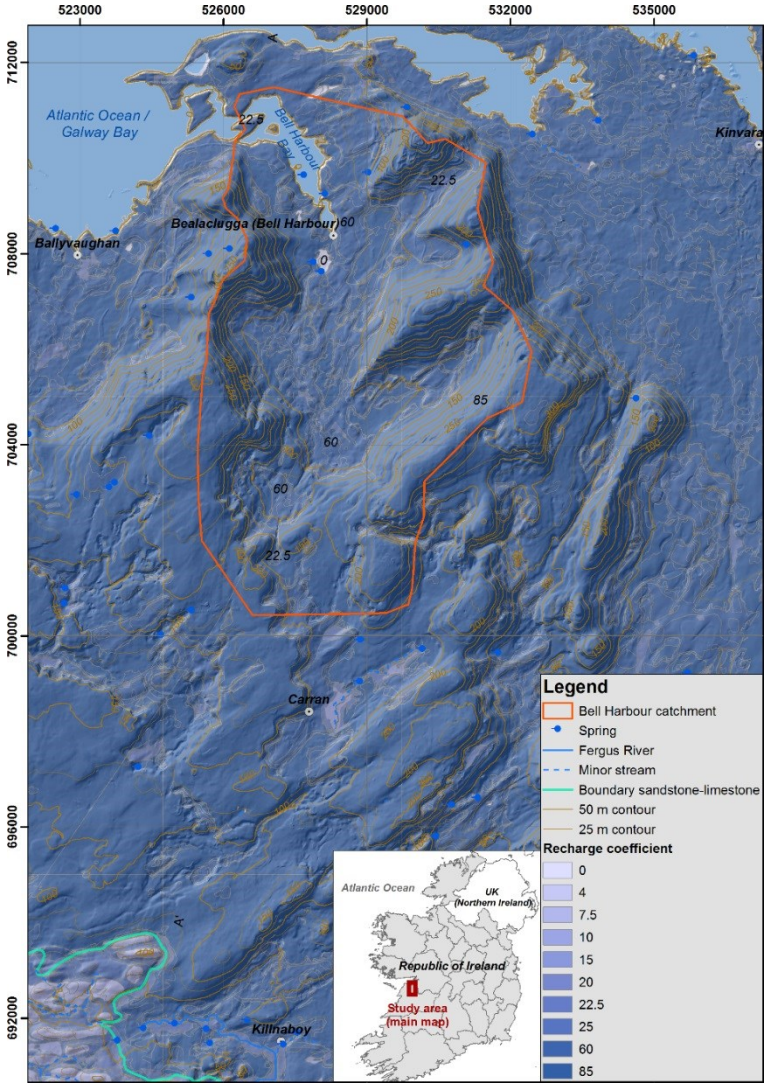

Figure 3.15: Groundwater recharge coefficients in the area of Bell Harbour.

Table 3.6: Areal contribution of recharge coefficients and weighted recharge coefficient for the entire catchment.

Recharge coefficient [%]	Land cover	Area [km^2]	Percentage [%]
0	Water	1.93	3.47
22.5	Moderate permeability subsoil and overlain by poorly drained gley soil / low permeability subsoil / till overlain by poorly drained gley soil	0.20	0.36
60	Moderate permeability subsoil overlain by poorly drained gley soil or well drained soil / till overlain by well drained soil	16.73	30.09
85	Bare rock	36.74	66.07
74.3	**Weighted average / total**	**55.6**	**100.00**

4. Materials and Methods

4.1. Monitoring, sampling and lab analysis

The majority of data used in this work was collected either manually or automatically in the field in the three study catchments.
Manual data collection describes, for example, the process of taking a discrete water quality sample or a single discharge measurement in a river while automated sampling refers to the installation of a sampler connected to a data logger that stores data continuously in a defined interval. While automated data sampling is indispensable for time series analysis in which a high temporal frequency in the range of minutes to hours is required, both approaches require much capital investment, know-how, and human resources for the inspection of monitoring sites, organising permission for land access, construction of samplers (e.g. tripod for a weather station), deployment of samplers, frequent maintenance of samplers in the field (cleaning of samplers, changing batteries, downloading data).

An extensive monitoring network was established to continuously monitor climate, surface water and groundwater (Table 4.1).

Table 4.1: Hydrometeorological monitoring network in Ballindine (BA), Bell Harbour (BH) and Manorhamilton (MH), parameters and periods (excl. data gaps) of monitoring: C = electrical conductivity, T = temperature, D = depth, WS = wind speed, WD = wind direction, RH = relative humidity, NETRAD = net radiation, BP = barometric pressure, P = precipitation.

	Catchment	Name/location	Elevation [masl]	Instrument	Data	Period of available data
Groundwater	BA	Ballindine spring	40.8	OTT CTD sensor	C, T, D	29-07-2017 to 01-10-2018
	BH	Pouldoody spring (SiGD1)	-0.6	AquiStar® CT2X / Solinst LTC	C, T, D	15-12-2014 to 01-10-2018
		Borehole (BH1)	30.4	AquiStar®Aqua4Plus INW CT2X	C, T, D	26-02-2015 to 01-10-2018
		Borehole (BH2)	142	Solinst LTC	C, T, D	21-05-2015 to 25-10-2016
		Gortboyheen turlough (T1)	16.3	Mini-Diver®502	D	17-07-2014 to 01-10-2018
		Luirk turlough (T2)	0.2	Mini-Diver®502	D	29-07-2014 to 19-07-2016
		Poll Gonzo (PG)	~70	Schlumberger CTD DI263	C, T, D	12-07-2017 to 14-04-2018
	MH	Manorhamilton spring (MH3)	112	Schlumberger CTD DI271	C, T, D	24-05-2017 to 04-06-2019
Surface water	BH	Bell Harbour Bay (top, BHB1)	~-0.5 below water surface	AquiStar® CT2X / Schlumberger CTD DI271	C, T, D	24-02-2016 to 01-10-2018
		Bell Harbour Bay (bottom, BHB2)	~-1 below water surface			

		Fergus River, Crossard bridge (FR)	~23	Solinst LT / Mini-Diver®502	T, D	09-06-2016 to 01-20-2018
		Carron south (CAS)	110.0	Solinst LT	T, D	19-12-2014 to 01-10-2018
		Carron north (CAN)	111.0	Solinst LTC	C, T, D	26-02-2015 to 01-10-2018
Climate	BH	Weather Station Burren Outdoor and Education Centre (C1)	37.7	Gill 2-D Sonic Wind Sensor	WS, WD	22-01-2016 to 01-10-2018
				Campbell Scientific CS215 Temperature & RH Probe	T, RH	
				NR-LITE Kipp & Zonen Net Radiometer	NETRAD	
				Casella CEL Tipping Bucket Rain Gauge	P	28-02-2016 to 01-20-2018
				AquiStar® PT2X	BP	15-12-2014 to 01-10-2018
		Fort Neylon (P1)	203	ARG100 precipitation sensor	P	17-04-2016 to 08-06-2017
	MH	MH 3	112	ARG100 precipitation sensor	P	24-05-2017 to 04-06-2019

The following two sections present the field equipment and lab instrumentation, and associated sampling procedure where applied.

4.1.1. Instrumentation

4.1.1.1. Field instrumentation

Rainfall samplers

Rainfall was recorded using a tipping bucket ARG100 rain gauge (Environmental Measurement Ltd., North Shields, UK) and a CEL Tipping bucket rain gauge (Casella, Bedford, UK) both attached to a Rainlogger Model 3002 (Solinst Canada Ltd., Georgetown, Canada) datalogger.

ARG100 rain gauges were deployed at MH3 (Manorhamilton) and at P1 (53.053° N; -9.119° W) at ~203 masl, 6 km south-west of C1 (World Geodetic System 84, WGS84) at 38 masl where a Casella CEL Tipping bucket rain gauge was deployed, to identify any orographic impact on the rainfall regime resulting in spatial heterogeneity across the Bell Harbour catchment.

All rain gauges recorded the amount of tipping (equivalent to 0.2 mm) every 15 min. Frequent maintenance including cleaning and cutting the surrounding grass was applied to avoid blockage of the inlet/funnel.

Climate station

A weather station (C1) was set up at the Burren Outdoor and Education Centre (BOEC) at 53.100° N and -9.068° W at 37.7 masl. The surrounding topography is flat, and the closest obstacles are a wall of ~1 m height and two trees of ~3 m height at 17.5 m distance to the north and a wall of ~1 m in height at 15.2 m distance to the east (Figure 4.1). The total height of the station is ~2.2 m.

Installation of the sensors was followed according to the standards of WMO (2008). The CS215 temperature & RH probe (Campbell Scientific Ltd., Shepshed, UK) was mounted between 1.2 m and 2 m and was protected by an unaspirated radiation shield. The NR-LITE net radiometer (Kipp & Zonen B.V., Delft, The Netherlands) was installed away from reflective sources and horizontally directed towards the south. The Ultrasonic wind sensor (Gill Instruments Ltd., Lymington, UK) was installed at 2 m above ground, as this is the reference height for observed wind speed using the Penman-Monteith equation for the estimation of evapotranspiration (instead of installing the wind sensor at 10 m for the observation of surface wind, as recommended by WMO (2008)).
The abovementioned sensors were attached to a CR800 Datalogger Module (4Mb SRAM memory) (Campbell Scientific Ltd.) contained in a Campbell weather-resistant enclosure, and all mounted on a constructed steel tripod (Figure A.7). Communication between computer and data logger was established using the software PC200W (version 4.3, Campbell Scientific Ltd.).
The station was powered by a 10 W solar panel (BO SX310) that was connected to a 12V lead-acid battery housed in the enclosure. A Solsum 6.6F 6A solar charge controller (Steca, Memmingen, Germany) was installed between the solar panel, battery, and data logger.
Frequent maintenance was applied to keep the vegetation at a low level, as well as cleaning the net radiometer if necessary.

Figure 4.1: Location of the weather station (C1) at the BOEC.

An INW PT2X (Seametrics, Kent, WA, USA) was separately attached to the tripod to continuously measure temperature and atmospheric pressure. Atmospheric pressure is essential for any water level readings as the latter ones are the sum of hydraulic pressure + atmospheric pressure, hence, air pressure is subtracted from any water level readings to account only for the water column.

Rainfall collectors

Rainfall was collected at C1 for stable isotope analysis using a rain sampler RS1 (Palmex Ltd., Zagreb, Croatia) (Gröning, et al., 2012), which is an evaporation-free, oil-free, rain and snow sampling device with minimal required maintenance for robust field operations.
Rainfall was collected in a 3 l sampling bottle that is filled through an intake-tube and a funnel. The sampler was installed at 1 m height. The sampler was emptied in intervals between 1 week and 1 month by the staff of the BOEC, and further, maintenance was applied to prevent blockage of the funnel/inlet.

dGPS

High-precision topographical measurements were taken using a Trimble 4700 (Trimble Navigation, Sunnyvale, CA, USA) differential global positioning system (dGPS) with horizontal/vertical accuracy of 0.01 m. The method of how to use the instrument is described in detail in Gill (2010). Topographic measurements were taken to increase locally the precision of the digital elevation model (DEM) used and to measure the elevation of monitoring sites.

Hand-held GPS

Coordinates and tracks on site were recorded using a water resistant GPSmap 60CSx (Garmin Ltd., Olathe, KS, USA). The instrument includes an electronic compass that determines the heading and direction, even when standing still. Further, it provides relative accurate elevation data using a barometric altimeter.
Data is stored on a 64 MB microSD card. Communication between the GPS and a computer was done using the software BaseCamp (version 4.6.2, Garmin Ltd.). Further, data were imported directly into Google Earth Pro (version 7.1.5.) using the designated Garmin GPS data import tool.

Zodiac

A Zodiac PVC thermobonded inflatable boat was used for sampling in Bell Harbour Bay and reaching the buoy sampler BHB1+2 for downloading data and sampler maintenance. Although an outboard motor can be installed, the boat was powered manually using oars. The Zodiac was inflated on site using a standard foot air pump.

Field laptop

Communication with the sensors/loggers deployed within the study sites was done using a GoBook XR-1 (General Dynamics, Falls Church, VA, USA) rugged notebook with a magnesium chassis/aluminium top.

Acoustic Digital Current meter

Spot discharge measurements were recorded in the Fergus River at Crossard bridge using an OTT Acoustic Digital Current) Meter (ADC, OTT Hydromet GmbH, Kempten, Germany). Spot discharge measurements were then used with measured water levels to establish a stage-discharge relationship.

During low flow of the River Fergus (~<0.5 m), vertical profiles of two discharge measurements were taken within a horizontal interval of 1 m within the river. During high flow (~>0.5 m) the density of the horizontal intervals was increased to 0.5 m, and discharge measurements had to be taken from the bridge. Under these circumstances, the OTT was installed on a 5 m long metal pole. The average velocity of each profile was calculated by the 2-point KREPS measurement where velocity measurements are taken near the surface and at 38% of the depth.

The total discharge per cross-section was calculated by the mid-section method (Figure 4.2), which has shown to yield more exact results than the mean-section method (OTT, 2013).

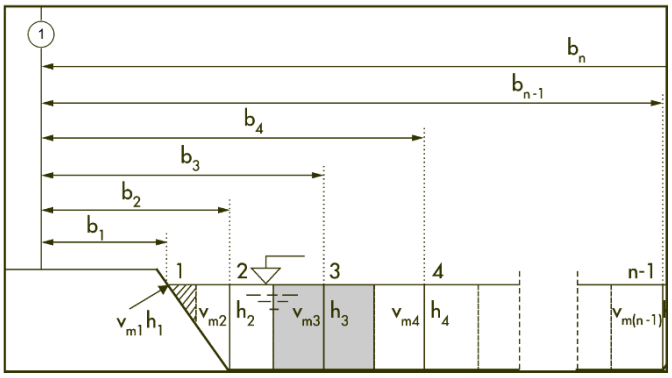

Figure 4.2: Mid-section method applied to yield the total discharge in a river cross-section (OTT, 2013).

Water level records were then plotted against respective discharge measurements in Microsoft Excel.

Water level meter

The water level in boreholes BH1 and BH2 were continuously monitored using CTD sensors. In addition, discrete water levels were recorded to cross-validate the monitored depth by the CTD sensors. Water levels were measured using a 101 P7 Water Level Meter (Solinst Canada Ltd.).

ISCO autosampler

Automated water quality samples were taken using an ISCO portable sampler model 6712 with 24 x 1,000 ml polypropylene sampling bottles (Teledyne Technologies Inc., Thousand Oaks, CA, USA). The autosampler is equipped with a peristatic pump that can lift a maximum suction head of 8.5 m (TeledyneISCO, 2015), however, tested in the lab, a maximum lift of ~9.5 m was achieved. Because of the relatively high head the pump can lift, the autosampler was used for collecting groundwater samples from a borehole as well as groundwater samples at spring outlets.
Before taking a sample, the tube was purged to push out 'old' stagnant water within the tube. In addition, for the application at BH1, two samples were taken at each defined sampling timestep: the first sample was discarded in order to ensure that the second sample was free of any old stagnant water.
A standard 44 Ah 12 V car battery was connected to the instrument for a power source. The battery was shielded in a marine air and water tight box. Before and after taking a sample, the autosampler purges the suction tube to remove any stagnant water.
The bottles in the autosampler are very well isolated from the surrounding environment and temperature influence. Yet, care was taken that the sampling filled bottles were emptied not later than 2 to 3 days after filling.

Discrete Interval sampler

Spot groundwater samples from a borehole were taken using a stainless-steel discrete interval sampler Model 425 (Solinst Canada Ltd.). It is a passive sampling method (without purging) that was considered not problematic given the rapid flow velocities within the borehole (BH1) used.
The discrete interval sampler has a pressure valve at its bottom inlet that is closed by increasing the internal pressure by pumping air into the interval sampler at the desired depth using a bicycle air pump attached to the tubing system. Air enters the interval sampler via a tube that connects the top of the sampler to the person at ground level. The pressure to be applied is a function of the water column above the level where the sample is taken.

Sampling bottles

Depending on the nature of the sample, different sampling bottles were used for the different successive analyses. For the analysis of stable isotopes (2H and 18O), 60 ml glass bottles (Thermo Fisher Scientific Inc., Waltham, MA, USA) were used, capped with a screw cap to exclude any head space.

For analysis of anions, polyethylene graduated narrow neck bottles (Kartell S.p.A., Noviglio, Italy) with a push-in lit and a capacity of 125 ml were used. For the analysis of cations, 30 ml polypropylene sampling tubes (Greiner Bio One International GmbH, Kremsmünster, Austria) were used. Every sample was filtered in the field using 0.45 µm cellulose nitrate membrane syringe filters (Whatman®) before acidifying the sample using one drop of a 10% nitric acid (HNO_3).

Conductivity, temperature and depth (CTD) sensors

CTD sensors were extensively deployed to measure these parameters continuously for spring discharge, turloughs, boreholes or within the bay of Bell Harbour or Galway. Instruments used were INW CT2X (Seametrics), DI271 CTD sensors (Schlumberger Water Services, BC, Canada), LTC Levelogger Edge (Solinst Canada Ltd.) and an OTT CTD (OTT Hydromet GmbH).

The four samplers have different sensors to measure single parameters. Since the conductivity of water increases with temperature, the measured conductivity is referenced to 25˚C (normalized) to yield the specific conductivity. Measurement is based on a 4-pole electrode technology constructed of epoxy/graphite (OTT, 2009; Seametrics, 2016a) or platinum (Solinst, 2017). For the deployment of CTDs in freshwater conditions, calibration was done using a one-point calibration using a 1,414 µS/cm standard while a 12.88 mS/cm solution was used for brackish/saline conditions.

Temperature was measured via a platinum resistance temperature detector (Solinst, 2017) or via a borosilicate glass encapsulated thermistor (Seametrics, 2016a).

Depth and level is measured via a vented pressure cell (OTT, 2009), a Hastelloy or stainless steel sensor with piezoresistive silicon (Seametrics, 2016a; Solinst, 2017), or using alumina as media (Eijkelkamp, 2016). In all cases the level is compensated for temperature. The range, accuracy and resolution for the three parameters of CTD samplers used are summarised in Table 4.2 (OTT, 2009; Eijkelkamp, 2016; Seametrics, 2016a; Solinst, 2017; Schlumberger, n.k.).

Table 4.2: Specification of CTD sensors used.

	Sensor		**Conductivity**	**Temperature [˚C]**	**Depth [cm, m, %]**
Range	INW CT2X		0-300,000 µS/cm	-5 to 40	0 to 70 m H_2O
	Schlumberger	DI271	0-120,000 µS/cm	-20 to 80	0 to 10 m H_2O
		DI263	0-80,000 µS/cm	-20 to 80	0 to 30 m H_2O
	Solinst LTC		0 to 100,000 µS/cm	-20 to 80	0 to 200 m H_2O
	OTT CTD		1 to 2,000,000 µS/cm	-25 to +70	0 to 4 m H_2O
Accuracy	INW CT2X		±0.5%	±0.25	±0.05% to ±0.1%
	Schlumberger	DI271	±1%	± 0.1 to ±0.2	± 0.5 to ± 2 cm H_2O
		DI263	±1%	± 0.1	3 cm H_2O
	Solinst LTC		±30µS < 500 µS/cm; ±2% 500 to 30,000 µS/cm;	±0.05	±0.05%

			±1% > 30,000 µS/cm		
	OTT CTD		± 0.05 %	± 0.1	± 0.05 % full scale
Resolution	INW CT2X		0.1 µS/cm	0.1	0.0034%
	Schlumberger	DI271	0.1%	0.01	0.2 cm H_2O
		DI263	0.1%	0.01	0.6 cm H_2O
	Solinst LTC		±0.1 µS/cm	0.003	-
	OTT CTD		0.001 mS/cm	± 0.01	0.1 cm

Communication with the instruments was established using different software products, i.e. Aqua4Plus (version 1.9.7, Seametrics), Diver-Office (version 2016r 8.0.0.4, vanEssen Instruments), Levelogger Software 4 (version 4.1.1 and 4.3.1, Solinst Canada Ltd.), and OTT Water Logger Operating Program (version 1.67.0, OTT Hydromet GmbH). Schlumberger, Solinst and OTT sensors have the advantage that they communicate via an optical or infrared (IrDA) interface with the computer whereas Seametrics sensors have a pinned plug for interaction. An optical/infrared interface is favourable as water, dirt or air cannot harm any exposed metal connectors.

Temperature and depth sensors

Depth and temperature as single parameters were measured using DI501 Mini-Diver (Schlumberger Water Services) deployed in turloughs and the River Fergus, and a Levelogger Edge M20 (Solinst Canada Ltd.) deployed in Carron depression, both with depth corrected for temperature. Its specifications are listed in Table 4.3 (Eijkelkamp, 2016; Solinst, 2018).

Atmospheric pressure was continuously measured using an INW PT2X (Seametrics) attached to the weather station (C1) at the BOEC. Sensor specifications are summarised in Table 4.4 (Seametrics, 2016b).

Table 4.3: Specification of TD sensors used.

	Sensor	**Temperature [°C]**	**Depth [cm, m, %]**
Range	Schlumberger DI501	-20 to 80	0 to 10 m H_2O
	Solinst Levelogger	-20 to 80	0 to 20 m H_2O
Accuracy	Schlumberger DI501	± 0.1 to ±0.2	± 0.5 to ± 2.5 cm H_2O
	Solinst Levelogger	± 0.05	± 0.05% FS
Resolution	Schlumberger DI501	0.01	0.2 cm H_2O
	Solinst Levelogger	0.003ºC	

Table 4.4: Specification of the INW PT2X.

	Temperature [°C]	**Depth [m, %]**
Range	-15 to 55	0 to 10 m H_2O
Accuracy	±0.5 (0 to 55)	±0.05% to ±0.1%
Resolution	0.1	0.0034%

Communication with the instruments was established using Aqua4Plus (version 1.9.7, Seametrics) and Diver-Office (version 2016r 8.0.0.4, vanEssen Instruments).

GGUN field fluorometer

Albillia GGUN-FL30 flow-through field fluorometers along with the designated software GGUN-FI Field Fluorometer (version 28.3, Albillia Co., Neuchâtel, Switzerland) were used for artificial tracer tests. The instruments were either borrowed from the GSI (instrument #949, #950, #951) or from the Federal Institute for Geosciences and Natural Resources (BGR, Hannover, Germany) (instrument #640, #641).

GGUN-FI field fluorometers can measure three distinct dyes in parallel as well as turbidity for a sampling interval ≥10 s (Figure 4.3). Readings are taken in millivolts (mV), which is converted into ppb using the calibration results. The smallest detectable concentration variation in clear water is 0.02 ppb for uranine and 0.14 to 0.2 ppb for the other tracers (Schnegg, 2002).

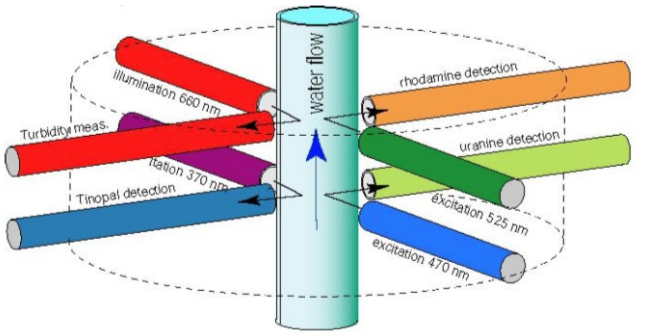

Figure 4.3: Functioning of the field fluorometer with four light sources and distinct excitation wavelengths for the three tracers uranine (Na-fluorescein), rhodamine and Tinopal CBS-X, as well as turbidity (Schnegg, 2002).

4.1.1.2. Lab instrumentation

Konelab - anions

Chloride (Cl^-), sulphate (SO_4^{2-}), nitrate (NO_3^-), nitrite (NO_2^-), ammonium (NH_4^+), alkalinity ($CaCO_3$) and silica (SiO_2) were photometrically analysed using a Konelab 20XT (Thermo Fisher Scientific Inc.) (Thermo, 2004) located in the Environmental Engineering Laboratory, Trinity College Dublin (TCD). The workflow of the instrument's analysis is displayed in Figure 4.4.

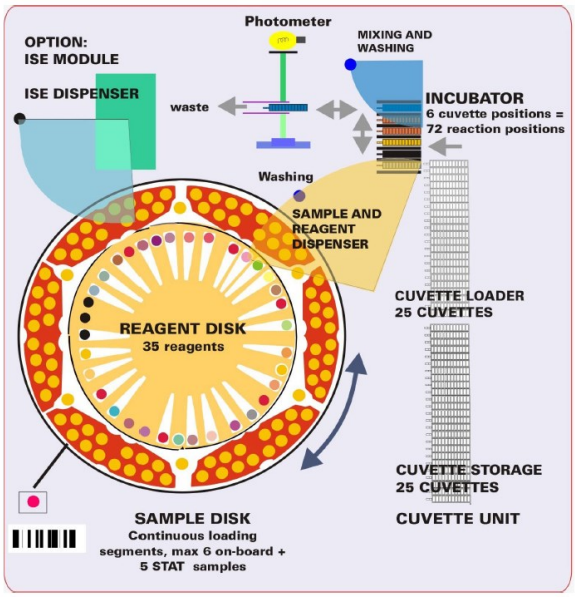

Figure 4.4: Photometric analysis proceeding in Konelab 20 XT (Thermo, 2004).

ICPAES - cations

Calcium (Ca^{2+}), potassium (K^{+}), magnesium (Mg^{2+}) and sodium (Na^{+}) were planned to be analysed in filtered samples with standard sample preparation, using inductively-coupled plasma atomic emission spectrometry (ICPAES) (Varian Liberty® Series 2, Figure 4.5) located in the Environmental Engineering Laboratory, Trinity College Dublin.

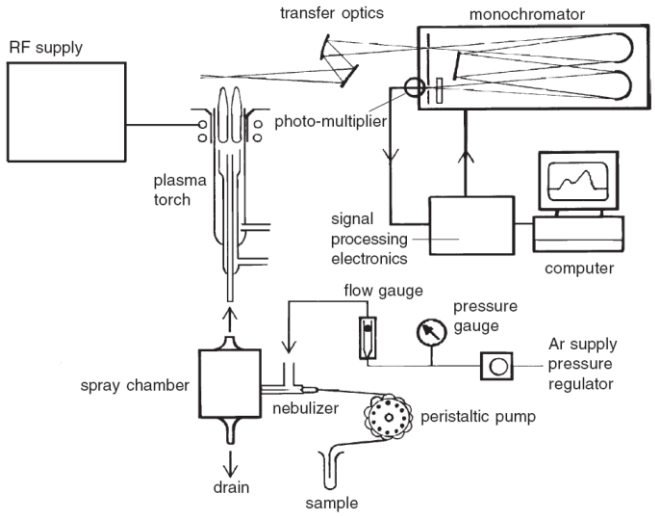

Figure 4.5: Components of an ICP atomic emission spectrometer (Varian, 1999).

As summarised in Morgan (2014), ICPAES can be used for determining all stable elements in the periodic table, apart from gases. A total of 120 samples were taken and filtered through a 0.45 µm pore diameter membrane filter (cellulose nitrate) in the field using a syringe filter. All samples were stored in a Greiner bio-one 30 ml sampling tube before acidifying the filtrate using nitric acid (10%).

It was aimed to analyse samples within 6 months after taking them. However, due to ongoing malfunction of the department's instrument, none of the samples could actually be analysed. Attempts to analyse the samples in other departments on campus had to be given up, unfortunately.

Picarro L2120-I – stable isotopes

Isotope samples were filled on site into 60 ml glass bottles with a screw cap (Thermo Fisher Scientific Inc.). The sample bottles were flooded to avoid any head space to exclude potential fractionation in the sample bottle, systematically labelled and shipped by post to the groundwater laboratory of the Federal Institute for Geoscience and Natural Resources (BGR) in Hanover, Germany, for stable isotope analysis of 2H and 18O.

The analysis followed the procedure outlined in Koeniger, et al. (2017): the water samples were analysed for δ2H and δ18O simultaneously using a Picarro L2120-i cavity ring-down laser spectrometer (Picarro, Inc., Santa Clara, CA, USA) after vaporization with a VAP 214 vaporizer. All samples were measured at least four times, and the reported value is the mean value. All values are given in the standard delta notation in per mill (‰) versus Vienna Standard Mean Ocean Water (VSMOW). Raw data were corrected for memory effect and excluded if necessary. The data sets were corrected for machine drift during the run and normalized to the VSMOW/Standard Light Antarctic Precipitation scale.

An additional post correction scheme for machine drift and memory effects was applied as recommended by van Geldern and Barth (2012). External reproducibility, defined as standard deviation of a control standard during all runs, was better than 1.0‰ and 0.30‰ for δ2H and δ18O, respectively. Deuterium excess (d) values ($d = \delta 2H - 8 * \delta 18O$) that are calculated from δ18O and δ2H values show more consistent values than those derived from earlier isotope-ratio mass spectrometry measurements, because here both isotopes are measured simultaneously. In this work, standard deviations of d excess values are better than 1‰ for a continuously measured quality check sample. All samples were checked for dissolved organic carbon (DOC) contamination using ChemCorrect™ with unaltered factory settings. However, it was not necessary to discard samples collected during this study, as DOC contents were low.

Cary Eclipse Fluorescence Spectrophotometer

Activated charcoal samplers were used in artificial tracer studies. In order to analyse the used activated charcoal samplers for fluorescence, the charcoal samplers were eluted using appropriate solutions (Smart and Simpson, 2002). The eluents were then analysed using a Cary Eclipse Fluorescence Spectrophotometer (Agilent Technologies, Santa Clara, CA, USA). All the analysis was carried out in the water lab of the GSI, Dublin.

4.1.2. Meteorological data and processing

Meteorological data were sampled in the field independently as well as obtained from the following MetEireann stations downloaded from www.met.ie:

- Ballindine: Climate data provided in hourly time steps obtained from the MetEireann for the station Claremorris (ID 2175) located on 68 masl, 4.5 km north/northwest of Ballindine spring at 53.707º N and -8.989º W. Parameters provided include precipitation [mm], air temperature [ºC], vapour pressure [hPa], relative humidity [%], mean wind speed [m/s]. These parameters were used for estimating ET, rainfall-discharge analysis and numerical modelling;
- Manorhamilton: Historical climate data provided in daily time step were obtained from the MetEireann stations Manorhamilton (Amorset) (ID 2236) located on 76 masl at 54.304° N and -8.176° W, and Markree (ID 1275) located on 34 masl at 54.172° N and -8.453° W. Manorhamilton (Amorset) is 4.9 km east of Manorhamilton spring observing only daily rainfall. Markree is located 19 km south-west of Manorhamilton spring observing precipitation [mm], and maximum and minimum air temperature [ºC]. Because of the close proximity of Manorhamilton (Amorset), its rainfall data were used for water balances of Manorhamilton, while temperature data of Markree were used for estimating ET;
- Bell Harbour: Daily rainfall time series were obtained from MetEireann for the stations Ballyvaughan (ID 2321) and Carron (ID 1218) located on 23 masl and 145 masl. Both stations are located outside the delineated catchment boundaries at 53.120º N and -9.168º W, 53.026º N and -9.073º W, respectively.

While certain parameters are directly measured, e.g. rainfall, temperature, humidity or wind speed, evapotranspiration (ET) was estimated using the most appropriate methods. For Ballindine and Bell Harbour, daily and hourly ET was estimated using the Penman-Monteith equation (Allen, et al., 1998) applied on climate data measured at Claremorris and at the Burren Outdoor and Education Centre (C1) respectively. The method quantifies ET with reference to well-watered, short-cut grass, and therefore yields the reference ET (ET_0). The method accounts for variable landuse which results in ET that deviates from ET_0 by multiplication with a crop coefficient (K_c).
For the daily time step, the method follows,

$$ET_{0,PM,d} = \frac{0.408\Delta(R_n - G) + \gamma \frac{900}{T+273} u_2 (e_s - e_a)}{\Delta + \gamma(1 + 0.34\, u_2)} \qquad \text{Eqn. 4.1}$$

with the daily reference evapotranspiration $ET_{0,PM,d}$ [mm/d], net radiation at the crop surface R_n [MJ/m²/d], the soil heat flux density G [MJ/m²/d], mean daily air temperature at 2 m height T [°C], the wind speed at 2 m height u_2 [m/s], the saturation vapour pressure e_s [kPa], the actual vapour

pressure e_a [kPa], the slope vapour pressure curve Δ [kPa/°C], and the psychrometric constant γ [kPa/°C].

MetEireann measures wind speed at 10 m reference height, however, following Allen, et al. (1998), wind speed is related to 2 m reference height. Hence, MetEireann wind speed records were downscaled to 2 m following,

$$u_2 = u_{10} \frac{4.87}{\ln(67.8 \times 10 - 5.42)} \quad \text{Eqn. 4.2}$$

with the wind speed at 2 m elevation u_2 [m/s] and the observed wind speed at 10 m elevation u_{10} [m/s].

At Claremorris, all relevant climate parameters are monitored necessary to estimate ET_0 following Allen, et al. (1998), except radiation. Therefore, net radiation was estimated using daily minimum and maximum temperature and relative humidity values as outlined in Allen, et al. (1998).

At C1, all relevant climate data were available at an hourly time step, so ET could be estimated following the Penman-Monteith method. However, at Claremorris, net radiation data were missing which therefore had to be estimated following Allen, et al. (1998) to estimate the daily ET ($ET_{0,PM,d}$). Hourly ET time series ($ET_{0,PM,h}$) was then estimated following the same procedure. Because the daily estimated ET is considered more reliable compared to the hourly ET, the resulting $ET_{0,PM,h}$ was fitted against the sum of $ET_{0,PM,d}$ by adjusting the parameters used to estimate the soil heat flux density, evaluated against the root mean square error (RMSE) for the hydrological years 2010 to 2018.

For Manorhamilton, only temperature data from the MetEireann station Markree was available. Accordingly, the temperature-based method following Hargreaves (1994) was applied to estimate ET following,

$$ET_{0,Har,d} = H_A R_e (T + 17.8) \Delta T^{H_E} \quad \text{Eqn. 4.3}$$

with the daily reference evapotranspiration $ET_{0,Har,d}$ [mm/d], the empirical parameters H_A (standard H_A = 0.0023) and H_E (standard H_E = 0.5), the water equivalent of the terrestrial radiation R_e [mm/d], the daily mean temperature T (($T_{max} + T_{min}$)/2) [ºC], and the difference between T_{max} and T_{min} to be ΔT. R_e makes the link to solar radiation and was calculated following Shuttleworth (1993). The empirical parameters H_A and H_E were adjusted to the regional context by fitting $ET_{0,Har,d}$ against $ET_{0,PM,d}$ (Berti, et al., 2014) using the lowest RMSE. The weather station C1 was used as

reference station for $ET_{0,PM,d}$ as there were no closer meteorological stations that could provide the full list of parameters necessary.

4.1.3. Groundwater and surface water data

4.1.3.1. Ballindine

Groundwater discharge of Ballindine spring was monitored for conductivity and temperature at MH3 in 1 h sampling frequency using an OTT CTD sensor.
Further, groundwater discharge time series in 15 min sampling period were obtained for Ballindine spring (53.6740º N; -8.9655º W) from the EPA via the EPA HydroNet website (http://www.epa.ie/hydronet).
Water level and flow of the Robe River observed in 15 min interval at Christina S BR. (53.6846º N; -8.9924º W) was obtained via the EPA HydroNet website.

4.1.3.2. Manorhamilton

Groundwater discharge of Manorhamilton spring was monitored for conductivity and temperature at MH3 in 30 min sampling frequency using a Schlumberger CTD sensor. The diver was attached to the bottom of the stream channel 3 m upstream the EPA gauging station.
Further, groundwater discharge time series in 15 min sampling period were obtained for MH3 from the EPA via the EPA HydroNet website.
Discrete water quality samples were taken at MH1, MH2, and MH3.

4.1.3.3. Bell Harbour

Groundwater was monitored at Pouldoody spring (SiGD1), Luirk and Gortboyheen turlough (T1, T2), in Poll Gonzo cave (PG), and in two open boreholes (BH1, BH2). Surface water was monitored at the outlet of Bell Harbour Bay (BHB1, BHB2), in the southern and northern part of Carron depression (CAS, CAN), and at the River Fergus at Crossard bridge (FR).

Bell Harbour Bay (BHB1+2)

EC and temperature of the sea was monitored offshore in the centre of the outlet of Bell Harbour Bay (53.1438º N; -9.0988º W). The retrieved time series recorded the variation of the parameters during the changing tidal regimes (emptying and filling of Bell Harbour Bay). These data were necessary to estimate the freshwater discharge from the bay, i.e. SiGD into the bay.
The site is subject to strong currents due to tidal fluctuation. Accordingly, a robust sampler had to be constructed consisting of the following elements: a ~75 kg concrete slab was used as an anchoring weight. Attached to it, a 10 m long and 16 mm strong polypropylene rope connects the concrete weight with a buoy that floats on the sea surface. As additional security against potential cutting/vandalism of the rope, a 3 m long and 8 mm thick galvanized chain was welded to the buoy and connected along the rope to protect the upper 3 m.

CTD sensors were attached to the rope at two different levels using cable-ties.
At the beginning of the project, two INW CT2X sensors were installed. Both sensors malfunctioned after a few months - one due to sea water intrusion and the other for unknown reasons. Both instruments were replaced by Schlumberger CTD DI271 that recorded for >2 years.
Data were downloaded in intervals of 1 to 3 months. Frequent maintenance had to be applied to clean the sensors and remove barnacles, algae and other organisms from the sensors. The samplers were reached using an inflatable Zodiac, and data were downloaded using a field laptop.

Fergus River (FR)

The Fergus River is presumed to drain more than ~1/3 the area of the Burren (Drew, 1990). Therefore, it was decided to monitor its discharge as it was potentially beneficial for the delineation of the groundwater catchment of Bell Harbour.
The water level at Crossard Bridge (52.9662º N; -9.0854º W) was continuously monitored using a Solinst LT / Mini-Diver®502. The diver was located in a PVC housing permanently fixed onto the concrete base of the bridge at approx. 23 masl (Figure 4.6). The instrument had been previously installed by a TCD researcher (Ted McCormack).

Figure 4.6: Upstream view on the Fergus River at Crossard Bridge at low flow. The diver is installed at the left bottom of the right arch.

Carron depression (CAS & CAN)

At the beginning of the project, it was unknown if Carron is located within the groundwater catchment of Bell Harbour. Therefore, it was decided to include Carron within the monitoring strategy. Carron is a topographic depression similar to a polje that consists of two parts, a northern (CAN) and a southern (CAS) area. The southern part receives partially and/or temporarily inflow via a spring from the northern part (Bunce and Drew, 2017). Both parts are seasonally flooded due to spring discharge of the surrounding hill slopes.

CAN and CAS are both drained by a swallow hole. Both swallow holes are the monitoring locations with elevations of were monitored at the 110.0 masl (CAS, 53.0285º N; -9.0690º W) and 111.0 masl (CAN, 53.0392º N; -9.0582º W). At both locations, a sensor was attached within a vertically aligned perforated PVC pipe, which was attached to a concrete slab. In addition, a buoy was connected to the concrete slab in order to localise the sampler during flooded conditions. The PVC pipe ensured protection on the one side and allowed flux of sediments and water on the other side. Both instruments had been previously installed by Ted McCormack.
The samplers were visited once a year for downloading data and maintenance.

Lowland borehole (BH1)

The 'lowland borehole' (BH1, 53.0808º N, -9.0734º W) was drilled in 2014/2015 as explorative 2" borehole with the top at 30.4 masl. The borehole is 492 m deep and is completely uncased, i.e. open. The top is cased with a screw-cap that prevents any influx from the surface. BH1 is located on the grounds of a GAA pitch, 4.6 km south-west of the southern end of Bell Harbour Bay. Because BH1 is located in the centre of the presumed catchment of Bell Harbour, it was used for groundwater monitoring.
Prior to the start of this project, groundwater monitoring was started by Ted McCormack who installed a INW CT2X sensor attached on a stainless-steel rope wire at 22.0 mbgl.
Data were downloaded within infrequent intervals.

Upland borehole (BH2)

The upland borehole (BH2, 53.0591º N, -9.0827º W) was drilled in 2014 as explorative 2" borehole with the top at 141 masl. The borehole is 207 m deep and is completely uncased. BH2 was also used initially for groundwater monitoring but data are only available until October 2016 – shortly after, the borehole was back sealed again, so it could not be used anymore.
During time of operation, the borehole remained open, so the water column was subject to atmospheric influence.
Prior to the start of this project, groundwater monitoring was started by Ted McCormack who installed a Solinst LTC sensor attached on a Teflon-rope.
Data were downloaded within infrequent intervals.

Pouldoody spring (SiGD1)

Pouldoody spring (SiGD1, 53.1291º N, -9.0738º W) is assumed to be the main intertidal spring within Bell Harbour Bay, linked to the Bell Harbour groundwater catchment. The spring discharges at -0.1 masl into Pouldoody Bay, which is a sub-bay within the larger Bell Harbour Bay.
The spring has a relatively well-concentrated outlet, which is not captured. Spring discharge was measured using a CTD sensor attached to a PVC pipe/concrete slab and floating buoy. The concrete slab was placed into the intertidal zone or shoreline approx. 2 m off the spring outlet at -0.6 masl. Accordingly, the data sampled may be a mixture of sea water and discharged spring water.

Further, because the spring is not captured, and discharge is impacted by tidal fluctuations, there is no possibility of measuring the spring discharge.
Again, the sampler was installed by Ted McCormack prior to this project.

Luirk turlough (T2)

Luirk (53.1170º N, -9.0733º W) is a seasonally flooded turlough located 0.5 km south-west of Bell Harbour Bay. The turlough is presumably filled and emptied through an estavelle at 0.2 masl, yet, the estavelle has not yet identified due to very dense vegetation. Groundwater monitoring was executed at the lowest point identified using a PVC pipe/concrete slab sampler attached with a pressure sensor.
Again, the sampler was installed by Ted McCormack prior to this project.

Gortboyheen turlough (T1)

Gortboyheen (53.0871º N, -9.0742º W) is a seasonally flooded turlough with its estavelle located at 16.3 masl 0.7 km north-west of BH1. Groundwater monitoring was executed at the estavelle using a PVC pipe/concrete slab sampler attached with a pressure sensor.
Recording at the estavelle commenced in Jul 2014 and lasted until Oct 2016 when land access 0was not granted anymore by the land owner. Following this, a pressure sensor was placed at a new location into the crack of rock within the turlough located at 18.1 masl. Accordingly, any water level between the bottom of the turlough and 18.1 m (a total of 3 m) could not be recorded for the period after October 2016.

Poll Gonzo cave (PG)

Poll Gonzo (53.1170º N, -9.0733º W) is a vertically elongated cave along a mineral vein discovered between its top at 116 masl and the bottom sump at 31 masl (Figure 4.7) (Bunce, 2010). The cave is only accessible with professional speleological equipment. At approx. 70 masl a perennial underground river discharges approx. 10-100 l/s from south to north into the main chamber forming a spectacular waterfall whose water is separated: a smaller share enters the conduit network in the northern branch, while the larger share follows the explored cave to the bottom sump.
Prior to this study, different studies have unsuccessfully attempted to trace the waterfall (Bunce, 2010). Even without knowledge on the discharge of Poll Gonzo, the underground river upstream of the waterfall was equipped for 9 months with a Schlumberger CTD sensor. These data were thought to be informative in terms of rainfall response dynamics.
Besides using Poll Gonzo as monitoring site, the waterfall was also used as injection site for artificial tracer testing to identify its discharge location(s) – see Sections ‘4.1.4.2. Artificial tracers’ and ‘8.1.5. Tracer study’.

Furthermore, time series on tidal water level fluctuations in the sea were obtained from the Marine Institute (MI) at a sampling frequency of 6 min. The monitoring station is Galway Port at 0 masl and 53.269° N and -9.048° W.

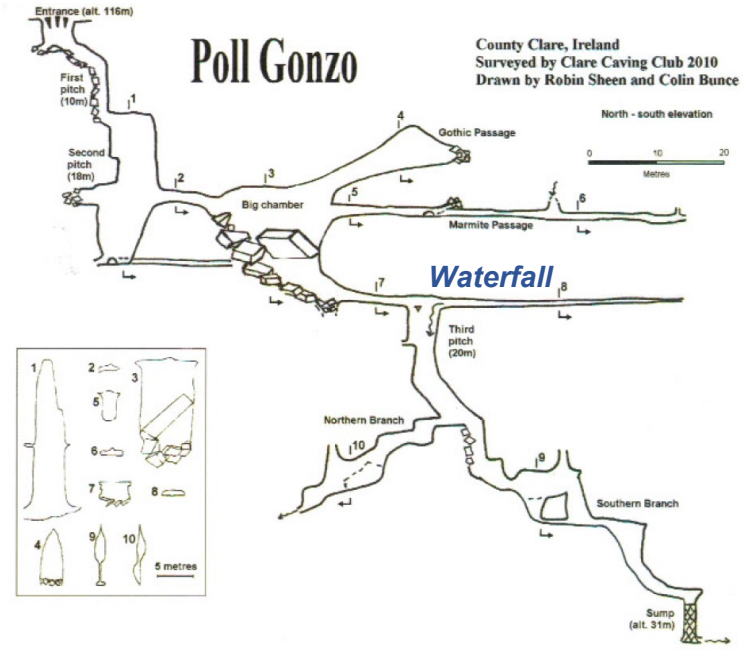

Figure 4.7: Cross-section of Poll Gonzo cave with highlighted location of the waterfall (Bunce, 2010).

4.1.4. Tracer techniques

4.1.4.1. Environmental tracers

Generally, ions, i.e. Na^+, Mg^{2+}, Ca^{2+}, K^+, Cl^-, SO_4^{2-}, $CaCO_3$, silicon dioxide (silica, SiO_2), and the parameters EC and temperature were used to characterise the response of systems to rainfall, as well as to evaluate their behaviour during recessions related to their source areas. This type of analysis is rather descriptive, yet, it allows conclusions to be drawn on the hydrodynamic behaviour and understanding of recharge, flow and spring discharge.

Further, for the determination of components in the spring signal, mixing models in form of TCMA was applied to separate a groundwater component from the overall hydrograph using 2H and 18O.

4.1.4.2. Artificial tracers

Artificial tracer tests were used to establish hydraulic (delineate the catchment of the study areas), and - where possible – to quantify mean flow velocities in the conduit/saturated zone.

Four different conservative and non-conservative fluorescent tracers were used: a) uranine (sodium-fluorescein, acid yellow 73, $C_{20}H_{10}O_5Na_2$), b) rhodamine WT (acid red 388, $C_{29}H_{29}N_2NaO_5$, c) and c) optical brightener (Durawhite A-01 liquid, Town End PLC, Leeds, UK). While much

information can be found in the literature on rhodamine WT and uranine, Durawhite is a less common tracer frequently applied though by the GSI.

All four tracers were sampled qualitatively using activated charcoal bags (rhodamine and uranine), cotton wool (optical brightener) and/or quantitatively in parallel using Albillia GGUN-FL30 flow-through field fluorometers and the designated software GGUN-FI Field Fluorometer.
For qualitative sampling, granulated activated charcoal (technical grade, AppliChem GmbH, Darmstadt, Germany) was used filled in nylon bags. Elution of fluorescence from charcoal was done following the 'Smart method' (Smart and Simpson, 2002) lasting for 1 to 2 hours. The analysis was carried out in the environmental laboratory of the GSI using a Cary Eclipse Fluorescence Spectrophotometer.
In the Manorhamilton and Ballindine catchments, field fluorometers were deployed at the EPA gauging station (MH3) and the main outlet MH1 to assess the connection between injection points and the observation site as illustrated in Figure 2.21. Accordingly, the concentration of up to three different dyes was monitored in spring water for a time interval ≥10 s. The plot of recovered tracer in time yields the tracer break-through curve (TBC). The TBC in combination with measured spring discharge then allows an estimate of: a) the total recovered tracer mass M_t [mg] and b) the mean residence time $\bar{t}$ [s], and c) the mean travel time $\bar{v}$ [m/s].

The total tracer recovery M_t [mg] was estimated by (Field, 2002),

$$M_t = \int_0^\infty C(t)\, Q(t)\, dt \qquad \text{Eqn. 4.4}$$

with the tracer concentration C [mg/l] at time t [s] and the discharge Q [l/s] accounting for the background tracer concentration.

The mean vertical travel time $\bar{v}$ was calculated based on the mean residence time $\bar{t}$, which is given by (Field, 2002),

$$\bar{\bar{t}} = \frac{\int_0^\infty tC(t)\, Q(t)\, dt}{\int_0^\infty C(t)\, Q(t)\, dt} \qquad \text{Eqn. 4.5}$$

While the method of artificial tracer testing follows standard procedures in the catchments of Ballindine and Manorhamilton, dye tracing in the coastal catchment of Bell Harbour was more challenging. Discharge at Bell Harbour occurs via a) intertidal springs as well as via b) known and unknown submarine springs. Intertidal springs can be monitored in the same way as it has been done using CTD sensors deployed at the outlet of Pouldoody spring (SiGD1). The resulting monitored concentrations are, however, not representative as pure spring discharge due to the occurring dilution

effect of the sea. Therefore, a clear TBC cannot be established. Further, measured concentrations of dye cannot be used to quantify the recovered tracer mass M_t as due to the nature of the discharge location, the spring discharge cannot be directly measured. Therefore, the results of dye testing at intertidal springs can be considered as semi-quantitative.

Concerning purely submarine springs, the method is even more complex. Complications arise due to:

- Limited knowledge concerning the exact location of submarine springs;
- Strong dilution effect of the sea on submarine groundwater discharge (SGD);
- Absence of knowledge which potential submarine springs may be hydraulically connected to a catchment and its injection sites; and
- Physical obstacle of deploying a fluorometer in the sea.

As it turned out in the framework of this research, it was necessary to develop a method to apply dye tracing on submarine springs in order to verify the hypothesis of the functioning of the coastal karst aquifer of Bell Harbour outlined in Schuler, et al. (2018a). The development of a tracer method for submarine springs was financed through a grant from the GSI thanks to the successful application for a GSI Short-Call project by Laurence Gill, Peter Croot and the author. This project lasted from November 2017 to October 2018.
In fact, the developed method aims to mitigate the problems (a)-(d) mentioned above, and it is summarised in Table 4.5.

Table 4.5: Summary of tracer method for submarine groundwater discharge.

Challenge	Mitigation measure
Limited knowledge concerning the exact location of submarine springs.	▪ Desktop study on (historical) reports on submarine springs and structural geology; ▪ Quantify and map temperature anomalies of the sea surface as indicator of submarine groundwater discharge.
Strong dilution effect of the sea on submarine groundwater discharge.	▪ Apply visible biodegradable solid tracers with neutral buoyancy in freshwater and positively buoyant in salt water; ▪ Use large amounts of fluorescent dyes.
Absence of knowledge which potential submarine springs may be hydraulically connected to a catchment and its injection sites.	▪ Conduct 'mobile offshore sampling' in the areas of potential submarine groundwater discharge in the sea to monitor for floating solid tracers and fluorescence of the sea water.
Physical obstacle of deploying a fluorometer stationary in the sea.	▪ Conduct monitoring over several days along transects in the sea with fluorometer attached to a vessel.
Erroneous readings of the fluorometer due to turbulent environment in the sea.	▪ Development of systematic approach to filter out erroneous data and threshold level to ensure validity and reliability of filtered data.

The general occurrence of SGD was evaluated using literature and understanding concerning the impact of structural geology on groundwater flow. More precisely, potential locations of SGD were mapped based on fact that SGD has a different density and temperature than sea water. The lower density of SGD promotes its rise towards the sea surface, where patterns of temperature anomalies may then be interpreted as indicator of that phenomenon (Johnson, et al., 2008; Wilson and Rocha, 2012; Tamborski, et al., 2015). Sea surface temperature maps were generated for as many dates as possible using optical Landsat 8 OLI imagery with a spatial resolution of 15 m (Band 8), 30 m (Band 1 – 7 and 9) and 100 m (Band 10 - 11, TIRS). (Data available from the USGS, available at https://earthexplorer.usgs.gov/).

Because Landsat is a passive system, images are frequently disturbed by cloud cover. The level of acceptable cloud cover was therefore defined as 20%, so that any imagery with a cloud cover >20% was neglected for this study. Surface temperatures were generated in ArcGIS using a designated ArcGIS toolbox and method (Walawender, et al., 2012). The analysis and plotting of temperature layers provide then reasonable results on potential SGD locations.

In a next step, suitable artificial tracers were chosen. Because of the strong dilution effect in the sea, two approaches were undertaken, which are both based on the very well-developed conceptual understanding of the study site: a) developing suitable solid tracers that would float on the surface once discharged into sea, and b) choosing large amounts of fluorescent dyes:

- Concerning a), the suitability of wood chips as a natural and biodegradable tracer was tested, which were to be injected into an underground river/waterfall within the cave system of Poll Gonzo. The ideal solid tracer would have a density between fresh water (1 kg/m^3) and sea water (~1.035 kg/m^3) to float neutrally buoyant within the underground river and conduits, before floating on the surface of the sea once being discharged into the bay. Once floating on the sea surface, these wood chips may be visually observed by persons over a longer period (~days/week). However, in reality it was found very difficult to find these properties in wood, as densities of woods may change from tree to tree. Further, due to sorption of water by wood, the density of wood chips changes over time. Therefore, chips of different types of wood were tested in a stirring freshwater tank over the period of 10 days. The types of wood tested, and their average densities provided by the wood species database of the UK Timber Research and Development Association (TRADA, 2018) are Denya (960 kg/m^3), European Oak (720 kg/m^3), Iroko (660 kg/m^3), Keruing (740 kg/m^3 ±20%) and Opepe (750 kg/m^3) (Figure 4.8a). The chips tested were of the size 4 x 40 x 50 mm.

Figure 4.8: Wood chips (a) tested in a stirring tank (b).

At the beginning of the test, all wood chips floated on the surface (Figure 4.8b). After 10 days, all wood chips sank to the ground, except Keruing, which was weakly buoyant and stayed more or less in the vicinity of the water surface. When tested, buoyancy was slightly higher in salt water where the tested wood was floating on the surface. Accordingly, this wood was used as solid tracer. Wood chips in ranging dimensions of approx. ≤5 x 40 x 50 mm were manufactured manually using a band saw and a wood chipper. The total mass of wood chips was then soaked in fresh water for approx. 5 days (to account for additional 'soaking' during time in the aquifer). Finally, the soaked chips were filled into 10 x 30 l caving bags used for transportation to and in the cave Poll Gonzo.

- Concerning b), the amount and type of tracer must be considered. In the study area, more than 12 tracer tests were previously conducted with tracer masses ranging between 50 g and 20 l using optical brightener, rhodamine, and uranine. Four of the 12 tests aimed to trace intertidal and submarine springs, with negative results (Bunce and Drew, 2017). Based on these results and the conceptual understanding of the catchment of Bell Harbour, it was decided to use fluorescein and rhodamine, each with a mass of 25 kg.

In a next step, the mobile offshore sampling strategy was outlined. Because multiple locations or areas of potential SGD were identified, which could all – if proven to be indeed related to SGD – be hydraulically connected to the injection points, sampling was designed to consider these different locations or areas. Hence, 'dynamic' or 'mobile' marine offshore sampling was conducted rather than deploying a fluorometer 'stationary' fixed at one location. Accordingly, the vessel was iteratively and systematically passing over the areas of potential SGD while monitoring for fluorescence in the sea and observing the sea surface for floating wood chips. Based on estimated mean travel times (<~270 m/h), it was decided to start sampling 36 h after injection lasting for 3-4 days as many hours as possible per day. The fluorometer was tied on ropes to be pulled in the back of the vessel while being connected to the data logger and a computer on board (Figure 4.9a-c). Additional weights were installed on the ropes to make sure the fluorometer stays under the sea surface.

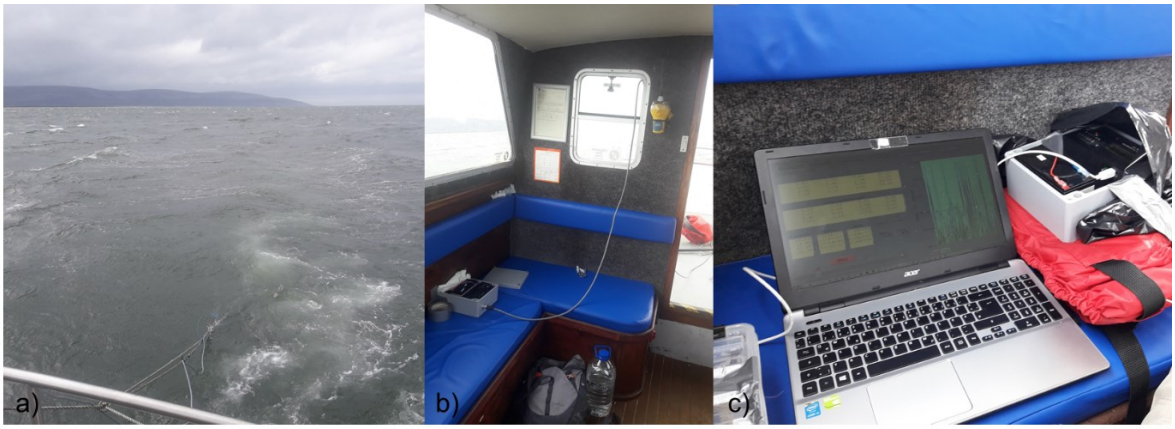

Figure 4.9: Offshore sampling in the sea using a field fluorometer (a) connected to a data logger (b) and laptop (c).

Further, a CTD (LTC M200 Levelogger) sensor was attached close to the fluorometer to sample for depth, temperature, as well as conductivity as indicator for submarine groundwater discharge.
In order to obtain the spatial reference of each reading of the CTD and the fluorometer, both instruments were synchronised with a hand-held GPS (GPSmap 60CSx) recording the geographic position of the vessel in 3 s intervals.

The functioning of the fluorometer was ensured during real-time monitoring on board the vessel, yet, the validity of recorded data was analysed after returning from the field. It turned out that the analysis of the data was not as straight-forward as in the case of 'stationary' sampling spring discharge. While monitoring of a spring yields a rather clean continuous signal in time, sampling in the sea is impacted by perturbation through currents, drag of the boat and air bubbles. Most likely air bubbles caused potentially erroneous readings, which, in some instances could clearly be detected while in other instances it was less clear. For example, Figure 4.10 shows readings of tracer 1 (uranine), tracer 2 (rhodamine) and tracer 3 (Tinopal) [mV] (column E-G), and the converted ppb signal based on the calibration (column S-U), and turbidity [NTU] (V). Lines in green are highlighted as valid records, lines in red are highlighted as invalid records. In principle, higher mV readings are converted into higher ppb values. However, in some instances, exceptionally high mV readings occur for tracer 1,2 and 3 (line 1770). Such high values are anomalous discrete high readings, which do not occur within a trending sequence of higher values, which would be the assumption if passing through an area where a 'plume' of dye was discharging. Therefore, these individual high readings were considered as not valid.
A method or procedure had to be applied to systematically and objectively filter out these discrete invalid readings.

	B	C	D	E	F	G	S	T	U	V
1	Time_UTC	lat	lon	Tracer1_mv	Tracer2_mv	Tracer3_mv	Tracer1_ppb	Tracer2_ppb	Tracer3_ppb	Turbidity NTU
1750	17/04/2018 15:01:10	53.186	-9.091	6.02	3.27	0.72	0.19	0.23	0.01	0.53
1751	17/04/2018 15:02:40	53.186	-9.093	5.26	2.99	0.68	0.13	0.19	0.01	0.42
1752	17/04/2018 15:02:50	53.186	-9.093	4.99	3.03	0.28	0.11	0.19	0.01	0.46
1753	17/04/2018 15:03:30	53.186	-9.094	5.05	3.10	1.42	0.11	0.21	0.01	0.33
1754	17/04/2018 15:03:40	53.186	-9.094	5.29	3.48	1.42	0.12	0.28	0.01	0.64
1755	17/04/2018 15:03:50	53.186	-9.094	5.76	2.64	1.31	0.19	0.12	0.01	0.57
1756	17/04/2018 15:04:20	53.185	-9.094	5.29	3.19	0.30	0.13	0.22	0.01	0.44
1757	17/04/2018 15:04:30	53.185	-9.095	5.95	2.57	0.91	0.20	0.10	0.01	0.40
1758	17/04/2018 15:04:40	53.185	-9.095	4.95	2.36	1.41	0.13	0.07	0.01	0.48
1759	17/04/2018 15:05:00	53.185	-9.095	4.95	18.44	0.93	0.00	3.03	0.01	3.09
1760	17/04/2018 15:05:10	53.185	-9.095	8.89	4.19	2.88	0.40	0.38	0.01	1.08
1761	17/04/2018 15:05:20	53.185	-9.096	8.89	4.19	1.20	0.40	0.38	0.01	4.77
1762	17/04/2018 15:05:30	53.185	-9.096	36.26	6.08	1.20	2.64	0.55	0.01	2.49
1763	17/04/2018 15:06:10	53.185	-9.097	21.01	7.01	2435.04	1.33	0.82	0.01	1.92
1764	17/04/2018 15:06:20	53.185	-9.097	12.49	7.01	2435.04	0.61	0.88	0.01	0.00
1765	17/04/2018 15:06:30	53.185	-9.098	20.61	7.01	2435.04	1.30	0.83	0.01	0.00
1766	17/04/2018 15:07:00	53.185	-9.099	13.15	725.39	6.87	0.00	132.92	0.01	4.64
1767	17/04/2018 15:07:10	53.185	-9.100	13.14	725.39	6.87	0.00	132.92	0.01	4.64
1768	17/04/2018 15:07:20	53.185	-9.100	34.45	7.51	6.87	2.44	0.83	0.01	1.04
1769	17/04/2018 15:07:30	53.185	-9.100	6.91	23.40	4.94	0.00	3.93	0.01	0.77
1770	17/04/2018 15:09:00	53.184	-9.104	1225.94	2490.45	2491.62	25.15	449.51	0.01	0.28
1771	17/04/2018 15:09:20	53.184	-9.105	4.90	14.03	0.69	0.00	2.22	0.01	0.00
1772	17/04/2018 15:10:00	53.184	-9.106	46.07	33.15	5.02	2.62	5.47	0.01	5.45

Figure 4.10: Sample of data collected by the fluorometer in the sea.

The systematic approach for filtering out erroneous readings was done in close communication with the manufacturer of the instrument, Pierre-André Schnegg. The principle behind the validity check is to compare the ratio of observed mV signals of given tracers with the ratio of mV signals of the same tracers as established during the calibration procedure using the values of the four photo-detectors namely L1, L2, L3 and L4, or as in the case of the two tracers rhodamine and uranine, only the ratios of L1 and L2 in the recorded raw files.

First, the ratio of measured mV signals for a tracer T_n of interest is established using the measured signals of L1 during calibration $L1_{cal}$ [mV] and L2 during calibration $L2_{cal}$ [mV]. The calibration ratio r_0 is then given by,

$$r_{0,T_n} = \frac{L2_{cal,T_n} - L2_{cal,W}}{L1_{cal,T_n} - L1_{cal,W}} \qquad \text{Eqn. 4.6}$$

with the associated signal for water W [mV] and the tracer with n = 1 for uranine and n = 2 for rhodamine.

The result is a characteristic ratio for each of the three tracers that can be monitored, corrected by subtracting the background signal of water. Next, the actual observed ratio between photodetector 1 $L1_{obs}$ [mV] and photodetector 2 $L2_{obs}$ [mV] at time step t is established to yield r_t following,

$$r_t = \frac{L2_{obs} - L2_{cal,W}}{L1_{obs} - L1_{cal,W}} \qquad \text{Eqn. 4.7}$$

again, corrected for the background value of water.

Ideally, $r_t = r_{0,T_n}$ but this is never exactly the case. Since L2 is measured 100 ms after L1, the measurement is rejected if a large deviation of r_t from r_{0,T_n} is observed, indicating the occurrence of air bubbles during the measurement of L1 or L2. Here, an observation was considered reliable if its r_t ranges between the lower and upper limit of the ratios of the two tracers considered, which are r_1 = 0.035 for uranine and r_2 = 2.597 for rhodamine. In addition, a threshold deviation of ±20% was defined as acceptable so that $0.8 \times r_{0,T_1} < r_{t,T_n} < 1.2 \times r_{0,T_2}$.
Because of its nature, the method is called 'quotient method'. This approach was considered to be very conservative in order to reliably define the validity of a single tracer reading following a transparent filtering sequence.

4.1.4.2.1. Calibration

It is important that fluorometers must be calibrated freshly for each tracer test to yield accurate concentrations especially when measuring multiple tracers at the same time. Calibration was done using the standards 1, 10 and 100 ppb for each specific tracer used throughout the test. The calibration standards were manually done using the respective dye diluted in source water where the fluorometer was deployed, where applicable. A very good reference for calibration of the fluorometers can be found in Margane and Abi-Risk (2011). Examples of calibration results are displayed in Figure 4.11a-b for uranine and rhodamine WT.

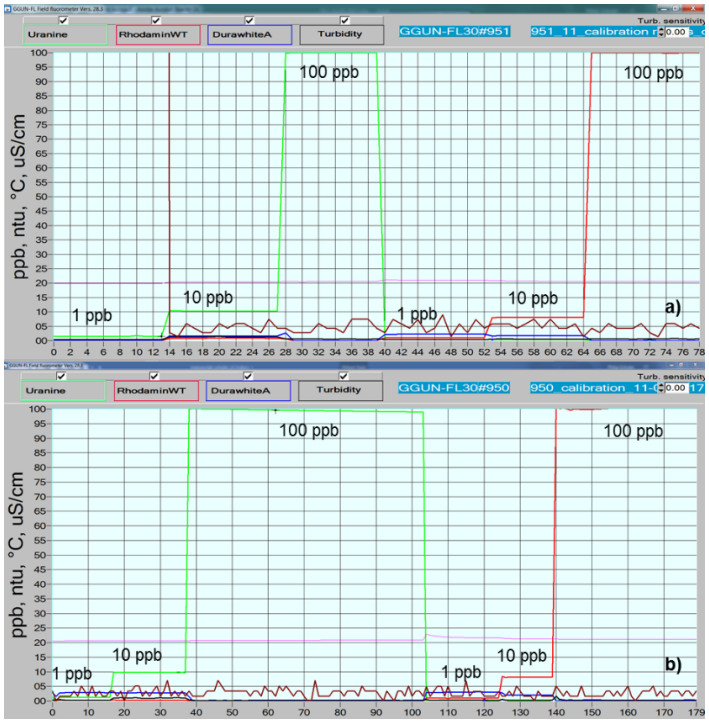

Figure 4.11: Calibration results of a) fluorometer #951 and b) a) fluorometer #950 for rhodamine WT and uranine.

4.1.5. Single borehole dilution tests (SBDT)

Ambient groundwater dynamics including water level, temperature and conductivity were continuously measured in BH1 using a CTD sensor. However, the collected data do not yield information on vertical flow (direction and velocity), as well as potential zones of groundwater inflow or outflow. Single borehole dilution tests (SBDT) were therefore conducted in BH1 to identify groundwater flow directions and mean flow velocities under ambient conditions. The approach follows the method outlined by Maurice, et al. (2011) using concentrated emplacements of tracer cocktails with a concentration of 125 or 62.5 g NaCl/l as well as using deionised water. Tracer cocktails were mixed in the lab and filled into 500 ml PET bottles.

The field application (see Figure 4.12) includes the following: a 0.6 cm diameter hosepipe of 25 m length at which end a Schlumberger DI263 CTD sensor was installed and released into the borehole. The top of the hose was connected to a funnel and fixed at the top of the borehole.

The sampling frequency of the CTD sensor at the bottom end of the hose was set to 1 s. Above and below the bottom of the tube, a set of CTD sensors were independently installed on wire ropes sampling at a frequency of 1 or 2 s in variable depths. All instruments were synchronised before deployment.

Injections were carried out by filling the desired tracer cocktail into the funnel. Flushing was done to ensure that all tracer was pushed out of the tube. The necessary flushing volume to be used was calculated by the part of the hose below the groundwater level multiplied with the inner diameter of the tube. When possible, turlough water (T1) was used for flushing. Flushing was commenced directly following the emptying of the tracer cocktail, and the time of flushing start was defined as the 'injection time'. Once the flushing water was all emptied, the injection was considered finished.

The total tracer recovery M_t [mg] and the mean vertical travel time $\bar{v}$ [m/s] were estimated following Eqn. 4.4 and Eqn. 4.5.

Zones of inflow and/or outflow of groundwater were determined by repeating the concentrated tracer injections after lowering or lifting the CTD sensor. For example, after a first tracer injection, the tracer plume may migrate upwards where it is recorded 10 m above the injection point. Successively, tracer injections were repeated with lifting the recording CTD sensor by e.g. 5 m each injection. When the tracer was not recorded at a certain level anymore, it was assumed that the tracer plume must have migrated out from the borehole between the levels of the CTD sensor during the last two tracer injections.

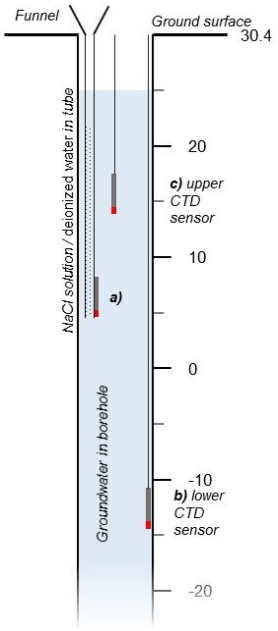

Figure 4.12: SBDT setup – inflow of tracer at the outlet of the tube (a), sampling below (b) and above (c) the injection depth.

4.2. Spatial data sets

Raster and vector files used in this study are summarised in Table 4.6, all freely available.
A 5 m bathymetry grid provided by the GSI was used to calculate the volume of Bell Harbour bay at different water levels. The bathymetry grid was combined with the Shuttle Radar Topography Mission (SRTM) digital elevation model (DEM) (data available from the U.S. Geological Survey, USGS, available at https://earthexplorer.usgs.gov/) and complemented with data from extensive topographical field surveys using the Trimble 4700 differential GPS to derive an improved 5 m elevation grid for the study area. This grid was used to calculate the volume of turloughs followed by the establishment of a stage-volume curve, carried out using ArcGIS (version 10.2, ESRI, Redlands, CA, USA). All spatial analyses and map design were done using the geographic coordinate system and projection Irish Transverse Mercator (ITM) displayed in meter.

Table 4.6: Spatial datasets used (GSI = Geological Survey Ireland, USGS = United States Geological Survey, EPA = Environmental Protection Agency).

Name	Type/resolution	Extent	Data source
Bathymetry	Grid, 5 m	Left-right: 515065.3, 541265.3, top-bottom: 719003.5, 707458.5	GSI
SRTM Digital Elevation Model, 1 Arc-Second Global	Grid, ~30 m	left-right: 462655.9, 600018.6 top-bottom: 806118.8, 583564.2	USGS

Landsat 8 OLI	Grid, 15-100 m	Rep. of Ireland	USGS
groundwater recharge	Vector	Rep. of Ireland	GSI
Bedrock rock units 1:100,000	Vector	Rep. of Ireland	GSI
Irish National Soils Map, 1:250,000k, V1b(2014)	Vector	Rep. of Ireland	Teagasc, Cranfield University
Bedrock Aquifers	Vector	Rep. of Ireland	GSI
Karst features	Vector	Rep. of Ireland	GSI
OSI Geometric River Network	Vector	Rep. of Ireland	EPA
OSI Rivers and Lakes	Vector	Rep. of Ireland	EPA

4.3. Methods overview

4.3.1. Time series analysis

In the case of spring discharge time series, master recession curves (MRC) were established using the software RC (version 4.0, HydroOffice, Mojtin, Slovakia). The software is freely available at https://hydrooffice.org.
MRCs were established by plotting rainfall and spring discharge time series together in order to identify periods where the spring discharge is not affected by significant rainfall (Figure 4.13). Individual spring discharge segments are then cropped and assembled. In the next step, all segments are plotted together, and fitted along the x-axis (time) to match a most coherent single recession. Finally, at every time step the average discharge is calculated to optimise the result, i.e. the averaged MRC representative for the discharge time series.

For a first analysis of the hydrological functioning of the aquifers of Ballindine and Manorhamilton, including the characterisation of infiltration and storage, respective MRCs were evaluated using the method of Mangin (1975) and El-Hakim and Bakalowicz (2007). This approach seems relevant as it yields two parameters, the infiltration delay i (describing the infiltration conditions, i.e. slow vs. fast) and the regulating power k (describing the mean residence time of groundwater in the phreatic zone). This assessment links groundwater recharge and discharge dynamics, and it provides first indications of spring hydrodynamics relevant to the overall research topic.
Further, the method estimates the dynamic storage in the phreatic zone $Max(V_d)$ [m³] by integrating the baseflow function from the flood peak time t_0. Referring to Forkasiewicz and Paloc (1967), the result of such baseflow function may be linked to the low storage component resembling the low-permeability domain, or rather to a 'lowest permeability domain' (i.e. an aquifer can be composed different levels of low permeabilities but only one is the lowest).

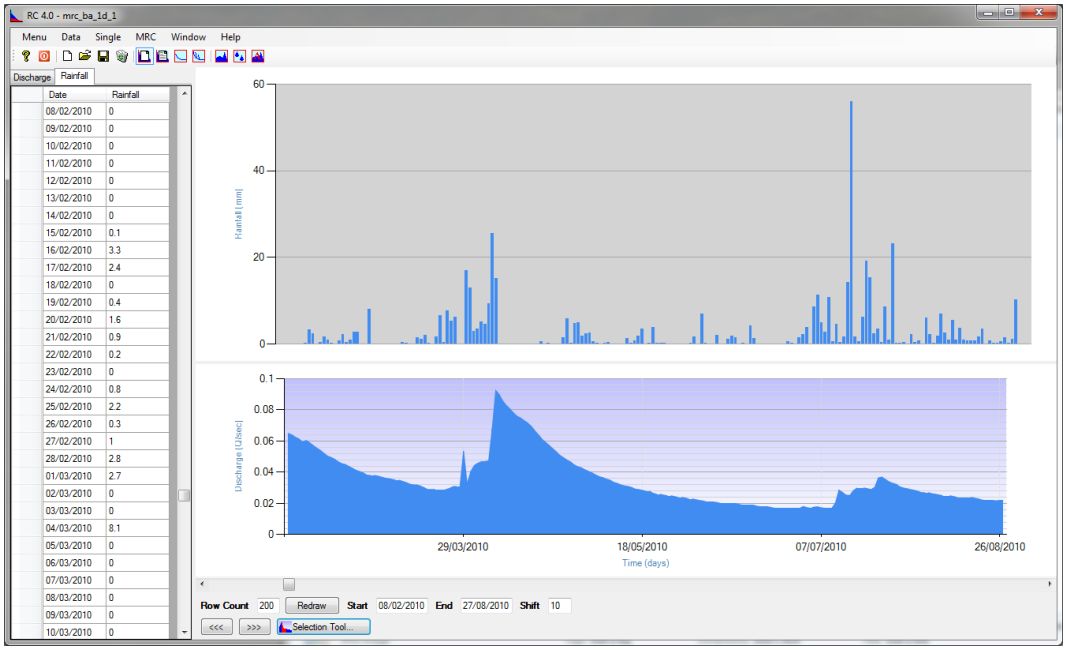

Figure 4.13: Establishing master recession curves using the software RC (HydroOffice).

4.3.1.1. Autocorrelation function

Autocorrelation was calculated for different time series (e.g. spring discharge, water level, rainfall, etc.) based on Venables and Ripley (2002); Valdes, et al. (2006).

The evaluation of a memory effect was done based on the widely used threshold of 0.2 and 0.05.

The autocorrelation function was executed using the freely available software R (version 3.2.3, www.r-project.org) and the interface RStudio (version 1.1.453, www.rstudio.com).

4.3.1.2. Cross-correlation

Cross-correlation was carried out between different time series (e.g. rainfall, water level, discharge, etc.) based on the assumption that the time series can be regarded as bivariate stochastic processes that are stationary (Box and Jenkins, 1976; Jukić and Denić-Jukić, 2015). Cross-correlation was calculated following Venables and Ripley (2002).

Cross-correlation analysis was applied on hourly or daily time series of different monitoring sites to identify the strength (cross-correlation function) and the dynamics (time lag) of linear input-output relationships between series.

Cross-correlation was executed using the software R (version 3.2.3, www.r-project.org) and the interface RStudio (version 1.1.453, www.rstudio.com).

4.3.1.3. Frequency analysis (Fourier transforms)

Computation of the Discrete Fourier Transform (DFT) of hourly and daily time series was done using a fast algorithm, i.e. Fast Fourier Transform (FFT) implemented in the software R based on Cooley and Tukey (1965) and Singleton (1979).

The FFT was then analysed for frequency patterns, which were also used for wavelet analysis to identify frequency patterns in time.
FFT was applied on discharge time series to identify frequencies associated with the drainage of permeability domains of karst aquifers. Accordingly, changes in frequencies are marked by significant changes in slopes, which were identified using Pettitt (1979) where,

$$K_T = \max\left|U_{t,T}\right| \qquad \text{Eqn. 4.8}$$

and,

$$U_{t,T} = 2\sum_{i=1}^{t} r_i - t(n+1)k = 1, \dots n \qquad \text{Eqn. 4.9}$$

with the change point of the series located at K_T and the ranks $r_1 \dots r_n$. The significance of K_T is approximated for p ≤0.05 with,

$$\mathrm{p} \cong 2\exp\left(\frac{-6K_T^2}{T^3 + T^2}\right) \qquad \text{Eqn. 4.10}$$

applied in the software R. The Pettitt test can only detect a single change point, which is a limitation if multiple change points are to be identified. Hence, the Pettitt test was applied iteratively: a first breakpoint was generated, and this breakpoint was then used to cut the entire time series into two segments, where the remainder of the time series was then again analysed to find the next breakpoint. This breakpoint was then used to cut the previously analysed time series into two segments, and so on. This repetition was done until no statistically significant breakpoint with a p value <0.05 was generated. Hence, only significant breakpoints were used.

Each segment of Fourier spectra separated by breakpoints following the Pettitt method in a log-log power spectrum can be approximated by a linear regression to yield the spectral coefficient β. Further, β is assigned to a 'noise domain' including the domains of Gaussian (random) and Brownian (structured) noise.
As a working hypothesis of this study, the drainage from distinctive permeability domains can be differentiated by the following steps:

1. Generating the Fourier spectra of each hydrograph;
2. Statistically separating different slope segments of the Fourier spectra applying the Pettitt test to generate significant change points; and

3. Using noise analysis to then select the change points that separate different segments of distinct noise, representing frequency segments characteristic for an individual permeability domain.

4.3.1.4. Wavelet analysis

The DWT is limited to continuous time series without interruption. While this could be achieved for Ballindine by filling some days of data gaps using a reservoir model, the length of time series for Manorhamilton is shorter as it contained significant data gaps that could not be filled.
Both, the continuous wavelet transform (CWT) in form of the Morlet wavelet (Torrence and Compo, 1998; Labat, et al., 2001) and discrete wavelet transform (DWT) in the form of the Daubechies wavelet (Labat, et al., 2000b) were applied using the software R. The transformation of a continuous signal into wavelets series decomposition through discrete wavelets is done on a dyadic scale (Valens, 1999). Decomposition is done into different scales, i.e. details (D), and the residual or smooth (S) (Labat, et al., 2000b).
Different orders of Daubechies wavelets were tested in this research, as there is no general rule of which to apply in hydrology. Here, db10 and db20 were applied.
Cross wavelet transform (XWT) and wavelet coherence (WTC) including mean phase angles were simulated using MATLAB R2016b (version 9.1.0., MathWorks Inc., Natick, MA, USA) and the code provided by Grinsted, et al. (2004).

4.3.2. Hydrograph analysis and low-flow component separation

The baseflow, or low-flow component (LFC), is conceptualised (although not necessarily only) to represent the discharge signal of a spring hydrograph linked to diffuse groundwater recharge. This diffuse recharge is believed to be associated with the low permeability domain of the aquifer.
This section addresses the methods applied for the separation of the LFC pathway for spring hydrographs of Ballindine and Manorhamilton. LFCs were generated using different methods according to the workflow presented in Figure 4.14. The here outlined workflow is split into sub-sections of Chapters ‘Catchment Studies’ and ‘Time Series Analysis’. The aim is to establish continuous time series that can be used as reference in groundwater flow modelling. Hence, where applicable, the LFC time series shall be used to calibrate a diffuse groundwater recharge and flow component.

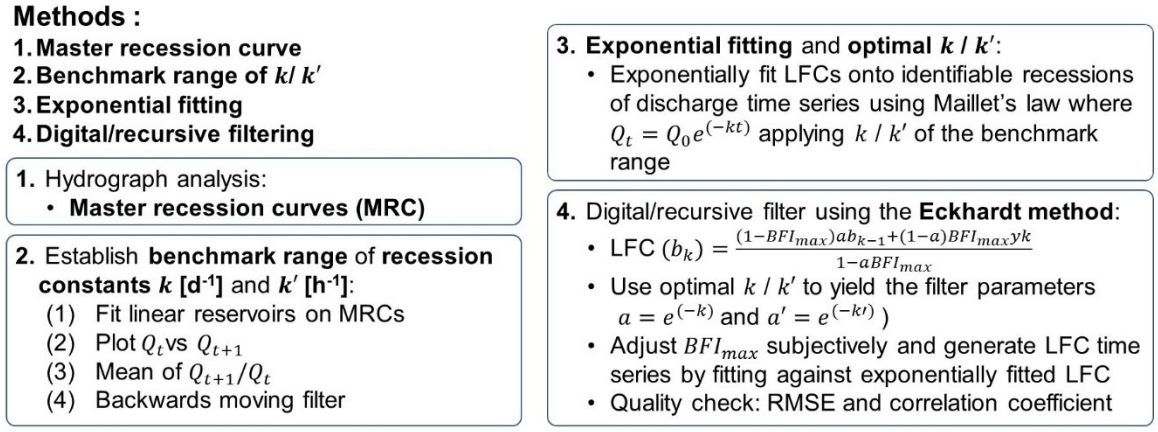

Figure 4.14: Workflow for the separation of LFCs.

The workflow presented in Figure 4.14 is based on the premises that:

1. A hydrograph is a response to a recharge event. While the rising limb expresses the characteristics of the recharge event, the recession following the inflection point is the stable part that is site-specific, and which informs about the discharge characteristics (internal structure) of the aquifer;
2. A karst hydrograph recession can be decomposed into multiple exponential segments, each representing a distinctive permeability domain of the karst aquifer. For symmetric block shape, three exponential components can sufficiently resemble the recession;
3. A master-recession curve (MRC) resembles the average recession (drainage) response of a karst spring following a recharge event;
4. Each exponential segment is described by Q_0 and a k value or recession coefficient a;
5. The LFC is defined as the low-frequency component. It is the exponential component with the lowest k value, active for a longer period than all other exponential components during a recession or low flow;
6. The permeability domain related to the LFC is site-specific, yet, it is rather associated with fissured matrix (if present). The LFC concentrates towards larger fractures and conduits towards the spring. Hence, the LFC may be subject to different flow regimes, potentially laminar and/or turbulent.

LFCs of each time series was established based on the recession (the stable and ideally undisturbed part of a hydrograph). The recession reveals information on aquifer characteristics via the recession constant k or coefficient a. Conceptually, the different recession segments are linked to different flow and recharge regimes based on the principles of Forkasiewicz and Paloc (1967). However, most commonly in Ireland undisturbed recession may be rare. Therefore, recession analysis was applied using the average recession, i.e. MRC. The number of exponential segments that can be distinguished along an MRC was identified fitting the least as possible linear reservoirs

along the MRC, starting with the lowest part of the recession. Fitting of the exponential components yields straight lines in a semi-logarithmic plot.

For the late recession (LFC), benchmark ranges of optimal recession constants k and recession coefficients a were established using 4 different methods: methods 1 to 3 were recommended by Eckhardt (2008) and Rimmer and Hartmann (2014), method 4 by Collischonn and Fan (2013), as follows:

1. Fitting multiple linear reservoirs following Maillet (1905) against the MRC where $a = \exp(-k)$;
2. Plotting Q_t against Q_{t+1} where the slope of the recession line through the origin is considered as the optimal recession constant a;
3. Calculating the mean of Q_{t+1}/Q_t; and
4. Applying a backwards moving filter.

The backwards moving filter applies,

$$q_{bf,t-1} = \frac{q_{bf,t}}{a} \qquad \text{Eqn. 4.11}$$

with the maximum possible baseflow of the previous time step $q_{bf,t-1}$ that would result in the present time step baseflow $q_{bf,t}$.

Using the benchmark range of k and/or a values, individual exponential components for single events were fitted against the late recession along the observed undisturbed hydrograph. These exponential components are discrete segments potentially short in time, which limits their use as calibration reference in groundwater flow modelling. Therefore, based on the k and a values and discrete exponentially fitted LFC segments, digital recursive filtering was applied. The benchmark range of optimal k and a values was used to fit digital recursive filters against the exponentially separated LFCs. Fitting was evaluated against the single exponential components using the RMSE and the correlation coefficient.

Another method that was applied to separate the LFC from the hydrograph was done using a two-component mixing model (TCMA) using stable isotope analysis (Section '4.1.4.1. Environmental tracers'). However, it should be noted that such event-based analysis could only be done for quick-responding systems, such as Bell Harbour and Manorhamilton.

4.3.2.1. Spring hydrography

Spring discharge time series and MRCs of Ballindine and Manorhamilton were decomposed into multiple exponential components with individual recession coefficients a where α_1 is the low flow

recession coefficient, α_2 is intermediate recession coefficient, and α_3 is fast recession coefficient. Accordingly, for each component, the discharge Q at time t is estimated following Maillet's law, while the sum of Q of all flow components at time t is given by,

$$Q_t = q_{0_1} e^{-a_1 t} + q_{0_2} e^{-a_2 t} + q_{0_3} e^{-a_3 t} \quad \text{Eqn. 4.12}$$

with the discharge q_0 at t = 0 and individual recession components a for the individual segments (Kovács and Perrochet, 2008).

The slope λ of each straight-line component is given by,

$$\lambda = \ln\left(\frac{Q_1}{Q_2}\right) / \left(\frac{t_2}{t_1}\right) \quad \text{Eqn. 4.13}$$

with the discharge Q_1 at the beginning of the segment at time t = 1 and discharge Q_2 at the end of the segment at time t = 2 (Moore, 1992).

The recession coefficient α_1 was established using the methods 1 to 4 outlined above.

The transformation from α_1 for daily time series into to $\alpha_1{}'$ another time step (e.g. hourly) the following relationship applies,

$$\alpha_1{}' = \alpha_1{}^C \quad \text{Eqn. 4.14}$$

where the time frequency of $\alpha_1{}'$ is given by $\Delta t' = c\Delta t$ (Eckhardt, 2008).

4.3.2.2. Well hydrography

Borehole level (piezometric head) time series and MRCs of BH1 and BH2 were decomposed following the same principles as spring discharge time series as outlined in Moore (1992); Shevenell (1996); Kovács, et al. (2015).
Accordingly, also the recession of borehole hydrographs was decomposed into individual exponential components with their own recession coefficient a so that Eqn. 4.12 can be rewritten as,

$$H_t = h_{0_1} e^{-a_1 t} + h_{0_2} e^{-a_2 t} + h_{0_3} e^{-a_3 t} \quad \text{Eqn. 4.15}$$

with the total head H at time t, head h_0 at t = 0 and individual recession components a for the individual segments.

The slope λ of each straight-line component is given by,

$$\lambda = \ln\left(\frac{h_1}{h_2}\right) / \left(\frac{t_2}{t_1}\right) \quad \text{Eqn. 4.16}$$

with the head h_1 at the beginning of the segment at time t = 1 and head h_2 at the end of the segment at time t = 2 (Moore, 1992).

4.3.2.3. Digital recursive filtering

Two different filters were used in this work, firstly the one-parameter filter (Chapman and Maxwell, 1996; Chapman, 1999) estimating the LFC Q_b at time i by, Eqn. 2.57. And secondly, the two-parameter algorithm (Eckhardt, 2005) was applied given by Eqn. 2.58.

The filter parameters a and BFI_{max} were estimated trying different methods:

a) According to the method of Collischonn and Fan (2013) where in addition to Eqn. 4.11, Eqn. 2.59 is applied; and
b) Estimating a based on the MRC and deriving its recession constant k according to Maillet's law, (O'Brien, et al., 2014; Rimmer and Hartmann, 2014) where $a = \exp(-k)$, while BFI_{max} can be optimised applying a root-mean square error (RMSE) following Eqn. 2.60 and Eqn. 2.61 (Rimmer and Hartmann, 2014).

Recursive digital filtering was applied on hourly time series of spring discharge Q at Ballindine and Manorhamilton using Microsoft Excel.
Spring discharge time series were separated using the one-parameter algorithm of Chapman and Maxwell (1996) and Chapman (1999), and the method of (Eckhardt, 2005). For the two methods the coefficient a was selected based on the optimal benchmark range (Table 5.3) while the BFI_{max} parameter of the Eckhardt method was established using the methods of Collischonn and Fan (2013) and Rimmer and Hartmann (2014).
For all methods, the benchmark of fitting was defined as the exponential LFC separated in the previous section using Maillet (1905). The aim was that the results using digital/recursive filters neither underestimate nor overestimate the observed discharge at the end of the recession. The estimated LFC was optimised by assessment of the correlation coefficient and minimising the value of the RMSE between the exponentially separated LFC and the LFC separated using different digital/recursive filters.

4.3.2.4. Two-component mixing model

Hydrograph separation was applied using 18O and 2H for individual high-frequency sampled time series of Manorhamilton spring following the principles of Fritz, et al. (1976) to distinguish quantitatively between pre-event water or groundwater component and the event water or flood (rainfall) component of short-term rain events following Eqn. 2.65. While this method separates a 'baseflow

component', this can relate to flow contributions from a different permeability than in the case of other baseflow separation methods (as discussed later in the Results' Sections).

The methods described above were established for discharges Q, yet, since Q can be equally expressed as head H (Moore, 1992; Shevenell, 1996; Kovács, et al., 2015), Eqn. 2.65 was rewritten for head data to express the total head H [m/t] as a function of single components h,

$$H_R = h_T \frac{\delta_T - \delta_S}{\delta_R - \delta_S} \qquad \text{Eqn. 4.17}$$

with the isotopic content δ of 2H or 18O, measured head h_T, pre-storm head component S, and the storm water component of head R. The idea behind this approach is to apply TCMA in the context of a catchment where spring discharge time series don't exist, such as in Bell Harbour. To the knowledge of the authors, the approach of using borehole or well data for TCMA has never been used or published, yet, it is tried in the study site of Bell Harbour using samples from BH1.

4.3.3. Quantification of SiGD

SiGD was estimated for the catchment of Bell Harbour Bay using a) the water balance approach, and b) a mass-balance approach in the form of a tidal prism model. The combination of these two approaches were deemed to be the most suitable given the scope the work and available budget.

Water balance

The water balance for the hydrological cycle is a statement of mass conservation for which the following applies,

$$P = GWR + R + ET + \Delta S \qquad \text{Eqn. 4.18}$$

with rainfall P, groundwater recharge GWR, runoff R, evapotranspiration ET and change in storage ΔS.

Changes in storage are only relevant and quantifiable for existing turloughs and their seasonal change in storage. Turlough volume fluctuations were considered in the water balances estimated for Bell Harbour.

Mass-balance

SiGD was estimated for the catchment of Bell Harbour Bay using a mass-balance approach in the form of a tidal prism model whereby the discharge from Bell Harbour Bay out into the main Galway Bay was quantified. Therefore, the discharge from Bell Harbour Bay has been considered as equivalent to the SiGD into Bell Harbour Bay.

Based upon the Simplified Tidal Embayment Assessment Model (STEAM) (DiLorenzo, et al., 1994), Barber (2003) and Barber and Wearing (2004b) developed a tidal prism approach for the flushing and discharge of a conservative pollutant in a well-mixed tidal embayment. The model is valid for small basins of the order of a few kilometres (one tidal excursion) with average depths ranging between 1 and 10 m.

The periodic variation in pollutant concentrations according to ebb tide and flood tide is modelled using a 'zero-dimensional approach', which is based on the concept of repeated exchange of the intertidal volume, taking into account the continuous release of pollution. Amongst others, the model assumes a constant inflow of freshwater from the shore for a tidal cycle.

The method was applied on the Central Harbour in New York (Barber and Wearing, 2004a), demonstrating that results are very encouraging and show that the tidal prism approach has considerable promise for predicting the water quality response of well-mixed tidal basins.

While this method was developed for estimating the flushing characteristics of conservative pollutants, it may be in turn used to quantify the freshwater input. This approach is therefore relevant for the study site 'Bell Harbour', as its discharge is in the form of SiGD, and hence not directly measurable.

To quantify the freshwater discharge into bay, a pollution flushing model was applied, which has been formulated to model the concentration of continuously released pollutants in a well-mixed tidal embayment at the end of ebb tide n, considering the concentration of the same pollutant at the previous flood tide and inflow of freshwater from land into the bay (Barber, 2003),

$$C_{e(n)} = C_{f(n-1)} exp\left\{\frac{\pi Q_f}{\omega\sqrt{V_m^2 - V_t^2}}\right\} \qquad \text{Eqn. 4.19}$$

where $C_{e(n)}$ is the pollutant concentration at the end of ebb tide *n*, $C_{f(n-1)}$ is the pollutant concentration at the end of the previous flood cycle, Q_f is the freshwater discharge into the bay [m^3], ω is the tidal angular frequency given by $\omega = 2\pi/T$ where T is the period of the tide [h], V_m is the mean volume of the basin [m^3] and V_t is the amplitude of the oscillatory component of the tidal volume [m^3].

The assumptions of the model are:

a) The pollutant is conservative;
b) The initial pollutant concentration in the harbour is uniform;
c) Zero pollution in the exterior water body;
d) Complete internal mixing of the contaminant each tidal cycle;
e) No vertical stratification in the basin due to thermal or density effects;
f) Continuous internal pollution loading;
g) Vertical basin walls; and
h) No other source of flow into the harbour other than from the sea.

For the estimation of the pollution concentration at the end of a tidal section, Barber (2003) differentiated between the ebb tide and the flood tide. The pollutant concentration at the end of a flood tide is calculated by a different equation other than Eqn. 4.19.

For the study presented here, the salinity of the sea water was considered as a conservative pollutant that varies in concentration according to the tidal fluctuation (and according to freshwater input): during a flood tide, sea water from outside enters the bay, increasing EC while during an ebb tide, EC drops due to the mixture of incoming terrestrial freshwater and sea water. In fact, this means that assumption c) does not hold true, as the fluctuation of the 'pollutant' EC in Bell Harbour Bay is (amongst others) the result of interaction with the Atlantic Ocean. However, this is accounted for by only considering the results of the ebb tide when Bell Harbour Bay is flushed. Therefore, the net SiGD can only be estimated for the ebb tidal cycle when the discharge of fresh water into the bay and a consequential drop in salinity can be picked up by the sampling devices. Accordingly, Eqn. 4.19 is rearranged and solved after Q_f to quantify the total volume of SiGD for ebb tide *n* and flood tide $n-1$, to yield,

$$\mathrm{Q_{(n)}} = \frac{-2\sqrt{\mathrm{V_m^2 - V_t^2}}}{\left(\mathrm{T_{e(n)} - T_{e(n-1)}}\right)} \cdot \ln\left(\frac{C_{e(n)}}{\mathrm{C_{f(n-1)}}}\right) \qquad \text{Eqn. 4.20}$$

with the combined discharge $Q_{(n)}$ of the flood tide $n-1$ and ebb tide n at the end of ebb tide n [m³], the specific conductivity $C_{e(n)}$ [µS/cm] at the end of ebb tide n, the specific conductivity $C_{f(n-1)}$ [µS/cm] at the end of the previous flood cycle, the time $T_{e(n)}$ [h] at the end of the ebb tide n, and the time $T_{e(n-1)}$ [h] at the end at the previous ebb tide $n-1$.

$C_{e(n)}$ and $C_{f(n-1)}$ were sampled at the outlet of the bay, using two CTD sensors installed at different depths to account for a potential vertical heterogeneity of EC records at the sampling location (Figure 4.15). The vertical heterogeneity of salinity of the sea water in the bay was assessed at different times by establishing EC transects through Bell Harbour Bay.
For the quantification of SiGD, an average of $C_{e(n)}$ and $C_{f(n-1)}$ was calculated (Figure 4.15). Barber (2003) and Barber and Wearing (2004b) introduced a return-flow factor that explains a share of the pollutant concentration in the bay through the return of a discharged pollutant during flood tide. Under idealized conditions the return-flow factor can be evaluated theoretically although in more realistic situations the value has to be found by calibrating the analytical model against observed pollution data. However, this study uses measured EC values (equivalent to pollution concentrations) to estimate the inflow of freshwater. This is done using the peak EC values at ebb and flood tide. Accordingly, the return flow can be neglected since only the difference between the peak EC values matters.

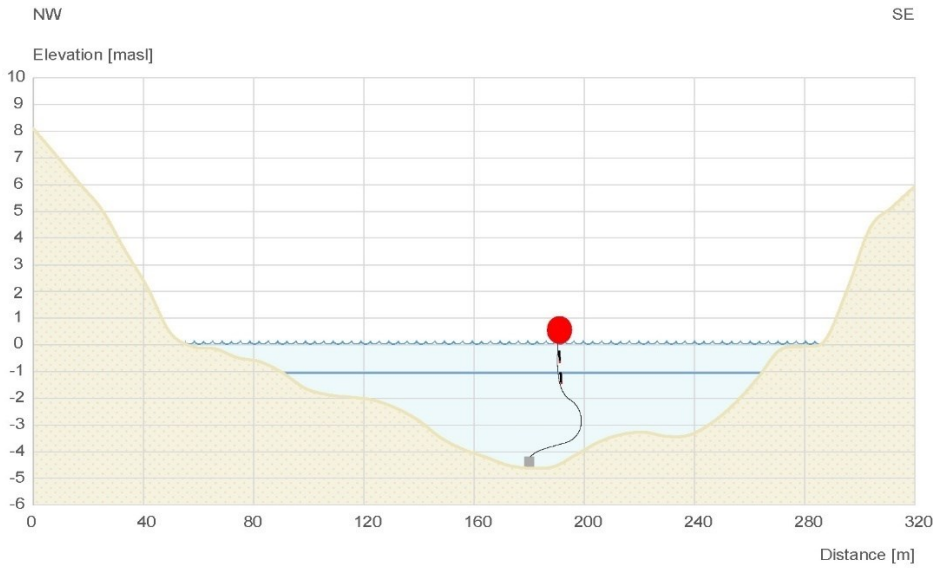

Figure 4.15: Cross-section at the buoy sampler showing two different levels of samplers below the mean sea level.

4.4. Numerical modelling

A major focus of this work is related to modelling groundwater flow dynamics, mainly related to the aspect of integrating diffuse groundwater recharge and different flow components into semi-distributed pipe network modelling using InfoWorks ICM (version 7.0.5., Innovyze Ltd., Wallingford, UK). Yet, in addition, lumped rainfall-discharge models were applied using the software KarstMod (version 2.2.0s, available at www.sokarst.org, Mazzilli and Bertin (2018)) in order to fill short data gaps of time series as well as to analyse hydrological processes (Mazzilli, et al., 2017) in terms of the prevailing recharge/flow dynamics in the different karst aquifers.

4.4.1. Lumped modelling

Rainfall-discharge modelling was carried out using KarstMod. The reasoning behind using this tool as a lumped modelling approach was because:

- Rainfall-discharge modelling allows filling of data gaps;
- KarstMod is a freely available and a straightforward tool that has been successfully applied in other studies related to the investigation of karst aquifer (internal) discharge dynamics; and
- Analysis of the best-fitting model characterises the aquifer in terms of prevailing flow conditions (conduit vs. fissured matrix), which then adds knowledge to the semi-distributed modelling approach.

KarstMod includes four different reservoirs organised in two hierarchical levels. The top level contains reservoir ‘E’ (epikarst) that represents the unsaturated zone subject to infiltration. The lower

level represents the saturated zone and its heterogeneous permeabilities accounted for by three optional reservoirs, i.e. 'C' (conduit), 'M' (matrix), and 'L' (Figure 4.16). Simulation of discharges of reservoirs can be simulated as finite (classical approach) or infinite. Infinitely modelled discharge applies a time transfer function to account for multiple transfer time scales, but using a single compartment maintains model structure simplicity.

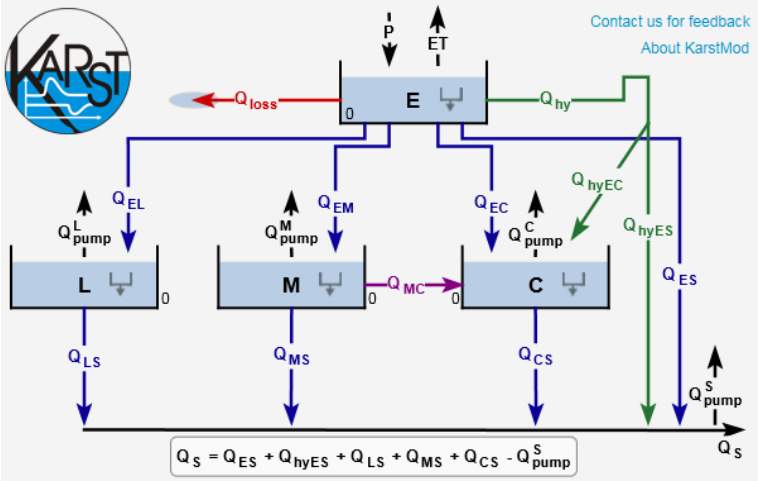

Figure 4.16: KarstMod structure for the classical (finite) setup.

Reservoir E is recharged by rainfall (P) and subject to evapotranspiration (ET). P and ET are imported as hourly or daily time series. Loss from 'E' (Q_{loss}) can be simulated by a threshold function. Flux from compartment E to the compartments C, M, L or directly to the spring S follows exponential functions in the finite configuration. A hysteretic discharge accounts for variations of soil moisture content and the capillary fringe, and it can be accounted for by flows between E and C and/or S using Q_{hy}, Q_{hyEC}, and/or Q_{hyES}.

Reservoirs C, M and L may be subject to groundwater abstraction that can be accounted for by hourly or daily time series. Matrix-conduit exchange flow can be considered by Q_{MC}, which can be negative at times when the conduit discharges into the matrix.

Water levels in all reservoirs and discharges at each time step are solved after the principle of mass balance using four balance equations, and the total outflow at the spring Q_S,

$$Q_S = R_A \times (Q_{ES} + Q_{LS} + Q_{MS} + Q_{CS} + Q_{hyES} + Q_{rE} + Q_{rLS} + Q_{rMS} + Q_{rCS} + Q_{bLS} + Q_{bMS} + Q_{bCS} - Q_{pump}^{S}) \quad \text{Eqn. 4.21}$$

with the catchment area R_A [L²], the internal discharge rates per unit surface area for classical configuration of reservoirs E, C, M and L Q_{ES}, Q_{LS}, Q_{MS}, Q_{CS}, and Q_{hyES}, the internal discharge rates per unit surface area for infinite configuration of reservoirs E, C, M and L Q_{rE} Q_{rLS}, Q_{rMS}, Q_{rCS}, Q_{bLS}, Q_{bMS} and Q_{bCS}, and the abstraction rate per unit surface area Q_{pump}^{S} [l/t].

The software calibrates the model by applying a quasi Monte-Carlo procedure with a Sobol sequence sampling of the parameter space that was previously defined by the user. The length of the calibration procedure can be defined by the user either according to a given time for modelling run, and/or by a number of simulations that satisfy the conditions of a user-defined model quality using e.g. the Nash-Sutcliffe efficiency (NSE) (Nash and Sutcliffe, 1970) or the Kling-Gupta efficiency (KGE) (Gupta, et al., 2009). Calibration may consider a warm-up period at the beginning, as well as a validation period. All of these are defined by the user.
The simulation results are exported as *.csv file, and there are different plots provided in the software that can be accessed directly after a successful simulation.

4.4.2. Pipe network modelling

Based on the geometrical architecture of the Discrete Conduit Network (DCN) approach (Jeannin, 2001; Kovács and Sauter, 2007), semi-distributed groundwater flow modelling is done using the software InfoWorks ICM (version 7.0.5., Innovyze Ltd., Wallingford, UK). InfoWorks was developed to model urban drainage networks and to evaluate, for example, its capacity or response to pluvial floods (e.g. Rubinato, et al. (2013). The software allows simulating different flow dynamics within a network.
While the DCN approach only accounts for groundwater flow in conduits or in connections between fractures, the semi-distributed pipe network model used here aims to more realistically simulate different flow components that have been quantified using various methods previously outlined in Section ‘4.3. Methods overview’. The ability of InfoWorks of simulating turbulent/open-channel flow as well as laminar flow shall be used to represent a karst aquifer. Further, the process of developing groundwater flow models, including the calibration procedures, may yield additional information about the behaviour of the different flow components.
This work builds upon the previous work of Gill (2010) who used InfoWorks CS (version 8.5, Innovyze Ltd., Wallingford, UK) in modelling the heads of a network of turloughs. The following sections outline the hydraulic principles of the key components of InfoWorks used for this study.

4.4.2.1. Hydraulic principles of the model

4.4.2.1.1. Ground Infiltration Module (GIM)

The Ground Infiltration Module (GIM) is the key component relevant for this study. The GIM consists of two reservoirs, a) a soil store, and b) a groundwater store (within the reference manual sometimes called ‘Ground store’). The two reservoirs allow modelling a highly attenuated response to rainfall by representing the below ground processes of infiltration through the soil and contribution from the groundwater store (Figure 4.17).

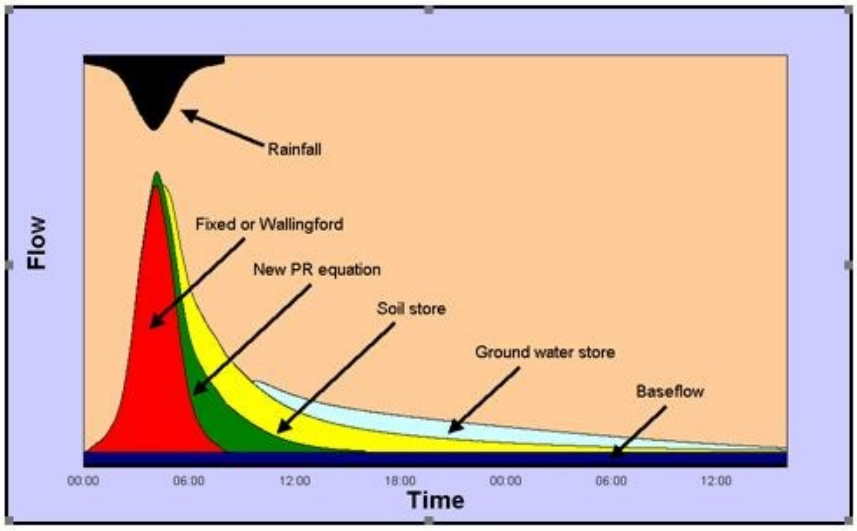

Figure 4.17: Groundwater recharge components incorporating the GIM (Wallingford, 2006).

The GIM has its own terminology of parameters that are manually adjusted (Table 4.7).

Table 4.7: Ground Infiltration Module (GIM) parameters.

Field Name	Description
Ground Infiltration ID	A unique identifier for the ground infiltration record. This field is used to associate a Ground Infiltration ID with a particular sub-catchment.
Soil Depth [m]	An estimate of the soil depth.
Percolation Coefficient	A time coefficient, determined by calibration from existing data. It is recommended that the value should be between 0.1 and 10.
Baseflow Coefficient	A time coefficient, determined by calibration from existing data. It is recommended that the value should be between 100 and 10,000.
Infiltration Coefficient	A time coefficient, determined by calibration from existing data. It is recommended that the value should be between 0.1 and 10.
Percolation Threshold [%]	The percentage saturation level of the soil at which water starts to percolate downwards.
Percolation Percentage Infiltrating [%]	The percentage of percolation flow that infiltrates directly into the drainage network.
Porosity of Soil	A coefficient representing the porosity of the soil (upper storage reservoir).
Porosity of Ground	A coefficient representing the porosity of the ground (lower storage reservoir).
Baseflow Threshold Level	The groundwater level at which secondary infiltration occurs.
Baseflow Threshold Type	The Baseflow Threshold Level can be either an *absolute* value (relative to Model Datum) or a level *relative* to the chamber floor of the node to which the sub-catchment drains.
Infiltration Threshold Level	The level of the groundwater storage reservoir at which groundwater infiltration occurs. It is recommended that the Infiltration Threshold Level should be between 0 and 5 m above the Baseflow Threshold.
Infiltration Threshold Type	The Infiltration Threshold Level can be either an *absolute* value (relative to Model Datum) or a level *relative* to the chamber floor of the node to which the sub-catchment drains.

4.4.2.1.2. Soil store

The soil store is the upper reservoir within the GIM. It is defined by three parameters: depth, saturation threshold (percolation threshold) D_t and porosity P_{Soil}. When the water level in the soil reaches the given percolation threshold D_t following infiltration, a percentage of water (percolation percentage infiltrating) starts infiltrating into the pipe network while the remainder percolates downwards to feed the groundwater store. Note, there is no possibility that flow from the groundwater store can move back into the soil store.

The 'losses' from the soil store are evaporation to the atmosphere and percolation Q_P to the groundwater store. The input is infiltration to soil store Q_{Soil}. The continuity equation for the soil store is,

$$\frac{dS}{dt} = \frac{Q_{Soil}}{P_{Soil}} - Q_P - \frac{Q_{Evap}}{P_{Soil}} \qquad \text{Eqn. 4.22}$$

with the soil porosity P_{Soil} and the evaporation Q_{Evap}.

Accordingly, the rise in the soil store is inversely proportional to the soil porosity. For example, if P_{Soil} = 40%, an inflow of 1 mm will result in a rise in the soil store of 1/0.4 = 2.5 mm. The lower the soil porosity the higher the soil store level will be following infiltration Q_{Soil}.

Evaporation Q_{Evap} is modelled as the product of the potential evaporation E_P and soil saturation as,

$$Q_{Evap} = \frac{D \times E_P}{D_{max}} \qquad \text{Eqn. 4.23}$$

with the depth of water in the soil D and the soil depth D_{max}. Accordingly, the higher the depth in soil store, the higher the rate of Q_{Evap}. If $D = D_{max}$, Q_{Evap} equals the potential evaporation.
Percolation flow Q_P is modelled according to,

$$Q_P = (D - D_t)Ak_1^{-1} \qquad \text{Eqn. 4.24}$$

with the threshold value D_t [% of soil depth] for D above which there is percolation flow, the catchment area A and the percolation coefficient k_1. If the depth of water in the soil $D < D_t$, percolation flow Q_P will be zero. There will only be percolation flow for $D > D_t$, modelled as the product of A and k_1. The higher the percolation coefficient, the smaller Q_P, and so the slower drainage of the soil store will be.
Any generated percolation flow Q_P is split into: a) soil store inflow Q_{ri}, and the remainder, b) as inflow into the groundwater store Q_{Ground}.

Soil store inflow Q_{ri}, i.e. the rainfall-induced infiltration of water above the percolation threshold into the pipe network, is modelled by,

$$Q_{ri} = \alpha_i Q_P \text{ x } P_{Soil} \quad \text{Eqn. 4.25}$$

with the percolation percentage infiltrating α_i.
The remainder of the percolation flow (100% - α_i) is directed into the groundwater store, so that the inflow into the groundwater store Q_{Ground} is modelled as,

$$Q_{Ground} = (1 - \sum a) Q_P \text{ x } P_{Soil} \quad \text{Eqn. 4.26}$$

The concept of the soil store is displayed in Figure 4.18.

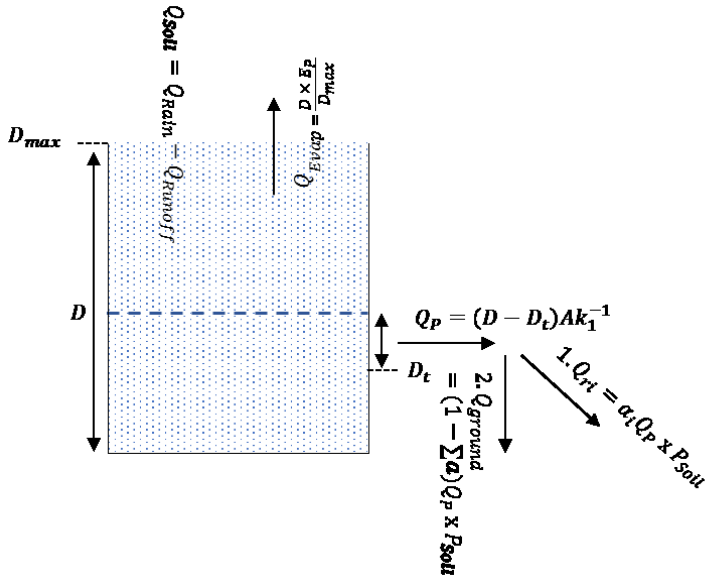

Figure 4.18: ICM soil store of the Ground Infiltration Module (GIM).

4.4.2.1.3. Groundwater store

Inflow into the groundwater store from the soil store is Q_{ground}.
The continuity equation for the groundwater store is,

$$\frac{dS}{dt} = \frac{Q_{Ground}}{P_{Ground}} - Q_{Gi} - \frac{Q_{Baseflow}}{P_{Ground}} \quad \text{Eqn. 4.27}$$

with the porosity of the ground P_{Ground}, the baseflow $Q_{Baseflow}$, and the groundwater infiltration Q_{Gi}.
Baseflow $Q_{Baseflow}$ accounts for losses from the system while groundwater infiltration Q_{Gi} accounts for drainage from the groundwater store into the pipe network.

Baseflow $Q_{Baseflow}$ is assumed to occur only when the depth of the groundwater reservoir is above some threshold value (baseflow threshold level) and is modelled according to,

$$Q_{Baseflow} = (H - H_{t1})Ak_2^{-1} \qquad \text{Eqn. 4.28}$$

with the height of the groundwater reservoir H, the minimum groundwater table level (baseflow threshold) at which baseflow occurs H_{t1}, and the reservoir time constant (baseflow coefficient) k_2, for $(H - H_{t1}) > 0$. If $(H - H_{t1}) < 0$, $Q_{Baseflow} = 0$. Accordingly, the higher the baseflow coefficient, the smaller $Q_{Baseflow}$, and so the slower drainage of the groundwater store will be.

The model for infiltration flow into the pipe network (groundwater inflow) follows the standard orifice equation. Infiltration into the network (groundwater store inflow) Q_{Gi} within a sub-catchment follows a variation of a linear reservoir model using,

$$Q_{Gi} = k_3^{-1}\sqrt{(H - H_{t2})} \qquad \text{Eqn. 4.29}$$

with the minimum groundwater table level (baseflow threshold) at which infiltration (groundwater store inflow) occurs H_{t2}, the infiltration coefficient k_3 [s/m$^{5/2}$] that determines the rate of flow into the pipe valid for $(H - H_{t2}) > 0. \; for < 0$, $Q_{Gi} = 0$. The larger k_3, the slower the flow from the groundwater store into the network.
The concept of the groundwater store is displayed in Figure 4.19.

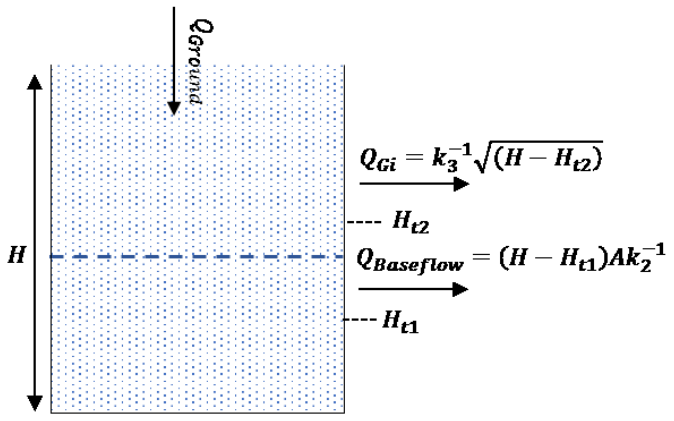

Figure 4.19: ICM groundwater store of the Ground Infiltration Module (GIM).

The combination of contribution from the groundwater store and soil store is called groundwater inflow.

4.4.2.1.4. Surface runoff

In principle, surface runoff, here referred to as runoff, should not be particularly significant as at least two of the three study sites are highly karstified where runoff may only be existent locally on a micro scale.
However, runoff constitutes the quick component of the total hydrograph (Figure 4.17). In InfoWorks, runoff is the process where rainfall lands on the catchment surface and runs overland to the nearest manhole and into the pipe network. Accordingly, runoff may be conceptually considered in the model as the fast-flow component of karst spring hydrographs as a result from quick and concentrated recharge.

Three components of runoff contribute to the shape and magnitude of runoff: a) runoff volume, b) runoff routing, and c) initial losses.
The runoff volume is defined by the amount of rainfall falling on the surface that will end up in the pipe network. The 'fixed percentage' is the simplest approach. In other models (e.g. SCS), runoff is generated according to the antecedent conditions; runoff routing defines the speed at which runoff will enter the pipe network, acting in a form of a unit hydrograph to attenuate the flow; and finally, initial losses account for evaporation of rainfall on the surface and its small depressions (depression storage) resulting in net, i.e. effective, rainfall.

The initial contribution from a rain event is assumed to cause no runoff because it is conceptually 'lost' by wetting the ground surface and forming puddles. Rainfall that falls on land is initially stored in surface depressions, i.e. depression storage, where it is subject to evaporation described by one of the three different rainfall loss models (initial loss type), i.e. a) absolute, b) slope, and c) SCS. Depth of storage $S_{Depression}$ is defined for the initial loss type 'absolute' or modelled for the initial loss type 'slope' according to,

$$S_{Depression} = \frac{initial\ loss\ value}{\sqrt{s}} \qquad \text{Eqn. 4.30}$$

with the ground slope s. The ground slope s can be defined for each sub-catchment as for example representing the general topography in the sub-catchment.

Once the surface depressions are fully saturated, runoff is generated and described by,

$$\sum_{t=0}^{r} \frac{Q_{Rain}(t)\Delta t}{A} > S_{Depression} \qquad \text{Eqn. 4.31}$$

with the surface area A, and the amount of rainfall Q_{Rain}.

The model assumption is that any rainfall that does not contribute to runoff will be subject to infiltration into the soil store if it is not fully saturated. The continuity equation for runoff is given by,

$$Q_{Soil} = Q_{Rain} - Q_{Runoff} \quad \text{Eqn. 4.32}$$

with the runoff flow Q_{Runoff} and the flow into the soil store Q_{Soil}. In general, runoff Q_{Runoff} is generated by,

$$Q_{Runoff} = PR \times Q_{Rain} \quad \text{Eqn. 4.33}$$

with the percentage runoff PR for a given surface. However, different runoff volume models, i.e. runoff volume types, determine how much runoff is generated (following initial losses).

Runoff routing volume

InfoWorks ICM integrates the following 14 runoff routing volume methods that model the contribution to runoff:

1. Constant Infiltration (ConstInf);
2. Deficit and Constant Loss Model (DefConLoss);
3. f1-Rsa;
4. Fixed percentage runoff;
5. Green-Ampt;
6. Horner;
7. Horton / HortonSWMM;
8. New UK (Variable) PR;
9. Probability Distributed Model (PDM);
10. ReFH;
11. Simple Runoff Model (SRM);
12. UKWIR;
13. USA Soil Conservation Service method (US SCS);
14. Wallingford Procedure (Fixed) PR.

Table 4.8 summarises the runoff volume models and potential suitability or applicability in this context of the study.

Table 4.8: InfoWorks ICM 7.0 Runoff volume models (red = not suitable, orange = potentially suitable, green = suitable).

Method	Description	Suitability
Constant Infiltration (ConstInf)	The ConstInf model allows to define a constant infiltration from the surface into groundwater. This is effectively a loss to the system. When the storage capability of the surface is fully used, the surface acts as a fixed runoff surface.	Not suitable as integration of loss from the system is not desirable as this results in erroneous water balances.
DefCon-Loss	The method is based on the HEC-HMS model (US Army Corps of Engineers, 2010), modelling the surface as a single soil layer in which incident rainfall is initially stored and which is subject to evaporative loss. When the soil layer reaches saturation capacity, infiltration may occur, with the excess rainfall going to runoff.	Suitable, as physical runoff can be avoided or largely reduced by choosing the saturation capacity appropriately. HEC-HMS applied on karst catchments, e.g. Kong-A-Siou, et al. (2013). However, not compatible with the GIM.
f1-Rsa	The f1-Rsa Model calculates the effective rainfall using the Quasi Linear Reservoir Method. First, an initial runoff rate, f1, is applied until the cumulative rainfall reaches a specified saturated rainfall value; standard runoff model used in Japan.	Potentially suitable.
Fixed percentage runoff	User defines a fixed percentage of the net rainfall, which becomes runoff. A range of 0% to 10% is suggested for permeable areas.	Suitable, applied by Gill (2010).
Green-Ampt	The Green-Ampt infiltration equation uses the parameters average capillary suction, saturated hydraulic conductivity, and initial moisture deficit to model runoff.	Potentially, although challenging to apply as to define the three parameters throughout sub-catchments.
Horner	A runoff volume model used to determine the net rainfall on urban sub-catchments using the parameters Horner Alpha, Horner Beta, and Horner Recovery.	Not suitable - designed for urban catchments; challenging to apply three parameters.
Horton / Horton-SWMM	Method designed for rural catchments using the parameters Horton Decay, Horton Initial, Horton Limiting, Horton Recovery, Horton SMS (rainfall event initial condition).	Not suitable - although designed for rural catchments; the number of parameters makes the method too complex leading to arbitrary results.
New UK (Variable) PR	This model is designed to consider the changes of catchment conditions (wetness) during long storms throughout the simulation for a pervious surface.	Potentially suitable, although the formation of runoff/groundwater recharge is believed to be relative constant in highly karstified catchments, and therefore the method may be redundant.
PDM	The method is a general-purpose, lumped conceptual model for continuous rainfall-runoff simulation using a probability distributed soil moisture storage.	Challenging, as many of the parameters are not physically meaningful. Potentially suitable.
ReFH Model	The ReFH Model is a rainfall-runoff model combining a loss model, a routing model and a baseflow model. The loss model is based on the Probability Distributed Model (PDM). Effective rainfall is	Not compatible with GIM, therefore not suitable.

	evaluated sequentially during a storm and if soil storage is filled, runoff will equal 100%. The baseflow model is based on the linear reservoir concept with a characteristic recession defined as an exponential decay.	
SRM	The Simple Runoff Model (SRM) uses a soil moisture deficit time series in conjunction with a constant runoff coefficient to modify input rainfall to get an effective rainfall.	Not suitable - soil moisture deficit is not the major driving in generating runoff/groundwater recharge.
UKWIR	The UKWIR equation was designed to replace the New UK PR Model using 10 different parameters.	Not suitable; too many parameters need to be defined.
US SCS	The SCS method is a widely accepted model for predicting storm flow volumes from rural catchments. The method is used in the USA, France, Germany, Australia and parts of Africa. It was derived for rural catchments with uniform conditions. This is a simple runoff model that allows for variation in the runoff coefficient depending on the catchment wetness. The wetness is updated during the storm and the runoff coefficient increases as the catchment wetness increases.	Suitable according to description of method, however, Norbiato, et al. (2009) faced challenges modelling runoff in karstified sub-catchments using the US-SCS curve number.
Wallingford Procedure (Fixed) PR	The default model, which is calibrated for the UK and applied on urban catchments using a regression equation to predict the runoff coefficient depending on the density of development, the soil type and the antecedent wetness of each sub-catchment.	Not suitable as none of the study areas can be classified as urban.

The runoff volume type chosen in this study is the fixed percentage runoff. All surfaces were defined as ‘pervious surfaces’ (as opposed to impervious or unknown).

Runoff routing model

There are 13 different runoff routing models determining how quickly the rainfall enters the drainage system from the catchment:

1. Clark Model;
2. Desbordes Model;
3. Kadoya Model;
4. Large Contributing Area Model;
5. Non-Linear Routing Model;
6. ReFH Unit Hydrograph Model;
7. SCS Unit Hydrograph Model;
8. Snyder Unit Hydrograph Model;
9. SPRINT Model;
10. SWMM Model;
11. Unit Hydrograph Model;
12. Wallingford Runoff Routing Model;

13. Rational Routing Model.

The response to rainfall is controlled by the runoff routing value – the larger the value, the quicker the response. Table 4.9 illustrates the different routing models and suitability for the modelling exercises in this study.

Table 4.9: InfoWorks ICM 7.0 Runoff routing models (red = not suitable, orange = potentially suitable, green = suitable).

Method	Description	Suitability
Clark	Flow is routed using the Clark unit hydrograph method based on linear reservoirs accounting for attenuation. Two parameters, lag time and time of concentration, are defined by the user. Method used in conjunction with the HEC-HMS model.	Potentially suitable, allows use of GIM.
Desbordes	Flow is routed using a single linear reservoir, whose routing coefficient depends on sub-catchment area, ground slope and percentage impermeable. Sub-events defining storm must be specified in the rainfall data.	Potentially suitable, allows use of GIM. Yet, event-based: for example, the liner reservoir coefficient is defined according to the length of the rainfall sub-event, which is difficult to apply on long time series.
Kadoya	Flow is routed using the Japanese Quasi Linear Reservoir Method.	Potentially suitable, allows use of GIM. Only parameter C to be adjusted.
Large Catch	The method is applied for sub-catchments > 1 ha; flow is routed using two equal linear reservoirs in series, whose routing coefficient depends on rainfall intensity, contributing area and surface slope as in the Wallingford model. Characteristics of the catchment and represents them using one pipe. The software applies a timestep lag and routing factor multiplier. The timestep lag and routing multiplier are functions of sub-catchment area, ground slope and catchment length.	Potentially suitable, allows use of GIM.
Non-Linear Routing Model	The non-linear routing model routes flow using the Storage Function Method adjusting seven different parameters.	Unsuitable due to large number of parameters to be adjusted.
ReFH	Flow is routed using a kinked triangle unit hydrograph. Time of peak flow, unit hydrograph peak and degree of kink are defined by the user.	Not compatible with GIM, therefore not suitability.
SCS Unit	Flow is routed using an SCS unit hydrograph. Time of peak flow and total runoff time are either user defined or calculated from built in methods.	The method is not suitable for mountainous or flat wetland areas. Potentially suitable due to simplicity, allows use of GIM.
Snyder Unit	Flow is routed using the Snyder unit hydrograph method. Lag time and peaking coefficient are defined by the user.	Potentially suitable, allows use of GIM.
Sprint	Flow is routed using a single linear reservoir applicable to lumped catchments, whose routing coefficient depends on sub-catchment area, ground	Potentially suitable, allows use of GIM.

	slope and percentage impermeable. The method does not account for rainfall intensity.	
SWMM	The SWMM runoff model uses a non-linear reservoir and the kinematic wave equation to route sub-catchment runoff to the manhole. To use SWMM routing, specify the sub-catchment width and Manning's roughness on impervious and pervious surfaces.	Potentially suitable, allows use of GIM.
Unit Hydrograph	A Unit Hydrograph for the sub-catchment is determined from user defined parameters, or from parameters calculated by built in methods. The Unit Hydrograph is then used to calculate runoff resulting from the sub-catchment net rainfall.	Potentially suitable, very simple approach, allows use of GIM.
Wallingford	Flow is routed using two equal linear reservoirs in series, whose routing coefficient depends on rainfall intensity, contributing area and surface slope. This method is usually applied on catchments < 1 ha.	Potentially suitable, very simple approach, allows use of GIM. Applied by Gill (2010), however, catchment size might be constraint.
Rational	The Rational Routing Model is a triangular Unit Hydrograph Routing Model using the parameters Tp (time of peak) = Tc (time of concentration), Tb (base time) = 2 * Tp. The difference between the rational and unit routing models is that the input hydrograph is discretised at intervals of Tc instead of the run time.	Potentially suitable due to simplicity and the fact that input hydrograph is discretised at intervals of Tc instead of the run time. Allows use of GIM.

The shape of the runoff hydrograph is then determined by the 'unit hydrograph' and associated runoff routing models (Figure 4.20, Table 4.10). Essentially, the models calculate the time of concentration T_c based on different parameters associated with the catchment. However, for this modelling approach, not only T_c seems to be relevant but also the general shape and the length of the runoff event. The methods 'User-Tc' and 'User-Tp-Tb' lets the user define the hydrograph based on the time of concentration T_c, or the time of peak flow T_p and total runoff time T_b.

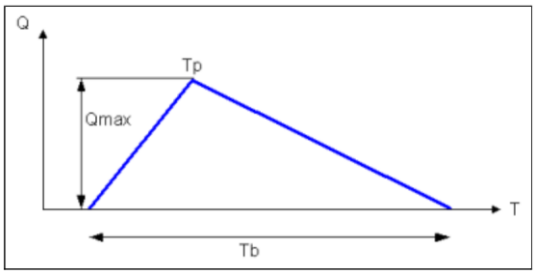

Figure 4.20: Unit Hydrograph Model, including time of peak flow T_p and total runoff time T_b.

Table 4.10: Available hydrograph models in InfoWorks ICM (red = not suitable, orange = potentially suitable, green = suitable).

Unit hydrograph model	Associated routing model	Suitability
Clark	Clark	Potentially suitable.
Desbordes-Tc	Unit Hydrograph	Potentially suitable.
Giandotti-Tc	Unit Hydrograph	Potentially suitable.
Kirpich-Tc	Unit Hydrograph	Potentially suitable.
Passini-Tc	Unit Hydrograph	Potentially suitable.
Rational	Unit Hydrograph	Potentially suitable.
ReFH	ReFH	Not compatible with GIM, therefore not suitability.
SCS-Forest-Tc	Unit Hydrograph	Not suitable as only one parameter is defined to shape the hydrograph.
SCS-Rural-Tc	Unit Hydrograph	Not suitable as only one parameter is defined to shape the hydrograph.
SCS-User-Tc	SCS	Not suitable as only one parameter is defined to shape the hydrograph.
Snyder	Snyder	Potentially suitable.
User-Tc	Unit Hydrograph	Too simplistic approach.
User-Tp-Tb	Unit Hydrograph/SCS	very simple approach, yet, linear recession simplistic.

From the perspective of this research, runoff may be considered as recharge variable /input function into the pipe network and flow component concentrating into the pipe network. Therefore, a useful hydrograph model can relate the modelled hydrograph to the fast segment of an exponential recession of karst hydrograph. The only possibility of calibrating the runoff hydrograph against some measured data is using spring discharge time series or well hydrograph time seriesm, if available.

As routing model, the ‘Unit Hydrograph’ seems very plausible and useful, as it can be directly related to the magnitude and duration of single events rising and falling limbs. The routing model was coupled with the ‘Soil Conservation Service’ (SCS) hydrograph (Figure 4.21a). This hydrograph has a curvelinear shape, including an inflection point on the recession limb at 1.7 times the time to peak. The shape is associated with and based on the triangular hydrograph (Figure 4.20), as shown in Figure 4.21b (McCuen, et al., 2002). The associated hydrograph model was chosen as the ‘User-Tp-Tb’ as it allows defining T_p and T_b in an easy way. In other methods, for example ‘SCS-User-Tc’, T_p is calculated based on T_c.

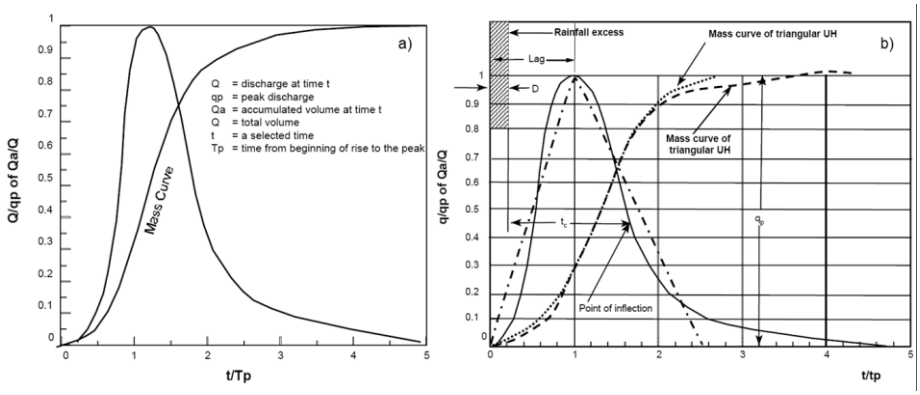

Figure 4.21: a) dimensionless curvelinear SCS unit hydrograph Model; b) SCS hydrograph and equivalent triangular hydrograph (McCuen, et al., 2002).

4.4.2.1.5. Pipes

The contribution of each GIM (soil store inflow and groundwater store inflow) and runoff of a single sub-catchment is diverted into a specified pipe connected to this sub-catchment. Once the flow enters the pipe network, it follows then the hierarchy of the pipe network, as designed by the user. Two different solution models governing pipe flow were used modelling different flow dynamics: a) permeable, i.e. Darcy flow, and b) full, i.e. turbulent/open-channel flow.

4.4.2.1.5.1. Permeable pipes

Laminar flow for R_e ranging between 1 and 10 following Darcy's law is modelled in 'permeable pipes' describing a linear relationship between the specific discharge u and the hydraulic gradient dh/dl (or i) when water molecules move in parallel in the direction of flow.

4.4.2.1.5.2. Full pipes

Flow in pipes can be either full (pressurised) or open-channel. The governing model equations are the Saint-Venant equations (as they allow a time transient effect to be modelled in open channel flow) that include the equation for continuity (conservation of mass) (Eqn. 2.9) and the equation for momentum (Eqn. 2.10).

The conveyance function is based on the Colebrook-White expression. The transition between free surface flow and pressurised pipe flow is enabled by using a 'Preissmann slot' at the top of the conduit. The Preissmann slot is a conceptual vertical and narrow slot that provides a conceptual free surface condition when the water level exceeds the top of the conduit (Figure 4.22).

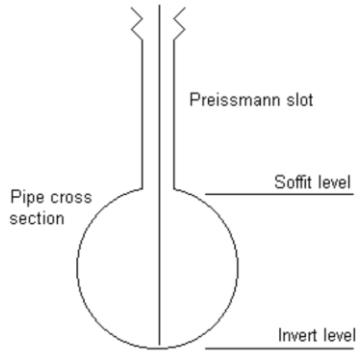

Figure 4.22: Integration of a Preissmann slot into the modelling of flow in conduits (Innovyze, 2015).

The Preissmann slot is used in the hydraulic simulation to model pressurised flow in closed conduits. The width of the Preissmann slot is defined such that the wave celerity (speed) in the slot is ten times that at half of the conduit height. This enables accurate modelling of pressurised flow and results in a slot width that is 2% of the conduit width. The Preissmann slot (and baseflow) impact on the storage in the network, which can be numerically corrected in InfoWorks. In this research, a numerical correction was not applied.

4.4.2.2. Translation of general concepts of karst aquifers into InfoWorks

One major aspect of this research is the question of how to model diffuse groundwater recharge and flow - along other flow components - within InfoWorks ICM.

Diffuse recharge and flow can be integrated in two different ways: 1.) diffuse recharge can be resembled by the discharge of the groundwater store (groundwater store inflow, Q_{Gi}) and/or potentially the soil store (soil store inflow, Q_{ri}) into the pipe network; 2.) diffuse laminar flow (as the result of diffuse recharge) can be modelled within permeable pipes. If a sub-catchment drains into a permeable pipe, diffuse recharge and flow is represented in series by discharges of the soil/groundwater store and flow in the connected permeable pipe.

On its way towards the spring outlet, diffuse recharge will eventually concentrate towards the full conduits in which pressurised turbulent flow or open-channel flow occurs. This diffuse flow component resembles lateral infiltration and percolation of rainfall through a medium of soil/epikarst, following the hierarchy of fractures within the aquifer (from small narrow fissures towards larger diameter fractures and eventually conduits).

Most concentrated and very fast recharge can be modelled using ‘runoff’. This recharge-flow signal corresponds to direct infiltration and percolation into swallow holes and large fractures and connected conduits, bypassing any soil/epikarst. Conceptually, following recharge, the runoff component must then be directed towards a full pipe entering turbulent/open channel flow, rather than into a permeable pipe where concentrated recharge would be subject to laminar flow. However, since

all flows generated by the GIM are diverted into the same conduit, if using the runoff component to represent fast recharge, modelling of laminar flow within permeable pipes must be ruled out. Between the diffuse and fast concentrated recharge and flow component, an intermediate recharge and flow signal can be modelled as soil store inflow Q_{ri}. This signal may correspond to diffuse recharge that quickly concentrates within the within the soil/epikarst into conduits.

The abovementioned distinction between the model set-up considering fast recharge or not is illustrated in Figure 4.23(a) and (b). Figure 4.23a illustrates three recharge components originating from the GIM, hence, the sub-catchment must be connected to a full pipe. Figure 4.23b illustrates the set-up where no (fast) concentrated recharge is considered. In the latter case, the GIM may drain into a permeable pipe modelling laminar flow before concentrating towards a full pipe modelling turbulent/open-channel flow.
This research proposes the use of pipe characteristics coupled with the GIM to model different recharge and flow components of the study sites. Hence, the soil store is conceptualised as a soil-epikarst reservoir, and the groundwater store resembles the fissured matrix domain system generating diffuse flow.
Referring to Figure 4.18 and Figure 4.19, Table 4.11 summarises the individual flow components of the InfoWorks environment representing physical processes in a karst aquifer.

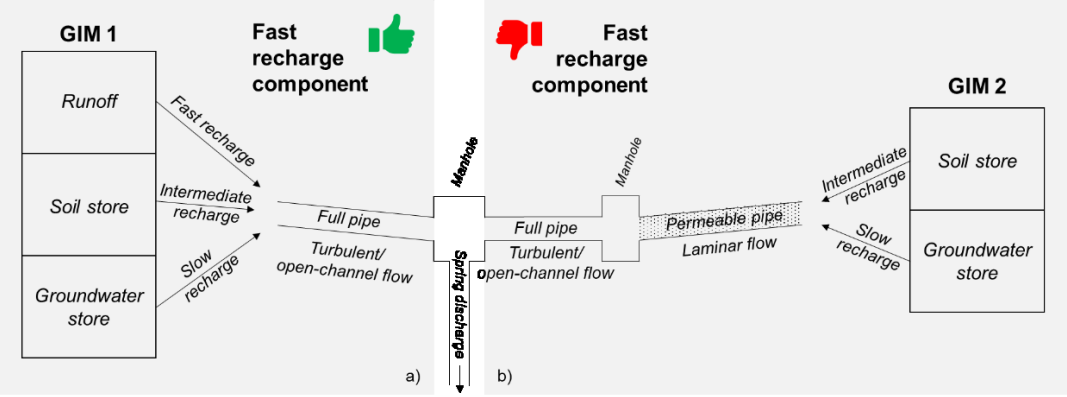

Figure 4.23: Conceptual set-up of InfoWorks considering (a) fast recharge or (b) not-considering fast recharge.

Table 4.11: ICM components representing duality of flow in karst aquifers.

ICM element	Equation	Karst aquifer representation
Soil store	-	Soil/epikarst
Groundwater store	-	Fissured matrix
Infiltration to soil store	$Q_{Soil} = Q_{Rain} - Q_{Runoff}$	Water available for recharge
Head in soil store	$\frac{dS}{dt} = \frac{Q_{Soil}}{P_{Soil}} - Q_P - \frac{Q_{Evap}}{P_{Soil}}$	Head in soil-epikarst driving percolation, and providing water for evaporation

Percolation flow	$Q_P = (D - D_t)Ak_1^{-1}$	Percolation into conduits and fissured matrix sub-system
Soil store inflow	$Q_{ri} = \alpha_i Q_P \text{ x } P_{Soil}$	Intermediate recharge and flow into the conduit network
Inflow into ground-water store	$Q_{ground} = (1 - \sum a)Q_P \text{ x } P_{Soil}$	Diffuse recharge into fissured matrix domain and rate of LFC
Groundwater inflow	$Q_{Gi} = k_3^{-1}\sqrt{(H - H_{t2})}$	
Runoff	SCS model	Fast concentrating flow component
Permeable pipes	Darcy	Laminar flow
Full pipes (con-duits)	Saint-Venant	Pressurised pipe/open-channel flow

4.4.2.3. Calibration

There is no automated calibration or parameter estimation tool in InfoWorks ICM, therefore, calibration is done manually by trial and error. The calibration period was at least one year for each study site. The performance indicators used are the NSE, KGE and the volume conservation criteria (VCC).

The calibration procedure depends on the outline of the model, and the order of calibrated elements (1. to 5.) differs between each study site. The model and its components were calibrated considering the following elements:

1. A water balance (input-output) is achieved, which is largely controlled by evaporation from the soil store. The water balance should be the first element to be calibrated. Calibration of the water balance uses the soil store parameters of the GIM, as they control the rate of evaporation losses (depth of soil, soil porosity, percolation coefficient, percolation threshold). This approach assumes that spring discharge is the only outlet of the aquifer, although this might be not case. If there are additional outflows (e.g. deep flows), this must be considered in the calibration of the soil store.

2. Observed spring discharge is calibrated against simulated discharge. The simulated discharge is the sum of the LFC, intermediate and fast recharge and flow components and flow characteristics in the pipes. Spring discharge is modelled using an outfall node that is connected to the 'final' conduit of the drained system. The modelled spring discharge is controlled by the different inflows into the pipe network, as well as by the parameters of the pipe network, namely the solution model ('full' vs. 'permeable'), the height and width [mm], the roughness type (Colebrook-White) and roughness height [mm] for empty conduits, the hydraulic conductivity K [m/s] and porosity [%] for permeable pipes, and the gradient (length [m] and downstream and upstream elevation [masl]).

3. The intermediate recharge and flow component (soil store inflow) is calibrated against the observed hydrograph and the intermediate recession component of the MRC. Discharge from the

soil store into the conduit network (intermediate recharge and flow component) depends on the infiltration to soil store, the soil porosity, the percolation threshold, and the percolation percentage infiltrating. Partly, these parameters were already set-up when matching the water balance, so care must be taken which parameters to change.

4. Depending on the built set-up (Figure 4.23a or Figure 4.23b), the contribution of diffuse recharge (and flow) is calibrated differently: Assuming that diffuse (slow) recharge is followed by diffuse (laminar flow) (in absence of fast concentrated recharge, Figure 4.23b, LFC is represented by flow in the permeable pipes.
   On the other hand, assuming that diffuse (slow) recharge directly enters the full pipe (along intermediate and fast recharge, Figure 4.23a), the slow/diffuse contribution is only resembled by the discharge of the groundwater store.
   In either case, the total volume discharged from the groundwater store or the total flow within the permeable pipe should then match the total volume of the LFC for the same period. Mismatches between the volumes should be adjusted by tuning the percolation percentage infiltrating. The rate of discharge depends on the groundwater store level (which depends on the porosity), and the infiltration coefficient. Hence, these parameters must be adjusted to match the groundwater store infiltration and the time series of the LFC. Flow in the permeable pipes should be adjusted by tuning the pipe parameters (K, porosity, gradient, diameter).

5. Quick recharge component resembled by runoff is calibrated against observed spring discharge and the fast recession component of the MRC. The runoff hydrograph depends on the volume of runoff (e.g. fixed percentage) and on the time of peak flow T_p and total runoff time T_b (Figure 4.20). By reducing T_p, the peak appears faster following a rainfall event. The duration of the runoff is defined using T_b, which essentially also impacts on the recession of the modelled runoff, which then can be matched the fast recession of the MRC and its recession constant k'.

The simulation results are either analysed per InfoWorks ICM element (individual sub-catchment, link or node) or ‘in bulk’. In bulk refers to the sum of specific flows. For example, the results of all soil store inflows from all sub-catchments’ GIM can be exported into a *.csv file using the ‘CSV export’ function in InfoWorks.

5. Catchment Studies

This section aims to highlight the functioning of the aquifers of Ballindine and Manorhamilton in terms of recharge and discharge dynamics within the delineated groundwater catchments. Relatively extensive studies had to be undertaken since only little or no systematic research has been conducted in both areas prior to this study.

As part of the catchment studies, for both springs, water balances were estimated, tracer tests were conducted, and reservoir modelling using KarstMod was executed. In a first step, the discharge hydrograph and its representative average recession, i.e. the master recession curve (MRC) was established and analysed with regard to corresponding recession constants k. For the LFC, a benchmark range of optimal recession constants k was established. Further, the MRC was related to infiltration dynamics following Mangin (1975); El-Hakim and Bakalowicz (2007).

5.1. Ballindine

The study area was previously illustrated in Figure 3.1. Figure 5.1 shows a semi-log plot of the hourly discharge hydrograph of Ballindine spring along with discharge of the River Robe and daily rainfall at the MetEireann station Claremorris. The discharge time series covers more than 9 years, as summarised in Table 5.1. One major data gap was present in the time series covering the period 1 Jul to 20 Nov 2015. This data gap was filled using simulated records (see Section '5.1.4. Reservoir modelling').

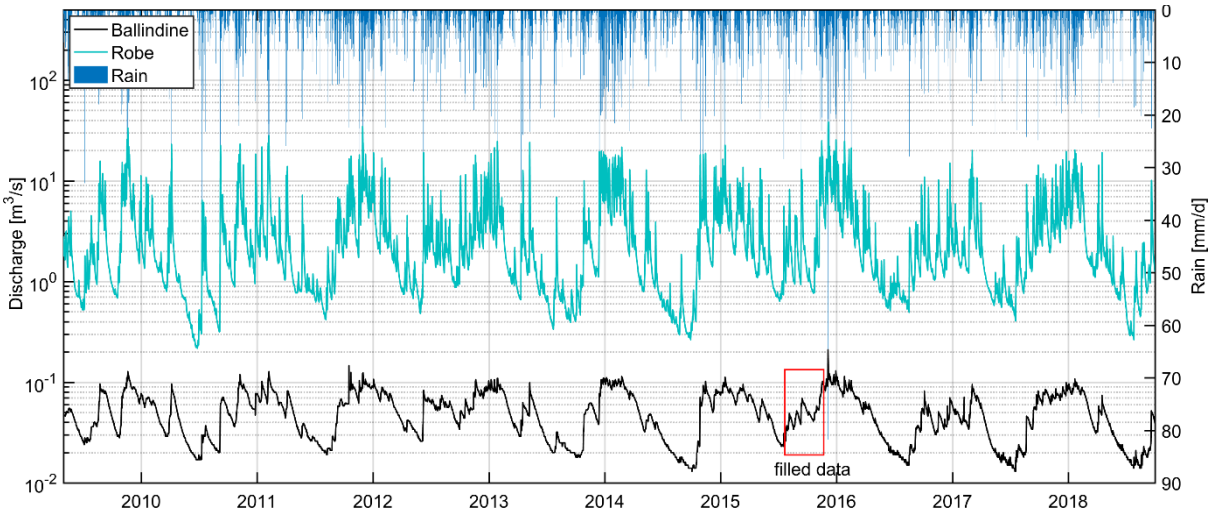

Figure 5.1: Hourly discharge of Ballindine spring, the River Robe and daily rainfall at Claremorris for hydrological years 2010 to 2018. The red box indicates a data gap that was filled with simulated discharge of the KarstMod reservoir model.

Discharge of Ballindine spring shows a clear seasonal pattern, with one or two larger recessions during the summer and peak discharges during the winter. Spring discharge ranges between a minimum of 0.013 m^3/s (measured in Oct 2014 and Jul 2017) and a maximum of 0.56 m^3/s (measured on 29 Nov 2011). However, the measured maximum of 0.56 m^3/s was considered as an artefact or outlier. It was therefore replaced modelling results of the KarstMod reservoir model to account for 0.122 m^3/s.
The spring hydrograph indicates a relatively slow response of the majority of discharge to rainfall. The time scale of the recession is in the range of months.

Discharge of the River Robe shows a very flashy signal, presumably rapidly responding to rainfall. River discharge ranges between 0.22 m^3/s (26 Jun 2011) and 38.45 m^3/s (06 Dec 2015). However, it is evident that the seasonal patterns of both discharge time series indicate some form of correlation.

Table 5.1: Summary of available data for Ballindine spring; Q = discharge [m3/s], T = temperature [ºC], EC = electrical conductivity [µS/cm], P = rainfall [mm/d], σ = standard deviation.

Station	Start date	End date	No of days	Parameters	Min.	Max	Mean	σ
Ballindine spring	29/04/2009	30/09/2018	3,442	Q [m^3/s]	0.013	0.562	0.052	0.025
	01/10/2017		438	T [ºC]	9.29	10.93	10.10	0.42
				EC [µS/cm]	607.0	784.0	744.4	25.45
Claremorris	29/04/2009		3,442	P [mm/h]	0	81.8	3.48	5.38
Christina S BR. (River Robe)	29/04/2009		3,442	Q [m^3/s]	0.22	38.4	3.12	3.72

Figure 5.2 summarises all available hydroclimatic variables/time series, including i) hourly discharge of the River Robe and Ballindine spring and temperature and electrical conductivity (EC) of Ballindine spring, and ii) rainfall and air temperature measured at the MetEireann climate station at Claremorris.
The temperature of spring discharge shows a) a seasonal pattern with temperatures ranging between 10.9 ºC in Oct 2017 and 9.3 ºC in Mar 2018, and b) a diurnal pattern where temperatures changes between day and night is >0.5 ºC during summer. The diurnal change may be associated with the monitoring station, which is an open pond that is subject to atmospheric temperatures. However, the seasonal pattern is very interesting, as it suggests a very slow temperature response, which doesn't seem to be correlated with the ambient air temperature. This temperature pattern may suggest a delayed contribution from a large reservoir.
EC of spring discharge is relatively high with an average of 744 µS/cm. In the context of the shallow outflow of Ballindine, EC can be interpreted in relation to the contact time between groundwater and the rock, which suggest a rather 'long' contact or residence time.

The course of EC during the hydrological year 2018 shows to some extent the typical response of a karst spring with clear drops of EC after a rise in discharge and an exponential rise in EC during periods of prolonged recessions. Yet, the EC records are relatively noisy. Periods of prolonged 'EC recessions' are usually associated accompanied by additional discrete EC drops which may be associated with contributions from conduit drainage via faster flow paths and/or contributions from reservoirs that have a lower EC (e.g. the River Robe). Notably, EC drops do not necessarily correlate either with rainfall or discharge peaks in the River Robe or Ballindine spring. Accordingly, the origin of the EC drops remains indefinite at this point.

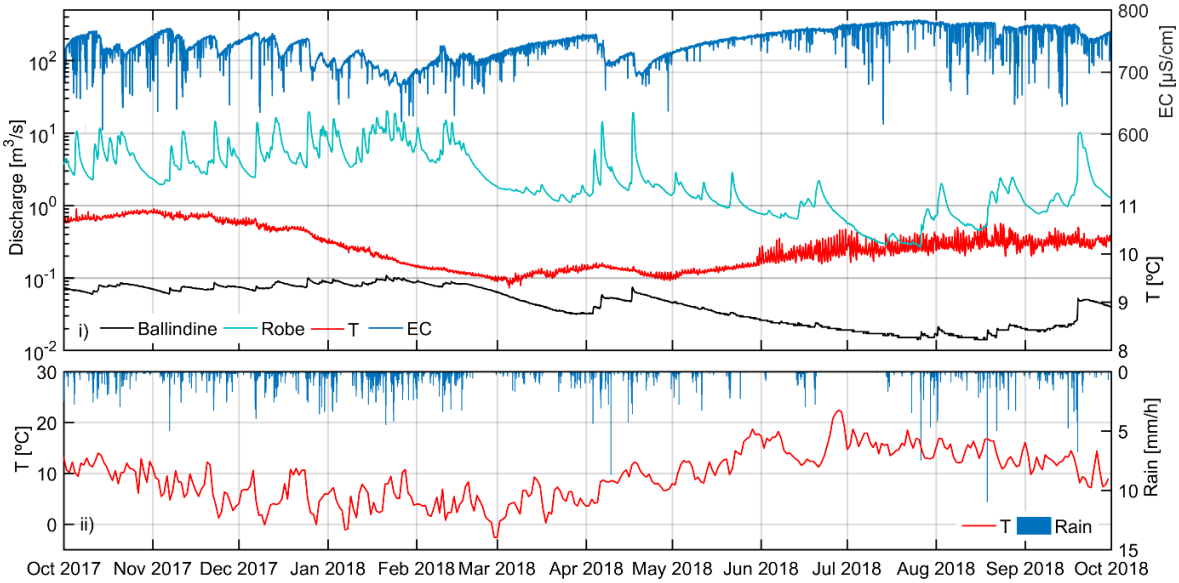

Figure 5.2: i) hourly discharge, EC and temperature of Ballindine spring and discharge of the River Robe and ii) hourly rainfall at Claremorris and mean daily temperature (T) for the hydrological year 2018.

As part of a tracer test (Section '5.1.3. Tracer tests'), the EC of both Ballindine spring and the River Robe were investigated further at a 5 min time step as well as their water levels between 30 Jan and 10 Feb 2019 (Figure 5.3). EC records of the Robe are relatively high for surface waters, ranging between 309 and 612 µS/cm. EC clearly responds to rising water levels and the recession of the river. There is no apparent correlation between the River Robe and Ballindine spring, yet, the 5 min time step reveals an interesting pattern, namely step-wise drops and surges in EC. For Ballindine, these steps are relatively large of up to 50 µS/cm. For Ballindine, the steps are relatively small in the range of 10 µS/cm. The specific reason for this pattern is unclear, but it may be related to the activation/deactivation of flow channels, perhaps due to a syphon-like effect. Hence, it indicates that the Robe is in interaction with the aquifer, and therefore, exfiltration towards Ballindine seems plausible.

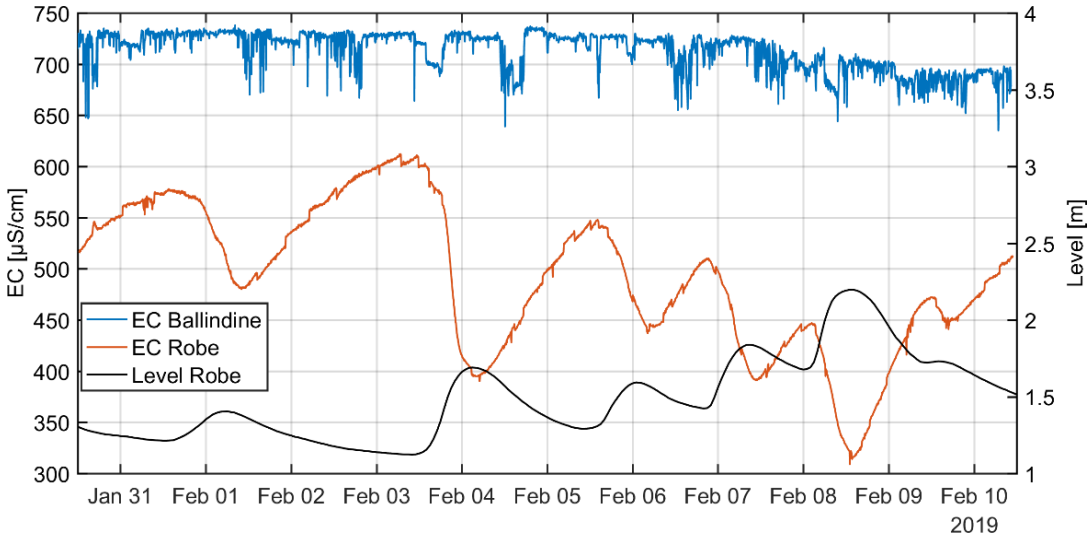

Figure 5.3: EC of Ballindine and the Robe along with water level of the Robe between 30 Jan and 10 Feb 2019.

5.1.1. Master recession curve analysis

While the previous section illustrated the overall discharge response of Ballindine over longer periods, this section focusses on the characterisation of the 'ideal' or average recession, namely the master recession curve (MRC) with regard to recharge, flow and discharge of the Ballindine aquifer. Therefore, different exponential components were identified. Further, different methods were applied to establish a benchmark range of recession constants k with regard to the LFC.

In a first step, the MRC for Ballindine was established from daily discharge between 2009 and 2018 using 20 undisturbed recession segments with a discharge ranging between 0.016 and 0.16 m^3/s (Figure 5.4). The minimum observed flow was reached after approx. 100 days.

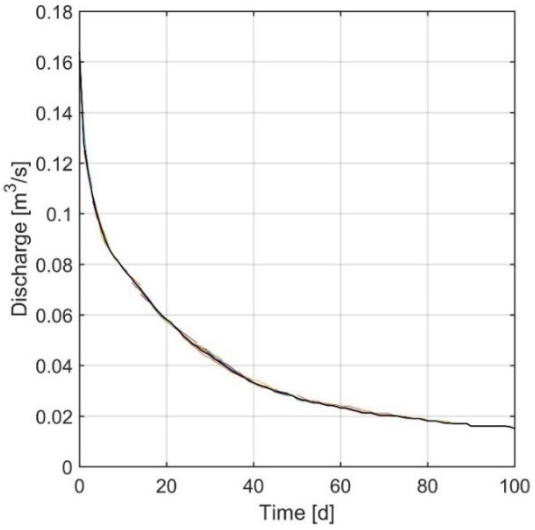

Figure 5.4: 20 fitted components and master recession curve for daily discharge of Ballindine spring.

Next, linear reservoirs following Maillet's law were fitted along the MRC. The MRC can be simulated by at least three linear reservoirs in parallel, which are interpreted as flow and discharge from different permeability domains: the upper most segment 'A' is the flood recession (k = 0.90 d^{-1}), 'B' is the intermediate recession (k = 0.05 d^{-1}) and the lowest segment 'C' is the low flow recession (k = 0.005 d^{-1}) (see semi-logarithmic plot Figure 5.5). In the context of Ballindine, 'A' may be considered as the very small fraction of conduit discharge, while 'B' and 'C' both resemble contribution from the fissured matrix domain. As it will be shown, the aquifer of Ballindine is almost exclusively described by diffuse and slow groundwater flow. Therefore, 'B' and 'C' must be considered as flow components of different permeabilities, potentially linked to diffuse flow within the fissured matrix domain. Segment 'A' may potentially be described by turbulent flow or at least deviating from laminar flow.

The respective recession coefficients for 'A', 'B', and 'C', are 0.407, 0.951, and 0.995 d^{-1}. Accordingly, the maximum contribution from low flow is at 0.025 m^3/s. For the daily k = -0.005 the daily recession coefficient a is calculated according to $a = \exp(-0.005) = 0.995$ d^{-1}. The hourly recession coefficient $a' = a^{1/24}$ will yield the hourly recession coefficient a' = 0.999 h^{-1}. Therefore, hourly recession coefficients a' for 'A', 'B', and 'C' are 0.963, 0.998 and 0.999 h^{-1}.

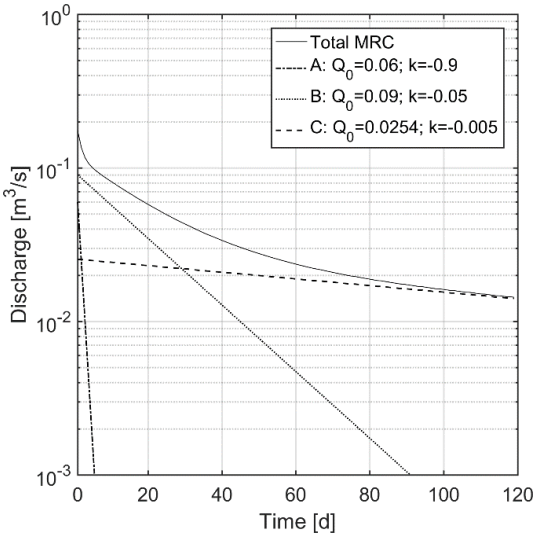

Figure 5.5: Master recession curve for daily discharge of Ballindine spring split into three contributing linear reservoirs.

Table 5.2 gives an overview of the individual straight-line components of Ballindine representing drainage from a linear reservoir. For comparison with Manorhamilton, the daily recession constant k was converted into hourly k' values. Figure 5.5 suggests that the intermediate component dominates the majority of the recession and hence, this component may be considered as contributing the majority of the flow.

Table 5.2: recession constants k of straight-line components for daily discharge of Ballindine (m^3/s).

Time step	LFC	Intermediate	Flood
k' [h^{-1}]	-0.0002	-0.0021	-0.0375
k [d^{-1}]	-0.005	-0.05	-0.90

In a next step, the benchmark range for the optimal recession coefficients was generated for the LFC ('C') of daily time series. The optimal recession coefficient was found by: a) plotting Q_t against Q_{t+1} where the slope represents a, b) calculating mean of Q_{t+1}/Q_t, and c) applying a backwards moving filter.

Plotting Q_t against Q_{t+1} yields a = 0.967 d^{-1} or k = -0.034 d^{-1} (Figure 5.6).

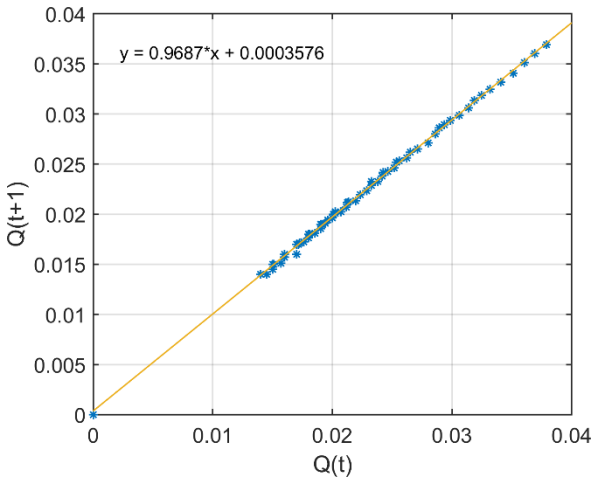

Figure 5.6: Plot of Q_t against Q_{t+1} to estimate the optimal recession coefficient for Ballindine spring.

In a next step, calculation of the mean of Q_{t+1}/Q_t yields a recession coefficient of a = 0.988 d^{-1} or k = -0.012 d^{-1}. Finally, the backwards moving filter yields a = 0.994 d^{-1} or k = -0.006 d^{-1} (Figure 5.7).

Table 5.3 summarises the recession coefficients calculated using the different methods. The results are considered as the benchmark range for fitting exponential LFCs along observed discharge. Accordingly, a ranges between 0.9667 and 0.995 d^{-1}. Again, for comparison with Manorhamilton, hourly k' and a' have been calculated as well.

The baseflow component or LFC is further used to characterise the aquifer following Mangin (1975); El-Hakim and Bakalowicz (2007) (Figure 5.8). The resulting associated parameters are displayed in Table 5.4. The simulated discharge $Q_{sim} = \psi(t) + \varphi(t)$ matches very well with the derived MRC proven by a NSE of 0.98.

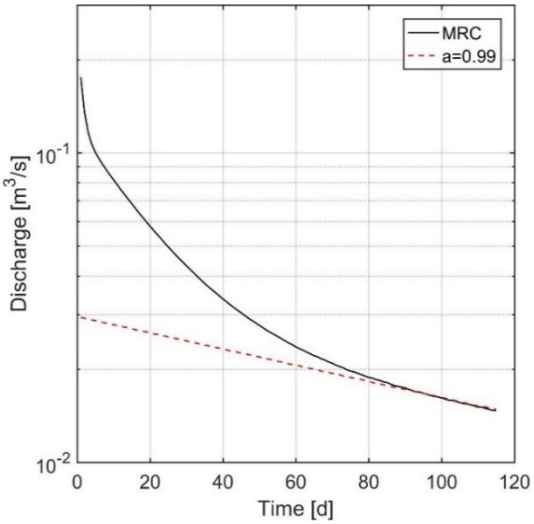

Figure 5.7: Estimation of a for the master recession curve of Ballindine according to Collischonn and Fan (2013).

Table 5.3: Range of optimal hourly and daily low flow recession coefficients (a and a') and recession constants (k and k') for Ballindine spring.

Method	Time resolution [h, d]	Constant	
Method 1 (fitting linear reservoirs)	h	a'	0.9998
		k'	-0.0002
	d	a	0.9950
		k	-0.0050
Method 2 (plotting Q_t against Q_{t+1})	h	a'	0.9987
		k'	-0.0014
	d	a	0.9687
		k	-0.0318
Method 3 (mean of Q_{t+1}/Q_t)	h	a'	0.9995
		k'	-0.0005
	d	a	0.9876
		k	-0.0125
Method 4 (backwards moving filter)	h	a'	0.9998
		k'	-0.0002
	d	a	0.9941
		k	-0.0059
Average	h	a'	0.9994
		k'	-0.0006
	d	a	0.9859
		k	-0.0143

The value of Q_{R0} is the result of fitting the exponential baseflow component $\boldsymbol{\varphi(t)}$ with α = 0.005 along the MRC. As a result, the dynamic storage $Max(V_d)$ accounts for 400,00 m^3, which may be

interpreted as low-flow storage component. The mean annual volume flowing through the phreatic zone V_{trans} accounts for 359,442 m³, and consequently the regulating power k = 1.11; k is considered as a relatively high, which suggests a relative high regulating power of the aquifer, and hence less influence of well-developed conduits in terms of functioning of the karst system. For an effective conduit controlled karst system, k is assumed to be <1 (El-Hakim and Bakalowicz, 2007). Further, the k value expresses the mean residence time of groundwater, which is therefore 1.11 years or 405 days.

The parameters η and ε are both <0.1, which also indicates aquifers of poorly developed conduit systems, or covered (not directly exposed karst bedrock) aquifers resulting in slow infiltration. As a consequence, i = 0.84 tends towards 1, as it is the case for slow or delayed infiltration.

The aquifer falls into category '5' of the classification system, i.e. "aquifers with a deep phreatic zone partly or totally confined under low permeable sediments with a complex drainage structure responsible for very long, multiannual or secular residence times". As previously stated in Section '3.1.3. Hydrogeology', deeper groundwater flow may be circulating along the Claremorris fault and/or discharging into Lough Mask/Lough Corrib. Hence, the notation of a "deep phreatic zone" may be related to this hypothesis.

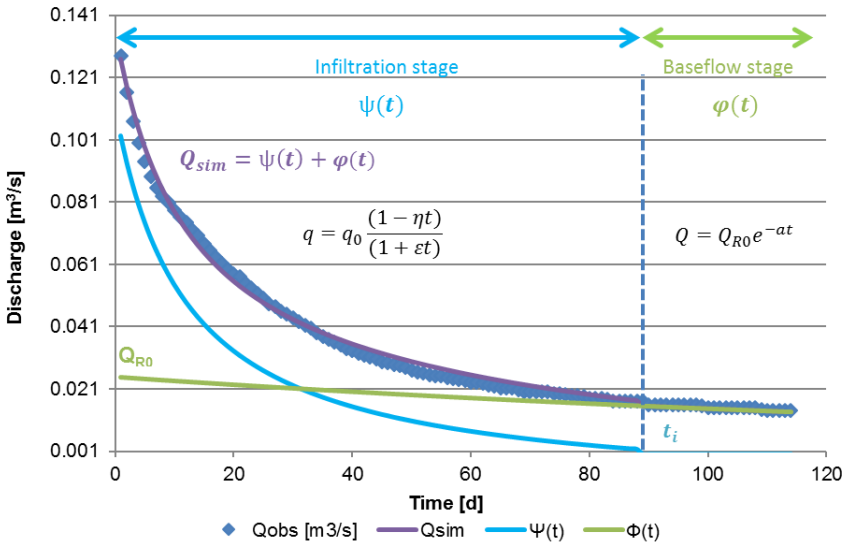

Figure 5.8: Analysis of the master recession curve (Q_{obs}) of Ballindine following Mangin (1975); layout modified after Duran (2015).

Table 5.4: Fitted parameters for the master recession curve of Ballindine following Mangin (1975); El-Hakim and Bakalowicz (2007).

t_i [d]	Q_{R0} [m³/s]	a [d⁻¹]	η [d⁻¹]	ε [d⁻¹]	$Max(V_d)$ [m³]	V_{trans} [m³]	k	i	Class
90	0.25	0.005	0.01	0.085	400,000	359,442	1.11	0.84	5

5.1.2. Water balance

Water balances were established to provide an indication of a reasonable catchment extent, and hence to evaluate the boundaries of the previously established catchment boundaries of 8.9 km^2 (EPA, 2011a). Fortunately, long time series of discharge and climate variables were available for this analysis.

The assumption is that over a period of one hydrological year, the input (rainfall) shall equal the output (discharge) given groundwater recharge is the difference between total rainfall and ET. Water balances for nine hydrological years are presented in Table 5.5: ET_0 is the daily reference ET for short cut, well-watered grass, which is considered representative for the mix of landuse in the area of the catchment. Groundwater recharge is the difference between ET and rainfall, and its share of total rainfall given in percentage. Discharge is the cumulative observed spring discharge, and the mismatch is the difference between presumed groundwater recharge and spring discharge.

Table 5.5 shows that groundwater recharge is estimated to be relatively low compared to the groundwater recharge map and the estimated weighted bulk recharge of 71% following Hunter Williams, et al. (2013). In addition, for each of the presented hydrological years, there is a significant mismatch between the observed discharge and estimated groundwater recharge, ranging between 1.64 and 3.59 million m^3. Hence, higher discharge would be expected for the size of the delineated catchment, assuming that all recharge is discharged at Ballindine spring. In fact, given the extent of the catchment of 9.92 km^2, the spring discharge accounts between 11.8 and 16.7% of total rainfall, with very little variation. This seems to be unrealistic and so it is surmised that the actual catchment size must be significantly smaller.

Table 5.5: Water balance for the Ballindine catchment based on original EPA defined catchment area of 8.9 km^2 (numbers in million m^3 if not stated differently, GW = groundwater).

Water year	Rainfall	ET_0	GW recharge	GW recharge [%]	Discharge	Mismatch
2010	10.60	5.49	5.11	48.23	1.52	3.59
2011	10.70	5.15	5.56	51.92	1.69	2.27
2012	12.03	5.13	6.90	57.33	2.00	2.45
2013	10.57	5.12	5.45	51.56	1.64	2.28
2014	11.59	5.35	6.24	53.83	1.62	2.67
2015	12.56	5.15	7.41	58.99	1.79	2.86
2016	13.34	5.48	7.86	58.93	1.58	3.36
2017	9.09	5.39	3.70	40.67	1.24	2.12
2018	8.72	5.66	3.06	35.15	1.58	1.64
Average	11.02	5.32	5.70	50.74	1.66	2.72

To estimate an appropriate catchment size in relation to the water balance, the annual observed spring discharge was matched with the estimated groundwater recharge (%) necessary to explain the discharge.

Assuming recharge rates ranging between 35 and 59%, with the given discharge of Table 5.5, the catchment would need to have a mean size between 1.8 and 4.6 km^2 as displayed in Table 5.6. This target catchment size is related to a target catchment size to yield the appropriate amount of rainfall and clearly indicates a smaller catchment size than previously assumed by the EPA delineation.

Table 5.6: Target catchment size of Ballindine based on the water balance (numbers in million m^3 if not stated differently).

Water year	Discharge	Target rainfall	Target catchment size [km^2]
2010	1.52	3.15	2.65
2011	1.69	3.25	2.71
2012	2.00	3.49	2.59
2013	1.64	3.17	2.68
2014	1.62	3.01	2.32
2015	1.79	3.04	2.16
2016	1.58	2.68	1.79
2017	1.24	3.05	2.99
2018	1.58	4.51	4.61
Average	1.63	3.32	2.72

The water balance approach taken here is based on the assumption that Ballindine spring constitutes a single discrete outlet of the aquifer receiving only recharge from rainfall. This assumption, however, may be challenged by the existence of multiple outlets of the karst aquifers and/or by the existence of drainage channels that are ubiquitous in the catchment as well as by additional recharge from the River Robe.
These aspects must be kept in mind for finalising the catchment size following the upcoming methods.

5.1.3. Tracer tests

The main goal of the tracer tests was to investigate hydrogeological connections in relation to the EPA (2011a) delineated catchment, to quantify tracer recovery and assess the mean travel time. Two tracer tests were carried out: Firstly, three injections into an estavelle and supposed swallow hole were conducted under low-flow conditions on 08 Aug 2018 using the artificial tracer rhodamine WT, fluorescein and optical brightener.
In the east of the previously assumed catchment, the Irishtown Group Water Scheme (GWS) abstracts approx. 500 m^3/d via two boreholes. Groundwater is treated using UV and chlorination before being supplied to approx. 600 connections in the region of Ballindine. This meant that the tracer approach taken had to be designed to avoid any potential visible tracer recovery occurring within the production wells.

Secondly, one injection of fluorescein was done into the River Robe on 30 Jan 2019. The aim of this test was to investigate a hydraulic connection between the river and Ballindine spring through river bed exfiltration.

The objectives of the test were mainly to:

- Identify hydraulic connections between
  - the estavelle (turlough) and the abstraction wells of the GWS;
  - the estavelle (turlough) and Ballindine spring;
  - a swallow hole (presumably) outside the catchment and Ballindine spring; and
  - the River Robe and Ballindine spring via surface water-groundwater interaction;
- Characterise groundwater flow dynamics between the injection sites and observation sites.

5.1.3.1. Tracer test 08 Aug 2018

Because of the absence of swallow holes within the previously assumed catchment, only two suitable injection sites (IS) were identified. IS(a) is the estavelle of a turlough at 59.51 masl (Figure 5.9).

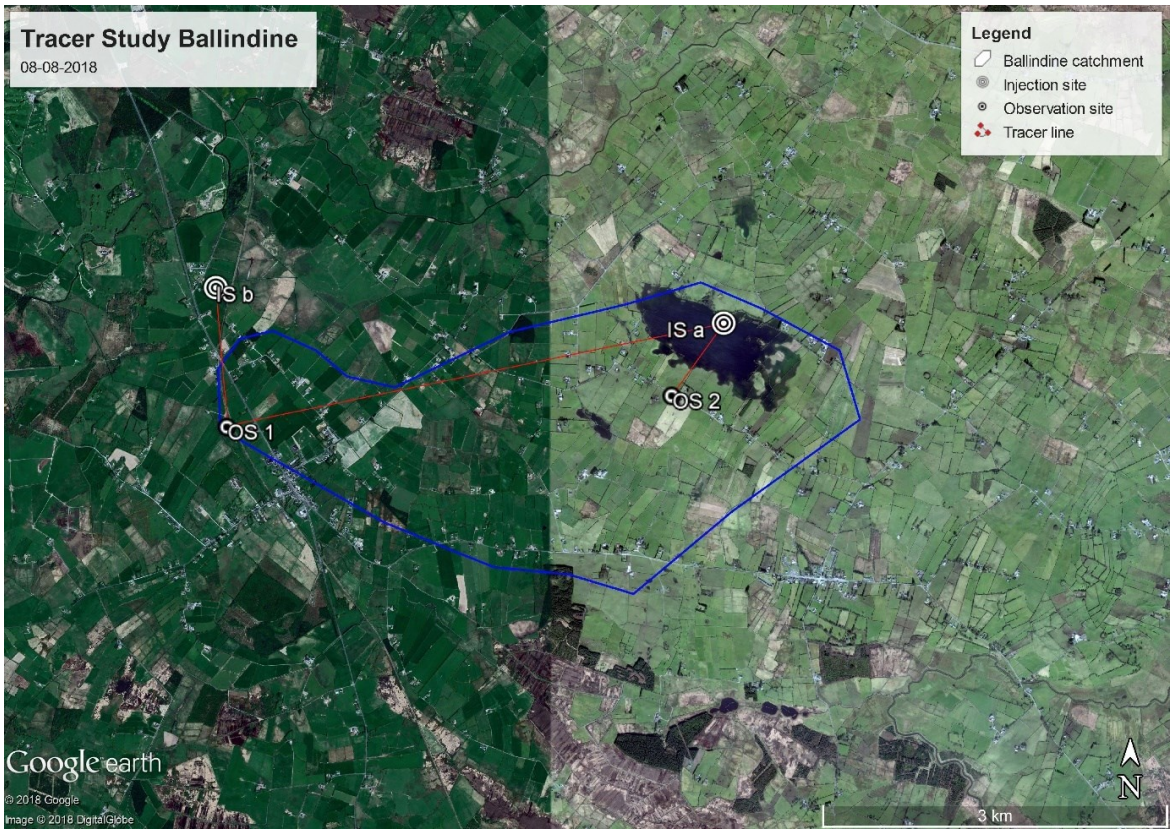

Figure 5.9: Outline tracer test 08 Aug 2018.

Due to consistent dry weather throughout the summer 2018, the turlough was completely empty, yet, precedent rainfall of 1.3 mm within 24 h prior to the first injection may have contributed to

generate flow of a few l/s into the estavelle. IS(b) was mapped as swallow hole according to the karst database of the GSI. Yet, in fact, the location of the swallow hole marks the disappearance of a drainage ditch into a man-made underground channel at approx. 54 masl. There was no information as to whether the channel discharges into a swallow hole in the underground, as the entrance to the underground channel was fenced off.
Two injections were carried out at IS(a): in order to ensure that the abstraction wells of the GWS are not impacted by any tracer, a first injection was done using a moderate mass of optical brightener (Durawhite). The subsequent monitoring for Durawhite did not indicate any arrival of tracer, hence, a second injection was carried out using fluorescein. In addition, and one injection was done at IS(b) using rhodamine WT (Table 5.7).

Table 5.7: Injection sites 08 Aug 2018.

Injection site	Injection	Coordinates	Altitude [masl]	Tracer and mass	Injection time	Flushing volume [l/s]
IS(a): Estavelle	1	53.6825°; -8.2682°	59.5	50 l Durawhite	11:00	~3-6
	2			760.5 g fluorescein	19:50	~3-6
IS(b): Assumed swallow hole	1	53.6853°; -8.9674°	~54	226 g rhodamine WT	12:55	~2-5

Tracer was monitored at two observation sites (OS), namely Ballindine spring (OS 1) and at a supply well of the GWS at OS 2 (Figure 5.9, Table 5.8).

Table 5.8: Observation sites 08 Aug 2018.

Observation site	Coordinates	Altitude [masl]	Linear distance to IS [m]	Instrumentation	Recording frequency
OS 1: Ballindine spring	53.6745°; -8.9659°	48.8	IS(a): 4,400 IS(b): 1,200	Albillia GGUN-FL30 (#950)	5 min
OS 2: Supply well	54.6770°; -8.9073°	~72 (groundwater abstraction between 58-60)	IS(a): 760	Albillia GGUN-FL30 (#951)	30 s

Automatic sampling was conducted using Albillia GGUN-FL30 field fluorometers provided by the GSI and deployed at both OSs. Monitoring continued at OS 1 for almost 25 days while monitoring at OS 2 lasted for only 8.7 h, as the only aim was to rule out that any tracer from injection 1 was recovered in OS 2.

Figure 5.10 shows the results of fluorometer #950 installed at the abstraction well of the GWS (OS 2) where monitoring was conducted for 8.7 h.
Turbidity is constantly <1 NTU while the signal for optical brightener shows a generally slightly decreasing trend >20 ppb until a rapid surge occurs from 20.2 to 21.5 ppb at 11:19. This, however,

was related to the adjustment of inflow through the field fluorometer. A check revealed that the inflowing tube was kinked, preventing constant inflow. This was fixed, causing an immediate surge in ppb. Hence, it was concluded that the readings of the first 1 ½ h are most likely not representative, and that no tracer break-through was observed in that period.

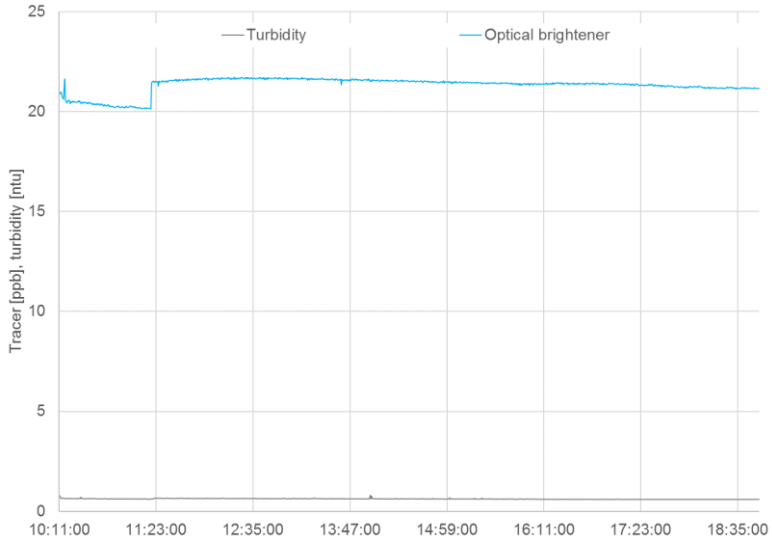

Figure 5.10: Tracer break-through curve for optical brightener [ppb] and turbidity [NTU] using fluorometer #950 at OS 2.

Because no tracer was observed at the water supply well, a second injection was done using fluorescein. The results of the tracer study are displayed in Figure 5.11 as monitored at Ballindine spring between 08 Aug 2018 and 02 Sep 2018 (24.9 days).

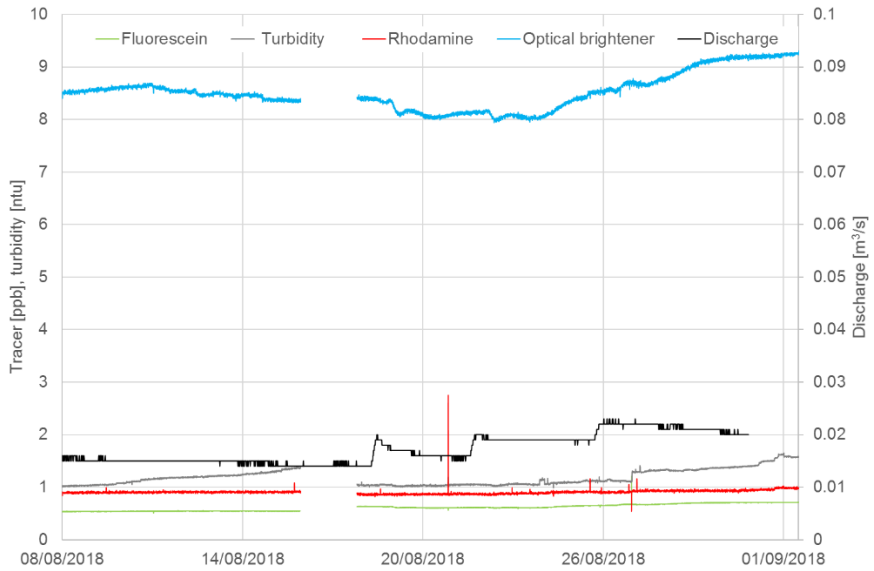

Figure 5.11: Tracer break-through curves for rhodamine WT, fluorescein and optical brightener [ppb], turbidity [NTU] and discharge [m^3/s] using fluorometer #951 at OS 1 (Ballindine).

During that period, a gap of monitoring occurred between 16 Aug 10:15 and 18 Aug 7:20. It is not known why the instrument stopped recording during that period.
During the entire monitoring period, rainfall caused three minor rises of discharge. There is an indication that turbidity increased with the third rise, although the level is comparably low. However, no rhodamine or fluorescein was recovered during the monitoring period. The few sharp spikes must be considered as artefacts/erroneous readings.
Optical brightener shows a fluctuating signal. From other tracer tests, it is known that the signal for optical brightener can fluctuate largely due to natural and artificial (e.g. detergents) background values. Further, the plot does not indicate the presence of a break-through curve. Therefore, it is considered as the result of natural, or more likely anthropogenic influence of nearby houses (wastewater).
In conclusion, no tracer was recovered at any of the two OS. It is believed that injection site IS(b) does indeed follow a drainage channel rather than infiltration via a swallow hole, but further investigations were not carried out as to where the injected dye might re-appear. The negative trace between IS(a) and OS 1 may be due to different reasons. Firstly, the tracer may have become trapped in a cavity. The test was executed during extreme low flow conditions, which are not favourable. Although there was a constant inflow of water providing flushing, trapping could have easily occurred along the flow path. Secondly, flow velocities may have been too low during the period, and hence monitoring not long enough. This could be related to the long residence time, as previously mentioned applying the method of El-Hakim and Bakalowicz (2007). On the other hand, this, however, would mean that flow velocities were lower than 177 m/d (7.4 m/h), which is unlikely. Alternatively, this might show that groundwater does not flow westwards across the Claremorris fault to Ballindine spring, but instead somewhere else, potentially towards the north, discharging into the River Robe.

5.1.3.2. Tracer test 30 Jan 2019

To investigate the exfiltration from the River Robe in the aquifer of Ballindine spring, 1.84 kg of fluorescein was injected into the River Robe at IS(c), ~600 m upstream of the supposed exfiltration zone of the Robe (Figure 5.12). This point was mainly due to it being the closest place to access the river upstream of the suspected exfiltration zone, but also because it allows sufficient time for mixing between the dye and river water, en route (Table 5.9).
Tracer was monitored at Ballindine spring (OS 1) (Figure 5.12, Table 5.10) using an Albillia GGUN-FL30 field fluorometer (#951) provided by the GSI. Because of the potentially partially rapid flux between the River Robe and Ballindine spring, as previously indicated by the noisy EC signal observed at the spring, the monitoring frequency was set to 1 min lasting for almost 11 days between 30 Jan 11:20 and 10 Feb 2019 10:15.

In addition, EC, temperature and depth of the River Robe was observed downstream of the supposed exfiltration site (Figure 5.12) using a Schlumberger CTD sensor (DI263) installed on the bank of the river.

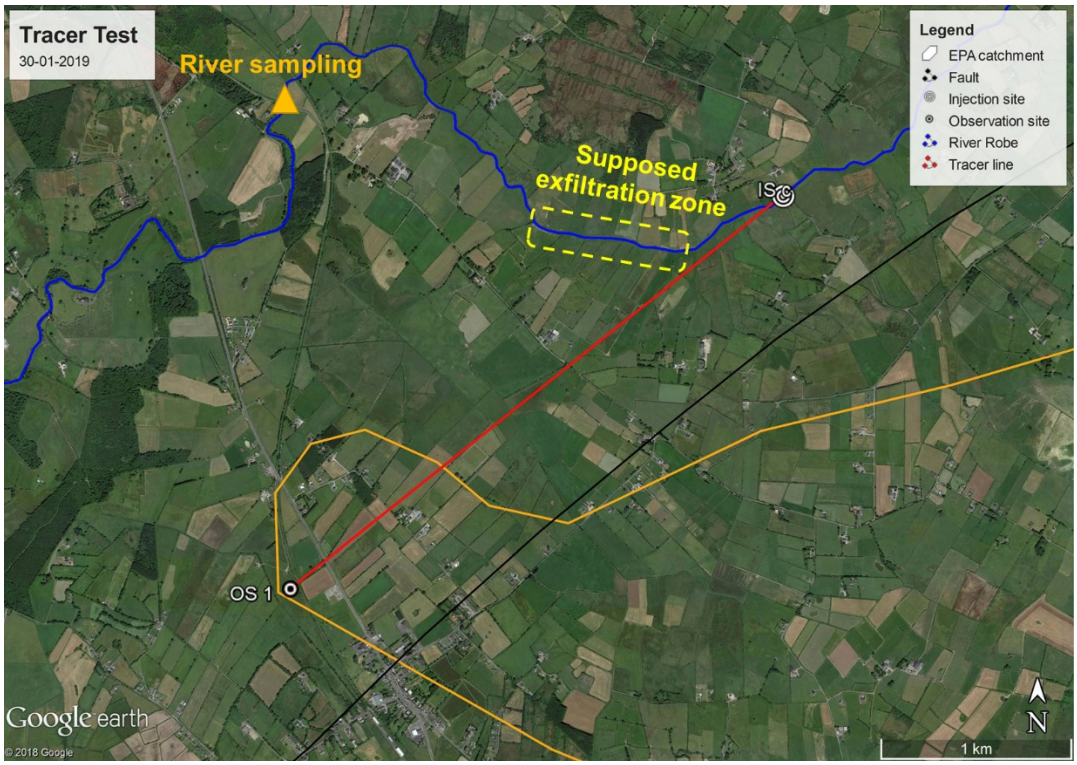

Figure 5.12: Outline tracer test 30 Jan 2019.

Table 5.9: Injection site 30 Jan 2019.

Injection site	Injection	Coordinates	Altitude [masl]	Tracer and mass	Injection time	Flushing Volume [l/s]
IS(c): River Robe	1	53.6929°; -8.9268°	~58	1,840 g fluorescein	13:10	-

Table 5.10: Observation sites 08 Aug 2018.

Observation site	Coordinates	Altitude [masl]	Linear distance to IS [m]	Instrumentation	Recording frequency
OS 1: Ballindine spring	53.6745°; -8.9659°	48.8	IS(c): 3,290	Albillia GGUN-FL30 (#951)	1 min

The results of the tracer test are summarised in Figure 5.13. Concerning the fluctuation of EC of Ballindine and the River Robe, the results were already discussed in the context of Figure 5.3 (Section '5.1. Ballindine').

Figure 5.13b shows the fluctuation of discharge of the River Robe, which corresponds clearly to rainfall events plotted below. The pattern of EC shows a clear inverse correlation to the river discharge.

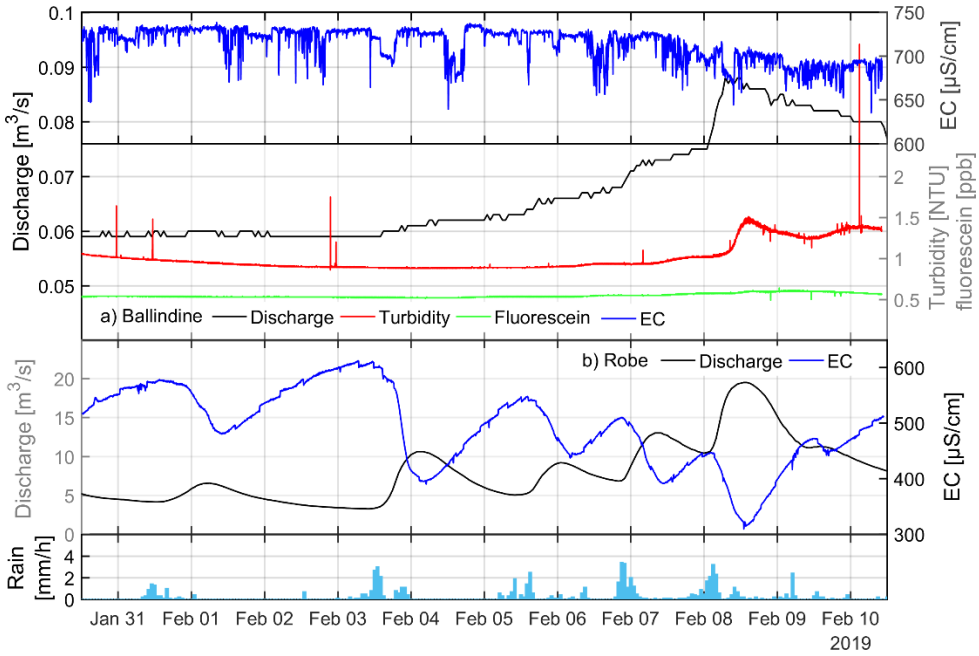

Figure 5.13: Summary of the tracer test between the River Robe and Ballindine spring between 30 Jan and 10 Feb 2019: bottom plot shows rainfall observed at Claremorris [mm/h]; b) shows EC [µS/cm] and discharge [m^3/s] of the Robe, and a) shows the concentration of fluorescein [ppb], turbidity [NTU], EC [µS/cm] and discharge [m^3/s] observed at Ballindine spring.

Figure 5.13a shows the results obtained at Ballindine spring. There is no indication for a breakthrough of fluorescein, hence, the trace between the river and the spring is interpreted as negative. The spring discharge gradually increases over the period of observation, yet, there are no fluctuations present as exhibited by the River Robe. However, on 06 Feb and 08 Feb, surges of discharge are obvious, the latter one seems significant in magnitude. These two surges clearly correlate in time with surges in discharge of the Robe. Further, the latter, second surge of discharge is accompanied by an increase in turbidity. Hence, it is hypothesised that the surge in river discharge may have impacted on flow within the aquifer of Ballindine spring, mobilising and/or transporting suspended solids along the flow path between river and the spring. This, again, is a hypothesis, and further tests would have to be carried out to clearly confirm this theory. Hence, until now, it is believed that the surge in river discharge >10 m^3/s (equivalent to >1.66 m) may be considered as threshold level after which the river rapidly impacts on the spring.

5.1.3.3. Conclusions

Figure 5.14 summarises the three results of all the tracer injections and their negative results. It is concluded that the injections on the eastern side of the Claremorris fault (06 Aug 2018) did not cross the fault, but instead more likely flowed towards the River Robe. The injection on the western side (IS b) most likely flowed into a drainage channel.

No tracer injected into the River Robe (30 Jan 2019) was recovered at Ballindine spring. This negative result may be caused by different reasons: the quantity of dye may have been too low while dispersion within the river and the aquifer may have been too high to yield measurable concentrations of dye at the spring. Further, insignificant quantities of tracer may have exfiltrated from the river bed. In fact, high frequency (5 min interval) sampling of the River Robe and Ballindine spring downstream river sampling suggest that there might be a threshold level at a water level of 1.7 m (equivalent to a discharge of 10 m^3/s) in the River Robe causing concentrated exfiltration, exemplified by an increase of turbidity at Ballindine spring. However, at the time of the tracer test, the discharge the River Robe was at 5 m^3/s, hence, it is possible that river exfiltration was very low at that time.

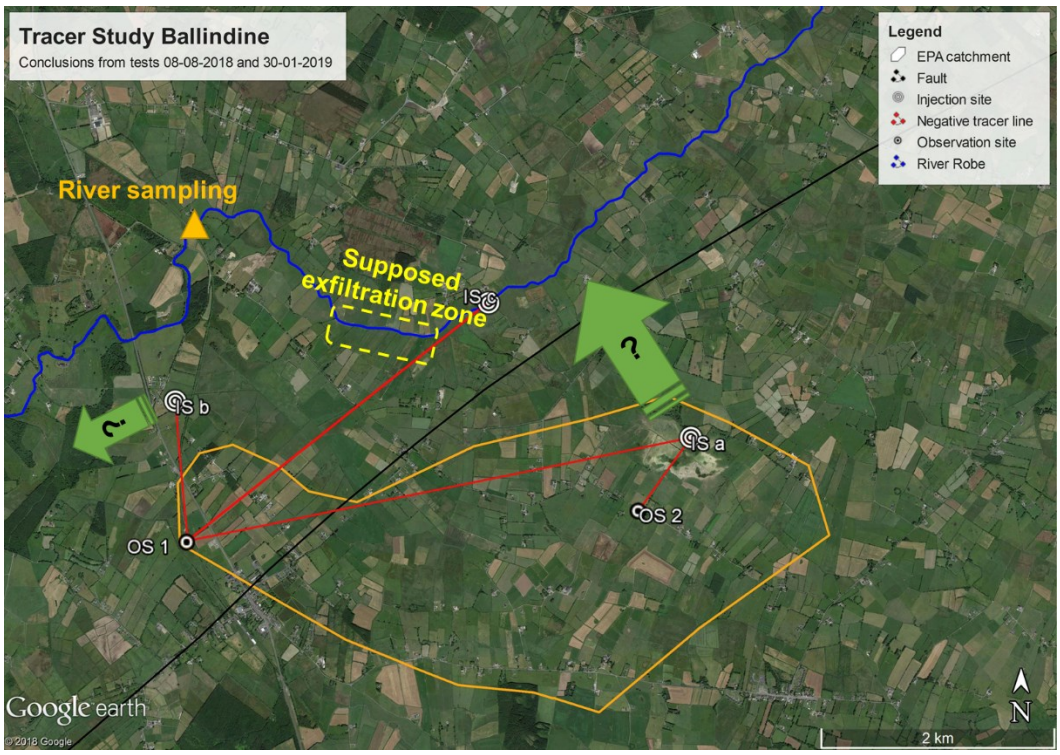

Figure 5.14: Negative tracer connections from injections on 06 Aug 2018 and 30 Jan 2019.

5.1.4. Reservoir modelling

A rainfall-discharge reservoir model was built using the software KarstMod (version 2.2.0.s) (Mazzilli, et al., 2017). The aim of this modelling exercise was, a) to generate simulated time series that can be used to fill data gaps and replace outlier(s) of the observed time series, and b) to determine how many and which reservoirs would be needed to simulate the spring discharge in the best way in order to characterise the role of the different internal flow paths within the karst network that comprise the total spring discharge.

The modelling period was 29 Apr 2009 to 30 Sep 2018, including 82,591 hourly time steps. A warm-up period was initiated for the period 29 Apr 2009 to 30 Sep 2010. The calibration was

carried out for the hydrological years 2012 to 2015 while validation was done for the hydrological years 2016 to 2018.

The best model was found by trying all different combinations of reservoirs and flows (Table 5.11, Figure 5.15).

Table 5.11: Fitted parameters of the KarstMod reservoir model of Ballindine spring, including data gaps.

R_A [km²]	E_0 [mm]	Q_{EM}		Q_{EC}		M_0 [mm]	Q_{MS}		C_0 [mm]	Q_{CS}	
		k_{EM} [mm/h]	a_{EM}	k_{EC} [mm/h]	a_{EC}		k_{MS} [mm/h]	a_{MS}		k_{CS} [mm/h]	a_{CS}
1.80	3.77	1.83	0.612	0.0127	0.02	4.30	0.0015	-	9.66	3.22	2.77

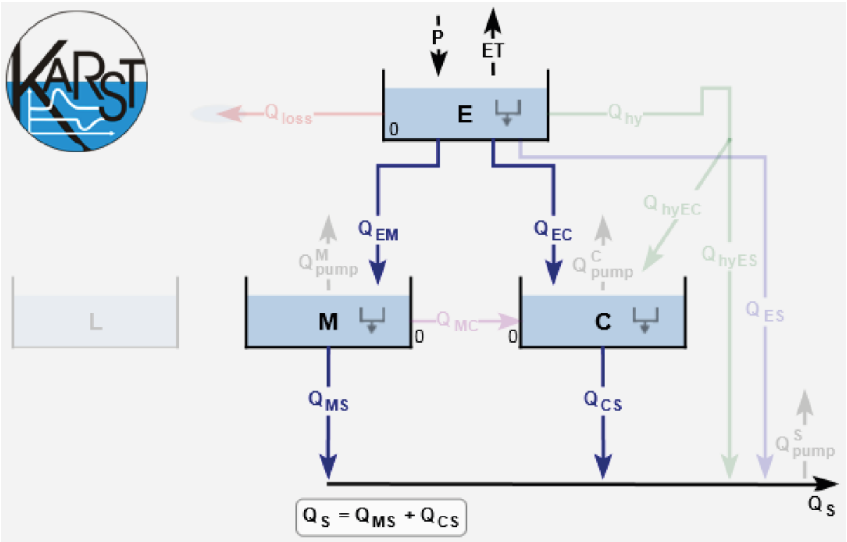

Figure 5.15: KarstMod reservoir model for Ballindine spring.

Each combination was then fine-tuned by reducing the parameter range after each model run. The best performing model was found to perform using the 'classical' model set up with the reservoir 'E' along 'C' and 'M' resulting in a NSE and KGE of 0.814 and 0.888 for the calibration period, and 0.470 and 0.740 for the validation period (Figure 5.16, Table 5.15). The optimum results were achieved when the catchment size is estimated at 1.8 km². Although Q_{MS} accounts for >99.99% of the total simulated spring flow compared to only <0.001% for Q_{CS}, reservoir 'C' is necessary to gain such high NSE/KGE. For example, by using only a single reservoir, i.e. 'M', (and a modified set of parameters) the model yields a NSE and KGE of 0.713 and 0.733 for calibration and 0.489 and 0.709 for validation.

Figure 5.16 shows modelled against observed discharge. In general, the model is capable of re-sembling the overall discharge dynamics, yet, it does underestimate or overestimate certain peri-ods of high flow or low flow. The difference varies, so no systematic pattern of mismatch can be identified.

The results show that observed discharge of Ballindine can be almost exclusively represented by drainage of the reservoir M, which represents slow or diffuse groundwater flow. There is a very small contribution of conduit flow that is nevertheless relevant for the simulation of observed discharge.

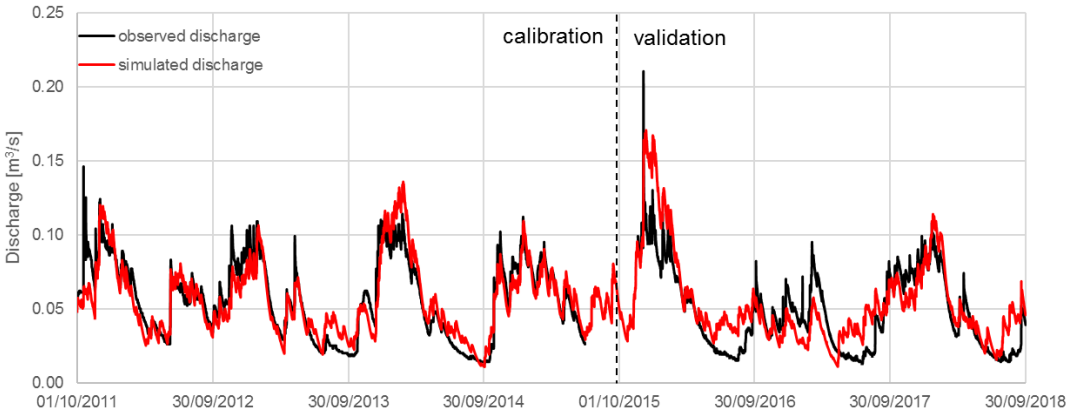

Figure 5.16: Observed and simulated discharge of Ballindine spring [m³/s] during calibration and validation, including data gaps.

Table 5.12: Performance of the simulated discharge and contributions from the 'C' and 'M' reservoirs for the period including data gaps.

Parameter	Calibration		Validation	
NSE	+0.814		+0.470	
KGE	+0.888		+0.740	
VCC	-0.11 MCM	-1.36%	+0.54 MCM	+12.50%
Q_{MS}	>99.99%		>99.99%	
Q_{CS}	<0.001%		<0.001%	

In a next step, the results were used to fill the data gap between 1 Jul to 21 Nov 2015. The model was then re-run, and the parameters were modified (Table 5.13).
Figure 5.17 and Table 5.14 illustrate and summarise the model performance for the time series with filled data gaps. Noticably, the model's performance is almost identical for the calibration period. During validation, the model performance decreases for all the parameters: the simulated discharge is overestimated by 10.85%.

Table 5.13: Fitted parameters of the KarstMod reservoir model of Ballindine spring.

R_A [km²]	E_0 [mm]	Q_{EM}		Q_{EC}		M_0 [mm	Q_{MS}		C_0 [mm]	Q_{CS}	
		k_{EM} [mm/h]	a_{EM}	k_{EC} [mm/h]	a_{EC}		k_{MS} [mm/h]	a_{MS}		k_{CS} [mm/h]	a_{CS}
1.80	3.71	1.85	0.602	0.0163	0.0465	4.08	0.0014	-	9.34	3.03	2.27

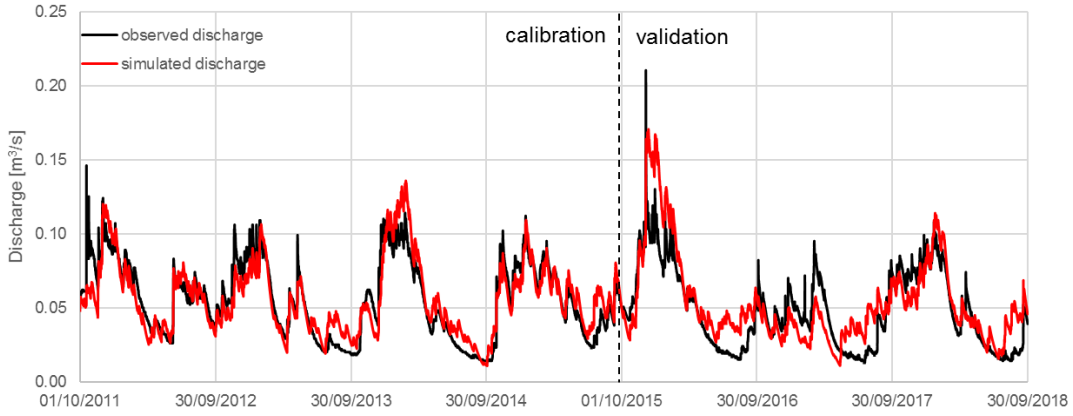

Figure 5.17: Observed and simulated discharge of Ballindine spring [m^3/s] during calibration and validation.

Table 5.14: Performance of the simulated discharge for the period including data gaps.

Parameter	Calibration		Validation	
NSE	+0.810		+0.573	
KGE	+0.868		+0.772	
VCC	-0.02 MCM	-0.23%	+0.49 MCM	+10.85%
Q_{MS}	>99.99%		>99.99%	
Q_{CS}	<0.001%		<0.001%	

In conclusion, the reservoir model indicates the dominant role of the matrix reservoir 'M' to simulate the observed discharge. This is interpreted as a dominant role of diffuse recharge and/or diffuse and slow groundwater flow components. Nevertheless, the necessity to integrate reservoir 'C' suggest that there is a very small contribution from a fast recharge and flow component.

5.1.5. Final catchment delineation

The results of the previous sections were used to update and improve the catchment boundaries. Based on the water balance approach which assumes that Ballindine spring is the only outlet draining the aquifer, the catchment size must have a minimum size of 1.8 km^2 as estimated by the KarstMod reservoir model and may have an average size of 2.76 km^2 as established by the water balances across 9 hydrological years.

However, additional surface water discharge out of the catchment through the drainage channels also has to be assumed, although it is very difficult to quantify this outflow given their ubiquity. Even an estimate seems challenging, yet necessary and so an additional outflow in the order of 20% of total discharge was chosen as a reasonable figure. Accordingly, the catchment size may be approximated by 3.3 km^2.

The results of the tracer tests can neither confirm a hydraulic connection between the turlough and the abstraction wells of the GWS, nor a connection between the turlough and Ballindine spring.

Therefore, there is no plausible explanation that groundwater flows east-west across the mapped fault/syncline.
Consequently, the most plausible and likely lateral extent of the aquifer would consider the Claremorris fault as flow barrier so to limit the catchment extent to the western side of the fault up towards the Robe River (Figure 3.1). This delineated catchment integrates the influence between surface water and groundwater along the River Robe.
The water level of the Robe River is measured 2.2 km north-west of Ballindine spring at Christina S BR. At this location, the river bed is lower than the outlet of Ballindine. However, along the northern catchment boundary, the river flows at an elevation of 54 masl, providing a head difference of >5 m to the spring.
The stream and spring hydrographs correlate very well in time, and indeed, as outlined in the results Section 'Time Series Analysis', the river does clearly exhibit influence on the aquifer of Ballindine spring. Such influence may be either via flow or via pressure transfer.
Accordingly, it seems most plausible to extend the catchment of Ballindine in the north-east up to the River Robe. The eastern and south-eastern boundary was defined as the course of the fault, considering some error with respect the precise course of the fault.
In the west, the catchment may actually extend further towards the river – this boundary may be dynamic in time.

5.1.6. Summary from Ballindine catchment studies

The final delineated catchment boundaries, as previously illustrated in Figure 3.1 in the solid red line, differ very much to the previously assumed EPA catchment boundaries illustrated in the dashed black line. The analysis of long-term time series, water balances for nine water years, reservoir modelling and tracer tests were used to delineate the final catchment boundaries. These boundaries are in line with the geological dip on the western side of the Claremorris fault, which is likely to act as a flow boundary and pathway for preferential flow. Further, a comparison of discharge time series between the River Robe and Ballindine spring provide evidence that the river influences the spring. A tracer test between the river and the spring did not directly confirm flow between the river and spring, but observed surges were interpreted as threshold effect for rapid surface water-groundwater interaction. The dynamics between the river and spring will be further discussed in the next chapter 'Time Series Analysis'. At present, it seems the most plausible to delineate the catchment towards the river.
Yet, it is not known if water sinks from the River Robe into the aquifer of Ballindine, or if it is only the head of the river that imposes a pressure transfer impact onto the head in the aquifer and consequently on discharge of the spring. Therefore, in the water balance approach, rainfall is the only input variable taken into consideration.
The MRC of Ballindine spring suggests the presence of three exponential flow components: a flood component with k' = -0.0375 h^{-1}, an intermediate component with k' = -0.0021 h^{-1} and an LFC with

k' = -0.0002 h^{-1}. The major part of the recession is governed by the intermediate component; hence, this component is interpreted as the dominating flow.
Aquifer dynamics are evaluated using the method of Mangin (1975); El-Hakim and Bakalowicz (2007) based on recharge-discharge relationships applied on the MRC. Interestingly, the aquifer of Ballindine is described as the type with a “deep phreatic zone partly or totally confined under low permeable sediments with a complex drainage structure responsible for very long, multiannual or secular residence times”. Accordingly, it seems plausible that Ballindine spring drains a large or deep reservoir. Perhaps the discharge dynamics of Ballindine spring are largely controlled by the top of such deep system, namely by the head differences between the Robe and the spring.
Within the contributing aquifer, dynamic storage $Max(V_d)$ accounts for 400,00 m^3 exposed to a relatively high regulating power of the aquifer with poorly developed conduit networks with a mean residence time of 405 days. Such behaviour can almost exclusively be represented by a single reservoir M using the KarstMod model. Hence, this indicates that infiltration is delayed or slow, as it is the case in diffuse-type karst groundwater systems.

5.2. Manorhamilton

The catchment of Manorhamilton was previously illustrated in Figure 3.6.
Discharge time series of Manorhamilton date back to April 2009, although unfortunately, there are many data gaps in the time series. Methods such as discrete wavelet transform rely on uninterrupted time series, which imposes limitation on the usage of the entire time series. In addition, the collection of hourly rainfall data representative for the catchment commenced with this project, hence, no historical hourly rainfall is available that could be used for rainfall-discharge analysis for periods prior to this research. Therefore, the time series used in this study are limited to certain periods, namely periods of the longest uninterrupted period (summarised in Table 5.15) and/or the period during which hourly rainfall data were collected within this project.

Figure 5.18 shows the hourly discharge hydrograph of Manorhamilton spring alongside daily rainfall measured at the MetEireann station Manorhamilton Amorset. Discharge ranges between 2.08 m^3/s (measured on 04 Oct 2017) down to 0.004 m^3/s (measured between 27 Jun 2010 and 04 Jul 2010). The average discharge is in the range of 0.14 to 0.16 m^3/s, yet, this is not a very meaningful figure given the relatively high standard deviation ranging between 0.21 and 0.23 m^3/s. The spring shows a flashy discharge behaviour.

Figure 5.19 shows the spring response to rainfall during the hydrological year 2018, including discharge, temperature and EC. Due to a malfunction of the rainfall data logger - presumably related to the connection between logger and sampler - a data gap of rainfall data occurred between 05 Oct 2017 and 15 Dec 2017.

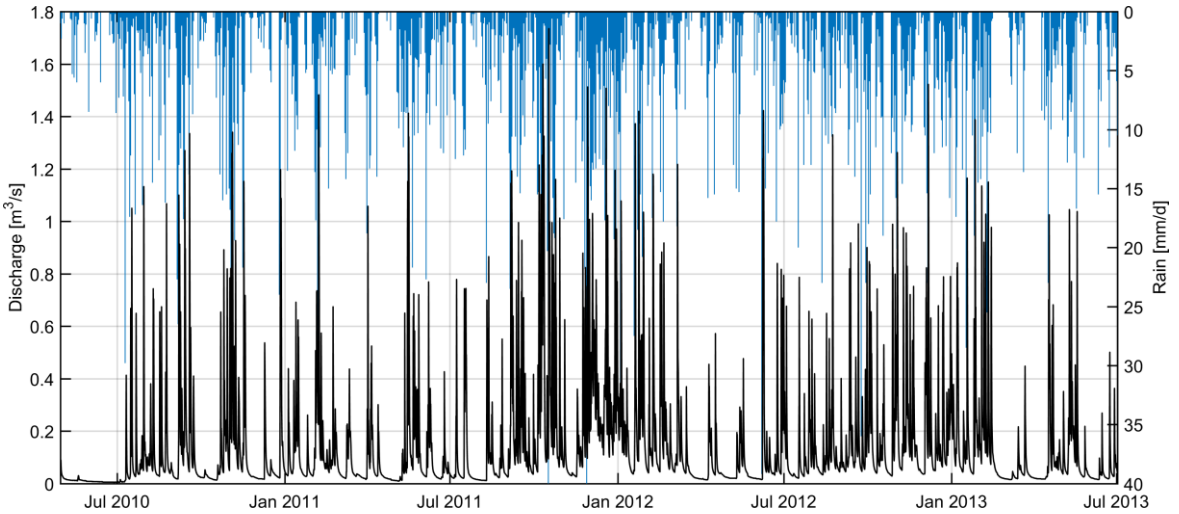

Figure 5.18: Hourly discharge of Manorhamilton spring and daily rainfall at Manorhamilton (Amorset) for the period 20 Apr 2009 to 02 Jul 2013.

Table 5.15: Summary of available data for Manorhamilton spring; Q = discharge [m³/s], T = temperature [ºC], EC = electrical conductivity [µS/cm], P = rainfall, σ = standard deviation.

Station	Start date	End date	No of days	No of hours	Para-meters	Min	Max	Mean	σ
MH3 (spring)	30/04/2009	02/07/2013	1,526	36,573	Q [m³/s]	0.004	1.72	0.14	0.21
	29/06/2017	04/06/2019	705	16,928	Q [m³/s]	0.009	2.08	0.16	0.23
					T [ºC]	6.04	12.4	9.76	0.72
					EC [µS/cm]	56.00	579.0	440.9	85.41
Amorset (rain)	30/04/2009	02/07/2013	1,526	36,573	P [mm/d]	0	44.7	4.27	6.0
MH3 (rain)	24/05/2017	04/06/2019	536	12,874	P [mm/h]	0	22.2	0.21	0.67

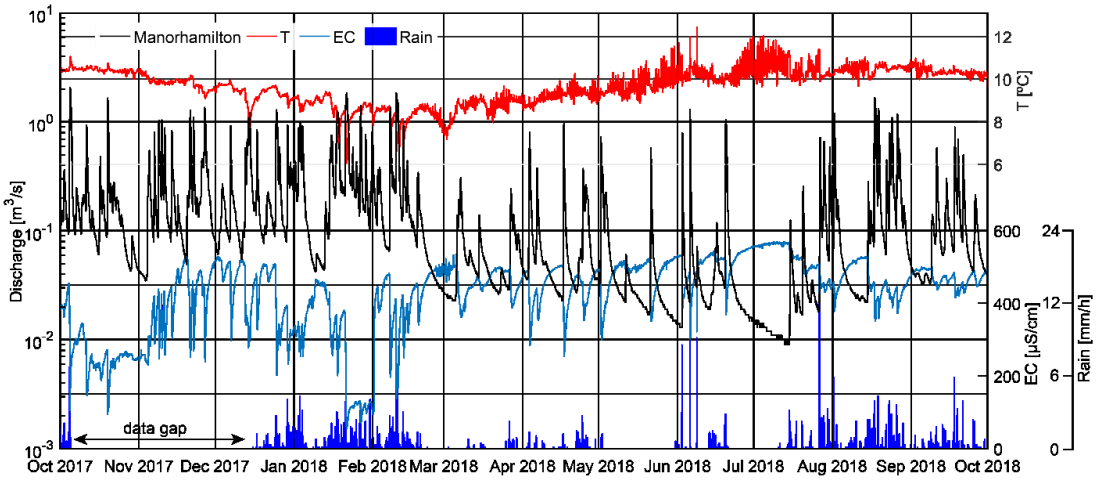

Figure 5.19: Hourly discharge of Manorhamilton spring along with temperature and electrical conductivity (EC) and rainfall monitored at the spring site (MH3) for the hydrological year 2018. Due to malfunction of the rainfall data logger, a data gap occurred between 05 Oct 2017 and 15 Dec 2017.

The spring shows a typical response as expected from a conduit dominated karst spring. The response of the rising limb to rainfall is very quick and almost instantaneously accompanied by a drop of EC due to dilution with freshly infiltrated rainfall. The recession of EC follows a similar course as the recession of spring discharge.
Levels of EC are much lower than in case of Ballindine spring, suggesting a shorter residence time of groundwater. Conduit discharge dominates through the high permeable domains with less contact to the rock matrix.
The lowest EC records below 100 µS/cm down to 56 µS/cm were monitored between 21 Jan 2018 and 01 Feb 2018. During this period, 130 mm of persistent rainfall is associated with such continuous low EC level at the spring. As another response, temperature dropped to the lowest record in the hydrological year 2018 reaching 6.04 ºC underlining the quick response of the system.
Throughout the year, temperature shows a seasonal pattern related to the air temperature. During summer, a strong diurnal component is present as the temperature fluctuates between a daily maximum at 13:00 to 16:00 and a daily minimum at 1:00 to 6:00. The diurnal fluctuation may be further enhanced by the fact that monitoring of spring discharge occurs approx. 100 m downstream the two spring outlets.
Overall, EC and temperature records suggest a very shallow and mostly quick component of groundwater recharge and flow in absence of any deeper groundwater component.

5.2.1. Master recession curve analysis

Again, this section focusses on the characterisation of the MRC in the context of overall aquifer recharge, flow and discharge dynamics, including the evaluation of recession constants k' for the different recession segments, including the LFC.
Figure 5.20 shows the MRC of Manorhamilton at an hourly time step with a discharge ranging between 0.002 and 0.9 m^3/s.

Figure 5.21 shows the MRC of hourly discharge of Manorhamilton spring, again decomposed into three linear reservoirs on a semi-logarithmic plot where ‘A’ is the flood recession (k' = -0.15 h^{-1}), ‘B’ is the intermediate recession (k' = -0.03 h^{-1}) and ‘C’ is the low flow recession (k' = -0.0025 h^{-1}). Respective recession coefficients a' for A, B, and C are 0.861, 0.971, and 0.998 h^{-1}. The maximum contribution from low flow is 0.035 m^3/s.
The ranges of k' values and recession coefficients reflect the flashiness of the discharge pattern.

Table 5.16 gives an overview of the individual straight-line components of Manorhamilton representing drainage from a linear reservoir. For comparison with Ballindine, k' was converted into daily k. As it can be seen, k/k' varies largely between the different reservoirs/components.

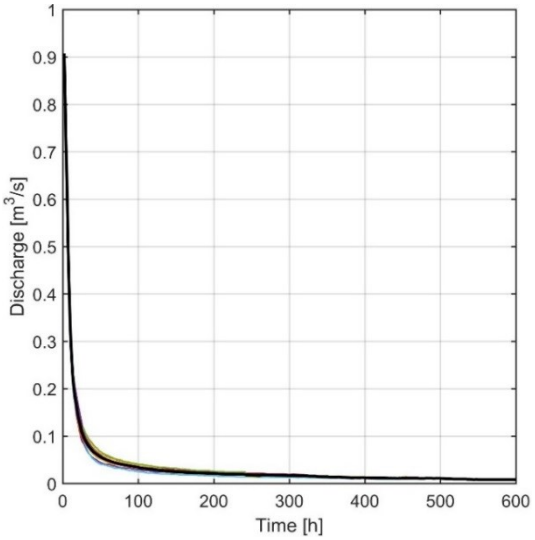

Figure 5.20: 18 fitted components and master recession curve for hourly discharge of Manorhamilton spring.

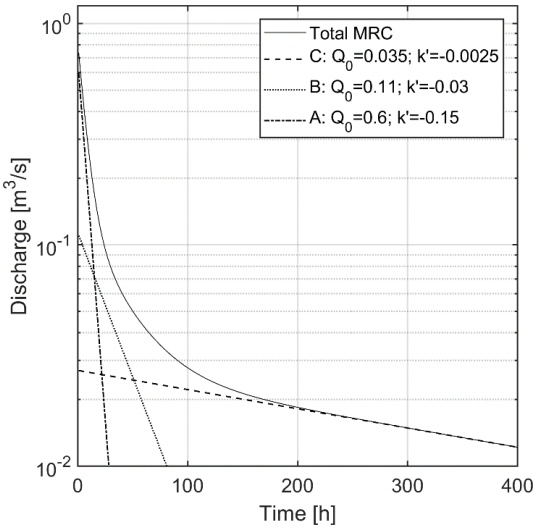

Figure 5.21: Master recession curve for hourly discharge of Manorhamilton spring split into three contributing linear reservoirs.

Table 5.16: recession slopes (k' and k) of straight-line components based on the hourly discharge of Manorhamilton.

Time step	LFC	Intermediate	Flood
k' [h^{-1}]	-0.0025	-0.03	-0.15
k [d^{-1}]	-0.06	-0.72	-3.6

The benchmark range for the optimal recession coefficient was then generated, as before, by: a) plotting Q_t against Q_{t+1} where the slope represents a', b) calculating mean of Q_{t+1}/Q_t, and c) applying a backwards moving filter.

Plotting Q_t against Q_{t+1} yields the hourly recession coefficient a' = 0.997 h^{-1} for hourly time series (Figure 5.22).

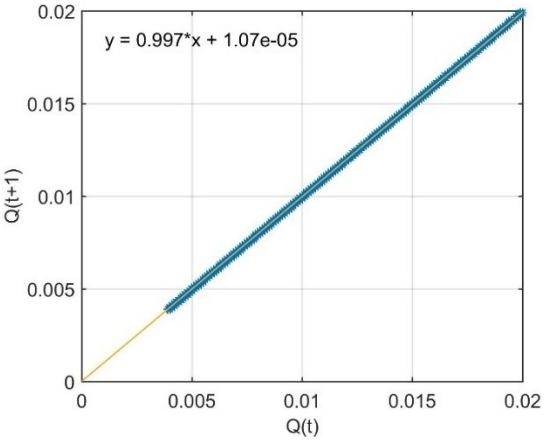

Figure 5.22: Plot of Q_t against Q_{t+1} to estimate the optimal recession coefficient for Manorhamiton spring using hourly discharge.

The calculation of the mean of Q_{t+1}/Q_t yields a recession coefficient of a' = 0.994 h^{-1} for Manorhamilton.

Finally, the application of the backwards moving filter (Collischonn and Fan, 2013) yields an hourly recession coefficient of a' = 0.998 h^{-1} (Figure 5.23).

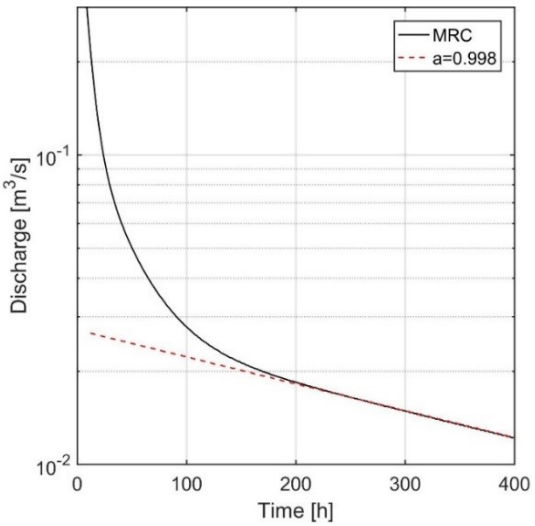

Figure 5.23: Estimation of a for the master recession curve of hourly discharge of Manorhamilton according to Collischonn and Fan (2013).

Because of the fast flow dynamics of Manorhamilton spring, the recession coefficients were established using hourly time series.

Table 5.17 summarises the recession coefficients of Manorhamilton, which again forms the benchmark range for fitting exponential LFCs along observed discharge.

Table 5.17: Range of optimal hourly and daily low flow recession coefficients a' and recession constants k' for Manorhamilton spring.

Method	**Time resolution [h, d]**	**Constant**	
Method 1 (fitting linear reservoirs)	h	a'	0.9975
		k'	-0.0025
Method 2 (plotting Q_t against Q_{t+1})	h	a'	0.9967
		k'	-0.0033
Method 3 (mean of Q_{t+1}/Q_t)	h	a'	0.9940
		k'	-0.0060
Method 4 (backwards moving filter)	h	a'	0.9980
		k'	-0.0020
Average	h	a'	0.9966
		k'	-0.0035

As for Ballindine spring, the MRC of Manorhamilton was decomposed into three distinct exponential components. The baseflow component or LFC is further used to characterise the aquifer following Mangin (1975); El-Hakim and Bakalowicz (2007) (Figure 5.24). The resulting parameters are displayed in Table 5.18. The simulated discharge $Q_{sim} = \psi(t) + \varphi(t)$ matches very well with the MRC as proven by a NSE of 0.99.

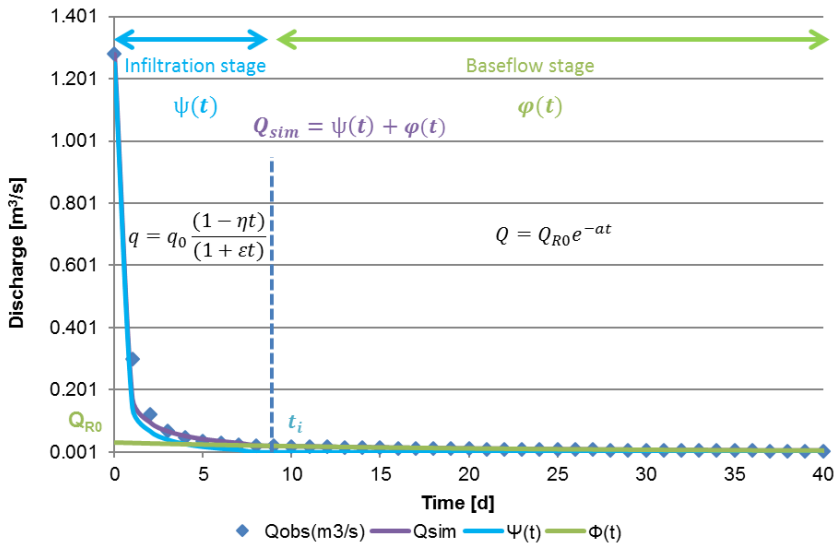

Figure 5.24: Analysis of the master recession curve (Q_{obs}) of Manorhamilton following Mangin (1975); layout modified after Duran (2015).

The value of Q_{R0} is the result of fitting the exponential baseflow component $\boldsymbol{\varphi(t)}$ with α = 0.05 along the MRC. This is a relatively high recession coefficient, which results in a dynamic storage $Max(V_d)$ of 51,840 m³. In turn, the mean annual volume flowing through the phreatic zone V_{trans} [m³] accounts for 200,325 m³. Accordingly, there is a discrepancy between the storage extent $Max(V_d)$ and the mean annual flow volume V_{trans} that explains the regulating power k = 0.26. This means, the aquifer exhibits a relatively low regulating power (rainfall input is little transformed towards the spring outlet), and the mean residence time is 0.26 years or 95 days.
The parameters η and ε are 0.1, 6.85 respectively. A value of 10 > ε > 1 indicates a dominance of fast infiltration, which therefore applies to Manorhamilton. As a consequence, i = 0.05 tends towards 0, as it is the case for fast infiltration.
The aquifer falls into category '4' of the classification system, i.e. "aquifers with a well karstified infiltration zone and extended conduit network ending into a flooded phreatic zone".

Table 5.18: Fitted parameters for the master recession curve of Manorhamilton following Mangin (1975); El-Hakim and Bakalowicz (2007).

t_i [d]	Q_{R0} [m³/s]	a [d⁻¹]	η [d⁻¹]	ε [d⁻¹]	$Max(V_d)$ [m³]	V_{trans} [m³]	k	i	Class
9	0.03	0.05	0.1	6.852	51,840	200,325	0.26	0.05	4

5.2.2. Event-based recession analysis using stable isotopes

As part of a preliminary hydrograph analysis, event-based hydrograph separation was applied on Manorhamilton spring to evaluate the possibility of separating a low-flow component (LFC) chemically using a two-component mixing analysis.
Therefore, high frequency event sampling was conducted at Manorhamilton over a period of almost 10 days to analyse the samples for anions, silica as well as stable isotopes (2H and 18O) following rain events.
The overall aim of the high-frequency sampling campaigns was to:

- Identify characteristic chemical signatures associated with the fissured matrix domain and fracture/conduit domain; and to
- Separate hydrographs into a flood component and low-flow component.

A two-component mixing model was then applied on the single rainfall runoff events in order to separate out the LFC using the isotopic signals. Due to the relatively fast spring response at Manorhamilton, the system was deemed suitable for this analysis, as the complete impact of single rain events on the spring can be monitored over a period of several days.

Chemical baseflow separation was applied on the spring discharge of Manorhamilton using 18O and 2H following the method of Fritz, et al. (1976). Spring discharge was sampled in intervals of 3 hours and 6 hours over almost 10 days between 12 and 21 Sep 2017 using an ISCO auto sampler

collecting 18 grab samples, although due to malfunctioning of the instrument, loss of data occurred between 16 Sep 17:30 and 21 Sep 07:30. Four rainfall samples were collected at MH3.
Data is shown in Figure 5.25 with daily rainfall data used from the MetEireann station Manorhamilton (Amorset) (76 masl) 4.9 km east of Manorhamilton spring.
As it can be seen from the plot, at the start of the sampling period, discharge was 0.26 m^3/s which is above the estimated low flow of approx. ≤0.15 m^3/s, thus not reflecting pure low flow conditions, had the lowest concentration of $\delta_S O18$ = -5.79‰ and $\delta_S 2H$ = -35.76‰. It is reasonable to assume that the concentrations of $\delta_S O18$ and $\delta_S 2H$ were higher prior to the beginning of the storm event. Therefore, the pre-storm water component δ_S (see Eqn. 2.64) was defined using a sample from 18 Aug 2017 as concentrations of $\delta_S O18$ and $\delta_S 2H$ were slightly higher with -5.52, -34.20‰ respectively.
The isotopic concentration of water at the gauging station δ_T was measured in intervals between 3 and 6 hours, and <5 days. Concentrations were interpolated and applied on 30 min discharge records q_T.

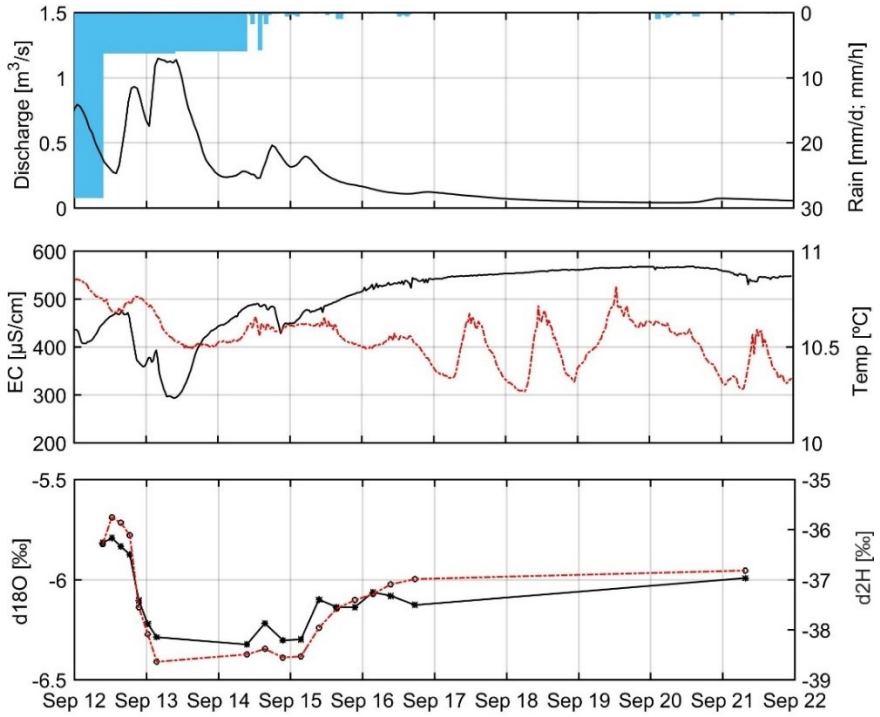

Figure 5.25: High frequency sampling at MH3. Solid line refers to the left axis and dashed lines/bars refer to the right axis; daily rainfall data between 12 and 14 Sep 2017 originates from MetEireann.

The isotopic concentration of the storm water component of the streamflow δ_R, i.e. rainfall, was measured at one location (MH3) at four different times showing a relatively high variation ranging between -52.93 and -41.93‰ for $\delta_S 2H$ and -8.30 and -7.01‰ for $\delta_S O18$ within one hour (Figure 5.26). This indicated the challenge or uncertainty in assigning the storm water component δ_R.

It was found that sufficient separation of the flood component could only be achieved using the lowest concentration of $\delta_S O18$ and $\delta_S 2H$, as the higher the concentration assigned to the pre-storm water component, the higher the lower the flood component. More realistic results, closer to the previously exponentially separated LFC, were found with assigned concentrations of $\delta_R O18$ = -7.01‰ and $\delta_R 2H$ = -41.93‰.

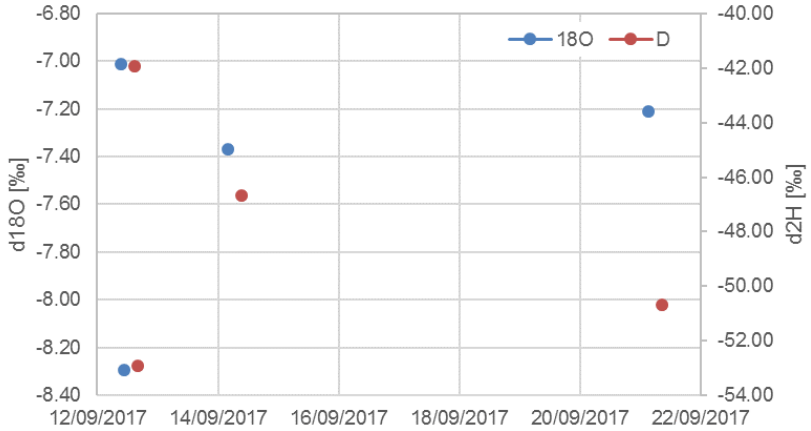

Figure 5.26: Concentration of d18O and d2H [‰] in rainfall measured at MH3.

The resulting low flow estimates are displayed for 2H in Figure 5.27. The relatively high LFC at the start of the period is a result of the rising concentrations of $\delta_S 2H$ (and $\delta_S O18$) near to the pre-storm water component δ_S.

It can be seen that even though the lowest concentrations of $\delta_R 2H$ were assigned, the LFC still comprises a relatively large proportion of the overall discharge. The results raise the question of 'what was separated'. With reference to Rimmer and Hartmann (2014) the results of baseflow separation using chemical parameters applied on a mixing model indicate that results depend on the nature of the tested component, rather than on a particular flow component, and in particular the representativeness of the input signal.

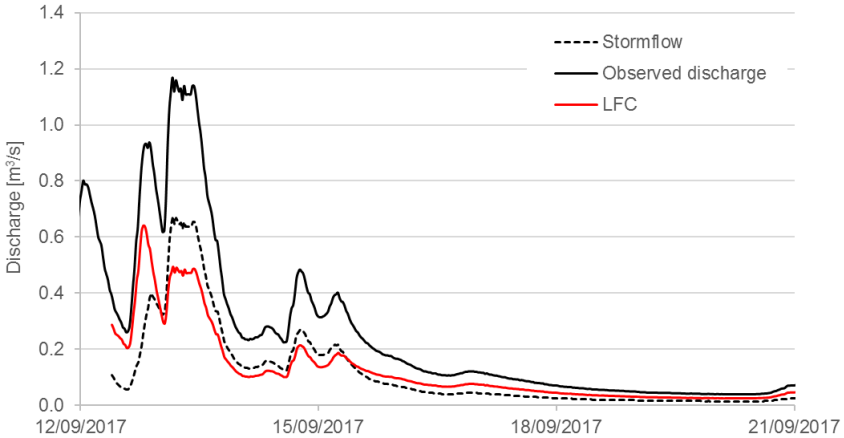

Figure 5.27: Low flow separation using 2H.

Two-component mixing analysis was applied on 18 groundwater samples (18O and 2H) from discharge at Manorhamilton, taken over almost 10 days. Rainfall samples were taken at the spring site at different times, which proved to be temporal highly variable.
The results show that in general, the concentrations of 18O and 2H resemble the dynamics occurring during and after the rain events, yet, the two-component mixing model achieves what is subsequently considered (see Chapter 'Time Series Analysis') a very (or unrealistically) high low-flow component representing the fissured matrix domain of the spring. This component exceeded 0.03 m^3/s, which was previously established as maximum low-flow component contribution using the other separation techniques. The reason for this may be related to the fact that at the beginning of the sampling campaign, discharge was clearly above low-flow conditions, thus, any mixing model with over-estimate such component (hence, incorporation additional flow components), as well as a limited representativeness of the input signal applied in time and space.

5.2.3. Water balance

Water balances were established to improve the previously delineated groundwater catchment boundaries of 1.95 km^2 (EPA, 2011b). Water balances cover the hydrological years 2010 to 2012, 2014 to 2016, and 2018 as for these years, spring discharge time series have very little interruption.
The climatic data used for estimating evapotranspiration originate from the MetEireann climate station at Markree, which provides daily minimum and maximum temperatures that allow estimating ET_0 following Hargreaves (1994). Adjustment of the empirical parameters H_A and H_E was done using climate data of C1 and fitting $ET_{0,Har}$ against $ET_{0,PM}$. The best fit was achieved with H_A = 0.00197 and H_E = 0.512 resulting in a RMSE of 0.578. Interestingly, these results are similar to the findings of Berti, et al. (2014) who found the optimal parameters H_A = 0.00193 and H_E = 0.517.
The water balances are presented in Table 5.19, along with the calculation for the mismatch between estimated groundwater recharge (difference between rainfall and ET) and observed discharge at the spring.

Table 5.19: Water balance for the Manorhamilton catchment for the catchment size of 1.95 km^2 (numbers in million m^3 if not stated differently; GW = groundwater).

Water year	Rainfall	ET	GW recharge	GW recharge [%]	Discharge	Mismatch
2010	2.59	1.06	1.53	58.95	3.66	-2.13
2011	2.73	1.02	1.71	62.62	3.80	-2.51
2012	3.55	1.00	2.55	71.82	5.67	-4.00
2014	2.87	1.05	1.82	63.31	3.96	-2.62
2015	3.24	0.99	2.25	69.38	4.82	-3.09
2016	3.50	1.03	2.47	70.53	5.24	-3.59
2018	2.97	1.08	1.89	63.72	5.01	-3.62
Average	3.06	1.03	2.03	65.76	4.56	-3.08

To estimate an appropriate catchment size, the annual observed spring discharge was matched with the percentage of groundwater recharge (Table 5.19) necessary to explain the discharge. Assuming recharge rates ranging between 58.9 and 71.8% and applying the observed discharge listed in Table 5.19, the catchment size ranges between 3.9 and 5.03 km^2 with a mean size of 4.3 km^2 (Table 5.20). This is more than twice the size previously delineated.
There is no indication of additional major outflows from the catchment (as in the case of Ballindine where drainage channels partly drain the catchment), which would impact on the water balance. The only additional outflows draining the aquifer relate to some small (epikarst) springs within the catchment. In the lower part of the catchment, such discharge may leave the catchment unaccounted, while in the upper part of the catchment, such discharge will infiltrate back into the aquifer. Hence, the water balance approach seems to yield reasonable results for this catchment.

Table 5.20: Target catchment size of Manorhamilton based on the water balance (numbers in million m^3 if not stated differently).

Water year	Discharge	Target rainfall	Target catchment size [km^2]
2010	3.66	6.20	4.55
2011	3.80	6.06	4.22
2012	5.67	7.90	4.22
2014	3.96	6.26	4.15
2015	4.82	6.65	3.90
2016	5.24	7.42	4.03
2018	5.01	7.87	5.03
Average	4.56	6.91	4.30

5.2.4. Tracer tests

The main goal of the tracer test was to investigate hydraulic connections between injection sites and observation sites, and to characterise the tracer break-through curve (TBC) in terms of tracer recovered and mean travel times.
The objectives of the test were mainly to:

- Confirm the hydraulic connections between the injection sites and observation sites to improve the delineated catchment, mainly to the north and to the south-west;
- Evaluate the mean travel time and total recovered tracer mass;
- Potentially link the tracer study to rainfall events and high-resolution hydro-chemical data sampling (d18O, d2H, anions, turbidity) at MH3 during flood and recession periods.

A total of five injections were done: three injections on 12 Sep 2017, followed by two injections on 16 Sep 2017. The meteorological conditions were very favourable during the tests. Much rainfall supported flushing and transportation of the dyes (Figure 5.28).

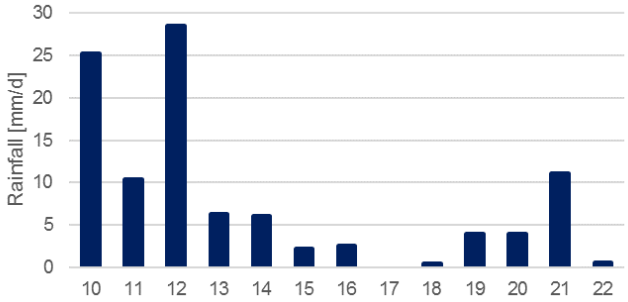

Figure 5.28: Daily rainfall in Sept 2017 at Manorhamilton (data 10 to 14 Sep from the MetEireann station Manorhamilton Amorset, data 15 to 22 Sep from MH3).

In the coming sections, the approach and results of the second tracer test (16 Sep) are presented prior to the first test (12 Sep).

5.2.4.1. Tracer test 16 Sep 2017

The two chosen IS are outside of the previously assumed catchment boundaries (IS(b)) and within the boundaries (IS(d)) (Figure 5.29 and Table 5.21). Both of them are swallow holes.
The tracers were flushed using 40 l of water that was carried to the site. This amount was sufficient since rain before and during the injection supported effectively flushing of the tracers.

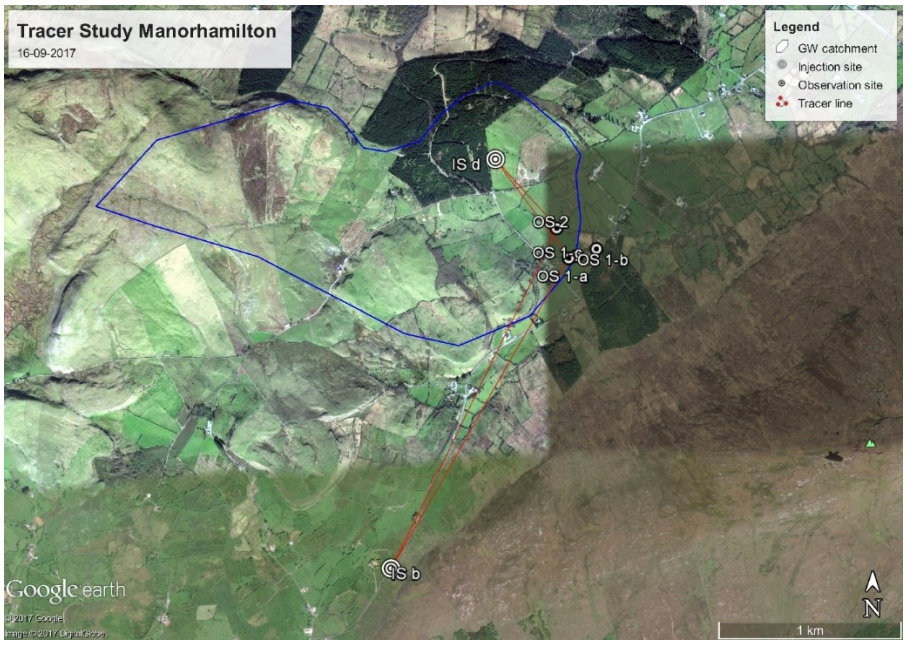

Figure 5.29: Outline tracer test 16 Sep 2017.

The observation sites (OS) correspond to the three locations at the outlet of the catchment at MH1 (OS 1-a), MH2 (OS 1-b) and MH3 (OS 1-c), and one OS within the catchment at a minor spring (OS 2) (Figure 5.29 and Table 5.22).

Table 5.21: Injection sites 16 Sep 2017.

Injection site	Coordinates	Altitude [masl]	Tracer and mass	Injection time	Flushing volume [l]
IS(b)	54.2813°; -8.2656°	~195	200 g rhodamine WT	14:17	40
IS(d)	54.3002°; -8.2574°	~167	100 g fluorescein	14:00	40

Table 5.22: Observation sites 16 Sep 2017.

Observation site	Coordinates	Altitude [masl]	Linear distance to IS [m] and gradient i [m/m]	Instrumentation	Recording frequency
OS 1-a (MH1)	54.2957°; -8.2513°	122	IS(b): 1,850, i = 0.039 IS(d): 636, i = 0.071	Albillia GGUN-FL30 (#950)	30 s
OS 1-b (MH2)	54.2958°; -8.2507	118	Similar as 1(a)	Charcoal bags	-
OS 1-c (MH3)	54.2961; -8.2490	112	Similar as 1(a)	Albillia GGUN-FL30 (#951), Charcoal bag	30 s
OS 2 (minor spring)	54.2971°; -8.2523°	~128	IS(b): 1,966, i = 0.034 IS(d): 476, i = 0.082	Charcoal bag	-

Automatic sampling was conducted using two Albillia GGUN-FL30 field fluorometers deployed at OS 1-a and OS 1-c. By monitoring the upper spring (MH1) and the downstream EPA monitoring station (MH3), conclusions could be made about discharge at MH2.
Manual sampling was conducted using activated charcoal bags to detect rhodamine WT and fluorescein deployed on 16 Sep 2017 and collected on 21 Sep 2017 at OS 1-a, OS 1-b and OS-2. Bags installed at OS 1-c (MH3) purely functioned as backup in case of malfunctioning of the automatic fluorometers.
The results of the tracer test are presented hereafter.

Qualitative analysis: activated charcoal

Activated charcoal was eluted at the GSI lab on 18 Sep 2017. Figure 5.37 shows the emission of the charcoal samples for the sampling sites OS 1-b (MH2) and OS 2 (minor springs) to detect rhodamine WT and fluorescein.
OS 1-b (MH2) shows relatively high intensities and clear peaks for rhodamine at ~575 nm and for fluorescein at 519 nm. Both readings were interpreted as positive for OS 1-b (MH2).
In turn, OS 2 (minor springs) shows lower intensities, no clear or definite peak for rhodamine WT, and no signal for fluorescein. Therefore, the results are interpreted as negative for both dyes.

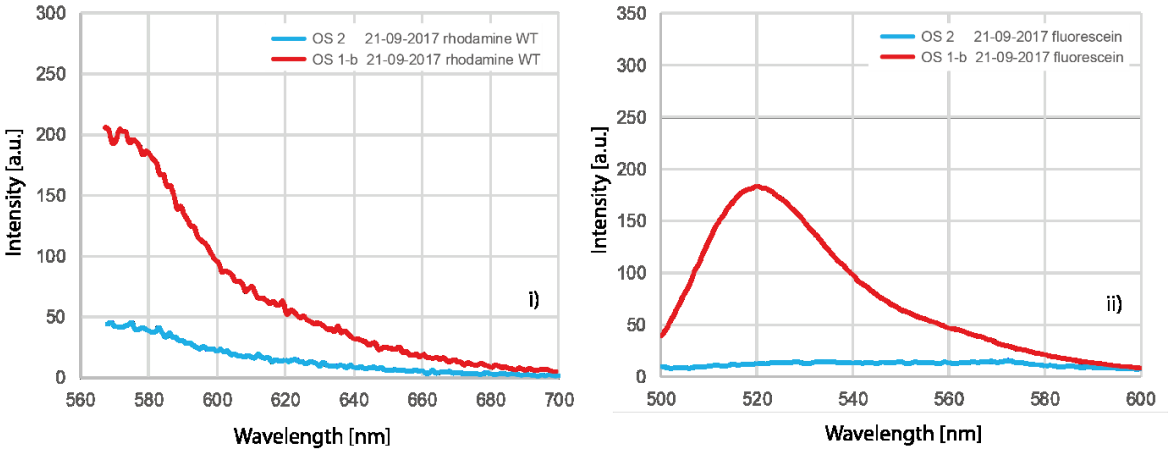

Figure 5.30: Emission spectra of charcoal samples analysed for i) rhodamine WT and ii) fluorescein at OS 1-b (MH2) and OS 2 (minor springs) resulting from tracer test on 16 Sep 2017 (samples collected on 21 Sep 2017).

Quantitative analysis: Tracer break-through curve

Figure 5.31 and Figure 5.32 show the TBCs and turbidity time series for the two fluorometers #950 and #951 installed at OS 1-a (MH1) and OS 1-c (MH3). Both plots show an excellent TBC, even though the TBC at MH3 exceeds the calibration range (>100 ppb).

Before the first tracer injection, the background value for fluorescein prior to the tracer test was 2.7 ppb while the background concentration of rhodamine WT was ~0.4 ppb.

No rhodamine WT was detected. The negative result for rhodamine WT at MH3 contradicts the result from the charcoal sample at MH2, which was interpreted as positive (if it was positive at MH2, it must be positive at the downstream monitoring station MH3). A possible reason for this contradiction may be related to the fact that a minor quantity of rhodamine WT from the first tracer test (12 Sep 2017) was still in the aquifer prior to the second tracer test (16 Sep 2017). While concentration may have been too low to be detected by the automatic fluorometer, it is possible that rhodamine WT has cumulatively adsorbed on to the charcoal sampler over the period of the second tracer test. Another reason could be that the charcoal sample of OS 1-b (MH2) was cross-contaminated.

Fluorescein was recovered at OS 1-a (MH1) and consequently downstream at OS 1-c (MH3). Arrival of the first fluorescein signal at OS 1-c (MH3) is at 19:25 on 16 Sep 2017 (5 h 25 min after injection) with a concentration of 2.8 ppb while first detection of fluorescein at OS 1-a (MH1) is at 19:57 with 2.8 ppb (5 h 57 min after injection). Both arrival times are very prominent. Interestingly, tracer at OS 1-a (MH1) arrives ~30 min later than at OS 1-c (MH3). Therefore, MH2 seems to be better connected to the injection locations, as the earlier arrival time of tracer at OS 1-c (MH3) than at MH1 must be related to discharge at OS a-b (MH2).

Tracer concentration at OS 1-c (MH3) is beyond the calibrated range (1 to 100 ppb), reaching 155 ppb. The maximum concentration at OS 1-a (MH1) reaches 58 ppb. Accordingly, the contribution of fluorescein from MH2 must have been in higher concentration than in the contribution from MH1.

Table 5.23 gives an overview of different parameters of the tracer injections.

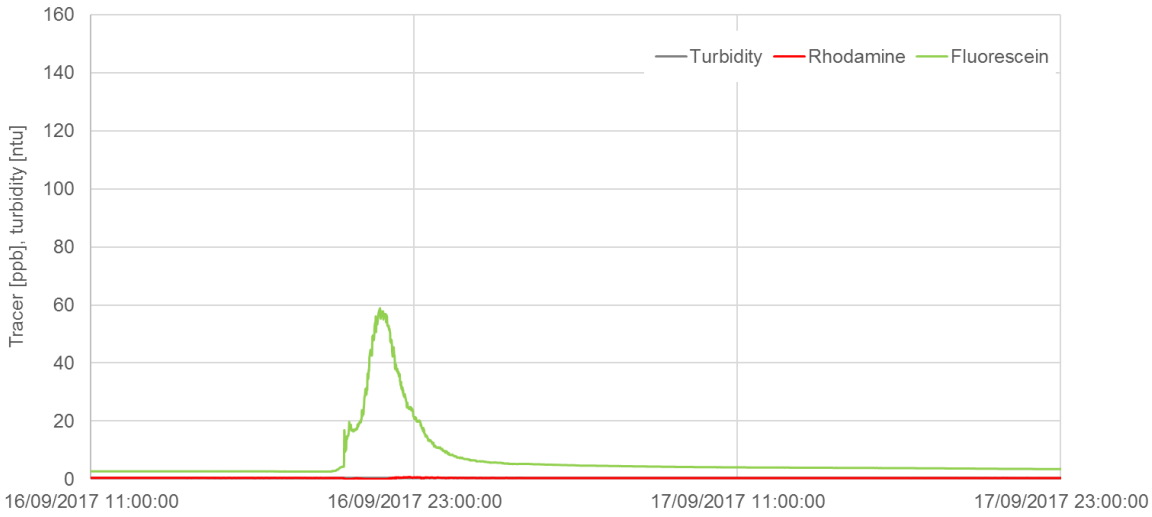

Figure 5.31: Tracer break-through curves of fluorometer #950 at OS 1-a (MH1).

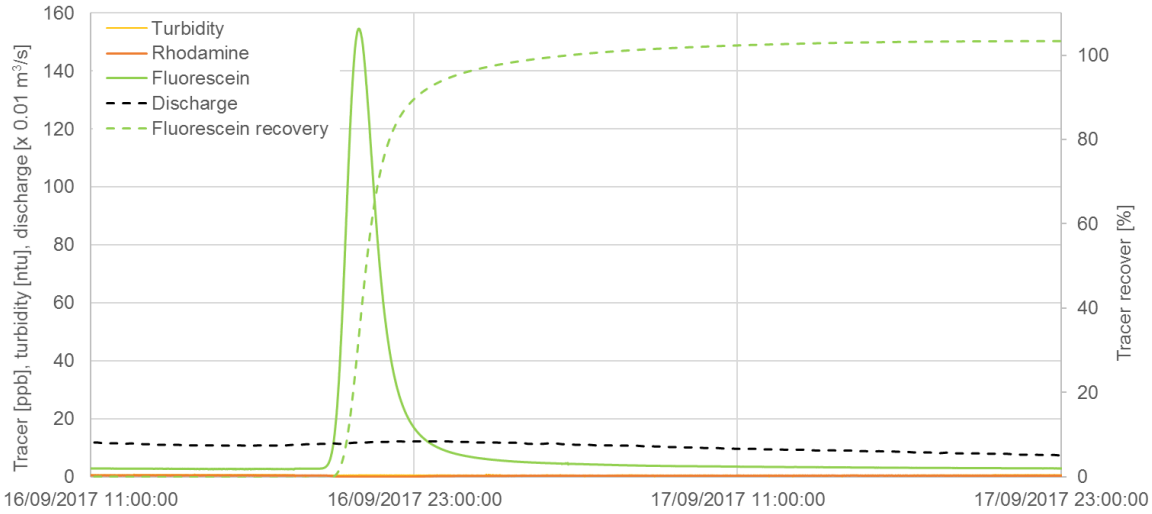

Figure 5.32: Tracer break-through curves of fluorometer #951 at OS 1-c (MH3).

Table 5.23: Interpretation of tracer break-through curves from the tracer test on 16 Sep 2017.

Observation site	**OS 1-a (MH1) #950**		**OS 1-c (MH3) #951**	
Tracer	Rhodamine WT	Fluorescein	Rhodamine WT	Fluorescein
Peak concentration [µg/l]	-	58.89	-	154.64
Time to first tracer arrival [h]	-	5.95	-	5.42
Max. flow velocity [m/h]	-	106.9	-	117.3
Peak concentration time [h]	-	7.7	-	7.0
Flow velocity to peak concentration [m/h]	-	82.2	-	91.5
Recovery [%]	-	-	-	~100
Mean travel time $\bar{v}$ [m/h]	-	-	-	88

The TBC for fluorescein at OS 1-c (MH3) lasts between 16 Sep 2017 19:25 and 18 Sep 2017 14:40 (1 d, 9 h, 15 min). The TBC for fluorescein at OS 1-a (MH1) lasts between 16 Sep 2017 19:57 and 19 Sep 2017 07:05 (2 d, 11 h, 8 min). Accordingly, the TBC at the upstream OS 1-a (MH1) last longer than at the downstream monitoring station at OS 1-c (MH3). This seems contradictory as OS 1-c measures the contribution from MH1 (OS 1-a) and MH2. However, it may be explained by a very short-lasting TBC at OS 1-b – this would mean that following the TBC, the discharge at MH2 actually dilutes the contribution coming from MH1 (OS 1-a) by flows with a lower fluorescein concentration in at OS 1-b (MH2).
Tracer recovery was calculated for fluorescein considering the background value of 2.7 ppb at the beginning of the test is 103% for the total period. The fact that recovery exceeds 100% is explained by the extrapolated concentration of fluorescein >100 ppb and/or uncertainties with regard to the background concentration.
50% of the total tracer was recovered on 16 Sep 2017 at 21:13:30, 433.5 minutes after injection at 14:00. The mean travel time $\bar{v}$ is estimated for the linear distance x = 636 m between IS d and observation sites 1. Correcting x for sinuosity S_d = 1.5, yields x_s = 954 m. Using Eqn. 4.10 yields $\bar{v}$ = 88 m/h.

5.2.4.2. Tracer test 12 Sep 2017

Three injections sites (IS) were chosen – two of them outside the previously assumed catchment boundaries (IS(a) and IS(b)) and one within the boundaries (IS(c)) (Figure 5.33 and Table 5.24). All three sites are swallow holes. Rhodamine and fluorescein were flushed using 40 l of water carried to the swallow holes. Again, this was sufficient as heavy rain before and during the injection caused shallow (epikarst) flow concentrating into the swallow holes, which greatly supported flushing of the tracers. Optical brightener was poured into a small stream discharging into a swallow hole, hence, no additional flushing was needed.

Monitoring was conducted at the outlet of the catchment at MH1 (OS 1-a), MH2 (OS 1-b) and MH3 (OS 1-c), as well as at a small (minor) spring (OS 2) (Figure 5.33 and Table 5.25).

Automatic sampling was conducted using two Albillia GGUN-FL30 field fluorometers deployed at OS 1-a and OS 1-c.
Manual sampling was conducted using activated charcoal bags for to detect rhodamine WT and fluorescein. Cotton wool bags were used for optical brightener deployed on 12 Sep 2017 and collected on 16 Sep 2017 at OS 1-a, OS 1-b and OS-2. Bags installed at OS 1-c (MH3) purely functioned as backup in case of malfunctioning of the field fluorometers.
The results of the tracer test are presented below.

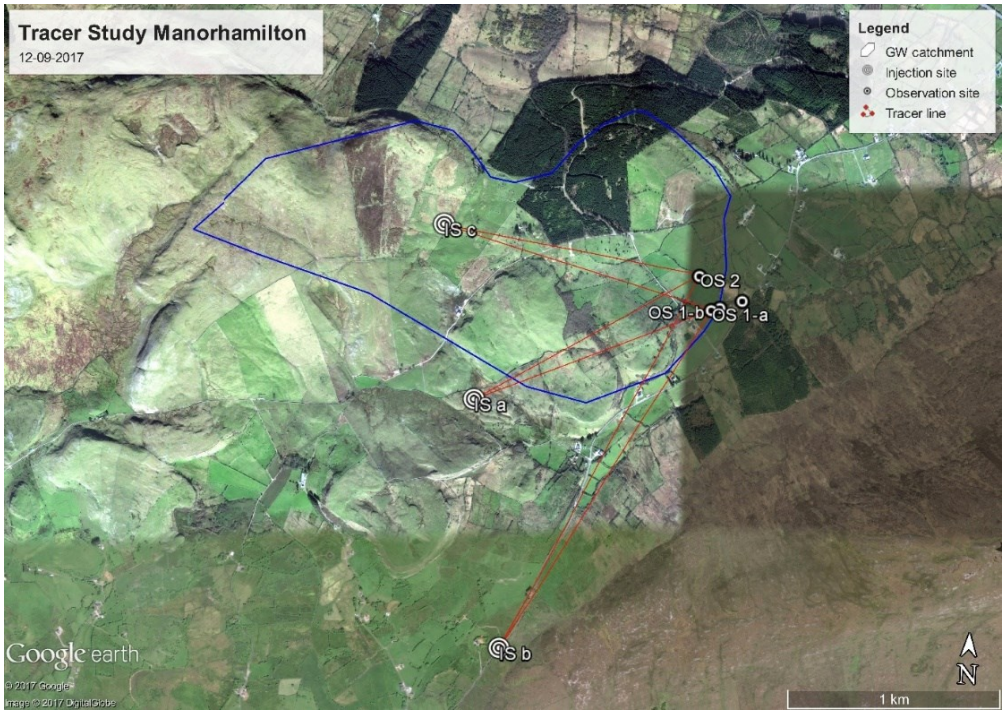

Figure 5.33: Outline tracer test 12 Sep 2017.

Table 5.24: Injection sites 12 Sep 2017.

Injection site	Coordinates	Altitude [masl]	Tracer and mass	Injection time	Flushing volume [l]
IS(a)	54.2914°; -8.2682°	~198	200 g rhodamine WT	12:25	40
IS(b)	54.2813°; -8.2656°	~195	40 l optical brightener	13:10	-
IS(c)	54.2985°; -8.2709°	~218	200 g fluorescein	14:27	40

Table 5.25: Observation sites 12 Sep 2017.

Observation site	Coordinates	Altitude [masl]	Linear distance to IS [m] and gradient i [m/m]	Instrumentation	Recording frequency
OS 1-a (MH1)	54.2957°; -8.2513°	122	IS(a): 1,196, i = 0.064 IS(b): 1,850, i = 0.039 IS(c): 1,310, i = 0.073	Albillia GGUN-FL30 (#950)	30 s
OS 1-b (MH2)	54.2958°; -8.2507	118	Similar as 1(a)	Charcoal & cotton wool bags	-
OS 1-c (MH3)	54.2961; -8.2490	112	Similar as 1(a)	Albillia GGUN-FL30 (#951) Charcoal & cotton wool bags	30 s
OS 2 (minor spring)	54.2971°; -8.2523°	~128	IS(a): 1,212, i = 0.058 IS(b): 1,966, i = 0.034 IS(c): 1,220, i = 0.074	Charcoal & cotton wool bags	-

Qualitative analysis: activated charcoal & cotton wool

Cotton wool

Cotton wool bags remained installed at OS 1-b (MH2), OS 1-c (MH3), and OS 2 (minor springs) for a period of 4 days until 16 Sep 2017.

Figure 5.34i shows a dry sample of cotton wool prior to deployment under UV light.

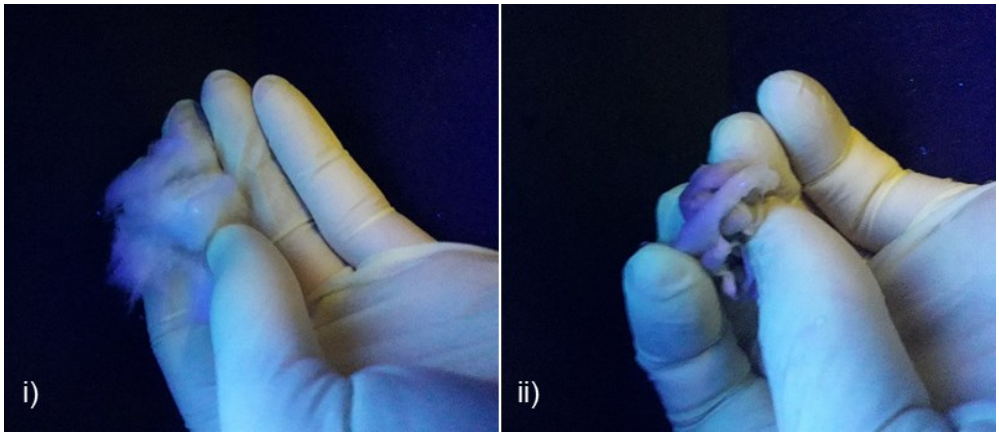

Figure 5.34: Dry sample of cotton wool prior to deployment (i) and sample OS 1-c collected on 16 Sep 2017 (ii).

There is generally no fluorescence of the cotton wool visible, yet, single small particles do show a glimpse of fluorescence, yet, not to a level to be considered contaminated.

Hence, no apparent residuals of tracers were found in any of the three cotton wool samples as exemplified in Figure 5.34ii.

It was concluded that no optical brightener had arrived apparently at any of the observation points.

Charcoal bags

Figure 5.35 shows the emission of the charcoal samples for the sampling sites OS 1-b (MH2) and OS 2 (minor springs) to detect rhodamine WT and fluorescein.

OS 1-b shows relatively high intensities and peaks for rhodamine at ~575 nm and for fluorescein at 519 nm. While the peak for fluorescein is very clear, as its peak is very close to 516 nm as stated in the literature, the signal for rhodamine WT is less clear. However, for rhodamine WT the peak emission is given as approximate value at 586 nm (Leibundgut, et al., 2009) indicating potential variation in the resulting emission. Therefore, the result for OS 1-b (MH2) is interpreted as positive for rhodamine WT and clearly positive for fluorescein.

In turn, OS 2 shows lower intensities, no peak for rhodamine WT but a very damped peak for fluorescein at ~520 nm. Therefore, the results are interpreted as carefully positive for fluorescein and negative for rhodamine WT at OS 2 (minor springs)

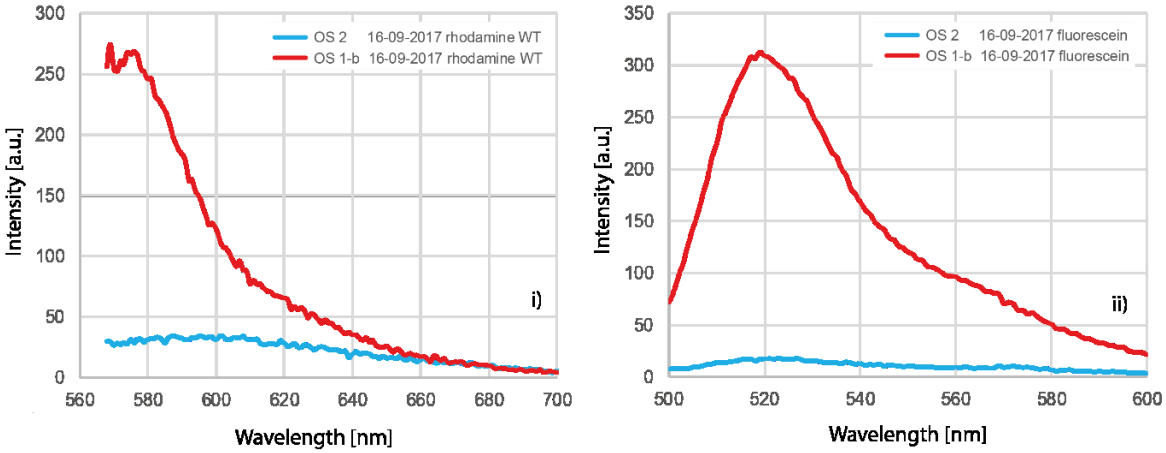

Figure 5.35: Emission spectra of charcoal samples analysed for i) rhodamine WT and ii) fluorescein at OS 1-b (MH2) and OS 2 (minor springs) resulting from the tracer test on 12 Sep 2017 (samples collected on 16 Sep 2017).

Quantitative analysis: Tracer break-through curve

Figure 5.36 and Figure 5.37 show the TBC and turbidity time series for the two automatic fluorometers #950 and #951 installed at OS 1-a (MH1), OS 1-c (MH3) respectively, as well as estimated tracer mass recovery at MH3. The results are shown in Figure 5.36 and Figure 5.37.

During the period of the tests, multiple rain events caused surges in discharge and two turbidity peaks: the first one during the peak of both observed tracers reaching 7 NTU; and the second one following the tracer peak reaching 20 NTU.

Fluorometer #950 (Figure 5.36) shows very noisy records for all the different tracers and turbidity compared to #951 (Figure 5.37). The reason is unclear. Both instruments were installed in standard submerged conditions without indication of any apparent influence of the surrounding environment. Because of the clear signal of #951 and associated observed discharge at this location, the following analysis focusses primarily on #951.

Overall, the shape and magnitude of the two tracer TBCs or fluorescein and rhodamine WT are very similar. The signal for optical brightener shows some variation over time, however, there is no clear TBC visible. It is believed that the variation is caused by natural background fluorescence, as already prior to arrival of the first tracers, values of optical brightener are elevated at 12.2 ppb (#951) and 17.8 ppb (#950).

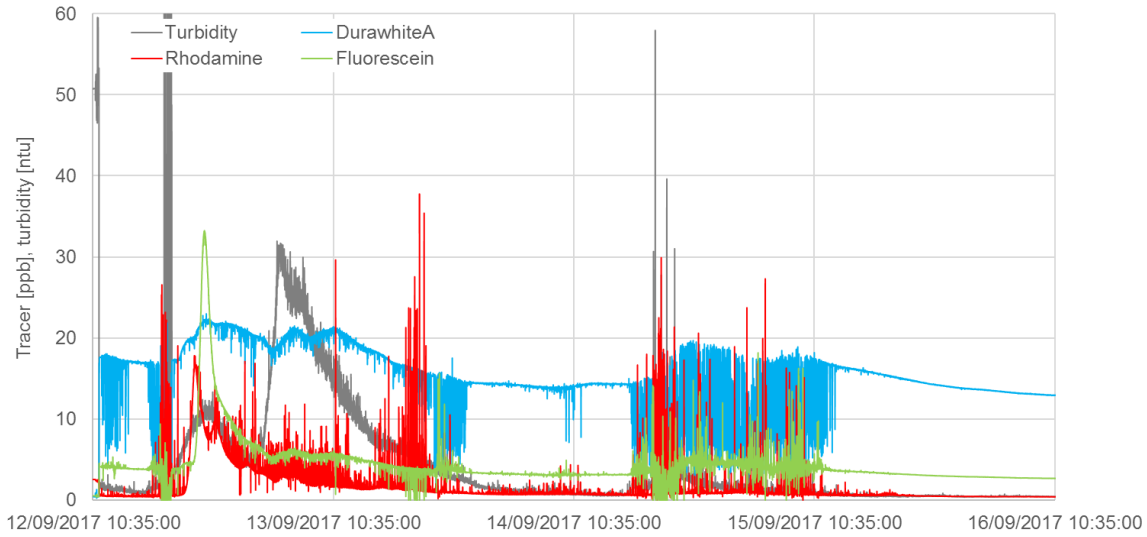

Figure 5.36: Tracer break-through curves of fluorometer #950 at OS 1-a (MH1).

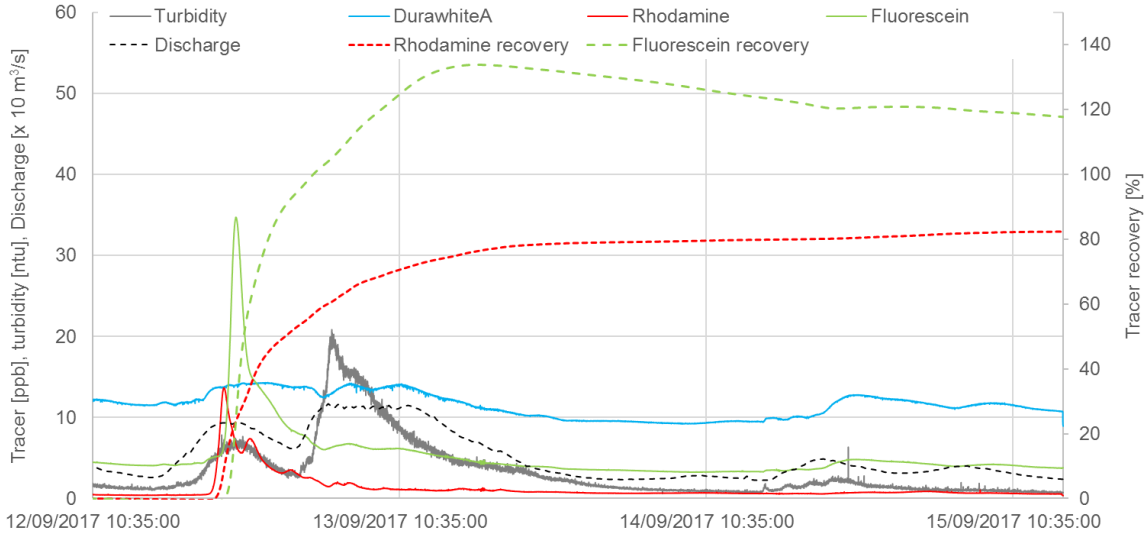

Figure 5.37: Tracer break-through curves of fluorometer #951 at OS 1-c (MH3).

Fluorescein shows a relatively high natural background value between 4 and 4.5 ppb while the fluorescence of rhodamine WT is ~0.4 ppb prior to any detection of tracer.

Arrival of the first rhodamine WT signal at OS 1-c is ~19:17 on 12 Sep 2017 (6 h 52 min after injection) at 0.5 ppb, while the first detection of fluorescein was at ~19:20 with 4.5 ppb (4 h 53 min after injection).

Peak tracer concentrations of rhodamine and fluorescein coincide with peak discharge of the event on 12 Sep 2017. The peak fluorescein concentration reaches 33.2 ppb at MH1 and 34.7 ppb at MH3. This result suggests that the concentration of fluorescein in MH2 is at least as high as in MH1.

Rhodamine WT reaches a concentration of 13.7 ppb at MH3, while the correspondent peak in the noisy plot for MH1 reaches 17.8 ppb. This suggests that the concentration of rhodamine at MH2 is lower than at MH1.

The duration of the TBC for rhodamine WT (time between the detection of the first and the last tracer signal) lasts between 12 Sep 2017 19:20 and 15 Sep 2017 14:25, so 2 days, 19 hours and 4.5 min.

The duration of the TBC for fluorescein lasts between 12 Sep 2017 19:20 and 13 Sep 2017 20:45, so 1 d, 1 h 25 min.

Table 5.26 gives an overview of different parameters of the tracer injections with regard to #951.

The tracer recovery for fluorescein (considering the background value of 4.5 ppb at the beginning of the test) reached 134%, well above 100%. The reason for this remains unclear. The application of the 'quotient method' did not filter out any records. Exceedance of 100% may be related to high turbidity or other disturbances occurring during the test influencing the optics of the fluorometer. This was further investigated as shown in Figure 5.38.

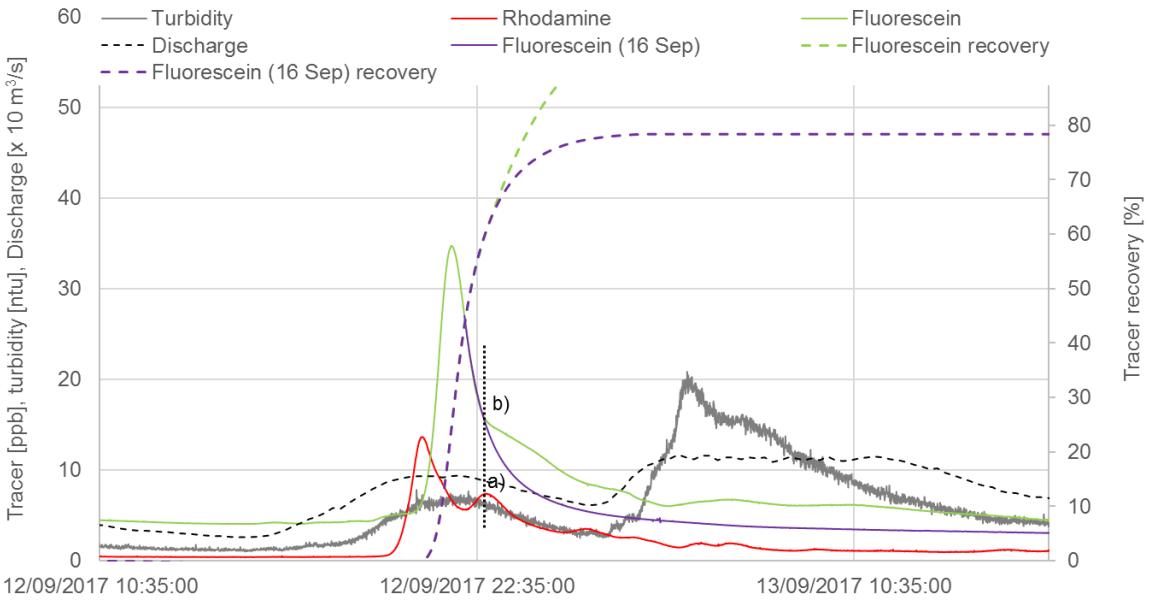

Figure 5.38: Modified tracer recovery for fluorescein for the tracer test on 12 Sep 2017 (#951). The lower part of the fluorescein recession was fitted using the results from the test on 16 Sep 2017.

The rhodamine TBC shows a distinct secondary peak (a). Interestingly, this peak coincides with an obvious deviation in the recession of fluorescein (b). It is believed that this deviation from the fluorescein recession is caused by underlying reading troubles. To 'fix' this, in a next step, the recession of the tracer test on 16 Sep was fitted along the present fluorescein recession. The fitting is excellent along the recession, until point 'b' where both recessions deviate from each other (another indicator for the modification of the observed recession).

Table 5.26: Interpretation of TBCs from the tracer test on 12 Sep 2017.

Observation site	**OS 1-a (MH1) #950**		**OS 1-c (MH3) #951**		
Tracer	Rhodamine WT	Fluorescein	Rhodamine WT	Fluorescein	
				raw	modified
Peak concentration [µg/l]	17.82	33.25	13.66	34.73	34.73
Time to first tracer arrival [h]	-	-	6.9	4.9	4.9
Max. flow velocity [m/h]	-	-	173.3	267.3	267.3
Peak concentration time [h]	8.3	7.3	8.4	7.3	7.3
Flow velocity to peak concentration [m/h]	144.2	180.3	141.7	178.6	178.6
Recovery [%]	-	-	82	134	78
Mean travel time $\bar{v}$ [m/h]	-	-	161	223	257

Finally, the tracer recovery of fluorescein was estimated using a 'combined TBC' that uses the results of the test on 12 Sep from the beginning until the deviation point 'b', and the results from the tracer test on 16 Sep after point 'b'. The total recovered tracer mass is 157 g (78%). The recovery of rhodamine WT is estimated at 82%. However, considering the fact that the recovery of fluorescein was over-estimated, the same may apply to rhodamine. Hence, the true recovery is likely to be less than 82%. The 'loss' of tracer may be related to a proportion of tracer being subject to sorption, and/or lost due to additional flow paths transporting tracer outside the catchment.

The results for both dyes show a very similar total recovery (considering the results of the modified TBC of fluorescein). While a recovery of rhodamine of <100% would be expected due to the location (outside the previously delineated catchment) and non-conservative characteristics of the dye (sorption), the overall result for fluorescein is ambiguous. The raw data suggests a recovery rate of >100% while the modified results suggest a recovery of 78%. Both results are actually unsatisfying: due to the central location of the injection site, previous to the test, a recovery of 100% was expected. At this stage, it is unclear what caused the secondary elevated ppb readings for both dyes, and hence, the precise recovered tracer mass remains unclear for both dyes.

Nevertheless, based on the abovementioned figures, 50% of the total recovered fluorescein (raw data) broke through on 12 Sep 2017 at 23:17:00, 530 minutes after injection at 14:27:00. The mean travel time $\bar{v}$ is estimated for the linear distance x = 1,310 m between IS c and OS 1. Correcting x for sinuosity S_d = 1.5 yields x_s = 1,965 m. Applying Eqn. 4.5 yields $\bar{v}$ = 222.5 m/h.
Using the modified TBC of fluorescein, 50% of the total recovered fluorescein (modified data) broke through on 12 Sep 2017 at 22:05:30, 459 minutes after injection at 14:27:00. The mean travel time $\bar{v}$ is estimated at 257.1 m/h.
Regarding rhodamine WT, 50% of the total recovered tracer broke through 12 Sep 2017 at 23:35:30, 671 minutes after injection at 12:25:00. The mean travel time $\bar{v}$ is estimated for the linear distance x = 1,196 m between IS c and OS 1. Correcting x for sinuosity S_d = 1.5 yields x_s = 1,794

m. Using Eqn. 4.10 yields $\bar{v}$ = 160.5 m/h. No correction could be applied to the rhodamine TBC since there was no previous rhodamine TBC available.

5.2.4.3. Conclusions

Figure 5.39 shows all negative and positive traces from both tracer tests.
The injection of fluorescein at IS(d), and negative result at OS 2 and positive result at OS 1-b (MH2) on 16 Sep 2017 shows that in fact, the minor spring (OS 2) was bypassed by the tracer. This suggests the functioning of shallow discharge (minor springs) that may be related to an epikarst sub-system.

As it can be inferred, the results of the tracer tests confirm the present catchment boundaries to the north, west and east; in the south, the catchment boundaries extend beyond the current outline (Figure 5.40).
Mean travel times were much faster in test 1 (12 Sep) compared to test 2 (16 Sep). One reason for that could be different hydraulic gradients between the IS and OS. However, the gradients are actually very similar and hence, this is not necessarily the driving factor. Another reason may be the characteristics of the conduits. For example, tortuosity and roughness (e.g. caused by debris) of the conduit network may be lower in the centre of the catchment (between IS(c) and MH1-3) than in the northern stretch (between IS(d) and MH1-3).

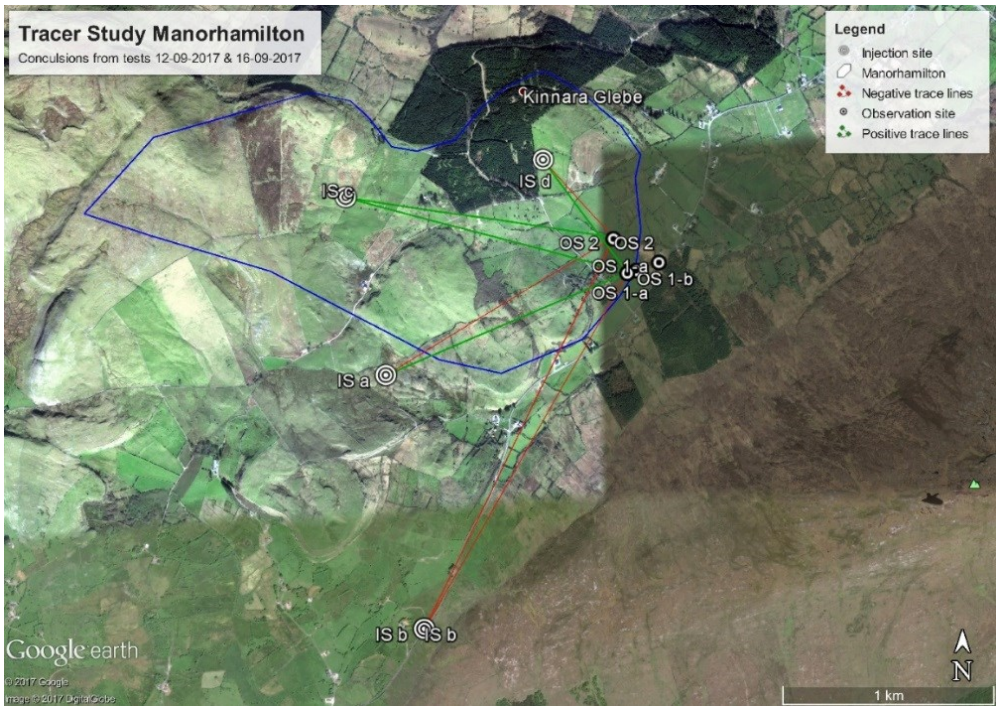

Figure 5.39: Positive and negative tracer connection from injections on 12 Sep 2017 and 16 Sep 2017.

Based on tracer recoveries the previous extent of the catchment boundaries has been further enlarged towards the south (Figure 5.40). The updated catchment now covers an area of 2.4 km^2 as opposed to the previous catchment size of 1.95 km^2.

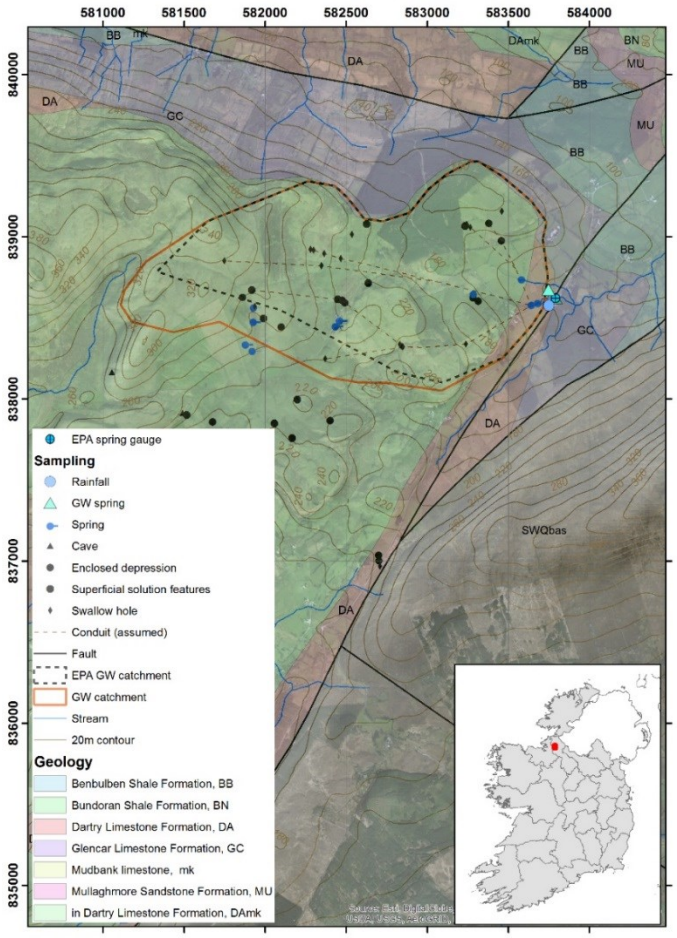

Figure 5.40: Updated catchment boundaries based on the two tests from 12 Sep 2017 and 16 Sep 2017.

5.2.5. Reservoir modelling

A KarstMod reservoir model was built to simulate the rainfall-discharge response of Manorhamilton spring.

The total modelling period was 15 Dec 2017 to 04 Jun 2019, including 12,874 time steps. This period was chosen, as it is the only period without any data gaps in conjunction with observed hourly rainfall at Manorhamilton. Data used are hourly discharge and rainfall observed at MH3. Hourly evapotranspiration (ET) data originates from daily ET time series that was estimated using climate data of the MetEireann station Markree. Conversion of daily into hourly time series was done by a simple disaggregation.

A warm-up period was initiated for the first two weeks. Calibration was applied on the period 01 Jan 2018 to 31 Dec 2018 while validation comprises the period 01 Jan 2019 to 04 Jun 2019.

The best model was found by trying all different combinations of reservoirs and flows (Table 5.27). Each combination was then fine-tuned by reducing the parameter range after each model run. The best performing model was found with a simple setup of reservoir 'E' and 'C' resulting in a NSE and KGE of 0.824 and 0.896 for the calibration period and 0.880 and 0.909 during the validation periods (Figure 5.41, Figure 5.42, Table 5.28). It was found that adding reservoir 'M' reduces the overall performance of the model, hence, this reservoir was neglected.

Table 5.27: Fitted parameters of the KarstMod reservoir model of Manorhamilton spring.

R_A [km²]	E_0 [mm]	Q_{EC}				C	
		k_{EC} [mm/h]	a_{EC}	C_0 [mm]	h_{maxC} [mm]	T_C [h]	a_C
3.23	9.91	0.00011	3.78	6.28	259	2.00	0.482

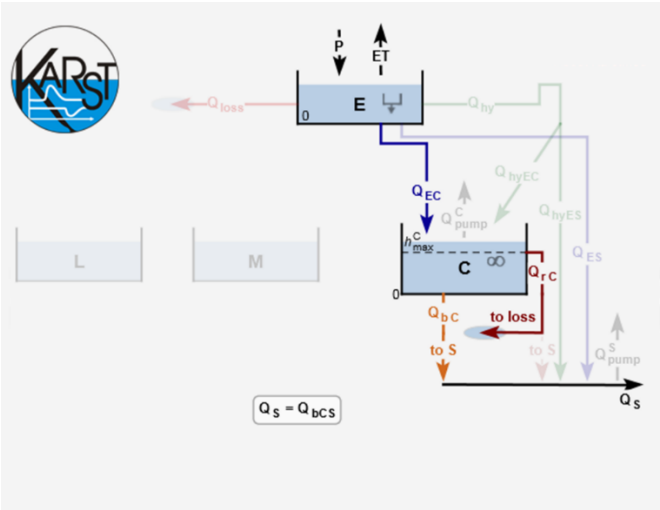

Figure 5.41: KarstMod reservoir model for Manorhamilton spring.

Table 5.28: Performance of the simulated discharge for the period including data gaps.

Parameter	Calibration		Validation	
NSE	+0.824		+0.880	
KGE	+0.896		+0.909	
VCC	-0.14 MCM	-3.1%	+0.09 MCM	+3.9%
Q_{EC}/Q_{bC}	100%		100%	

The model results suggest a catchment size of 3.2 km². This catchment size is smaller than the previously estimated average catchment size of 4.3 km² applying water balances. The reason for this difference is related to the different time series used for the water balances (daily rainfall from the MetEireann station Amorset) as opposed to the time series used for the reservoir model (hourly rainfall monitored at MH3). For the hydrological year 2018, the total rainfall observed at Amorset

sums up to 1,565 mm as opposed to 1,812 mm observed at MH3. The higher rainfall observed at MH3 relates to smaller catchment boundaries compared to smaller rainfall observed at Amorset.

Figure 5.42 shows modelled against observed discharge. In general, the model is capable of resembling the overall discharge dynamics. Peak discharges and recessions are relatively well matched. However, between March and June 2018, the observed spring hydrograph is poorly simulated. Both, the peaks of discharges as well as single events are poorly matched, or not simulated at all. This mismatch may be caused by faulty recording of rainfall (e.g. a loose connection between the sampler and logger), however, no obvious problem was noticed on site This mismatch during the calibration periods is believed to be the reason for the better performance of the model during validation.

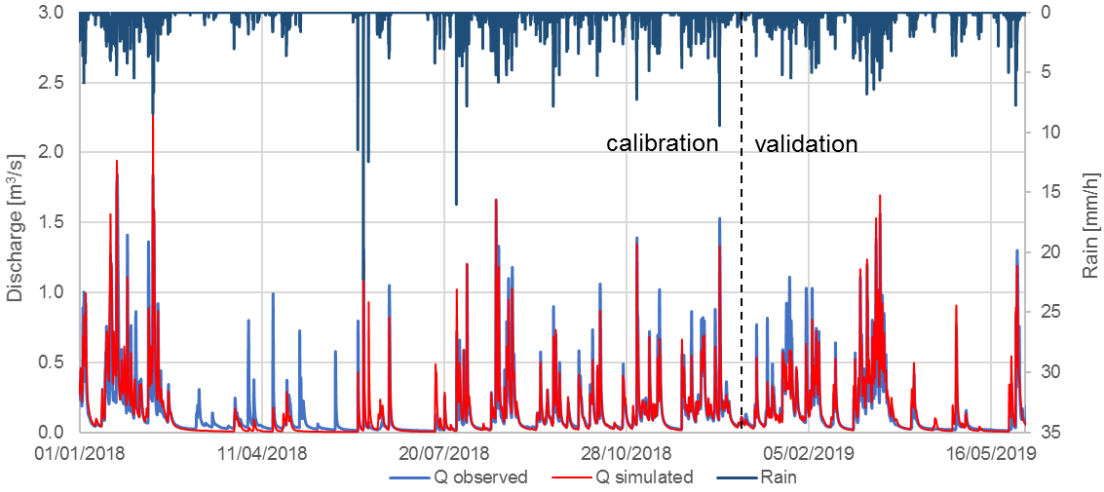

Figure 5.42: Observed and simulated discharge [m^3/s] during calibration and validation.

Given that, the NSE and KGE of 0.824 and 0.896 are considered as sufficient performance.
The results show that observed discharge of Manorhamilton can exclusively represented by drainage of the reservoir C, which represents rapid and concentrated recharge and groundwater flow. Integration of reservoir 'M' representing diffuse and slow flow reduced the model performance, hence, according to the model, no such flow contribution is present.
The model suggests that diffuse groundwater recharge is rapidly concentrating towards conduits. Hence, the LFC may be expected to be very low.

5.2.6. Final catchment delineation

Tracer tests confirmed hydraulic connections that were previously not considered in the catchment delineated by EPA (2011b) resulting in an increase of the catchment area to 2.4 km^2 outlined in the previous Section '5.2.4. Tracer tests'.

The water balance presented in Section ‘5.2.3. Water balance’ indicated a catchment size ranging between 3.9 and 5.03 km^2 with a mean size of 4.3 km^2. Accordingly, even the updated boundaries had to be enlarged.

The alignment of swallow holes indicates the course of connected conduits in the sub-surface, presumably aligning northwest-west – southeast-east, from the Leean Mountain towards the spring (rather than southwest-northeast, which would be favourable for additional contribution from the south). Following a northwest/west-southeast/east conduit alignment leads potential further upland towards the Leean Mountain. As previously presented, the dip of the Dartry Limestone formation is gently towards southeast-south/southeast (Figure 3.10), from the Leean Mountain towards Manorhamilton spring.

Therefore, it seems to be more favourable that additional contribution comes from the west, rather than from the south. Accordingly, the catchment was delineated as displayed in Figure 5.43 for a rather conservative size of 3.6 km^2. Additional contributions may originate from the south though.

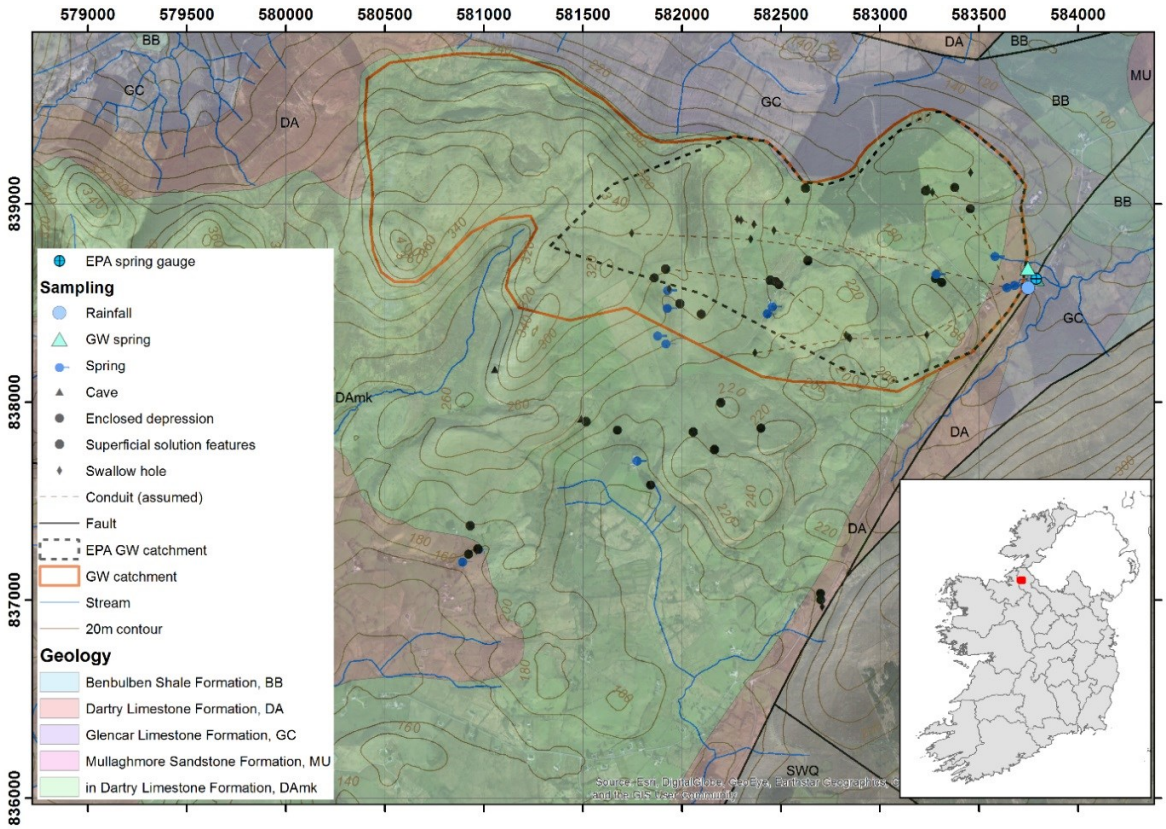

Figure 5.43: Final delineated catchment of Manorhamilton.

5.2.7. Summary from Manorhamilton catchment studies

The groundwater catchment of Manorhamilton was delineated as the single main outlet of the aquifer. This seems plausible, as there are only relatively small springs located in the area. These springs are conceptualised as epikarst discharges. Because of the absence of streams in the

centre region of the study area, any discharge from the epikarst springs must infiltrate back into the aquifer. Therefore, the concept of the water balance seems to be applicable.
The catchment is believed to vary between 3.9 and 5.0 km² (average 4.3 km²). The KarstMod reservoir model suggests a catchment size of 3.2 km². All these figures are larger than the previously delineated catchment size of 1.95 km². It is assumed that the catchment extends further to the west, upland towards the Leean Mountain.
The existence of many swallow holes in the regions suggests concentrated groundwater recharge. In fact, the system was classified as aquifer with a well karstified infiltration zone and extended conduit network ending into a flooded phreatic zone. The discrepancy between the storage extent $Max(V_d)$ and the mean annual flow volume V_{trans} highlights the relatively low regulating power (transformation of the rainfall signal towards the spring outlet) and the mean residence time is estimated at 0.26 years or 95 days. The dominance of fast infiltration was provided by 10 > ε > 1. Further, the KarstMod reservoir model suggests that discharge of the spring is best represented using reservoir C (concentrated flow), hence, a fast groundwater flow component in absence of a diffuse or slow-flow component.
The MRC of Manorhamilton spring suggests the presence of three exponential flow components: a flood component with k' = -0.15 h^{-1}, an intermediate component with k' = -0.03 h^{-1} and an LFC with k' = -0.0025 h^{-1}. The major part of the recession is governed by the flood and intermediate component; hence, these components are interpreted as the dominating flows.
Mean groundwater flow velocities within the conduits were estimated in the order of 88 to 223 m/h. The TBC indicate relatively low dispersion.

5.3. Conclusions

Both of the finally delineated groundwater catchments of Ballindine and Manorhamilton spring differ to the previously defined boundaries (EPA, 2011a; EPA, 2011b): Manorhamilton spring drains an upland-lowland catchment comprising 3.6 km², while Ballindine spring constitutes a lowland catchment of approximately 3.3 km² that is conceptualised to be largely influenced by surface water-groundwater interaction.
The characterisation of the catchments was done using available hydrogeological information, but most importantly using high frequency (1 h) and long-term, multi-annual hydroclimatic time series that enabled annual water balances and reservoir modelling to be carried out. In fact, these activities provided the basis for field studies, such as tracer methods, which provided insights into the catchment dimensions, as well as into average flow velocities in functioning of minor springs for Manorhamilton.
Further, the available hydrographs of both springs allowed recession analysis to be applied. Manorhamilton shows a very short recession compared to Ballindine, which exhibits a much longer recession with the significant contribution constituted by the intermediate recession component as

well as a continuous level of the LFC. Manorhamilton clearly shows a steeper recession than Ballindine. In fact, the intermediate recession of Ballindine corresponds in magnitude to the LFC recession of Manorhamilton, and the flood recession of Ballindine corresponds to the intermediate recession of Manorhamilton (Table 5.29).

Table 5.29: Recession constants k / k' of Ballindine and Manorhamilton.

Site	Time step	LFC	Intermediate	Flood
Ballindine	k' [h^{-1}]	-0.0002	-0.0021	-0.0375
	k [d^{-1}]	-0.005	-0.05	-0.90
Manorhamilton	k' [h^{-1}]	-0.0025	-0.03	-0.15

The LFC of Manorhamilton is limited up to maximum of 0.035 m^3/s. This is a relatively small flow contribution given the range of discharge at the spring reaching up to 1.72 m^3/s. This is reflected by the small recession constant k' for the LFC of 0.0025 h^{-1} as opposed to the intermediate k' of 0.03 h^{-1} and the flood k' of 0.15 h^{-1}. As a result, overall the LFC contributes very little to the discharge regime. Hence, in conclusion, it must be assumed that diffuse infiltrated rainfall rapidly concentrates towards larger permeability domains and that the contribution of diffuse groundwater flow is very small. While this finding was already partly raised in the previous chapters, the results of this chapter provides an upper limit to the component related to diffuse groundwater flow in the overall spring discharge hydrograph.
Following Mangin (1975); El-Hakim and Bakalowicz (2007), Ballindine spring is fed by an “aquifer with a deep phreatic zone partly or totally confined under low permeable sediments with a complex drainage structure responsible for very long, multiannual or secular residence times”. Equally, Manorhamilton is fed by an “aquifer with a well karstified infiltration zone and extended conduit network ending into a flooded phreatic zone”. Both of these definitions seem to be coherent with the existing information, and thus, provide valuable information for the upcoming analysis.

With regard to TCMA, this analysis has yielded a relatively high proportion of a groundwater component as opposed to the storm component (Fritz, et al., 1976; Laudon and Slaymaker, 1997; Pellerin, et al., 2008). This is also the case for Manorhamilton spring. Yet, such a high groundwater component or LFC contradicts all other results that can be interpreted towards a smaller contribution of such LFC. While this groundwater component is conceptually related to drainage from the phreatic zone, it cannot be further sub-divided into different permeability domains associated with the aquifer (soil, epikarst, etc.). This is clearly a limitation of the method. Further complexity arises given the spatial and temporal heterogeneity of rainfall and its isotopic composition, making it difficult to assign a single 18O or 2H value to the input. However, while the method was not supportive in this study, it is believed that it may be an interesting research topic for further investigation of karst aquifer heterogeneity linked to other hydrograph separation techniques.

6. Time Series Analysis

In this chapter, different time series analyses are applied providing information and reference parameter values for the semi-distributed pipe network modelling that follows.
Firstly, uni- and bivariate statistical methods are applied aiming is to quantify linearity within and between time series representing input-output relationships. Such information is used to gain insights into recharge and flow dynamics.
In a next step, spectral analysis linked to noise analysis and multi-resolution analysis (MRA) are applied. Spectral analysis and MRA are used to characterise the time-amplitude signal in the frequency domain. The fundamental premise is that different flow components or dynamics are linked to distinct 'physically meaningful' frequency ranges, which may provide the framework for 'constructing' specific signals related to flow components using discrete wavelet transforms (DWT): for example, a low-frequency signal that relates to diffuse flow(s). Finally, digital/recursive filtering is applied to distinguish an LFC signal of the lowest (diffuse) permeability domain.
Throughout the previous chapters it was shown that Manorhamilton and Ballindine are very distinct aquifer systems: Manorhamilton is conceptualised as a single discrete outlet compared to Ballindine which is conceptualised as an aquifer that is in interaction with the River Robe and drainage channels. Therefore, these systems were analysed separately.

6.1. Autocorrelation

The autocorrelation function (ACF) was applied to quantify the linear relationship within a time series. The lower the ACF, the lower the linear relationship of a signal with its preceding signal in time. The rate of decrease of the ACF corresponds to what can be considered as the 'loss in memory' of the signal. In this case different segments of the declining ACF have been interpreted in relation to drainage from different flow components.
Further, the ACF is a measure of randomness, and can be applied on time series to rule out any systematics, e.g. errors.

6.1.1. Ballindine

Autocorrelation was applied on time series of spring discharge, rainfall (measured at Claremorris) and the River Robe (measured at Christina S BR., corrected for contribution from Ballindine).

The results are illustrated in Figure 6.1 distinguishing between daily (long-term, (a)) and hourly (short-term, (b)) analysis for the period 29 Apr 2009 to 30 Sep 2018.
On a daily time step, the ACF of Claremorris drops immediately below the significance level of 0.05, and then follows the pattern of white noise, i.e. type 'B' (see Figure 2.15). There might be a slight tendency of small structures present in the frequency of one year for rainfall time series,

which can be interpreted as seasonal variation of the rainfall regime. Nevertheless, the ACF suggests quasi-stochastic characteristics of the rainfall pattern, as would be expected.
The ACF of Ballindine and the River Robe shows a strikingly similar pattern, which in fact exhibits a correlation coefficient of 0.995. Both patterns show the same characteristic peaks and slopes reaching <0.2 and <0.05 after 78 and 91 d (in the case of Ballindine) and 67 and 85 d (in the case of the Robe).

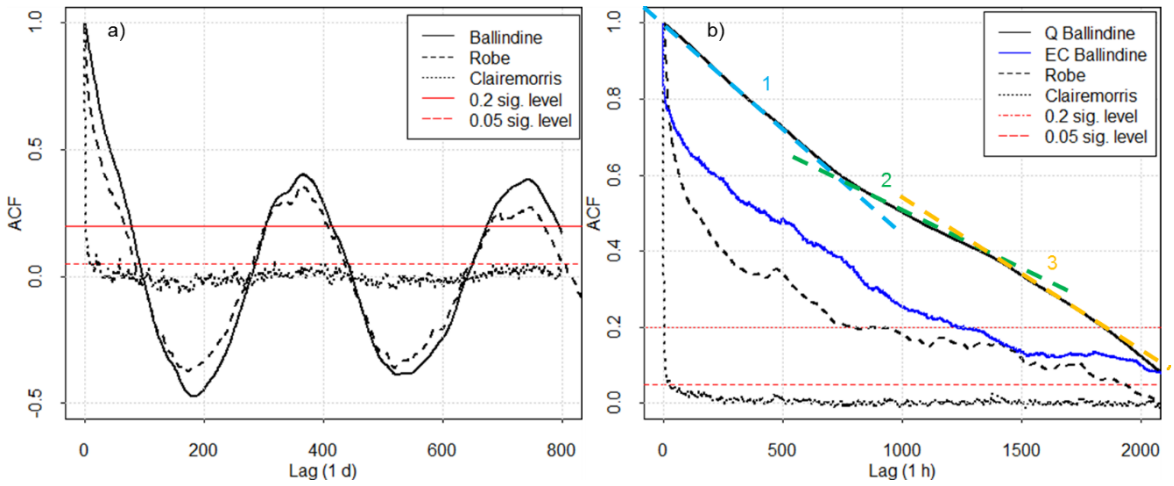

Figure 6.1: ACF for daily rainfall (Claremorris), spring discharge (Ballindine) and river discharge (Robe) up to lag = 800 d (a) and hourly ACF for the same monitoring sites and EC of the Ballindine (b), and significance level at 0.2 and 0.05 between 29 Apr 2009 and 30 Sep 2018.

The ACF of Ballindine and the Robe applied over the range of one year shows a cycle of positive and negative correlation. This dynamic is interpreted as a time series with a clear seasonal component following type ‘G’ as illustrated in Figure 2.15. Both ACFs show regular peaks without any tendency of approaching to 0. The minimum and maximum ACF of Ballindine and the Robe range between -0.47 and 0.38, and -0.37 and 0.35 respectively. These are relatively high values and confirm again the high degree of linearity of the discharge time series. Yet, the higher magnitude of fluctuation of the ACF of Ballindine indicates a higher level of linearity, as opposed to the ACF of the Robe. Hence, this may be related to the storage of the aquifer, indicating a more static system in case of Ballindine. Nevertheless, the relatively high level of linearity of both systems characterises the relatively high memory effect.
Further, the very smooth course and high linearity suggests a very homogeneous discharge regime of Ballindine without significant heterogeneities that would interrupt such linearity.

The shorter-term hourly time series indicate again the randomness in the rainfall signal (Figure 6.1b). Further, the ACF of the Robe shows an exponential decline of autoregressive type (type ‘E’ in Figure 2.15).

The ACF of discharge of Ballindine shows slight changes, which can be noticed in Figure 6.1b. Three straight lines (‘1’, ‘2’, ‘3’) can be fitted subjectively to the three sections. Even though the slope of the fitted lines looks very similar to each other, they may be interpreted as different rates of memory loss which can be linked to different dynamics on the hydrograph and so, potentially linked to different flow components.

The ACF of EC observed at Ballindine spring recesses between discharge of the spring and the River Robe. Interestingly, the course of the recession shows changing slopes that correspond roughly to changing slopes of the ACF of discharge of the River Robe. The similar pattern of memory loss may be indicative of similar underlying driving dynamics.

6.1.2. Manorhamilton

Figure 6.2 shows the ACF for daily (long-term, (a)) and hourly (short-term, (b)) rainfall observed at MH3 and Manorhamilton spring discharge. Discharge and daily rainfall refer to the period from 30 Apr 2009 to 03 Jul 2013 while hourly rainfall refers to the period 15 Dec 2017 to 31 Dec 2018.

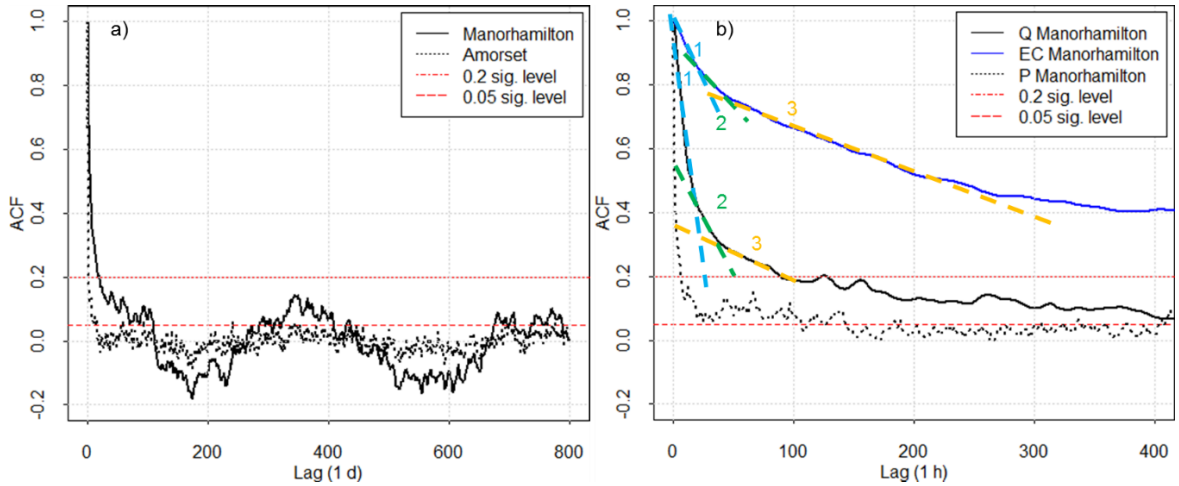

Figure 6.2: ACF for daily discharge of Manorhamilton up to lag = 800 d between 30 Apr 2009 to 03 Jul 2013 (a), and ACF for hourly discharge, EC and rainfall (P) up to lag = 400 h between 15 Dec 2017 and 31 Dec 2018 (b), and significance level at 0.2 and 0.05.

The ACF of both rainfall time series shows the typical signal as to be expected for a random signal or white noise.

The ACF of Manorhamilton applied over the range of one year shows a cycle of positive and negative correlation (Figure 6.2a). This dynamic is interpreted as a time series with a clear seasonal component following type ‘G’ as illustrated in Figure 2.15. Yet, the ACF ranges between -0.16 and 0.14, indicating a relatively low level of linearity.

The shorter term ACF of hourly discharge time series for Manorhamilton decreases very steeply for the first 40 hours before a more gradual decline with small structures appears. The ACF reaches <0.2 after 89 h and <0.05 not before 560 h (23.3 d).
The recession of the ACF for the first 22 h may be regarded as distinct loss of memory compared to the remaining recession. This component is indicated by the blue line '1' in Figure 6.2b. From this, another distinct recession can be approximated between 22 and 40 h ('2'), followed by another longer recession ('3).
The first rapid memory loss for the first 22 hours may be accounted to a high fluctuation of the signal and conduit flow whereas the remaining decreasing pattern may be indicative for a slower discharge contribution. The change from '1' to '2' or '3' indicates changing discharge dynamics (Mathevet, et al., 2004). However, the overall loss is very high – even the third recession cannot prevent the ACF dropping below 0.2 after 89 h.
The ACF of observed EC shows a very gradual decline, yet, for the upper recession, three distinct straight lines ('1', '2', '3') can be fitted. These correspond more or less to the same lag periods (h) as previously plotted for the ACF of discharge.

6.1.3. Summary from autocorrelation analysis

The results show that the discharge signal of Manorhamilton is characterised by a low degree of linearity and a rapid loss of memory. The recession of the ACF is steep for all three fitted segments. In comparison, the discharge time series of Ballindine shows a relatively high level of linearity and a smooth inter-annual fluctuation. There is a slight indication of three distinct discharge regimes, but nowhere near as clear as in the case of Manorhamilton.
The level of linearity is linked to the heterogeneity of the aquifer, which impacts on a) storage, and b) on discharge dynamics. High linearity is the result of a well organised aquifer, which significantly transforms a rainfall signal towards the outlet due to a low degree of karstification and/or high storage. In comparison, a very heterogeneous aquifer with a high level of karstification would transform a given rainfall signal towards the spring to a much lesser extent as a result of lower storage potential and rapid discharge.
Accordingly, it is concluded that Manorhamilton is characterised by a highly karstified aquifer in which groundwater recharge rapidly concentrating towards the conduits. The segments '1' and '2' may be account for rapid recharge and flow. However, even segment '3' rapidly declines below the significance level. The dominant share of discharge must be linked to concentrated recharge. It can be expected that the proportion of diffuse recharge and flow is very low.
Due to the low range of ACF fluctuation during the seasons, storage is also considered to be low.

The discharge signal of Ballindine, however, shows a high level of linearity between the seasons. This is interpreted as important storage component, which gradually drains. Such drainage may be linked to the role of the fissured matrix domain. There is not necessarily any indication of conduit

flow components, which would be characterised by a steep recession at the beginning. Therefore, the discharge of Ballindine may conceptualised as a system dominated by diffuse groundwater recharge characterised by a low degree of karstification.

6.2. Cross-correlation

While the previous section analysed the linearity of individual time series, this section quantifies the linear relationship and the delay (lag) between two time series, i.e. input (rainfall and/or potentially river flow) and output (discharge) by applying the cross-correlation function (CCF).

6.2.1. Ballindine

The cross-correlation was analysed between rainfall (Claremorris) and discharge of the River Robe (input) and Ballindine spring (output) on a daily times step (Figure 6.3a, long-term) and an hourly time step (Figure 6.3b, short-term) for the period 29 Apr 2009 to 01 Oct 2018.

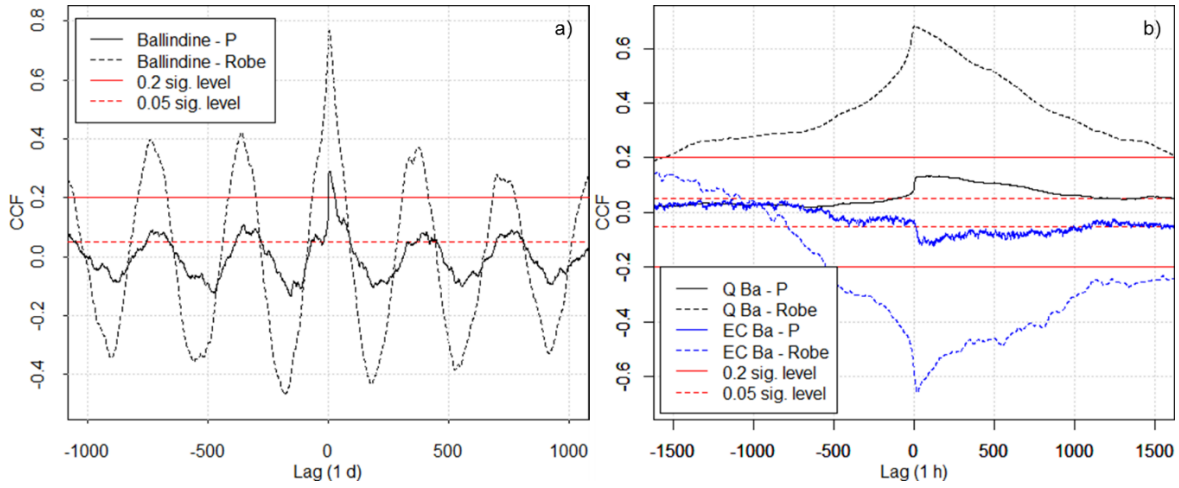

Figure 6.3: CCF between daily (a) and hourly (b) discharge and EC of Ballindine spring and rainfall observed at Claremorris and discharge of the River Robe between 29 Apr 2009 and 01 Oct 2018, and significance level at 0.2 and 0.05.

Over the long-term analysis, both CCFs show an inter-annual fluctuation (Figure 6.3a). While the CCF between rainfall and Ballindine varies around 0.1 and -0.1, the CCF between the Robe and Ballindine fluctuates in the range of 0.4 and -0.4. Hence, linearity between the Robe and Ballindine spring is much stronger than between rainfall and the spring. This is confirmed in the short-term analysis (Figure 6.3b). Both CCF for discharge peak positively indicating a clear response of Ballindine spring to rainfall and to the Robe. Yet, the two CCFs vary substantially in quality.
The CCF between rainfall and Ballindine spring reaches the peak after a lag of 60 h at 0.13. This value lies between the significance levels of 0.05 and 0.2 and expresses therefore a weak

relationship between rainfall and spring discharge. In fact, there is no dominant peak, and the following recession is very wide, recessing between CCFs of 0.13 and 0.06. The CCF of Ballindine therefore indicates a significant transformation of the rainfall signal towards the spring outlet, und underlines the relative inertia of the system to rainfall. In fact, the CCF decreases relatively slowly or gently, which is interpreted as absence of a fast-flow component (Padilla and Pulido-Bosch, 1995; Angelini, 1997) or at least as a relatively slow contribution of fast-flow.

The CCF between discharge of the River Robe and Ballindine exhibits a relative similar pattern as the one between rainfall and spring discharge, with a Pearson's correlation coefficient of 0.80, which suggests that both CCFs follow a similar pattern. However, the CCF between the River Robe and Ballindine spring peaks with a lag of 2 h at a CCF of 0.68 indicating a high linearity between both time series.

Further, the CCF between rainfall/river discharge and the observed EC at the spring is shown. Clear anti-correlation can be observed between the Robe and EC at Ballindine with a peak of -0.66 at a lag of 19 h. The high linearity indicates rapidly dropping EC at the spring with increasing river discharge. Conversely, the linearity between rainfall and EC is very weak.

Correlation does not necessarily imply causality. Yet, the high level of correlation must be regarded in the context of limited input variables, namely rainfall and river flow. Therefore, in this context, the high degree of cross-correlation is interpreted as causality, so that the River Robe exhibits presumably an important influence on the aquifer of Ballindine spring, and its discharge regime. The results therefore also indicate that the lateral extent of the catchment of Ballindine spring should reasonably extend up to or close to the River Robe.

6.2.2. Manorhamilton

Over the long-term, a clear seasonal effect can be observed between rainfall and discharge time series (Figure 6.4a).

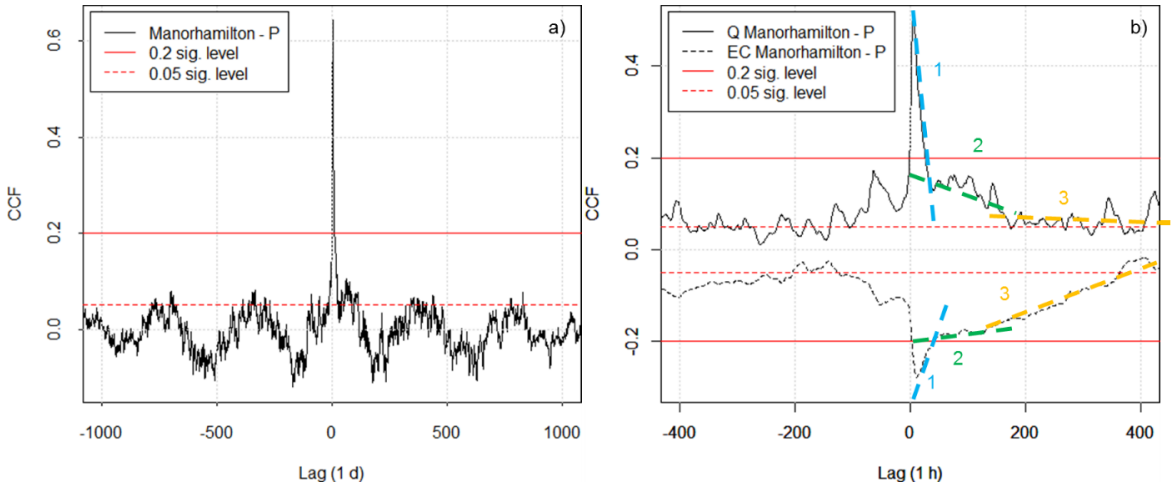

Figure 6.4: CCF between daily discharge of Manorhamilton and rainfall measured at Manorhamilton (Amorset) for the period 30 Apr 2009 to 03 Jul 2013 (long-term, a), and between hourly

discharge and EC and rainfall measured at MH3 for the period 24 Mai 2017 to 01 Oct 2018 (short-term, b).

The CCF peaks at 0.64 at a lag of 2 d, indicating again the rapid response of spring discharge to rainfall, and decreasing below 0.2 after 11 d. After this, the seasonal pattern of the CCF shows a very noisy tendency fluctuating mostly below the significance level of 0.05.

6.2.3. Summary from cross-correlation analysis

Ballindine and Manorhamilton have revealed different patterns of CCF.
The relatively high CCF peaks of Manorhamilton shows that the rainfall input signal is directly transformed towards the spring discharge, with the conclusion that the aquifer of Manorhamilton is less structured; the spring shows a clear direct response to rainfall input. Infiltrated water travels relatively fast and concentrated towards the aquifer outlet. Accordingly, it seems that there is little influence of storage on the discharge signal of Manorhamilton. This matches the conclusions drawn from the autocorrelation analysis, as discussed previously in Section '6.1. Autocorrelation', and the conclusions drawn from the method of Mangin (1975); El-Hakim and Bakalowicz (2007). Ballindine, conversely, shows relatively little correlation with the rainfall time series. The rainfall signal seems to be largely transformed by the aquifer which may be a result of the well-structured characteristics of the aquifer, and/or the influence of the head or infiltrating river water of the Robe, which may overlap the rainfall signal. Ballindine shows a very high CCF peak with the discharge time series of the River Robe, which suggests that the river exhibits significant influence on the Ballindine spring.

6.3. Spectral and noise analysis

Spectral analysis was used to evaluate the observed time-amplitude signal in the frequency (Fourier) spectrum as well as in the time-frequency domain using wavelet transform.

In this study, it is believed that different flow components correspond to distinct frequencies, as previously applied by different authors (Mathevet, et al., 2004; Fournillon, 2012; Duran, 2015; Dufoyer, et al., 2018). Here, flow components are linked to different frequencies using noise analysis. Accordingly, changes in slopes within the power spectrum are interpreted to coincide with a change in discharge dynamics, finally then characterised by distinct spectral coefficients. For example, discharge through the fissured matrix is believed to generate a structured low-frequency signal as opposed to the high-frequency signal related to flow through larger fractures or conduits. However, all these signals of course are integrated by the time the water arrives at the spring outlet. Hence, the assumption is that spectral analysis can be applied on spring hydrographs to extract time-amplitude signals that resemble contributions from different permeabilities.

The power spectra of hourly discharge time series of Ballindine and Manorhamilton was established using the Fast Fourier Transform (FFT). The time series were not detrended before the analysis (as a comparison of results between detrended and non-detrended time series did not indicate any relevant difference).
The aim of the spectral analysis was to: a) characterise the overall frequency pattern, and b) identify distinctive segments of different slopes on power spectra that may be characterised by individual spectral coefficient β (β_1, β_2,… β_n), which may be linked to distinctive flow or discharge components of the karst aquifer.
To distinguish objectively between individual slope segments within the power spectrum, the method after Pettitt (1979) was applied iteratively to detect significant breakpoints. A linear regression is then fitted along each segment in log-log space to describe a characteristic slope, i.e. the spectral coefficient β.

Based on the time-invariant frequency analysis, time-variant spectral analysis is applied in the form of continuous wavelet transform (CWT), cross-wavelet (XWT) and wavelet coherence (WTC).
The aim of CWT is to identify the 'nature' of the previously analysed frequency signals – how these frequencies occur in time, and if there is some temporal pattern or seasonality within a single time series, which may indicate a relation to discharge dynamics of the aquifer.
XWT is then applied to evaluate the cross wavelet power between two time series (input and output) that is interpreted as the local relative phase between the two signals in time and frequency phases (Grinsted, et al., 2004). The aim is to identify common features or common powers between the input (rainfall and potentially river discharge) and the output (spring signal) for discrete periods. Regions of high power are interpreted as high influence of the input onto the output signal, while periods of lower power are interpreted as lower influence.
WTC measures the cross-correlation between the two time series as a function of frequency. By quantifying the relative phase of the two signals to each other, causality between input and output can be evaluated.
For both, XWT and WTC, the relative phase can be expressed in degree using phase angles, which indicate under caution which of the two signals is leading in time – for example, if arrows point to the right, the signal are in-phase, and the phase difference is 0º. If the two signals are completely out of phase, their phase difference is 180º and arrows point to the left. If arrows point downwards, the input variable leads over the output variable by 90º, and the opposite of the angle shows upwards. Further, a cause-effect relationship would be characterised by a constant phase angle, i.e. i.e. all arrows pointing in the same direction, within the contours of significant common powers.

6.3.1. Ballindine

Figure 6.5 shows the power spectrum of the entire hourly discharge time series of rainfall decomposed into its frequencies (Hz) using FFT and significant breakpoints. Breakpoints result in individual slope segments, which correspond to spectral coefficients β, which were labelled starting from the lowest frequency segment β_1 to the highest frequency segment β_8 (from 'left' to 'right'), labelled in black. The difference between neighbouring spectral coefficients is labelled in blue.

The spectra show spectral coefficients exclusively in the Gaussian domain, hence, the complete signal is characterised by randomness, as might be expected for a rainfall signal. The lowest spectral coefficient reaches -1.02 (β_7), which is strictly in the Brownian noise domain between 11 and 5.1 h, hence, a slight structured component is present. However, the spectrum confirms rainfall as being a random input variable. Therefore, the transformation of the random rainfall signal towards a partially structured spring discharge signal must be related to the aquifer.

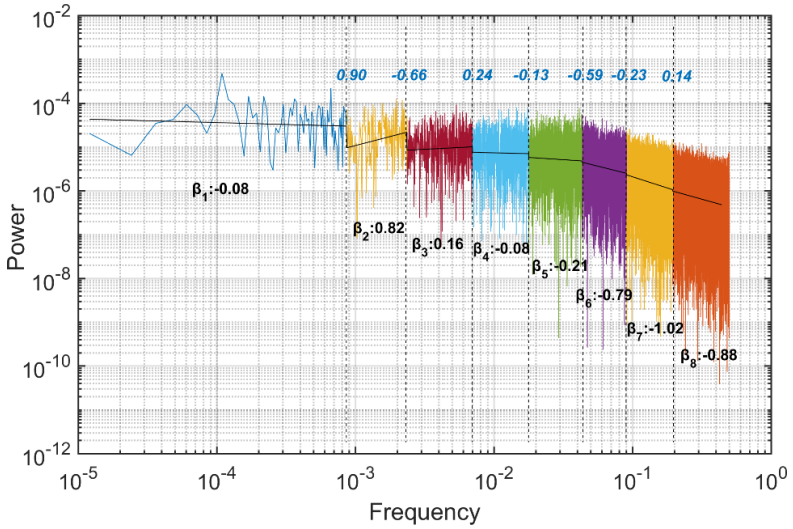

Figure 6.5: Frequencies (Hz) associated with hourly rainfall at Claremorris between 01 Apr 2009 and 30 Sep 2018 and frequency segments following the Pettitt method with associated spectral exponents β with β_1 to β_8 (black) and changes between spectral exponents (blue).

Next, discharge time series were analysed. Figure 6.6 shows the power spectrum of the entire hourly discharge time series of Ballindine (9 years). The Pettit method yields nine breakpoints and associated segments with β coefficients ranging between 0.28 and -2.21 (Figure 6.7). Accordingly, only β_1 and β_2 lie in the Gaussian domain and can be considered as the stochastic and the non-structured component of the discharge time series, while β_3 to β_{10} lie within the Brownian domain and can be considered as a more organised component. In fact, β_4, β_5, β_6 and β_{10} correspond to anti-persistent Brownian noise, while β_3, β_7 β_8 and β_9 correspond to persistent Brownian noise with a memory effect. The lowest spectral coefficients (-2.01, -2.15, -2.16 and -2.21) are the most structured ones (persistent Brownian noise) between red and black noise.

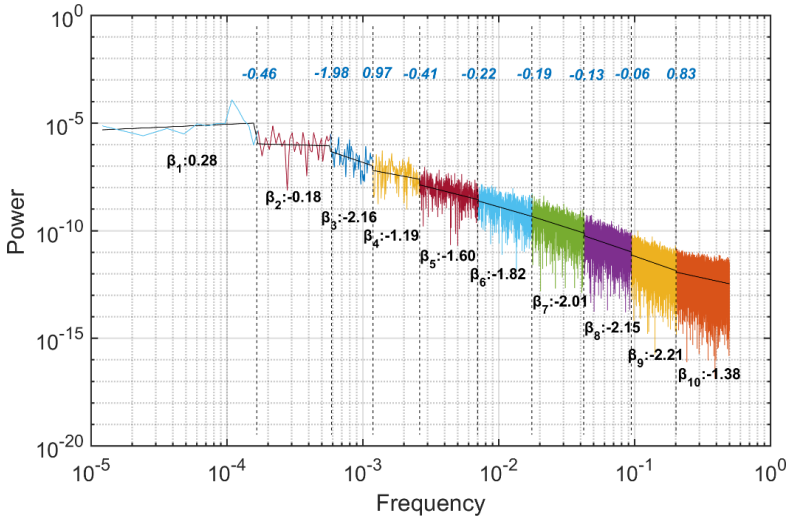

Figure 6.6: Frequencies (Hz) associated with hourly discharge of Ballindine between 19 Apr 2009 and 30 Sep 2018 and frequency segments following the Pettitt method with associated spectral exponents β with β_1 to β_{10} and changes between spectral exponents (blue).

The plot of β coefficients (Figure 6.7) shows an interesting pattern in the non-Gaussian range: the persistent Brownian spectral coefficient β_3 is separated from the other persistent Brownian spectral coefficients β_7 to β_9 by three anti-persistent Brownian spectral coefficients β_4 to β_6.

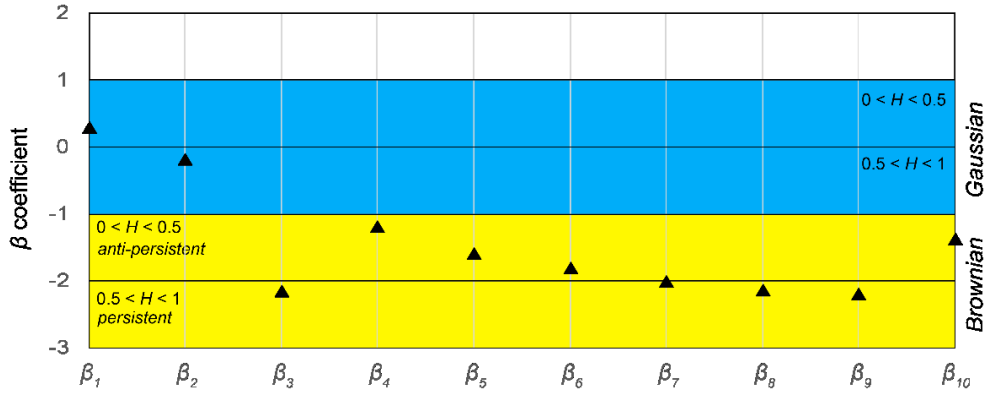

Figure 6.7: Spectral coefficients β_1 to β_{10} for Ballindine spring, including the Hurst exponent and noise domain.

Two potentially suitable ways of classifying distinct frequency segments were found:

1. Considering the difference between persistent and non-persistent noises, distinct structured signal ranges may be defined: a) a low-frequency signal β_3, b) an intermediate frequency signal β_4 to β_6 and c) a high-frequency signal β_7 to β_9.
   Dufoyer, et al. (2018) labelled the frequency interval of the highest frequency signal (here β_{10}) as distinct high frequency component as a result of highly transmissive zones in the aquifer.

Hence, the high-frequency range β_7 to β_9 may be extended also β_{10} to finally result in a high-frequency range of β_7 to β_{10}.

Accordingly, the low-frequency signal (β_3) corresponds to a frequency range of 0.0006 to 0.0012 Hz (1,720.6 to 842.8 h; 72 to 35 d), the intermediate signal (β_4 to β_6) corresponds to the frequency range of 0.0012 to 0.0176 Hz (842.8 to 56.8 h; 35 to 2 d), and the high frequency signal (β_7 to β_{10}) corresponds to a frequency range of 0.0176 to 0.5000 Hz (56.8 to 2 h; 2 to <1 d).

2. Another way of classifying the spectral signals is using the change between β coefficients as the indicator for distinct frequency sections associated to flow components (Dufoyer, et al., 2018). Accordingly, β_3 and β_{10} show the largest and most pronounced differences to their neighbouring spectral coefficients. In comparison, the difference between the coefficients β_4 to β_9 seems relatively low. Hence, one may classify distinct structured signal ranges as: a) a low-frequency signal β_3, b) an intermediate frequency signal β_4 to β_9 corresponding to the frequency range of 0.0012 to 0.2033 Hz (842.8 to 4.9 h),and c) a high-frequency signal β_{10} corresponding to the frequency range of 0.2033 to 0.5000 Hz (4.9 to 2 h).

Given the remarkable difference of β_3 and β_{10} to their neighbouring spectral coefficients, it was decided to apply option 2.) for the non-Gaussian range. Hence, the low-frequency signal applies to β_3 (0.0006 to 0.0012 Hz, 1,720.6 to 842.8 h), the intermediate frequency signal applies to β_4 to β_9 (0.0012 to 0.2033 Hz, 842.8 to 4.9 h) and the high-frequency signal apples to β_{10} (0.2033 to 0.5000 Hz, 4.9 to 2 h).

This interpretation and concept was further investigated using the Morlet continuous wavelet transform (CWT). The aim is to identify the ‘nature’ of the signal – how these frequencies occur in time, and if there is some temporal pattern or seasonality, which may indicate a relationship to discharge dynamics of the aquifer.

The CWT plot is shown in Figure 6.8, illustrating the area of randomness (white noise) and the range for structured low frequency signal (1,720 to 842.8 h), the structured intermediate signal (842.8 to 4.9 h), and the structured high frequency signal (4.9 to 2 h).

The higher frequency range is clearly characterised by very short-lasting, high energy impulses. These patterns can be related to a physical meaning and have been assigned to the influence of rapid discharges related to conduits. While previously, autocorrelation and cross-correlation did not clearly indicate the existence of a fast-flow component, the results of the KarstMod reservoir model did suggest the existence of a very small fraction of fast-flow component. In addition, the hydrograph and chemograph of Ballindine suggests that low-conductivity water from the River Robe may be rapidly transmitted (via conduits) towards the spring causing sharp EC drops. Therefore, the pattern of discrete high frequencies seems plausible in this context.

The low frequency range shows a more continuous occurrence of moderate to high energies lasting for longer periods as compared to the higher frequency range. Per se, it does not seem clear

how to relate this frequency pattern to a physical meaning of certain aquifer heterogeneity. However, based on the previous assessments that highlight the low inertia of the system characterised as a matrix-domain aquifer type, this frequency range may be considered as fissured matrix contribution or 'physically meaningful' diffuse recharge proportion.
The intermediate frequency range shows rather continuous powers in time in its lower frequency boundary (<842.8 h), while powers are more discontinuous at the upper frequency boundary (>4.9 h). Hence, this segment may relate to a more fractured, yet still diffuse, flow component.

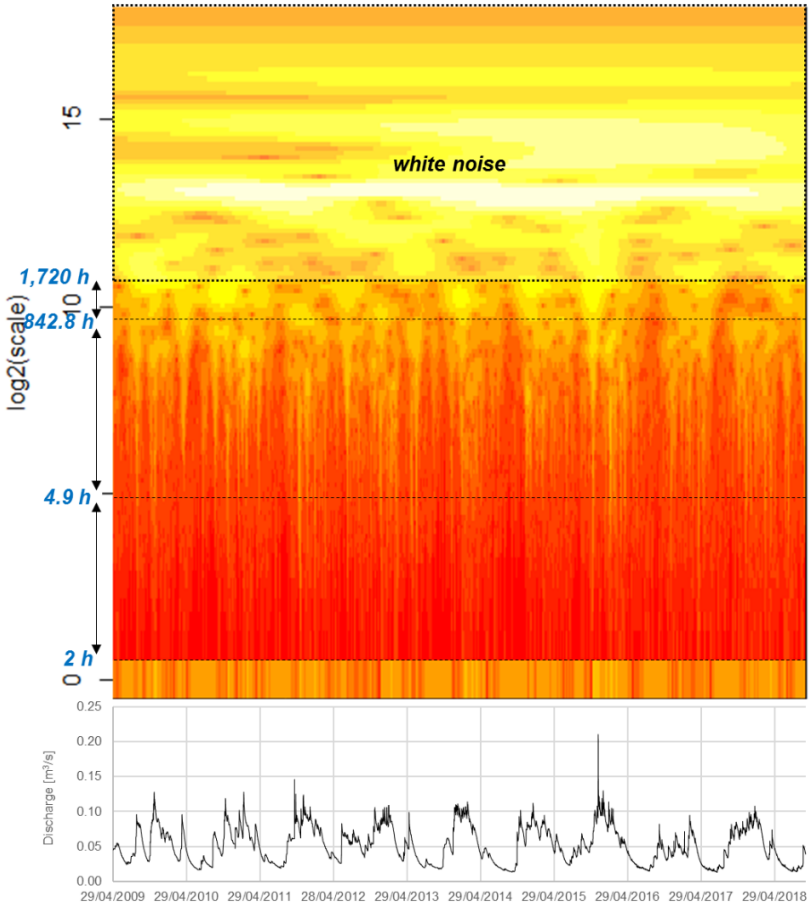

Figure 6.8: CWT of hourly discharge of Ballindine between 29 Apr 2009 and 01 Oct 2018.

In the previous two sections, a linear relationship between the River Robe and Ballindine spring was indicated as causality. The relationship between the Robe and Ballindine was examined in more detail in order to be able to draw conclusions on the driving forces of groundwater recharge of Ballindine spring. Hence, the discharge hydrograph of the Robe was also examined using noise analysis.
For the discharge signal of the Robe, eight significant change points were generated resulting in nine segments (Figure 6.9, Figure 6.10).

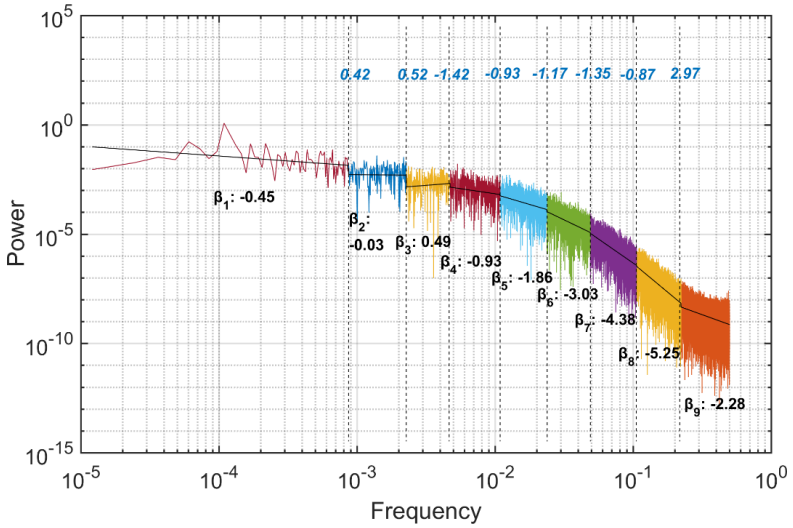

Figure 6.9: Frequencies (Hz) associated with hourly discharge of the River Robe between 19 Apr 2009 and 06 Jul 2018 and frequency segments following the Pettitt method with associated spectral exponents β with β_1 to β_9 (black) and changes between spectral exponents (blue).

The plots highlight that the low frequency segments (β_1 to β_4) relate to the random component. The remainder of the discharge signal is characterised by partially very low spectral coefficients in the higher frequency domain. The spectral coefficient β_5 (0.0109 to 0.0236 Hz, 91.6 to 42.3 h) characterises anti-persistent Brownian noise while β_9 characterises persistent Brownian noise and β_6 to β_8 characterises structured black noise.

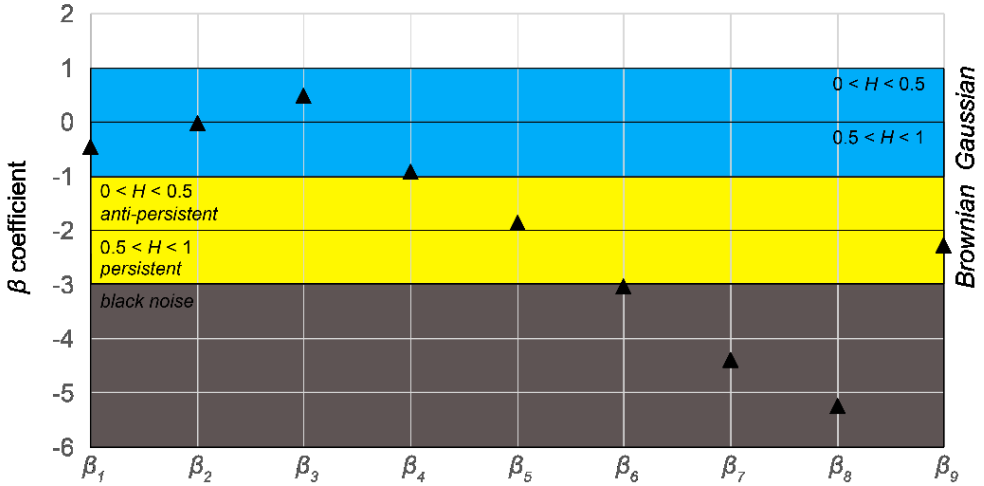

Figure 6.10: Spectral coefficients β_1 to β_9 for the River Robe, including the Hurst exponent and noise domain.

Comparing the results between the Robe and Ballindine shows that the spectral coefficients of the Robe cover a much wider range than the coefficients of Ballindine spring. Further, 4 out of 9

spectral coefficients of the Robe are associated with random noise as opposed to 2 out of 10 in case of Ballindine.
The difference between the signals suggests that if water of the Robe infiltrates into the aquifer of Ballindine spring, much of the input signal is transformed en route by the aquifer acting as a filter.

Until now, spectral analysis indicated the presence of physically relevant (or structured) frequency segments of two different time series. In a next step, common powers in the frequency-time domain are analysed in order to better illustrate cause-effect relationships in time, and further to evaluate the pattern of the high frequency signal (0.2033 to 0.5000 Hz, 4.9 to 2 h, <1 d), the intermediate frequency signal (0.0012 to 0.2033 Hz, 842.8 to 4.9 h, 35 to 24 d) and the low frequency signal (0.0006 to 0.0012 Hz, 1,720.6 to 842.8 h, 24 to 12 d) of Ballindine spring, in relation to the potential input variables in time.
The main part of the XWT plot illustrates the cross wavelet transform for hourly time series (Figure 6.11). On the bottom of the XWT plot, the spring discharge and rainfall amplitudes are plotted in time. Periods of high common powers exist throughout all frequencies in time being more pronounced and continuous >128 h. Below 128 h, the common high powers are more discontinuous. Below 16 h in the high frequency, the power changes periodically, whereas the periods of commonly high powers are rather associated with high flows of Ballindine spring, while during low flow the common power drops.

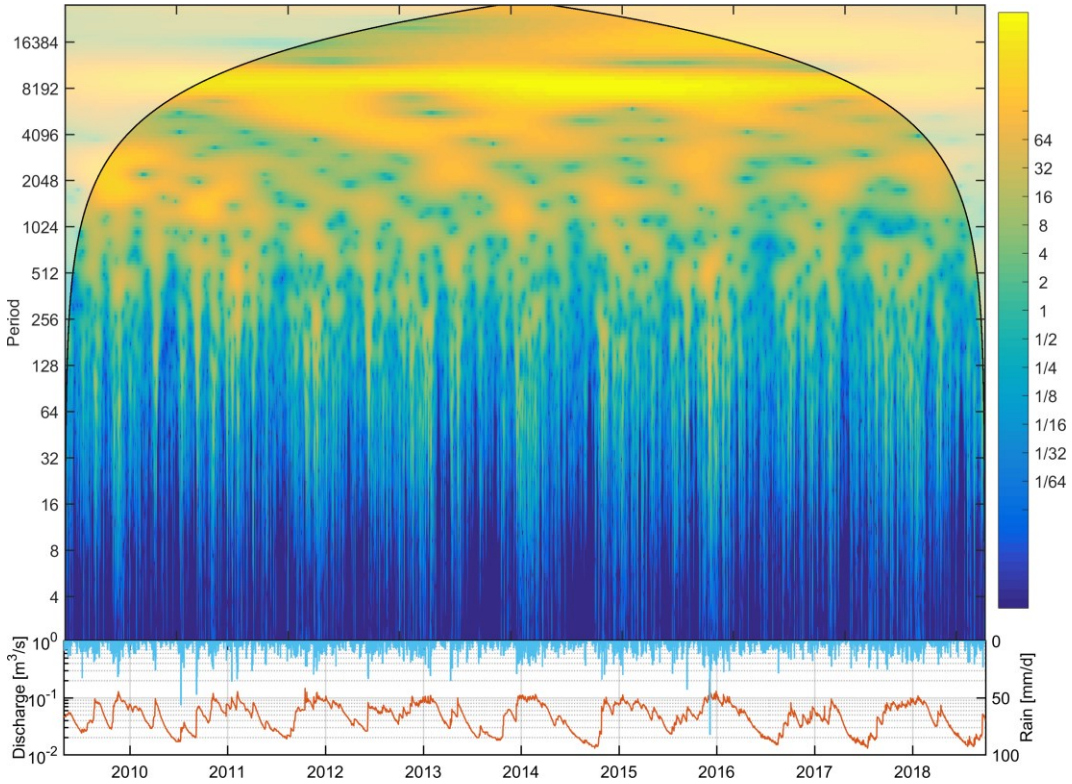

Figure 6.11: XWT plot of hourly rainfall and discharge of Ballindine spring between 29 Apr 2009 and 01 Oct 2018.

In a next step, wavelet coherence (WTC) was applied to quantify the powers in terms of correlation between Ballindine spring and rainfall (Figure 6.12). The plot shows the coherence along with phase angles indicated by the black arrows in areas of high coherence (Figure 6.11). For reference, the three previously identified frequencies at 4.9, 842.8 and 1,720 h were plotted distinguishing between a high, intermediate and low frequency range.

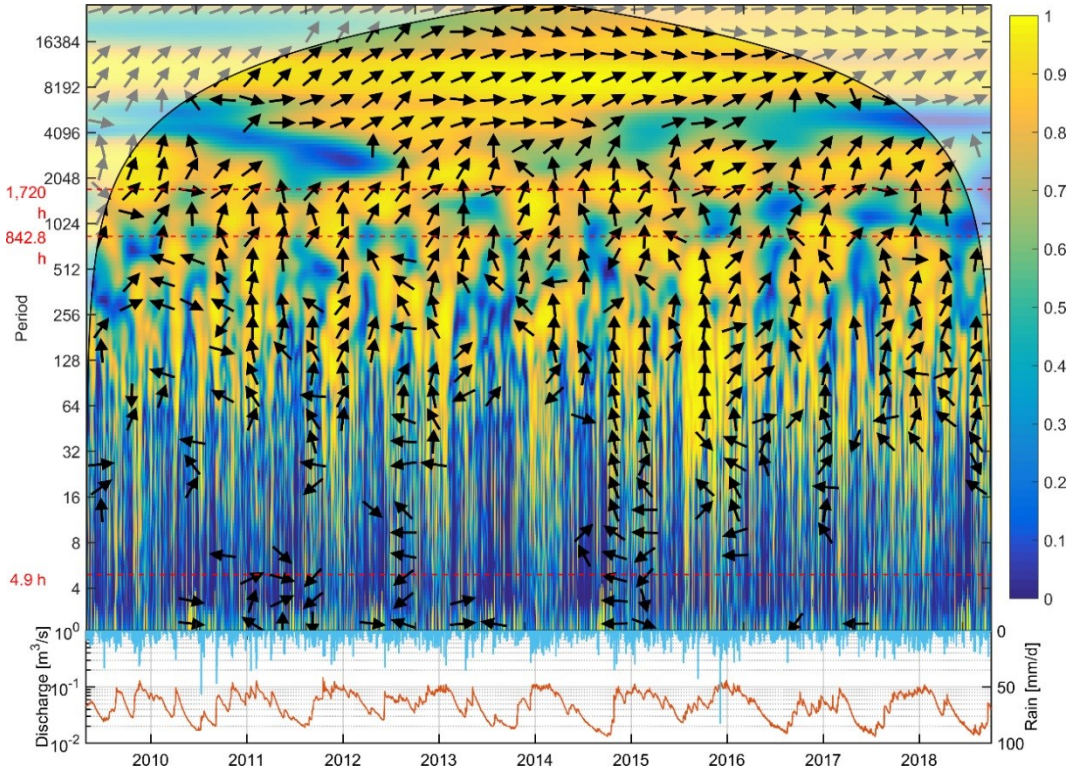

Figure 6.12: WTC plot of hourly rainfall and discharge of Ballindine spring between 29 Apr 2009 and 01 Oct 2018.

The WTC plot illustrates the strength of coherence between frequencies, ranging between 0 (dark blue) and 1 (yellow) at a given time (x-axis, h) and frequency (y-axis, y), where 1 indicates a linear relationship. In addition, for high coherence areas the black arrows illustrate the difference in phase ranging between 0 (linear relationship is direct), 180 (linear relationship is indirect) to 360º. Patterns of interest may follow either horizontal orientation at a given frequency, or vertical orientation at or during events. A consistent direction of arrows along the y-axis suggests causality between the input and output variable.

The coherence between Ballindine and rainfall (Figure 6.12) suggests a localised and discrete arrangement of patches of high coherence in time and frequency as opposed to a more general background of low coherence: where rain events and discharge surges coincide, a phase-lock behaviour results in high coherence.

Overall, three distinct areas of relationships can be identified: 1.) Below 256 h (10.7 d) fine strips of coherence interleaved with non-coherence areas represent the alternation of rainfall events (and

discharge peaks) and absence of rain and recession periods (even if short). Below 16 or 4.9 h there is no clear phase relationship as indicated by the varying arrow directions. However, there seems to be a rather continuous high coherence in the very high frequency range at 2 h, which relates to quick responses between rainfall events and discharge peaks; 2.) between ~842 and 1,720 h (35 and 72 d) high and low coherence areas alternate presumably linked an inter-annual or seasonal pattern. The phase angles generally point upwards and increasingly towards the right with increasing period indicating a decreasing time lag; and 3.) above 8,000 h (333 d) the coherence is very high throughout the entire period being related to the annual or bi-annual cyclicity. The phase angles are mostly to the right (in-phase) where the time lag is negligible.

The lack of coherence for the low frequencies may be explained by a time delay of the aquifer dynamics compared to the input dynamics of rainfall. Hence, the low coherence within high frequencies suggests that either the impact of rainfall is low, and/or the rainfall signal is largely transformed as a result of the filtering effect due to low karstification of the aquifer. In terms of the higher frequencies (e.g. <4.9 h), high coherence may be expected as a result of rapid and unfiltered transfer of the rainfall signal towards the spring.

Next, the XWT was applied between the hourly discharge time series of the Robe and Ballindine (Figure 6.13).

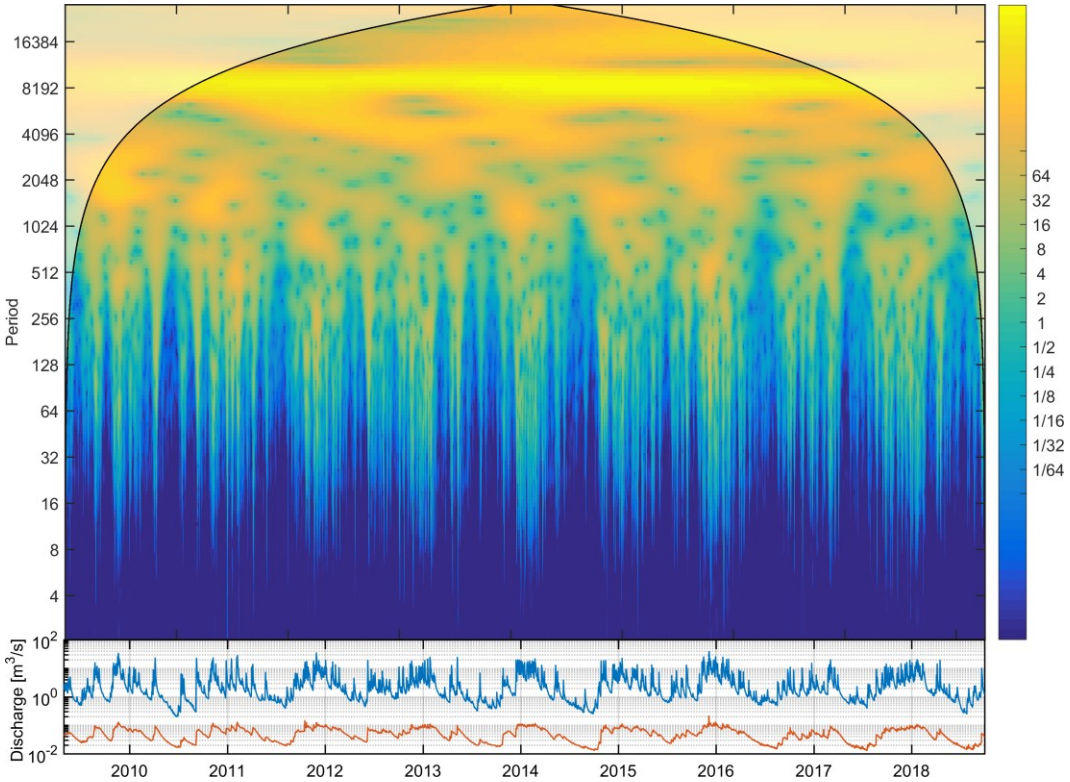

Figure 6.13: XWT plot of hourly discharge of the River Robe and Ballindine spring between 29 Apr 2009 and 01 Oct 2018.

Similar to Figure 6.11, common high powers are more pronounced and continuous in time for frequencies >128 h. Below 128 h, it seems that periods of low common power are more continuous while at the same time periods of high common power are also more continuous in time. In fact, the periods of low common power are highly limited in time by periods of relatively low discharge of the Robe. Below a frequency of 5 h, there seems to be almost no common power between the Robe and Ballindine spring.
Because of the discrete periods of continuity and discontinuity in common high power, it is believed that the pattern follows a systematic process suspected to be the interaction between the Robe and Ballindine spring, which seems to vary in time according to season/discharge/water level of the River Robe.

The WTC between Ballindine spring and the River Robe is shown in Figure 6.14, along with the plotted phase angles. Again, the three levels of frequencies distinguishing between the low, intermediate and high frequency range are plotted.

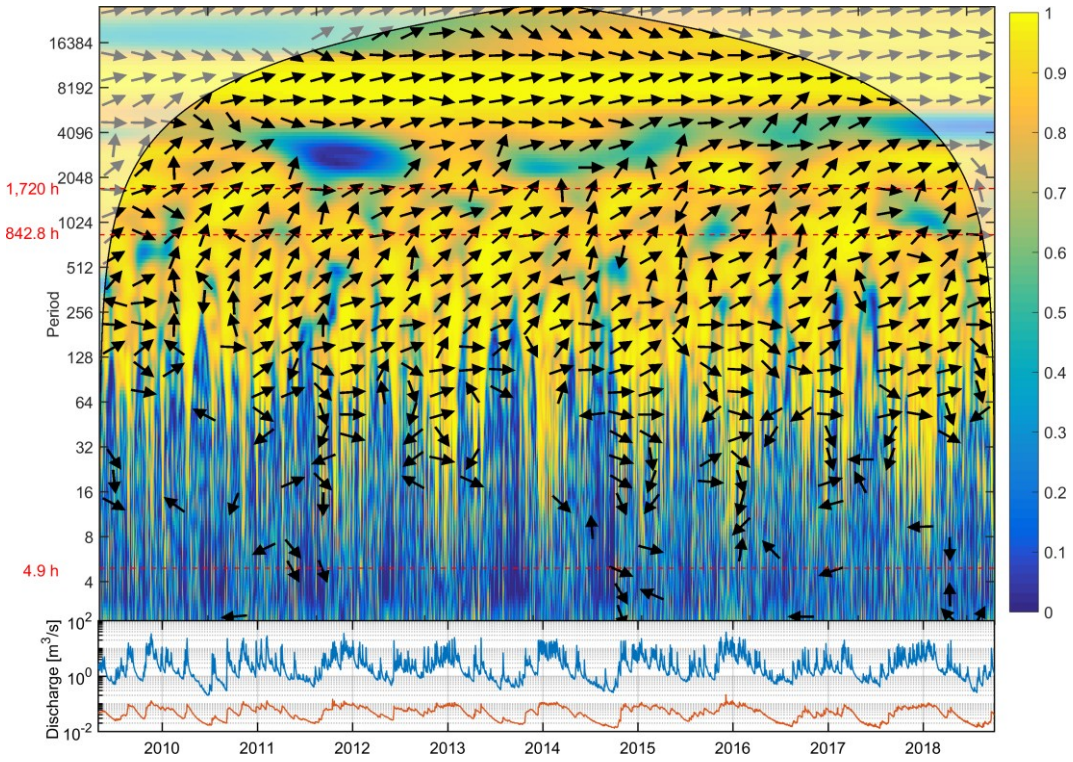

Figure 6.14: WTC plot of hourly discharge of the Robe and Ballindine spring between 29 Apr 2009 and 01 Oct 2018.

The plot shows a strikingly high coherence throughout frequency and time. Yet, strong discontinuities in time are visible for frequencies of 2,048 to 4,096 h (83 to 170 d). These exceptions are very interesting as it is also present in the coherence plot between rainfall and Ballindine (Figure 6.12). These low coherences indicate a deviation of linearity between input and output, which is highest

during the rainy period of 2012. The frequency range relates to a seasonality, and it is interpreted that the power of spring discharge may be relatively low as compared to the power of the river discharge for the given spectrum. A reason for that may be a physical limitation (transmissivity/effective porosity) of the aquifer, limiting the overall spring discharge, while such limitation is not given for the river discharge. Other possible or additional reasons may be a temporal clogging of filling of conduits as well as the impact of the drainage channels cutting into the topography of the catchment: given a high water level in the aquifer, the top level of the aquifer may be drained directly by the drainage channels, hence, cutting off flow to the spring. Both, or one of these reasons may result in the low coherence at the given spectrum and time.
On the annual/bi-annual cyclicity (>8,000 h), the coherence is continuously high, and the frequencies are in phase, which suggests an obvious common annual /bi-annual periodicity.
Between 8,000 and 128 h, the coherence is still very high, only intersected by locally low coherence. The phase angles range between 0º (in-phase) and 90º (upwards) showing generally a very consistent pattern which is an argument for causality between the frequencies/time series.
The high degree of coherence above ~128 h suggests that the River Robe and Ballindine spring exhibit very similar dynamics, also at low discharge rates. The high coherence may be the result of a similar response to input variables, yet, the consistency of phase angles suggests causality, hence, clear SW-GW interaction.
Below frequencies of 128 h, the pattern indicates periods of strong coherence down to 8/16 h during periods of high flow alternating with periods of strong coherence down to 32/64 h during periods of low flow. Despite the occurrence of high frequency discharge surges of the River Robe during low flow periods, the signal is not transposed towards the spring, and thence, the coherence remains low. Therefore, this seasonal alternation of coherence between 8/16 h and 32/64 h is interpreted as a change in the impact regime that the river exhibits onto the spring. This may be explained by a threshold effect, previously discussed in Section ‘5.1.3.2. Tracer test 30 Jan 2019’.

6.3.2. Manorhamilton

The power spectrum of the entire hourly rainfall at MH3 was decomposed yielding six significant breakpoints and four spectral coefficients β (Figure 6.15). Four spectral coefficients are >-1 and hence confirm the randomness of the signal as they are associated with the Gaussian domain. However, to exponents (β_4 and β_5) are <-1 between 8 and 35 h associated with anti-persistent Brownian noise. It remains unclear where the structure originates from. Yet, the spectral coefficient (β_{total}) of the entire power spectrum is -0.78 and can be considered as random. Therefore, the transformation of the random rainfall signal towards a partially structured spring discharge signal must be related to the aquifer.

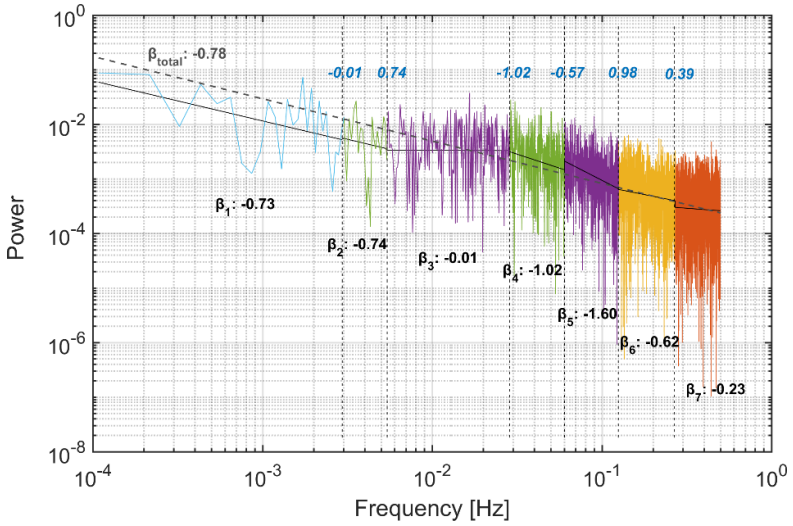

Figure 6.15: Frequencies (Hz) associated with hourly rainfall at Manorhamilton between 15 Dec 2017 and 04 Jun 2019 and frequency segments following the Pettitt method with associated spectral exponents β with β_1 to β_7 (black) and changes between spectral exponents (blue).

The discharge time series of Manorhamilton spring provide by the EPA is interrupted by several periods of missing data.

Firstly, the analysis was limited to the short period of the latest discharge data for which there is also hourly rainfall available, and which covers the calibration and validation period of the numerical pipe network model ('7.2. Manorhamilton') namely between 29 Jun 2017 and 04 Jun 2019 (Figure 6.16).

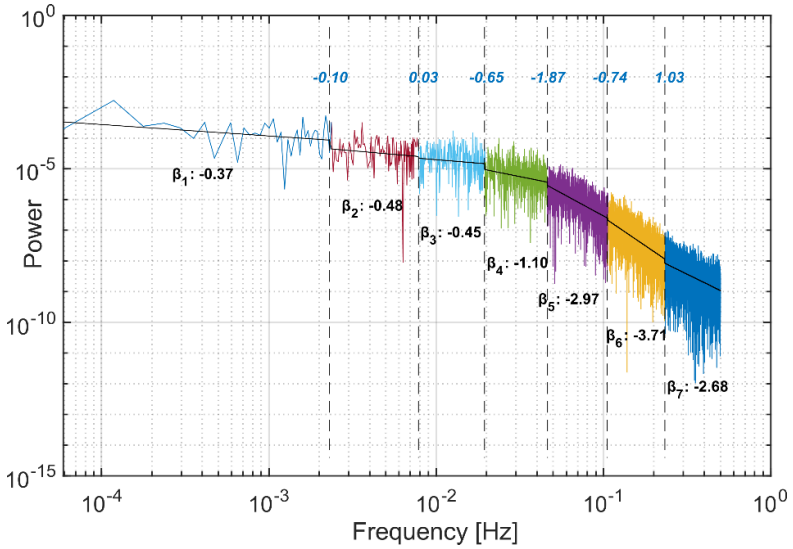

Figure 6.16: Frequencies (Hz) associated with hourly discharge of Manorhamilton between 29 Jun 2017 and 04 Jun 2019 and frequency segments following the Pettitt method with associated spectral exponents β with β_1 to β_7 (black) and changes between spectral exponents (blue).

The Pettitt test yields six significant breakpoints, sub-dividing the power spectrum into 7 segments with β coefficients ranging between -0.37 and -3.71 (Figure 6.17).

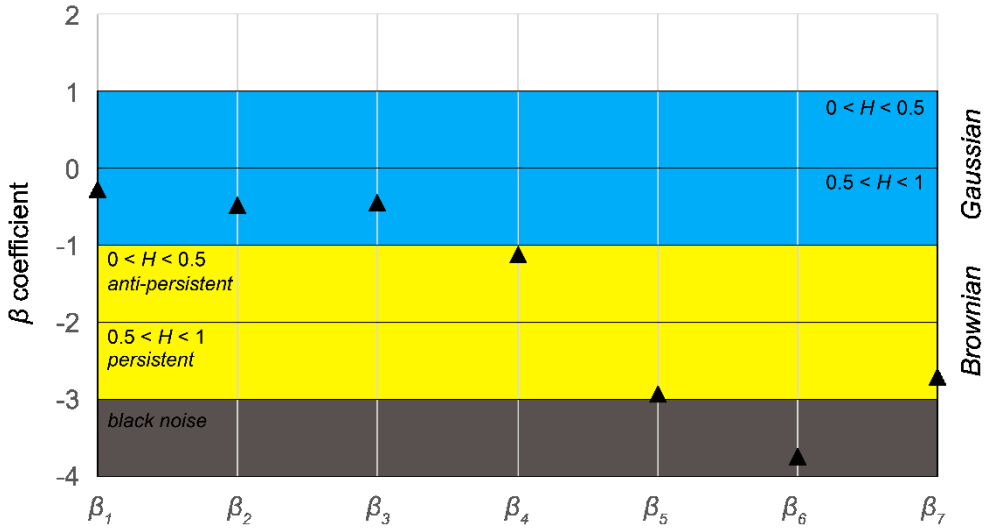

Figure 6.17: Spectral coefficients β_1 to β_7 for Manorhamilton spring between 29 Jun 2017 and 04 Jun 2019, including the Hurst exponent and noise domain.

The course of the frequencies is dramatic with drastically changing slopes and powers. The spectral coefficients β_1 to β_3 relate to the Gaussian domain (stochastic and non-structured component) with associated frequencies ≤0.0196 Hz (≥51.1 h). Anti-persistent Brownian noise is associated with β_4 corresponding to a frequency range of 0.0196 to 0.046 Hz (51.1 to 21.7 h), while persistent Brownian noise corresponds to β_5 (0.046 to 0.1061 Hz, 21.7 to 9.4 h) and β_7 (0.2322 to 0.500 Hz, 4.3 to 2 h). The lowest spectral coefficient β_6 reaches -3.71 and is associated with black noise, which corresponds to a frequency range of 0.1060 to 0.2322 Hz (9.4 to 4.3 h).

Next, the long-term hourly discharge time series of Manorhamilton was analysed between 20 Apr 2009 and 01 Oct 2018 with the power spectrum (Figure 6.18) yielding 8 significant breakpoints. The spectral coefficients β range between 0.19 and -3.97 (Figure 6.19). The spectral coefficients β_1 to β_4 are clustered around 0 and are therefore considered as random components with associated frequencies ≤0.0130 Hz (≥77.2 h). The coefficients β_5 and β_6 are associated with anti-persistent Brownian noise with associated frequencies 0.0130 to 0.0517 Hz (77.2 to 19.4 h), while β_9 relates to persistent Brownian noise (0.2246 to 0.500 Hz (4.5 to 2 h). The coefficients β_7 and β_8 resemble structured black noise with associated frequencies 0.0517 to 0.2246 Hz (19.4 to 4.5 h). Interestingly, there is a large difference between β_6 and β_7 of -1.56, and between β_8 and β_9 of -1.18, clearly separating the spectral coefficients between Brownian noise and black noise.

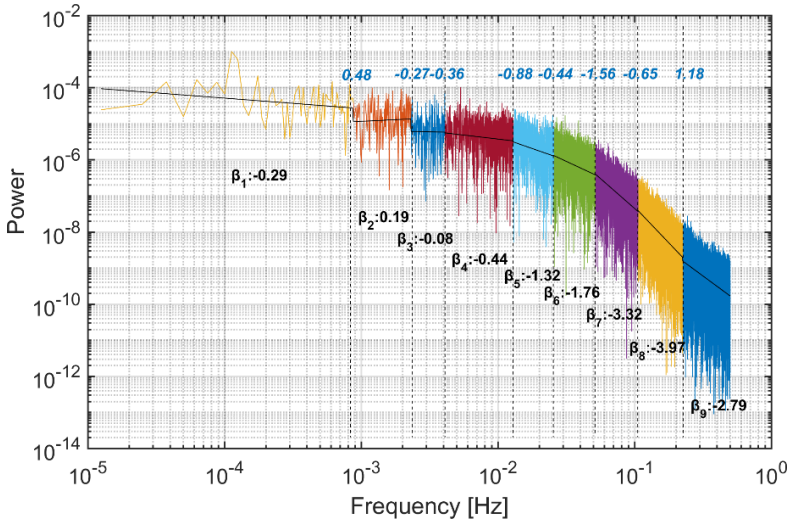

Figure 6.18: Frequencies (Hz) associated with hourly discharge of Manorhamilton between 30 Apr 2009 and 01 Oct 2018 and frequency segments following the Pettitt method with associated spectral exponents β with β_1 to β_9 (black) and changes between spectral exponents (blue).

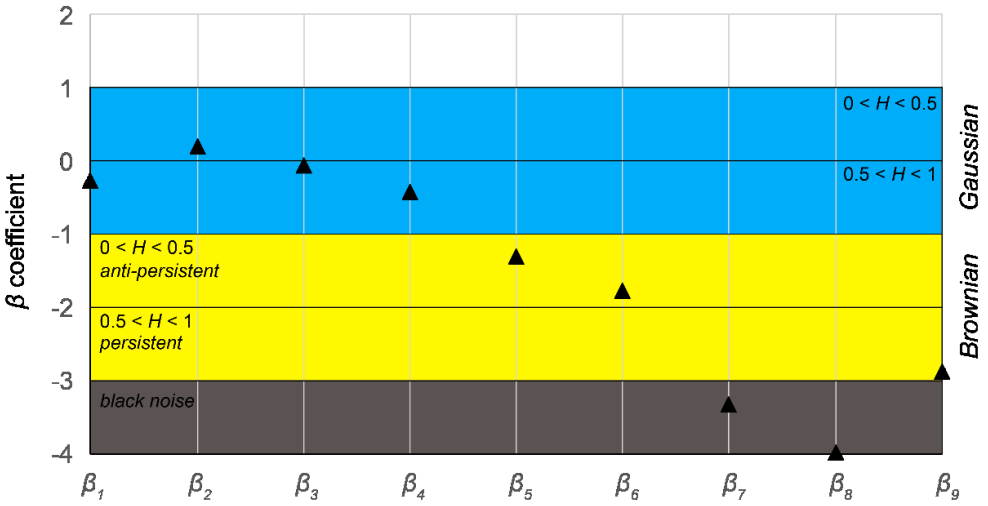

Figure 6.19: Spectral coefficients β_1 to β_9 for Manorhamilton spring between 30 Apr 2009 and 01 Oct 2018, including the Hurst exponent and noise domain.

The interpretation of the spectral coefficients of Figure 6.18 and Figure 6.19 suggests four distinct segments: a) a random noise segment (β_1 to β_4) and associated frequencies <0.0130 Hz (>77.2 h); b) a low frequency segment of anti-persistent Brownian noise (β_5 to β_6) and associated frequencies 0.0130 to 0.0517 Hz (77.2 to 19.4 h); c) an intermediate frequency segment (β_7 to β_8) and associated frequencies 0.0517 to 0.2246 Hz (19.4 to 4.5 h); and a high frequency segment (β_9) and associated frequencies 0.2246 to 0.5 Hz (4.5 to 2 h).

This interpretation applies similarly to the short analysis for the period 29 Jun 2017 and 04 Jun 2019. Accordingly, the random frequency segment corresponds to β_1 to β_3 (≤0.0196 Hz, ≥51.1 h),

the low frequency segment is assigned to β_4 (0.0196 to 0.0460 Hz, 51.1 to 21.7 h), the intermediate frequency segment relates to β_5 to β_6 (0.0460 to 0.2322 Hz, 21.7 to 4.3 h) while the high frequency segment relates to β_7 (0.2322 to 0.5 Hz, 4.3 to 2 h). Although β_5 (-2.97) corresponds to persistent Brownian noise, it is very close to black noise, and hence, it was decided to match it with the black noise of β_6.

Next, the period 29 Jun 2017 to 04 Jun 2019 was interpreted using the CWT approach (Figure 6.20). The plot highlights again the frequency ranges previously assigned to random noise, the low, intermediate and high frequency.

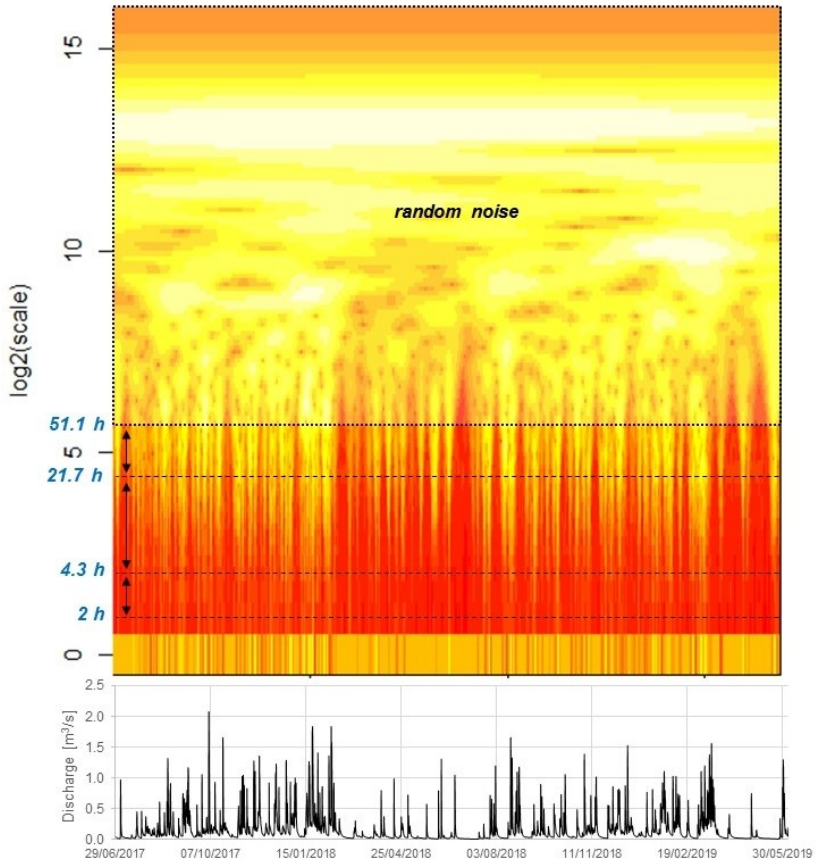

Figure 6.20: CWT and hourly discharge of Manorhamilton between 29 Jun 2017 and 04 Jun 2019.

A large proportion of the plot is associated with random noise (>51.1 h). The high and intermediate frequency ranges (21.7 to 2 h) show alternating periods of high and low energies across the spectrum. Localised high energies relate do discharge peaks, and hence, conduit discharge of the aquifer.

Within the low frequency range (51.1 to 21.7 h), the periods of high energies are more continuous in time with the pattern suggesting a systematic behaviour. Generally, power is visible within this spectrum throughout the period of analysis, yet, an exception occurs during a period of relatively low discharge (≤0.015 m^3/s) between 29 Jun to 01 Jul 2018. Again, the absence of power may be

an indicator that the associated flow components are not visible within the discharge signal at this period, with the tentative conclusion that no contribution from the related permeability domain occurring.

Next, the common power in the time-frequency space is analysed between rainfall and spring discharge using cross wavelet transform (XWT) applied on the period 15 Dec 2017 to 04 Jun 2019 (during which hourly rainfall was available with no data gap). The XWT plot is again compared to the rainfall and spring discharge time series below (Figure 6.21). Further, the three frequencies 51.1, 21.7 and 4.3 h are highlighted, separating the three frequency segments.

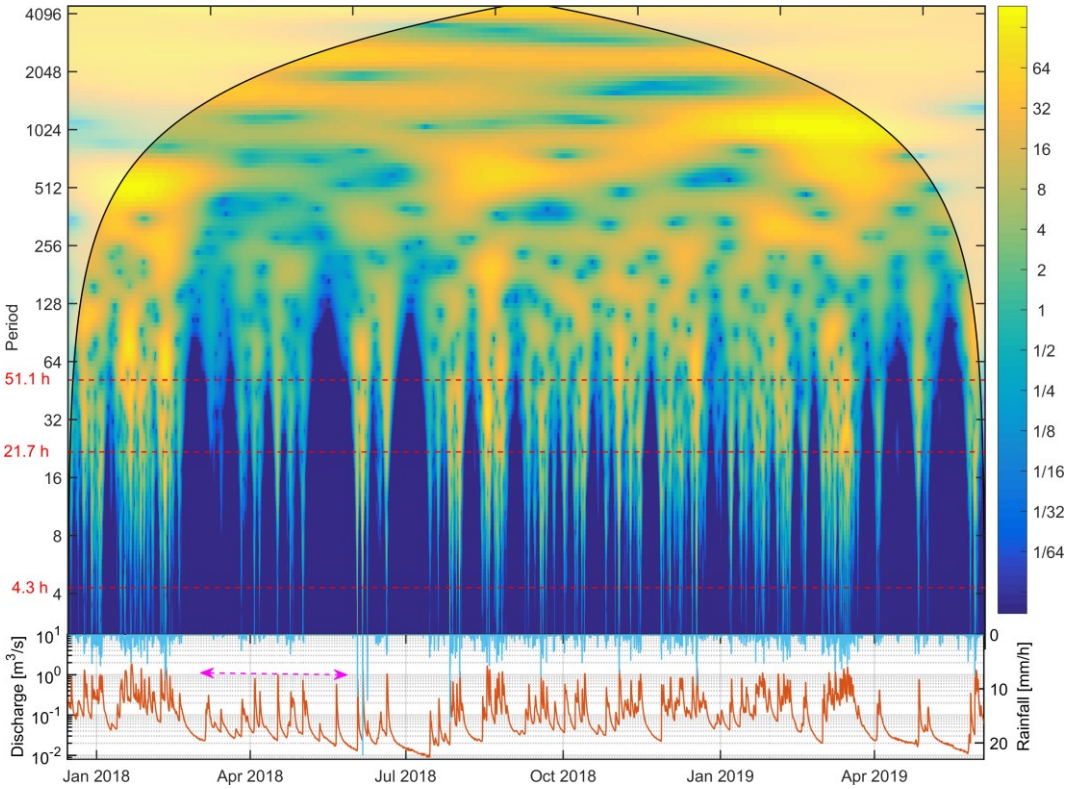

Figure 6.21: XWT plot of hourly rainfall and discharge of Manorhamilton spring between 15 Dec 2017 and 04 Jun 2019. The pink double arrow indicates the period of potentially missing recorded rainfall.

Strikingly, common powers vary throughout the spectrum and in time. The high frequency range (<4.3 h) shows highly discontinuous and very localised and short periods of high power across the entire spectrum. These localised powers correlate very well with rainfall events. Strangely though, between 05 Mar and 02 Jun 2018 (the period highlighted by pink double arrow), the observed discharge does not correspond to high powers. The reason for this seems to be missing rainfall, as some discharge peaks (e.g. 21 May) are not accompanied by any recorded rainfall. Hence, it seems that the measurement of rainfall was faulty during this period.

The interpretation of the results therefore focusses on the period before 05 Mar 2018 and after 02 Jun 2018. Outside of this period, the power remains very localised and discontinuous, indicating that this frequency range represents very fast and short-lasting responding dynamics. During recessions, no power is exhibited in this range. Thus, clearly this high frequency range can be attributed to conduit flow.
The intermediate and low frequency range (51.1 to 4.3 h) shows more continuous periods of high common powers with rainfall. However, because of the alternating low and high powers, also these frequency ranges seem to be directly impacted by rainfall events. Hence, the cross wavelet power indicates that this range is rather associated with relatively quick flow dynamics, as opposed to, for example, a long-term or seasonal flow component as in the case of a low flow component.

Finally, the coherence of both time series, hence, the cross correlation of frequencies in time, is analysed using wavelet coherence (WTC). The result is plotted in Figure 6.22 along with the phase angles, the frequency range boundaries (51.1, 21.7 and 4.3 h) and the observed spring discharge and rainfall.

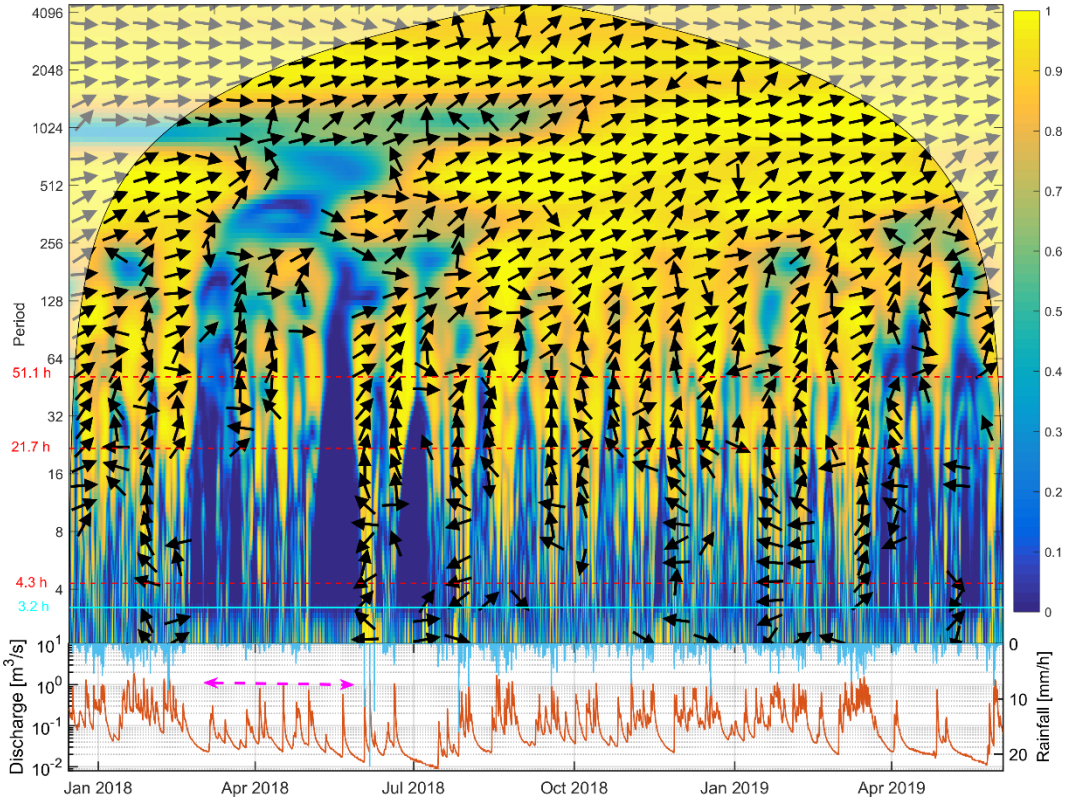

Figure 6.22: WTC plot of hourly rainfall and discharge of Manorhamilton spring between 15 Dec 2017 and 04 Jun 2019. The pink double arrow indicates the period of potentially missing recorded rainfall.

Outside the period of unreliable rainfall (05 Mar to 02 Jun 2018), the coherence is generally high with the plot indicating a clear input-output relationship.
Above 51.1 h, the phase angles are mostly in-phase (0º). For the low and intermediate frequency range (51.1 to 4.3 h), the phase angles are generally 90º upwards, while within the high frequency range (<4.3 h), the phase angles are out of phase (180º). Within the high frequency range, the coherence is relatively high, especially below 3.2 h (cyan line), indicating actually higher consistency in time than in the intermediate frequency range. This pattern is interpreted as the potentially quickest response of the spring to rainfall.

6.3.3. Summary from spectral and noise analysis

Noise analysis of the Fourier spectra was applied to relate frequencies of rainfall and discharge time series in terms of randomness and structure. This showed that the rainfall signals exhibited complete randomness. Hence, such rainfall time series can be used to assess the filtering effect of the aquifer between its input (rainfall) and output (discharge).

In the case of Ballindine, such input-output relationship is complicated due to the role of the River Robe as an additional input time series. In fact, the discharge of the Robe shows a partly structured signal associated within black noise. The discharge signal of Ballindine, in turn, shows a less structured signal, exclusively associated to the Gaussian and Brownian domain. The Brownian domain was sub-divided into: a) low, b) intermediate and c) high frequency segments, which were interpreted to correspond to a) very diffuse, b) diffuse, and c) conduit contributions, respectively.
With regard to input-output relationships, the XWT between rainfall and Ballindine spring suggests common high powers throughout all frequencies during periods of high discharge of the spring, although the WTC and the corresponding phase angles suggest an unclear cause-effect relationship. Further, a relatively low coherence in the high frequency range suggests the potentially strong filtering effect of the aquifer.
In turn, the XWT between the Robe and Ballindine shows discrete periods of continuity and discontinuity in common high power following a systematic pattern. This pattern indicates the interaction between the Robe and Ballindine spring, which seems to vary in time according to season/discharge. A generally very high coherence and constant phase angles are strong indicators for a cause-effect relationship. Moreover, low coherence during low flow periods suggests that the river doesn't exhibit a strong impact on Ballindine during these periods. The observation of low coherence during flood events occurring during generally low flow periods was interpreted as threshold water level, below which the River Robe does not significantly impact on Ballindine spring.

The frequency and noise analysis of Manorhamilton spring suggests that the spectrum can be subdivided into four segments: a) a random noise component, b) a low frequency segment of anti-persistent Brownian noise, c) an intermediate frequency segment of black noise and d) a high

frequency segment of persistent Brownian noise. All non-Gaussian frequency components show partly low powers during periods of recessions, and hence, it seems that a diffuse slow-flow component could not be identified, as it might be related to lower frequencies.
With regard to the input-output relationship, XWT suggests highly localised and discontinuous powers in time across all frequencies. Yet, the intermediate frequency range shows more continuous powers in time than the high frequency range, which again was interpreted as a quick responding system. This interpretation was confirmed by the WTC. Further, relatively high coherence is visible for the frequency range 3.2 to 2 h, which may represent the fastest flow response of the spring towards rainfall.

Finally, Figure 6.23 shows a comparison between one year WTC plots between rainfall and Ballindine spring (Figure 6.23a), discharge of the Robe River and Ballindine spring (Figure 6.23b) and between rainfall and Manorhamilton spring (Figure 6.23c).
The three plots suggest the highest and most continuous coherence in time and frequency occurs between the Robe and Ballindine spring. This coherence is similar to the coherence between rainfall and Manorhamilton spring. Hence, this high coherence confirms again an input-output relationship between the river and Ballindine spring. Yet, while for single events significant coherence can be observed between rainfall and the Manorhamilton spring across the entire upper frequency range (<128 h), such continuous high coherence does not apply for the relationship between rainfall and Ballindine spring for the upper frequency range. Instead, the coherence is relatively low below 64 or 128 h, presumably linked to a water level in the River Robe below a threshold level.

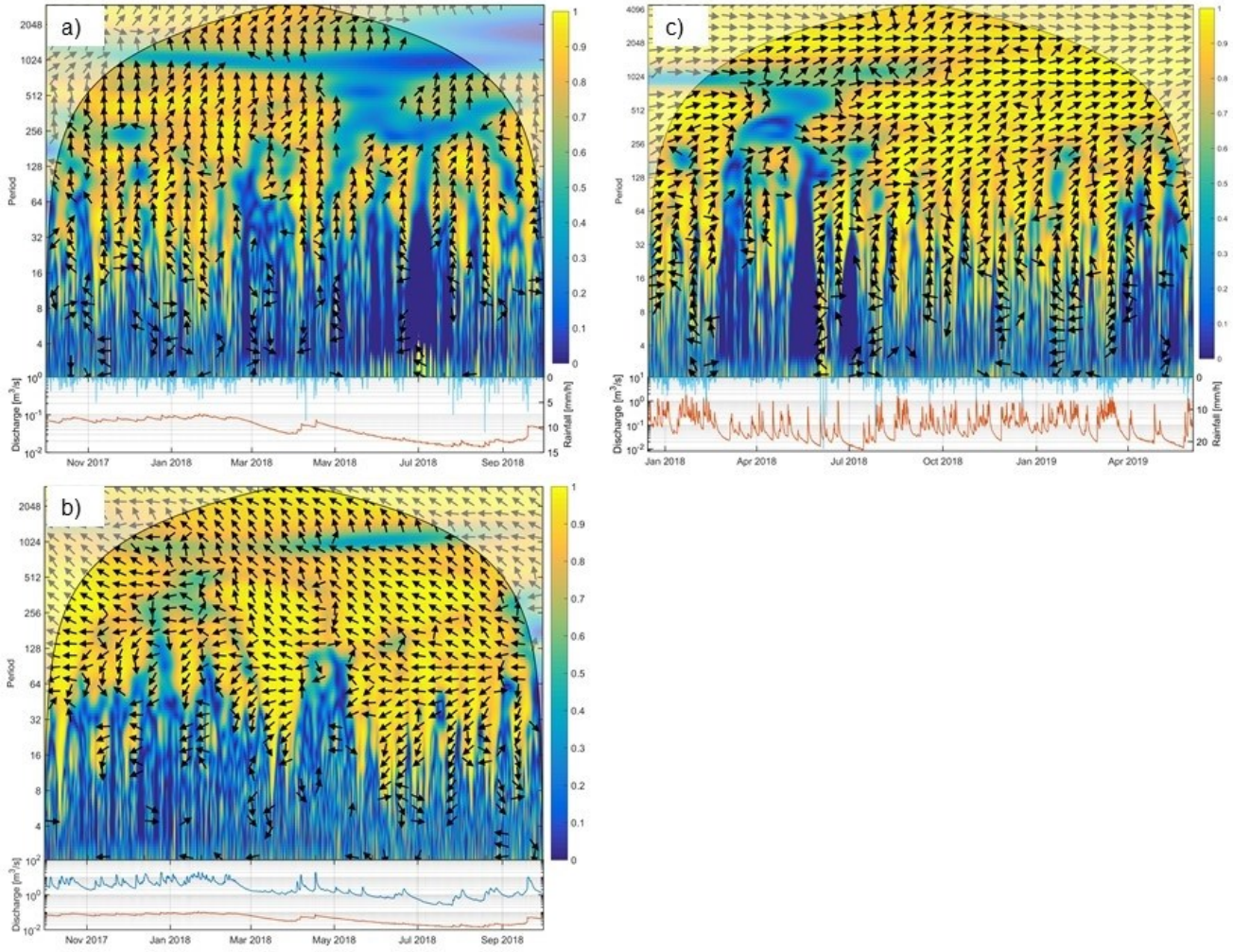

Figure 6.23: Comparison of WTC between a) Ballindine spring and rainfall; b) Ballindine spring and the River Robe; and c) Manorhamilton spring and rainfall, limited to one year to facilitate comparisons.

6.4. DWT

The previous section showed that certain frequency ranges of discharge time series may contain 'physically meaningful' information linked to groundwater recharge and flow dynamics as result of the heterogeneity of the respective aquifers.
Following on, this section aims to apply discrete wavelet transforms (DWT) to decompose the time series into timescale domains according to previously identified physically meaningful frequency ranges. A DWT is able to decompose a time-amplitude signal into time-frequency components (details, D, and the trend, S). Hence, the individual details can be linked to the previously identified frequency to analyse the occurrence of powers in time.
Further, DWT is used to 'construct' discharge time series that relate to distinct flow components (related to specific frequency ranges). The question, therefore, is whether certain frequency components can be linked to distinct flow components.
It should be noted that given there is no specific guideline as to which discrete wavelets to use in hydrology, it was decided to test two different orders of Daubechies wavelets (db10 and db20) in order to broadly cover the range of the existing Daubechies wavelets db4 to db20.

6.4.1. Ballindine

Decomposition of the time-amplitude signal of spring discharges into discrete frequencies was carried out using the db10 and db20 wavelets applied on hourly discharge time series between 2009 and 2018. This results in 16 levels (details, D) and the residual or trend (S). These 16 details and their frequencies are then associated with the spectral coefficients β and their upper and lower frequency boundary (established in Section '6.3.1. Ballindine'), displayed in Table 6.1. For example, β_1 is associated with the details 12 to 16 and S of db10, because these details cover the frequency range of β_1 which is spans from 1.21E-05 to 1.70E-04.
Table 6.1 further shows the domain and noise in which each detail lies. Accordingly, D11 to D16 can be considered stochastic while D1 to D10 lie within the domain of Brownian noise.

Table 6.1: 16 details of db10, db20 and the residual S, their frequencies and associated spectral exponents β of Ballindine. The coloured shade in the column β indicates the noise: blue = Gaussian, yellow = Brownian.

Detail	db10			db20		
	Frequency		β	Frequency		β
	Hz [s^{-1}]	Time [h]		Hz [s^{-1}]	Time [h]	
1	3.42E-01	2.9	10	2.96E-01	3.4	10
2	1.53E-01	6.5	9	1.37E-01	7.3	9
3	7.37E-02	13.6	8	7.66E-02	13.1	8
4	4.18E-02	23.9	7	4.18E-02	23.9	7
5	1.77E-02	56.5	7	1.77E-02	56.5	7
6	9.31E-03	107.4	6	8.60E-03	116.3	6

7	4.77E-03	209.6	5	4.77E-03	209.6	5
8	2.18E-03	458.8	4	2.18E-03	458.8	4
9	1.16E-03	860.3	3	1.05E-03	949.3	3
10	5.81E-04	1,720.6	3	5.45E-04	1,835.4	2
11	2.42E-04	4,129.6	2	3.03E-04	3,303.6	2
12	1.21E-04	8,259.1	1	1.33E-04	7,508.3	1
13	1.09E-04	9,176.8	1	1.09E-04	9,176.8	1
14	3.63E-05	27,530.3	1	3.63E-05	27,530.3	1
15	2.42E-05	41,295.5	1	2.42E-05	41,295.5	1
16	1.21E-05	82,591.0	1	1.21E-05	82,591.0	1
S	1.21E-05	82,591.0	1	1.24E-05	80,512.0	1

Previously, three distinct (and presumably physically meaningful) frequency ranges were identified, a) a low-frequency signal β_3; b) an intermediate frequency signal β_4 to β_9; and c) a high-frequency signal β_{10}. With regard to these frequency ranges, the individual details D associated with these frequency ranges were combined and plotted with the residual S above the hourly discharge of Ballindine spring and the River Robe (Figure 6.24). The aim of this plot is to indicate the powers of the combined details in time in relation to the discharge dynamics.

Details 11 to 16 relate to the random component (Gaussian domain), largely fluctuating in time. Above this, details 9 and 10 (structured low frequency segment) show also their associated flow throughout the entire period. In fact, the flow is very consistent in time, only with smaller oscillations during the seasonal low flows. The details 2 to 8 (structured intermediate frequency segment) are discontinuous in time, exhibiting no contribution during the seasonal low flows. Interestingly, high oscillations correspond to the periods of high flows of the River Robe. And finally, detail 1 shows only very localised flows associated with this high frequency component.

In summary, the combined details related to the three frequency segments show distinct behaviours: the high frequency segment related to conduit discharge shows highly localised flows in time; the details related to the intermediate frequency range exhibit different levels of oscillations in time, while being correlated to the high flows of the River Robe; and the details related to the low frequency segment seem to be continuous in time and power.

Further to the above analysis, the cumulative summation of all details D and the residual S yield the original observed discharge time series. As presented previously by different authors, the DWTs can be used to build a signal that resembles different flow components. For example, a signal representing the fissured matrix domain would be characterised by the absence of high frequency components that would resemble conduit discharge.

The cumulative summation of the trend S together with the details starting at the lowest detail yields a designated discharge signal. For example, the summation of the trend S, the random component (D11 to D16), and the frequencies D9 and D10 related to β_3 may yield a (partly) structured slow-flow component resembling long lasting processes, perhaps related to a fissured matrix domain, as shown in Figure 6.25.

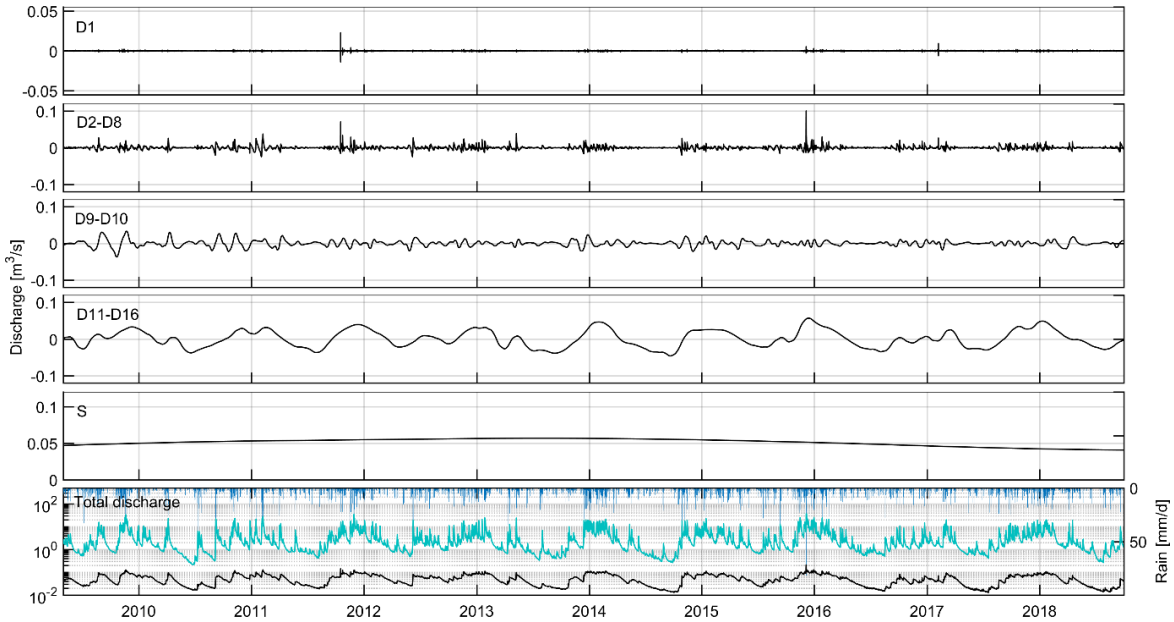

Figure 6.24: Hourly discharge of the River Robe (green) and Ballindine spring (black) and daily rainfall (bottom plot) and combined wavelet details (D) of Ballindine spring using db10: D11 to D16 (β_1 to β_2), D9 to D10 (β_3), D2 to D8 (β_4 to β_9) and D1 (β_{10}) and the trend S.

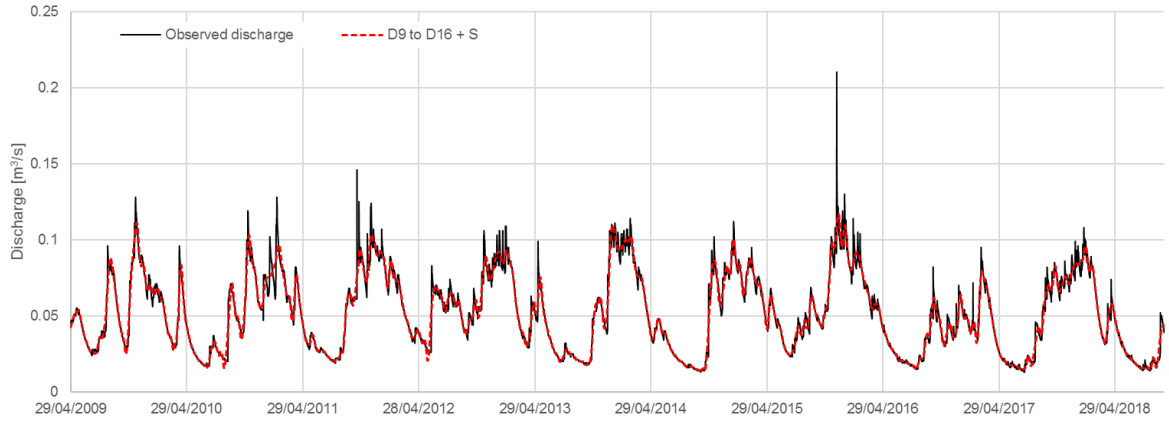

Figure 6.25: Low frequency signal (detail 9 to 16 +S) of db10 for discharge of Ballindine spring between 2009 and 2018.

The composed signal shows a relatively high proportion of flow. In fact, it is very similar to observed discharge, yet, with reduced maximum peaks. The related recessions of the constructed low-frequency signal seem to clearly exceed the recession of the LFC previously established using the MRC (Section '5.1.1. Master recession curve analysis').

During the previous assessments (reservoir modelling, ACF, CCF) it became evident that the conduit contribution is a relatively small fraction of the total discharge. Accordingly, it seems that realistically only a relatively small share presumed to be associated with the direct conduit discharge is missing from the overall discharge time series in Figure 6.24, which can be seen in the composed discharge time series for S and D9 to D16 illustrated in Figure 6.25.

6.4.2. Manorhamilton

Decomposition of the time-amplitude signal of spring discharges into discrete frequencies was carried out using the db10 and db20 wavelets applied on hourly discharge time series between 2017 and 2019. This results in 14 details (D) and the residual (S).
These 14 details and their frequencies are then associated with the spectral coefficients β and their upper and lower frequency boundary (established in Section '6.3.2. Manorhamilton'), displayed in Table 6.2.

Table 6.2: 15 details of db10, db20 and the residual S, their frequencies and associated spectral exponents β for the period 2017 to 2019. The coloured shade in the column β indicates the noise: blue = Gaussian, yellow = Brownian, black = black noise.

Detail	db10			db20		
	Frequency		β	Frequency		β
	Hz [s^{-1}]	Time [h]		Hz [s^{-1}]	Time [h]	
1	2.98E-01	3.4	7	2.50E-01	4.0	7
2	1.67E-01	6.0	6	1.38E-01	7.3	6
3	7.03E-02	14.2	5	6.78E-02	14.7	5
4	4.03E-02	24.8	4	3.97E-02	25.2	4
5	2.37E-02	42.2	4	2.37E-02	42.2	4
6	1.29E-02	77.7	3	1.26E-02	79.5	3
7	5.49E-03	182.0	2	5.14E-03	194.6	2
8	2.24E-03	445.5	1	2.24E-03	445.5	1
9	1.06E-03	940.5	1	1.71E-03	583.8	1
10	5.91E-04	1692.9	1	5.91E-04	1692.9	1
11	2.95E-04	3385.8	1	2.36E-04	4232.3	1
12	1.18E-04	8464.5	1	1.18E-04	8464.5	1
13	5.91E-05	16929.0	1	1.18E-04	8464.5	1
14	5.91E-05	16929.0	1	5.91E-05	16929.0	1
S	5.91E-05	16929.0	1	5.91E-05	16929.0	1

Previously, three distinct and presumably physically meaningful frequency ranges were identified, a low frequency segment of anti-persistent Brownian noise, an intermediate frequency segment of black noise and a high frequency segment of persistent Brownian noise. The individual details associated with these frequency ranges were combined and plotted in conjunction with the random component and the residual S above the hourly discharge of Manorhamilton spring (Figure 6.26).

Details 6 to 14 relate to the random component (Gaussian domain), largely fluctuating in time except during periods of low flow. Above, detail 4 and 5 (structured low frequency segment) shows a discontinuous pattern of high amplitudes localised in time during major discharge events. During recessions, the flow associated with this frequency is very close to 0. Detail 2 and 3 (intermediate frequency component) shows even more localised flows limited to discharge events. And lastly, detail 1 resembling the high frequency component is highly localised in time.

None of the assembled details exhibits oscillations during major recessions, which is plausible.

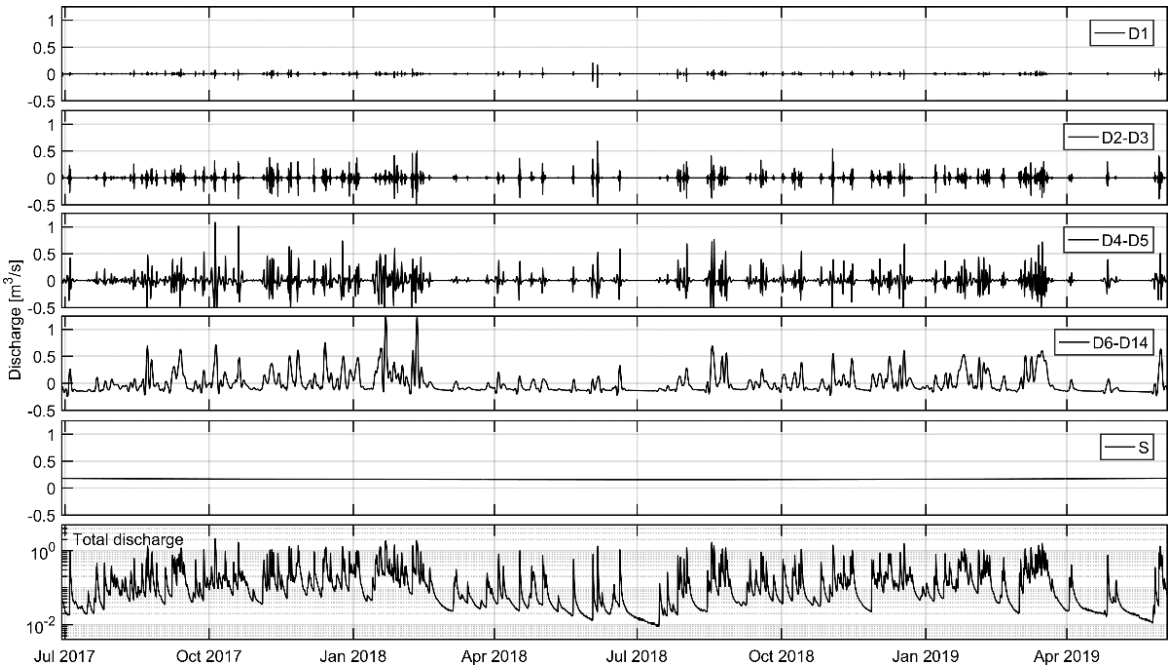

Figure 6.26: Hourly discharge of Manorhamilton spring (bottom plot) and combined wavelet details (D) using db10: D6 to D14 (β_1 to β_3), D4 to D5 (β_4), D2 to D3 (β_5 to β_6), D1 (β_7) and the trend S.

Again, details and the trend S were aggregated to resemble a structured low-frequency signal. Given the previous results, S was aggregated with the random component (D6 to D14) and the structured low frequencies D4 and D5 to resemble a signal related to the LFC (Figure 6.27).

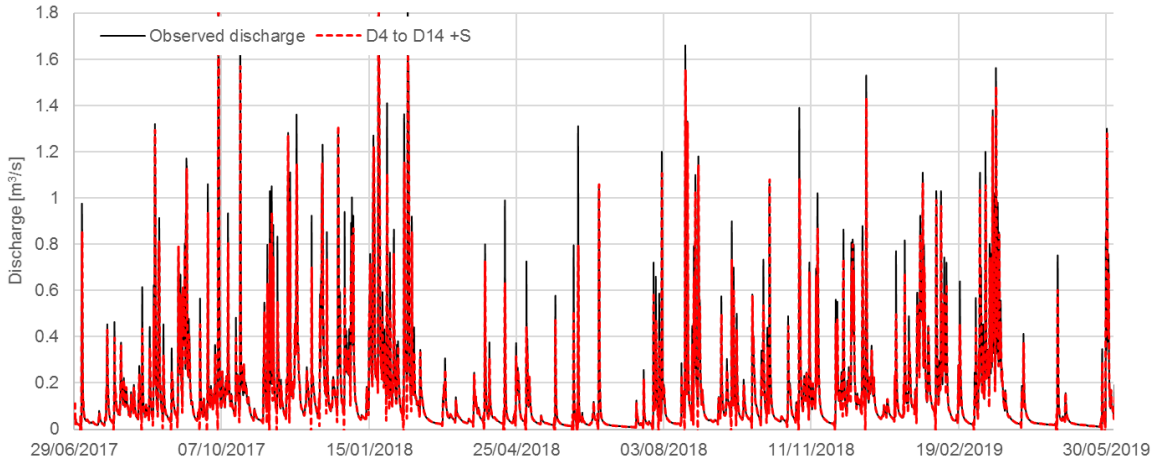

Figure 6.27: Low frequency signal (detail 4 to 14 +S) of db10 for discharge of Manorhamilton spring between 2017 and 2019.

The plot shows that the composed signal is almost identical with the observed time domain discharge signal, presumably related to the relatively large contribution of Gaussian noise. However, if

the low frequency segment represents diffuse flow processes in the aquifer, the question is then if the random signal covers any ‘structured’ fissured matrix drainage, hence, if there is no detectable fissured matrix signal in the spring hydrograph.

The assembled ‘diffuse’ flow components (Figure 6.27) shows a relatively large proportion of the overall flow. Again, the related recessions seem to clearly exceed the recession of the LFC previously established using the MRC (Section ‘5.2.1. Master recession curve analysis’). Therefore, the resulting low-frequency flow component using DWT suggests another contribution as well as the exponential LFC originating from the MRC.

6.4.3. Summary from DWT

DWT was applied on discharge time series (time-amplitude signal) of Ballindine and Manorhamilton spring. The aim was to relate the decomposed details - derived from the time-amplitude signal - to previously identified spectral coefficients, which are believed to inform about the ‘physical meaning’ or ‘relevance’ of the signal in terms of distinct flow dynamics. Further, the assigned details were used to re-build time-amplitude signals that represent distinct physical domains that were interpreted as distinct flow components related to aquifer porosities.
For Ballindine and Manorhamilton, details were related to four different frequency ranges: a) the random component; and the structured b) low; c) intermediate; and d) high frequency segment. For Ballindine, the intermittent and high frequency segment are relatively localised in time potentially linked to high flows of the River Robe, while the low frequency details appear to exhibit flows rather continuous in time.
Conceptually, the high frequency segment is interpreted to relate to fast conduit flow, the intermediate frequency segment relates to a more diffuse flow potentially impacted by the Robe, while the low frequency segment relates to diffuse flow.
Further, using the random component along with the trend S and the lowest structured component, the low frequency segment, a structured low frequency discharge signal is built, which is totally free from fast-flow components and believed to resemble diffuse flow and/or drainage from the low permeability domain.

For Manorhamilton, all assembled details exhibit highly localised powers in time which seem to be related to the highly fluctuating spring discharge signal. The aggregated low-flow signal is almost identical to the observed time domain discharge signal.

The constructed low-frequency signals of Ballindine and Manorhamilton spring both exceed the contribution related to a LFC recession, as previously established using respective MRCs. Therefore, the resulting low-frequency signals suggest an additional flow contribution than just the contribution related to the exponentially separated LFC.

6.5. Low-Flow Component (LFC) separation

In the previous Section, relatively large proportions of low-frequency signals were separated using DWT. However, the aim of this section is to establish a low-frequency signal representative and linked to the exponential LFC of the MRCs. The LFC is considered to represent the proportion of laminar/diffuse groundwater recharge and flow within the fissured matrix domain.
Whilst recharge for Manorhamilton spring is only related to rainfall on the catchment, it appears that Ballindine spring receives recharge from rainfall and from riverbed exfiltration. Therefore, the classical approach of rainfall-discharge does not apply to Ballindine and hence, conclusions drawn about recharge based on spring hydrography are more limited in this sense.

The workflow used to separate the low-flow component from discharge time series of Ballindine and Manorhamilton spring is outlined in Section '4.3.2. Hydrograph analysis and low-flow component separation' (Figure 4.14).

6.5.1. Ballindine

6.5.1.1. Exponential fitting

The previously established benchmark ranges of k/ k' or a/a' values were used to create exponential LFCs along the most undisturbed segments of recessions of daily discharge time series for the period 2009 to 2018 (Figure 6.28). Fitting was carried out starting at the beginning of a recession, which commences when rainfall decreases or ceases.

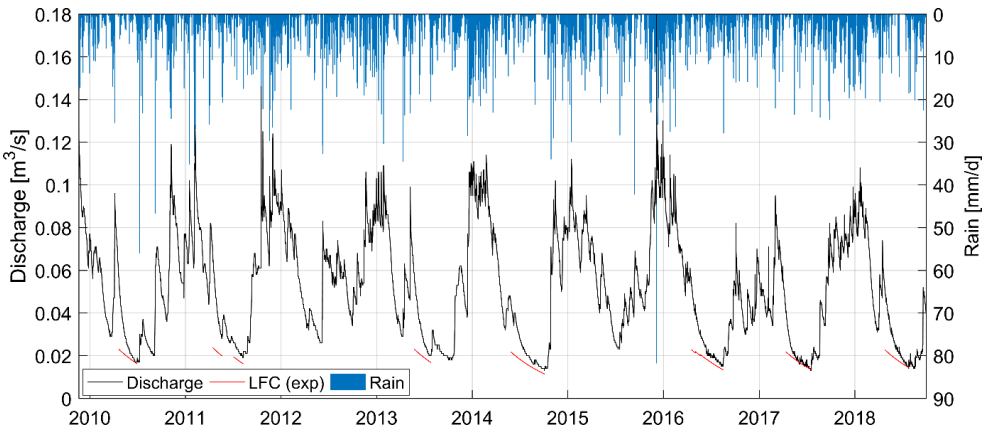

Figure 6.28: Exponentially separated LFC following Q_0 = 0.025 m³/s and k = -0.005 of daily discharge of Ballindine between 2009 and 2018.

Q_0 at the beginning of the exponentially fitted recession was applied as established previously by the MRC (Figure 6.29). The best fitting of exponential components according to the slope of the low discharge component was achieved using a high recession coefficient a of 0.994 to 0.995 d^{-1} or k value of -0.006 to -0.005 d^{-1}. As it can be seen, the fitted LFCs are not necessarily tangential to the

discharge Q during the late recession, which indicates that besides the LFC, the intermediate component was still actively draining during these periods. Hence, what might be considered as a 'pure LFC' is only reached in summer 2010, 2017 and 2018.

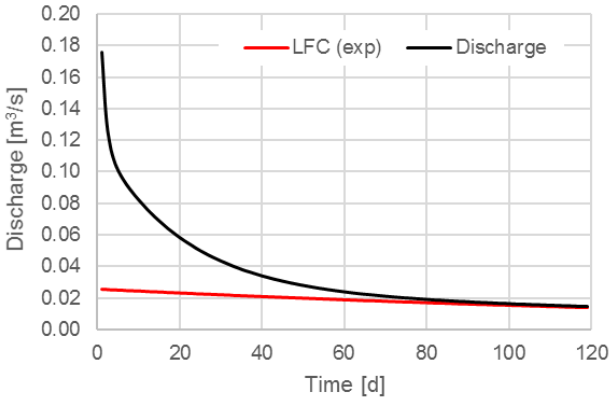

Figure 6.29: Relationship between Q_0 of the LFC and the MRC for Ballindine.

Based on the optimal benchmark range of recession coefficients, it was found that for Ballindine spring, low flow is reasonably explained using k = -0.005 d^{-1} or a = 0.995 d^{-1}, which corresponds to the upper end of the benchmark range resembling the value achieved by method 1, i.e. fitting linear reservoirs along the MRC.

6.5.1.2. Digital filtering

This section presents the results of fitting different digital recursive filters against observed discharge and exponentially separated LFCs for clearly identifiable low flow periods.

The Eckhardt filter and (for comparison) the one-parameter filter were numerically fitted along the exponentially separated LFC segments (Figure 6.28) for the period 2009 to 2018 by minimising the RMSE, as well as by visually fitting along the observed discharge graph. The correlation coefficient was applied for comparison. Recession coefficients were fitted according to the optimal benchmark region ranging between 0.995 and 0.967 d^{-1} where it was previously found that a higher a fits the late recession better.

The optimal benchmark region was applied for estimating a for the one-parameter filter, yielding the best fit with a = 0.992 d^{-1} with a RMSE of 0.006 and a correlation coefficient of -0.929. However, the method clearly overestimates the maximum LFC of 0.047 m^3/s, and it also shows unrealistically sharp inclinations (Figure 6.28).

For the application of the Eckhardt method, the optimal benchmark region was applied for estimating a. Further, the filter parameter BFI_{max} was estimated based on the optimisation procedure

outlined by Rimmer and Hartmann (2014). In the case Ballindine, TDS was the only continuously monitored quality parameter (along with temperature). However, TDS is highly fluctuating between seasons as well as individual rainfall events. Therefore, it was found to be neither physically meaningful to assign a single TDS value as representative for the low-flow or quick-flow component, nor was its application successful in terms of generating a consistent low RMSE result.

A more practical approach for estimating BFI_{max} according to Collischonn and Fan (2013) was applied on the master recession curve previously established. The results yield BFI_{max} = 0.994. Using this parameter along the estimated a = 0.994 d^{-1} yields a highly exaggerated LFC almost identical with the observed discharge, with a RMSE of 0.014 and consequently a high linear correlation 0.890. Because the result (Eckhardt 1) was not meaningful, this approach was also rejected, so that finally, BFI_{max} was adjusted manually (Eckhardt 2). The best fit was achieved with a = 0.995 d^{-1} and BFI_{max} = 0.34, resulting in a RMSE of 0.003 and a correlation coefficient of 0.760. The maximum simulated low flow is modelled to be at 0.028 m^3/s, very close to the maximum low flow contribution of 0.025 m^3/s established by the MRC.

The resulting separated LFCs are displayed in Figure 6.30. RMSE and correlation coefficients are displayed in Table 6.3 for all methods applied. Based on this assessment, the Eckhardt method yielded similar results, close to the maximum LFC as established using method 1. Although the methods yield the lowest correlation coefficient, they achieve the lowest RMSE (which is considered to be the relevant performance indicator).

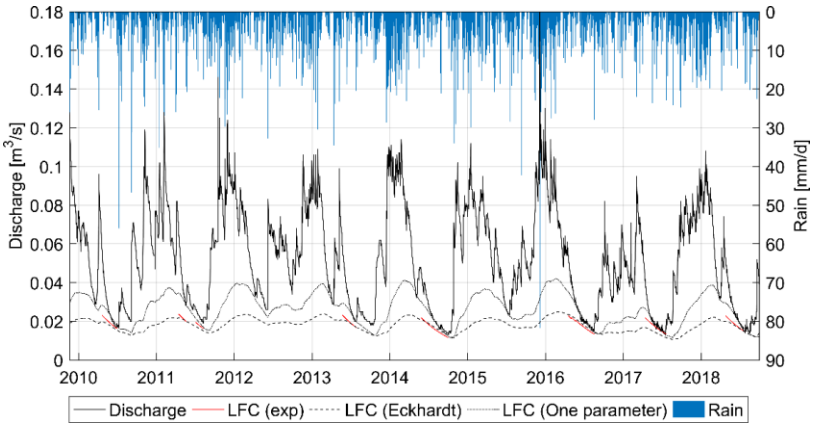

Figure 6.30: LFC separation of daily discharge of Ballindine between 2009 and 2018 using exponential fitting (exp), Eckhardt filter (Eckhardt 2) and the one-parameter filter.

Table 6.3: Fitting between digital/recursive filters and exponentially separated low flow for daily discharge of Ballindine spring (m^3/s) 2009 to 2018.

Filter	a [d^{-1}]	BFI_{max}	RMSE	Correlation coefficient	Max Q [m^3/s]	% of observed discharge
Eckhardt 1	0.994	0.994	0.014	0.890	0.129	99.4
Eckhardt 2	0.995	0.34	0.002	0.767	0.025	34.6
One-parameter	0.992	-	0.006	0.929	0.042	50.2

From the overall assessments, all filters fit the late low flow recession of the observed time series reasonably well. Major differences occur during periods of dominating flood or intermediate recession, during which the filters estimate the LFC differently. The evaluation of a low, intermediate and flood components was previously carried out using multi-resolution analysis (Sections '6.3. Spectral and noise analysis' and '6.4. DWT').

6.5.2. Manorhamilton

6.5.2.1. Exponential fitting

The exponential LFC was separated for the hourly discharge time series at Manorhamilton spring for the period 29 Jun 2017 to 01 Oct 2018 across which hourly rainfall data were also available. The results are shown in Figure 6.31, which shows a log-linear plot of discharge and exponentially fitted LFCs against hourly rainfall. The best fit of the exponential LFC of the hourly MRC of Manorhamilton was achieved by applying Q_0 = 0.035 m^3/s and k' = 0.0025 h^{-1} (Figure 5.21).

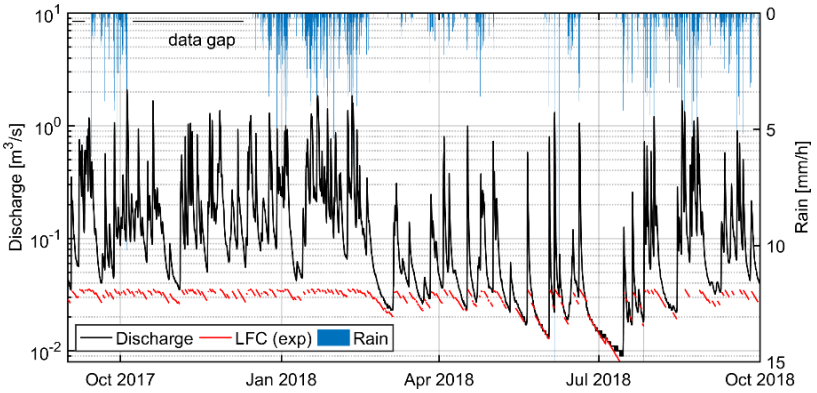

Figure 6.31: Exponentially separated LFC following Q_0 = 0.035 m^3/s and k' = -0.0025 h^{-1} of hourly discharge of Manorhamilton 29 Jun 2017 and 01 Oct 2018.

6.5.2.2. Digital filtering

Different filters were numerically fitted along the exponentially separated LFC for the hourly discharge at Manorhamilton spring by minimising the RMSE, as well as visually fitted along the observed discharge time series graph. The hourly discharge time series was analysed for the period 29 Jun 2017 to 01 Oct 2018.

The optimal benchmark region was applied for estimating a for the one-parameter filter, yet, no meaningful results can be achieved. Hence, it is concluded that one parameter is not sufficient to explain the low frequency baseflow signal of Manorhamilton spring.

Also, for the application of the Eckhardt method, the optimal benchmark region was applied for estimating a. Further, the filter parameter BFI_{max} was estimated based on the optimisation procedure,

as outlined by Rimmer and Hartmann (2014). This, however, was difficult to realise due to the method procedure, which implies that the LFC and a quick-flow component can be described by a representative water quality parameter, e.g. SO_4^{-2} or total suspended solids. Again, TDS (EC) and temperature were the only continuously monitored quality parameter. However, TDS is highly fluctuating, and may vary largely between individual rainfall events. Therefore, it was neither found to be physically meaningful to assign a single TDS value as representative for the baseflow or quick-flow component, nor was its application successful in terms of generating a consistent low RMSE optimisation result.

Estimating BFI_{max} according to Collischonn and Fan (2013) was applied on the MRC previously established resulting in BFI_{max} = 0.97. Using this parameter along the estimated a' = 0.997 h^{-1} yields again a highly exaggerated LFC with a maximum LFC of 0.25 m^3/s, almost identical with the total discharge, with a RMSE of 0.013 and correlation coefficient of 0.001 for hourly data. This LFC constitutes 11.5% of the observed discharge. Therefore, this approach (Eckhardt 1) was rejected for Manorhamilton spring, so that finally, BFI_{max} was adjusted manually (Eckhardt 2). The best fit was achieved with BFI_{max} = 0.093 and a' = 0.998 h^{-1} resulting in a RMSE and correlation coefficient of 0.015 and 0.54. Maximum discharge of the LFC reaches 0.035 m^3/s making 9.4% of the observed discharge, which is identical to the maximum value of 0.035 m^3/s as established using method 1.

The resulting separated LFCs are displayed in semi-log Figure 6.32. All two different approaches using the Eckhardt filter, including the RMSE, correlation coefficient and the maximum LFC are displayed in Table 6.4. Based on this assessment, fitting of the Eckhardt method (2) using a' based on the optimised benchmark range achieves the lowest RMSE, which is considered as the relevant criteria with a' = 0.998 h^{-1}. Further, maximum low flow of this method is closest to 0.035 m^3/s. This LFC accounts for 9.4% of the observed discharge.

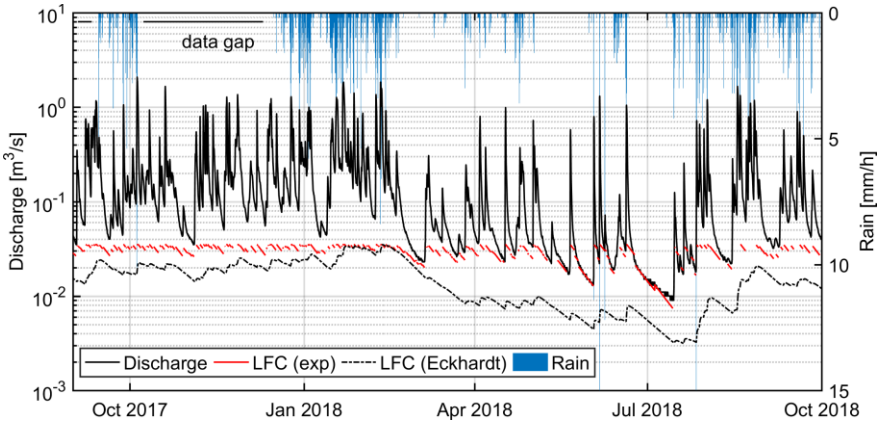

Figure 6.32: LFC separation of hourly discharge of Manorhamilton between 29 Jun 2017 and 01 Oct 2018 using exponential fitting (exp) and the Eckhardt filter (Eckhardt 2).

Table 6.4: Fitting between digital/recursive filters and exponentially separated LFC for hourly discharge of Manorhamilton 2017.

Filter	a' [h^{-1}]	BFI_{max}	RMSE	Correlation coefficient	Max Q [m^3/s]	% of observed discharge
Eckhardt 1	0.9967	0.974	0.013	0.001	0.025	11.5
Eckhardt 2	0.9980	0.099	0.015	0.542	0.035	9.4

Overall, it was found that the one-parameter filter does achieve a useful or meaningful result while the Eckhardt method matches the exponentially fitted LFCs relatively well.
The Eckhardt method (2) achieves LFCs that are identical to the maximum contribution of 0.035 m^3/s as established by method 1 (which has method has been previously applied in the context of baseflow separation of karst springs/rivers), which makes it a justifiable approach.

6.5.3. Summary from LFC

The aim of this section was to establish a continuous time series of a LFC resembling diffuse flow or drainage from the low permeability domain related to the lowest recession constant k / k' established from the MRC. Therefore, two digital recursive filters were applied, namely the Eckhardt filter and the one-parameter filter.
For both springs, the Eckhardt filter yielded a continuous low-frequency time series fitted along individually separated exponential LFC segments.
For Ballindine, the established LFC signal contributes a relatively high proportion of the overall discharge. Further, the LFC signal shows a seasonal fluctuation. These findings are in good agreement with the statistical analysis of the time series, which previously suggested the presence of a high-storage domain that is subject to seasonality.
For Manorhamilton, the LFC signal shows a very small contribution compared to the overall discharge signal. This result is in good agreement to the previous statistical assessment which suggested a low contribution of fissured matrix-domain permeability, and a very low seasonality of the spring which would be the result of significant storages, i.e. fissured matrix permeability.
The application of a digital recursive filter on spring hydrographs resulted in a further or additional refinement of a 'diffuse' signal, as compared to the previously applied DWT.

6.6. Conclusions

The spring discharge hydrographs of Ballindine and Manorhamilton were analysed using autocorrelation, cross-correlation, spectral and multi-resolution analysis and digital/recursive filtering. Ultimately, the aim was to, a) further characterise the hydrogeology (especially of the Ballindine system and its surface water-groundwater interaction), and b) to characterise and distinguish the (mainly diffuse) recharge and flow components based on the time-amplitude hydrographs. A hydrograph is the result of the filtering effect of the system (in case of a spring: the aquifer), hence, the

underlying principle of this Section's input-output analysis is the transformation of a random input signal (i.e. rainfall) into a structured output (spring discharge). The findings are then used to develop and calibrate pipe network models in the next Chapter 7.
The availability of long-term hydroclimatic data turned out to be of high value for the time series analysis, especially for Ballindine spring, which exhibits only one major recession throughout a hydrological year. For the faster-responding system Manorhamilton, multi-annual hourly hydroclimatic data is not necessary, although it may have improved the analysis.

A crucial aspect of a hydrological input-output analysis is the randomness of input time series. The randomness of the rainfall time series was evaluated using ACF and signal analysis coupled with noise analysis.
Although, complexity arises for Ballindine spring: The River Robe is conceptualised as a losing stream and hence, a part of the river runoff is considered as an additional input time series for the aquifer. Yet, as shown by the noise analysis, the river runoff exhibits partly highly structured components. Therefore, the structured components of the Ballindine hydrograph are likely to be the result of a combination of the structured river runoff infiltrating into the aquifer and the filtering effect of the aquifer itself, further transforming the river input as well as the random signal input from the rainfall.

The differences between the hydrogeology of Ballindine and Manorhamilton spring have been revealed by the analyses carried out in this Section: The diffuse-type system of Ballindine shows a low loss of memory underlining the inertia of its system (ACF), which largely transforms the rainfall signal (low CCF between rainfall and discharge time series). The corresponding spectral coefficients (8 out of 9) are dominantly attributed to the Brownian domain. The pattern of spectral coefficients is interpreted as the result of a rather uniform or homogeneous system that is governed by a systematic of diffuse recharge and flow.
The catchment of Ballindine does not contain any known karst features but instead is covered by relatively thick soil. Essentially, almost all recharge can therefore be considered as diffuse, meaning a predominant diffuse groundwater flow which is also shown by the results of the KarstMod model (Section '5.1.4. Reservoir modelling'). In fact, this may explain a relatively large proportion of a 'diffuse' component that was constructed using DWT. As part of such diffuse signal, a continuous time series resembling the LFC could be established using the Eckhardt digital/recursive filter. The corresponding LFC is limited up to 0.025 m^3/s with a k value of 0.005 d^{-1}. Importantly, this LFC signal could be well matched with periods of exponentially separated LFCs.

On the other hand, the conduit-dominated system of Manorhamilton shows a high loss of memory (ACF). The filtering effect of the aquifer is relatively small given the relatively high peak of the CCF. Different flow components are apparent in the discharge hydrograph. The corresponding spectral

coefficients range between Gaussian noise and black noise. The latter one may be attributed to large flood events and the influence of concentrated recharge and conduit flow.
The construction of a ‘diffuse’ recharge and flow signal using DWT yielded a relatively high proportion of the total hydrograph. Yet, the proportion seems small compared to Ballindine. This diffuse component though seems not to sustain the very low flow of the spring hydrograph, as indicated by the DWT. Instead, it was suggested that the trend S may be the only component sustaining such low flow towards the end of long-lasting recessions. Therefore, the application of a digital/recursive filter (Eckhardt) was considered to be relevant in order to generate a representative diffuse signal that also includes contributions into the very late recession. The resulting LFC signal shows a very small contribution compared to the overall discharge signal, which again suggests and/or confirms previous findings concerning the very small contribution of a low-permeability (e.g. fissured matrix) domain, and small groundwater storage.

With regard to the following chapter on the InfoWorks pipe network model, this chapter has gained important findings with regard to the different recharge and storage dynamics of both aquifers, as well as a threshold effect of the river runoff. In addition, it has provided continuous time series resembling a diffuse signal as established by DWT and time series corresponding to the low-permeability domain using a digital/recursive filter, which is based on the MRCs.

7. Groundwater Modelling using InfoWorks ICM

This chapter presents the pipe network models established for Ballindine and Manorhamilton, simulating the total spring discharge, as well as individual flow components as identified and separated within the previous chapters. By doing so, this part presents the cornerstone of this research.

7.1. Ballindine

The conceptual model of the Ballindine aquifer underlying the pipe network model is based on the following conclusions that were achieved from the previous results within this study:

1. **Change of the catchment boundaries:** Tracer tests did not confirm the catchment boundaries (EPA, 2011a) covering 8.9 km^2 across the Claremorris fault, at least during prevailing low flow conditions during which the tests were conducted. A smaller catchment size is proposed ranging between 1.8 and 4.6 km^2 as indicated by water balances and reservoir modelling. However, the exact size remains uncertain due to suspected additional outflows of unknown quantities via drainage channels, which are ubiquitous on the western side of the Claremorris fault.
   The proposed catchment boundaries extend on the western side of the Claremorris fault being connected to the River Robe;
2. **Hydraulic connection to the River Robe:** a tracer test within the River Robe suggested the existence of a threshold water level upon which flow and transport (turbidity) impacts Ballindine spring. This finding is partly in compliance with the noisy EC readings and drops, which were interpreted as related to river exfiltration, although being persistent in time and therefore not only linked to a threshold level of river discharge. The impact of the river on the spring is strongly supported by the high linearity between discharge of the River Robe and Ballindine spring (cross-correlation) as well as by the high coherence. The correlation and coherence between these time series is much more pronounced than the relationship between rainfall and spring discharge;
3. **Diffuse type karst aquifer:** The entire catchment is underlain by luvisols presumably originating from glacial till, and locally gleysols, which suggest a very limited vadose zone, and the effectiveness of drainage channels on diverting recharge to surface water. Such soil cover is expected to largely filter the rainfall input signal towards the spring outlet, which is suggested by autocorrelation, cross-correlation between rainfall and spring discharge and frequency analysis. No swallow holes are known within the catchment and its surrounding, which could promote concentrated infiltration.
   Following Mangin (1975) and El-Hakim and Bakalowicz (2007) the recession of the spring discharge suggests that the aquifer exhibits a relatively high regulating power with a poorly developed conduit system with primarily slow infiltration. The mean residence time is estimated at 1.11 years. Further, the aquifer is classified as ”aquifer with a deep phreatic zone partly or

totally confined under low permeable sediments with a complex drainage structure responsible for very long, multiannual or secular residence times". 'Deep' groundwater flow may be flowing along the Claremorris fault and discharging into Lough Mask/Lough Corrib;

4. **Flow components:** Establishing a master recession curve (MRC) was crucial to establish a continuous recession because the discharge regime of Ballindine is very seasonal without complete undisturbed recessions. Fitting linear reservoirs onto the MRC suggests that the aquifer is drained via three flow components: one minor fast component resembling conduit drainage and two slow components (one major and one minor) resembling drainage from the fissured matrix. The results of the KarstMod reservoir model suggest the major importance of a slow-flow component on the spring discharge. However, a fast-flow component, albeit small in absolute terms, is also necessary to achieve a reasonable model performance.
   Based on exponentially fitting, a continuous low-flow component (LFC) could be established using a digital recursive filter and a decomposition method in the form of discrete wavelet transform, both matching relatively well with the exponentially fitted components. These LFCs are believed to resemble discharge from the low(est) permeability domain of the aquifer sustaining discharge during the periods of lowest flows.

Accordingly, three flow components are integrated within the pipe network model: a) a minor proportion of conduit flow, b) a major proportion of diffuse slow-flow, and c) a minor continuous proportion of LFC:

a) The minor conduit contribution is conceptualized to originate from river inflow being activated above a water level threshold in the river;
b) The major diffuse slow-flow component is conceptualized to originate from river infiltration of the River Robe, being the reason to cause continuously drops in EC throughout the year. The input signal is highly transformed through the structure of the aquifer; and
c) The minor continuous LFC contribution is conceptualized to originate from the surface of the catchment and therefore subject to slow and diffuse infiltration and flow towards the spring.

The drainage channels act as another output from the catchment; the channels receive a proportion from diffusely infiltrating recharge.

Based on the abovementioned results, a conceptual site model (CSM) (Figure 7.1) was developed with regard to the GIM architecture, altogether underlying the ICM pipe network model. Where applicable, the GIM terminologies are added to the labels of the individual flows.
The aquifer compartment of the CSM is split into a soil layer (soil store) and bedrock layer and fissured matrix (groundwater store). Flow from the soil store and groundwater store is modelled in permeable and full pipes. Interaction with drainage channels and the River Robe are accounted through connections with the pipe network.

Rainfall (a) falls on the land surface from where it infiltrates into the soil layer (soil store) via soil store inflow (c). Within the soil store, losses occur via evapotranspiration (b).
Percolation/infiltration through and from the soil (percolation flow) occurs in two ways: firstly, conceptualised as diffuse flow through the soil matrix into the groundwater store via percolation flow from where drainage occurs as infiltration flow (d); hence, percolation to the groundwater store resembles recharge of the lowest permeability domain. And secondly via preferential flow paths through macropores (e) via rainfall-induced infiltration into a permeable pipe. The relative proportions of the two different components had to be estimated. It was assumed that the proportion of matrix component was much more relevant than the component of macropores.
Altogether, d and e account for diffuse groundwater recharge from the land surface, eventually discharging into a permeable pipe (Figure 7.3a). Losses from the aquifer occur via deep percolation (k, assumed to occur along the Claremorris fault) modelled as 'baseflow' from the groundwater store and via drainage channels. The latter losses (f, g) are incorporated in the model using a combined sewer overflow (CSO) (Figure 7.3b): overflow is activated at a calibrated threshold diverting flow towards the drainage channels, which then carry these flows towards the River Robe. The remainder share of inflow from the permeable pipe originating from the sub-catchment is continuously discharging towards the centre conduit (d'+e').

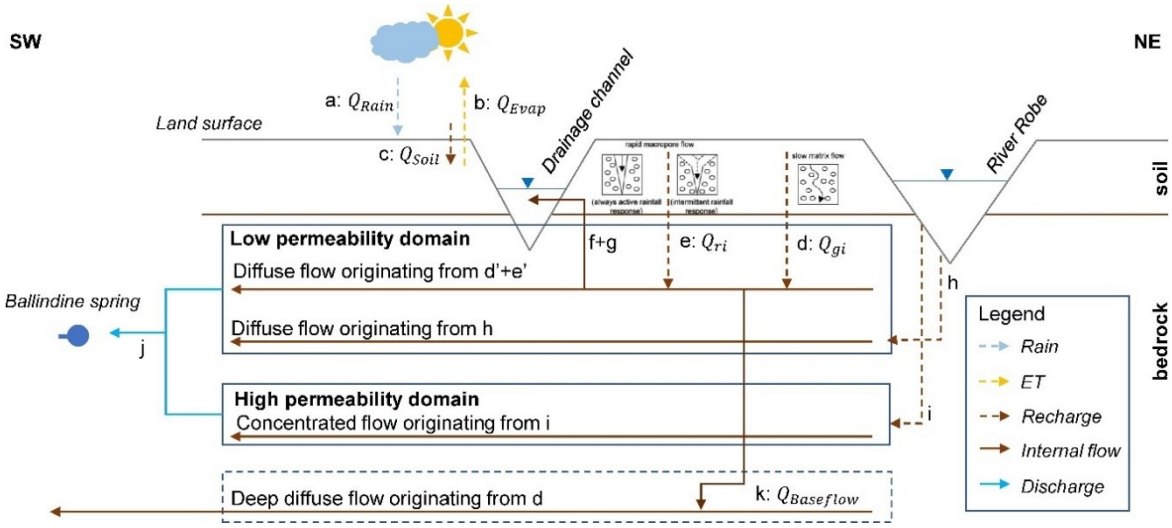

Figure 7.1: Conceptual site model for Ballindine spring. Where applicable, the GIM terminology was included in the description of individual flows.

Two recharge and flow components originate from the River Robe (h, i), namely a diffuse component (h) and a concentrated component (i). The diffuse flow component is believed to resemble the major contribution to the overall discharge of Ballindine spring.
A fast-flow component is believed to originate through concentrated exfiltration/percolation from the river bed (i) after the water level reaches a threshold level, here modelled as 100 cm. This concentrated recharge directly enters the central conduit where flow is modelled as pressurized pipe /

open-channel flow. Within the central conduit the other diffuse flow components merge together to drain the aquifer constituting the overall discharge of Ballindine spring (j).

7.1.1. General model outline

The CSM (Figure 7.1) was built in InfoWorks ICM and is illustrated in Figure 7.2 and Figure 7.3. The entire catchment of Ballindine spring is sub-divided into 4 sub-catchments (SC) each of 0.825 km^2 in size.

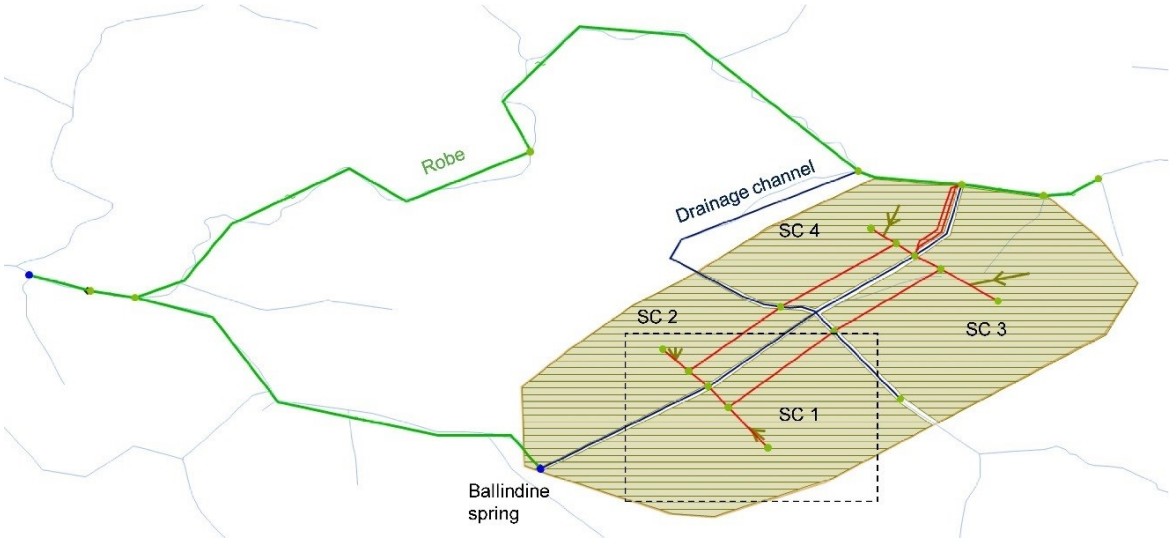

Figure 7.2: InfoWorks ICM model for Ballindine spring. Dark blue lines are full pipes (open-channel/pressurised pipe flow), red lines are permeable pipes (Darcy flow) and the light blue lines are streams 'channels' including the River Robe. The entire catchment was split into four sub-catchments (SC 1 to 4). The dashed area is illustrated in Figure 7.3.

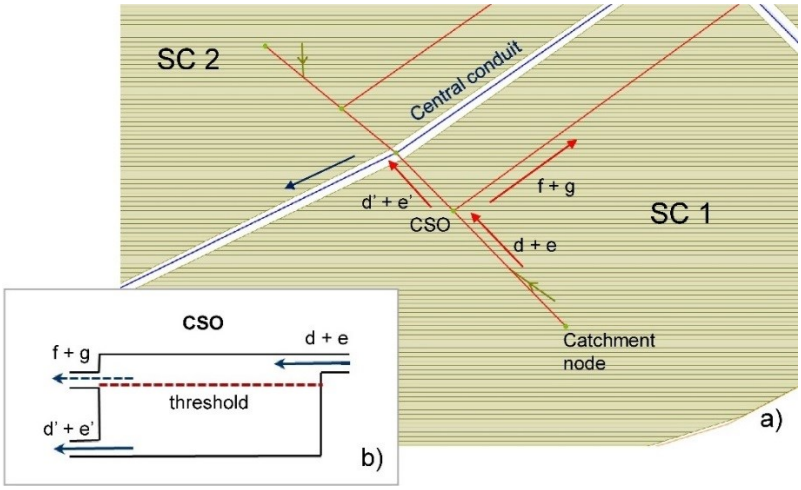

Figure 7.3: a) Detailed view on the model structure, including b) the combined sewer overflow (CSO) manhole. The CSO diverts the inflow from the sub-catchment (d+e) towards the central conduit (d'+e') while an overflow is diverted towards the drainage channel (f+g).

Each sub-catchment has its own GIM that models the behaviour of the soil store and groundwater store. Flows are then drained laterally into an associated permeable pipe that is connected to a catchment node. Each catchment node has a chamber floor level of 55 masl and a chamber roof level of 64 masl, while the connected permeable pipe has a K of 0.005 m/s and a porosity of 0.9. The entire flow within each permeable pipe is then split within a downstream manhole (CSO, Figure 7.3) into a minor (d+e) and major (f+g) permeable pipe. The major permeable pipe with K = 0.005 m/s and porosity of 0.5 is the overflow (f+g) draining into a conduit that resembles the flow towards the drainage channels. This flow is then diverted back to the River Robe leaving the catchment. The minor permeable pipe (d+e) with K = 0.005 m/s and porosity of 0.9 drains into a central conduit. The central conduit integrates all flow components towards the outlet (Ballindine spring) via an outfall located in the south-west. The discharge of Ballindine is then diverted towards the River Robe (downstream section) via a rectangular channel of 1 x 1 m and a gradient of 4.85 x 10^{-4} m/m (3,092 m over an elevation difference of 4.5 m).
The Robe is represented as a channel, originating in the north-east and ending after the confluence with the inflow from Ballindine spring further downstream. The channel gradient is 1.7 x 10^{-3} m/m (6,000 m over an elevation difference of 10.4 m) and its width and central depth is 6.5 and 5 m (Figure 7.7).The River Robe channel is modelled as a losing stream. Exfiltration from the river into the Ballindine spring catchment is modelled by using three pipes: 1.) an upper rectangular permeable pipe (170,000 x 5,000 mm) with K = 0.08 m/s and porosity of 0.9 resembling the general and major inflow from the river; 2.) a lower permeable pipe (170,000 x 700 mm) with K = 0.0005 m/s and a porosity of 0.1 resembling a low-permeable exfiltration zone of the river bed filled by mud and sediments; and 3.) a single full pipe (⌀ 170 mm) with a Colebrook-White roughness of 0.5 mm. The empty conduit is elevated 100 cm above the river bed to resemble the threshold level of concentrated inflow, as previously discussed (Section ‘5.1.3.2. Tracer test 30 Jan 2019’) (Figure 7.4). The upper (1.) and lower (2.) rectangular permeable pipes overlap vertically by 50 mm to constitute a transition zone (Figure 7.4). This overlap was necessary to avoid abrupt changes of inflow into the pipe network, hence, to smoothen the input signal.
These inflows from the Robe then discharge into the central main conduit of the Ballindine catchment integrating flows to the spring.

Hourly data input time series for calibration reference of the model comprise rainfall observed at Claremorris, evapotranspiration as estimated by the Penman-Monteith equation using climate data from Claremorris and observed spring discharge at Ballindine and river runoff observed at Christina S BR. The upstream head of the River Robe at the supposed exfiltration area is determined by calibrating the River Robe channel using the observed downstream flow (head) as upstream inflow and matching the channel dimensions over a length of 6,000 m to then match the simulated the downstream head against the observed head.

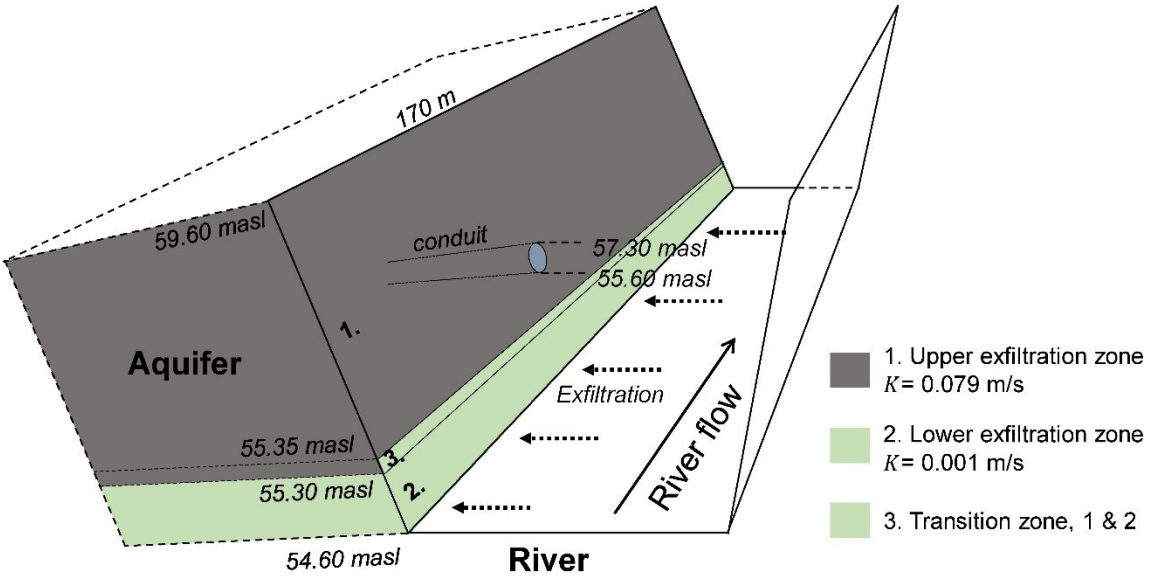

Figure 7.4: Outline of the exfiltration zone of the Robe River channel in InfoWorks: 1. upper and 2. lower exfiltration zone, and an overlapping 3. transition zone. A conduit (⌀ 170 mm) drains the river at 55.60 masl, providing concentrated recharge into the Ballindine aquifer.

7.1.2. Flow components

Three distinct flow components that were previously identified are represented in the model: diffuse recharge constitutes a major diffuse flow component in the fissured matrix (Section '6.4.1. Ballindine') and the LFC sustaining the lowest flow of Ballindine spring (Section '6.5.1. Ballindine'). Concentrated recharge constitutes a minor concentrated conduit component (Sections '5.1.4. Reservoir modelling' and '6.4.1. Ballindine') (Figure 7.5). The minor concentrated component and the major diffuse component originate from the River Robe while the minor diffuse component originates from recharge through rainfall infiltrating within the four SCs.

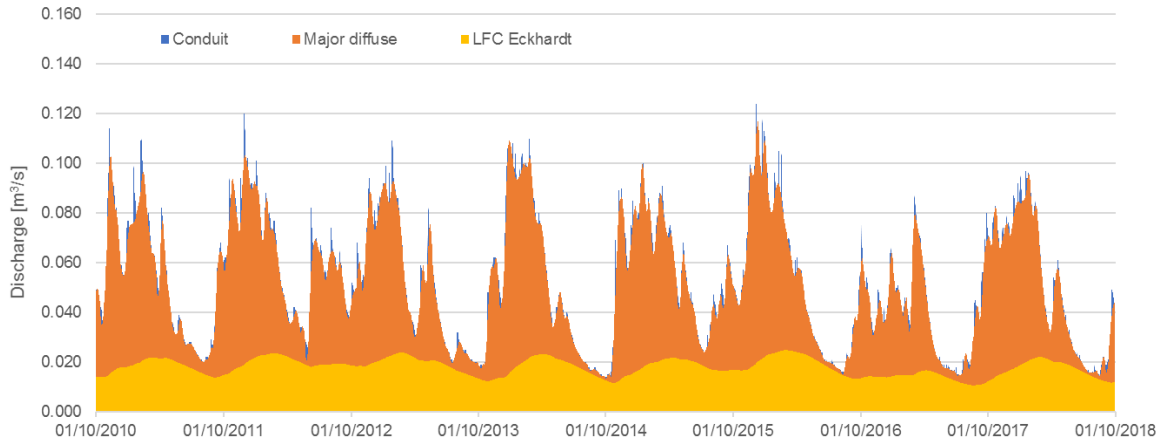

Figure 7.5: Flow components of Ballindine spring: minor conduit, major diffuse and minor diffuse (LFC). The LFC was established by using the Eckhardt filter.

Since concentrated recharge from the river was modelled within an empty conduit that originates 100 cm above the river bed, this proportion of conduit flow is intermittently activated.
Major diffuse flow was modelled within two rectangular permeable pipes representing an exfiltration zone via Darcy flow. This exfiltration zone is sub-divided into a lower low-hydraulic conductivity zone and an upper (main) higher hydraulic conductivity zone, as previously shown in Figure 7.4.

The minor diffuse flow component originates exclusively from all four SCs modelled as flow within permeable pipes resembling Darcy flow. This component originates from the soil store and the groundwater store within the GIM. Accordingly, all discharge originating from the GIM resembles diffuse groundwater recharge, as well as diffuse groundwater flow towards Ballindine spring in the form of the minor diffuse flow component.
The two discharges into the pipe network originating from the GIM can be distinguished, i.e. inflow from the soil store (e: Q_{ri}, Figure 7.1) and inflow from the groundwater store (d: Q_{gi}, Figure 7.1). Q_{ri} can be interpreted as the quick response of the diffuse recharge; it is understood as macropore recharge through the soil. In turn, Q_{Gi} is conceptualised as perennial recharge through the soil matrix, which sustains recharge even periods of no rainfall. This is the dominating driving force behind minor diffuse recharge and flow.
Deep percolation in the aquifer, essentially bypassing Ballindine spring, is modelled as drainage from the groundwater store (k: $Q_{Baseflow}$, Figure 7.1).

The conceptual model of the hydrograph is illustrated in Figure 7.6.

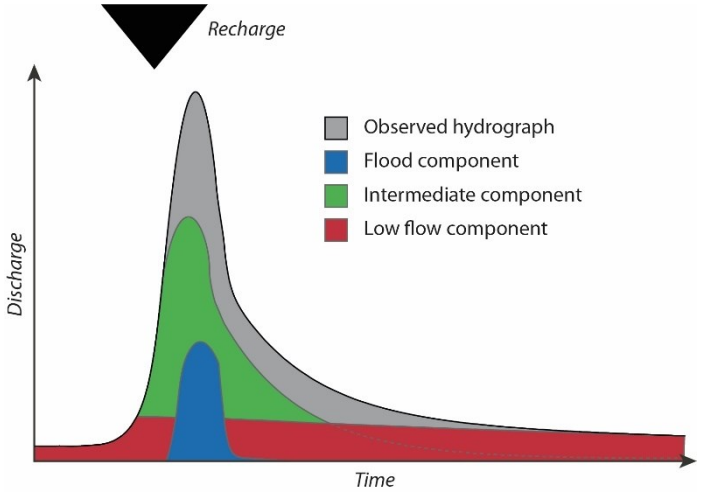

Figure 7.6: Flow components of Ballindine spring: minor flood component (concentrated inflow from the River Robe), major intermediate component (diffuse inflow from the River Robe) and the minor LFC (diffuse catchment recharge).

7.1.3. Calibration

The numerical parameters used to evaluate the model performance are the volume conservation criteria (VCC), the Nash-Sutcliffe efficiency (NSE) and the Kling-Gupta efficiency (KGE). In addition, the spectra of observed and modelled spring discharge were compared, as well as their ACF. The model was run on an hourly timestep.
The calibration period used was the hydrological years 2012 to 2015 (01 Oct 2011 to 30 Sep 2015) while validation was performed over the hydrological years 2016 to 2018 (01 Oct 2015 to 30 Sep 2018). The 2011 hydrological year was used as warm-up / initialisation period for the model.

The following components of the InfoWorks model and their discharges were calibrated against reference time series, prioritised as follows:

1. The river flow in the Robe along its entire 6,000 m length around the catchment was calibrated using the observed river discharge at Christina S BR. The goal of this calibration was to represent the Robe channel realistically in order to achieve the optimal and most realistic upstream head, at the point of supposed exfiltration. At this step, no sub-catchments were connected to the river, hence, no exfiltration was considered, in order to provide an optimal baseline upstream river head for the calibration steps 2. to 4.;
2. The minor diffuse flow component originating from the sum of all four sub-catchments' GIMs (Figure 7.3b, d'+e') and discharging through the minor permeable pipes into the overall pipe network was calibrated against the LFC;
3. The simulated total discharge of the pipe network model at the outfall was calibrated against observed time series at Ballindine spring by modifying the dimensions of the permeable pipes and the conduits connected to the River Robe;
4. The major diffuse flow component (originating from river bed infiltration) was calibrated against the diffuse flow component established by spectral analysis (Figure 6.25) but with the LFC subtracted;
5. The contribution of conduit flow (the difference between the observed discharge and the major diffuse flow component determined by the DWT) was used as reference for the contribution of the concentrated conduit inflow originating from the River Robe.

1. River flow

Runoff data for the River Robe observed at the monitoring station Christina S BR. was used as input in the upstream region where river bed exfiltration was modelled to occur into the aquifer of Ballindine spring. Hence, discharge of Ballindine spring was subtracted from the observed river runoff. The corrected river runoff was then used as upstream input for river flow.
In order to achieve realistic upstream flow and head dynamics of the river, the channel (river), namely its dimension and roughness coefficient, were fitted so that the upstream inflow flows through the 6,000 m long channel finally matches the downstream head as observed at Christina S

BR. This calibration procedure was done without associated catchments in order to simply and speed up the calibration procedure, and because the goal was limited to achieve realistic channel dimensions and upstream heads.

Since there was no detailed topographical data of the river bed available, a synthetic channel profile was created. The parameters that were adjusted are the geometries of the channel (length, depth) and the roughness of the channel surface (Manning's n) by trial and error.

2. Minor diffuse flow component (LFC)

The LFC was established applying a set of different methods (Section '6.5.1. Ballindine'), including the use of a digital recursive filter.

The LFC was modelled as the contribution from the four SCs via the GIM discharging through permeable pipes into the central conduit (d'+e', Figure 7.1). Calibration of simulated LFC against previously established LFCs was done by modification of the GIM and pipe parameters as well as the CSO manhole.

The GIM controls the quantity and magnitude that is drained laterally into the associated permeable pipe. Further, the GIM controls the dynamics of groundwater being 'lost' via deep percolation. Some of the parameters of the GIM are conceptually related to physical meaningful dimensions, e.g. porosity of reservoirs. However, it is important to bear in mind that in the framework of the model, such parameters are adjusted to fulfil the functioning of the CSM rather than representing a real world observation of soil porosity (Figure 7.1).

The calibration procedure (applied to all four SCs) was as follows: First, the proportion of runoff (fixed runoff coefficient) was set to a very low number, 0.0001 to generate practically no runoff. Next, it was decided to split the proportion of quick macropore recharge and slow diffuse soil matrix recharge as 1:99; ergo, 1% of recharge was drained from the soil store into the network as soil store inflow Q_{ri} controlled by the percolation percentage infiltrating. The remaining share of 99% percolated into the fissured matrix domain (groundwater store).

Drainage of the soil store and groundwater store is controlled by the porosity, the threshold level above which outflow is generated and the percolation and infiltration coefficient. The latter coefficients are of major importance in controlling the magnitude of drainage, as well as to prevent a continuous rise in the water level in any of the reservoirs.

Both reservoirs' porosity was set to 1%. Again, this number is not directly related to a physically meaningful porosity, rather it just controls the magnitude of head fluctuation in the reservoir. Drainage of the soil store via percolation flow Q_P was generated with a percolation coefficient of 100 after reaching a threshold level of 0.8 m in the soil.

Drainage from the groundwater store into the network was continuously modelled with an infiltration coefficient of 10 and a threshold level of 0. Deep percolation flow was modelled after reaching a baseflow threshold level of 0.05 m. The final GIM parameters are displayed in Table 7.1.

Table 7.1: GIM parameters adjusted to model minor diffuse recharge and flow for Ballindine spring.

Soil depth [m]	Percolation Coefficient [t^{-1}]	Baseflow Coefficient t^{-1}]	Infiltration Coefficient t^{-1}]	Percolation Threshold [%]	Percolation percentage infiltrating [%]	Porosity of soil [%]	Porosity of ground [%]	Baseflow threshold level [m]	Baseflow threshold type	Infiltration threshold level [m]	Infiltration threshold type
0.8	100	100	10	0.8	1.0	1.0	1.0	0.05	Abs.	0.0	Abs.

The permeable pipes receiving lateral inflows from the GIM were defined to have a K of 0.04 m/s and a porosity of 0.9. Lateral inflow was then split by the CSO into a major pipe discharging into a drainage channel and a minor pipe discharging into the overall pipe network. The size of the minor pipe controlled at the end, how much LFC was generated in total. The optimum diameter was found to be 2,370 mm circular shape, as opposed to 6,000 mm for the larger drainage pipe.

3. Simulated total discharge of Ballindine

The total simulated discharge of the modelled spring is the sum of the three flow components. which was therefore calibrated against the observed discharge at Ballindine spring.

4. Major diffuse flow component

According to the conceptual model, the major diffuse component is the sum of LFC and diffuse river bed infiltration. The latter constitutes the major share of recharge to the saturated zone, as it conceptually relates to the dominating intermediate recession (k = 0.05 d^{-1}) and accounts for the generally large impact of the river onto Ballindine spring as indicated by the wavelet coherence analysis.

The calibration of river bed infiltration through the permeable pipes yielded two dimensions of the permeable pipes: a) 5,000 x 170,000 mm, a porosity of 0.9 (90%) and a hydraulic conductivity of 0.08 m/s, and b) 750 x 170,000 mm, a porosity of 0.1 (10%) and a hydraulic conductivity of 0.0005 m/s.

5. Conduit component

The share of conduit contribution of the total spring hydrograph was determined by the difference between the observed discharge, and the major and minor diffuse components. This difference was then used to match the inflow of the conduit draining the river above a threshold. The conduit was modelled with ⌀ 170 mm, a gradient of 0.0066 m/m and a roughness of 5 mm.

7.1.4. Results

The calibration parameters previously outlined were optimised to yield the following results.

1. River flow

The final channel cross-section and associated roughness are illustrated in Figure 7.7. A 'global' roughness coefficient of n = 0.015 was applied, and the river bed was then fitted to cover a width of 6.5 m and a maximum depth in the centre of 5 m.

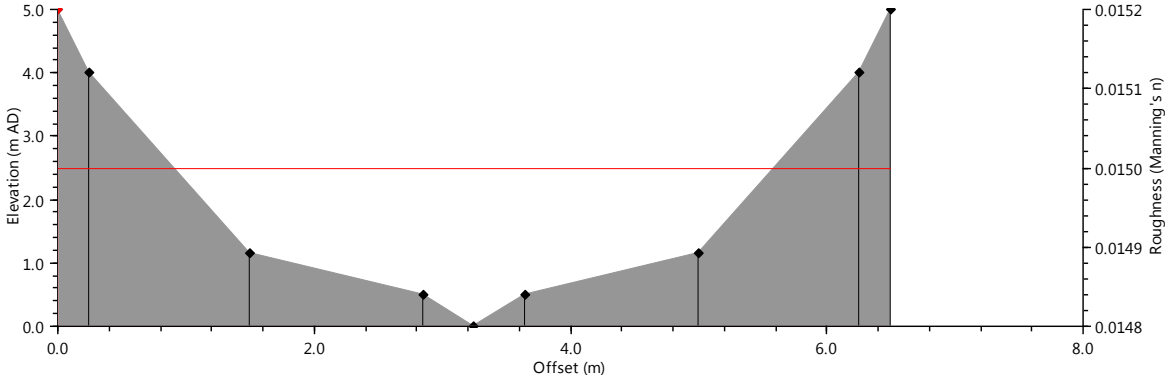

Figure 7.7: Final channel properties representing the River Robe in InfoWorks.

The observed and simulated river heads for the hydrological years 2011 to 2018 are illustrated in Figure 7.8. Overall, the simulated head matches very well the observed head. The NSE is 0.973 and the KGE is 0.953 .

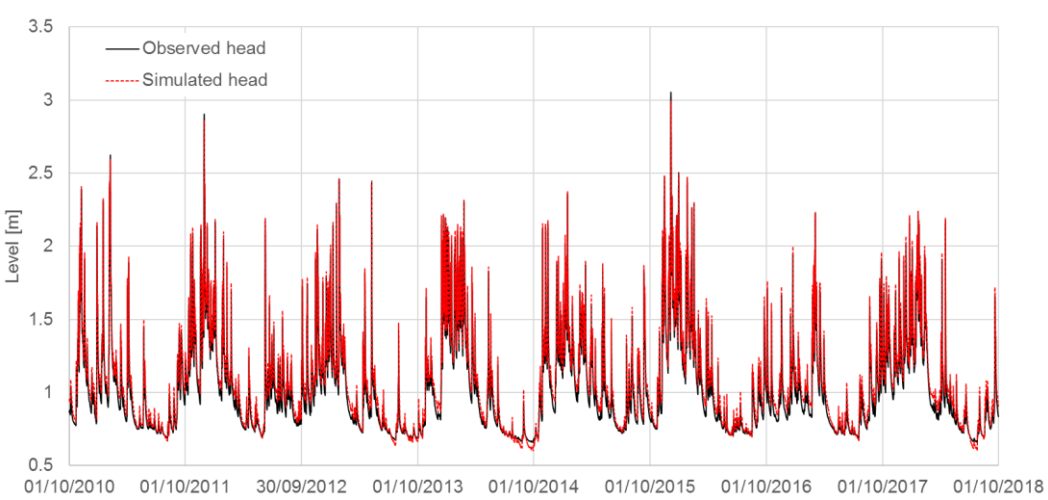

Figure 7.8: Simulated and observed river head [m] of the River Robe downstream of the confluence with the inflow of Ballindine spring for the 2011 to 2018 hydrological years.

2. Minor diffuse flow component (LFC)

The simulated LFC is largely the result of drainage of the groundwater store according to a variable head and flow dynamics within the associated permeable pipes. Figure 7.9 shows the fluctuation of the head within the groundwater store. This fluctuation could be calibrated against observed piezometric data, if available. In this case, the absolute level of the piezometric head becomes more meaningful. However, in this study, there were no piezometric records available. Therefore, the head fluctuation was the result of fitting the GIM parameters along with the parameters for the permeable pipes to match the overall LFC.

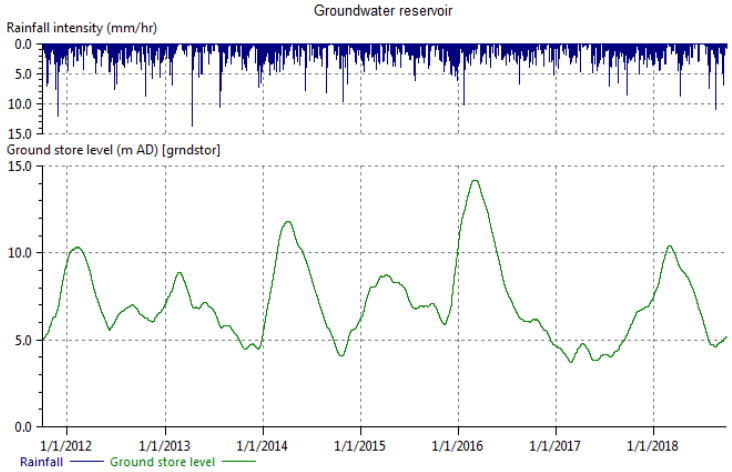

Figure 7.9: Simulated water level fluctuations within the sub-catchments.

Figure 7.10a shows the calibrated and validated simulated LFC against the LFC (Eckhardt), and Figure 7.10b illustrates their cumulative flows.

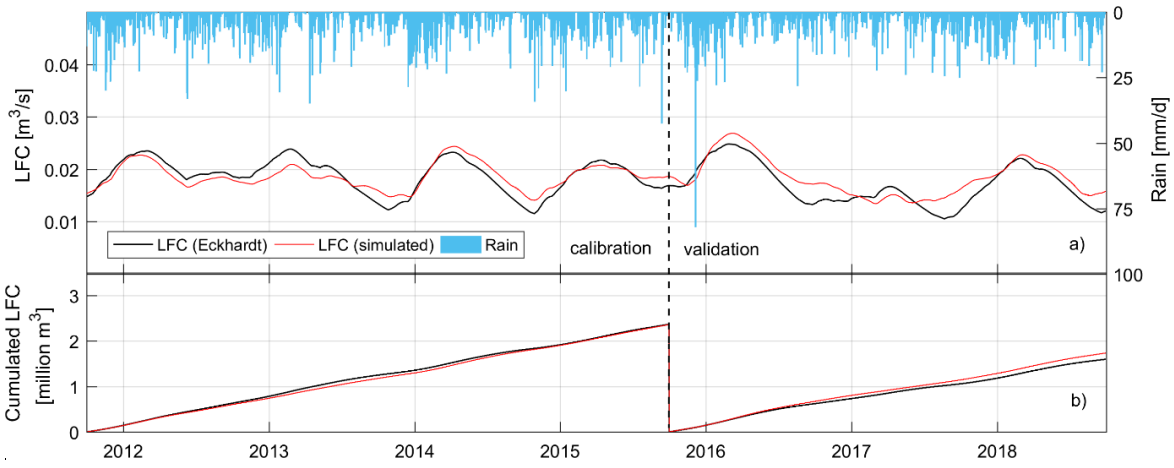

Figure 7.10: Results of simulated hourly discharge of LFC (a) and cumulative LFC (b) for the 2012 and 2015 hydrological years (calibration period) and 2016 to 2018 hydrological years (validation period).

The simulated LFC could be relatively well matched against the LFC established by the Eckhardt method, in terms of overall pattern but also in relation to the total discharge. The performance of the model simulating the LFC in relation to the LFC established by the Eckhardt method is illustrated in Table 7.2.

Table 7.2: Performance of the simulated LFC compared to the LFC established by the Eckhardt method.

Parameter	Calibration		Validation	
NSE	+0.739		+0.694	
KGE	+0.718		+0.865	
VCC	-0.003 MCM	-0.7%	+0.138 MCM	+8.2%

The overall pattern of the simulated LFC is largely controlled by the GIM. However, since the drainage of the reservoirs is modelled according to a variable head, the drainage from the reservoirs appears as a direct function of the water level, which results in a rather flashy discharge pattern. In order to smooth this discharge pattern, the permeable pipes with their hydraulic conductivity of 0.04 m/s played an important role (Figure 7.11).

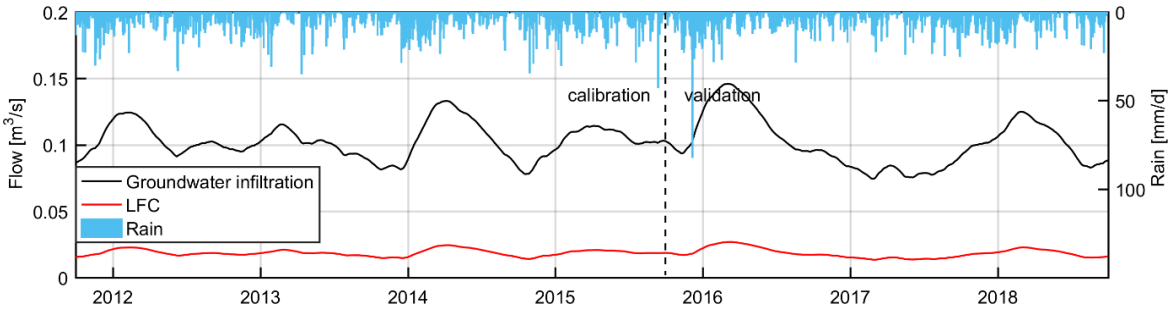

Figure 7.11: Inflow from the GIM (Groundwater infiltration) of which a part constitutes the low-flow component (LFC) for the 2012 and 2015 hydrological years during calibration and validation.

3. Simulated total discharge of Ballindine

The simulated hourly discharge of Ballindine along with its LFC (Eckhardt method) during calibration and validation are displayed in Figure 7.12a. The cumulative discharges are illustrated in Figure 7.12b. The performance of the model simulating the discharge is summarised in Table 8.1.

The overall pattern of the simulated discharge is very well represented, as indicated by the three performance indicators. For the calibration period, both NSE and KGE are relatively high with values ≥0.8. Further, the total simulated discharge over the four years can be considered as identical to the observed discharge. During validation, the performance decreases. Importantly, the total simulated discharge is 13.0% above the observed discharge and the NSE and KGE drop to 0.76 and 0.78.

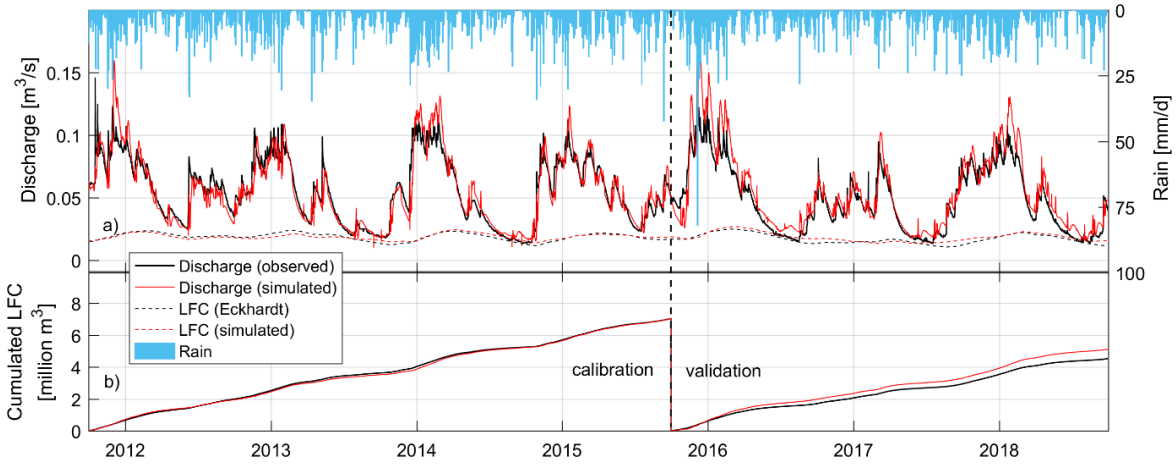

Figure 7.12: Results of simulated vs. observed hourly discharge of Ballindine spring and LFC along with rainfall (a) and cumulative discharges of Ballindine spring during calibration and validation (b).

Table 7.3: Performance of the simulated discharge of Ballindine spring.

Parameter	Calibration		Validation	
NSE	+0.844		+0.761	
KGE	+0.886		+0.767	
VCC	0.00 MCM	-0.01%	+0.59 MCM	+13.00%

Another way of analysing the performance of the model is looking at the observed and modelled spectra of the spring discharge. The spring discharge integrates the different flow components that are believed to be resembled by the spectra. Hence, the comparison of spectra reveals information on the integrated observed and modelled flow components.

The different spectra were analysed for the entire modelling period (the hydrological years 2012 to 2018) for observed (Figure 7.13a) and simulated (Figure 7.13b) time series.

The different plots suggest a very similar frequency pattern with almost identical powers. Yet, deviations can be observed in the high-frequency range, approximately between 5 and 10 h. While for the observed time series the two upper most spectral coefficients β_8 and β_9 lie within the domain of persistent Brownian noise, the corresponding spectral coefficients β_9 and β_{10} of the simulated time series are associated with black noise. Further, the relative changes between the third and second upper most spectral coefficients is much stronger for the simulated time series (-1.84) than for the observed time series (-0.04). This difference suggests indeed a stronger role for the high frequency component for the simulated time series than for the observed time series. Hence, the conduit contribution is likely to be exaggerated for the simulated time series.

However, the pattern of the spectrum of the simulated time series is considered to be very close to the observed time series' spectrum. Hence, the representation of flow components is considered to be realistic.

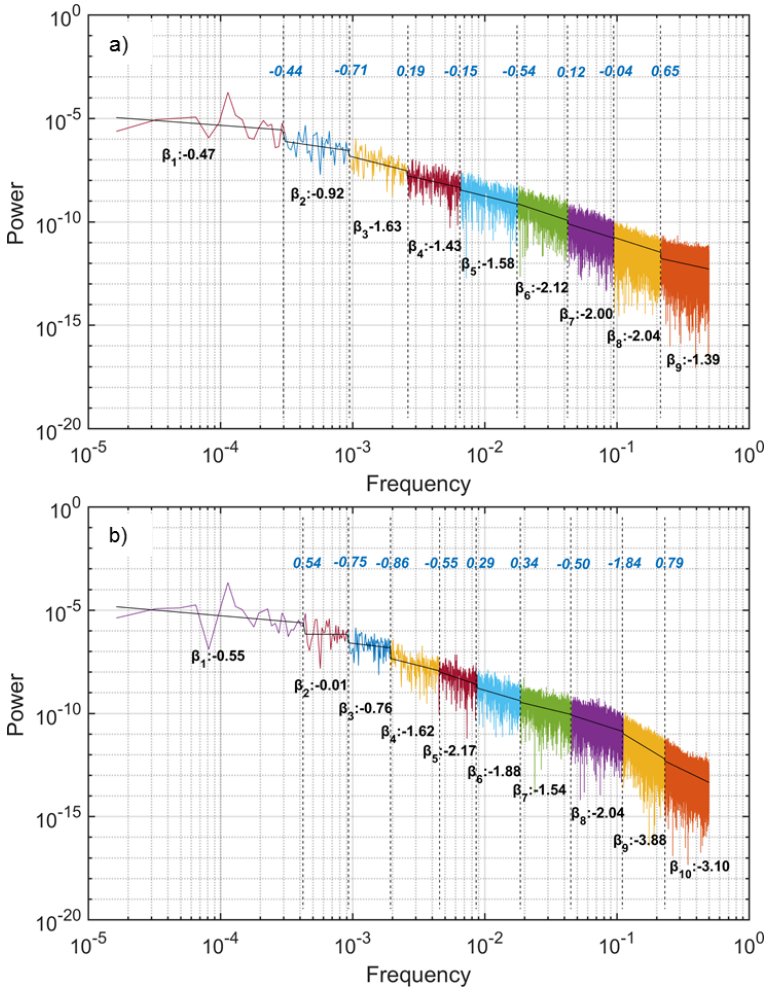

Figure 7.13: Power spectrum and spectral coefficients of the observed discharge time series (a) and simulated time series (b) of Ballindine spring for the hydrological years 2012 to 2018.

The rate of loss of memory of the observed and simulated spring discharge is further displayed as ACF for 83 d in Figure 7.14. It is obvious that the rate of loss between the observed and simulated discharge is almost identical, which indicates the good representation of the modelled time series. The changes in slopes previously noted in Figure 6.1b correspond to changing slopes of the ACF of the simulated time series.

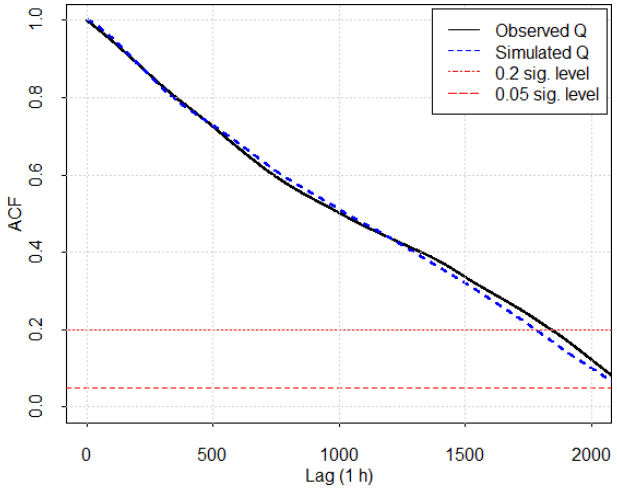

Figure 7.14: ACF of hourly observed and simulated discharge of Ballindine.

4. Major diffuse flow component

The major diffuse component comprises the difference between the inflow through the two permeable pipes from the river channel and the minor diffuse flow component originating from the sub-catchments. This inflow was matched to the diffuse flow component established by DWT (Section '6.4. DWT').

Figure 7.15 illustrates the performance of the simulated hourly major diffuse component for the calibration and validation period (a) and cumulative discharges (b). Table 7.4 summarises the performance indicators.

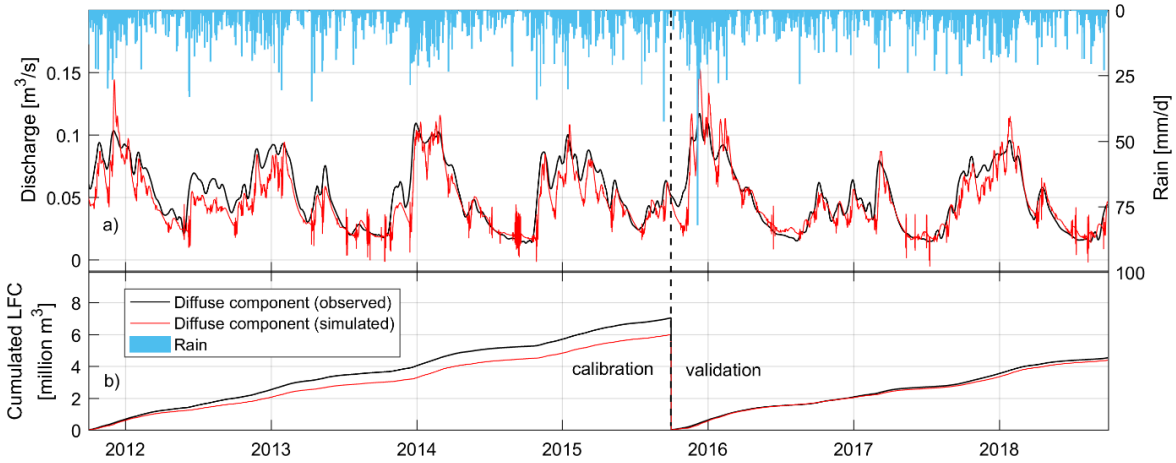

Figure 7.15: Results of simulated vs. observed major diffuse component and rainfall (a) and cumulative major diffuse discharge (b) during calibration and validation.

Table 7.4: Performance of the simulated major diffuse flow component of Ballindine spring.

Parameter	Calibration		Validation	
NSE	+0.763		+0.838	
KGE	+0.835		+0.913	
VCC	-0.86 MCM	-12.3%	-0.15 MCM	-3.3%

The NSE and KGE differ between the calibration and validation period, with a NSE of 0.763 and a KGE of 0.835 during calibration, which increases to 0.838 and 0.913 during validation. The simulated flows are underestimated during both periods, which is expressed by the VCC which accounts for -12.3% during calibration, and an improvement to -3.3% during validation.
Overall, the pattern of the estimated major diffuse flow can be represented by the model, yet, the model performance shows deficiencies. An increasing share of the major diffuse flow component resulted in a worse performance of the model simulating the overall discharge.

5. Conduit component

The simulated conduit inflow from the river bed was matched against the difference of the observed discharge and the major and minor diffuse flow component (Figure 7.16).
The simulated conduit contribution is very different compared to the 'observed' conduit inflow. In fact, the difference between the 'observed' and simulated time series may be related to the differences in the high frequency spectrum, as previously discussed with regard to Figure 7.13.
No NSE and KGE were calculated, because it is obvious that the patterns largely deviate. Instead, the comparison was limited to the VCC, which accounts for +0.52 million m^3 (+250%) during calibration and +0.36 million m^3 (+254%) during validation. Hence, the simulated conduit contribution is largely overestimated compared to the 'observed' conduit contribution. At the same time, such high conduit inflows were necessary to achieve the previously presented performance of the simulated spring discharge – any reduction in conduit inflow caused a drop in performance of the simulated spring discharge.

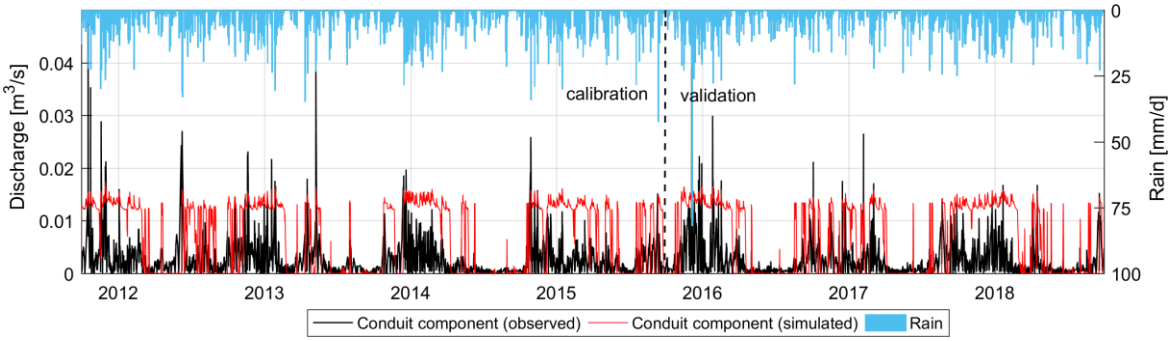

Figure 7.16: Results of simulated and 'observed' conduit component and rainfall during calibration and validation.

7.1.5. Summary of Ballindine pipe network model

Overall, the pipe network model proves to be capable of simulating the discharge regime of Ballindine spring as the result of three distinct recharge processes and two distinct flow dynamics (open channel/pressurized pipe flow vs. laminar diffuse). By doing so, the model is shown to be capable to resemble the conceptual site model (Figure 7.1), and in fact, it excels better than the reservoir model discussed in Section '5.1.4. Reservoir modelling'. This is remarkable because given the

simple structure, few parameters and neglecting any spatial component, the performance of global models can be expected to be superior to the performance of a (semi-)distributed model. The performance of the reservoir model and the pipe network model decreases during validation, and both models almost identically overestimate the simulated discharge during this period.

The modelled spring discharge shows almost an identical loss of memory compared to the observed discharge, as indicated by the ACF. Further, the spectrum of the modelled discharge matches very well the spectrum of the observed discharge, which suggests that flow components of the model and the 'real world' karst network integrate similarly towards (or at) the spring outlet. Major differences between the simulated and 'observed' time series relate to the high-frequency conduit contribution. Either the model is not representing this component adequately, or else, the reference conduit flow time series (which has been derived from other data) contains too high flows.

Figure 7.17 summarises the simulation of the total discharge and flow components for observed (a) and simulated (b) time series. Again, the total discharge and LFC match very well. However, the major diffuse flow component is underestimated by the model; as a result, the modelled conduit discharge is probably overestimated.

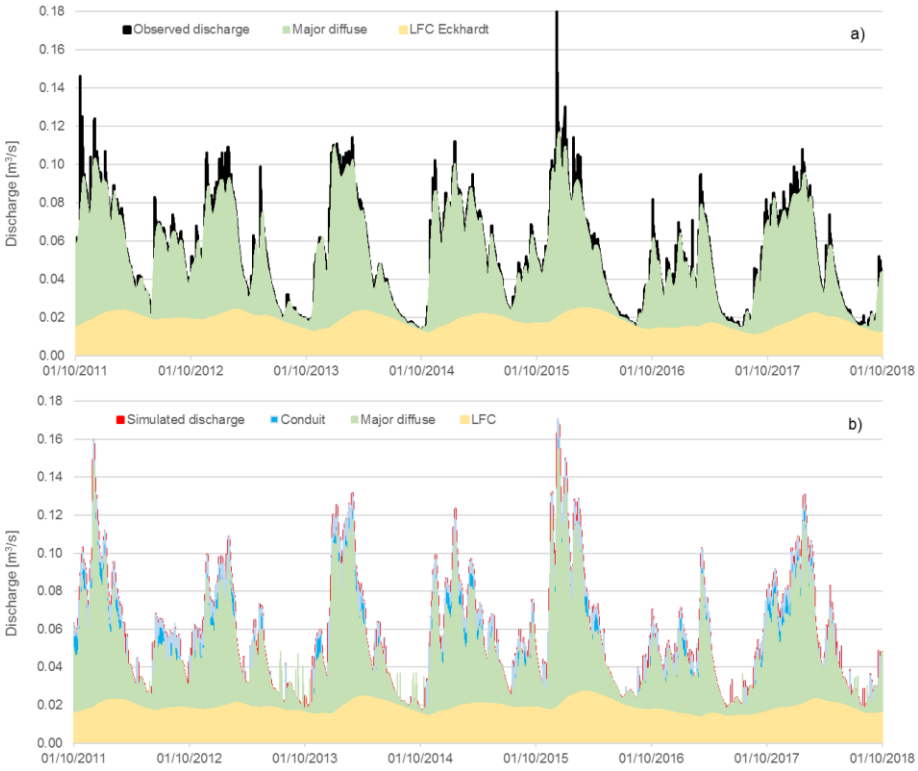

Figure 7.17: Summary of recharge and flow components for a) observed and b) simulated time series for the hydrological years 2012 to 2018.

7.2. Manorhamilton

The conceptual model of the Manorhamilton aquifer underlying the pipe network model is based on the following conclusions that were achieved from the previous results within this study:

1. **Change of the catchment boundaries:** The tracer tests conducted suggest larger catchment boundaries than that delineated by the EPA (2011b) covering 1.95 km^2. This is supported by water balances and the KarstMod reservoir model suggesting that the catchment may range between 3.3 and 5.0 km^2. The average catchment size based on the water balance is 4.3 km^2. Based on the dip of the Dartry formation, it is assumed that the catchment extends further to the west upland towards the Leean Mountain;
2. **Upland-lowland conduit type karst aquifer:** Where present, the soil cover is relatively shallow in the catchment (<1 m). Bare limestone outcrops are widespread; hence, the role of the soil as attenuation system must be assumed to be very limited. Swallow holes are ubiquitous in the catchment, and artificial tracer tests conducted confirm their connection to a conduit system: mean travel times range between 88 and 223 m/h with a generally low dispersion. The two TBCs of fluorescein suggest a very similar recession, hence, conduit parameters between the two injection sites and Manorhamilton spring may be very similar. The hydrograph and chemograph show the typical pattern of a conduit-dominated karst aquifer: almost every large rain event causes a rising limb and drop in EC and temperature. There is no indication of contribution from a deeper reservoir, hence, the aquifer is conceptualized as being relatively shallow and unstructured, as indicated by the cross-correlation function (CCF).
   Further, following the classification of Mangin (1975) and El-Hakim and Bakalowicz (2007) the aquifer exhibits a relatively low regulating power with a dominance of fast infiltration. The mean residence time is estimated at 95 d. The aquifer is classified as “aquifer with a well karstified infiltration zone and extended conduit network ending into a flooded phreatic zone”;
3. **Flow components:** Fitting linear reservoirs onto the MRC of Manorhamilton spring suggests that the aquifer is drained via three flow components: a major fast flood component resembling conduit drainage (k' = 0.15 h^{-1}), an intermediate component (k' = 0.03 h^{-1}) and a minor low flow component (k' = 0.0025 h^{-1}).
   Different analyses highlight the dominance of the fast and intermediate recharge and flow component: The results of the KarstMod reservoir model suggest that the entire hydrograph can be simulated by only using the reservoir ‘C’ resembling conduit flow. The dominance of the fast recharge and flow results in little storage, expressed by relatively low linearity of the discharge time series through the ACF. Further, linearity between rainfall and spring discharge is relatively high, hence, the spring clearly responses quickly to rainfall input whereby the rainfall signal becomes only moderately transformed towards the spring, as indicated by the high peak of the CCF.

In turn, the role of a matrix or low-permeability flow component must be considered as negligible: the integration of reservoir 'M' resembling a slow and diffuse flow component reduced the performance of the KarstMod model. Further, frequency and noise analysis suggest the presence of three non-stochastic frequency segments: a low, intermediate and high frequency component associated with different spectral exponents. Based on exponentially fitted low-flow components (LFC), continuous LFCs were established using a digital recursive filter and a decomposition method in the form of discrete wavelet transform. Both match poorly the exponentially fitted components, although the LFC established using the digital recursive filter seems more plausible. Hence, it seems challenging to generate a realistic LFC that can be used as calibration reference.

Accordingly, three flow components are integrated within the pipe network model: a) a major proportion of conduit flow, b) a contribution of intermediate flow, and c) minor proportion of diffuse slow-flow (LFC) that sustains the flow during periods of drought: the major conduit contribution (a) and the intermediate component (b) are conceptualized to originate from concentrated infiltration directly via swallow holes and/or rapidly concentrating diffuse recharge. The minor diffuse-slow LFC (c) is conceptualized to originate from the fissured matrix and low permeability domain that drains the aquifer during periods of absence of rainfall.

Based on the abovementioned results, a CSM (Figure 7.18) was developed underlying the InfoWorks ICM pipe network model.

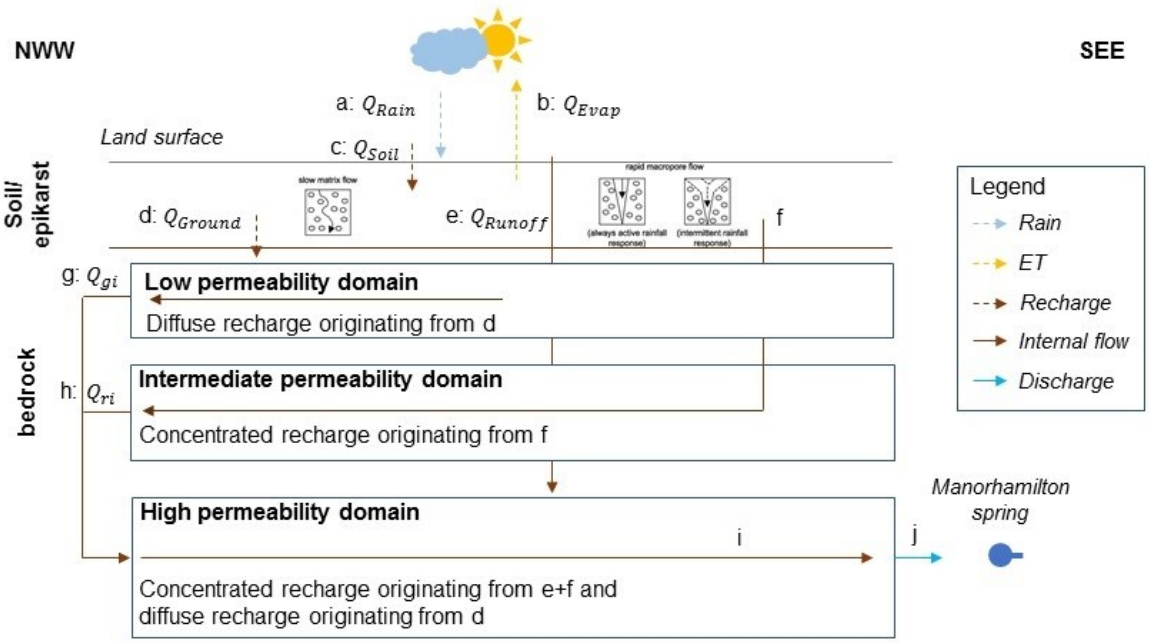

Figure 7.18: Conceptual site model of Manorhamilton spring.

The CSM is split into a soil-epikarst layer (soil store) and bedrock layer (groundwater store). Rainfall (a: Q_{Rain}) falls on the land surface from where one share infiltrates into the soil-epikarst layer (soil store) via soil store inflow (c: Q_{Soil}), while another share is concentrated groundwater recharge that directly enters the conduit network (e: Q_{Runoff}). The latter one resembles the very quick recharge component that relates to the high permeability domain discharge component (k' = 0.15 h^{-1}).

Within the soil store, losses occur via evapotranspiration (b: Q_{Evap}). The discharge of the soil store, i.e. percolation flow, is split into two sequences of flows: 1.) the components f and h: Q_{ri} (rainfall-induced infiltration) correspond to intermediate recharge and flow. This intermediate recharge drains into the conduit network and is conceptualised as relating to the intermediate component of the spring hydrograph recession (k' = 0.03 h^{-1}). The other sequence of flows is 2.) the components d: Q_{Ground} and g: Q_{gi} constitute percolation flow into the groundwater store, which resembles recharge into the low permeability domain, i.e. the fissured matrix, and drainage of the groundwater store via infiltration flow into the conduit network resembling the LFC. Altogether, the drainage of the three permeability domains is the combined flow in the centred conduits (i) that finally constitutes the spring hydrograph of Manorhamilton spring (j).

7.2.1. General model outline

The entire catchment was sub-divided into six sub-catchments (Figure 7.19, Table 7.5). The outline is based on the results of tracer tests in conjunction with the perception of the alignment of conduits in the catchments and the apparent landcover.

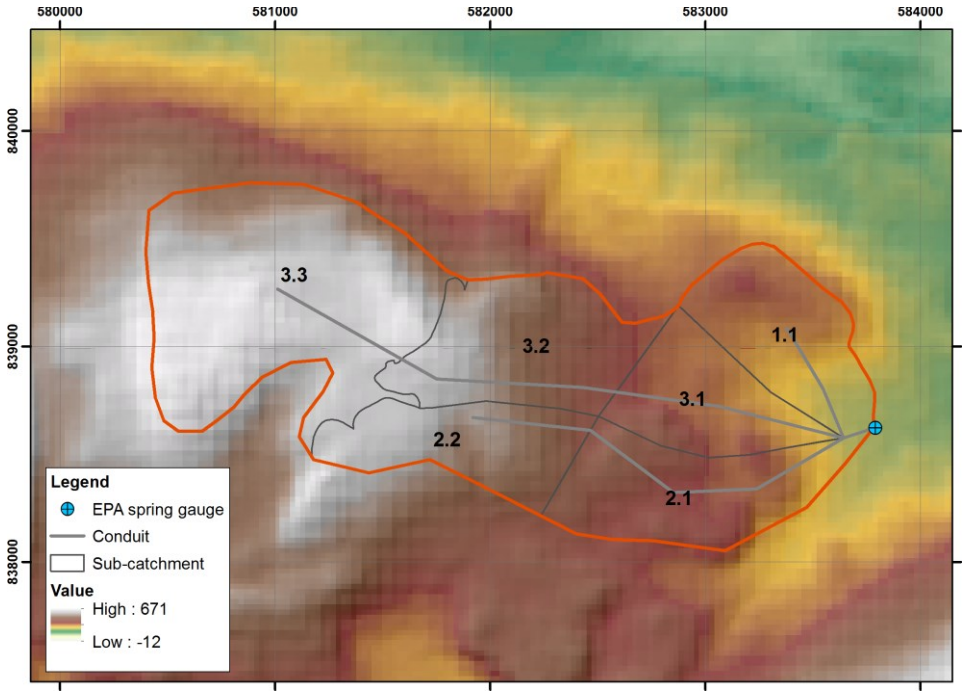

Figure 7.19: Manorhamilton sub-catchments as modelled in ICM.

Table 7.5: Sub-catchments of the catchment of Manorhamilton spring.

Sub-catchment	Area [km²]	Mean elevation [masl]
1.1	0.444	158.9
2.1	0.536	191.0
2.2	0.407	272.7
3.1	0.384	175.6
3.2	0.577	250.6
3.3	1.210	315.4
Total	3.558	227.37

Sub-catchment 1.1 drains the northern part as proven by the tracer test on 16 Sep 2017. Sub-catchment 2.1 and 2.2 drain the southern part, as proven by the tracer test on 12 Sep 2019. Sub-catchments 3.1, 3.2 and 3.3 drain the centre and upland of the catchment. Numerous swallow holes in the centre suggest the alignment of east-west trending conduits. The topography of the catchment was accounted for by assigning mean elevations to the sub-catchments, ranging between 158.9 and 315.4 masl. In sub-catchment 1.1 to 3.2, shallow soils and bare rock outcrop with numerous swallow holes dominate the landcover. In turn, sub-catchment 3.3 is completely covered by peat and so it is believed that recharge in sub-catchment 3.3 is more damped and slower than in the other sub-catchments. This aspect was resembled in the model: sub-catchment 3.3 drains laterally into a permeable pipe with a porosity of 50% and K = 0.1 m/s (Figure 7.20).

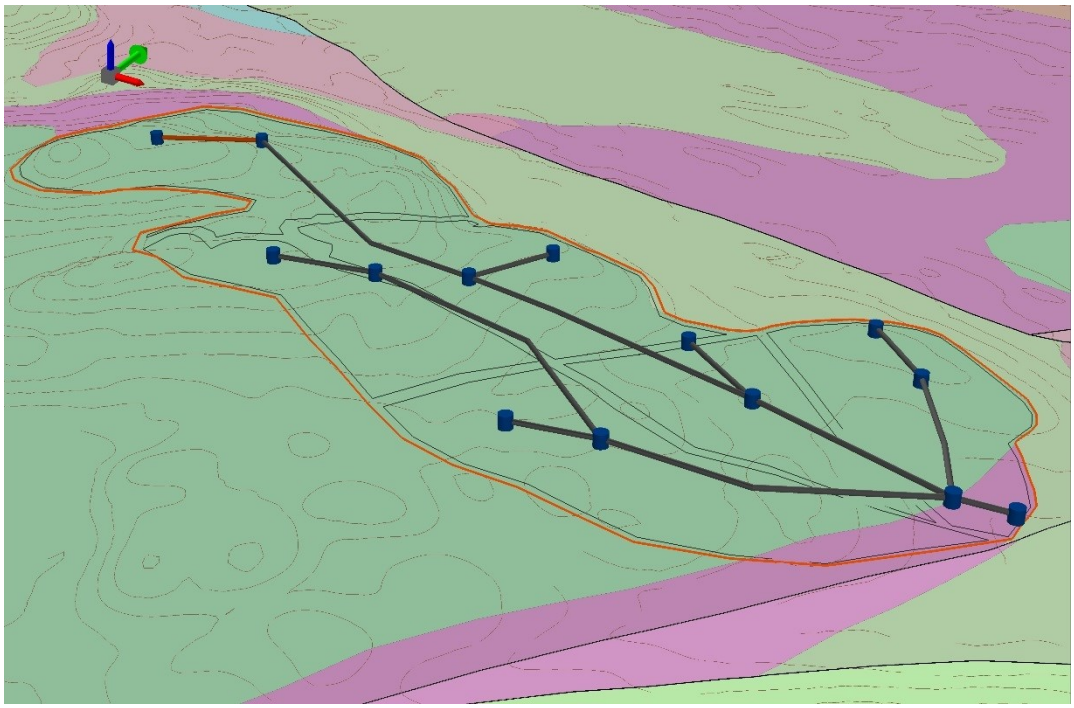

Figure 7.20: ICM model outline and sub-catchments for Manorhamilton spring. Dark grey lines are ‘full pipes’ and the red line is a ‘permeable pipe’. The blue cylinders are manholes.

In turn, sub-catchments 1.1 to 3.2 drain directly into conduits with roughness (Colebrook-White) of 10.0 mm.

The input time series for the model are hourly rainfall observed at MH3, daily evapotranspiration (Hargreaves, 1994) based on climate data Markree and the observed hourly discharge at the EPA monitoring station.

7.2.2. Flow components

The MRC showed that that the spring's recession can be decomposed into three distinct exponentials resembling recharge and/or drainage from distinct permeability domains. A continuous time series resembling LFC was established by the Eckhardt method characterised by k' = 0.0025 h^{-1} (Sections '6.5.2. Manorhamilton' and '6.5.2.2. Digital filtering').
A second intermediate recession component was identified with k' = 0.03 h^{-1} ('6.5.2. Manorhamilton'). However, no truly realistic continuous time series of a low-frequency signal could be established (Section '6.4.2. Manorhamilton'). And third, a major conduit component was identified with k' = 0.15 h^{-1} (Section '6.5.2. Manorhamilton'). Presumably, the dominance of this quick component is the reason that the discharge of the spring could be modelled using only the two reservoirs 'E' and 'C' in the KarstMod model (Section '5.2.5. Reservoir modelling').
However, in terms of continuous time series, only one could be established for the LFC, while the remainder of the hydrograph can be considered by combining contributions from both the high and intermediate flow components (Figure 7.21).

The fast-flow component was linked to direct and concentrated recharge, modelled using the triangular Unit hydrograph model. The intermediate flow linked to a more damped recharge signal was modelled as rainfall-induced infiltration from the soil store. The diffuse signal was modelled as discharge from the groundwater store. The conceptual model of the hydrograph is illustrated in Figure 7.22.

All flows were generated per sub-catchment. Each sub-catchment drains into an empty conduit that models turbulent/open channel flow, except sub-catchment 3.3 which, as mentioned previously is covered by peat, and therefore drains into a permeable pipe to simulate a more damped flow response.

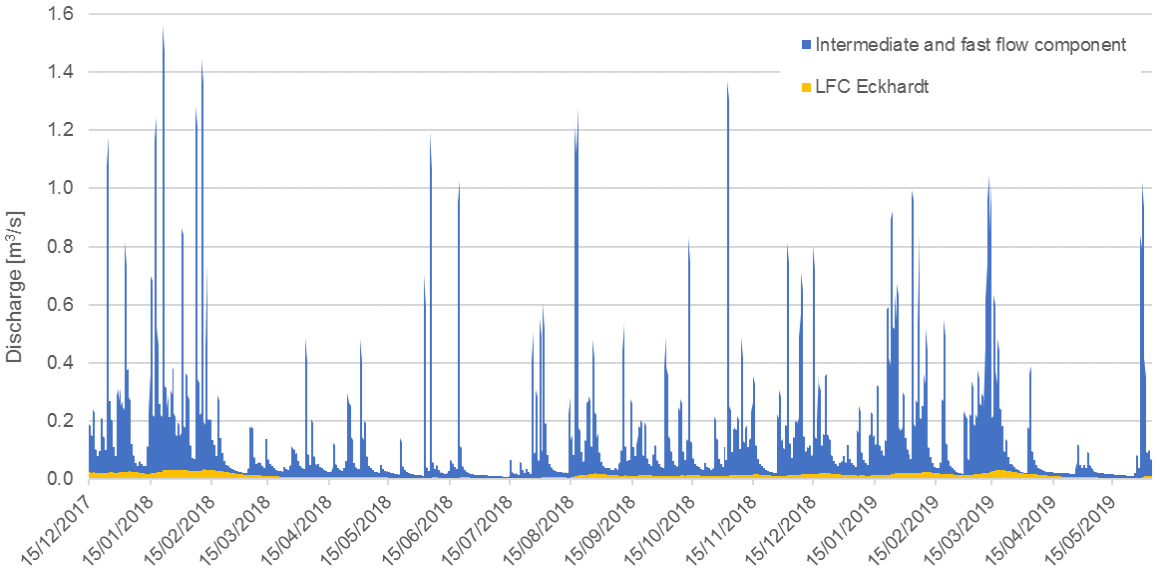

Figure 7.21: Flow components of Manorhamilton spring: fast- and intermediate flow and the LFC.

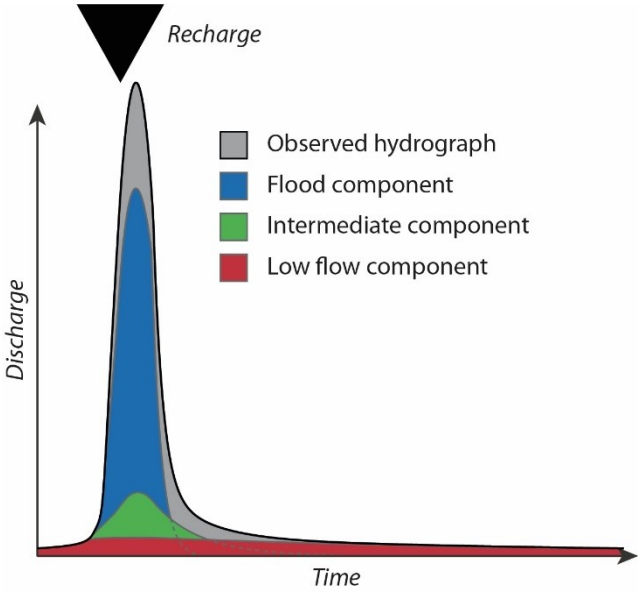

Figure 7.22: Flow components of Manorhamilton spring: flood component (runoff), intermediate component (soil store inflow) and the LFC (groundwater store inflow).

7.2.3. Calibration

The parameters used to evaluate the model performance are the VCC, the NSE and the KGE. Further, the spectra of modelled and observed spring discharges were compared, as well as their ACFs. The model was run on an hourly timestep between 15 Dec 2017 and 04 Jun 2019. The first 16 days of that period was used for warm-up / initialisation of the model. Calibration was applied onto the period 01 Jan to 31 Dec 2018, while the resulting model was evaluated using the period 01 Jan to 04 Jun 2019.

The following elements of the InfoWorks and their discharges were calibrated against reference time series in the following order:

1. To match the water balance, the soil store and groundwater store were calibrated, as the soil store models water losses via evaporation. Hence, the soil depth was matched against the percolation coefficient in order to have an initial set-up of approximate recharge into the soil store, which matches the overall observed discharge. Further, the percolation coefficient and infiltration coefficient were approximated to ensure drainage of the reservoirs (avoiding continuously increasing water levels because of too little drainage);
2. Fast concentrated recharge, modelled as runoff in InfoWorks, was calibrated against observed individual rising and falling limbs. Runoff was modelled using the triangular Unit Hydrograph routing model and the fixed percentage runoff modelling the volume. The shape of the runoff hydrograph was modelled using the curvelinear SCS unit hydrograph model (Figure 4.21). The occurrence and shape of the modelled runoff peak and the recession was fitted against the observed hydrograph and individual flood recessions following k' = 0.15 h^{-1} using the parameters T_p, T_b, the runoff routing value and the fixed runoff coefficient;
3. The shape and the total volume of LFC originating from the groundwater store was calibrated against the LFC as established using the Eckhardt filter using the sum of discharges of all sub-catchments;
4. The recession of the discharge of the soil store into the conduit network (rainfall-induced infiltration) resembling intermediate recharge/flow was fitted against the intermediate recession coefficient with k' = 0.03 h^{-1}. This was done using an event-based because no continuous intermediate discharge time series could be established. Therefore, the simulated recessions of the soil store were fitted against the course of the intermediate recession of the MRC;
5. The simulated total discharge of the pipe network model at the outfall resembling Manorhamilton spring was calibrated against the observed time series by adjusting parameters of the pipes (bottom and top roughness of empty conduits, K and porosity of the permeable pipe).

1. Soil and groundwater store

Table 8.1 summarises the final parameters of the GIM.

No loss due to baseflow was expected (no cross-catchment flow) and therefore the baseflow threshold was set to an excessive level (10 m). The infiltration threshold was set to 0 m meaning that no baseflow that would occur below that threshold.

For example, the combination of soil depth (0.1 m), percolation threshold (55%), soil porosity (60%) and the percolation coefficient of 1.5 ensures an even water balance.

Table 7.6: Final GIM parameters for all sub-catchments of Manorhamilton spring.

Soil depth [m]	Percolation Coefficient [t^{-1}]	Baseflow Coefficient t^{-1}]	Infiltration Coefficient t^{-1}]	Percolation Threshold [%]	Percolation percentage infiltrating [%]	Porosity of soil [%]	Porosity of ground [%]	Baseflow threshold level [m]	Baseflow threshold type	Infiltration threshold level [m]	Infiltration threshold type
0.1	1.5	100	35	55	76	60	1	10	Abs.	0.0	Abs.

2. Fast recharge

The fast-concentrated recharge (runoff) hydrograph was broadly matched against the occurrence of discharge peaks for the entire calibration period. Then more closely, the shapes of the runoff peaks and recession were fitted against the exponential recession following k' = 0.15 h^{-1}. The final parameters related to runoff are displayed in Table 7.7.

As a result, the fixed runoff coefficient was set to 44%, meaning that 44% of groundwater recharge was modelled as direct conduit recharge. Accordingly, the remainder, i.e. 56% of recharge, was directed into the soil store.

Since the fast and concentrated recharge and flow component largely controls the peak flow of an event, the time to peak t_p was found to match best the hydrograph peaks at t_p = 20 min. The base time t_b that controls the duration of the runoff event was best matched against the exponential recession of k' = 0.15 h^{-1} with t_b = 825 min.

Table 7.7: Final runoff parameters for all sub-catchments of Manorhamilton spring.

Runoff routing type	Runoff routing value	Runoff volume type	Surface type	Routing model	Fixed runoff coefficient [%]	Time to peak, t_p [min]	Base time, t_b [min]
Abs	1	Fixed	Pervious	Unit	44	20	825

3. LFC

The volume of modelled LFC is controlled by the volume of flow directed from the soil store into the conduit network, as the remaining share is diverted into the groundwater store. Hence, 'percolation percentage infiltrating' was found to be optimal at 76% (of 56% of the total flow) (
Table 7.6), which means that 24% (of 56% of the total flow) of drainage of the soil store is diverted into the groundwater store. The optimal discharge of the groundwater store, i.e. infiltration flow, was at an infiltration coefficient of 35.

4. Intermediate recharge

The volume of the intermediate recharge (rainfall-induced infiltration) was modelled with a percolation percentage infiltrating at 76%. The recession of the percolation percentage infiltrating was

fitted against single events and the exponentially separated intermediate recession of the MRC with k' = 0.03 h^{-1}. The best percolation coefficient was found at 1.5 (Table 8.1).

5. Total discharge

The total modelled spring discharge is the sum of the fast and concentrated recharge (runoff), the intermediate recharge (rainfall-induced infiltration) and the LFC (infiltration flow), which is then transformed by the characteristics of the pipe network model towards the spring outlet.

7.2.4. Results

The calibration parameters previously outlined were optimised to yield the following results.

1. Soil and groundwater store

Figure 7.23 shows the course of both the average soil store level and the groundwater store level of all sub-catchments in m, along with hourly rainfall. Again, it is important to note that these levels neither correspond to physical observations nor represent realistic water levels. Instead, these water levels constitute a representation of the notional stored volumes in these different conceptual reservoirs.

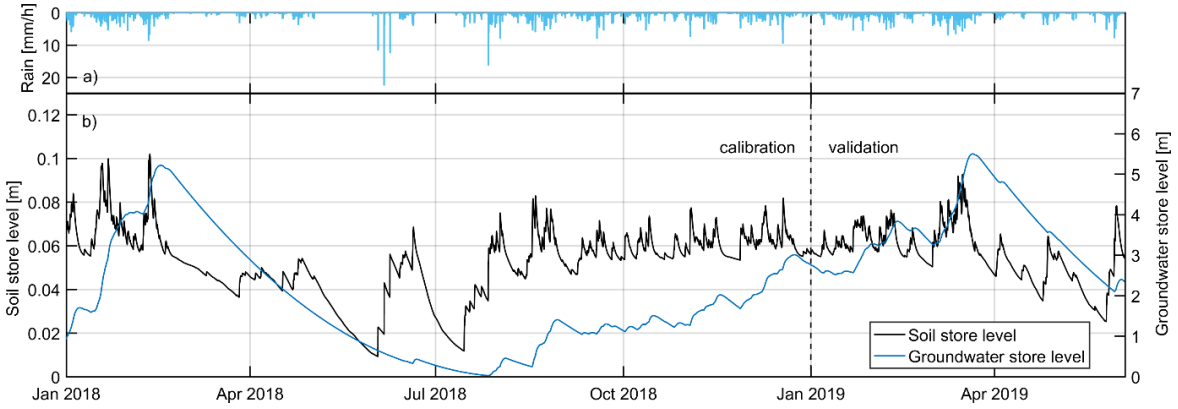

Figure 7.23: Rainfall (a) and water level of the soil and groundwater store (b) during calibration and validation.

None of the water levels shows an increasing or decreasing trend indicating too rapid or too slow drainage.

The soil store water level ranges between 0.01 and its maximum of 0.1 m where maximum evapotranspiration occurs. The groundwater store ranges between 0.02 and 5.5 m.

During the period Mar to Jun 2018, both reservoirs show a gradual declining trend. The soil store, however, shows events of influx associated to rainfall. In turn, the groundwater store does not show any increase in water level. Instead, a continuous decline of the water level can be observed between Mar and the middle of Jun 2018. This decline is related to very low inflow to the groundwater

store, which again is related to the generally very low rainfall during that period. It was previously mentioned in Section '6.3.2. Manorhamilton' that the total rainfall during that period seems to be biased, i.e. less rainfall was recorded than it should be. This may explain the gradual declining trend of the groundwater store. Hence, the results of this period may lack validity.

2. Fast recharge

Figure 7.24 shows the observed rainfall, observed discharge and simulated runoff. The simulated runoff is the direct result of rainfall, matching overall the pattern of discharge peaks (note that simulated runoff peaks are lower than observed discharge peaks because the discharges of the soil store and groundwater store are not incorporated).
Since the runoff signal will be modified within the conduit, the comparison really aims to match the magnitude and duration of runoff (concentrated recharge) against the actual discharge peaks.

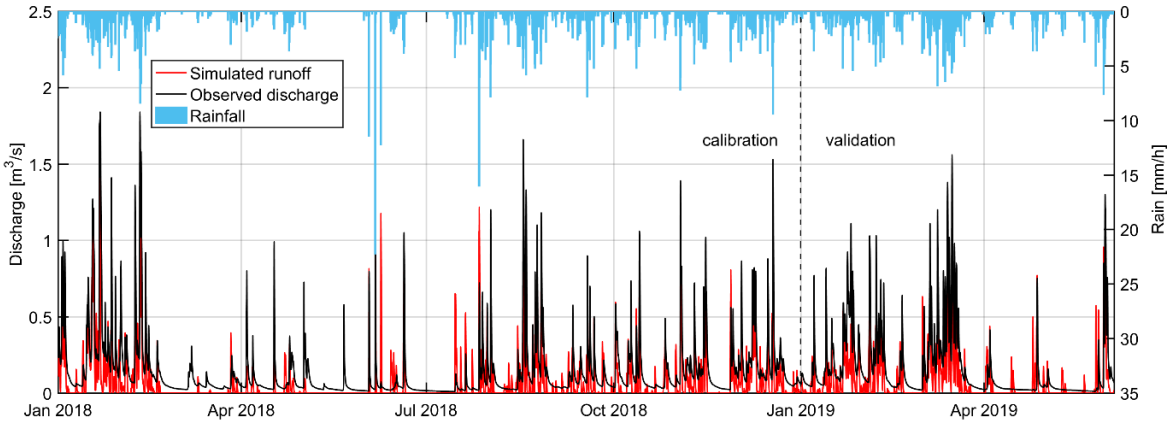

Figure 7.24: Observed discharge and simulated runoff resembling concentrated recharge along with rainfall during calibration and validation.

The duration and recession of runoff events was fitted against single events (Figure 7.25). The plot shows for the exemplified events a reasonable fit for the occurrence and magnitude of the simulated runoff peaks and their durations. An exception though is the observed rain event on Jun 9 to 10, which did not cause a response of the hydrograph, while the InfoWorks model clearly simulates a major flood event. The reason is believed to be unaccounted rainfall. Nevertheless, the simulated recessions match well the exponentially fitted recession with k' = 0.15 h^{-1} for most of the events. Yet, the bottom part of the recession is underestimated by the simulated runoff, which is related to the characteristics of the SCS hydrograph model. In addition, single small rain events seem to cause an overestimation of modelled flow.

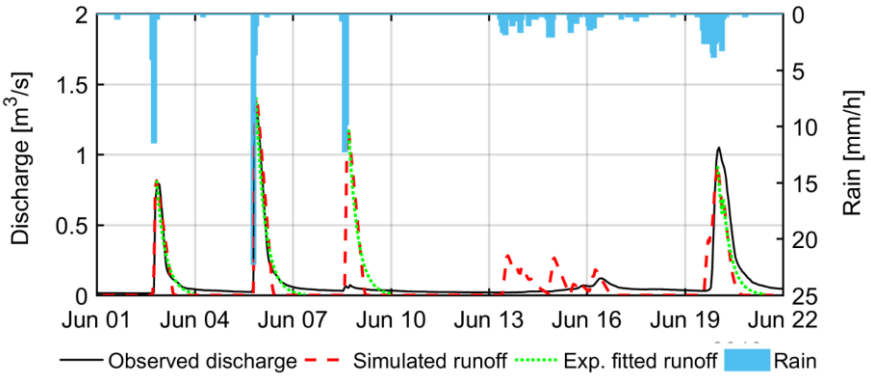

Figure 7.25: Observed discharge and simulated runoff resembling concentrated recharge along exponentially fitted fast recession with k' = 0.15 h^{-1} and rainfall between 01 and 22 Jun 2018.

3. LFC

Figure 7.26 shows the observed rainfall and the simulated discharge of the groundwater store compared to the LFCs generated using the Eckhardt filter.

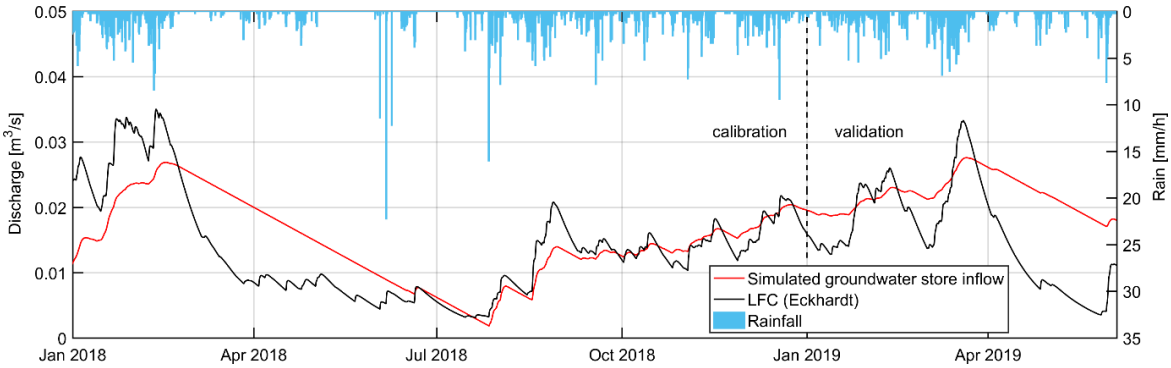

Figure 7.26: Rainfall, LFCs (Eckhardt filter) and the simulated groundwater store inflow resembling discharge of the low permeability domain during calibration and validation.

As mentioned above, the groundwater store is subject to a continuously declining water table between Mar and the middle of Jun 2018, which is reflected by the continuously declining discharge of the reservoir. In fact, during this period, the simulated discharge does not fit the LFC well.
For the remaining periods, the course of the simulated discharge fits the LFC (Eckhardt) better. During calibration, the KGE and NSE between the simulated discharge and the LFC (Eckhardt) are 0.638 and 0.494 (Table 7.8). Hence, the performance of the modelled LFC is in the range of 0.5, which is generally considered the threshold of acceptance (Moriasi, et al., 2007). However, the ~3 months period of suspected erroneous rainfall data must be considered, impacting on inflow into the groundwater store as well as discharge. During validation, the performance of the modelled LFC largely decreases, notably the absolute quantity is highly exaggerated (+39.2%). In consequence, the NSE and KGE drop to -0.332 and +0.185. Presumably, the LFC was modelled very

conservatively during calibration in order to match the flows during the period of erroneous rainfall. In consequence, modelled flows are overestimated during the periods of validation.

Table 7.8: Performance of the simulated LFC of Manorhamilton spring compared to the LFC established by the Eckhardt method.

Parameter	Calibration		Validation	
NSE	+0.494		-0.332	
KGE	+0.638		+0.185	
VCC	+0.030 MCM	+7.6%	+0.082 MCM	+39.2%

4. Intermediate recharge

Figure 7.27 shows the observed rainfall and the observed discharge and simulated soil store inflow.

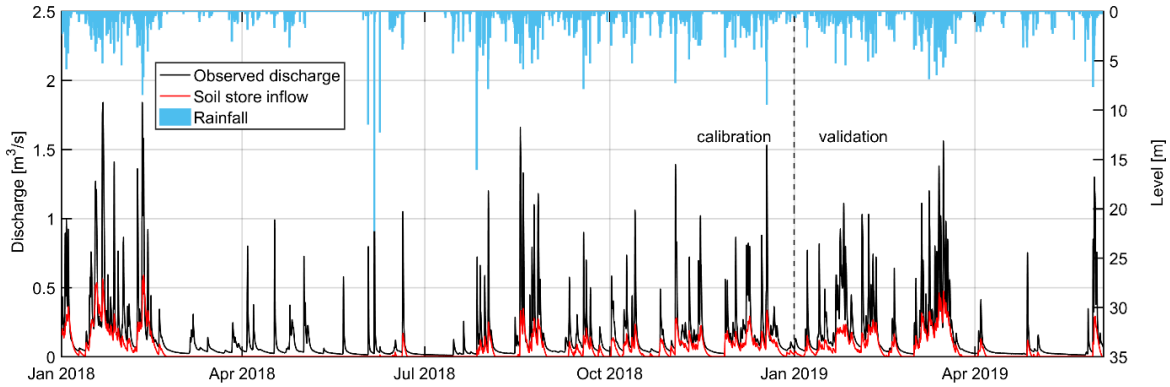

Figure 7.27: Observed discharge and simulated soil store inflow resembling intermediate recharge along with rainfall during calibration and validation.

The simulated soil store inflow is the intermediate result of rainfall following runoff and infiltration to soil store. The soil store inflow was matched against the intermediate recession with k' = 0.03 h^{-1}. Examples of single events and fitted soil store inflow are displayed in Figure 7.28.

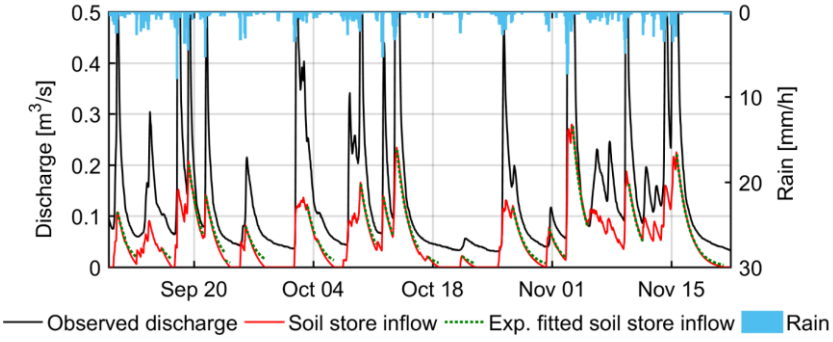

Figure 7.28: Soil store inflow resembling intermediate recharge along exponentially fitted fast recession with k' = 0.03 h^{-1} and rainfall between 10 Sep and 22 Nov 2018.

Overall, the simulated recession seems to fit well against the 'ideal' exponentially fitted recession based on the MRC. Yet, at low flows, the simulated recession starts to deviate for individual events. Nevertheless, the results seem plausible.

5. Total discharge

The total modelled spring discharge is the sum of the fast and concentrated recharge (runoff), the intermediate recharge (rainfall-induced infiltration) and the LFC (infiltration flow), which is then transformed by the characteristics of the pipe network model towards the spring outlet. Figure 7.29 illustrates the observed and simulated discharge of Manorhamilton spring. The performance indices are summarised in Table 7.9. During calibration, the NSE and KGE are 0.807 and 0.904, which is a very good fit. The simulated results differ, however, from the observed time series again during the period Mar to middle of Jun 2018 which, as previously highlighted, is believed to be the result of erroneous rainfall input. During validation, the NSE increases to +0.882 while the KGE slightly drops to +0.892. Notably, the simulated discharge exceeds the observed discharge by 9.04% during validation.

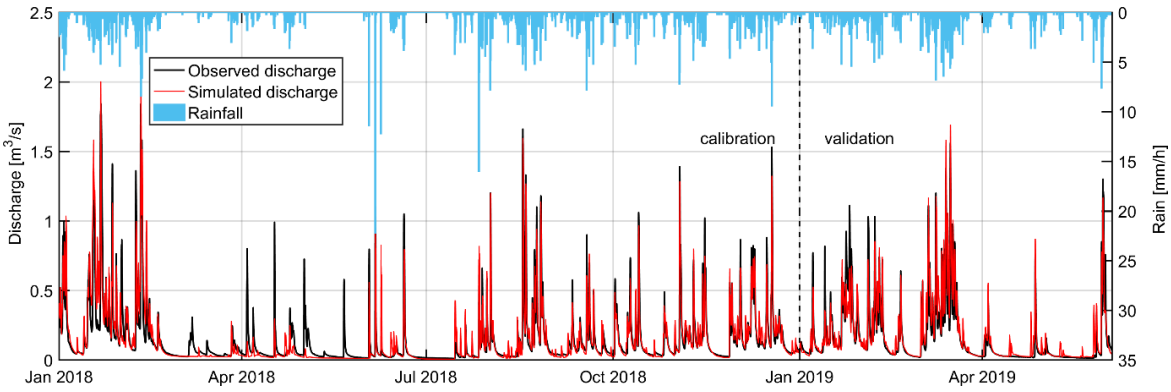

Figure 7.29: Observed and simulated discharge of Manorhamilton spring along with rainfall during calibration and validation.

Table 7.9: Performance of the simulated discharge compared to the observed spring discharge of Manorhamilton spring.

Parameter	Calibration		Validation	
NSE	+0.807		+0.882	
KGE	+0.904		+0.892	
VCC	+0.020 MCM	+0.21%	+0.196 MCM	+9.04%

Another way of checking the performance has been carried out by comparing the spectrum of the observed discharge time series (Figure 7.30a) against the spectrum of the simulated time series (Figure 7.30b). Overall, the patterns look very similar with the corresponding spectral coefficients all laying all in a very similar range. Differences can be observed in the higher frequencies (β_5 to β_7), however, the difference does not appear to be fundamental.

The differences between the spectral coefficients seems to be smoother within the observed time series than in the simulated one where relative differences of up to -2.96 occur. Notably, this difference occurs between β_4 and β_5; the same applies to the spectra of the observed time series, where the largest relative difference (-2.11) also occurs between β_4 and β_5. Such a difference may be explained with the abrupt changes of discharge regimes – in real karst aquifers, this is interpreted to relate to a change in dominating discharge regimes, while within the InfoWorks model, such a change may relate to a change in contributions from the different modelled flow components. Yet, overall, the simulated discharge seems to integrate well the different flow components to generate a very similar spectrum to the spectrum of the observed discharge.

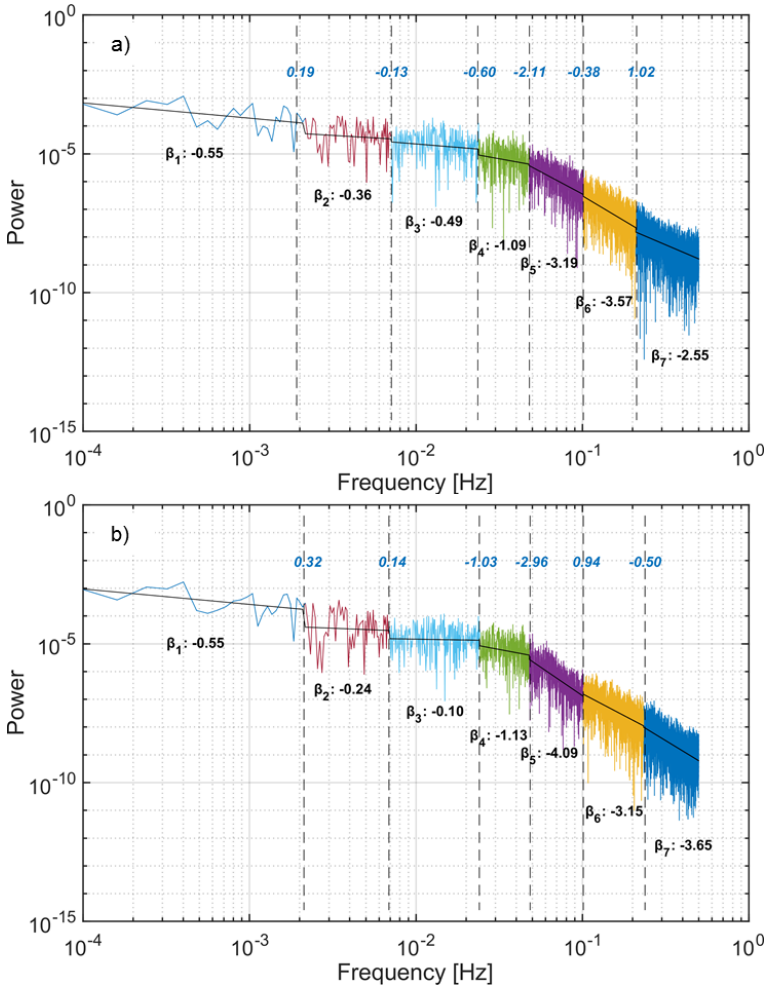

Figure 7.30: Power spectrum and spectral coefficients of the observed discharge time series (a) and simulated time series (b) of Manorhamilton for the calibration and validation period.

The loss of memory is compared using the ACF of the observed and simulated discharge during calibration and validation illustrated in Figure 7.31.

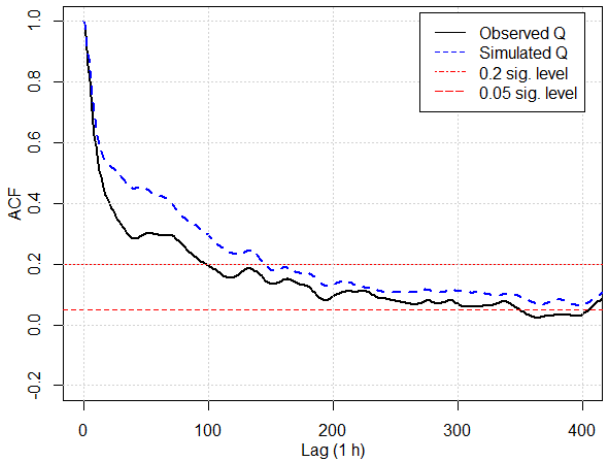

Figure 7.31: ACF of hourly observed and simulated discharge of Manorhamilton spring during calibration and validation.

Interestingly, the course is very similar, yet, the loss of memory is slower for the simulated discharge than for the observed discharge. The ACF of the observed and simulated time series reach <0.2 and <0.05 after 99 and 350 h, 146 and 650 h respectively. Hence, the simulated discharge time series indicates a higher degree of linearity, which may be related to the fact that the contribution of the soil store and groundwater store are simulated using linear equations.

7.2.5. Summary of Manorhamilton pipe network model

Overall, the model proved to be capable of simulating the discharge regime of Manorhamilton spring as the result of three distinct recharge processes, i.e. fast and concentrated, intermediate and diffuse. All these inputs are eventually discharged into the main conduits where they are subject to turbulent flow conditions modelled using the Saint Venant equations. The comparison of the spectrum of the observed and simulated spring discharge suggests that the simulated flow components are integrated towards the spring outlet. The ACF suggests a higher degree of linearity of the simulated time series as opposed to the observed discharge time series.
The model shows to be able to resemble the conceptual site model (Figure 7.18). For the calibration and validation period, the pipe network model reaches a NSE and KGE of 0.807 and 0.904, +0.882 and +0.892 respectively, which is almost the performance of the KarstMod reservoir model (‘5.2.5. Reservoir modelling’). The assumed catchment size seems to be plausible.
However, the performance of the simulated discharge differs from the observed discharge for the period Mar to the middle of Jun 2018, which is believed to be due to erroneous rainfall data input, as already previously stated, impacting on the modelled LFC, which is resembled by discharge of the soil store (soil store inflow). This explains the better model performance of modelled discharge during validation. Yet, the overall pattern of the estimated LFC is well matched outside the period of erroneous rainfall data. The recession of the soil store inflow matches reasonably well the MRC

with k' = 0.03 h^{-1} – the same applies to the fast and concentrated recharge that is modelled using runoff, and which was fitted to the fast recession of the MRC with k' = 0.15 h^{-1}.

Figure 7.32a shows the observed spring discharge and the separated LFC (Eckhardt method) referring to the spring discharge. Hence, the plotted LFC is the result of diffusely infiltrated rainfall that concentrates towards to the spring via different openings in the aquifer. It is likely that this LFC actually experienced different flow regimes, laminar as well as turbulent.

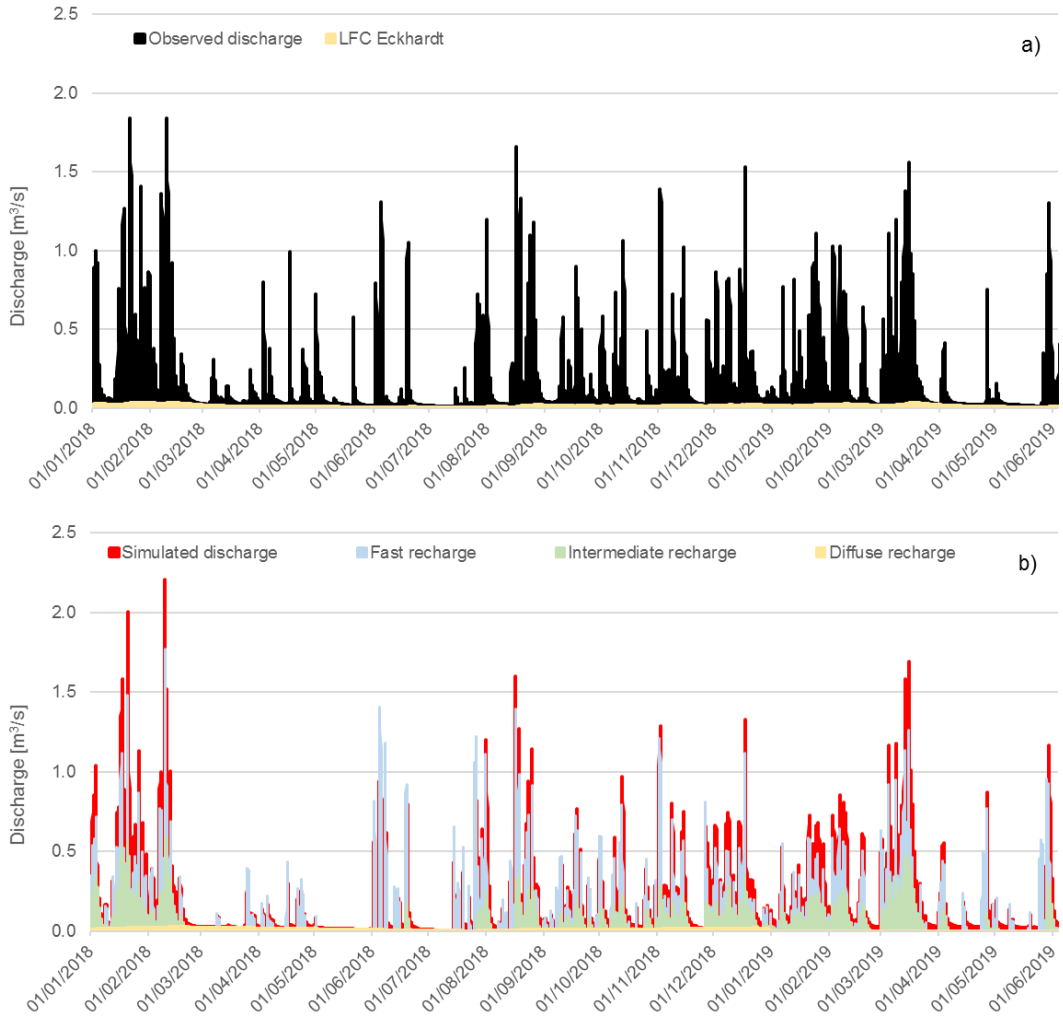

Figure 7.32: Summary flow components of a) observed and b) simulated time series during calibration and validation.

Figure 7.32b shows the modelled spring discharge, along with different recharge components. The time series of the recharge components do not refer to the spring outlet but to the moment when they concentrate and discharge into the conduit network. After they concentrate towards the conduit network, the combined flow is modelled as pressurised turbulent flow towards the spring outlet. The major influence of fast recharge in generating discharge peaks becomes apparent. While this

fast recharge components drops relatively quickly with the end of a rain event, the role of intermittent recharge and its discharge becomes important in sustaining the flow. Finally, the lowest flow is sustained by the LFC.

7.3. Conclusions

InfoWorks ICM was applied to simulate the discharge of Ballindine and Manorhamilton springs, and further to represent distinct recharge and flow components previously identified. Based on the results of this chapter, the following conclusions can be drawn:

Conceptual site models:

Previously, the catchment of Ballindine was newly delineated considering a surface water-groundwater interaction between the River Robe and Ballindine spring. Yet, it was unclear whether exfiltration along the river bed occurs, or if the river impacts on the spring/aquifer via a pressure transfer. The performance of the numerical model provides evidence that in fact, most flows originate from the river, and hence that the delineated catchment underlying the CSM is realistic.
Also, the catchment boundaries of Manorhamilton were newly delineated, and the system was modelled with a single outlet (Manorhamilton spring). The model structure does incorporate the characteristic topography by assigning the elevations to the pipe network. However, the main concern seems to be the catchment size, which was modelled as 3.6 km^2.

Modelling flow components:

Based on the master recession curve (MRC) of both springs, three distinct recharge and flow components were identified and linked to specific recharge and flow types: quick recharge was modelled as conduit inflow from the river (Ballindine) and as runoff (Manorhamilton). The intermediate recharge component was modelled as river inflow through permeable pipes (Ballindine) and as soil store inflow (Manorhamilton). And lastly, the low-flow component (LFC) was modelled as groundwater store inflow originating from rainfall and flowing through permeable pipes (Ballindine) and/or directly entering the conduit network of full pipes (Manorhamilton).
The simulated flows were calibrated against the occurrence of observed discharge events, the recession constant k, LFC time series (Eckhardt filter) and db10 time series, with different levels of success: for Manorhamilton, the timing, magnitude and recession of the quick-flow component (major concentrated component) could be very well simulated by applying the Unit Hydrograph routing model and the curvelinear SCS unit hydrograph model (Figure 4.21). The runoff parameters time to peak t_p and base time t_b correspond to 20 and 825 min, which can be considered in the order of the previously identified lag of 5 h (300 min) of the CCF.
For Ballindine, an intermittently occurring quick-flow component (minor concentrated component) was calibrated against the high-frequency component established by using DWT. This conceptual

understanding was very difficult to represent numerically – it must be assumed that the model over-simplifies the occurrence of concentrated recharge via a threshold-level functioning originating from the river.

The intermediate recharge component of Manorhamilton was calibrated against the occurrence of discharge events and against the recession following the MRC. It was found that again, the timing, magnitude and recession of this flow-component could be well matched against the observed data. Hence, the parameters of the soil store, including the soil store inflow (Eqn. 4.25), can be applied to represent this recharge component.

For Ballindine, the intermediate recharge and flow component (major diffuse component) was calibrated against the observed hydrograph and against the low-frequency signal established by using DWT and noise analysis. It was found that the model can reasonably well represent this component, with a NSE and KGE of 0.76 and 0.84 during calibration and 0.84 and 0.91 during validation. Hence, the use of permeable pipes (Darcy flow) to simulate river exfiltration proved to be applicable to represent these flows.

And finally, the groundwater store inflow resembling the LFC of Manorhamilton (minor diffuse component) was calibrated against the previously established low-frequency time series (Eckhardt filter). The performance of the model is fair during calibration, but very weak during validation. This raises the question, if either the parameters of the groundwater store, including groundwater store inflow (Eqn. 4.29) may not be applicable to represent the LFC signal, or if the reference LFC time series may be not realistic. Previously, the challenge was discussed of establishing a LFC signal for Manorhamilton, notably due to the absence of structured low-frequency components. Further, matching the separated LFC time series against exponentially fitted LFC segments was not feasible. Hence, it may be concluded that the established LFC time series may not be representative of a diffuse low-frequency flow signal. Hence, calibrating the groundwater store against such flow component may seem redundant after all.

The LFC signal of Ballindine was simulated by the discharge of the groundwater store and flow within permeable pipes, which was calibrated against the separated low-frequency time series (Eckhardt filter). It was found that the model excels well in representing the absolute flows (including the use of a CSO) but also the overall pattern as illustrated by a NSE and KGE of 0.74 and 0.72 during calibration and 0.69 and 0.87 during validation.

The LFC modelling results of Ballindine suggest that a LFC established by the Eckhardt filter can be modelled in InfoWorks – therefore, the poor modelling performance of the LFC for Manorhamilton may be indeed related to the way how the LFC was established, rather than by how it is numerically represented.

Modelling discharges:

Overall, both pipe models proved to perform reasonably well with regard to the overall spring discharge. The Ballindine model reaches a NSE and KGE of 0.84 and 0.89 during calibration and 0.76

and 0.77 during validation. The Manorhamilton model reaches a NSE and KGE of 0.81 and 0.90 during calibration and 0.88 and 0.89 during validation.
The better performance of the Manorhamilton model may be the results of a simpler CSM than in the case of Ballindine.
Besides representing the overall spring discharges, both models have been shown to mimic the spectra of the observed time series well. Especially the simulated spectra of Manorhamilton seems to be very close to the spectra of the observed time series, with exceptions in the high-frequency ranges. Similarly, it is also the high-frequency range of the spectra of the simulated discharge time series of Ballindine, which deviate from the spectra of the observed time series. Nevertheless, the comparison of the spectra is considered as a strong indicator that different recharge and flow components, which constitute the final spring discharge, were reasonably well matched.

Finally, based on these results, it is concluded that the CSMs are realistic for both sites, and that InfoWorks ICM is able to integrate different recharge components concentrating as diffuse and/or pressurized pipe/open-channel flows towards the spring outlet.

8. Bell Harbour

8.1. Catchment studies

8.1.1. Time series

Figure 7.32 shows hydroclimatic time series of all monitoring sites in the study area of Bell Harbour (except rainfall at Fort Neylon and water levels in Poll Gonzo) between 01 Jan 2015 and 30 Sep 2018. Arrows indicate periods of missing data. Importantly for the understanding of the catchment dynamics, blue shaded segments show 'high-flow periods' and yellow shaded areas 'low-flow periods'.

Figure 7.32a shows the daily rainfall observed at C1. Data gaps were filled with the average of time series from the MetEireann stations of Ballyvaughan and Carron. The maximum daily rainfall (00:00 to 24:00 h) recorded by the project was 51.4 mm on 03 Mar 2017. Further, Figure 7.32a shows the hourly temperature ranging between -5.6 ºC on 01 Mar 2018 and 31.1 ºC on 29 Jun 2018. Hourly ET established by the Penman-Monteith equation shows highest values in June 2018 reaching 0.8 mm/h. Temperature and ET show a clear seasonal pattern with minimum levels around Dec and Jan and maximum levels in Jun/Jul.

Figure 7.32b shows the water levels of the surface water features or polje CAS and CAN (previously shown in Figure 3.12). The water level of CAS ranges between 110 and 113.1 masl on 31 Dec 2015. The water level of the higher elevated CAN ranges between 111 and 113.4 masl also recorded on 31 Dec 2015. CAS and CAN are highly correlated as they are hydraulically connected. CAS and CAN may be flooded during the entire winter and periodically throughout the year.

Figure 7.32c shows the piezometric head observed within the upland and lowland borehole BH2 and BH1, and the water levels observed at the turloughs T1 and T2. The upland borehole BH2 was backfilled in 2017, thus, it could not be used since that time. Water levels in T1 were observed at the estavelle at 15.2 masl until 25 Oct 2016. After this date, land access to the estavelle was not given anymore, and so, the pressure sensor measuring the water depth had to be placed at an alternative site in the turlough, 2.9 m above the bottom (estavelle). Hence, the observed water levels recorded after 25 Oct 2016 don't show any flooding below 18.1 masl.

T1 is a typical seasonally flooded turlough with a maximum water level of 26.0 masl on 27 Jan to 1 Feb 2018 (equating to a water depth of 10.8 m). T2 is actually almost perennially flooded, thus, not strictly a turlough. The water level reaches a maximum of 5.5 masl on 07 Dec 2015.

The head in the upland BH2 ranges between 94.8 masl on 19 Jun 2016 and 126.7 masl on 22 Aug 2016 whilst the head in the lowland BH1 ranges between 8.7 masl on 25 Jun 2016 and 30.0 masl on 06 Dec 2015. The head in BH1 shows the impact of tidal fluctuation at low levels.

BH1 is located 0.7 km 'upstream' of the estavelle in T1. This explains the high correlation of the time series. During periods of flooded conditions in T1, the head is consistently high in BH1 and cannot drop below the water level of T1. In turn, if the turlough is empty, the head in BH1 can drop towards the minimum level, influenced by the tide. During periods of low water level and empty T1,

recharge events cause an instantaneous rise in head in BH1 that can exceed 10 m. Interestingly, the recession following the recharge events may be practically non-existent. Instead, the head may just drop back to its previous state. The relationship between the head in BH1 and water levels of CAS, CAN and T1 will be described more in detail in Figure 8.2.

Figure 7.32d also shows the observed EC at Pouldoody spring (SiGD1) and prevailing temperature. Due to the high fluctuation of the EC signal, a moving average (+/- 7 h) was plotted to facilitate the general course of the signal. Observed EC is measured below the outlet of the intertidal spring, on the sea floor. Therefore, different factors impact on the fluctuation of EC, such as discharge quantity of the spring, the water level due to the tidal fluctuation, and the EC of the sea water. Altogether, these variables pose a challenge on the interpretation on the signal.

In general, a very low variation of the EC amplitude between tides suggests either active discharge or inactive discharge. For example, the periods of continuously low EC records and low variation suggest periods of discharge of fresh-brackish groundwater (e.g. 15 Nov 2015 to 15 Apr 2016 or 26 Oct 2016 to 13 Jan 2017). In turn, periods of consistently high EC and low variation suggest periods of inactive discharge (e.g. 30 Sep to 09 Nov 2015 or 10 May to 10 Jul 2016), which was confirmed observations in the field several times. EC ranges between 53 mS/cm corresponding to sea water and <150 µS/cm corresponding to freshwater. Interestingly, the low EC records between 15 Nov 2015 and 15 Apr 2016 and following surge in EC until 10 Jul 2016 corresponds well with periods from high water levels in CAS, CAN and T1, and high piezometric head in BH1 towards lower levels of all of them. Obviously, intense rainfall resulted in recharge and flooded conditions, which subsequently impact on the discharge regime and associated low EC levels at Pouldoody spring. Temperatures range between 29.1 ºC on 19 Jul 2016 at 12:00 (at low water level) and 2.3 ºC on 07 Nov 2016 at 07:00 (at low water level).

Finally, Figure 7.32e presents the observed EC in the centre of the outlet of Bell Harbour Bay. The average EC of the upper (BHB1) and lower (BHB2) CTD sensors, i.e. BHB1+2, is presented, along with associated sea temperatures. The fluctuation of EC is a function of the tidal fluctuation, and filling and emptying of the bay. The differences of EC between high tide and low tide are thus interpreted as the result of SiGD into Bell Harbour Bay, which act to reduce the salinity in the bay. A rise in EC is then caused by incoming sea water from outside the bay (during flood tide), while a drop can be associated with drainage of the bay water (low tide). The plot shows a relatively high fluctuation during winter periods (e.g. 22 Feb to 28 Apr 2016, 22 Dec 2016 to 20 Apr 2017 or 20 Jul 2017 to 05 May 2018). Periods of very low fluctuation in EC occur during spring/autumn (e.g. 01 Jun to 05 Nov 2016 or 20 Apr to 20 Jul 2017). The recorded temperature shows a clear seasonal fluctuation, ranging between 20.2 ºC on 19 Jul 2016 and 4.5 ºC on 01 Mar 2018.

The presented time series are very important to understand the overall hydrodynamics affecting recharge, flow and discharge in the Bell Harbour catchment, which is the basis for any detailed analysis of these dynamics.

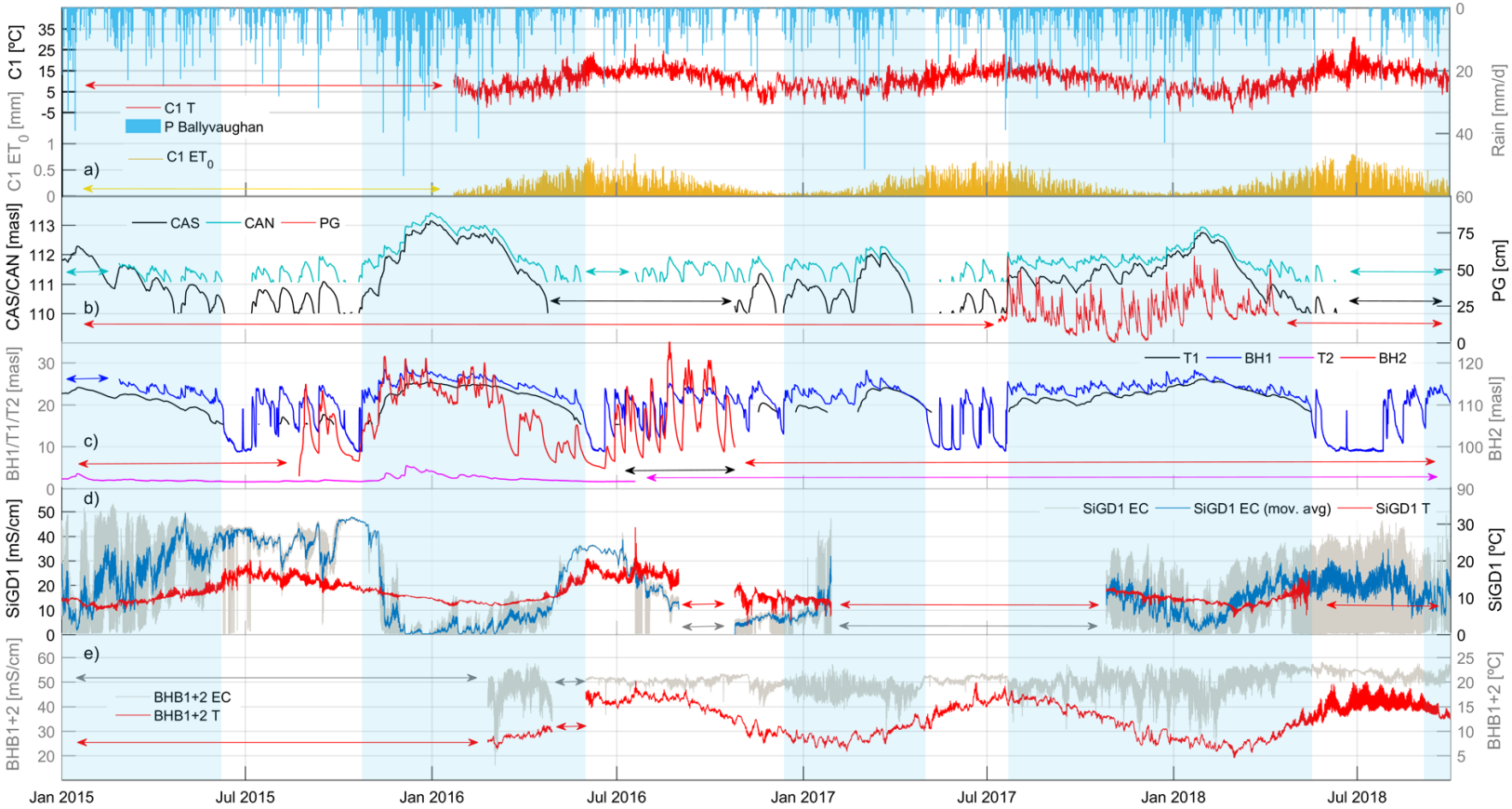

Figure 8.1: Hydroclimatic time series collected in Bell Harbour (all hourly except rainfall (P): a) rainfall at C1 (gaps filled by average of MetEireann station Ballyvaughan and Carron), temperature (T) and evapotranspiration (ET); b) water level of CAS, CAN and PG; c) water level of T1, T2, BH1 and BH2; d) EC at SiGD1, including a moving average to illustrate the pattern in time, and T; e) average minimum and maximum EC records per tidal cycle at BHB1+2 and T. Arrows indicate period of missing data. Blue shaded segments are 'high-flow periods' and remaining white shaded areas 'low-flow periods'.

The water level and head time series of BH1, T1, CAS and CAN are shown in more in detail (Figure 8.2), plotted during 'flooded' conditions (i.e.when the water column was above the level of the pressure sensor).

The period Apr to Jul 2015 marks the end of a high-flow period with dropping heads towards a low-flow period and low head levels in Jun and Jul.

Overall, rising and falling heads correlate very well in time. The dynamics seem to be slowest for T1, followed by CAS, CAN and BH1. High-flow periods describe the period in which BH1 is continuously high and T1 is flooded, potentially in combinatoin with CAS.

During low-flow periods, the hydrograph of BH1 shows very flashy responses and surges and drops of >10 m within a few hours. Such dynamics seem to occur below a head of ~20 masl. The shape of the limb suggests a pressure transfer (accompanied by flow) as the driver for surges and drops. However, these surges may be very short in time, presumably not allowing the fissured matrix to fully recharge, which explains the rapid drop.

A striking pattern of dynamics is visible between the plotted time series: if CAN, CAS and T1 are all empty, the head in BH1 is <21 masl. In fact, the moments of complete emptying of CAS and T1 coincide with a rapid drop in head in BH1. Conversely, as soon as a water table is generated in CAS or T1, the head in BH1 sharply rises. An exception is 28 Jun.

However, this pattern is interpreted as a pressure transfer between upland Carron and lowland BH1. Accordingly, the water table in Carron is able to transfer a proportion of head towards the lowland borehole BH1 4.9 km to the north. This is an interesting aspect as previously to this study, Carron was conceptualised to be outside of the Bell Harbour catchment (Bunce and Drew, 2017). Yet, the hydrographs suggest a hydraulic connection between Carron and BH1 (Schuler, et al., 2019a).

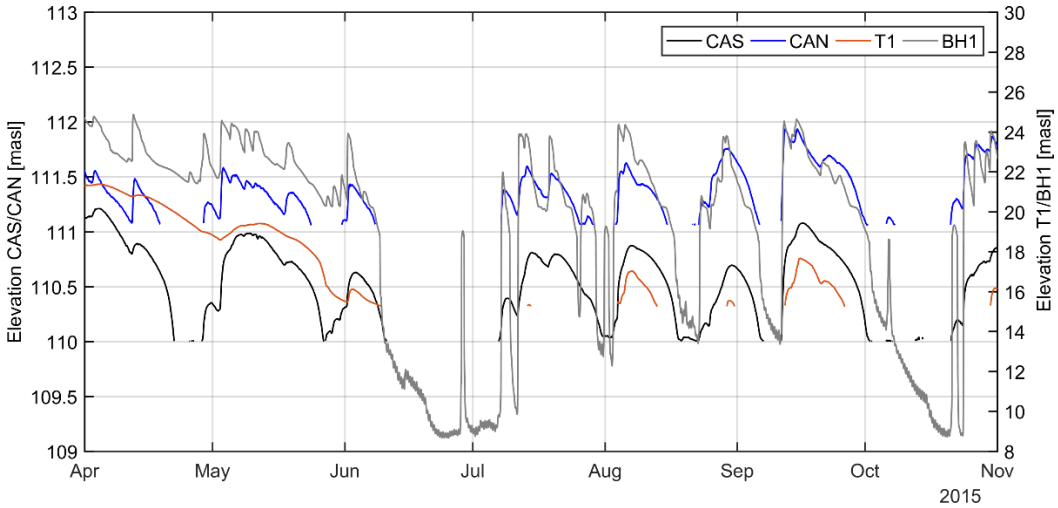

Figure 8.2: Water level in CAS, CAN and T1 and piezometric head in BH1 between 01 Apr and 01 Nov 2015.

A more detailed view on the dynamics in BH1 and the differences between a high-flow period and a low-flow period are illustrated within Figure 8.3 and Figure 8.4. Figure 8.3 shows the response of EC to rainfall (Figure 8.3), as well as head and d18O (Figure 8.3b) during three days of a low-flow period. The plot shows a remarkable plateau-like pattern of head and EC levels. For both parameters, an upper and a lower level can be observed. Potentially, both levels can be related to highly transmissive zones and groundwater in- and outflow (major groundwater outflow from the borehole between 4.8 and 24 masl was identified using single borehole dilution tests, Section '8.1.4. Single borehole dilution tests' and 'SBDTs'). The head rises and drops sharply, as it is indicative of a pressure transfer influence, and may perhaps suggest the existence of a syphon effect in the system. Importantly, there is yet no piston-effect visible in the EC series. It seems that the change in the inflow regime becomes active immediately, rather than any evidence of a forward pressure pulse through the aquifer which would mobilise high-EC water, and hence, cause an increase in EC before dropping down (as it often documented in other karst studies). With increasing head, the EC rapidly drops. Interestingly, with a sharp drop in head, the EC sharply increases, without exhibiting a lasting recession of increasing EC. This suggests that the sharp rise and drop in head is the result of pressure transmitted through inflowing water. Yet, the level of EC of the inflowing water is still relatively high, which suggests that it originates from internal reservoirs within the karst system (rather than very rapidly percolating rainfall). The contribution of another water source contribution during the rising head is in line with the observed increase in concentration of d18O.

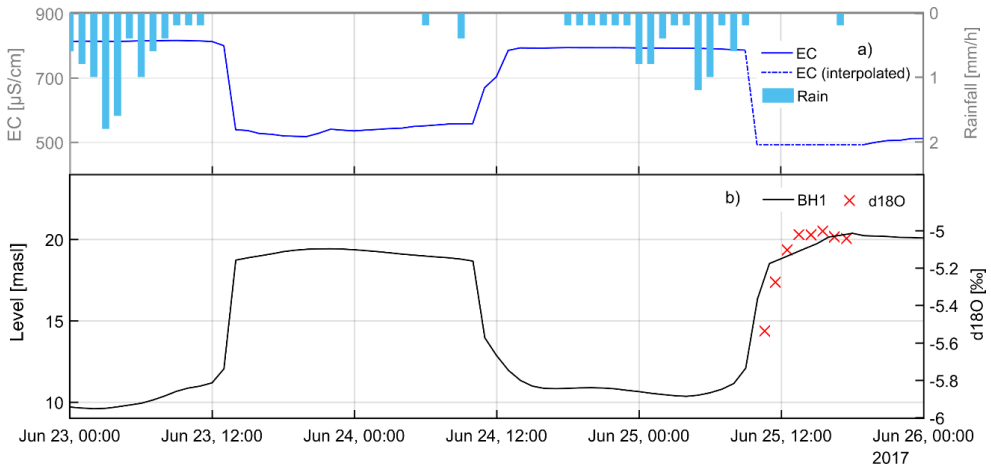

Figure 8.3: Rainfall and EC (a) and head and d18O (b) in BH1 during low-flow period (23 to 16 Jun 2017).

To exemplify the response of the borehole during a high-flow period, the head, EC and rainfall between 08 Mar and 15 Apr 2018 were plotted in Figure 8.4. Notably, the head is higher, and the EC is lower than the respective records in Figure 8.3. As can be seen, EC behaves more or less conversely to the head. During these higher levels the rainfall and resulting recharge do cause a piston-effect that leads to an event-based rise in EC prior to drop in EC. The recession of EC follows a gradual course, as opposed to the sharp and rapid changes observed in Figure 8.3. Hence, Figure

8.4 suggest that the response in BH1 during this high-flow period follows a more common karst aquifer response than during the previously shown low-flow period.

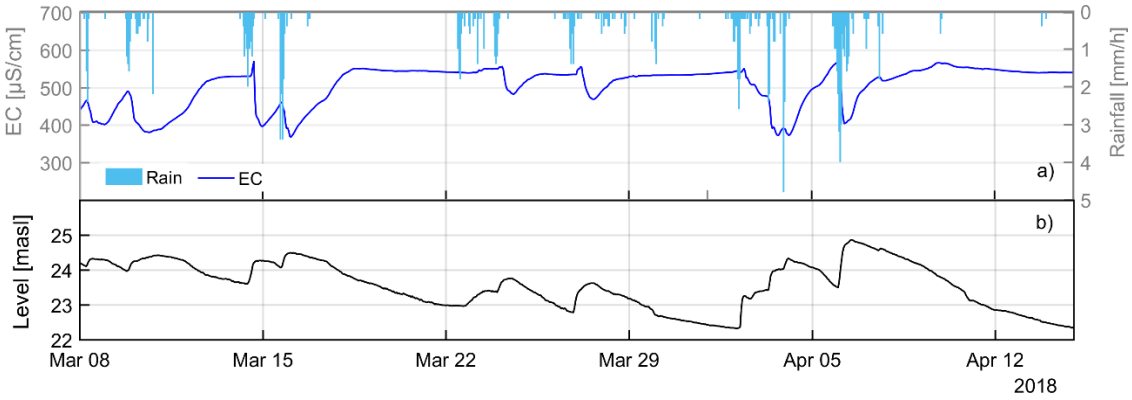

Figure 8.4: Rainfall and EC (a) and head (b) in BH1 during high-flow period (08 Mar to 15 Apr 2018).

Another perspective into the dynamics of BH1 is illustrated in Figure 8.5, which exemplifies the ambient borehole hydrograph exhibiting a rapid response to rainfall and multiple recessions. In addition, it shows the prevailing conditions during the single borehole dilution tests (SBDT, Section '8.1.4. Single borehole dilution tests').

Between the first recession on 05 Apr and 15 May 2017 almost no rainfall occurred. Strikingly, the recession consists of multiple convex and concave sections whereas two main recessions split up the total hydrograph into: a) above 20.2 masl, b) below 20.2 masl. Below 16.5 masl, the recession is clearly impacted by tidal oscillation. The lagged correlation between the tidal amplitude and the borehole hydrograph between 17 and 27 Jun 2016 (Figure 8.5) shows an oscillation pattern of ~6 h, with a delay of approx. ±3 h at the borehole hydrograph.
The hydrograph of BH1 suggests:

- high fluctuation of water levels ranging between 28.2 and 8.9 masl;
- the water level responds very fast to rainfall events confirming that the borehole is hydraulically well connected to the aquifer;
- at least 2 distinct major recessions with changes from concave sections to convex sections are present: a) >20.2 masl, and b) <20.2 masl suggesting the existence of multiple groundwater flow horizons;
- the water level oscillates in a frequency of 11 to 12 h below 16.5 masl. The lagged cross-correlation between the tidal oscillation and BH1 yields a correlation coefficient of +0.08 and -0.10 for a lag of +3.5 h, -2.5 h respectively, proving that BH1 is impacted by the tidal fluctuation and therefore connected to the sea;
- head fluctuation is governed by rainfall as well as by the overall piezometric level in the aquifer, including the level in the turlough T1.

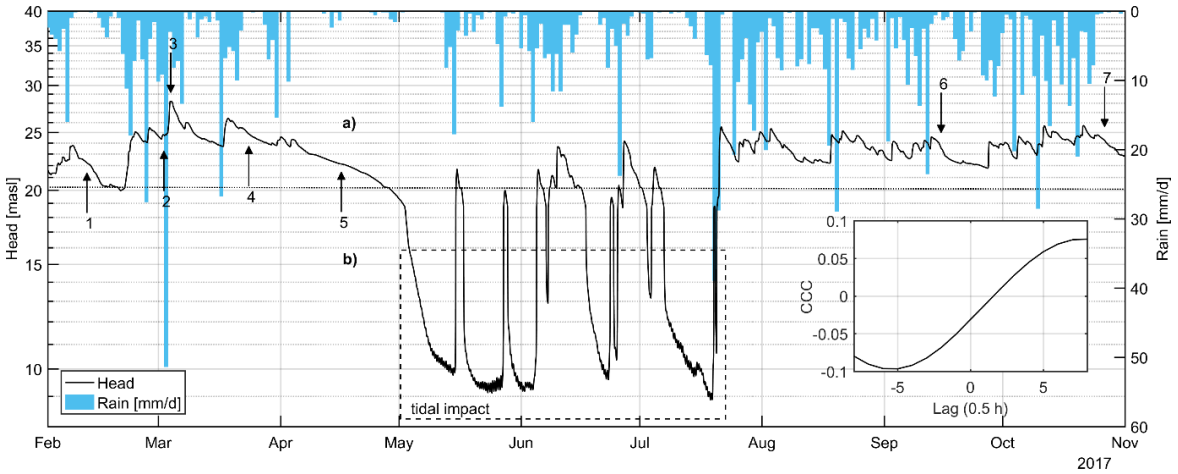

Figure 8.5: Ambient borehole recession at BH1 and daily rainfall between Feb and Oct 2017. The rapid response to rainfall and multiple recessions indicate different reservoirs. Numbers and arrows refer to tracer injections (single borehole dilution tests). For the period 17 Jul to 30 Sep 2017 rainfall data from the MetEireann station at Carron and Ballyvaughan was used due to a data gap at C1. Inset shows the correlogram between the tidal oscillation (masl) and groundwater level (masl) of BH1 for 30 min time series at low level.

Next, Figure 8.6 provides a more detailed overview on some of the climatic input variables, namely a wind rose diagram indicating that the prevailing wind originates from south and south-south/east with mostly wind speeds of 1 to 2 m/s. The highest average wind speed recorded within 15 min interval was 18.5 m/s (66.6 km/h) on 19 Sep 2018.

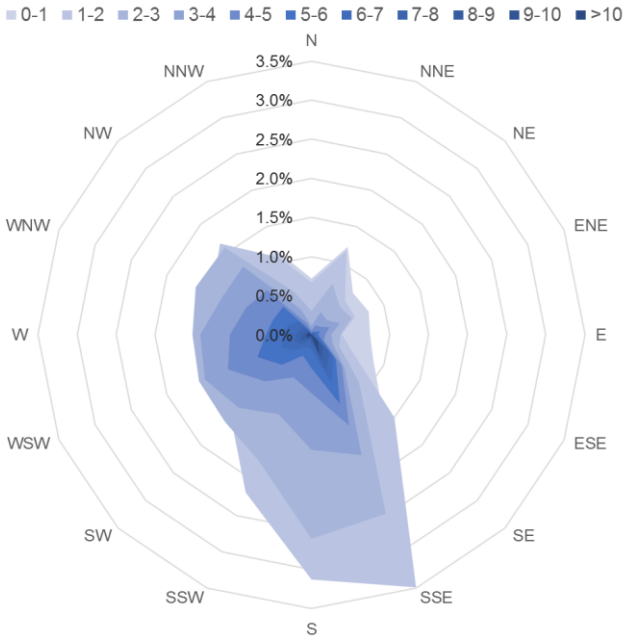

Figure 8.6: Relative occurrence of average wind speed in m/s and wind direction in 15 min intervals during the hydrological years 2017 and 2018 at C1.

Rainfall was recorded at two different locations, namely at C1 (at 37.7 masl in the centre valley) and P1 (up on the plateau at 203 masl), in order to evaluate the spatial variation of its input. Figure 8.7 shows the cumulative rainfall of the two sites for 417 consecutive days. Strikingly, the difference of recorded rainfall is only 16.8 mm over that period, which corresponds to 1.3%. Not only the absolute quantity, but also the pattern of occurring rainfall can therefore be considered as practically identical (i.e. there seems to be no orographic enhancement to the rainfall in this area).

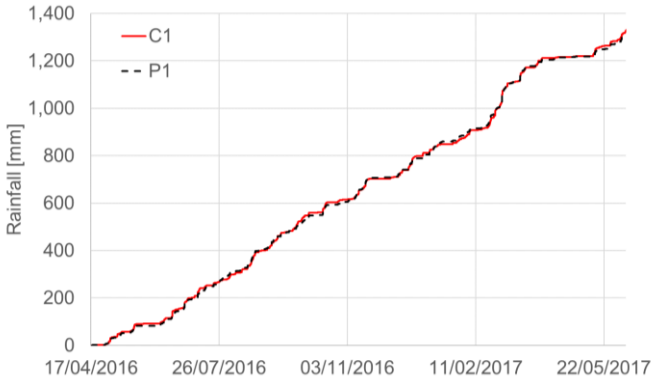

Figure 8.7: Cumulative rainfall at C1 and P1 between 17 Apr 2016 and 08 Jun 2017.

Figure 8.8 shows the records of 46 stable isotopes (2H and 18O) collected at C1 between 30 Mar 2017 and 01 Apr 2018. d18O ranges between -16.45 and -0.58‰ while d2H fluctuates between -119.50 and -1.57‰. Accordingly, all samples indicate a depletion of heavier isotopes compared to the reference standard. The most depleted samples were collected between 16 and 22 Jul 2017 and 07 and 14 Dec 2017.

Over the entire sampling period, a declining trend in concentrations can be seen. It is unclear if this trend reflects the true values or rather an artefact of the sampling or analytical methodology perhaps.

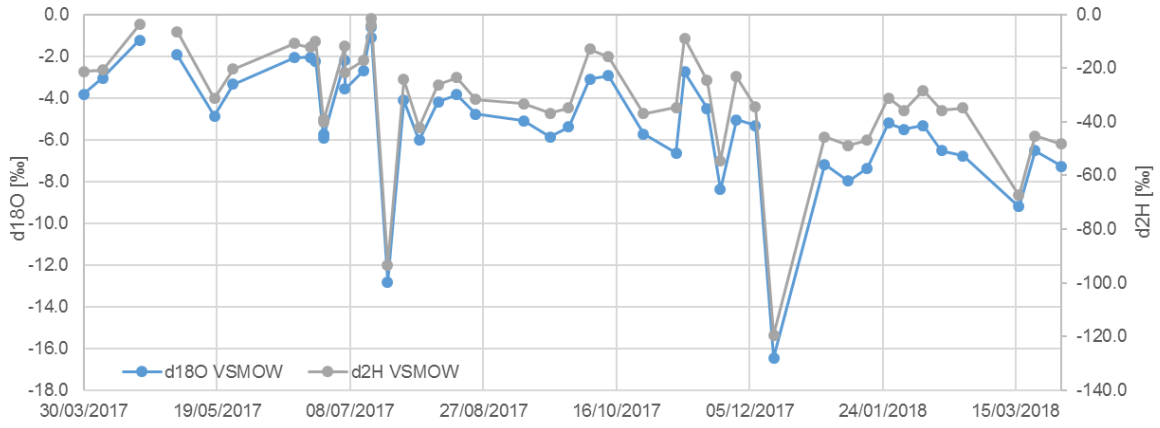

Figure 8.8: Weekly concentrations of d18O and d2H [‰] in rainfall collected at C1 between 30 Mar 2017 and 01 Apr 2018.

Figure 8.9 shows the isotopic composition of 123 collected samples in the study area compared to the GMWL and the regional meteoric water line (MWL) of Valentia ($\delta^2H = 7.269 \cdot \delta^{18}O + 4.8864$). A local MWL (C1) for the study area was established based on the 45 rainfall samples to yield $\delta^2H = 7.3555 \cdot \delta^{18}O + 6.1402$.

In fact, the C1 MWL lies in between the GMWL and the MWL of Valentia. However, the number of samples used for the C1 MWL is relatively low covering only one year, thus, being limited in terms of its representativeness.

All groundwater or surface water samples are very close to the C1 MWL. The only values that show depletion are two samples taken from Pouldoody spring (SiGD1), presumably impacted by evaporation, potentially indicating sea water intrusion into the aquifer.

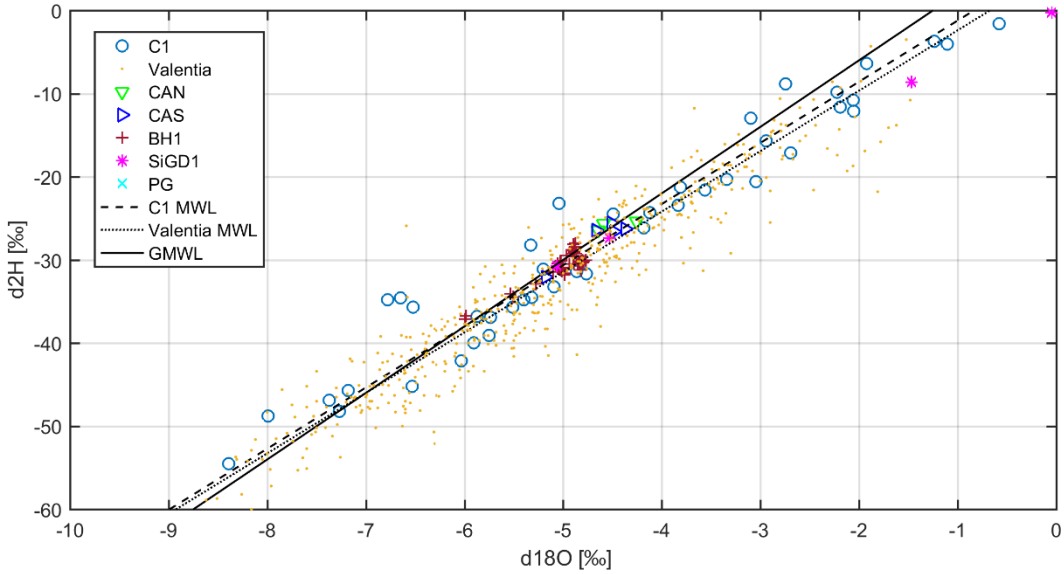

Figure 8.9: d18O and d2H [‰] of BH1, rainfall at the C1, CAS and Pouldoody spring compared to the Global Meteoric Water Line (GMWL), the isotopic composition of the MetEireann station Valentia (Valentia MWL) and the C1 MWL.

8.1.2. Quantifying submarine and intertidal groundwater discharge (SiGD)

The Bell Harbour catchment discharges at least partly into Bell Harbour Bay via SiGD. A few intertidal and submarine springs are known (Figure 8.10). However, it seems impossible to quantify their discharge individually. Therefore, the bay was considered ‘in bulk’, whereby the total ‘groundwater discharge’ from the bay into Galway Bay was estimated and considered to account for the SiGD from the Bell Harbour catchment.

SiGD was estimated according to the methodology in Section ‘4.3.3. Quantification of SiGD’ using continuous EC and tidal fluctuation measurements at the outlet of the bay (BHB1+2). The principle of estimating SiGD is based on a mass-balance approach between the salinity of the outgoing (low) tide and incoming (flood) tide. Hence, SiGD was estimated per tidal cycle.

The necessary parameters (Eqn. 4.20) were established as follows. The bathymetry of the bay was needed to establish the mean volume of the basin V_m [m^3]. The topography of the bay was derived using a 5 m bathymetry grid provided by the GSI. Missing grid cells were interpolated in ArcGIS using the nearest neighbour method to the final topography with a maximum depth of -10.2 masl (Figure 8.10).

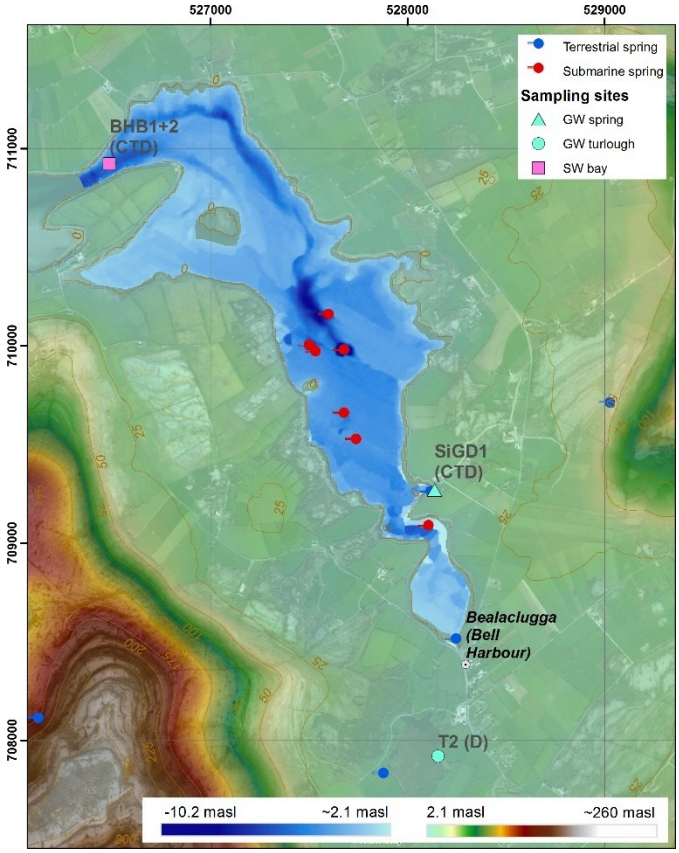

Figure 8.10: Bathymetry of Bell Harbour Bay along with submarine and terrestrial (including intertidal) springs.

The topography of the bay was further used to estimate the amplitude of the oscillatory component of the tidal volume V_t [m^3] in conjunction with tidal oscillations from Galway Port monitored in 6 min frequency at Galway Port by the Marine Institute (MI). To link the observed tidal level with the volume in the bay, a stage-volume relationship was established. A sequence of modelled volumes according to intervals of 0.02 m levels was done using the 'Surface Volume' tool in ArcGIS (Figure 8.11). V_m is then estimated as the long-term average of the bay volume, which is 2.67 million m^3. The amplitude of the oscillatory component of the tidal volume is given by V_t describing the fluctuation of the ebb tide and flood tide level around V_m. As such, the standard deviation of all peak flood volumes and peak ebb volumes were considered as representative resulting in V_t = 2.37 million m^3. The tidal period T is the time of the effective resultant tidal cycle in the bay (sum of ebb and flood tide). T was related to the occurrence of minimum and maximum EC values observed at the outlet

of Bell Harbour Bay, ranging between 11 and 14 h, resulting in a variation of ω between 0.57 and 0.45 (on average, T = 11.63 h, and accordingly, ω = 0.54).

Eqn. 4.20 was then solved for each tidal cycle considering the maximum and minimum observed EC (average of BHB1 and BHB2) for each flood and ebb tide.

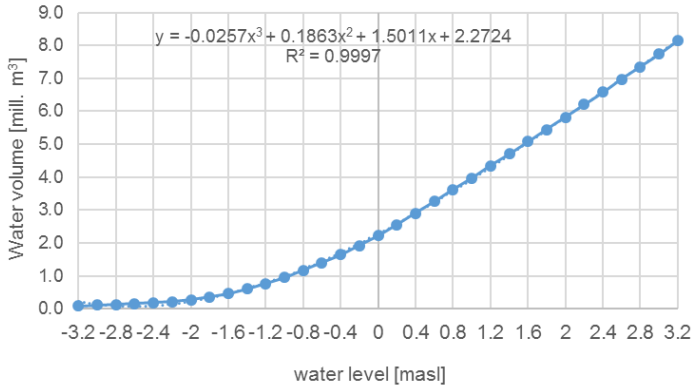

Figure 8.11: Stage-volume curve for Bell Harbour Bay.

Figure 8.12 shows the variation of EC as a result of tidal fluctuation observed at Galway Port. Clearly, there is a temporal delay of minimum and maximum EC records observed at BHB1+2 compared to observed tidal fluctuation related to the geographical location of the monitoring site BHB1+2 and various hydroclimatic factors impacting on the flood and drainage behaviour of Bell Harbour Bay. This phenomenon was accounted for by assigning the minimum EC value to the lowest water level (ebb tide) while assigning the maximum EC value to the highest water level (flood tide) per tidal cycle.

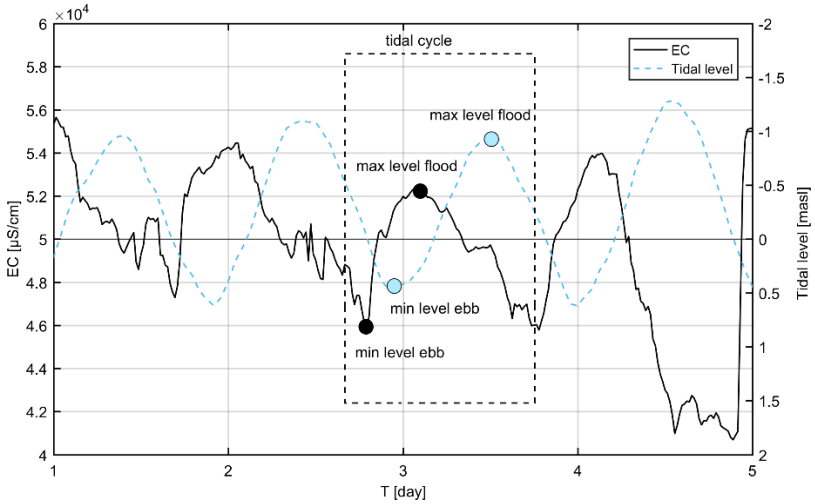

Figure 8.12: Example of fluctuation of EC measured at BHB1+2 and tidal oscillation observed at Galway Port.

In addition to Figure 8.1e, Figure 8.13 shows the observed EC values measured at the upper (BHB1) and lower (BHB2) CTD sensor attached to the buoy sampler at the outlet of Bell Harbour Bay. It should be noted that data losses occurred due to the breakdown of three CT2X sensors. The higher the amplitudes of EC values, the higher the difference of the salinity between the incoming and outgoing tide, and hence the estimated discharge from the bay (i.e. SiGD). Interestingly, both EC time series show generally a very similar pattern. Yet, the bottom sensor indicates smaller variations at certain periods which makes intuitive sense as the top sensor should be more influenced by salinity fluctuations due to the lower density of freshwater.

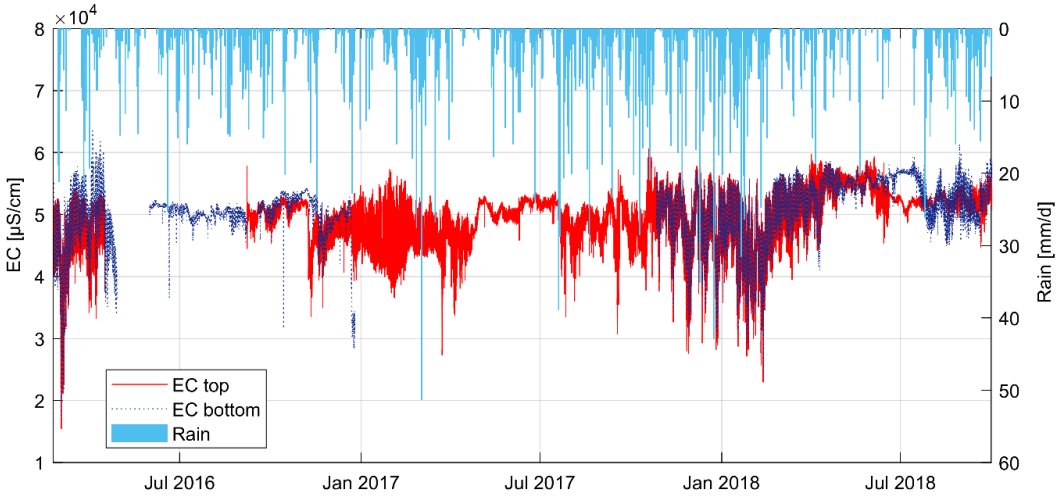

Figure 8.13: Measured EC at BHB1 (top) and BHB2 (bottom) at the outlet of Bell Harbour Bay and rainfall at C1 [mm/d] for the period of 24 Feb 2016 to 1 Oct 2018. Breakdown of CTD sensors resulted in loss of data and data gaps.

Figure 8.14a shows a plot of the resulting estimated averaged daily SiGD [m^3/s] draining Bell Harbour along with daily rainfall measured at C1 (gap filled). In spring 2016, SiGD reaches a peak discharge of 3.0 m^3/s discharging 5.8 million m^3 between 24 Feb and 28 Apr 2016. During summer and autumn 2016, the discharge from the bay clearly drops varying between close to 0 and 0.5 m^3/s whereby even significant rainfall events do not appear to cause a drop in EC in the bay and associated SiGD. In winter 2016, the SiGD starts to increase again. During the period 31 May 2016 to 15 Jul 2017 the total discharge accounts for 13.0 million m^3, with a peak discharge of 2 m^3/s. The plot indicates that the relationship between SiGD and rainfall is complex and non-linear. Across the entire study period, rainfall remained fairly constant for certain periods with a monthly mean of 119 mm and standard deviation of 55.7 mm. A period of high rainfall can be observed between Jun 2017 and Apr 2018 (1,787 mm).
There seems to be a slight correlation between monthly rainfall and the SiGD regime during periods of high rainfall. Conversely, it is not directly possible to relate periods of moderate rainfall (below average) to periods of low discharge.

During summer, it is expected that higher temperatures cause a drop of effective rainfall and the rate of groundwater recharge. Therefore, reduced recharge may be one reason for reduced SiGD. Figure 8.14b shows the daily ET at C1 using the Penman-Monteith equation along with the minimum and maximum EC values for all ebb and flood tides. ET shows a typical seasonal trend – there is indication that ET shows an anticorrelation with EC amplitudes and estimated SiGD. However, while the seasonal pattern of ET is rather smooth or transient, the fluctuation of EC amplitudes shows a rapidly changing dynamic, e.g. in Nov 2016 or between 25 Apr and 20 Jul 2017. These rapid changes of amplitudes seem unlikely to be caused by a change in recharge associated with effective rainfall and ET. Instead, the events of rising or declining amplitudes seem to correlate well with the piezometric head observed in BH1 (Figure 8.14c). During periods of low-flow (empty T1) in the aquifer, the EC amplitudes tend to be very small as compared to the periods of high-flow (filled T1). Hence, it is believed that the SiGD regime is related to the piezometric head in the lower part of the aquifer of Bell Harbour. The activation of SiGD may be related to an overflow mechanism.

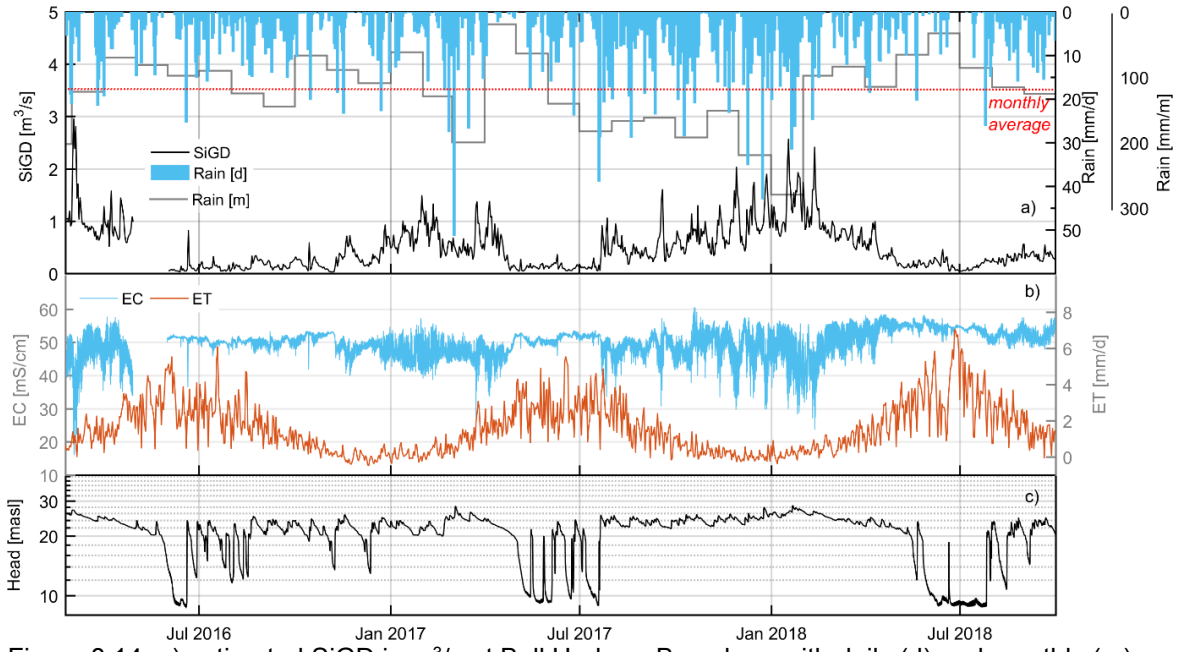

Figure 8.14: a) estimated SiGD in m^3/s at Bell Harbour Bay along with daily (d) and monthly (m) rainfall, b) minimum and maximum EC values [µS/cm] of ebb and flood tide and evapotranspiration [mm/d] as measured at C1, and c) hourly piezometric head (log scale) at BH1 [masl].

In conclusion, the low rates of SiGD during summer and autumn periods suggest much reduced SiGD during these periods. The discharge pattern of SiGD highly fluctuates between seasons while being correlated with the piezometric head in the aquifer, which is interpreted as being linked to an overflow mechanism in the karst system. Since there seems to be almost no fresh or brackish water diluting the bay during summer, it is believed that a significant quantity of groundwater from the

catchment must discharge into the sea via different springs, potentially bypassing Bell Harbour Bay.

8.1.3. Water balance

Water balances were established to compare the rainfall input in relation to the derived output of SiGD and ET from the bay and catchment respectively for the hydrological years 2017 and 2018. In the presupposed conceptual model that all of the water from the catchment enters into the bay as SiGD, the input (rainfall) should equal the output (SiGD and ET). Any missing figures in the water balance were considered as 'unaccounted resources' which were believed to drain the catchment via different (potentially deeper) flow paths (conduits) not accounted in the measurements taken in Bell Harbour Bay.
All relevant climate parameters were measured at C1 and P1, including temperature, relative humidity, net solar radiation and wind speed.
As mentioned before, the spatial pattern of rainfall is very homogeneous (Figure 8.7). Accordingly, rainfall data from C1 (or P1) was considered as representative for the entire catchment, and consequently used as global input for the water balances.

Daily ET was estimated using the Penman-Monteith equation (Allen, et al., 1998) applied on climate data measured at C1. The method quantifies ET in reference to well-watered, short-cut grass, and therefore yields the reference ET (ET_0). The method accounts for variable landuse which results in ET that deviates from ET_0 by multiplication with a crop coefficient (K_c). While ET_0 was believed to be representative for the land covered by soil, i.e. pasture, grass and farm land, which accounts for 36% of the catchment, ET was believed to be lower on the land covered by bare karst landscape rock (64% of the catchment) due to the fast infiltration of rainfall. Therefore, for the bare outcrop a K_c value of 0.5 was applied reducing ET by 50% as compared to grass land.
During the hydrological year 2017 the catchment received 63.8 million m^3 of rainfall (Figure 8.15a).

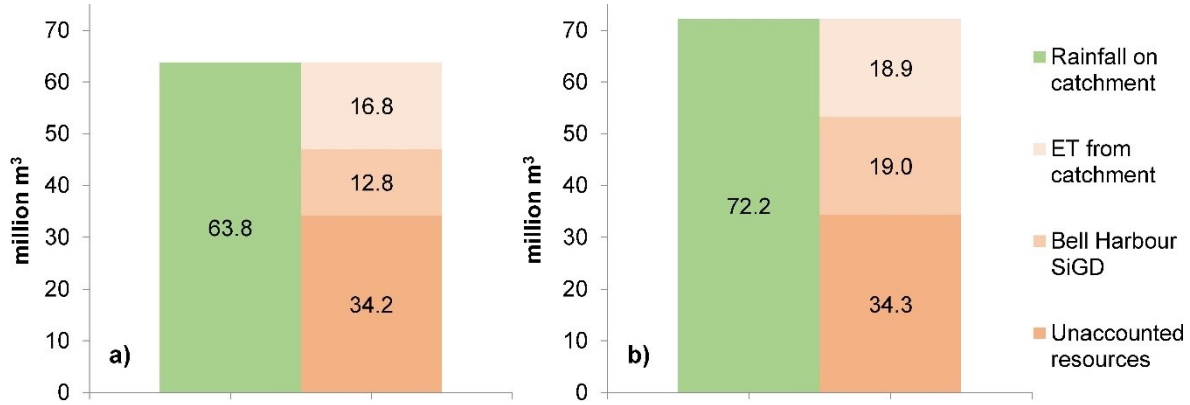

Figure 8.15: Water balance of Bell Harbour for the hydrological year a) 2017 and b) 2018 in million m^3: green = input, orange = output.

SiGD accounts for 12.8 million m^3 (20.1% of rainfall) and ET accounts for 16.8 million m^3 (26.3% of rainfall). Hence, there is a significant mismatch of 34.2 million m^3 (53.6% of rainfall), which is considered as unaccounted resources.
Throughout the hydrological year 2018 the catchment received 72.2 million m^3 of rainfall (Figure 8.15b). SiGD accounts for 19.0 million m^3 (26.3% of rainfall) and ET accounts for 18.9 million m^3 (26.2% of rainfall). Again, there is a significant mismatch of 34.3 million m^3 (47.6% of rainfall).

As shown in the previous section, there seems to be a seasonal variation of discharge. Therefore, a seasonal water balance from 2018 was established for three high-flow periods and two low-flow periods (Figure 8.16).

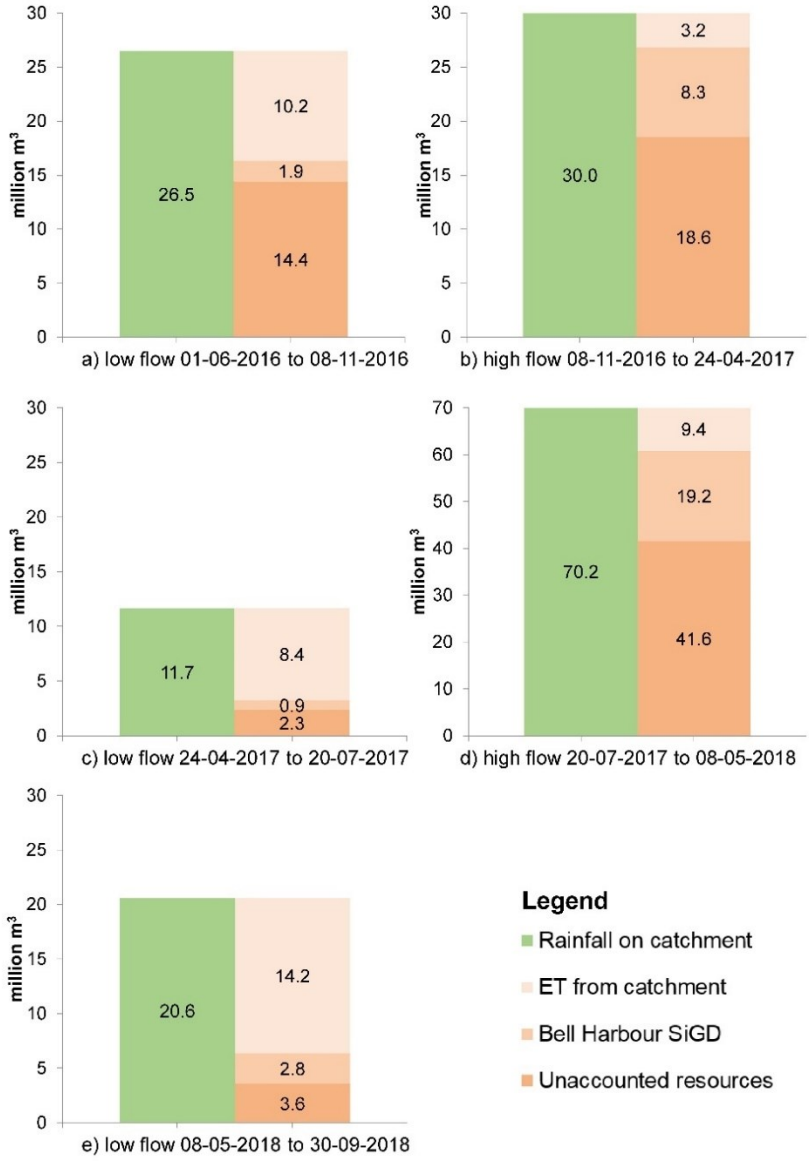

Figure 8.16: High (a, c, e) and low (b, d) flow water balances of Bell Harbour in million m^3: green = input, orange = output.

The low-flow periods are defined according to the estimated SiGD illustrated in Figure 8.14 with a) 01 Jun to 08 Nov 2016, b) 24 Apr to 20 Jul 2017 and c) 08 May to 30 Sep 2018 (Figure 8.16a, c, e). The two high-flow periods are defined by d) 08 Nov 2016 to 24 Apr 2017 and e) 20 Jul 2017 to 08 May 2018 (Figure 8.16b, d).
The high-flow periods coincide with the winter period and autumn and spring, while the low-flow periods correspond to the summer periods. This is reflected by the differing rates of ET, ranging between 38 and 72% during the low-flow periods and between 11 and 13% during the high-flow periods. The ET regimes impact on groundwater recharge, which is consequently higher during high-flow periods than during low-flow periods. As one consequence, unaccounted resources and SiGD are proportionally higher during high-flow periods. SiGD accounts for 0.9 to 2.8 million m^3 (7 to 14%) during low-flow periods while it reaches 8.3 to 19.3 million m^3 (27 to 28%) during high-flow periods. Further, unaccounted resources range between 2.4 and 14.4 million m^3 (17 to 54%) during low-flow periods and between 18.6 and 41.6 million m^3 (59 to 62%) during high-flow periods.

During the two different flow periods, significant resources are unaccounted (or missing) in the water balances. During periods of high-flow, proportionally more groundwater is discharged into the bay than during low-flow periods. It is believed that due to the higher piezometric state of the aquifer, SiGD is continuously activated during these periods.
Based on the figures stated, two outflow regimes were hypothesised, namely intermittent SiGD into Bell Harbour Bay and continuously outflow via deep conduits bypassing Bell Harbour Bay and draining as SGD into Galway Bay. It is believed that during low-flow periods, a higher share of groundwater bypasses Bell Harbour Bay than during high-flow periods.

8.1.4. Single borehole dilution tests

Vertical flow velocities and directions within the open borehole BH1 were investigated using SBDT. Alternative methods, such as using a heat pulse flow meter, had to be rejected due to the very small diameter of 2” of the borehole.

25 concentrated SBDTs were conducted on 7 different days in 2017 at different hydrological conditions using NaCl (125 g/l or 62.5 g/l) and deionized water as a tracer, defined as: campaign 1 (11 Feb), 2 (26 Feb), 3 (4 Mar), 4 (23 Mar), 5 (14 Apr), 6 (13 Sep) and 7 (26 Oct). Deionized water was used to rule out that downwards migration of NaCl tracer may be density driven.
Table 8.1 summarises and Figure 8.17 illustratively exemplifies the results of 21 successful tracer tests, including mean flow velocities and tracer recovery, considering prevailing hydrological conditions. The summary of each tracer campaign is presented in SBDTs.
Unsuccessful tracer tests were related to withdrawing the CTD sensor before complete recovery of the tracer (mainly following the first injection on a day) or unsuccessfully injecting the tracer.

Table 8.1: Summary tracer break-through curves of successful SBDT conducted in 2017 of Figure 8.17 including groundwater level, preceding rainfall (n.a. = not available) tracer injection depth, tracer sampling depth, tracer recovery and mean groundwater flow velocity and flow direction (upwards ↑ or downwards ↓).

Parameter		Date						
		11 Feb	**26 Feb**	**4 Mar**	**23 Mar**	**14 Apr**	**13 Sep**	**26 Oct**
Head (masl)		21.9	25.1	28.1	25.2	25.2	24.5	24.4
Number of injections (NaCl/deionised)		1/0	6/0	6/2	1/1	2/0	1/0	1/0
Preceding rainfall	12 h	0	24	1.6	0	1.4	n.a.	n.a.
	24 h	0	24.4	37.8	0	1.4	1.9	0.5
	36 h	0	31	53	2.6	1.4	n.a.	n.a.
	48 h	0	31.8	60	4.2	1.4	24.7	8.35
Tracer injection depth [masl]		-7	-4.3	4.8	4.8	5.1	4.8	4.8
Tracer sampling depth (range) [masl]		-16.9	-21.9 to -45.2	18.4 to 23.4	-44.7	-80.4	-129.4 to -176	-141.3
Tracer recovery (range) [%]		99.8	45.8 to 51.0	0.1 to 0.3	89.8	20.0	9.4 to 25.6	16.3
Mean groundwater flow velocity (range) [m/h]		185.0	146.3 to 242.2	198.0 to 262.9	54.7	97.9	43.3 to 97.0	83.5
Flow direction [↓/↑]		↓	↓	↑	↓	↓	↓	↓

In general, the groundwater flow direction was downwards, and tracer recovery and mean groundwater flow velocity decrease with increasing depth, suggesting continuous groundwater outflow along the depth of the borehole up to at least 176 mbsl (where tracer was still recovered).
Mean groundwater flow velocities reach high levels of up to 263 m/h confirming that the borehole must be well connected to highly transmissive fractures / conduits. Along the vertical borehole section, tracer was recovered between the top at 23.4 masl and on the bottom at 176 mbsl, which was the maximum sampling depth of the CTD sensor, and so migration of the tracer would continue below that level.
During tracer tests carried out on 4 Mar 2017, the groundwater flow direction was upwards during the peak of a rising limb following a rain event. The low recovery rate of 0.1 to 0.3% is a clear indication of outflowing groundwater along the borehole section and associated loss of tracer.

The results highlight the presence of multiple highly transmissive groundwater flow horizons, ranging between 23 masl down to below 176 mbsl. The prevailing flow direction is downwards, however, during recharge, the flow direction becomes upwards. The low recovery during upwards flow is interpreted as lateral outflow from the borehole.

The changing dynamics and high flow velocities are a clear indicator of pressure-induced flow via large conduits. The depth of recovered tracer below 176 mbsl proves the existence of such deep conduits.

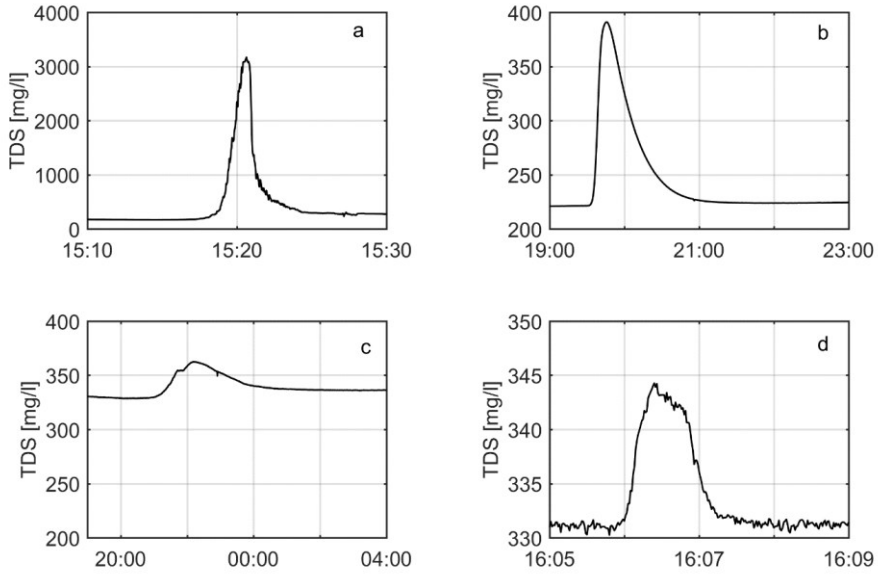

Figure 8.17: a), injection of 500 ml NaCl (62.5 g/l) at 4.3 mbsl, tracer recovery at 43.7 mbsl; b) injection of 500 ml NaCl (62.5 g/l) at 4.3 masl, tracer recovery at 130.0 mbsl; c) injection of 500 ml NaCl (62.5 g/l) at 4.3 masl, tracer recovery at 175.0 mbsl; d) injection of 500 ml NaCl tracer (125 g/l) at 4.8 masl, tracer recovery at 18.4 masl.

It is hypothesised that the existence of such deep conduit(s) must be linked to the groundwater flow regime in the catchment. Accordingly, deep flow paths are most likely the reason for groundwater bypassing Bell Harbour Bay. Such deep flow must discharge into the sea (e.g. Galway Bay) via submarine sprigs. Surcharge of these deep channels, driven by heads from the surrounding escarpments, temporarily / seasonally increases the head in BH1, activating more shallow conduits and draining as SiGD into the bay.

8.1.5. Tracer study

The results of this tracer study were published in Schuler, et al. (2018b); Schuler, et al. (2019b). The main goal of the tracer test was to investigate hydrogeological connections between two injection points on the Burren Plateau and several different potential outlet points. Three injections were conducted on 14 Apr 2018 using the artificial tracers rhodamine WT, fluorescein and wood chips.

The objectives of the test were mainly to:

- Evaluate hydraulic connections between the injection points and
    - the deep borehole (BH1);

- intertidal springs, potentially allowing for semi-quantitative analysis of tracer breakthrough at Pouldoody spring (SiGD1); and
- potential SGD locations/areas in Galway Bay;

- Characterise groundwater flow dynamics between the injection sites and observation sites;
- Evaluate the use of a solid particle tracer in the form of wood chips.

Offshore sampling of fluorescence and EC was carried out between 16 and 19 Apr 2018. Unfortunately, on Day 1 (14 Apr), the CTD was not recording for unknown reasons, so there are only fluorometer readings for that day.
While rainfall was very favourable in order to provide recharge and pressure pulses for the dyes to be transmitted, wind speeds imposed a limitation to sampling in the sea (Figure 8.18). On 16 Apr a red weather warning issued by the Irish meteorological service MetEireann limited sampling on that day in time and space.

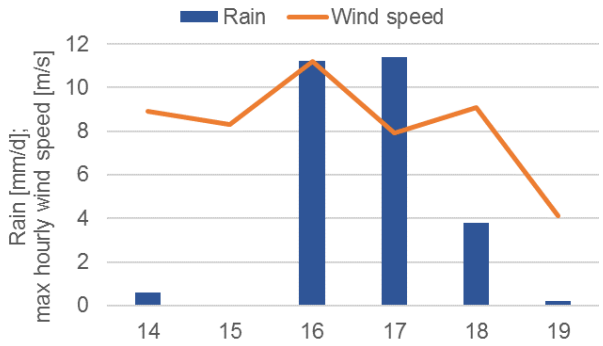

Figure 8.18: Meteorological conditions during the tracer test between 14 and 19 Apr 2018.

The results of the study are presented below.

8.1.5.1. Localising areas of SGD

Different submarine outlets for the Bell Harbour were believed to exist in Galway Bay based on the conceptual understanding that today's outlets may have developed as swallow holes or springs during periods of lower sea levels. Rising sea levels increased the base level, and hence connected the former swallow holes to higher elevated aquifer(s), which is today's Burren.
Therefore, firstly, areas of potential SGD were investigated by looking at sea surface temperatures which were mapped in ArcGIS using Landsat 8 OLI following Walawender, et al. (2012) (Figure 8.19). While the absolute temperatures exhibit some uncertainty due to atmospheric correction parameters, the relative pattern of temperatures clearly indicates discrete localised areas of temperature anomalies, i.e. lower temperatures than the surrounding sea temperature.

These discrete areas of temperature anomalies were interpreted as potential areas influenced by SGD, mapped, and used as reference for sampling for fluorescence in the sea following the tracer injections.

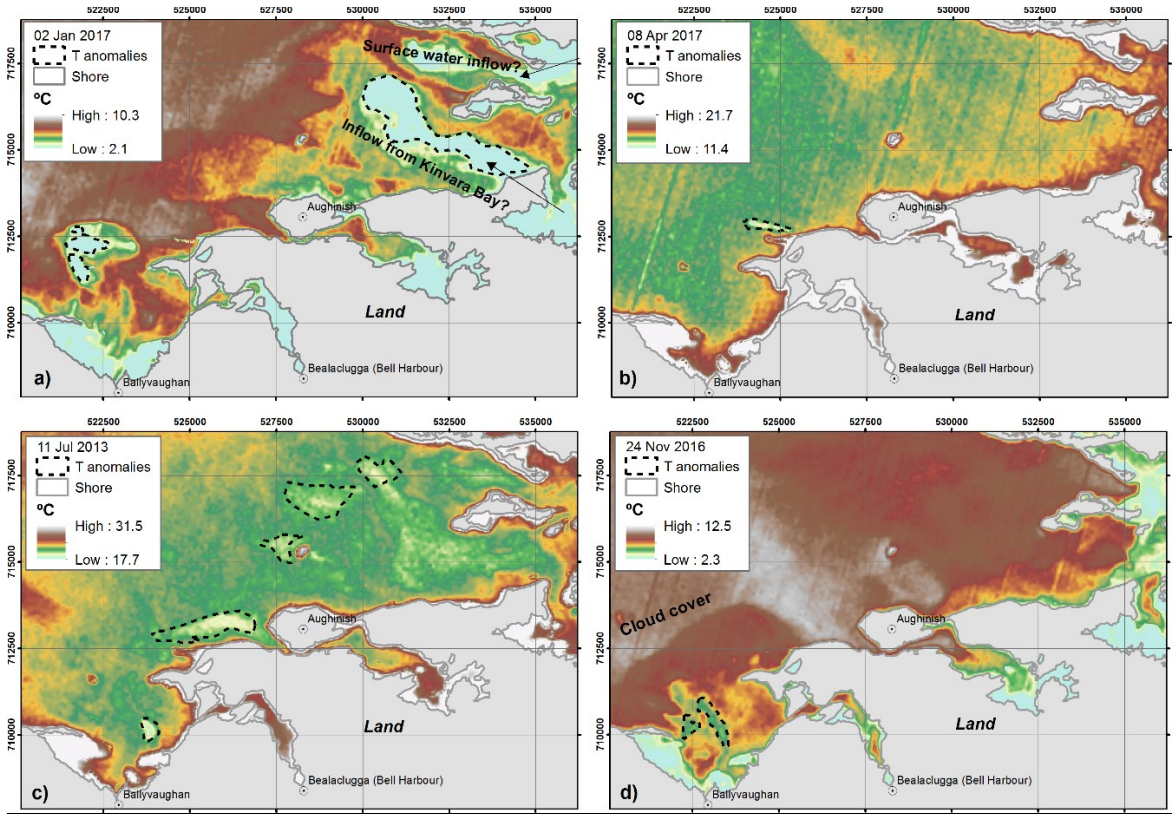

Figure 8.19: Sea surface temperatures derived from Landsat 8 OLI indicating localised temperature anomalies indicative for SGD on a) 2 Jan 2017, b) 8 Apr 2017, c) 11 Jul 2013 and d) 24 Nov 2016. Note that temperature is scaled differently in each scene.

8.1.5.2. Injection sites

The two fluorescent dyes and wood chips (three injections in total) were injected at two different sites on 14 Apr 2018: one injection site is the openly accessible swallow hole Deelin Pot (5.9 km south of Bell Harbour Bay) while the other site is the cave Poll Gonzo (7.5 km south of Bell Harbour Bay).

Access to Poll Gonzo required speleological equipment, with a team of six persons abseiling three (20 m approx.) pitches on fixed ropes. The uranine was dissolved in-situ within a 100 l inflatable swimming pool and released into the underground stream upstream of a waterfall at approx. 70 masl and 56 m below ground level (Table 8.2, site 1a).

The 250 l of wood chips were released at the bottom of the cave at ~31 masl at the local water table, where three experienced speleologists abseiled down another pitch with difficult access (Table 8.2, site 1b).

Rhodamine was injected into the bottom of Deelin Pot 1.67 km north-northwest of Poll Gonzo, where a 1 m^3 carbon-fibre tank with a release valve at its bottom was installed to dilute the dye in-situ (Table 8.2, site 2). The total volume of water used for dilution and flushing was 2.7 m^3.

Table 8.2: Injection sites 14 Apr 2018.

Injection site	Coordinates	Altitude [masl]	Tracer and mass	Injection time	Flushing volume
1a (Poll Gonzo, waterfall)	53.055°; -9.073°	~70	Uranine, 25 kg	13:00	~30 l/s
1b (Poll Gonzo, bottom sump)	53.055°; -9.073°	~30	Wood chips, 250 l	12:00	~30 l/s
2 (Deelin Pot)	53.070°; -9.080°	~84	Rhodamine, 25 kg	17:00	2.7 m^3

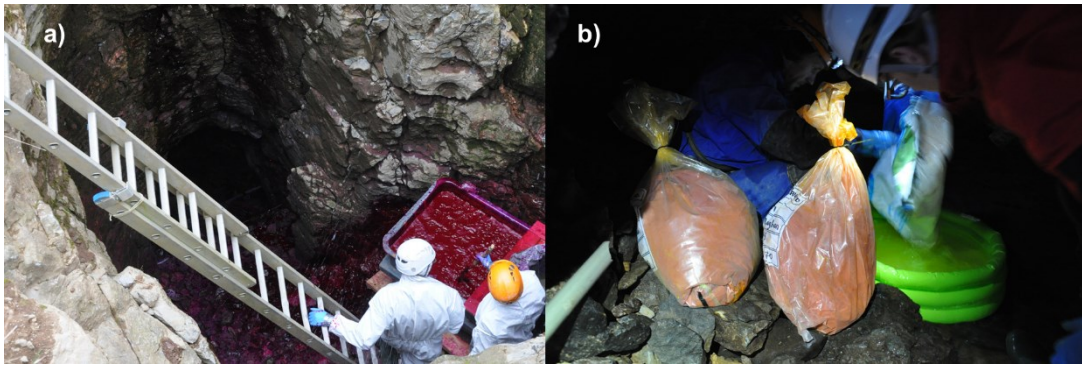

Figure 8.20: a) Dilution of 25 kg fluorescein within Poll Gonzo, and b) dilution of 25 kg rhodamine within Deelin Pot.

8.1.5.3. Observation sites

Onshore monitoring for the potential discharge of tracer was done qualitatively at 10 different sites using activated charcoal, and (semi-) quantitatively using field fluorometers (Table 8.3). The charcoal samplers were exchanged on the 19 Apr 2018 (except for BHB, which was collected on 25 Apr), so that for every location there were two phases of charcoal sampling carried out.

Offshore monitoring was designed to take place in transects passing through the areas of potential SGD previously identified, and iteratively monitoring with the fluorometer (#641) deployed in the sea pulled behind the vessel. The whole concept of the tracer study is outlined in Figure 8.21. Offshore monitoring routes were sub-divided into a ‘western section’ and an ‘eastern section’. Because of the higher number of potential SGD areas identified in the western part, the western section was prioritised in monitoring. The total duration and kilometres covered during the monitoring period is presented in Table 8.4. On Day 1, monitoring was limited to the eastern part of the bay due to a storm event and red weather warnings. Stormy conditions continued for the following two days, making the conditions problematic until Day 4, but monitoring was extended to the centre and western part of the Galway Bay from Day 2 onwards.

Table 8.3: Observation sites.

ID	Observation site	Coordi-nates	Altitude [masl]	Distance to injection site [m] to:		Instrumen-tation	Recording frequency/ duration
				Poll Gonzo	Deelin Pot		
1	Fergus River at Crossard Bridge	52.966°; - 9.085°	~23	9,392	10,878	Albillia GGUN-FL30	5 min; 14 to 25 Apr
2	Pouldoody spring	53.129°; -9.074°	-0.1	8,221	6,641	Albillia GGUN-FL30	5 / 15 min; 14 to 20 Apr
3	BH1, borehole	53.081°; -9.073°	15 to -170	2,848	1,339	Charcoal	14 to19 Apr 19 to 25 Apr
4	Ballyvaughan West	53.122°; -9.158°	~0	9,343	7,796	Charcoal	14 to 19 Apr
5	Ballyvaughan East	53.121°; -9.139°	~0	8,607	6,994	Charcoal	14 to 19 Apr
6	Corranroo West	53.141°; -9.010°	~0	11,327	10,265	Charcoal	14 to 19 Apr 19 to 25 Apr
7	Toberbreen	53.144°; -8.989°	~0	10,437	9,250	Charcoal	14 to 19 Apr 19 to 25 Apr
8	Kinvara West	53.140°; -8.937°	~0	13,148	12,433	Charcoal	14 to 19 Apr 19 to 25 Apr
9	Kinvara East	53.142°; -8.928°	~0	13,659	12,974	Charcoal	14 to 19 Apr 19 to 25 Apr
10	BHB, outlet of Bell Harbour Bay	53.144°; -9.099°	~0	10,111	8,356	Charcoal	14 to 25 Apr

Table 8.4: Offshore sampling periods from Day 1 (16 Apr) to Day 4 (19 Apr).

Date (Apr)	Start time	Finish time	Total duration [h]	Track covered [km]
16	08:55	12:30	3:35	41
17	11:00	17:55	6:55	80
18	08:28	16:25	7:57	69
19	07:50	10:37	2:47	29
Total			21:14	219

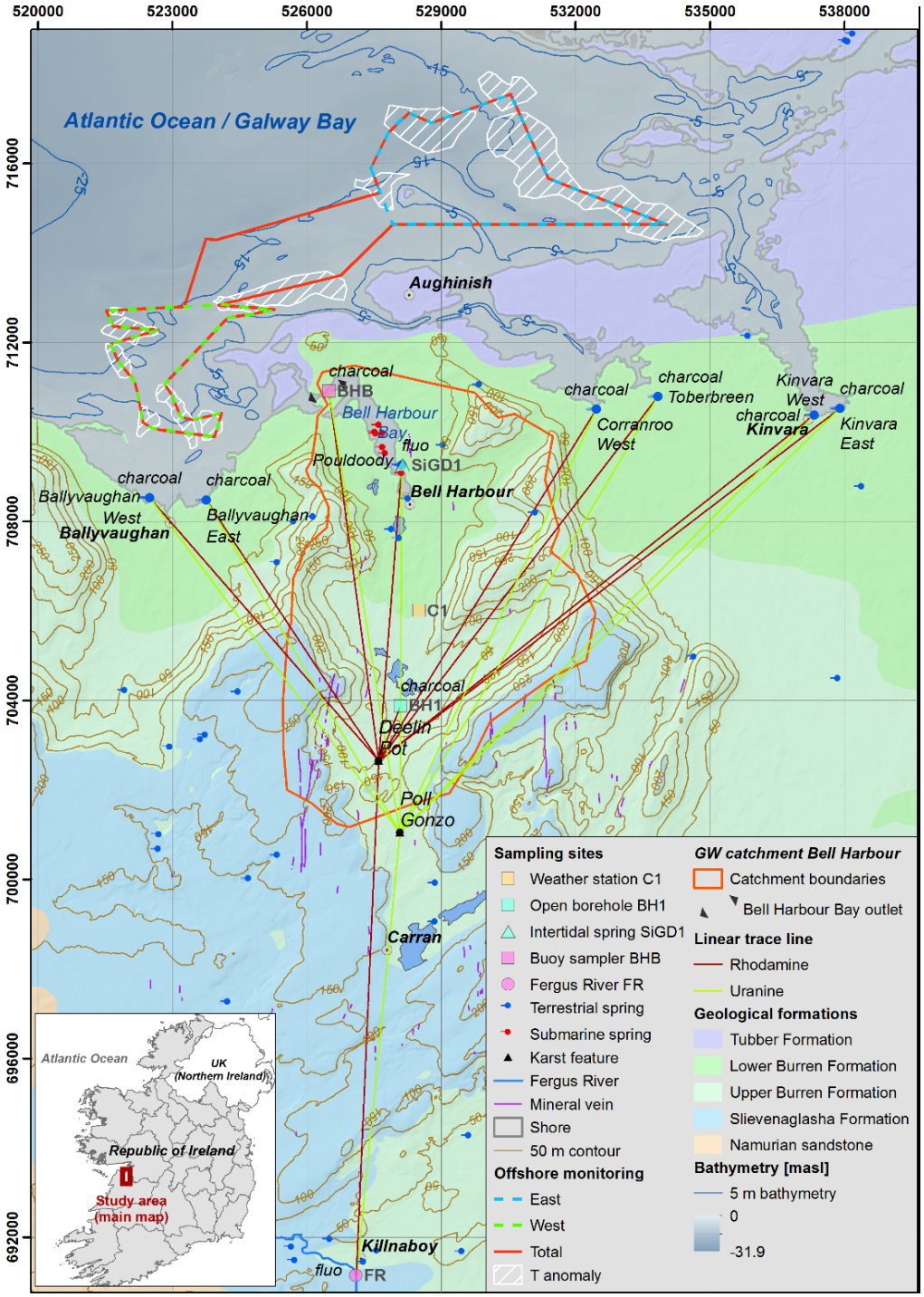

Figure 8.21: Outline of the tracer study, incl. injection points, onshore sampling locations and monitoring devices, and offshore monitoring routes.

8.1.5.4. Monitoring results

The monitoring results are distinguished between terrestrial stationary sampling and marine mobile sampling.

8.1.5.4.1. Stationary sampling

Figure 8.22 shows the data from the field fluorometer installed in the Fergus River to the south of the tracer injection points. The river flow exhibits a clear response to the two preceding rainfall events of 11.6 mm (15 April 3:00 to 16 April 1:00) and 14 mm (16 April 14:00 to 17 April 4:00) as illustrated by the rising limb and following recession. The discharge increases from 1.6 to 12.8 m^3/s, notably along with turbidity. Uranine and rhodamine time series both show a correlation with turbidity peaking at 2 ppb and 3 ppb respectively. Correlation between fluorescent dyes and turbidity within this range is common (Schnegg, 2002). In addition, measured fluorescence exhibits a negative correlation with the temperature in the stream. Hence, the observed dye concentrations are interpreted as a mixture of natural background and/or anthropogenic sources.

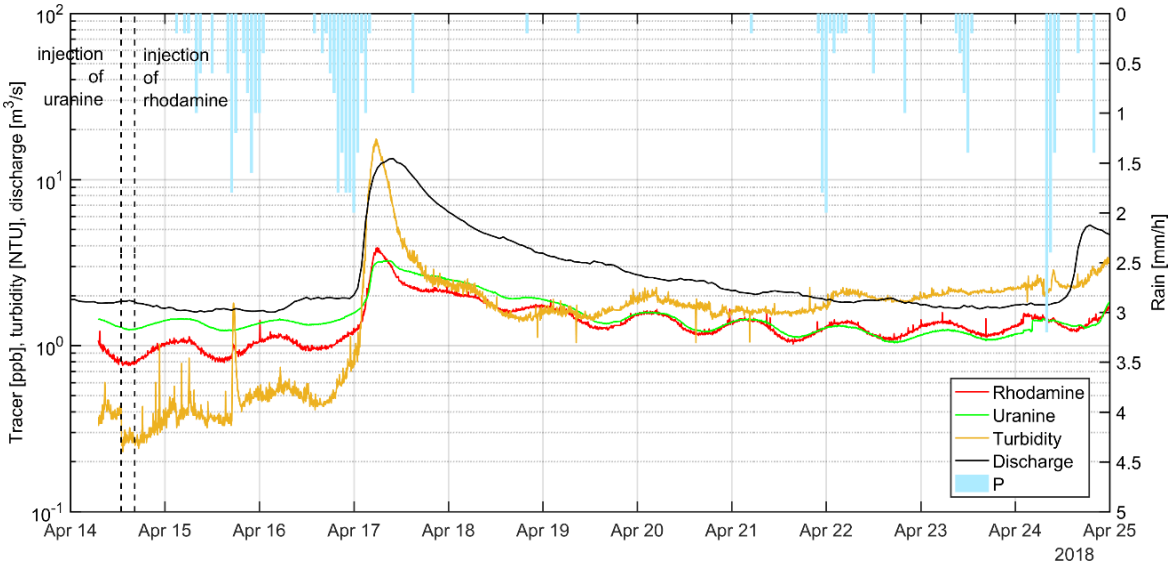

Figure 8.22: Readings of uranine and rhodamine in ppb, turbidity in NTU and discharge in m^3/s observed at the Fergus River between 14 and 25 April, as well as hourly rainfall measured at C1. The two dashed vertical lines indicate injection times of uranine and rhodamine, respectively.

Figure 8.23a-d shows the emission spectra of the eluted charcoal samples collected on 19 and 25 Apr along with an example of a positive result. Neither a clear visible emission peak of 516 nm for uranine (Figure 8.23a, b), nor an emission peak of 575 nm for rhodamine (Figure 8.23c, d) is present in any of the samples. As a result, all charcoal samples are interpreted to be free of any of the two dyes.

The results of the charcoal samples show that, a) there was no cross-contamination happening during the installation, replacement, and collection of charcoal samplers, and that b) none of the intertidal springs along the shore, the borehole (BH1) and the outlet of Bell Harbour Bay (BHB) proved to be hydraulically connected to the two injection sites.

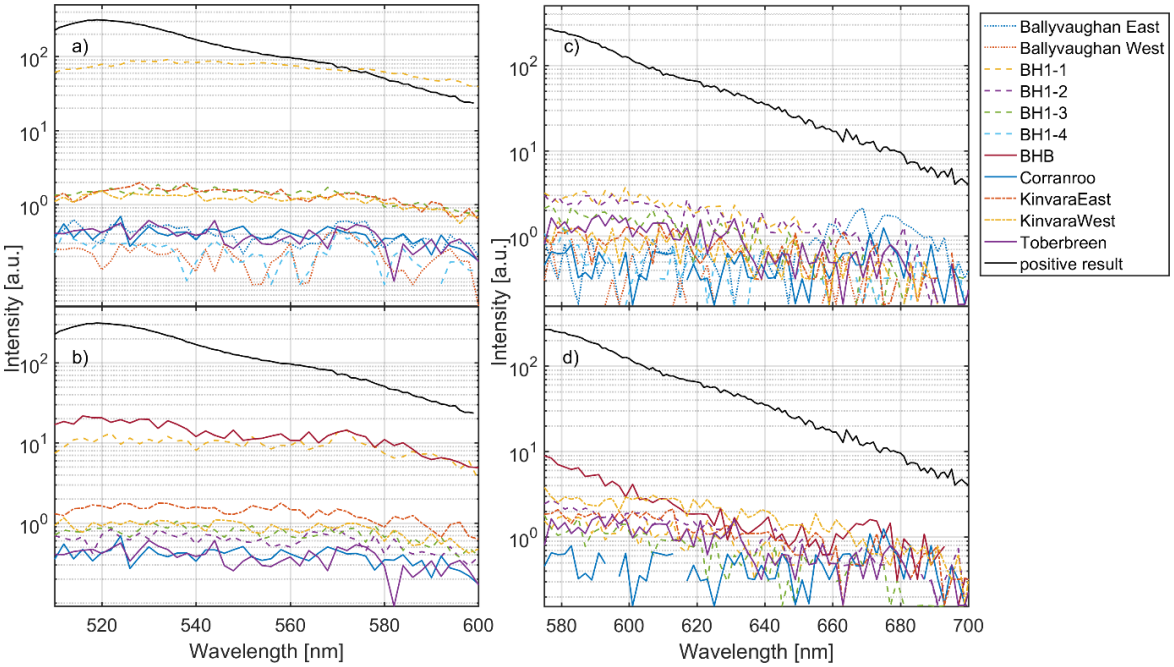

Figure 8.23: Emission spectra of activated charcoal samples for a) rhodamine and b) uranine. All samples were collected on 19 Apr, except BHB, which was collected on 25 April.

Figure 8.24 shows the results obtained from Pouldoody spring, along with water level fluctuations measured at the monitoring site.

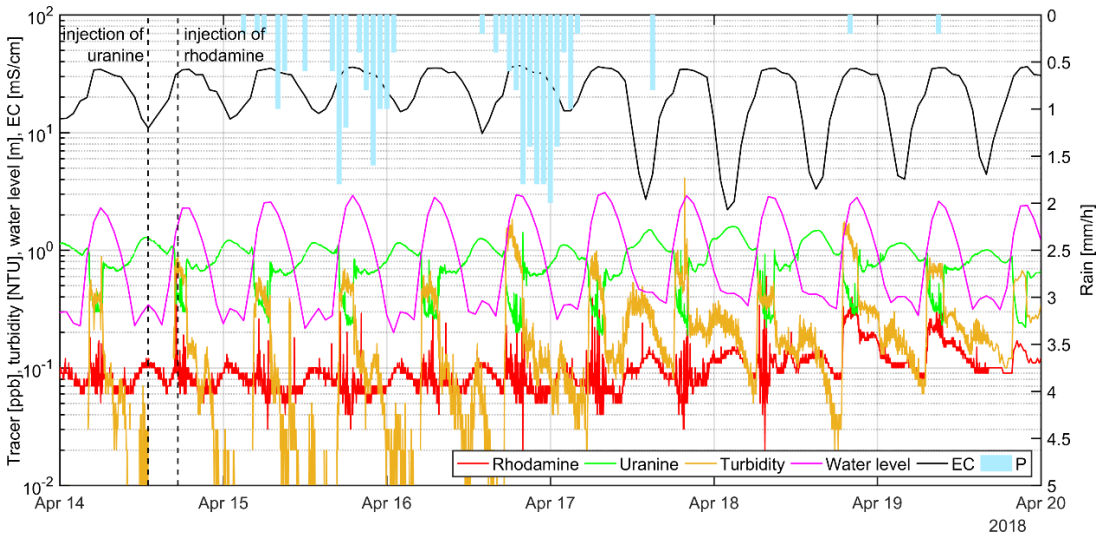

Figure 8.24: Concentration of uranine and rhodamine in ppb, turbidity in NTU and water level in m observed at the intertidal spring Pouldoody between 14 April and 20 April, and hourly rainfall (P) measured at C1.

The obvious twice diurnal water level fluctuation is a function of the tidal cycles. Further, the fluctuation of conductivity indicates active discharge of the spring, increasing on 17 April, which suggests increased discharge. The tidal fluctuation and spring discharge impact on the readings of both

dyes, which again is believed to be the result of changing chemistry and composition of the water at the site, probably from dissolved organic matter (DOM). The concentration of rhodamine is <0.3 ppb while uranine slightly exceeds 1 ppb. As a consequence of these low concentrations, the results are interpreted as negative.

8.1.5.4.2. Mobile sampling at sea

The previous section showed that no tracer was reliably sampled at any of the terrestrial sampling sites.

Figure 8.25a-b shows the concentrations of uranine and rhodamine for the filtered data in semi-log scale along with measured conductivity in the sea, depth of sampling and hourly rainfall. Conductivity records are missing for Day 1 (16 April). As discussed, monitoring was limited to the eastern transect on Day 1 due to very harsh weather conditions. During Day 2 to 3, sampling focussed on the centre and the western transect, particularly, due to the fact that more elevated tracer readings were noticed in real-time in the centre and the west on Day 2.

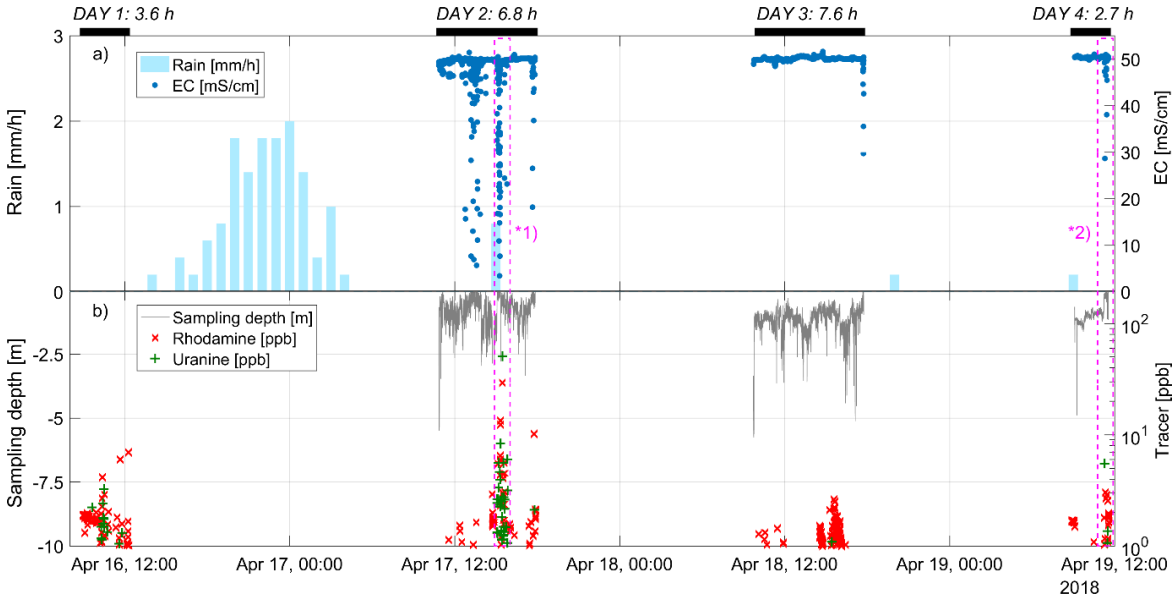

Figure 8.25: Concentrations of rhodamine and uranine [ppb] against measured EC [mS/cm] for a) the raw data and b) the filtered data using the quotient method between 16 and 10 Apr 2018 (Day 1 to Day 4). The black bars in the middle show the duration of sampling for each day.

The raw data shows 4,998 tracer readings with maximum values for rhodamine and uranine reaching 208.6, 457.8 ppb respectively (Figure 8.25b). The quotient method was applied to filter potentially erroneous readings, leaving 4,365 (87.3%) of the readings considered to be valid (Figure 8.25b). As a result, the maximum levels of rhodamine and uranine correspond to 29.3 and 50.7 ppb respectively.

Both maximum dye concentrations were recorded on sampling Day 2 (17 April) which correlate very well with the lowest conductivity <5 mS/cm values also recorded on Day 2. Periods of low

conductivity and high tracer readings are highlighted in pink rectangular hashed boxes (Day 2: 15:05 to 15:20; Day 4: 11:15 to 11:28). Importantly, the depth of the fluorometer and CTD sensor was very low during these two periods (0.18, 0.23 m). The average sampling depths on Day 1, 2 and 3 are 0.81, 1.20 and 0.96 m (average of 1.01 m). Therefore, the positive tracer readings within the upper 0.23 m of the sea water column may reflect a fresh or brackish water layer with cumulative dye concentrations.

Low conductivity levels may be linked to the two rainfall events between 15 Apr and 17 Apr with a total of 22.6 mm. It is hypothesised that the rapid recharge increased SGD with the resultant lowering of conductivity in the sea at these locations. In comparison, the conductivity readings on 18 and 19 April (during which period there continued to be no rainfall), are much more homogeneous and relatively constant. It is assumed that the impact of freshwater was reduced on these days and hence the impact of SGD lowered.

No correlation between conductivity and tracer concentration occurred on Day 3 with the conductivity readings remaining continuously high at 50 mS/cm (with a few exceptions).

The differences of either relatively strong spatio-temporal correlations between conductivity and tracer opposed to an absence of correlation suggest consistency of the method. Overall, it must be assumed that strong dilution and mixing of the signals in the sea weakened and spatially integrated the signal and therefore, a clear correlation cannot be expected.

As discussed previously, turbidity might impact on tracer readings and SGD may be associated with higher turbidity than the sea water. For example, Drew (2003) showed an SGD plume floating on the sea surface, differentiated by its colour and presumably linked to peaty water. Turbidity may be related to recharge at Deelin Pot, as it is known that its bottom shows a level of clay/sediments, as opposed to Poll Gonzo where all flow is clearly concentrated in a cave system/conduits. Therefore, turbidity was plotted against tracer readings to evaluate if there is a high linearity between the readings (see Figure 8.26a and Figure 8.26b).

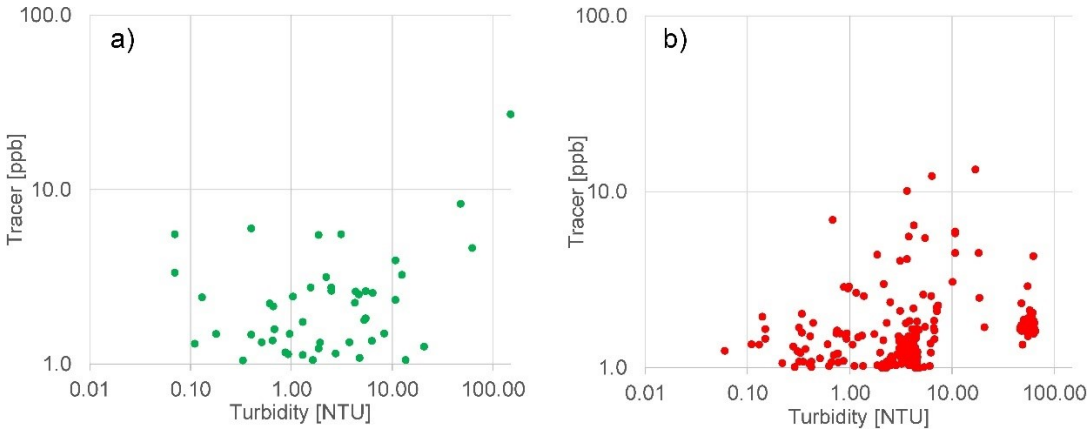

Figure 8.26: Fluorescein (a) and rhodamine (b) (≥1 ppb) against turbidity (NTU).

Both plots show elevated tracer readings at low turbidity readings. While there seems slightly linearity between rhodamine readings and turbidity, no linearity seems to exist between fluorescein and turbidity. The maximum fluorescein reading of 50.7 ppb is accompanied by a turbidity of 0.0 NTU (not shown in the plot because NTU is plotted >0).
Again, higher turbidity would be expected along tracer readings, even more in the case of Deelin Pot and associated rhodamine. Therefore, the plots do not seem to indicate a clear systematic relationship between turbidity and tracer readings.

In order to evaluate the spatial pattern of recorded values, Figure 8.27 shows the georeferenced and filtered ppb readings for rhodamine and uranine along with the conductivity of the sea water, and the total track recorded by the GPS. Both dyes are plotted for values >2 ppb in order to not overload the map with low (and presumably non-meaningful) concentrations.

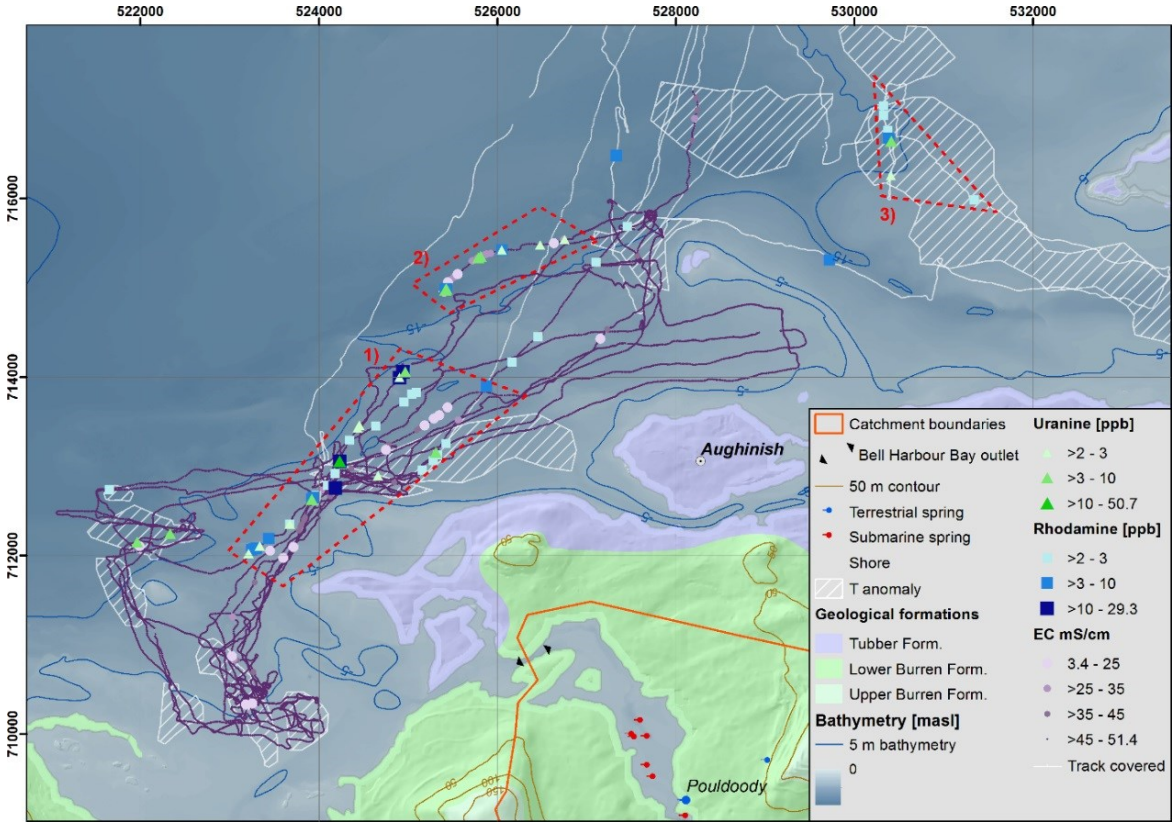

Figure 8.27: Measured and corrected tracer concentration of rhodamine and fluorescein [ppb] along measured EC.

In general, tracer was recovered in a relatively large geographical area, yet, three clusters are visible, Cluster 1 in the west, Cluster 2 in the centre and Cluster 3 in the east. In all clusters, both dyes were recovered. Altogether, a spatial correlation between dye readings and conductivity values can be confirmed. Cluster 1 contains the maximum observations for rhodamine and uranine reaching 29.3, 50.7 ppb respectively, associated with the low conductivity readings on Day 4 (Figure 8.25,

*2), which correspond to travel times of 100 and 105 m/h for rhodamine and uranine respectively. Cluster 2 relates mainly to the highly correlated low conductivity and high tracer readings observed on Day 2 (Figure 8.25, *1) with associated travel times of >184 and 197 m/h for rhodamine and uranine respectively. These areas are considered as SGD 'hot spots'.
The longest distance between injection sites and sampling locations occurred in Cluster 3, where on Day 1 uranine was sampled 15.8 km away from Poll Gonzo and rhodamine 14.6 km away from Deelin Pot, which correspond to travel times of 346 and 354 m/h.

No wood chips were observed during offshore monitoring. During the first three days of sampling, the sea was very rough due to strong winds with maximum average hourly wind speeds of 8 to 11 m/s. These conditions made the work onboard difficult and monitoring of wood chips on the sea surface challenging. On Day 4, the sea became very calm, but still no wood chips were seen or sampled. Therefore, the result of the tracer test using wood chips is considered as inconclusive / negative.

8.1.5.5. Summary of tracer study

Submarine groundwater discharge (SGD) is recognized as an important pathway for contaminant transport into the coastal environment, hence, it is of relevance in the context of coastal karst catchments. A good understanding of SGD dynamics linked to the drainage of coastal karst aquifer is therefore necessary.
This study combines methods to: a) first locate potential areas of SGD using remote sensing; b) apply a set of different artificial tracers, including fluorescent dyes and wood chips, and c) evaluate hydraulic connections between terrestrial injection points and offshore submarine discharge locations. The overall approach was successfully applied in the study area of the coastal aquifer of Bell Harbour. Both of the fluorescent dyes were recovered in the sea up to 15.8 km away from an injection point using the GGUN field fluorometers. Offshore sampling was conducted in transects in the sea over four successive days onboard a vessel. The estimated travel times are in the order 100 to 354 m/h. Fluorescence peaks localised in time and space correlated with lower conductivity values in the sea, indeed indicating the discharge of fresh or perhaps brackish groundwater. Two main areas of SGD were identified, whereas the spatial pattern of SGD is believed to resemble the multiplicity of SGD locations. It is hypothesised that the main outlets of the catchment are located in Cluster 1 and 2. However, additional studies are needed to confirm this conclusion.
None of the wood chips were recovered from the sea). Different factors may have prevented a positive result, including the potential sediment infill of submarine springs, trapping any larger particles, and/or maybe the rough sea conditions during sampling which prevented them being seen.

8.1.6. Conceptual model & catchment delineation

The results of the previous four chapters were used to conceptualise the functioning of the catchment, and further to update the catchment boundaries of Bell Harbour:

- Highly variable EC concentrations draining Bell Harbour Bay, and associated fluctuation of SiGD into the bay. During summer, SiGD is very low, while during winter, an increase can be observed;
- According to the previously assumed catchment boundaries of Bell Harbour (McCormack, et al., 2017) there is a significant mismatch in the water balance according to which the main discharge would occur via SGD bypassing Bell Harbour Bay (Schuler, et al., 2018a);
- EC measured at the outlet of Bell Harbour Bay and at the intertidal spring Pouldoody indicate rapid surges and drops than can be linked to surges and drops in the piezometric state of the aquifer observed at BH1, T1 and CAS/CAN;
- Periods of high-flow and low-flow were identified: During periods of low-flow, a smaller proportion of rainfall is drained via SiGD than during high-flow periods;
- Deep groundwater flow is plausible and confirmed beyond a depth of 176 mbsl using SBDT in BH1;
- While the general vertical flow direction in BH1 is ‘downwards’, during one recharge event ‘upwards’ moving groundwater was confirmed. This observation links deeper groundwater flow in the catchment to shallow flow horizons, at least temporarily;
- Tracer tests have shown that the upland of the Burren is directly connected to different SGD locations or areas in Galway Bay. No tracer was reliably recovered along the shore, suggesting that the tracers bypassed intertidal springs along the shore;
- The water levels of CAS, CAN and T1 correlate well with the piezometric head in BH1. During periods when T1, CAS or CAN exhibit a water level, the head in BH1 tends to be >21 masl. In turn, once the water level in CAS, CAN and T1 disappears, the head in BH1 rapidly drops several meters. This phenomenon was interpreted as pressure-influence between the upland (CAS and CAN) and the lowland (T1). Hence, CAS/CAN are assumed to be part of the Bell Harbour catchment. At the same time, CAS was previously successfully traced to the Fergus River (Bunce and Drew, 2017). Therefore, it is hypothesised that drainage of CAS can divert to both the south and north, perhaps with seasonal changes, or changes related to the overall head. Further, a syphon may affect the transfer of flow acting as a sort of valve.

The conceptual model describes a very complex, multi-layer coastal karst aquifer that is drained via SiGD and SGD (Figure 8.28).

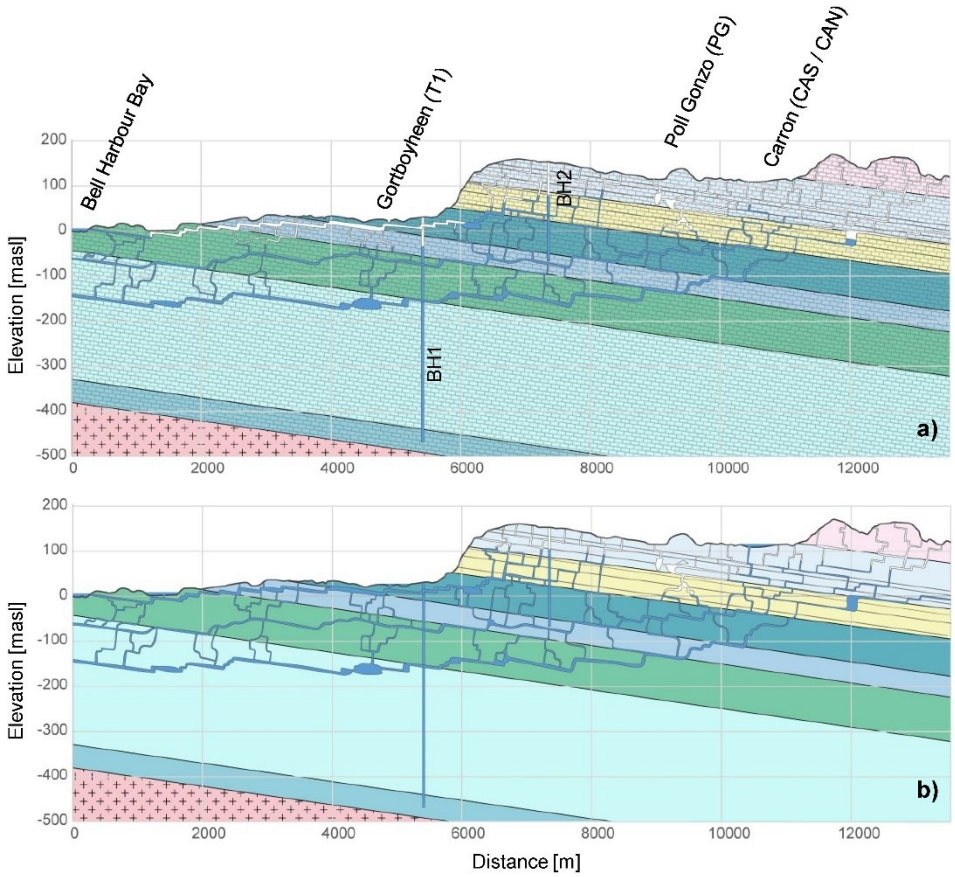

Figure 8.28: Conceptual model of the karst aquifer of Bell Harbour, described by a multi-level conduit dominated system: a) during summer, a low piezometric state of the aquifer causes less SiGD than in b) winter, when a higher piezometric state causes turloughs to be flooded and increased SiGD into Bell Harbour Bay.

Discharge via SGD must be perennial while discharge contribution to SiGD is rather intermittent. In fact, it is hypothesised that during the winter months and periods of higher head in the aquifer, there is a significant contribution to SiGD along the shore. Accordingly, shallow groundwater flow is connected to the shallower discharge regime. In turn, during the summer months and periods of lower head, SiGD is limited to localised contributions while deeper groundwater flow remains in deeper domains. Accordingly, the prevailing hydraulic conditions differs between a) summer (low-flow) and b) winter (high-flow).

8.2. Time series analysis

8.2.1. Autocorrelation

The autocorrelation function (ACF) was previously applied to quantify the linear relationship within the discharge time series of Ballindine and Manorhamilton springs. In this section, different time

series obtained in Bell Harbour are similarly analysed in order to characterise the linearity of the karst system measured at different locations.
Figure 8.29i shows the ACF for daily discharge of Ballindine (29 Apr 2009 to 01 Oct 2018) and Manorhamilton (30 Apr 2009 to 03 Jul 2013) and estimated SiGD into Bell Harbour Bay (25 Feb 2016 to 01 Oct 2018) for a lag of up to 400 d, including the significance level at 0.2 and 0.05. SiGD time series reaches <0.2 and <0.05 after 69 and 84 d indicating that the discharge from Bell Harbour Bay exhibits a memory effect that is slightly below Ballindine. The ACF rapidly declines for the first 5 to 10 d.
Following the first rapid decline after 5 to 10 d, the ACF of SiGD shows an unusual course, a mixture of different decreasing slopes and steps. This may be caused by the complex SiGD dynamics into Bell Harbour Bay, and further additional complexity by the drainage of the bay due to tidal fluctuation impacted by marine dynamics.
The interpretation of the estimated SiGD time series in terms of flow components is challenging: first of all, a daily time step is a low resolution for a fast responding system. Hence, contributions from individual flow components may be dissolved within such resolution. Secondly, the discharge into Bell Harbour Bay is conceptualised as being the overflow dynamics of the karst network system. Hence, it can be assumed that it is rather the head in the aquifer that drives the discharge as opposed to draining permeability domains adding additional non-linearity. And thirdly, other variables such as sea currents may impact on observed EC, and hence estimated SiGD. Such factors may also act to obscure the signal originating from individual flow components.

In the long-term a change in ACF is visible, which is interpreted as a seasonal variation of the discharge signal. The seasonal fluctuation of SiGD time series lies between at the ACF of Ballindine and Manorhamilton. Seasonal SiGD fluctuation may be related to aquifer storage potential and/or the characteristic of the discharge pattern of SiGD time series.
Based on that analysis, it may be inferred that the contribution of low-flow components of SiGD is similarly significant as in the case of Manorhamilton, and lower than in the case of Ballindine. Further, it may be inferred that the relatively strong seasonal fluctuation of Ballindine will also translate into a larger variation of low flow, as is the case in the Manorhamilton/Bell Harbour catchments, which again is a result of the aquifer storage that contributes to low flow, which is higher for Ballindine as for Manorhamilton/Bell Harbour.

Next, linearity within the catchment of Bell Harbour is assessed and compared on a daily scale using the measured head in the boreholes BH1 and BH2, CAS and CAN, in the underground river of Poll Gonzo (PG) and turlough T1. All ACFs are plotted for 800 d (including BH2 and Poll Gonzo even though both time series are shorter than 800 d).
The previously outlined seasonal pattern of the ACF of SiGD is confirmed by the fluctuation at approx. 365 d (Figure 8.29i). To a similar extent, the ACF of BH1 also shows a seasonal pattern, although it exhibits less linearity than in the case of SiGD (Figure 8.29ii). In fact, seaonal peaks of

its ACF reach >0.2. This pattern reflects the seasonal head in BH1, which is constantly high during high-flow periods, and intermittently low during low-flow periods. The ACF drops <0.2 and <0.05 after 52 d, 69 d respectively, indicating a faster loss of memory than for SiGD. Further, BH2 exibits an even faster loss of memory indicating less linearity becasue the ACF reaches <0.2 and <0.05 after 46 d, 62 d respectively. Again, these figures confirm that BH2 fluctuates more rapidly than BH1, and as a result, the head in BH2 has lower persistence than the head in BH1.

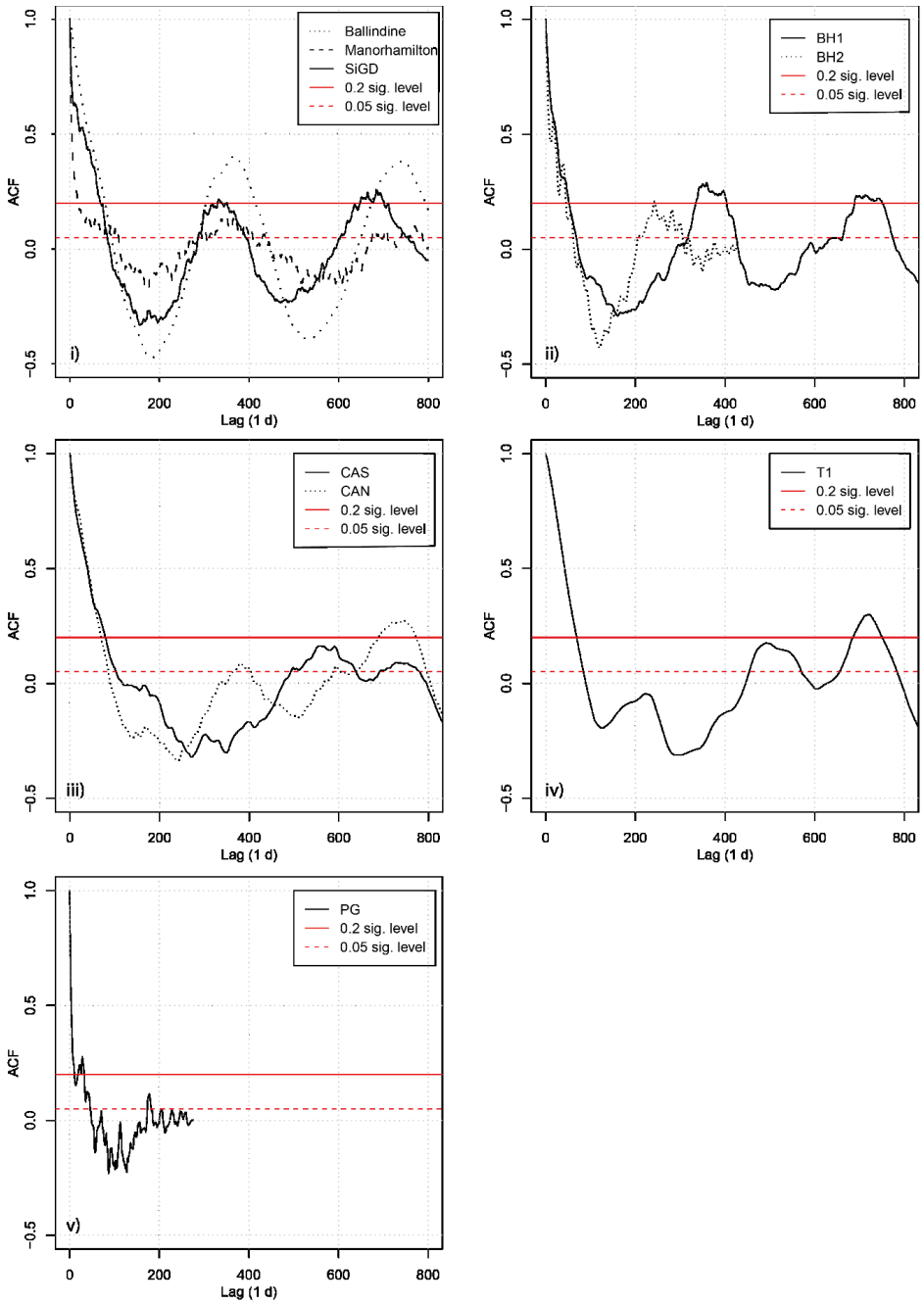

Figure 8.29: ACF for daily time series of i) SiGD draining Bell Harbour Bay and head measured at ii) BH1 and BH2, iii) CAS and CAN, iv) turlough Gortboyheen and v) the underground river in Poll Gonzo (upstream of the waterfall) up to lag = 800 d, and significance level at 0.2 and 0.05.

The ACF of CAN and CAS suggests a seasonal pattern, although the fluctuation is much disturbed, when compared to the ACF of SiGD or BH1 (Figure 8.29iii). CAS and CAN are both intermittently flooded, even during periods labelled as 'low-flow'. Hence, this may explain the disturbed seasonal pattern and the lower degree of linearity of the time series. The ACF of CAN and CAS reaches <0.2 and <0.05 after 70 and 80 d, 86 and 104 d respectively. Accordingly, the CAS time series exhibits less persistence than CAN. This again can be explained by the fact that CAS is impacted by discharge originating from CAN.
The ACF of T1 shows an even more disturbed seasonal pattern than in the case of CAS and CAN (Figure 8.29iv). The ACF <0.2 and <0.05 is reached after 70 d, 85 d respectively, which is very similar to the figures of CAN.
For the underground stream monitored in Poll Gonzo, the time series is limited to 276 days. Its ACF shows the fastest decline of all data analysed for Bell Harbour, reaching <0.2 and <0.05 after 11 d, 46 d respectively, indicating a high loss of memory. In fact, a first recession can be limited to the first 15 d, while for the period 15 to 106 d, a distinct secondary recession can be observed. The secondary recession may indicate additional flow component(s). Further, the ACF signal is relatively noisy. This fluctuation of linearity is interpreted to be related to the flashy nature of the water level time series.

Next, ACFs were computed for hourly time series up to a lag of 2,000 h (83.3 d) (Figure 8.30). CAS, CAN and T1 don't reveal much more information on an hourly time step, as compared to the daily time step previously assessed (Figure 8.30ii, iii). In turn, the ACFs of hourly head levels in BH1 and BH2 show more detail (Figure 8.30i). While the level of significance is the same as for the daily records, the recession of both ACFs are distinct. BH2 shows a sinusoidal decline fluctuating at 450 h (~19 d). Again, this is interpreted as the result of a highly reactive hydrograph. In turn, the ACF of BH1 shows a more gradual recession of convex and concave segments as well as a stagnant part between approx. 800 and 1,090 h. Clearly, different segments can be distinguished related to different degrees of loss in memory. The changing rate of linearity suggests changing dynamics: this can be related to impact of different flow components, or perhaps rather to different levels of karstification/transmissive zones along the borehole, and hence changing dynamics with changing heads.
The ACF of Poll Gonzo shows a relatively gradual decline for the first 140 h (6 d) followed by a second period of decline between 140 and 330 h (13.75 d), followed by a declining trend. Again, the ACF of Poll Gonzo shows a rapid loss of memory, and this ACF can be used as an indicator for the presence of at least two flow components impacting on the loss of memory.

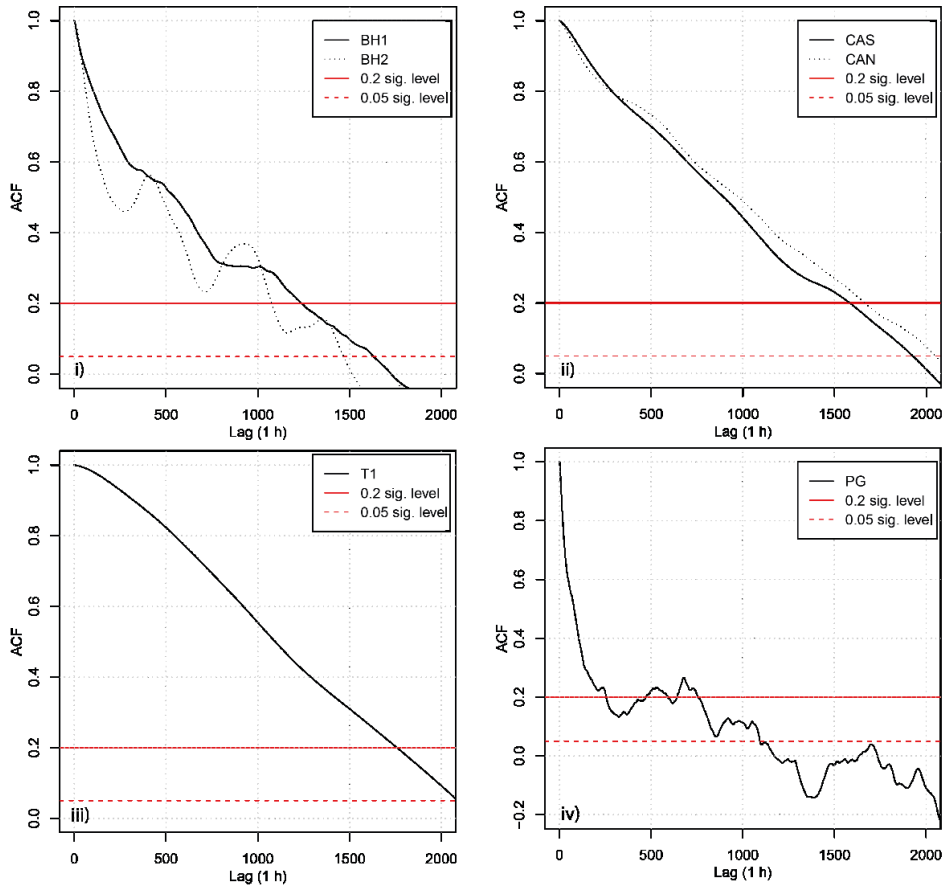

Figure 8.30: ACF for hourly time series of head measured at i) BH1, BH2, ii) CAS and CAN, iii) turlough Gortboyheen and iv) the underground river in Poll Gonzo (upstream of the waterfall) up to lag = 2,000 h, and significance level at 0.2 and 0.05.

8.2.2. Cross-correlation

While the previous three sections explained the complex pattern of time series from a single sampling location, cross-correlation was used to link individual time series in order to quantify linearity between input (e.g. rainfall) and output (e.g. head) time series as well as respective time lags.
First, a long-term analysis was done at a daily time step (Figure 8.31). Since SiGD was estimated per tidal cycle, respective time series could only be cross-correlated for mean daily records.
The results show a large range of peaks of the CCFs and lags ranging between 0.21 and 0.55 d, 0 and 21 d respectively.
SiGD peaks at a lag of 0 d with a CCF of 0.26, indicating a fast response to rainfall (Figure 8.31i). Yet, the quality of linear relationship is relatively low, and accordingly, additional variables must be influencing the SiGD regime into Bell Harbour Bay, as well as the drainage dynamics of the bay itself, based on the 'simple' assumption of input-output relationship between rainfall and SiGD. The significance level of 0.2 and 0.05 is passed after 7 d, 73 d respectively.
The water level of T1 shows a relatively low CCF of 0.23 at a lag of 21 d (Figure 8.31ii). The recession of the CCF is relatively slow, the level of 0.2 and 0.05 is reached after 32 and 66 d

respectively. These high values underline the functioning of the turlough T1, which is primarily driven by the piezometric state of the aquifer rather than by direct rainfall. Furthermore, drainage of a turlough via an estavelle is slow. Interestingly, correlation between the CCF series of T1 and the CCF series of SiGD reaches 0.48. This linearity indicates common dynamics driving the overall piezometric state of the aquifer, expressed by T1, and the SiGD regime of Bell Harbour Bay.
CAN and CAS both show a very similar pattern of the CCF (Figure 8.31iii). This is not a surprise, since CAN drains at least partly into CAS. CAS shows a relatively low CCF of 0.22 and a lag of 7 d with rainfall. In turn, CAN peaks at 0.37 and a lag of 3 d. These different figures therefore reveal the functioning of the system, where the CAN response to rainfall is faster and more linear compared to CAS, which responds both to rainfall, as well as discharge from CAN. The CCF of CAN and CAS show both relatively high linearity with the CCF of T1 reaching 0.66, 0.74 respectively. The fact that the correlation between the CCF of CAS and T1 is higher than the correlation between the CCF of CAN and T1 may be an indicator that CAS exhibits influence on T1. In this case, a hydraulic connection between CAS and T1 must be active, at least temporarily or seasonally.

The groundwater levels observed at BH1 and BH2 show distinct CCFs with rainfall (Figure 8.31iv). The upland borehole BH2 shows a relatively high peaking CCF reaching 0.43 at a lag of 3 d, indicating a quick response to rainfall. The recession is very fast, reaching <0.2 after 8 d and <0.05 after 14 d. In fact, the CCF shows a high variability which is very distinct from the previous CCF plots. This again suggests a highly non-linear response to rainfall, potentially related to different flow paths present which influence the water level. In turn, BH1 peaks with a CCF of 0.34 at a lag of 2 d, indicating less linearity. The CCF reaches <0.2 and <0.05 after 12 d, 71 d respectively. In fact, the recession shows two individual peaks that suggest the presence of additional flow components.
The difference between the CCF of BH1 and BH2 indicates the functioning of the aquifer of Bell Harbour: the upland borehole and its water level is largely or directly impacted by rainfall, while the lowland borehole is impacted by rainfall as well as by the head in the surrounding escarpments that influence on the lowland piezometric state.
The underground river in Poll Gonzo shows a very rapid response to rainfall indicated by a CCF of 0.55 and a lag of 1 d. The level of 0.2 and 0.05 is reached after 7, 10 d respectively. Interestingly, the recession shows several multiple peaks, which may be interpreted as additional flow components as well as the influence of upstream channel heterogeneity with potentially different rainfall response dynamics. However, they are all <0.2, and so their significance is questionable.

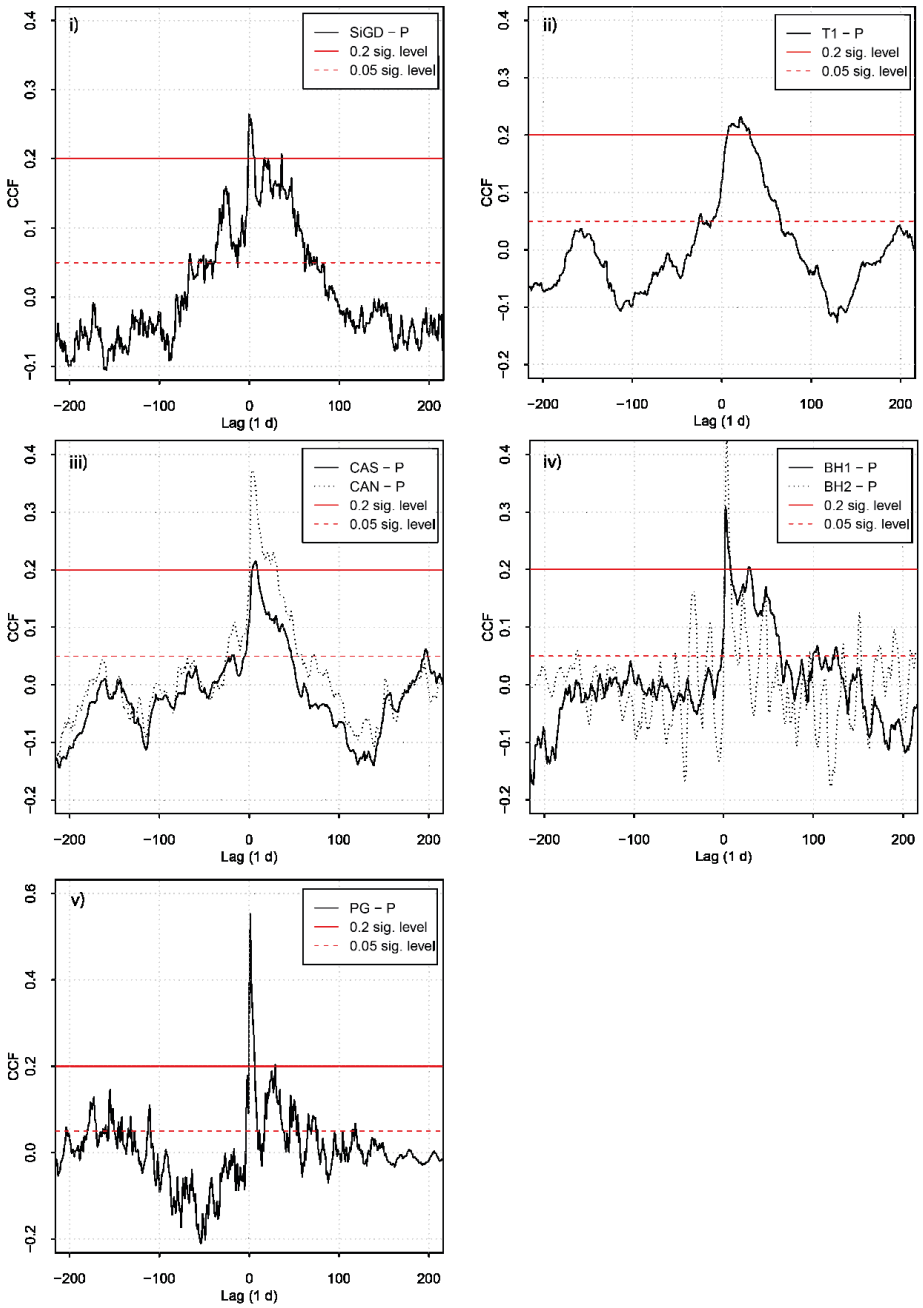

Figure 8.31: Cross-correlation functions (CCF) between daily rainfall and SiGD into Bell Harbour Bay (i), water level of turlough Gortboyheen (ii), water level of Carron south and north (iii), water level in boreholes BH1 and BH2 (iv) and water level upstream the waterfall in Poll Gonzo (v).

In a next step, hourly CCFs were evaluated to more closely identify a more detailed response to rainfall as well as to assess indicators of presence of additional flow components (Figure 8.32). The CCFs of CAN, CAS and T1 show very similar patterns dominated by seasonality. It is no surprise that these ‘storage’ systems do not contain high-temporarily resolved information towards the interpretation of flow components. Instead, the more dynamic time series of PG, BH1 and BH2 are more relevant.

Again, BH1 and BH2 show distinct courses with their CCFs (Figure 8.32i): BH2 peaking with a relatively low CCF of 0.19 at a lag of 50 h. The recession of the CCF is quick, reaching <0.05 after 206 h. In turn, the CCF of BH1 peaks with a CCF of 0.22 after 102 h. The recession of the hourly CCF is very slow. This pattern reflects the overall characteristics of BH1: the water level may respond quickly during low-flow periods, however, during high-flow periods, there may be very little linearity between rainfall and the water level. Certainly, there is no major recession of the borehole hydrograph during high-flow periods, which would translate into a higher loss of linearity between the rainfall and hydrograph time series. Accordingly, the CCF recesses relatively slow and smoothly. The water level of the underground river in Poll Gonzo shows high linearity with rainfall (Figure 8.32iv). The CCF peaks with 0.32 at a lag of 6 h. The loss of memory is relatively quick, reaching <0.2 after 34 h. In fact, the recession of the CCF is very steep for the first 50 h flattening out until approx. 140 h. The secondary slope of the recession is indicative of additional flow components.

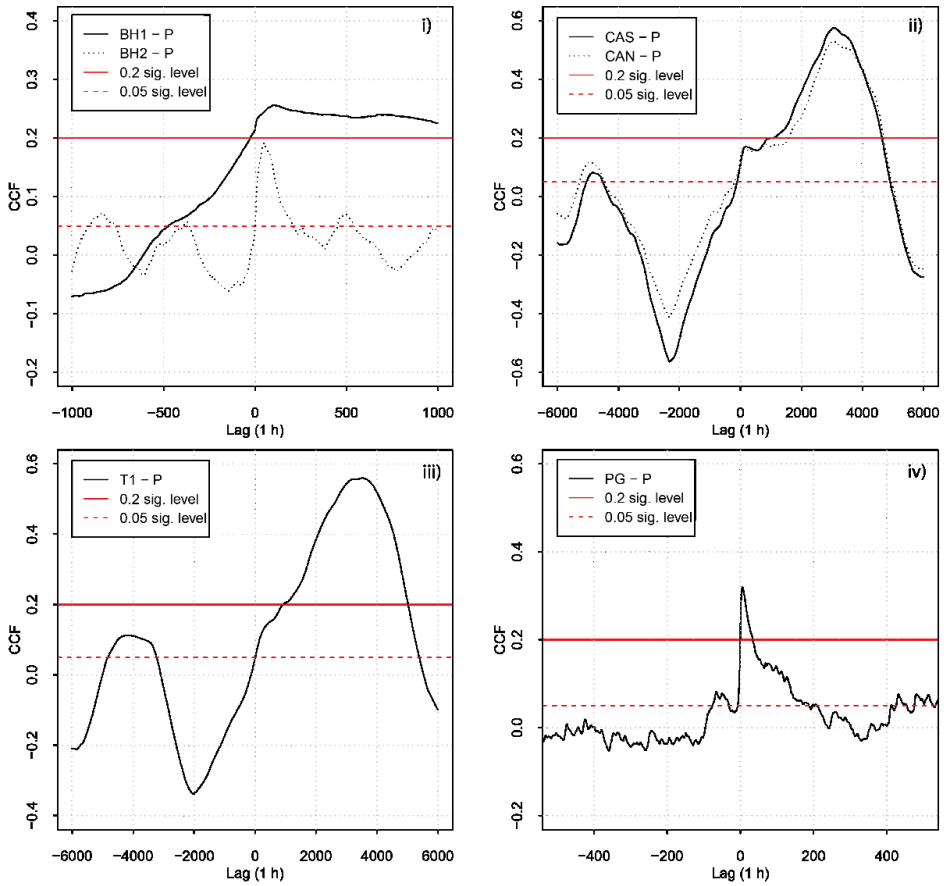

Figure 8.32: Cross-correlation functions (CCF) between hourly rainfall and water level in boreholes BH1 and BH2 (i), water level of Carron south and north (ii), water level of turlough Gortboyheen (iii) and water level upstream the waterfall in Poll Gonzo (iv).

Relevant CCFs between hourly or daily rainfall, water level and discharge time series were mapped in Figure 8.33 which highlights the spatial catchment dynamics. Each arrow links an input time

series (start of arrow) with an output time series (end of arrow). The combination of arrow and the +/- of the CCF indicates the direction of dynamics: if the CCF is positive, direction follows the arrow; if the CCF is negative, the direction of dynamics are against the arrow.

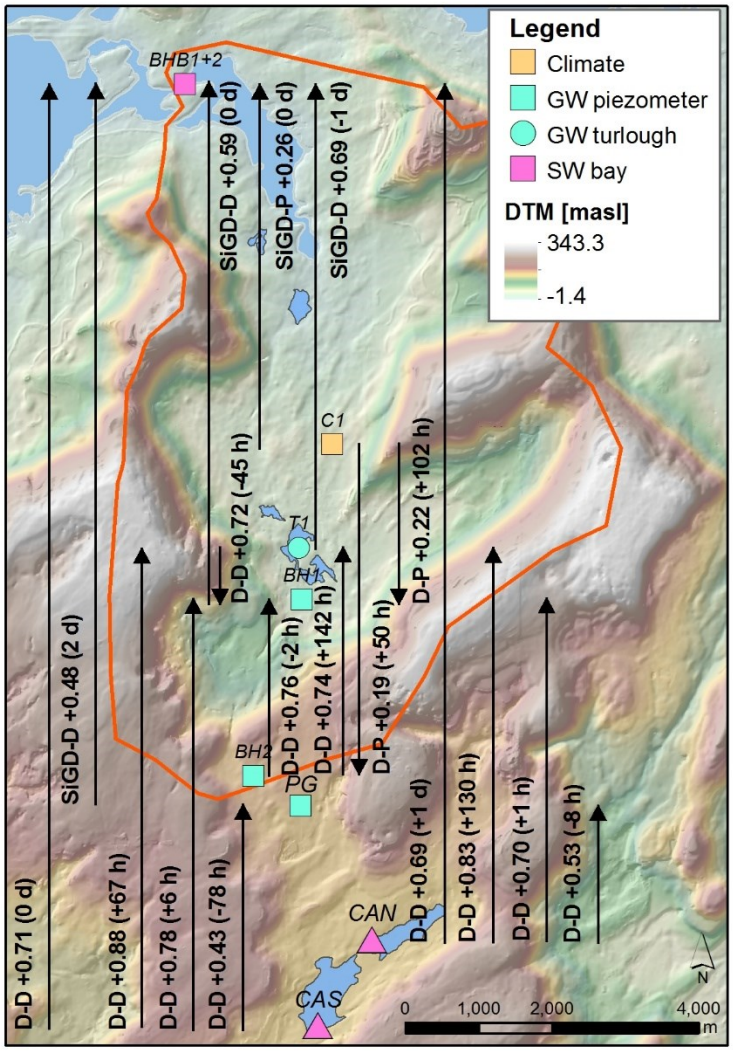

Figure 8.33: Cross-correlation functions with lag times in h/d in brackets for time series of rainfall (C1), borehole data (BH1, BH2), turlough level (T1), surface water level (CAS, CAN) and estimated SiGD (BHB); D = depth, P = rainfall, SiGD = submarine intertidal groundwater discharge. The arrows indicate the direction from input to output connecting the two sampling sites with the associated CCF and lag times.

All CCFs show positive peaks ranging between 0.19 and 0.88 with lag times ranging between -78 and 142 h. The lowest peaks of the CCFs are related to rainfall as the input variable ranging between 0.19 and 0.26. In turn, CCFs between groundwater levels and SiGD are much larger ranging between 0.48 and 0.88.

Groundwater levels in BH1 and BH2 show a positive peak of the CCF with water level of T1. The corresponding lag times indicate that the direction of dynamics is from BH1/BH2 towards T1, with a lag of 45 h, 142 h respectively. Further, T1 is highly correlated with water level in CAS. The CCF of 0.88 and a lag of 67 h suggests high linearity between the two time series. Again, a causal relationship between CAS and T1 may be hypothesised. Further, CAS shows a very high correlation with water level in BH1 with a peak of the CCF of 0.78 and a lag of 6 h. The shorter lag compared to T1 highlights the different dynamics driving the water levels in the turlough (slow) as opposed to the borehole (fast). Accordingly, a shorter lag time is the result of a fast response of the water level in BH1. CAS even shows a very high correlation with the SiGD regime in Bell Harbour Bay, expressed by a CCF peak of 0.71 and a lag of 0 d. In general, SiGD correlates very well with water level time series: 0.69 between SiGD and water level in CAN, 0.69 between SiGD and water level in T1, 0.59 between SiGD and water level in BH1 and 0.48 between SiGD and the water level in Poll Gonzo. All lags range between -1 and 2 d, indicating a relatively quick response from groundwater levels towards SiGD. All these figures underline linearity between the overall piezometric level in the aquifer and the SiGD regime into Bell Harbour Bay.
Interestingly, the CCF peaks between PG/BH1 and SiGD are the lowest in comparison to the CCF between SiGD and CAS, CAN and T1. This fact may be the result of the stronger seasonality of time series of CAS, CAN and T1 as opposed to the more rapidly fluctuating BH1 and water level in Poll Gonzo. Further, it suggests that seasonality is clearly a relevant factor with regard to the SiGD regime.
Another interesting aspect is the CCF between PG and CAS, PG and CAN respectively. The CCF between CAN and PG is higher (0.53) and faster (-8 h) than the CCF between CAS and PG (0.43, -78 h). The higher linearity of CAN and PG as opposed to CAS and PG may suggest that PG is hydraulically ‘better’ connected to CAN than it is connected to CAS, or else, that PG and CAN respond to rainfall more similar than PG and CAS.

To conclude, cross-correlation between rainfall and water level and flow time series show a variation in quality in time. In general, low CCFs between rainfall and observed time series are interpreted as the result of additional variables that alter the signal, such as groundwater recharge and flow dynamics related to the aquifer heterogeneity. This is the case at the lowland BH1 (as opposed to the upland BH2) or T1. Yet, the time step (h vs. d) is important to consider. The water level in Poll Gonzo shows a comparably high peak of the CCF as response to rainfall, for both, daily and hourly time series.
Mapping of the CCFs suggests linearity between CAS/CAN and other observed time series. This may be interpreted that CAS/CAN influences flow dynamics in Bell Harbour, and hence, that CAS/CAN are part of the catchment, at least temporarily/seasonally.
The SiGD regime into Bell Harbour Bay correlates very well to the overall piezometric state of the aquifer, which is believed to reflect the seasonality and high-flow system dynamics as opposed to low-flow periods.

8.2.3. Signal analysis

The time series of Poll Gonzo and BH1 indicated the presence of distinct flow components. Therefore, in a next step, signal analysis was applied to both of these head time series, which is later (Section '8.3. Low-flow component separation') used to separate out a low-flow component.

8.2.3.1. Poll Gonzo

The available head time series of PG is relatively short covering less than one year (12 Jul 2017 to 14 Apr 2018), hence, it does not contain the full spectrum of one hydrological year, which limits the interpretability of noise analysis.

The power spectrum shows the frequencies (Hz) and significant changes of slopes following Pettitt (1979) (Figure 8.34).

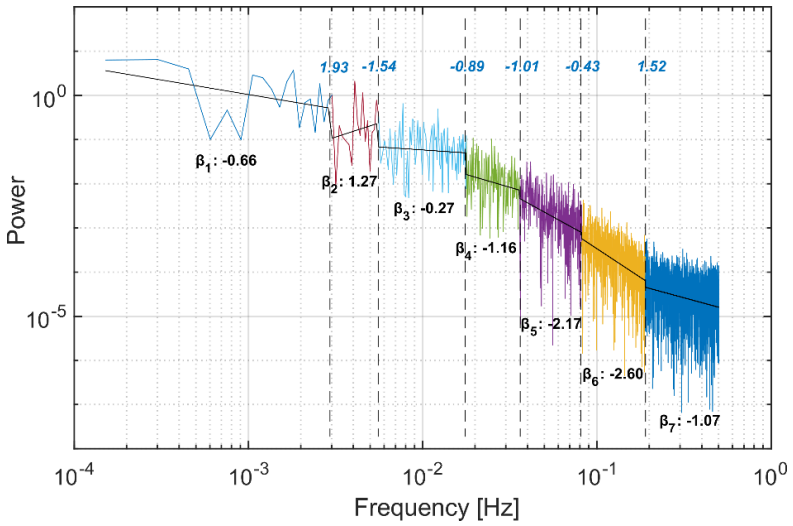

Figure 8.34: Frequencies (Hz) associated with hourly head in PG between 12 Jul 2017 and 14 Apr 2018 and frequency segments following the Pettitt method with associated spectral exponents β with β_1 to β_7 (black) and changes between spectral exponents (blue).

The spectral coefficients β_1 to β_3 (0.0002 to 0.0178 Hz, 6,621 to 56.1 h) relate to the stochastic component (although β_2 is >1, and therefore outside of the Gaussian domain) while β_4 to β_7 (0.0178 to 0.500 Hz, 56.1 to 2 h) relate to the Brownian domain (Figure 8.35).

Anti-persistent Brownian noise relates to β_4 (0.0178 to 0.0359 Hz, 56.1 to 27.8 h) and β_7 (0.1891 to 0.4999 Hz, 5.3 to 2 h), while persistent Brownian noise relates to β_5 and β_6 (0.0359 to 0.1891 Hz, 27.8 to 5.3 h).

With regard to the noise classification, as well as the relative changes between frequency segments, it seems reasonable to sub-divide the spectrum into: a random component (β_1 to β_3), a low frequency component of anti-persistent Brownian noise (β_4), b) an intermediate frequency component of persistent Brownian noise (β_5 and β_6) and a high frequency segment of anti-persistent Brownian noise (β_7).

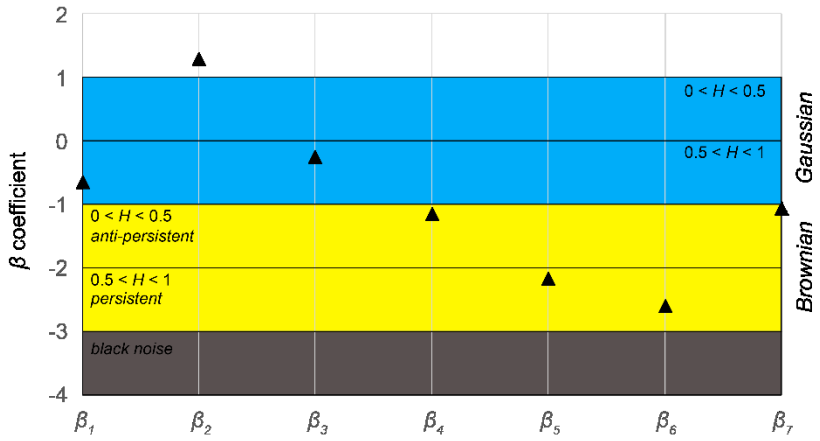

Figure 8.35: Spectral coefficients β_1 to β_7 for Poll Gonzo between 12 Jul 2017 and 14 Apr 2018, including the Hurst exponent and noise domain.

Next, Figure 8.36 shows the CWT of the head time series, including the frequency space for the random component, the low frequency segment (56.1 to 27.8 h), the intermediate frequency segment (27.8 to 5.3 h) and the high frequency segment (5.3 to 2 h).

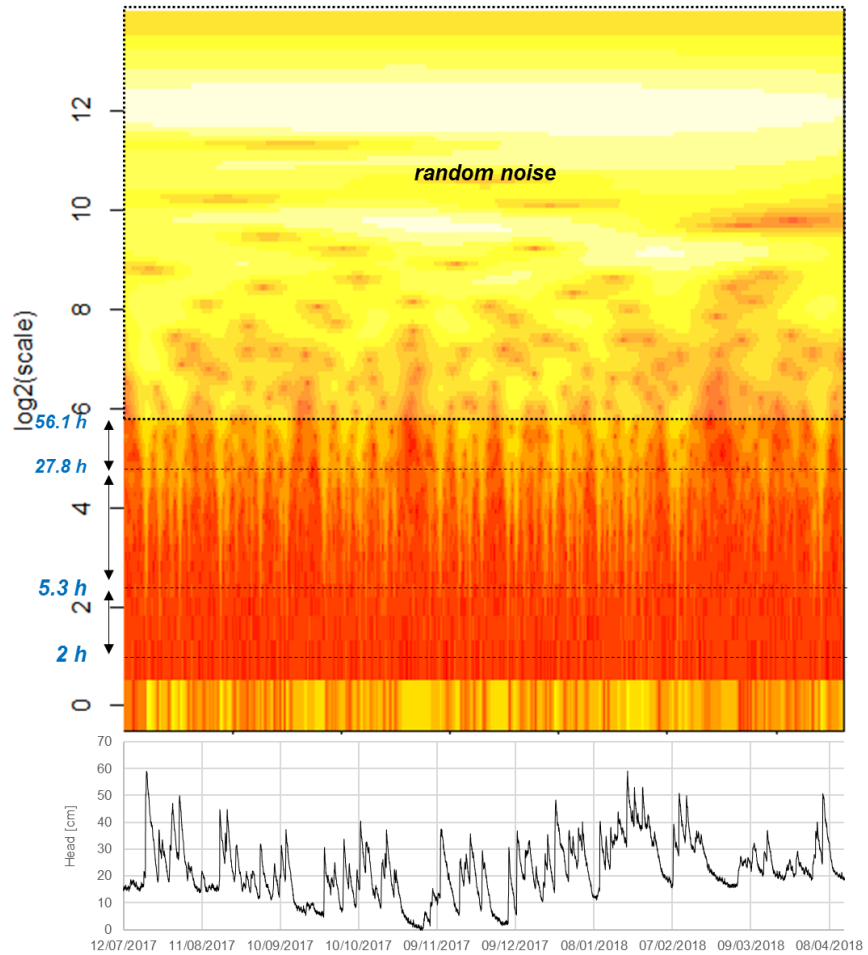

Figure 8.36: CWT of hourly head in PG between 12 Jul 2017 and 14 Apr 2018.

The high frequency segment shows very intermittent powers associated with the peaks of head. The intermittent frequency segments show more continuous power in time, although being concentrated on the times of high flows / flood events. During recessions, the power of this frequency segment is low.

The low frequency segment shows relatively continuous powers over time although, even during major recessions, e.g. 29 Oct to 03 Nov 2017, or 23 Feb to 04 Mar 2018, the powers are very low. Hence, the CWT suggests that the low frequency range does not necessarily relate to flows sustaining the late recession.

8.2.3.2. BH1

The power spectrum was again analysed with regard to significant changes of slopes following Pettitt (1979) (Figure 8.37). The spectral coefficients β_1 to β_3 (0.00003 to 0.0060 Hz, 31,561 to 166.1 h) relate to the Gaussian domain while β_4 to β_8 (0.0060 to 0.4999 Hz, 166.1 to 2 h) relate to the Brownian domain (Figure 8.38). Anti-persistent Brownian noise relates to β_4 (0.0060 to 0.0149 Hz, 166.1 to 67.0 h) and β_8 (0.1856 to 0.4999 Hz, 5.4 to 2 h). Persistent Brownian noise relates to β_5 to β_7 (0.0149 to 0.1856 Hz, 67.0 to 5.4 h).

In addition to the random component (β_1 to β_3), three frequency segments may be sub-divided: a low frequency segment of ant-persistent Brownian noise (β_4), an intermediate frequency segment of persistent Brownian noise (β_5 to β_7) and a high frequency segment again of anti-persistent Brownian noise (β_8).

A localised high power can be observed at the high frequency end of β_6 at 0.0805 Hz, which corresponds to a time of 12.4 h. This power is related to the tidal component present in the time series, and therefore relates to persistent Brownian noise.

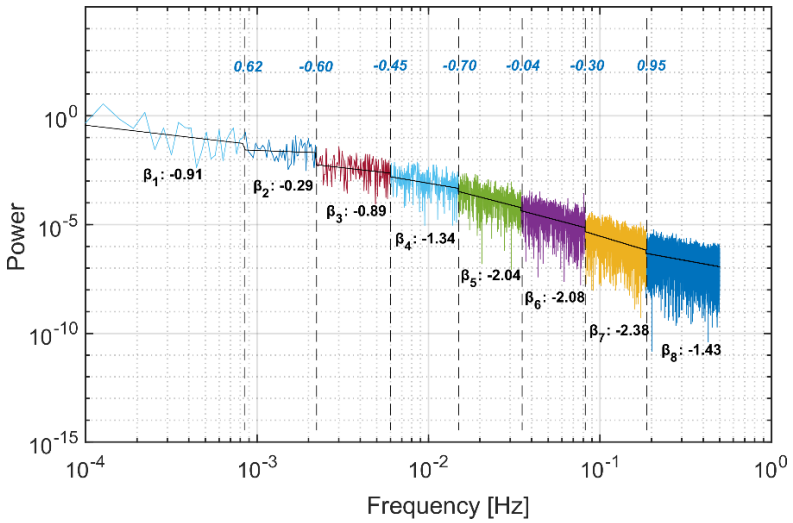

Figure 8.37: Frequencies (Hz) associated with hourly head in BH1 between 26 Feb 2015 and 03 Oct 2018 and frequency segments following the Pettitt method with associated spectral exponents β with β_1 to β_7 (black) and changes between spectral exponents (blue).

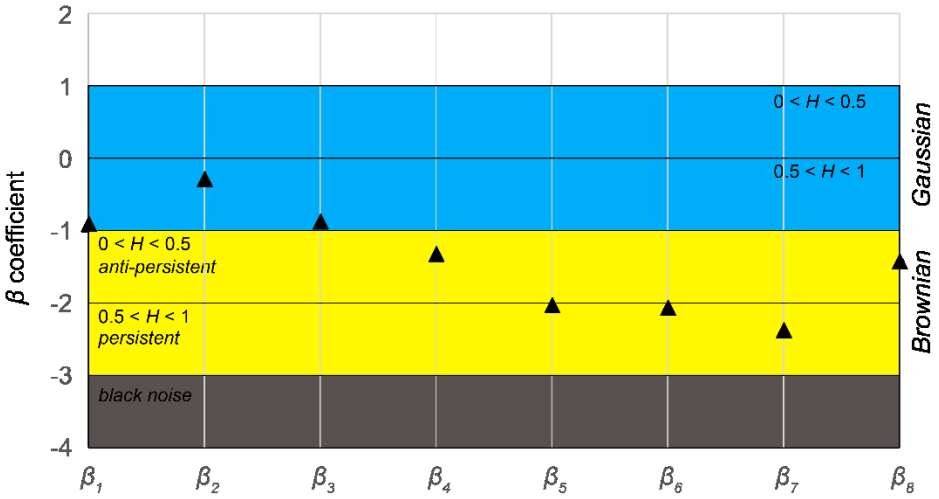

Figure 8.38: Spectral coefficients β_1 to β_8 for BH1 between 26 Feb 2015 and 03 Oct 2018, including the Hurst exponent and noise domain.

Figure 8.39 shows the CWT of the head time series, including the frequency space for the random component, as well as the low (166.1 to 67.0 h), intermediate (67.0 to 5.4 h) and high frequency range (5.4 to 2 h). In addition, a line for higher energies at 12.4 h associated with the tidal component is plotted.

The plot highlights the two different regimes of high-flow and low-flow periods: during high flow, high powers are almost exclusively limited to the low and intermediate frequency range. During low flow periods, high powers can be observed in the high frequency range. Further, powers <166.1 h are much stronger during the low-flow periods as opposed to the high-flow periods. This is comprehensible as the largest surges and drops of head occur during the low flow period.

However, it seems that the low frequency range (166.1 to 67.0 h) exhibits power throughout the entire year, although with different magnitude between high-flow and low-flow periods. Though, conceptually, recessions during high-flow periods may be related to a low-frequency component or LFC.

Powers related to the tidal component at 12.4 h are more pronounced during low-flow periods.

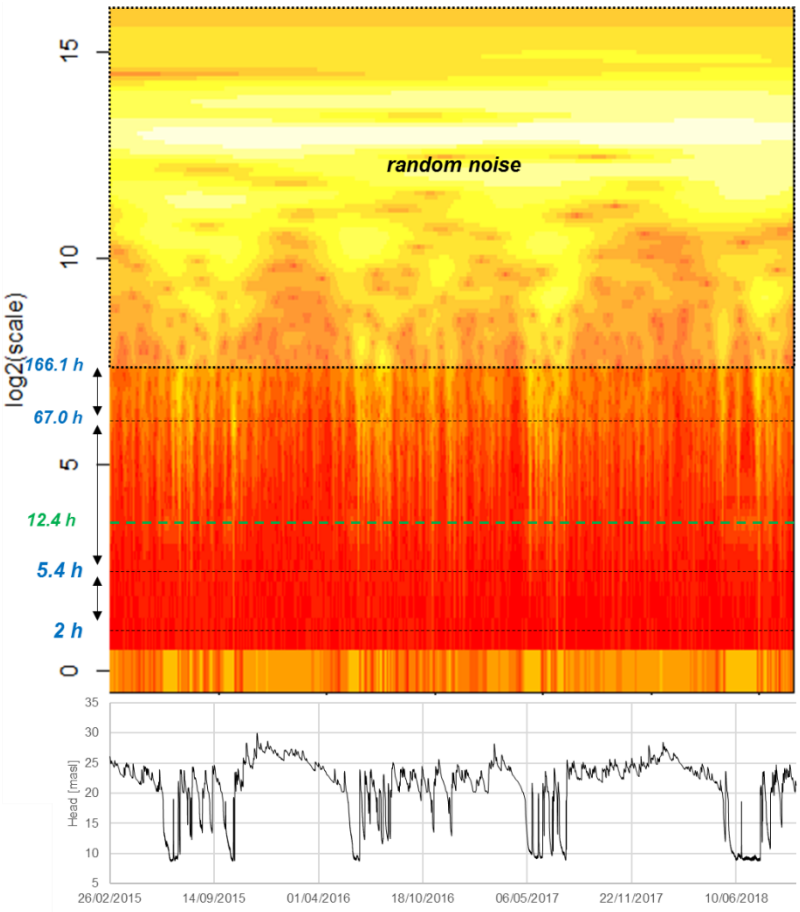

Figure 8.39: CWT of hourly head in BH1 between 26 Feb 2015 and 03 Oct 2018.

8.2.4. DWT

8.2.4.1. Poll Gonzo

As previously applied on the time series of Manorhamilton and Ballindine spring, the decomposition of the time-amplitude signal into discrete frequencies was carried out using the db10 and db20 wavelets applied on hourly head time series between 12 Jul 2017 and 14 Apr 2018. This results in 12 levels (details, D) and the residual or trend (S). These 12 details and their frequencies are then associated with the spectral coefficients β and their upper and lower frequency boundary, displayed in Table 8.5 which shows the domain and noise in which each detail lies.

Within the previous section, three distinct non-stochastic frequency ranges were identified: a) a low frequency signal β_4, b) an intermediate frequency signal β_5 to β_6 and c) a high frequency signal β_7. With regard to these frequency ranges, the individual details D associated with these frequency ranges were combined, and plotted above the hourly head of the underground river in Poll Gonzo in order to highlight the powers of the combined details in time in relation to the discharge dynamics (Figure 8.40).

Table 8.5: 12 details and the trend S of db10 and db20, their frequencies and associated spectral exponents β of Poll Gonzo. The coloured shade in the column β indicates the noise: blue = Gaussian, yellow = Brownian.

Detail	db10			db20		
	Frequency		β	Frequency		β
	Hz [s^{-1}]	T [h]		Hz [s^{-1}]	T [h]	
1	3.16E-01	3.2	7	3.11E-01	3.2	7
2	1.51E-01	6.6	6	1.48E-01	6.7	6
3	6.45E-02	15.5	5	6.84E-02	14.6	5
4	3.96E-02	25.3	5	3.41E-02	29.3	4
5	1.95E-02	51.3	4	1.63E-02	61.3	3
6	1.01E-02	98.8	3	1.22E-02	81.7	3
7	4.08E-03	245.2	2	4.08E-03	245.2	2
8	2.27E-03	441.4	1	2.57E-03	389.5	1
9	1.81E-03	551.8	1	1.81E-03	551.8	1
10	7.55E-04	1,324.2	1	7.55E-04	1,324.2	1
11	3.02E-04	3,310.5	1	4.53E-04	2,207.0	1
12	3.02E-04	3,310.5	1	3.02E-04	3,310.5	1
S	1.51E-04	6,621.0	1	1.51E-04	6,621.0	1

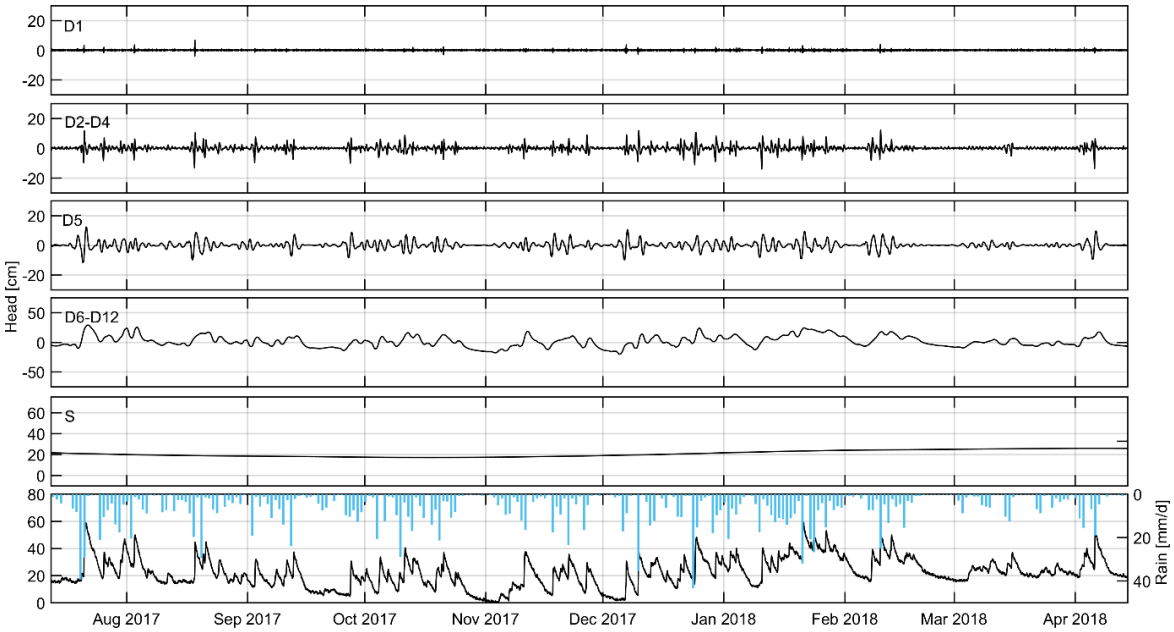

Figure 8.40: Hourly head of the underground river in Poll Gonzo (black) and daily rainfall (bottom plot), the trend S and combined wavelet details (D) using db10: D6 to D12 (β_1 to β_3), D5 (β_4), D2 to D4 (β_5 to β_6) and D1 (β_7).

Details 6 to 12 relate to the random component (Gaussian domain). Above, detail 5 (persistent Brownian noise, low frequency segment) shows powers of less magnitude and less continuity in time. The power is reduced to a minimum during the late recessions.

The details 2 to 4 (persistent Brownian noise, intermediate frequency segment) are very discontinuous in time, exhibiting only power during flood events and no power during recessions. Detail 1 (anti-persistent Brownian noise, high frequency component) shows only minor powers, which occur very localised at major flood events.
The combined details 1 to 5 related to the three frequency segments show distinct behaviours: the intermediate and high frequency segment show highly localised powers in time and hence, they may be linked to a faster flow component.
Detail 5 shows small powers during major recessions; hence, it may be linked to a slow-flow component that contributes discharge during the late recession.

In order to construct a partly structured low-flow component resembling long lasting processes, perhaps related to a fissured matrix domain, details 6 to 12 (stochastic component), detail 6 (non-stochastic component) and the trend S of db10 are summed up (Figure 8.41).
The constructed signal is very similar to the observed head. The major difference seems to be a reduction in noise, and therefore, the contribution of a low frequency signal may be considered to be relatively small.

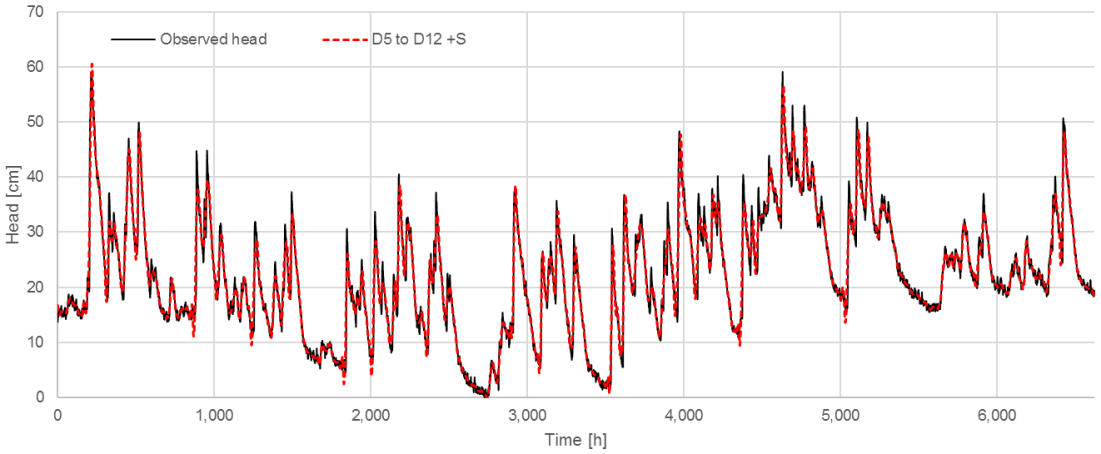

Figure 8.41: Observed head at Poll Gonzo and composed head of details 5 to 12 + residual S.

8.2.4.2. BH1

The decomposition of the time-amplitude signal into discrete frequencies was carried out using the db10 and db20 wavelets applied on hourly head time series between 26 Feb 2015 and 03 Oct 2018. This results in 14 details (D) and the trend (S). These 14 details and their frequencies are then associated with the spectral coefficients β and their upper and lower frequency boundary, displayed in Table 8.6 along with associated noise domain.

Table 8.6: 14 details and the trend S of db10 and db20, their frequencies and associated spectral exponents β of BH1. The coloured shade in the column β indicates the noise: blue = Gaussian, yellow = Brownian.

Detail	db10			db20		
	Frequency		β	Frequency		β
	Hz [s^{-1}]	T [h]		Hz [s^{-1}]	T [h]	
1	2.99E-01	3.3	8	3.19E-01	3.1	8
2	1.40E-01	7.1	7	1.40E-01	7.1	7
3	8.05E-02	12.4	6	8.05E-02	12.4	6
4	3.43E-02	29.1	5	3.43E-02	29.1	5
5	1.69E-02	59.3	5	1.69E-02	59.3	5
6	1.11E-02	90.4	4	1.06E-02	93.9	4
7	4.28E-03	233.8	3	4.28E-03	233.8	3
8	2.00E-03	501.0	2	1.96E-03	509.0	2
9	1.68E-03	595.5	2	1.17E-03	853.0	2
10	7.29E-04	1,372.2	1	6.02E-04	1,661.1	1
11	3.49E-04	2,869.2	1	3.49E-04	2,869.2	1
12	1.27E-04	7,890.3	1	1.27E-04	7,890.3	1
13	6.34E-05	15,780.5	1	1.27E-04	7,890.3	1
14	6.34E-05	15,780.5	1	3.17E-05	31,561.0	1
S	3.17E-05	31,561.0	1	3.17E-05	31,561.0	1

Within the previous section, three distinct non-stochastic frequency ranges were identified, a) a low frequency signal β_4, b) an intermediate frequency signal β_5 to β_7 and c) a high frequency signal β_8. With regard to these frequency ranges, the individual details D associated with these frequency ranges are plotted above the hourly head observed in BH1 (Figure 8.40).
Details 7 to 14 relate to the random component (Gaussian domain). These details characterise the overall pattern of the head in time, including periods of high-flow and low-flow.
Above, detail 6 (persistent Brownian noise, low frequency segment) shows powers of less magnitude and less continuously in time. Powers occur largely but not exclusively during periods of low piezometric head.
The details 2 to 5 (persistent Brownian noise, intermediate frequency segment) shows a similar pattern to D6, yet, with slightly larger amplitudes. These powers relate to major surges of head, as they occur at the beginning of the high-flow period, for example.
Finally, detail 1 (anti-persistent Brownian noise, high frequency component) shows only minor powers, which occur very localised exclusively during low-flow periods.

Overall, the plotted details share the same characteristics, namely the concentration of high amplitudes during high-flow periods and absence of amplitudes during low-flow periods. Hence, it seems that the details highlight the overall functioning of the aquifer (high-flow vs. low-flow periods) while at the same time, it seems impossible to relate these frequency details to individual flow components (as influencing the observed head).

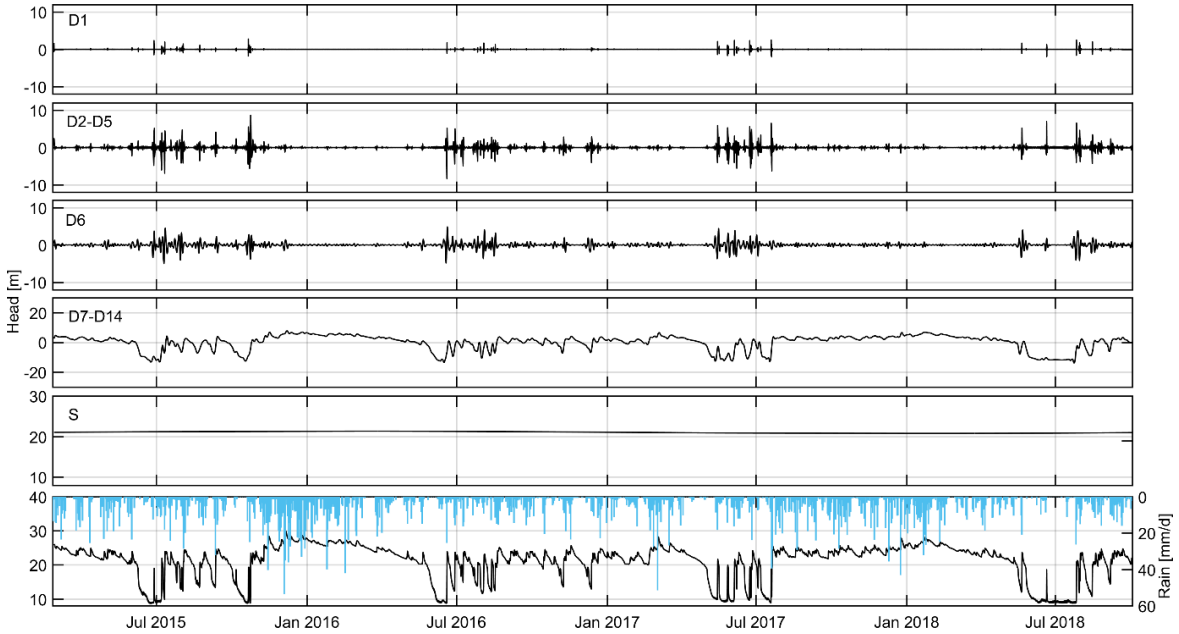

Figure 8.42: Hourly head of BH1 (black) and daily rainfall (bottom plot) and the trend S and combined wavelet details (D) using db10: D7 to D14 (β_1 to β_3), D6 (β_4), D2 to D5 (β_5 to β_7) and D1 (β_8).

8.2.5. Summary from Bell Harbour time series analysis

Time series analysis highlighted the seasonal variation of water levels / piezometric heads as well as providing insights into the regime of SiGD for Bell Harbour Bay, as shown by the ACF and CCF. The linearity of and between the corresponding time series suggests the characteristics of seasonally varying 'high-flow periods' and 'low-flow periods'. This specific pattern seems to be characteristic for the entire catchment ranging geographically between Carron in the south and Bell Harbour Bay in the north.

In general, linearity between rainfall and water level time series is low, which was interpreted as a major filtering effect of the aquifer. Hence, the degree of karstification of the aquifer highly transforms the rainfall input signal. Further, the seasonality of 'high-flow' and 'low-flow' periods further dampens the CCF, namely for the water level time series of the lowland impacted by high-flow periods.

This complexity is amplified by the presence of deep karst channels and the absence of a single, discrete and measurable spring draining the aquifer. Hence, the use of time series analysis for the quantification of diffuse groundwater recharge is much hampered.

Nevertheless, loss of memory of the water level time series of PG indicates locally the presence of at least two flow components. At the same time though, signal analysis was used to distinguish between three structured noise components. However, it seems that the contribution of quick-flow dominates the overall signal.

8.3. Low-flow component separation

The catchment of Bell Harbour is drained continuously via SGD and intermittently SiGD, hence, no high-resolution discharge hydrograph is available that could be used for the separation of a LFC. Instead the head time series of BH1 and PG were used to characterise the low-flow signal. Both sets of data must be considered as local information (as opposed to global information in case of a spring hydrograph). Hydrograph analysis, ACF and CCF have previously suggested the presence of distinct flow components to be present in either of the two time series, hence, it seems justifiable to further analyse these time series in terms of a LFC.

In case of the head time series of PG, the same workflow was applied as used previously for Ballindine and Manorhamilton springs.
In case of the borehole hydrograph, the workflow applied differs, as not all methods (digital recursive filtering) could be applied on the piezometric time series. The methods applied are: 1) establishing an MRC, 2) fitting linear reservoirs onto MRCs, and 3) event-scale two-component mixing analysis.

8.3.1. BH1

8.3.1.1. Exponential fitting

Figure 8.43 shows the MRC of BH1 in a semi-log plot. The recession shows a strikingly heterogeneous pattern with changes between concave and convex sections, including several smaller or larger individual recession segments, e.g. between 23.7 and 20.1 masl. A large drop occurs between 18.8 and 9.4 masl when the head time series is visibly impacted by tidal fluctuation.
The MRC may be separated into a lower section (<18.8 masl) and an upper section (>18.8 masl). The upper section shows multiple individual recession segments; hence, this section was considered as relevant in terms of recession analysis related to diffuse groundwater recharge.

Figure 8.43 shows a multiplicity of recession segments. These multiple recession segments are interpreted as individual levels of discharge within the aquifer. Hence, these levels of discharge may be related to multiple k' values, which impose complexity on hydrograph separation. In fact, hydrograph separation must be applied on individual recession segments. This approach was applied on three recession segments (Figure 8.44a-c).

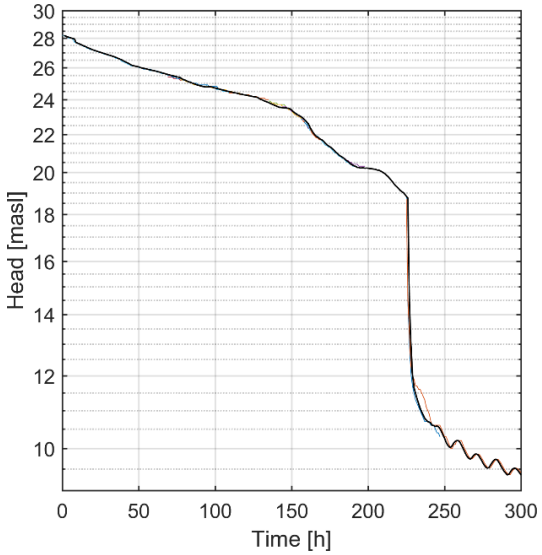

Figure 8.43: 20 fitted components and master recession curve of borehole hydrograph BH1.

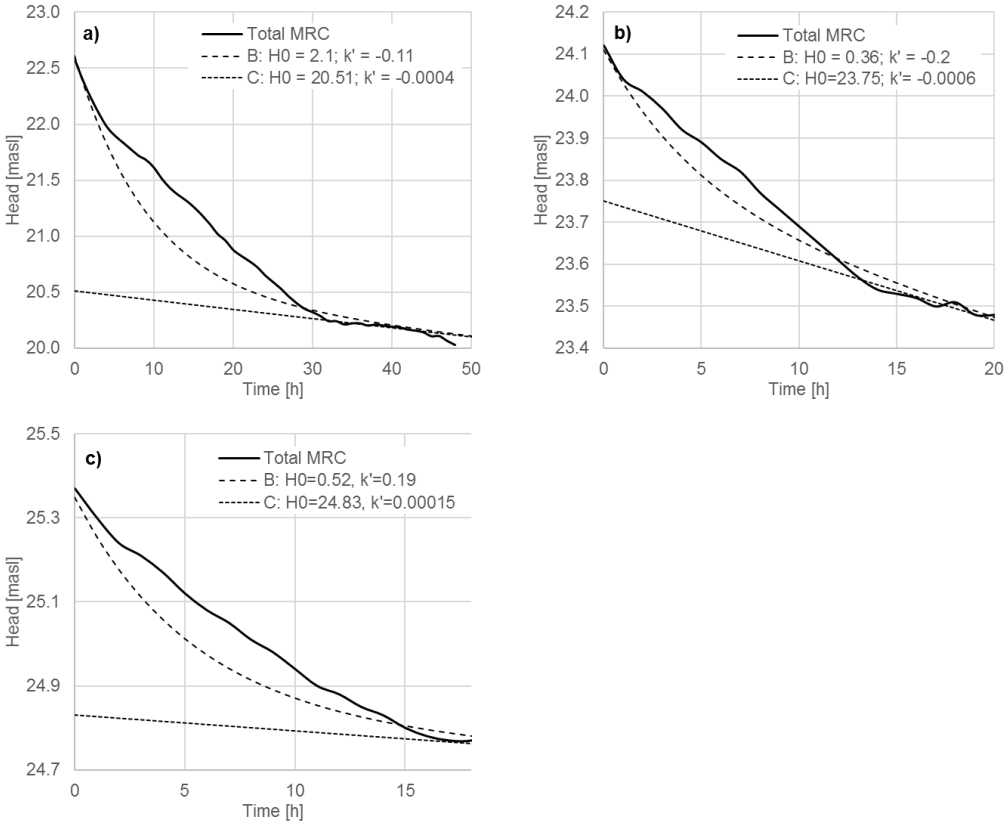

Figure 8.44: Three recession segments of the upper section of the BH1 MRC (a-c) along with fitted LFC using the head.

The first recession (Figure 8.44a) was decomposed into two exponential components. Only the baseflow or LFC (C) with H_0 = 20.51 masl and k' = 0.0004 h^{-1} fits reasonably well. However, the

additional component (B) between 20.1 and 22.6 masl fails to follow the concave shape of the MRC.

A second recession (Figure 8.44b) was again decomposed into two exponential components ranging between 23.4 and 24.2 masl. Again, only a LFC can be fitted reasonably well while an additional exponential component (B) cannot be fitted realistically along the established MRC, as it again follows a concave shape.

And lastly, a third recession (Figure 8.44c) was decomposed. Again, the exponential component (C) with H_0 = 24.83 masl and k' = 0.00015 h^{-1} fits reasonably well, while the upper exponential component B shows a major deviation from the MRC.

Altogether, all three recessions highlight the difficulty to fit more than one linear reservoir resembling the LFC along the course of the MRC head time series. However, at least the lowest exponential component fits reasonably well at each recession. Accordingly, k' for the LFC ranges between -0.00015 and 0.0006 h^{-1}.

8.3.1.2. Two-component mixing model

The previous section indicated the complexity of the analysis of flow components related to the hydrograph of BH1.

A further attempt was carried out to gain insights into the potential contribution of flow components by applying a two-component mixing model. The underlying principle is that different flow components dominate inflow into the borehole at certain heads in BH1.

Therefore, a high frequency sampling event of BH1 was conducted over a period of almost 15 days to analyse the samples for anions, silica as well as stable isotopes (2H and 18O) during recessions following rain events.

The overall aim of the high-frequency sampling campaigns was to:

- Identify characteristic chemical signatures associated with a slow/diffuse inflow component (potentially linked to the fissured matrix domain) and quick/concentrated inflow component (potentially linked to the fracture/conduit domain); and to then
- Separate hydrographs into a quick-flow or flood-component and LFC.

October/November 2017

An ISCO auto sampler was deployed between the period 26 Oct and 10 Nov 2017 to grab 52 groundwater samples at 20 mbgl. The sampling interval ranged between 1 h (during rain events) and 6 to 8 h (following rain events) (Figure 8.47).

Temperature and conductivity were measured in parallel using an INW CT2X sensor deployed at ~23 mbgl (the difference of observation level was due to the tightness in the borehole, hence, the sensor had to be released below the tubing system of the ISCO autosampler).

10 stable isotope samples of the rainfall input signal were collected at the sites C1, P1 and NUIG, displayed in Figure 8.45 and Figure 8.46. The concentrations in groundwater are displayed in Figure 8.47.

Head, rainfall, EC, temperature, SiO_2 and pH over the period of sampling are plotted in Figure 8.47, which can be divided into two periods, i.e. 1. before the beginning of the first rain event on 03 Nov 17:00, and 2., during and after the first (minor) and second (major) rain event between 03 Nov 17:00 and the end of the sampling campaign on 10 Nov 12:00.

Period1: 26 Oct 00:00 to 03 Nov 17:00

At the beginning of the sampling period, the head in BH1 was at the maximum of 24.5 masl dropping to the minimum of 22.3 masl (Figure 8.47) exhibiting the characteristic recession with smaller concave and convex segments, which were interpreted as heterogeneities in the limestone causing influence by fracture flow.

During the monitoring period, temperature and EC increase, not gradually but rather in individual segments. This is also interpreted as rapid changes in influence from different contributions of flow, contributing specific EC and temperature levels.

Due to a malfunction of the autosampler, SiO_2, pH, 18O and 2H samples were not withdrawn between 26 and 30 Oct. However, it can be assumed that all of these parameters would have shown an increase in concentrations in this period. Further, the deuterium excess decreases during these days which might be due to the influence of evaporation.

Following on, after 30 Oct, prior to any significant rainfall, pH, SiO_2, temperature, d18O and d2H start a (gently) declining trend.

Period 2: 03 Nov 17:00 to 10 Nov 12:00

Two major rain events occurred in that period, the first one between 03 Nov 17:00 and 04 Nov 13:00 (5.4 mm) and the second event during 06 Nov 19:00 and 07 Nov 16:00 (17.4 mm). Scattered rainfall persisted until the end of the sampling period, which was decided when there was no further evidence of a longer recession.

Rainfall samples were taken at C1 (37.7 masl), NUIG (~115 masl) and Fort Neylon (FN) (~200 masl), exhibiting a spatial and temporal variation (Figure 8.45 and Figure 8.46). NUIG and FN are off the LMWL as established for Bell Harbour using weekly rainfall data from BOEC, which is almost identical to the long-term rainfall data of Valentia (IAEA/WMO, 2016) (Figure 8.45). Hence, the heterogeneity of rainfall samples indicates the challenge when using such spatially distributed rainfall samples as a single input for a mass-balance analysis.

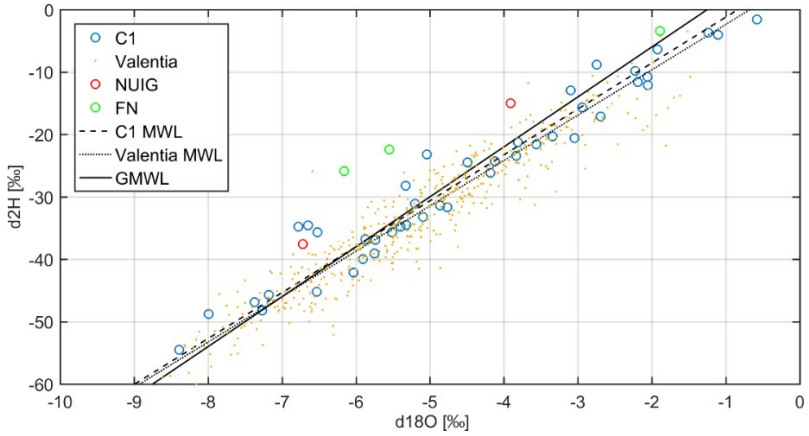

Figure 8.45: Isotopic composition (d18O, d2H) of rainfall in the Burren and western Ireland.

Overall, the first rainfall event on 03 Nov had a smaller impact on the chemical composition as well as on the head, than the second event on 06 Nov.

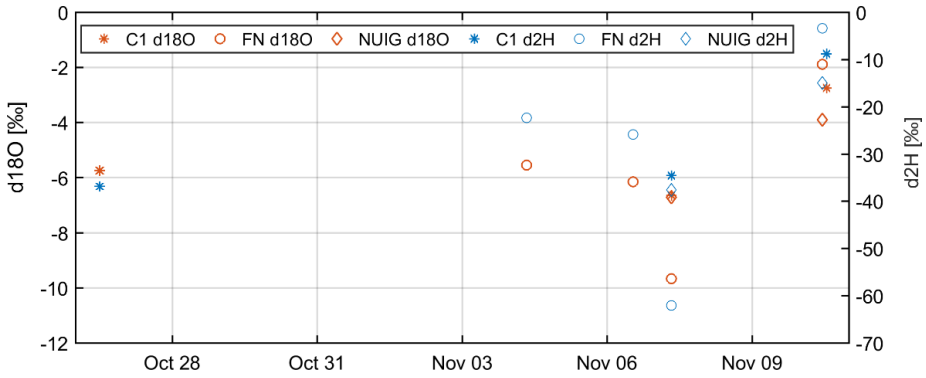

Figure 8.46: d18O and d2H content of rainfall samples at C1, NUIG research station at Carron (NUIG) and at Fort Neylon (FN).

Hydrograph/chemograph response

Regarding the influence of rainfall on the groundwater dynamics monitored in BH1, Figure 8.47 clearly confirms the rapid response of head to rainfall, proving its good connection to active groundwater flow paths in the aquifer.

The first rain event between 3 and 5 Nov caused:

- an increase in head by 0.35 m;
- an increase in temperature from 11.29 to 11.34 ºC at the middle of the rain event;
- a drop of EC from 727.9 to 707.6 µS/cm;
- peaks of SiO_2 at the beginning of the rain event, increasing twice from ~2.38 mg/l to 2.69, 2.64 mg/l respectively;
- a drop in pH from ~7.5 to 7.1;
- a slight increase in d18O and d2H.

The second larger rain event starting on 06 Nov is characterised by:

- a spatial and temporal variation of isotopic concentration in rainfall;
- an increase in head from 22.3 to 24.1 masl within 28 h;
- a drop in temperature from 11.31 to 11.02 ºC;
- a drop of EC from 727.6 to 429.5 µS/cm;
- a decrease in SiO_2 from 2.34 to 1.35 mg/l;
- an increase in pH from ~6.7 to 7.4, following a gradual further increase;
- a decrease in d18O to -5.1‰ followed by a surge in d18O to ~-4.9‰, and a drop in d2H to -31.8‰ followed by major increase to -28.1‰;
- a major increase in 2H excess, from 8 to 11.

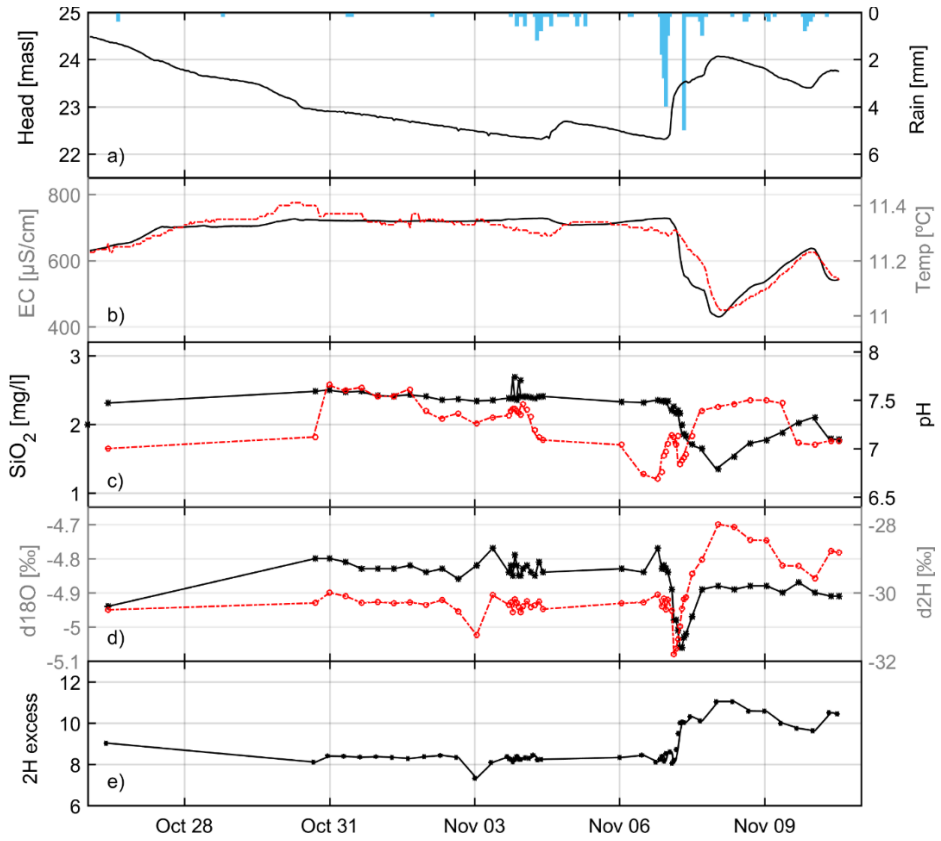

Figure 8.47: Water sampling at BH1 between 26 Oct and 10 Nov 2017; solid black line refers to the left y-axis while bars and red dashed lines refer to the right y-axis.

Interpretation of results

The temporal pattern of the abovementioned parameters is interpreted as follows:

- The slight decrease of EC and increase in temperature during event 1 corresponds to an increase in head: the increase in temperature may be related to inflow of groundwater stored in the aquifer. The decrease of EC indicates inflow of less mineralised water;
- The peaks of silica at the begin of event 1 are an indicator for the activation of flow paths (Laudon and Slaymaker, 1997), hence, contributions from different source waters;

- Peaks of d18O on 03 Nov and 06 Nov (occurring prior to event 1 and 2) may be indicative of influence by 'older' or different source water or water previously influenced by evaporation;
- Event 1 had no clear influence on the isotopic composition of water in the borehole;
- Event 2 had a major influence on all parameters sampled;
- During event 2, drops in temperature, EC, SiO_2, and d18O, as well as increase in d2H associated with influence of freshly infiltrated water. For example, the d18O concentrations get close to the values of sampled rainfall ranging between -6.3‰ at NUIG and -9.7‰ at FN;
- The increase of pH during event 2 leaves open questions, as it was expected that pH would drop.

The abovementioned results suggest various changes in the levels of observed physico-chemical parameters in time. Interestingly, these changes occur not only during flood events or periods of groundwater recharge, but also during recessions. Hence, the fluctuation of recorded parameters during recessions may indicate the contribution of different contributions of groundwater at different times. In fact, the results may suggest that different recorded levels may be linked to specific heads in BH1.

Based on the principles of baseflow separation for spring hydrographs, an attempt was made to separate a LFC as outlined in Section '4.3.2.2. Well hydrography' and '4.3.2.4. Two-component mixing model'.
LFC separation for BH1 was done in the same way as typically done for spring discharge using stable isotope data from rainfall, pre-event water and event water (Fritz, et al., 1976), although it should be noted that this approach has not been applied before on well/borehole time series to the author's knowledge.

Two-component mixing model

As mentioned above, rainfall exhibited a variation in time and space, which must be accounted for the two-component mixing model. Spatial variability was accounted for by weighting the input signal of each rainfall sampler according to its areal contribution estimated by applying Thiessen polygons upstream of BH1 (Figure 8.48).
The isotopic contribution could not be weighted by collected rainfall, as the quantity of rainfall was only recorded at C1 (and not at FN or NUIG).
For each rainfall collector, the estimated impact was differentiated between minimum catchment boundaries (50 km^2) (topographical boundaries) and a potential additional catchment component in the south (Bunce and Drew, 2017) of ~13 km^2. The percentage area in Figure 8.48 refers to each single polygon assuming the extended catchment boundaries. Accordingly, NUIG accounts for 52%, BOEC for 27% and FN for 21% of the input signal.

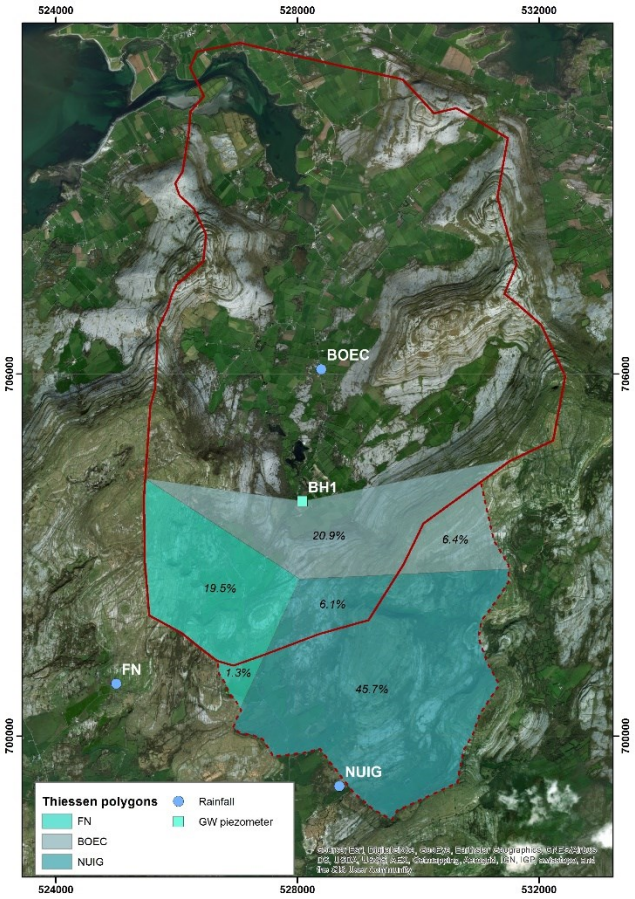

Figure 8.48: Thiessen polygons to delineate the spatial representation of the stations C1 (BOEC), NUIG and FN.

Figure 8.49 shows the plot of d18O concentrations against head for BH1. The conceptual idea is that the overall piezometric level is constituted by contributions from different vertically organised sub-systems of the karst system, i.e. fissures/fractures/conduits that contribute inflow and head to BH1.

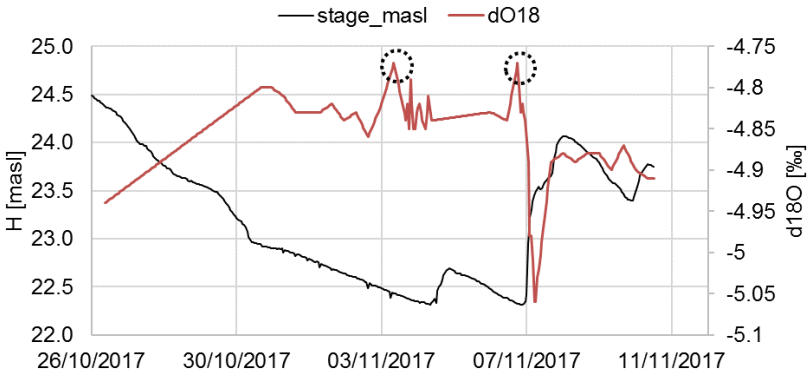

Figure 8.49: Head series of BH1 and d18O concentrations. The dashed circles highlight maximum records of d18O.

The LFC or contribution from the fissured matrix domain would be associated with higher concentrations of EC and increased temperature. Further, it can be assumed that higher concentrations of d18O are associated with longer residence times.

As already outlined above and shown in Figure 8.49, the plot shows first a decline in d18O until 30 Nov, followed by a slightly increasing trend until 02 Nov. Interestingly, the first peak of d18O (-4.78‰) occurs on 03 Nov at 09:00 at 22.42 masl, before the beginning of the first major rainfall event 03 Nov 2017 at 17:00. This may indicate a distinct contribution at the given piezometric level at 22.4 masl. Further smaller peaks of d18O occur with the rising of the water table on 04 Nov at 08:00, perhaps linked to fissured matrix outflow and potentially associated with an increase in pressure (piston effect) in the aquifer. Unfortunately, no samples were taken between 04 Nov 09:00 and 06 Nov 00:00 so that the dynamic of d18O during the rain event is not known. However, on 06 Nov 00:00 the concentration of d18O is identical to the concentration on 04 Nov 09:00.
A second peak of d18O occurs then on 06 Nov 18:00 (-4.77‰) at 22.33 masl before the first rainfall on 06 Nov 2017 19:00. Interestingly, this peak is almost identical in magnitude to the first peak, and at almost an identical piezometric level. This suggests that the piezometric head between 22.3 and 22.4 masl may be indeed linked to a distinct contribution in the limestone aquifer. A relatively high degree of groundwater outflow from the borehole was observed between 4.8 and 23.4 masl using SBDTs on 04 Mar 2017 (Section '8.1.4. Single borehole dilution tests' and 'Appendix C:') - hence, the occurrence of d18O peaks at 22.3 / 22.4 masl do suggest active groundwater flow at this level, as has been previously inferred.
Two-component mixing analysis separating the flood hydrograph H_R /low-flow hydrograph H_B from the total hydrograph H_{total} was performed according to Eqn. 4.17 using the isotopic concentrations of 18O in rainfall and groundwater samples.
The results previously described expressed the hypothesis that the two d18O peaks (Figure 8.49) are the result of a distinct contributions. If these contributions are considered as flow-components, a mixing-model may be applied (assuming that the falling head is not disturbed or influenced by upland pressure-transfers, but instead gradual draining of the aquifer via distinct flow components). Accordingly, the d18O concentrations of the two peaks were defined as representative of the contributions from the fissured matrix domain, i.e. the pre-storm head component δ_S (Eqn. 4.17). Along with the measured head component δ_T and the storm water component δ_R, the low-flow component of the hydrograph was estimated as the difference between the total hydrograph flood H_{total} and the flood hydrograph H_R using Eqn. 4.17. The results are illustrated in Figure 8.50.

The separation of low-flow from the borehole hydrograph was done using the observed hydrograph H_{total}. The separated low-flow component may be regarded as the overall contribution or share of the total hydrograph – e.g. while between 26 and 31 Nov the head is falling, H_B is increasing, which shall be interpreted as 'relative increasing contribution' rather than 'absolute contribution'. Accordingly, the two peaks of d18O on 03 and 06 Nov result in $H_{total} = H_B$, which may be interpreted that

the contribution from the fissured matrix domain during these two periods was the driving force for the concentration of d18O and potentially also the head in the borehole.

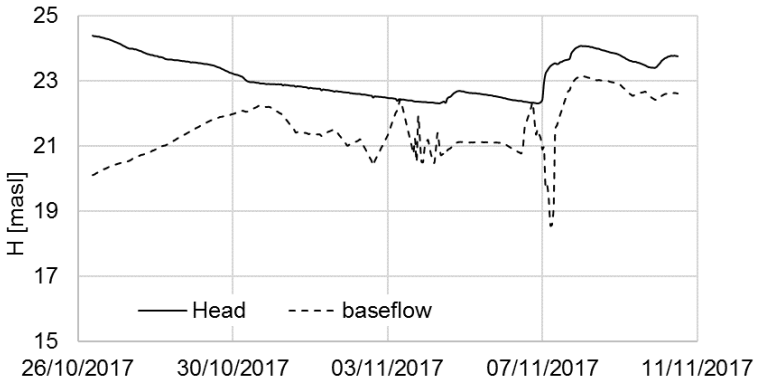

Figure 8.50: Decomposition of head time series of BH1 into a low-flow (or baseflow) component.

However, again, the application of the borehole hydrograph separation is tricky. Since the borehole is highly reactive as a result of presumably being well connected to hydraulically active fractures and conduits, it must be assumed that contributions from different fractures or conduits are active at the same time. Hence, a recorded chemical signal in the borehole is not the result of a single inflow, but rather a blend of different signals.
Further complication arises, as the activation of inflow from different fractures/conduits may be very complex, and the result of different factors that change in time, e.g. the surrounding head, groundwater recharge, head in the upland part of the aquifer, including CAS and CAN. Hence, the contribution of different flow paths may not only change according to the observed head in BH1, but according to local heads in the aquifer, which are in some way connected to BH1. Therefore, the assumption of a gradually falling head that is accompanied by gradually draining flow components in the aquifer is probably too simplistic.

Overall, the results suggest a fluctuation of physico-chemical parameters observed in BH1. This fluctuation coincides with certain head levels. In fact, the results of the analysis strongly suggest that different levels of active inflow (and outflow) occur. Hence, it is hypothesised that such inflow contributions may be related to different flow paths in the aquifer. The results indicate that the contributions from different flow domains of the limestone aquifer are very dynamic in time. Accordingly, it remains a challenge (which may be insurmountable) to generate a consistent time series of low flow or fissured matrix contributions from an open borehole.
And finally, the definition of a single isotopic input signature for a catchment of that size, changing in time is very difficult, and imposes uncertainty to the entire approach of TCMA.

8.3.2. Poll Gonzo (PG)

8.3.2.1. Benchmark range for optimal k value

First, a MRC for the underground river in Poll Gonzo was established (Figure 8.51) using 16 undisturbed recession segments for the period of 9 months (12 Jul 2017 to 14 Apr 2018). The head time series were used because no stage-discharge curve is available for the stream. Another limitation in this analysis is the fact that there is a gap in the rainfall time series between 16 Jul and 26 Oct 2017.

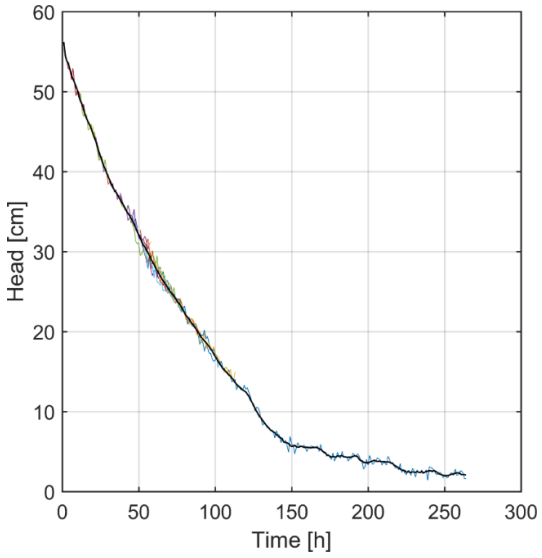

Figure 8.51: MRC of the underground river in Poll Gonzo upstream of the waterfall, using 16 recession segments.

The MRC of Poll Gonzo ranges between 56.2 and 2.0 cm. The minimum observed level is after 263 h. The MRC does not show a typical convex course from the beginning to the end. Between 32 and 130 h, the recession follows a slight concave shape as observed earlier over recession segments of the MRC of BH1.
Further, the individual recession segment used from the observed time series are relatively noisy, which is related to the relatively low accuracy (3 cm) and resolution (0.6 cm) of the sensor used (Schlumberger DI263).

Next, linear reservoirs were fitted along the MRC. Two exponential components (B and C) were fitted onto the MRC (Figure 8.52). The sum of 'B' and 'C' is displayed, along with the MRC for comparison.
The sum of the two components 'B' and 'C' (i.e. 'MRC (b+c)') is below the established MRC for the upper part (0 to 175 h), and below the MRC for the lower part (175 to 250 h). Poor fitting for the lower half may again be related to the low resolution of the CTD sensor, and its noisy signal.

However, the LFC can be reasonably fitted along the MRC considering the general noise with H_0 = 25 cm and k' = 0.0095 h^{-1}. However, the upper exponential component fails to follow the MRC, as the sum of B and C underestimate the head with regard to the MRC. Therefore, the analysis is limited to the LFC.

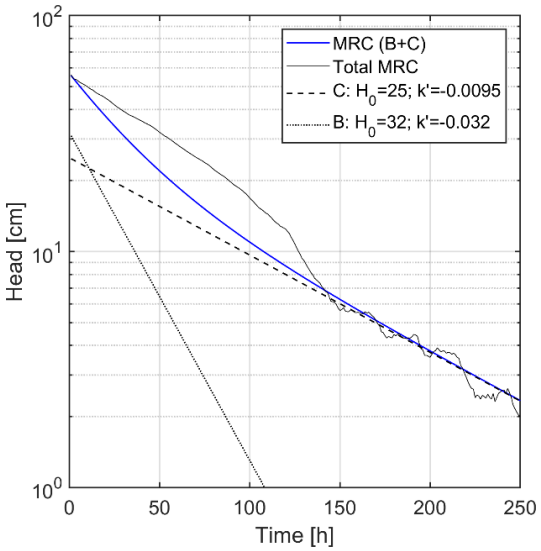

Figure 8.52: Master recession curve for hourly discharge of the underground river in Poll Gonzo split into two contributing linear reservoirs.

In a next step, the benchmark range for the optimal recession coefficients was generated for the LFC ('C') using the same methods as before for Manorhamilton and Ballindine springs. The only difference is that instead of discharge Q, the head H was applied. Accordingly, the methods are summarised as a) plotting H_t against H_{t+1} where the slope represents the recession coefficient a', b) calculating mean of H_{t+1}/H_t, and c) applying a backwards moving filter.

Plotting H_t against H_{t+1} yields a' = 0.988, which corresponds to k' = -0.0121 h^{-1} (Figure 8.53) and the calculation of the mean of Q_{t+1}/Q_t yields a recession coefficient of a' = 0.9876 or k' = -0.0124 h^{-1}. Further, the backwards moving filter suggests a' = 0.987 or k' = -0.0131 h^{-1} (Figure 8.54).

Table 8.7 summarises the recession coefficients and constants. The results are considered as the benchmark range for fitting exponential LFCs along observed discharge. Accordingly, a' ranges between 0.9870 and 0.9905 h^{-1} and k' between -0.0095 and -0.0131 h^{-1}. These are remarkably high values, exceeding the respective k'/ a' values of Manorhamilton or Ballindine. Hence, these high values may be an indicator for the very flashy response and high loss of memory, as was previously identified using the ACF.

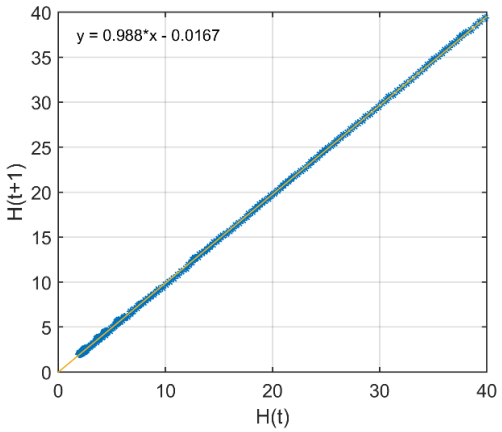

Figure 8.53: Plot of H_t against H_{t+1} to estimate the optimal recession coefficient for Poll Gonzo.

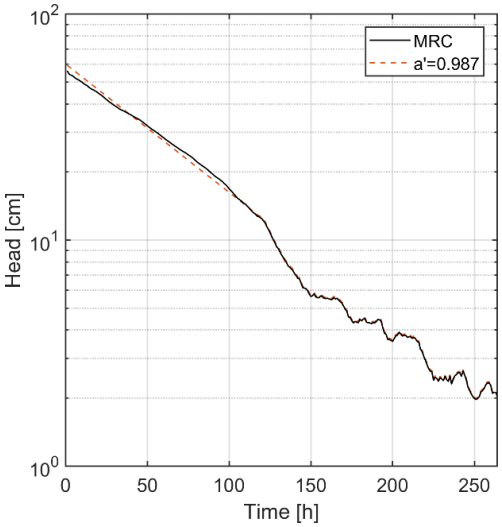

Figure 8.54: Estimation of a for the master recession curve of Poll Gonzo according to Collischonn and Fan (2013).

Table 8.7: Range of optimal hourly low flow recession coefficients (a') and recession constants (k') [h^{-1}] for Poll Gonzo.

Method	Constant	
Method 1 (fitting linear reservoirs)	a'	0.9905
	k'	-0.0095
Method 2 (plotting H_t against H_{t+1})	a'	0.9883
	k'	-0.0118
Method 3 (mean of H_{t+1}/H_t)	a'	0.9876
	k'	-0.0124
Method 4 (backwards moving filter)	a'	0.9870
	k'	-0.0131
Average	a'	0.9884
	k'	-0.0117

8.3.2.2. Exponential fitting

The previously established benchmark ranges of k' or a' were used to create exponential LFCs along the most undisturbed segments of recessions of hourly head time series for the period 12 Jul 2017 to 14 Apr 2018 (Figure 8.55).

Fitting was done starting at the beginning of a recession with H_0 following the LFC along the MRC (Figure 8.52, Figure 8.56).

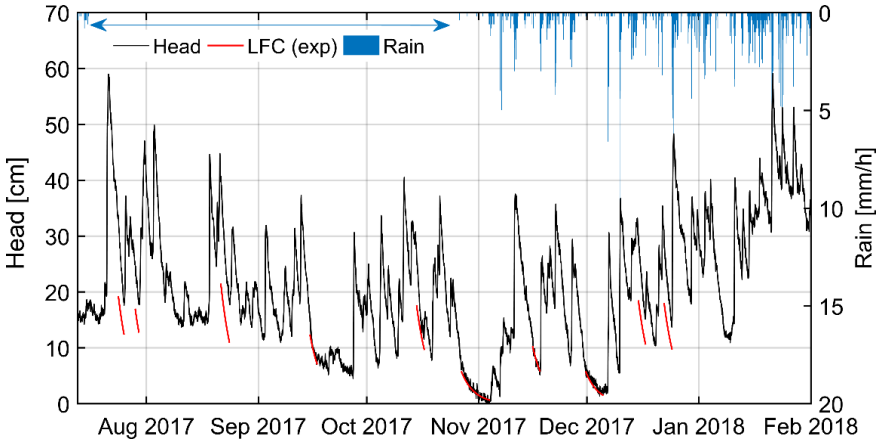

Figure 8.55: Exponentially separated LFC following H_0 = 24.8 cm and k' = -0.0117 of hourly head time series of PG between 12 Jul 2017 and 14 Apr 2018.

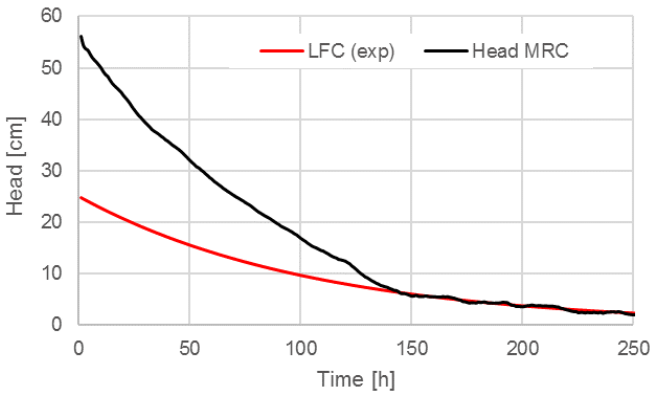

Figure 8.56: Relationship between H_0 of the LFC and observed head (resembled by the MRC) for Poll Gonzo.

Overall, only relatively few individual segments were reasonably undisturbed which might allow exponential exponents to be fitted along such observed time series.

The best fitting of exponential components according to the slope of the low head component was achieved using the actual average value of k' = -0.0117 h^{-1}.

As it can be seen, the fitted LFCs do very well follow the course of the head at lowest levels. It seems that the average k' of the benchmark range yields reasonable results.

8.3.2.3. Digital filtering

This section presents the results of fitting the Eckhardt filter and the one-parameter algorithm along exponentially separated LFCs.

The optimal benchmark region was applied to estimate a for the one-parameter filter, yielding the best fit with a = 0.983 (k' = -0.0172 h^{-1}) with a RMSE of 1.295 and a correlation coefficient of -0.980. Accordingly, the a coefficient is below the previously established benchmark range. The maximum LFC is 22.47 cm, which is below the maximum head of the LFC as established by the MRC (24.76 cm).

For the application of the Eckhardt method, the best fit was achieved with a = 0.979 and BFI_{max} = 0.54, resulting in a RMSE of 1.119 and a correlation coefficient of 0.984. Again, the a coefficient is below the previously established benchmark range. The maximum simulated head of the LFC is 24.95 cm, which is very close to the maximum head of 24.76 cm as established by the MRC.

The resulting separated LFCs are displayed in Figure 6.30. RMSE and correlation coefficients are displayed in Table 8.8.

Table 8.8: Fitting between digital/recursive filters and exponentially separated low flow for hourly head in PG between 12 Jul 2017 and 14 Apr 2018.

Filter	a	BFI_{max}	RMSE	Correlation coefficient	Max H [cm]
Eckhardt	0.979	0.540	1.119	0.984	24.95
One-parameter	0.983	-	1.295	0.980	22.47

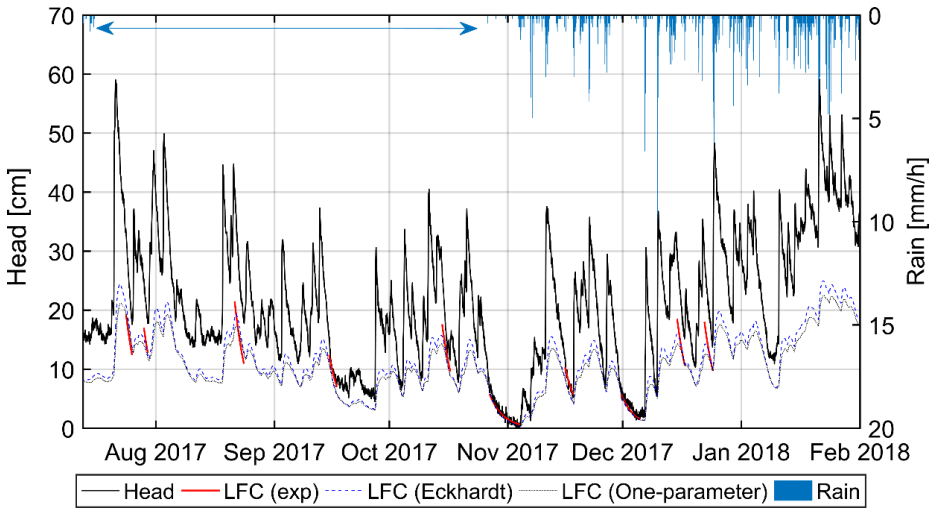

Figure 8.57: LFC separation of hourly head of PG between 12 Jul 2017 and 14 Apr 2018 using exponential fitting (exp), Eckhardt filter and the one-parameter filter.

The results show that both applied a coefficients are outside the previously established benchmark range.

However, both digital filters seem to perform well, although the Eckhardt filter achieves a slightly lower RMSE and a slightly higher correlation coefficient.

8.3.3. Summary from Bell Harbour LFC

Since the catchment of Bell Harbour does not have a discrete and directly measurable outflow in the form a single spring with associated hydrograph, alternative time series from two different sampling sites were used instead: borehole head time series (BH1) and head time series in the underground river of Poll Gonzo (PG).
The analysis of PG is constrained by a) relatively short time series (less than one year) not completely accompanied by available hourly rainfall time series; and b) relatively low resolution and accuracy of the measuring sensor, resulting in a noisy signal.
The MRC of PG does not show a completely convex recession, as a concave segment is also present. This may be due to the uncertainty and limitation of the time series, or else the results of the hydrograph characteristics. Only one linear reservoir could be fitted along the MRC, namely representing the LFC with H_0 = 25 cm and k' = 0.0095 h^{-1}.
Altogether, the benchmark range suggests that the k' of the head of the LFC may range between -0.0095 and -0.0131 h^{-1} with a mean of -0.0117 h^{-1}. In fact, the average k' fits very well relatively undisturbed recession parts of the hydrograph. However, the best fitting continuous LFC signal in the form of a digital recursive filter (Eckhardt) applies a recession coefficient a' of 0.979, which corresponds to k' of -0.0212 h^{-1}, which is below the benchmark range. This deviation from the benchmark range may be perhaps an indicator or the overall uncertainty with regard to the time series of PG.

The upper part of the borehole hydrograph (MRC) observed in BH1 was also analysed. The MRC shows many changes between convex and concave segments, which are believed to be the results of the heterogeneity of the aquifer related to hydraulically active fractures. The complex course of the MRC only allows sufficiently fitting of the lowest exponential component onto recession segments. The resulting k' values range between -0.00015 and -0.0006 h^{-1}.
The contribution of distinct chemical signals associated with contributions from fractures at different heads was indicated during a high-resolution sampling campaign. These signals are another indicator of the complex karstification of the aquifer, and presumably multiplicity of existing flow paths.

8.4. Modelling using InfoWorks ICM

This chapter presents the pipe network models established for Bell Harbour, considering the estimated SiGD into Bell Harbour Bay, head in T1, CAS and BH1 as well as the LFC as identified and separated within the previous chapters.

The presented model is a further development of the model published in Schuler, et al. (2018a), as it includes the results and conclusions from the subsequent tracer study extending the catchments to the south (thereby incorporating CAS/CAN), as well as integrating a separated LFC. Further, it incorporates results gained by the previous pipe network models for Ballindine and Manorhamilton.

The conceptual model of the Bell Harbour aquifer was outlined in Section '8.1.6. Conceptual model & catchment delineation', which is the base for the pipe network model here presented.

8.4.1. General model outline

In plan view, the entire catchment of 61.1 km^2 was sub-divided into nine sub-catchments according to landcover (soil or bare outcrop) and according to elevation (lowland or upland): four high elevated sub-catchments with bare outcrop; three low lying sub-catchments with a soil cover; one sub-catchment for Bell Harbour Bay and one sub-catchment for Carron (Figure 8.58, Table 8.9).

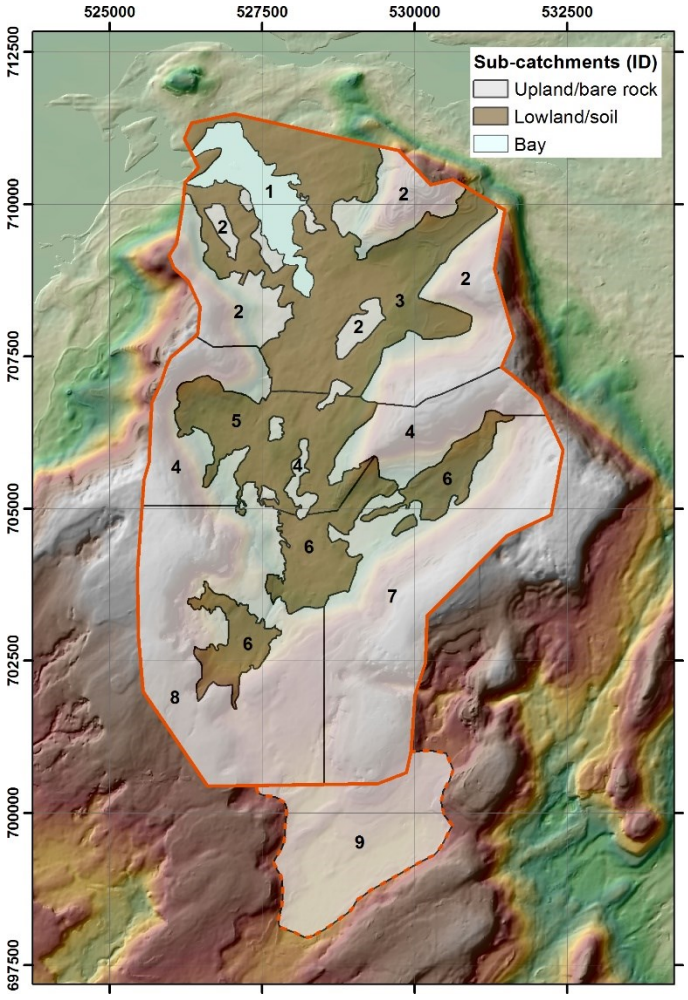

Figure 8.58: Bell Harbour sub-catchments as modelled in InfoWorks ICM.

The relatively large sizes of sub-catchments made it necessary to further disaggregate these in order to ensure numerical stability of the model. Hence, each sub-catchment was further sub-divided into sub-units, modelled as separate catchments in InfoWorks.
Mean elevations of each sub-catchment in the model were extracted from the improved digital elevation model. By doing so, the pipe network model realistically accounts for head differences between the low lying centre and the surrounding escarpments, which is believed to be the driving force of pressure transfer towards recharge, flow and discharge dynamics in the catchment.
The lowland sub-catchments are modelled as draining into permeable pipes, as done in the Ballindine model, accounting for a diffuse flow component (Figure 4.23b). In turn, the upland sub-catchments are modelled to drain into an full pipe, as done in the Manorhamilton model, representing a fast transfer of the recharge components (Figure 4.23a).
The parameters of the Ground Infiltration Module (GIM) were set differently, according to the best fit of the calibrated model (Table 8.9). The final parameters will be presented in Section '8.4.3. Calibration'.

Table 8.9: Sub-catchments of the catchment of Bell Harbour.

Sub-catchment No	Number of sub-units	Area [km^2]	Mean elevation [masl]	GIM ID	Type
1	0	1.84	1	0	Bell Harbour Bay
2	6	8.47	118	1	Upland
3	8	9.63	53	1	Lowland
4	6	6.31	153	1	Upland
5	4	4.05	43	1	Lowland
6	6	4.60	65	2	Lowland
7	4	10.05	184	1	Upland
8	4	10.66	163	1	Upland
9	0	5.47	126	3	Carron

The previously identified characteristic of shallow and deep groundwater flow was represented by two levels of conduits shown in the conceptual model in Figure 8.59. A shallow conduit that ranges between 10 and 0 masl and discharges periodically as overflow SiGD into Bell Harbour Bay and a deep conduit system at ~ 65 mbsl (~95 mbgl) that discharges as SGD into Galway Bay, bypassing Bell Harbour Bay. Both conduit levels are connected via vertical pipes to allow upwards and downwards flow.
This two-level system was built using empty conduits for pressurised open channel flow. The discretisation of the very heterogeneous aquifer with several flow horizons into 2 levels was considered to be a reasonable simplification and hence, a most parsimonious model.

The upper most sub-catchment of the model domain is resembled by the sub-catchment of Carron draining into CAS. CAS is integrated as a 'pond node'. Based on a detailed topographical survey and a resulting stage-volume relationship (Figure 8.60), a stage-area relationship for the pond node 'Carron' was entered in InfoWorks ICM (Figure 8.61).

The drainage of Carron enters the conduit network: the major share flows towards the north and Bell Harbour Bay/Galway Bay while a minor share flows towards an outfall representing discharge into the Fergus River in the south. Diversion was realised using a manhole with two outflow conduits. The division of the flows was realised using a manhole with two outflow conduits. The percentage split was arrived at as a result of the calibration procedure, namely by modifying the pipe network to fit the water level in T1 and the SiGD dynamics into Bell Harbour Bay. The resulting split was 36.9% (towards the Fergus River) to 63.1% (towards Bell Harbour).

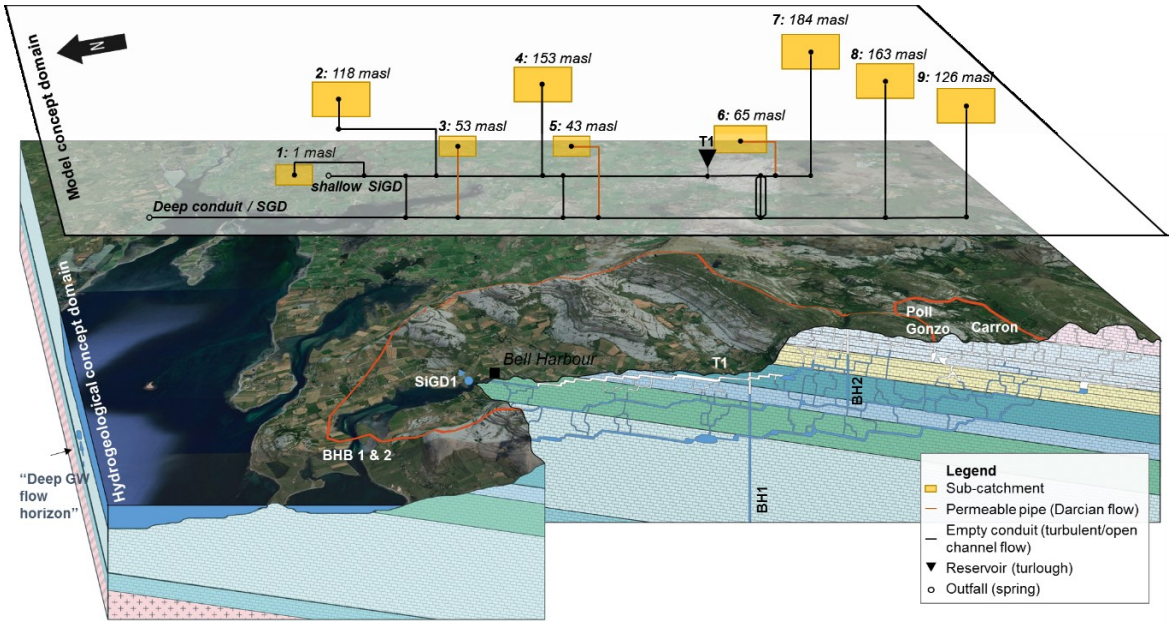

Figure 8.59: 3D Conceptual model of the hydrogeology of the Bell Harbour catchment, including conduit networks that are resembled in the pipe network model: permeable pipes (Darcy Flow) modelling diffuse recharge and full pipes (open channel and turbulent flow) model conduit flow. Yellow boxes represent conceptually sub-catchments with sub-catchment number and mean elevations.

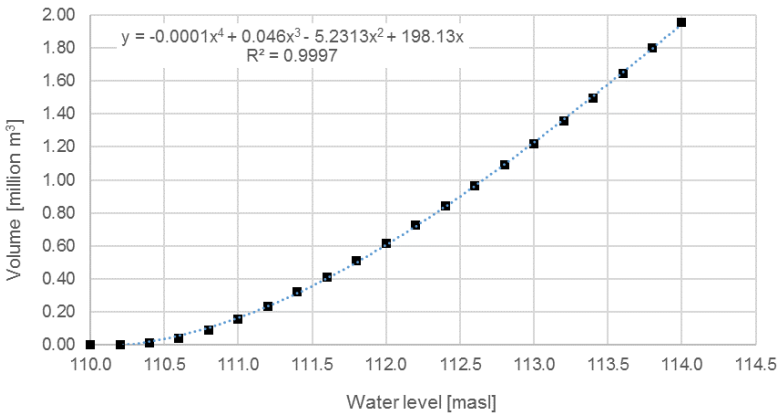

Figure 8.60: Stage-volume relationship of Carron south (CAS).

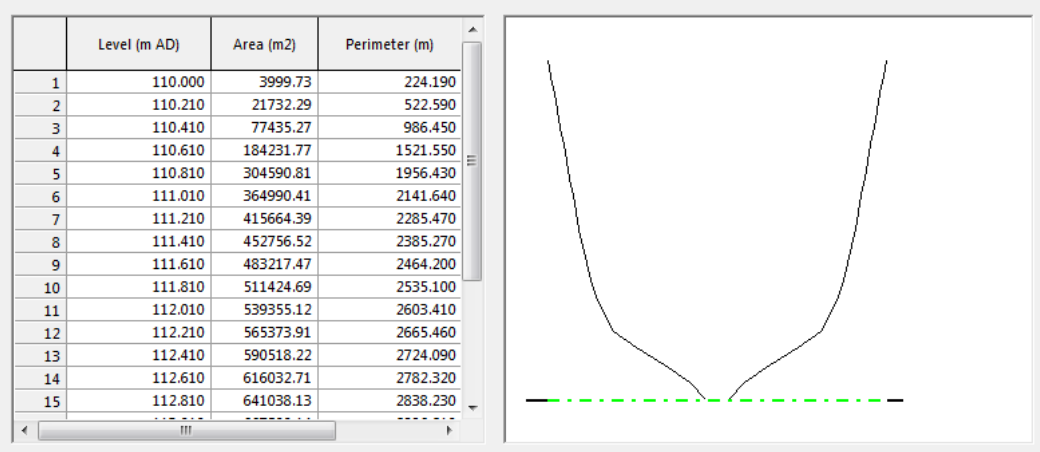

	Level (m AD)	Area (m2)	Perimeter (m)
1	110.000	3999.73	224.190
2	110.210	21732.29	522.590
3	110.410	77435.27	986.450
4	110.610	184231.77	1521.550
5	110.810	304590.81	1956.430
6	111.010	364990.41	2141.640
7	111.210	415664.39	2285.470
8	111.410	452756.52	2385.270
9	111.610	483217.47	2464.200
10	111.810	511424.69	2535.100
11	112.010	539355.12	2603.410
12	112.210	565373.91	2665.460
13	112.410	590518.22	2724.090
14	112.610	616032.71	2782.320
15	112.810	641038.13	2838.230

Figure 8.61: Stage-area relationship of Carron south (CAS) represented by a reservoir node in InfoWorks ICM.

Similarly, the turlough T1 was integrated using a pond node. Based on topographical measurements, a stage-volume relationship (Figure 8.62) was expressed, and further, a stage-area relationship derived and entered into the model (Figure 8.63).

The input time series for the model are hourly rainfall observed at C1, daily evapotranspiration based on climate data recorded at C1 following Allen, et al. (1998) (both uniformly applied on all sub-catchments) and tidal fluctuation observed at Galway Port (14 km north of the catchment) by the Marine Institute. For calibration reference the following time series were used: hourly head time series of Carron (CAS) and turlough Gortboyheen (T1) and mean daily estimated SiGD into Bell Harbour Bay.

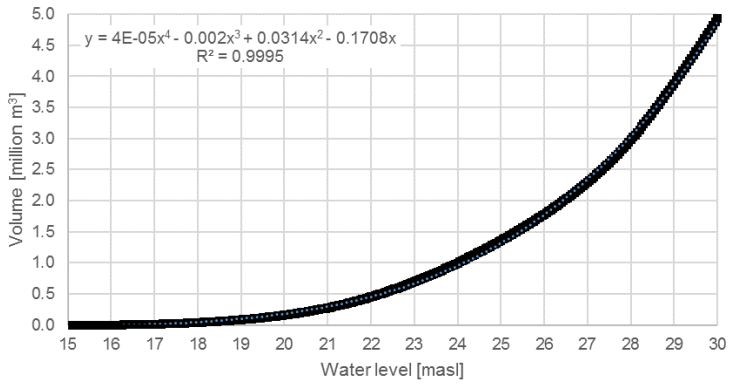

Figure 8.62: Stage-volume relationship of turlough Gortboyheen (T1).

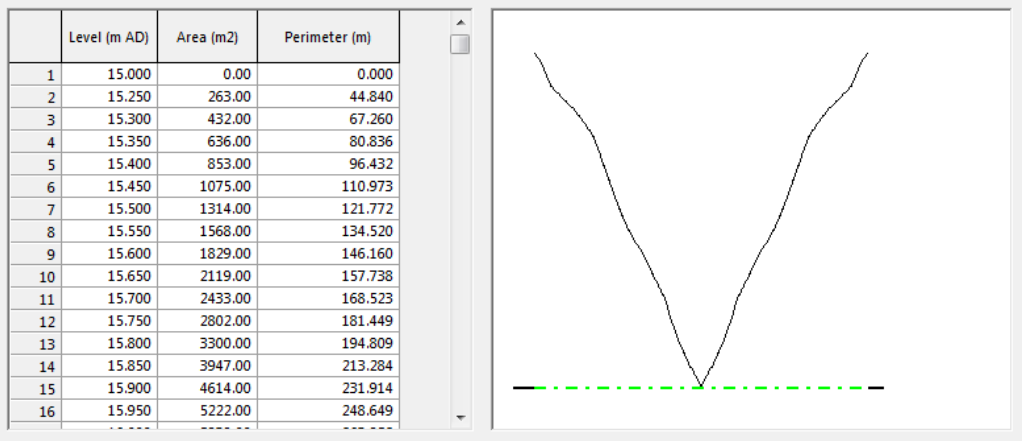

	Level (m AD)	Area (m2)	Perimeter (m)
1	15.000	0.00	0.000
2	15.250	263.00	44.840
3	15.300	432.00	67.260
4	15.350	636.00	80.836
5	15.400	853.00	96.432
6	15.450	1075.00	110.973
7	15.500	1314.00	121.772
8	15.550	1568.00	134.520
9	15.600	1829.00	146.160
10	15.650	2119.00	157.738
11	15.700	2433.00	168.523
12	15.750	2802.00	181.449
13	15.800	3300.00	194.809
14	15.850	3947.00	213.284
15	15.900	4614.00	231.914
16	15.950	5222.00	248.649

Figure 8.63: Stage-area relationship of Gortboyheen (T1) represented by a pond node in InfoWorks ICM

8.4.2. Flow components

The separation of a representative LFC and other flow components was challenging as discussed in Section '8.3. Low-flow component separation'). Using the head time series of PG and BH1, only a LFC (and not an intermediate or fast-flow component) could be separated, with k' ranging between -0.0117 and -0.0172 h^{-1} for PG, and between -0.00015 and -0.0006 h^{-1} for BH1. Hence, these ranges of k' were used as reference for the LFC.

The diffuse recharge signal was modelled as discharge from the groundwater store as previously done for Manorhamilton. Accordingly, each sub-unit (catchment) of a sub-catchment generates discharges flowing into a full or permeable pipe modelling turbulent or diffuse flow.

The conceptual model of the hydrograph is exemplified in Figure 8.64 using the MRC of Poll Gonzo.

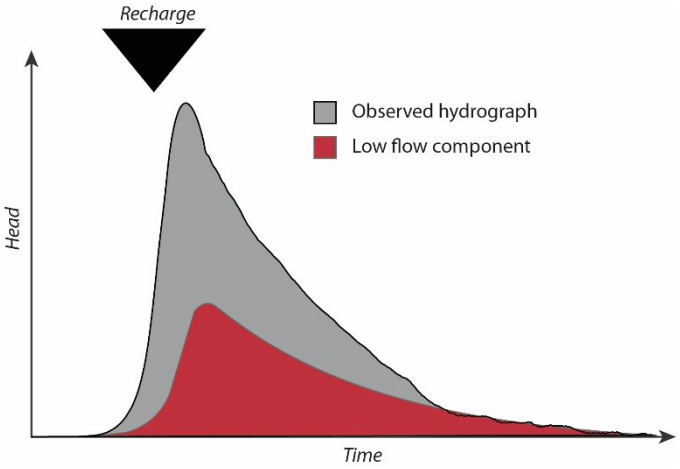

Figure 8.64: Low-flow component of Poll Gonzo as considered representative for the Bell Harbour catchment modelled as groundwater store inflow.

8.4.3. Calibration

The parameters used to evaluate the model performance are the VCC, the NSE and the KGE. Further, the ACF of modelled and observed/estimated time series was used.
The model was run on an hourly timestep between 28 Feb 2016 and 01 Oct 2018 with 28 Feb to 31 May 2016 used as initialisation / warm-up period. The period 01 Jun 2016 to 30 Sep 2017 was used for validation, and the period 01 Oct 2017 to 01 Oct 2018 was used for calibration.

The following elements of the InfoWorks and their discharges were calibrated against reference time series in the following order:

1. Water Balance: the parameters of the soil store and groundwater store were fitted to ensure that inflow equals outflow over the modelling period;
2. Head in Carron south (CAS): since CAS is the upper most pond node feeding into the conduit network, this was calibrated first. Calibration was done modifying the draining conduits of the pond node, and an attached node draining a share to the Fergus River;
3. Head in turlough Gortboyheen (T1): was matched against observed head by fitting the pipes that are connected to the pond node;
4. Total discharge of the pipe network model at the outfall SiGD into Bell Harbour Bay: calibrated against estimated time series by adjusting the geometries and parameters of the entire upstream pipe network.

The above elements 1 to 4 were used to ensure that the overall functioning of the aquifer was realistically simulated, including high-flow and low-flow periods and the associated regime of SiGD into Bell Harbour Bay.
Following the calibration procedure above (steps 1 to 4) the resulting model was cross-checked by:

5. The modelled recession of water levels of all groundwater stores was matched against the range of recession constants k' representing the LFC of PG and BH1; and
6. The head of the upper level of the pipe network upstream of T1 was matched against the observed head in BH1.

The parameter options with which to adjust the elements 5 and 6 were limited, as higher priority was given to the elements 1 to 4. Hence, elements 5 and 6 can be considered as cross-checking the model performance with regard to these two aspects - namely matching the LFC dynamics and fluctuation of the piezometric head in BH1.

1. Soil and groundwater store

Table 8.10 summarises the final parameters of the GIM applied for the different terrestrial sub-catchments as illustrated in Table 8.9 and Figure 8.58. Setting 3 applies to the sub-catchment of Carron, while settings 1 and 2 refer to sub-catchments between north of Carron and Bell Harbour

Bay. No GIM was used for the sub-catchment of Bell Harbour Bay because its contribution was modelled using runoff parameters only.

Table 8.10: Final GIM parameters for sub-catchments of Bell Harbour.

Setting	Soil depth [m]	Percolation Coefficient [t^{-1}]	Baseflow Coefficient t^{-1}]	Infiltration Coefficient t^{-1}]	Percolation Threshold [%]	Percolation percentage infiltrating [%]	Porosity of soil [%]	Porosity of ground [%]	Baseflow threshold level [m]	Baseflow threshold type	Infiltration threshold level [m]	Infiltration threshold type
1	0.1	25	100	25	55	56	60	1	10	Abs.	0.0	Abs.
2		15		35	55	76						
3		0.1		0.1	99	76						

All rainfall falling on the surface was modelled to enter the soil store, as no runoff was modelled representing fast and direct recharge (due to lack of any means of calibrating such a flow component).

The parameters of the GIM differ between sub-catchments with regard to the discharge dynamics of the GIM. The remaining parameters could be set globally. The same values for soil depth, porosity of the soil and ground were applied on all sub-catchments. Furthermore, no loss due to baseflow was expected (i.e. no cross-catchment flow) and therefore, the baseflow threshold was set to an excessive level (10 m). The infiltration threshold was set to 0 m, as there was no baseflow that would occur below that threshold.

2. Carron South (CAS)

The modelled head in the pond node CAS was matched against the observed head by fitting and adjusting the pipes draining the pond node (representing a polje) via an outfall (representing a swallow hole), namely their roughness and their dimensions (gradient and diameter).

It was found that a very good performance could be achieved using two empty conduits draining the pond node. The main drainage occurs via an empty conduit of ⌀ 255 mm at the bottom of the pond node at 110 masl. A second empty conduit drains the pond node at 111.5 masl with a width of ⌀ 250 mm. The combined flow is split into a) an empty conduit of ⌀ 470 mm towards an outfall resembling discharge into the Fergus River, and b) into an empty conduit of ⌀ 600 mm towards the pipe network of Bell Harbour.

The final design of the pond node CAS is illustrated in Figure 8.65.

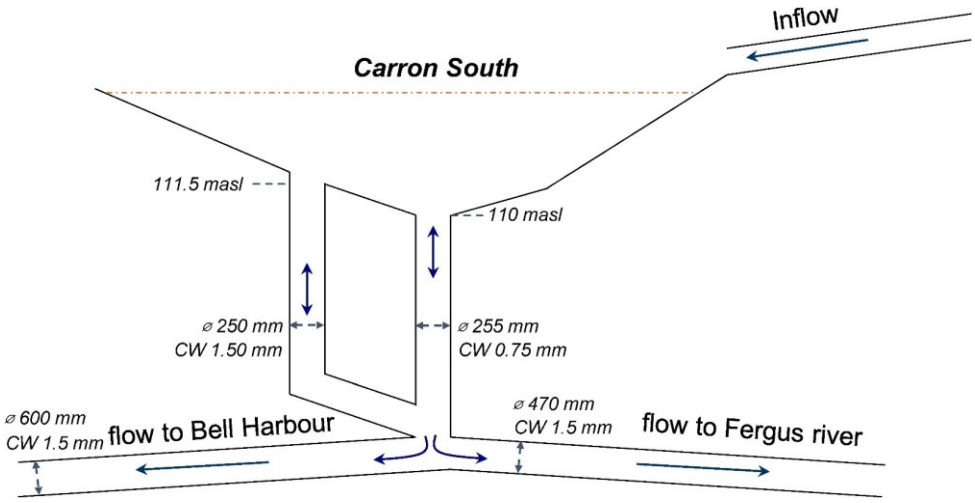

Figure 8.65: Final design of the pond node CAS and its outflows.

3. Gortboyheen (T1)

Again, the modelled head in the pond node of T1 was matched against the observed head by fitting and adjusting the pipes representing an estavelle, namely their number and their dimensions (diameter).

The inflow was modelled through two pipes: 1.) via an estavelle-type design constituted by a full pipe of ⌀ 800 mm that faces a throttle of ⌀ 435 mm, which forces flow into the storage node T1 through a vertical pipe of ⌀ 280 mm; and 2.) through a lateral inflow via a full pipe of ⌀ 525 mm at 20 masl that contributes overflow of the upstream pipe network at high-flows (>20.5 masl) Flow in the vertical 350 mm pipe is bi-directional, hence, upwards during periods of turlough inflow, and downwards during periods of drainage – i.e. it operates as an estavelle. Additional outflow from T1 occurs via three empty conduits of ⌀ 100, 300 and 370 mm respectively.

The final conduit setting is illustrated in Figure 8.66.

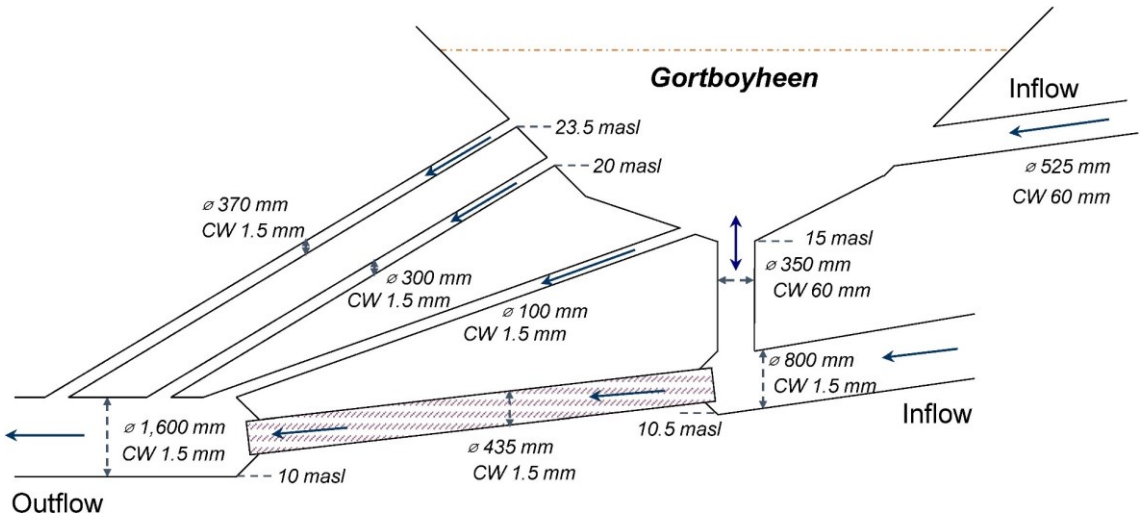

Figure 8.66: Final design of the pond node T1 and its outflows.

4. Estimated SiGD

The total modelled spring discharge is the sum of all flow components, and notably the result of the head distribution (potentiometric surface) in time over the two-level conduit network articulated by the head in Carron south, BH1 and turlough Gortboyheen. Hence, the calibration of head time series in CAS, T1 and BH1 was considered as most important in order to achieve the seasonal pattern of SiGD.

5. LFC

The LFC was resembled by the discharge of the groundwater store. However, since there is no known quantity of LFC, only the head, and in particular its recession, could be calibrated by fitting it against recessions associated with a range of k' values previously established using the time series of BH1 and PG.

The discharge of the groundwater store, i.e. infiltration flow, was optimised using an infiltration coefficient in the range of 15 to 25.

6.BH1

The simulated head in the upper pipe-level upstream of T1 was cross-checked against the observed borehole hydrograph in BH1. No modification of parameters was carried out anymore at this stage, as this would have resulted in re-iterating the calibration of elements 1. to 5.

8.4.4. Results

The model calibrated using the parameters previously outlined yielded the following results.

1. Soil and groundwater store

Figure 8.67 shows the water level of the soil store and groundwater store for setting during calibration and validation. Both water levels fluctuate in time, with neither showing an increasing trend that would lead to a deficit in recharge, and hence corrupt the water balance.

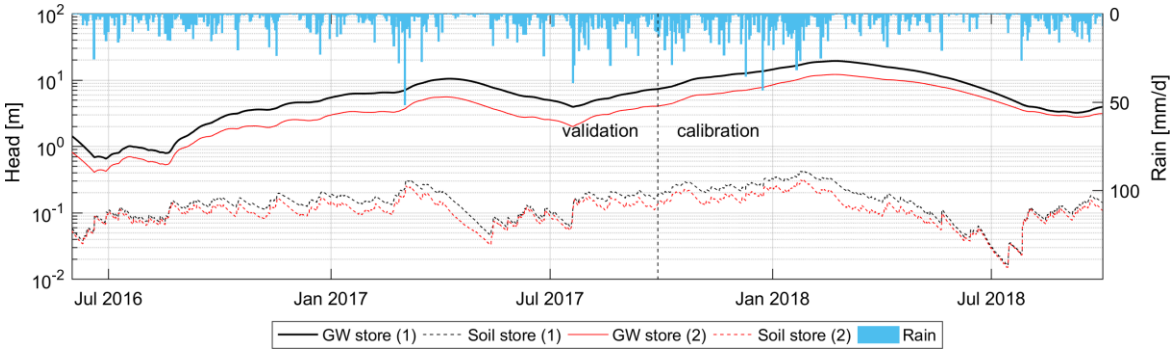

Figure 8.67: Simulated water level (m) of the soil store and groundwater (GW) store for setting 1 and 2 during calibration and validation.

2. Carron south (CAS)

The modelled head is plotted together with the observed head along with rainfall for the calibration and validation period (Figure 8.68). Periods of missing observations are illustrated by using horizontal double arrows.

The simulated head clearly matches the observed head well. All flood events are matched by the model. The model performance is summarised in Table 8.11. During calibration, this performance reaches a NSE and KGE of 0.946 and 0.975. During validation, the NSE and KGE decreases, reaching 0.883 and 0.853.

Table 8.11: Performance of the simulated head compared to the observed head of Carron south.

Parameter	Validation	Calibration
NSE	+0.883	+0.946
KGE	+0.853	+0.974

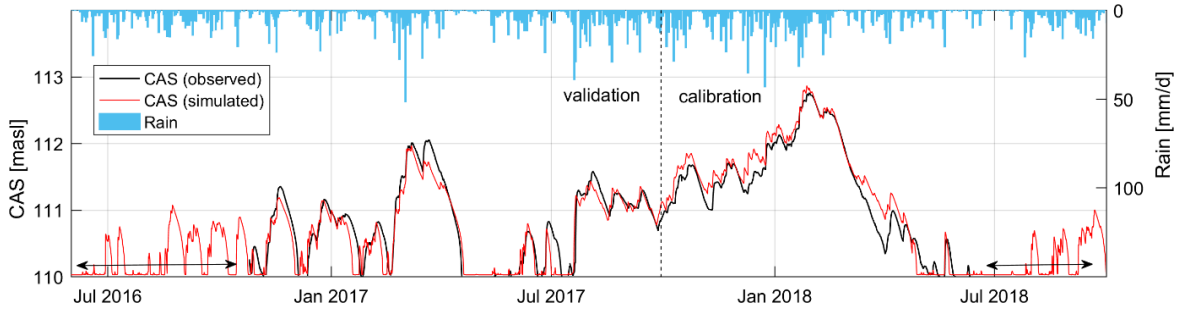

Figure 8.68: Observed vs. modelled head in Carron South (CAS) along with rainfall during the validation period 01 Jun 2016 to 30 Sep 2017 and the calibration period 01 Oct 2017 to 01 Oct 2018.

3. Turlough Gortboyheen (T1)

The modelled head is plotted together with the observed head (along with rainfall) for the calibration and validation period (Figure 8.69). Again, periods of missing observations are illustrated by black horizontal double arrows. No field observations of head in T1 could be measured for levels lower than 18.1 masl.

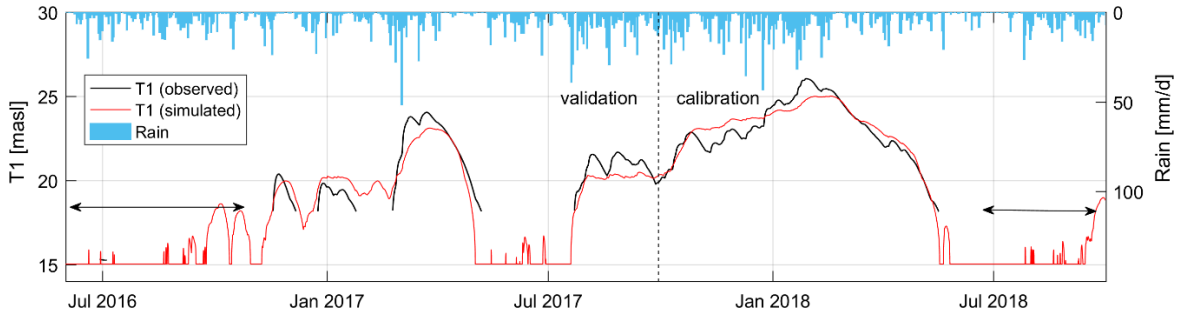

Figure 8.69: Observed vs. modelled head in turlough Gortboyheen along with rainfall during the validation period 01 Jun 2016 to 30 Sep 2017 and the calibration period 01 Oct 2017 to 01 Oct 2018.

The simulated head matches the observed head trend reasonably but does not exhibit the higher frequencies of fluctuations of the observed data. The model performance is summarised in Table 8.12.

Table 8.12: Performance of the simulated head compared to the observed head of turlough Gortboyheen.

Parameter	Validation	Calibration
NSE	+0.676	+0.884
KGE	+0.853	+0.879

4. Total discharge

The total discharge is the 'overflow' of the upper outfall representing SiGD into Bell Harbour Bay. Figure 8.70a shows the observed (estimated) and simulated SiGD during the calibration and validation period, along with daily rainfall. Figure 8.70b shows the cumulative discharges for both periods. Table 8.13 summarises the performance indicators, which relate to the average daily discharge.

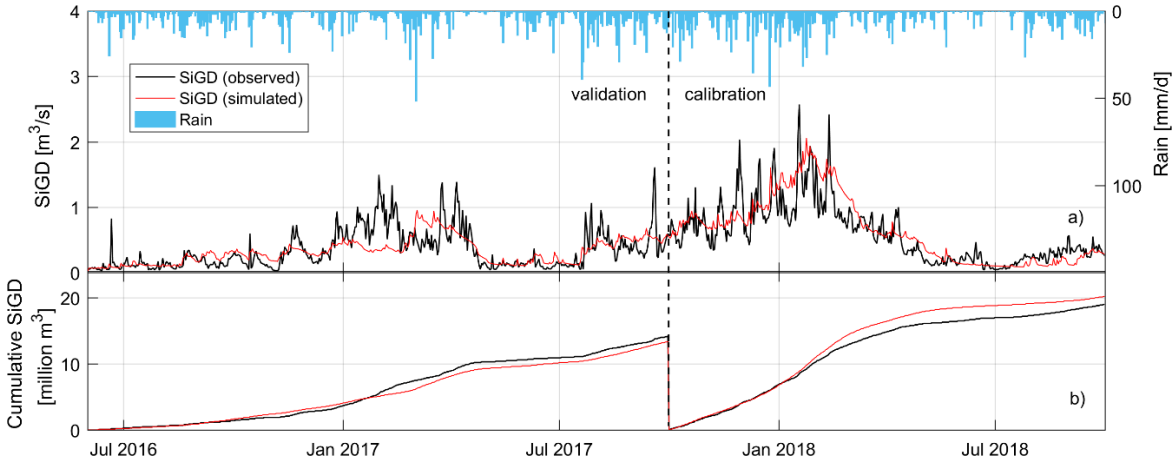

Figure 8.70: Simulated and observed (estimated) SiGD draining Bell Harbour Bay during calibration and validation: a) averaged daily discharge (m^3/s), and b) cumulative discharge (million m^3).

During calibration (01 Oct 2017 to 30 Sep 2018), the model performs relatively well. During this period, the estimated SiGD was 19.0 million m^3 as opposed to a simulated SiGD of 20.2 million m^3. The simulated SiGD matches the pattern of the estimated SiGD relatively well. A clear common pattern during high-flow and low-flow periods can be observed, presumably as there are no clear deviations occurring. Hence, the NSE reaches 0.65 and the KGE 0.81.

During validation (1 Jun 2016 to 30 Sep 2017) the estimated SiGD was 14.2 million m^3, while the simulated SiGD is 13.4 million m^3.

During the validation period, two periods of clear mismatch occur: first, between 10 Jan and 24 Feb 2017, when the simulated SiGD is too low; and secondly, between 24 Feb and 24 Mar 2017, when

the simulated discharge is too high. The deviation of modelling results in these periods remains unclear. However, it should be noted that the tidal prism method of estimating SiGD is susceptible to errors according to some of the assumptions made, as well as the calculation time step of each 'tidal cycle' of ~12 h acting to smooth out discharge peaks occurring in between. Further, it can be hypothesised that potentially strong marine currents at the monitoring site may have caused erratic measurements in salinity thereby challenging the assumptions made within the method.
These deviations seem to be the reason why the performance of the simulated discharge during the validation period is low, yielding a NSE of 0.36 and a KGE of 0.47. In fact, these two deviations were the reason why the model was calibrated against the period 01 Oct 2017 to 30 Sep 2018, instead of using the period that follows the warm-up period, which is considered as validation (1 Jun 2016 to 30 Sep 2017).
The model is capable of representing the periods of low flow as opposed to periods of high flows, matching reasonably well the estimated SiGD dynamics.

Table 8.13: Performance of the simulated SiGD compared to the estimated SiGD draining Bell Harbour Bay.

Parameter	Validation		Calibration	
NSE	+0.361		+0.646	
KGE	+0.467		+0.812	
VCC	-0.79 MCM	-5.56%	+0.20 MCM	+6.34%

Further, the performance is evaluated by comparing the loss of memory by using the ACF of the observed and simulated SiGD for the calibration and validation period (Figure 8.71a and b).

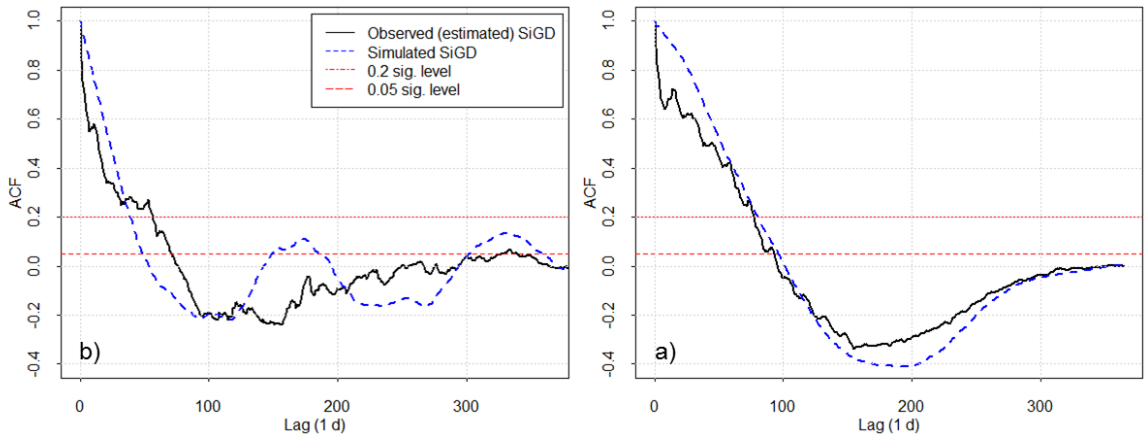

Figure 8.71: ACF of daily observed (estimated) and simulated SiGD during a) calibration and b) validation.

During calibration (Figure 8.71a) the courses of the ACFs show a very similar course. The loss of memory is almost identical reaching <0.2 after 78 days (estimated) and 81 days (simulated).

During validation, this pattern changes: the loss of memory is faster for the simulated time series reaching <0.2 after 40 days, as opposed to the observed (estimated) ones reaching <0.2 after 57 days. Overall, the course of the ACF of the simulated time series is smoother than the course of the ACF of the observed time series, and a deviation occurs.

To conclude, the comparison of the ACFs for both periods confirms the better performance of the model during the calibration period. The model seems to match the loss of memory very well. In turn, during validation, the loss of memory deviates, which again may be caused by the deviation of the simulated SiGD, as previously discussed.

5. LFC

Previously, the parameters of the GIM, including the groundwater store, were optimised by calibrating CAS, T1 and SiGD. This optimisation procedure left a limited parameter space in which to modify the GIM/groundwater store to match the simulated head against the previously established k' values as established for Poll Gonzo and BH1.

Figure 8.72 shows the finally simulated head of the groundwater store with setting 1 and 2. The best fitting along two major recessions was achieved using the k' value of the upper limit of the recession of BH1 with k' = 0.0006 h^{-1}.

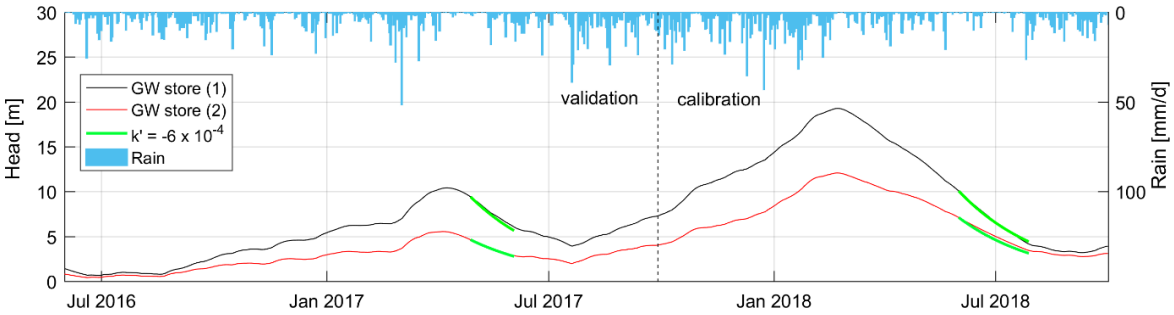

Figure 8.72: Head of the simulated groundwater (GW) store of setting 1 and 2 and exponentially fitted recessions with k' = 0.0006 h^{-1} (upper limit of BH1).

6. BH1

The simulated head in the upper level of the pipe network upstream of the pond node T1 was compared to the observed head in the borehole BH1. The simulated head is illustrated in Figure 8.73 and the performance of the model is summarised in Table 8.14.

Overall, the model matches the pattern of high-flow and low-flow periods. Single observed surges in head are very well matched by the model, and the simulated recessions generally follow the observed ones. The KGE during calibration and validation is 0.45 and 0.72. However, the absolute levels are insufficiently matched, which is indicated by the lower NSEs compared to the KGEs during calibration and validation.

The comparison of the NSE and KGE highlights the strength and weaknesses of the simulated head: the absolute heads are insufficiently matched, as expressed by the NSE, which evaluates

the match of the absolute simulated values. In turn, the KGE incorporates the correlation coefficient and the standard deviation (and the average) of both time series, hence, it evaluates more the linearity between time series. Therefore, the KGE considers if the overall 'pattern' or 'course' between two time series is matched.

While it would be desirable to achieve a better performance in modelling the head at BH1, this comparison shows some of the strengths and weaknesses of the pipe network model. Although the model is able to represent realistically the occurrence and timing of recharge and related flow dynamics within pipes, the flow dynamics occurring in pipes are bound to their own physical limitations (or potentially discharging into reservoirs). However, there is no medium surrounding the pipes, i.e. an "annex-to-drain system" (Mangin, 1975), which could receive groundwater during periods of high pressure (flow from the conduit into the matrix) and/or slowly discharging groundwater during periods of recessions. For example, the overestimation of modelled heads between December 2017 and March 2018 may be related to a missing storage system. At the same time, the simulated heads immediately recess or drop with the end of recharge, which indicates a missing inflow from a matrix, which would slow down this recession.

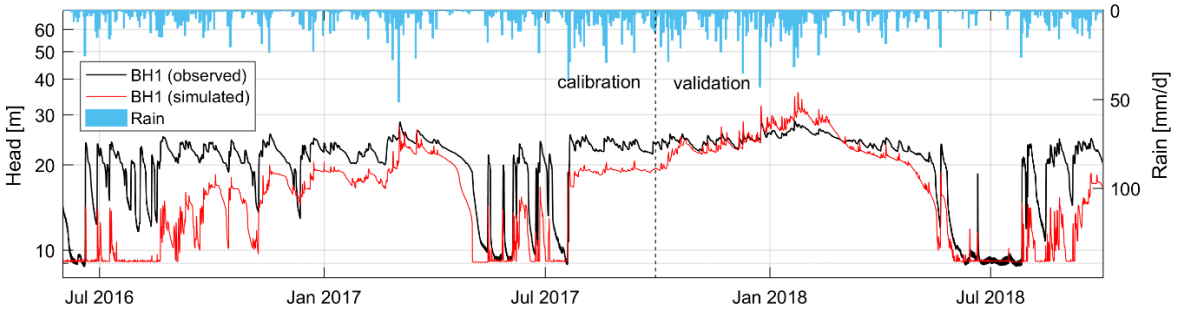

Figure 8.73: Observed head in BH1 and simulated head upstream of the pond node T1 ('BH1 simulated') during calibration and validation. Note that the absolute level (datum) of 'BH1 simulated' was adjusted to the datum of 'BH1 observed'.

Table 8.14: Performance of the simulated head in the upper pipe network compared to the observed head at BH1.

Parameter	Validation	Calibration
NSE	-0.712	+0.452
KGE	+0.633	+0.715

8.4.5. Summary from Bell Harbour pipe network modelling

The two-level pipe network model previously developed (Schuler, et al., 2018a) was extended to incorporate the sub-catchment of the polje Carron, creating a total catchment area of 61.1 km^2. The model was calibrated against observed head levels in CAS and T1 and against daily estimated SiGD draining Bell Harbour Bay. Further, the discharge of the groundwater stores was fitted

against established low-flow components (LFC), and heads were cross-checked against the observed head time series in BH1.

The model was run on an hourly timestep with a warm-up period applied between 28 Feb to 31 May 2016 and calibration and validation carried out across the periods 01 Oct 2017 to 01 Oct 2018 and 01 Jun 2016 to 30 Sep 2017.

The model excels simulating the head of CAS with a KGE and NSE >0.94 during calibration and >0.85 during validation. Lower performance however, is achieved for simulating the head of T1 with a NSE and KGE ≥0.88 during calibration and 0.68 and 0.85 during validation. This lower performance may be related to the complex structure of the model comprising two levels of pipe-flow, and hence, the distribution of heads. For example, the comparison between the observed head in BH1 and the simulated head in the upper-pipe level upstream of the pond node T1 indicates the strength and weaknesses of the model: while the overall pattern of heads in time can be simulated, including the timing of surges and recessions, the overall magnitude of heads is poorly modelled, being either underestimated or overestimated. It is believed that one limiting aspect is the physical limitation of flow within pipes: there is no “annex-to-drain” system connected to the pipes, which could receive water during periods of pressurised flow while discharging water into the conduits during periods of unpressurised flow in the pipes.

However, given the generally well-fitting timing or occurrence of rising heads indicates that recharge into the pipe network is reasonably well simulated. As part of that, a conceptual LFC originating from the master recession curve (MRC) of BH1 and hydrograph separation could be simulated as discharge from the groundwater store as part of the Ground Infiltration Module (GIM) in InfoWorks.

Overall, the seasonal or periodic discharge regime into and from Bell Harbour Bay could be reasonably matched. The NSE and KGE reach 0.65 and 0.81 during calibration and 0.36 and 0.470 during validation. The drop of performance during validation is believed to be related to two periods of clear deviations between the simulated and the observed results, namely between 10 Jan and 24 Feb 2017 and 24 Feb and 24 Mar 2017. During these periods, it is believed that the results of the model are more realistic than the estimated SiGD given the generally well-matching results of the head in CAS and within the upper pipe network compared to BH1. Again, these two periods of deviation may indicate the tidal prism method of estimating SiGD (against which the model is being compared) is susceptible to errors according to some of the assumptions made.

Nevertheless, the absolute discharges are relatively well simulated by the model. During calibration, the simulated SiGD accounts for 20.2 million m^3 compared to 19.0 million m^3 of estimated SiGD. During the validation, the estimate SiGD was 14.2 million m^3, while simulated SiGD is 13.4 million m^3.

8.5. Conclusions from Bell Harbour

Relatively little was known about the recharge and flow dynamics in the Bell Harbour catchment, with the relevant studies being carried out very recently (Perriquet, et al., 2014; McCormack, et al., 2017; O'Connell, et al., 2018). This study was able to further deepen the understanding of hydrodynamic processes in the Bell Harbour catchment covering the north-eastern part of the Burren Limestone Plateau.

The basis of an improved understanding is a well-distributed monitoring network covering terrestrial sampling locations to monitor climate, groundwater and surface water, as well as marine sampling locations and the availability and analysis of high-frequency long-term time series. Importantly, the monitoring at the different sampling locations was carried out in parallel at the same time, not in sequence or succeeding. Only through parallel sampling, the picture of high-flow and low-flow system could be drawn and expanded in space between the upland (Carron) in the south and the bay in the north. In addition, the continuous monitoring of hydroclimatic parameters was extended by tracer studies, namely single borehole dilution tests (SBDTs) and catchment-scale artificial tracer tests between the Burren Plateau and submarine springs in Galway Bay.

Altogether, the analysis and results suggest that the coastal aquifer of Bell Harbour is a very complex multi-level aquifer system. The heterogeneity of the aquifer is expressed through autocorrelation while cross-correlation between distributed time series partially suggests linearity of the hydrodynamics but dominating non-linearity. Ultimately, the catchment discharges seasonally via shallow SiGD into Bell Harbour Bay, and continuously as SGD into Galway Bay. Groundwater flow paths from south to north seem to be largely controlled by the presence of calcite filled Variscan veins that extend for >10 km across the Burren (Moore and Walsh, 2013; Walsh, et al., in review) acting as potential inception horizons for the development of conduits. In fact, silica peaks observed in BH1 during a high-frequency sampling campaign would seem to comply with this hypothesis.

Daily SiGD of the catchment was estimated using a tidal prism approach. Over the period of the two hydrological years 2017 and 2018, the water balances suggest that the majority of groundwater is discharged via SGD into Galway Bay bypassing bell Harbour Bay. However, the temporal resolution and/or reliability of the estimated SiGD time series does not yield a hydrograph that could be used for source separation techniques as applied on the spring time series of Ballindine and Manorhamilton. Therefore, alternatively, separation techniques were applied on the borehole hydrograph of BH1. However, this borehole hydrograph is constrained by the existence of multiple well-connected hydraulically active fractures/conduits connected to the borehole resulting in a multiplicity of recessions along the total borehole recession. Further, the use of the hydrograph of the stream in Poll Gonzo is limited by its short time span, as is the case for BH1; these also represent local information which cannot be assumed to be representative for the entire aquifer. In consequence, the separation of an LFC was much constrained.

Nevertheless, such a LFC signal was considered in calibrating a two-level pipe network model using InfoWorks ICM. Most importantly though, the pipe network model is capable of resembling the

hydraulic heads in CAS and T1, as well as the seasonality and the absolute quantities of estimated SiGD into Bell Harbour Bay.
Altogether, the results of the pipe network model have helped to define and confirm the validity of the conceptual model of the aquifer.

9. Conclusions

9.1. Summary

Karst aquifers are highly heterogeneous systems usually described by dual or triple porosities and associated ranges of recharge and flow dynamics often comprising laminar (diffuse) and non-linear partly or fully turbulent groundwater flow. Such heterogeneity challenges the development of numerical models of karst aquifers with regard to groundwater flow and even more contaminant transport. At the same time, there is a need for the numerical representation of karst aquifers as decision support system, e.g. for water resources and landuse management. Hence, the development of parsimonious hydraulic models is an ongoing and highly relevant research topic.
The aim of this research was to characterise diffuse recharge and flow components of three distinct autogenic karst aquifers as basis and part of the development of semi-distributed hydraulic pipe network models using the urban drainage software InfoWorks ICM. The three study sites are 1.) Ballindine spring, a low lying catchment in interaction with a river; 2.) Bell Harbour, a coastal-upland catchment impacted by the tide and discharging as submarine and intertidal groundwater discharge; and 3.) Manorhamilton spring, an upland-lowland catchment. The research question and objectives comprised 1.) developing an hydrogeological understanding and conceptual site model (CSM) of each study site, 2.) applying a suitable set of statistical and hydrochemical (time series) analyses to distinguish between recharge and flow components, and 3.) numerically simulate these recharge and flow components in pipe network models, and by doing so, thereby evaluate 1.) and 2.).

This section concludes on relevant results notably that **InfoWorks is able to simulate recharge and flow dynamics, which were identified using time series and multi-resolution analysis, as well as the overall discharge of all studied karst aquifers. The performance of the three hydraulic models justify the representation of a karst aquifer into a pipe network model using InfoWorks as a novel tool for semi-distributed groundwater flow modelling, and further confirm the realistic representation of the developed CSMs.**

The CSMs were largely built using different **hydrogeological field investigations** that were necessary given the relatively poor knowledge about the functioning of all three sites prior to this research. It could be demonstrated that the use of various types of artificial tracer tests, continuously and automated observed basic hydroclimatic variables and further derived hydrological parameters (such as estimated SiGD) were indispensable for the development of a sound conceptual understanding.

The developed CSMs comprise a range of dynamics related (but not limited) to karst, namely concentrated recharge through swallow holes, diffuse recharge through the soil, surface water-

groundwater interaction along a river, submarine and intertidal groundwater discharge (SiGD), epikarst or fracture and conduit dominated groundwater flow. Hence, this research bears a lot of elements that can be further investigated or linked to other international studies related to the functioning of karst, or national studies related to practical applications, e.g. delineation of source protection zones, management of coastal water or groundwater flooding mechanisms.

A combination of **time series analysis**, including **uni- and bivariate statistical methods**, **frequency, noise and multi-resolution analysis** was applied to support the development of CSMs, but mainly to characterise and quantify different **flow components**: a concentrated, an intermediate and a **low-flow component (LFC)**. The LFC was conceptualised as the component that sustains the lowest discharge of a spring as part of an overall diffuse recharge and flow signal. In general, the multiplicity of recharge and flow components could be accounted for by the applied methods. The number of identified components was limited to 3 in this study to fit into the conceptual model – yet, the results of frequency and noise analysis suggest that identifiable components may be beyond this number. Further research focussing on multi-resolution analysis coupled with noise analysis may reveal a much deeper understanding. Preferably, such analysis would be undertaken for spring catchments that have been studied more in depth in the past using different methods, including hydrochemical methods. While in this study, the use of hydrochemical analysis was challenged by a lack of infrastructure able to analyse for cations as well as by a perhaps too simplistic approach of the **two component mixing analysis (TCMA)**, a more refined approach will likely yield valuable information that ideally could be linked to the above mentioned methods.

However, the numerically identified recharge and flow components – where reliably detected - as well as the final discharge of the study sites could successfully be modelled using InfoWorks. The conceptual understanding according to which different recharge and flow components integrate towards a spring outlet discharge is the sum of different recharge and flow components has proven to be adequate, at least in a numerical sense, which is largely based on the combination of triangular recharge function, linear reservoirs as well as laminar, turbulent and open-channel/pressurised pipe flow dynamics. The large variety of karst of the three study sites suggest that InfoWorks can be applied in various settings ranging between diffuse-type aquifers and conduit-dominated aquifers.

9.2. Recommendations

Based on the results and conclusions drawn, the following activities are recommended for further development of the approach outlined in this thesis, and/or more generally for application to other similar activities:

Hydrogeological investigations

In order to improve the conceptual site models, the following activities are suggested:

Ballindine

In order to improve the understanding of surface water-groundwater interaction, it is recommended to repeat the tracer test conducted on 30 Jan 2019 when the water level of the River Robe is >1.7 m. However, there is the concern that dispersion in the river and in the aquifer may actually decrease any tracer concentration at the spring outlet below detectable limits. Therefore, it is recommended to investigate the possibility of drilling a 20 m deep open borehole at the southern bank of the River Robe. This borehole then shall be used as injection location for a tracer study.

Further, for a better understanding of the functioning of the drainage channels, future studies may target continuous water sampling (conductivity and temperature) of the outlet of the main drainage channels, along with sampling of the River Robe and Ballindine spring. A first set of time series may be very informative concerning the connectivity of these drainage channels with regard to the river and the spring.

Altogether, this catchment may reveal much information concerning surface water-groundwater interaction in a low lying karst catchment, including the role of manmade drainage channels onto the local hydrogeology.

Bell Harbour

In order to improve the hydrodynamic behaviour during ‘high-flow’ and ‘low-flow’ periods, it is suggested to conduct artificial tracer tests between the borehole BH1 and Bell Harbour Bay and SGD locations in Galway Bay during different times of the year considering tidal fluctuations as well as wave and sea current dynamics. Depending on the head in BH1, the outflow of this borehole is likely to be sufficient for such tracer tests, which may yield different results depending on the prevailing period during which the test is conducted. However, such tests may improve the understanding of groundwater discharge into Bell Harbour Bay at different hydroclimatic conditions. This knowledge may be relevant also for other coastal karstified aquifers with shallow and deeper outflows.

With regard to groundwater flow from Carron to the Fergus River, a quantitative tracer study may indicate the proportion of groundwater flowing towards the south. Importantly, such test would have to be carried out at least twice during different hydrological conditions to yield meaningful results.

Manorhamilton

The final delineated catchment includes uncertainty with regard to contribution from the uplands in the west (Leean Mountain) as opposed to contributions from the south. Additional tracer tests from the uplands and the southern part may be easily conducted in order to improve the current catchment boundaries, given the availability of suitable swallow holes.

Altogether, the three studied catchments offer very distinct recharge, flow and discharge processes, and hence, the combined use of these three sites may yield valuable information on the parameters studied.

Flow component separation

In this research, different techniques were applied to separate flow components, with varying degrees of success.

The underlying principle of flow component separation was based on frequency and noise analysis, yet, it was not the central theme of this research. It is felt that much more information may be obtained from frequency and noise analysis: for example, the classification of frequency ranges according to noise types may be more thoroughly linked to karst aquifer heterogeneities. Such studies could be linked or supported by hydrochemical assessments (e.g. mixing analysis).

However, it remains a challenge to link the identified frequency segments to a real physical dimension of the aquifer, for example, distinct ranges of fracture openings associated with types of porosities as illustrated in Figure 2.4.

The application of a digital filter is straight-forward, as shown in this research. However, this approach may be improved by linking it to hydrochemical analysis based on the principle of mixing reservoirs. Such an approach was attempted in this research, but the results showed that a more thorough approach is required, for example, targeting high-frequency sampling over several rain events. Sampling of hydrochemistry should consider more than two end members (groundwater and rain) as carried out in this research, as it has been shown that this approach was insufficient for Manorhamilton. For example, for Manorhamilton, it seems relevant to account for soil pore water and epikarst water/discharge, while for Ballindine, reservoirs could be incorporated by soil pore water, drainage channels and the River Robe.

A profound hydrochemical study with sufficient temporal and spatial resolution is likely to provide a better understanding with regard to different recharge, flow and discharge dynamics, and may therefore be linked to baseflow separation. Ultimately, such study may be linked to event-based hydrological pipe network modelling.

In additional to a hydrochemical approach, discrete wavelet transforms (DWT) has indicated promise in establishing a specific time series, based on the overall observed time-amplitude signal of the spring. Future research in this field may improve the use of multi-resolution analysis (MRA) in the field of baseflow separation.

Pipe network modelling

InfoWorks offers an abundance of possibilities to represent an aquifer as a network of discrete pipes connected to sub-catchments that generate different types of flow. This clearly is a strength of InfoWorks, alongside its stability in simulation. Yet, using the GIM the simulation of discharge of

the soil and groundwater store is limited to Eqn. 4.25 and Eqn. 4.29. However, it may be promising to modify the way how the soil and groundwater store are discharged, namely applying linear or non-linear equations. Future work could explore the possibilities of realising this, e.g. by applying for an 'Open-Source-License' at Innovyze or the development of a new model, aiming to modify desired components.

Another limitation of using the GIM to represent karst aquifer dynamics is the 'uni-directional' discharge: the groundwater and soil store receives inflow from the 'top', and discharges through the 'bottom'. There is no possibility that a reservoir received inflow from its 'bottom'. Such inflow, however, may be relevant in order to more realistically represent flow dynamics within an aquifer, especially given the interaction between the 'fissured matrix' and the 'conduits': at current, conceptually, flow is only generated from the 'fissured matrix' towards the conduits. Yet, it is well known that under pressurized conditions, the flow direction can change from the conduit back towards the matrix. Hence, the possibility of a 'reverse flow' during times of saturated flow in the pipes associated with the GIM may improve the numerical model in terms of a more realistic representation of the reality.

A strength of InfoWorks is the simulation of upstream and downstream heads in the pipes. These parameters can be used to calibrate the model against observed piezometric levels observed in karst aquifers. In this research, the only available head time series of a piezometer/borehole comprise BH1 and BH2 in Bell Harbour. The use of the BH1 time series as reference for the Bell Harbour model showed that such data can be used for calibration despite the very complex dynamics. For the development of future InfoWorks models of karst aquifers, it is recommended that sites are prioritised with regard to available piezometric time series for calibration reference.

Besides the more conceptual use of pipe network models for an improved understanding of groundwater recharge and flow dynamics, one relevant topic for the development of such models are climate change scenarios. Especially with regard to surface water-groundwater interaction along rivers or considering sea water intrusion along coastal aquifers, such models may be useful.

InfoWorks does not incorporate a parameter estimation tool to facilitate the calibration procedure. However, given the large number of parameters that can be adjusted and depending on the complexity of the model, the calibration process may be very extensive. The minimum time for calibrating a model can be estimated at one full-time work week, reaching possibly up to (several) months. The possibility of at least partly optimising the parameter space would largely increase the efficiency in modelling, and most likely also improve the performance of the final model.

As an alternative to InfoWorks, the open source public software Storm Water Management Model (SWMM) (US EPA, Washington DC, USA) has been used for modelling karst aquifers. Because the abovementioned aspects are likely to be able to incorporate in SWMM, it might be worth directly comparing the performances between SWMM and InfoWorks concerning hydrogeological modelling, to then conclude on the strengths and weaknesses, and finally the suitability of both platforms.

Evaluation of pipe network modelling in conjunction with contaminant transport

In InfoWorks, the transport of conservative and non-conservative contaminants can be simulated using a ‘Pollutograph’. The mass influx over time is defined in conjunction with an ‘Inflow’ event and assigned to a specific link or node.

Therefore, the simulation of a concentrated contaminated event, represented by e.g. a tracer test, can be carried out. More complexity may arise though by modelling diffuse contamination: assigning inflow along a permeable pipe may be one approach, however, attenuation shall be accounted for. The possibility of further investigating such approach would be a relevant topic especially with regard to using InfoWorks for realistic catchment-scale contaminant transport modelling.

References

Aggarwal PK, Fröhlich K, Gat JR, Gonfiantini R (2012) Commentary on Papers Aq, A2, A3. In: Aggarwal PK, Fröhlich K, Gat JR, Gonfiantini R (eds) Isotope hydrology:11-13.

Akram W, Ahmad M, Tariq JA, Latif Z, Rafique M (2013) Study of the relationship between streamflow and groundwater in selected areas of the Indus basin, PakistanIsotopic Age and Composition of Streamflow as Indicators of Groundwater Sustainability - Results of a 2004-2009 Coordinated Research Project:125-167.

Allen RG, Pereira LS, Raes D, Smith M (1998) Crop evapotranspiration - Guidelines for computing crop water requirements - FAO Irrigation and drainage paper 56 FAO - Food and Agriculture Organization of the United Nations, Rome, 1998.

Angelini P (1997) Correlation and spectral analysis of two hydrogeological systems in Central Italy. Hydrological Sciences Journal 42: 425-438 DOI 10.1080/02626669709492038

Appleton P (1989) Limestones and caves of North Wales. In: Ford TD (ed) Limestones and caves of Wales:257.

Aquilina L, Ladouche B, Dörfliger N (2006) Water storage and transfer in the epikarst of karstic systems during high flow periods. Journal of Hydrology 327: 472-485 DOI http://dx.doi.org/10.1016/j.jhydrol.2005.11.054

Arnold JG, Allen PM (1999) Automated methods for estimating baseflow and ground water recharge from streamflow records. JAWRA Journal of the American Water Resources Association 35: 411-424 DOI 10.1111/j.1752-1688.1999.tb03599.x

Atkinson TC (1977) Diffuse flow and conduit flow in limestone terrain in the Mendip Hills, Somerset (Great Britain). Journal of Hydrology 35: 93-110 DOI https://doi.org/10.1016/0022-1694(77)90079-8

Baertschi P (1976) Absolute18O content of standard mean ocean water. Earth and Planetary Science Letters 31: 341-344 DOI https://doi.org/10.1016/0012-821X(76)90115-1

Bailly-Comte V, Martin JB, Screaton EJ (2011) Time variant cross correlation to assess residence time of water and implication for hydraulics of a sink-rise karst system. Water Resources Research 47: 1-16 DOI 10.1029/2010WR009613

Bakalowicz M (2004) The epikarst, the skin of karst. In: Jones WK, Culver DC, Herman JS (eds) Epikarst, Special Publication 9 Karst Waters Institute, pp. 16-22.

Barber RW (2003) Chapter 17 Analytical modeling of pollution flushing in well-mixed tidal embayments. In: Lakhan VC (ed) Elsevier Oceanography Series:467-489.

Barber RW, Wearing MJ (2004a) A mathematical model for predicting the flushing characteristics and pollution susceptibility of Centerport Harbor, New York. In: Latini G, Passerini G, Brebbia CA (eds) Development and Application of Computer Techniques to Environmental Studies X:135-146.

Barber RW, Wearing MJ (2004b) A Simplified Model for Predicting the Pollution Exchange Coefficient of Small Tidal Embayments. Water, Air and Soil Pollution: Focus 4: 87-100 DOI 10.1023/B:WAFO.0000044789.67230.3e

Barnes B (1939) The structure of discharge-recession curves. Eos, Transactions American Geophysical Union 20: 721-725 DOI 10.1029/TR020i004p00721

Behrens H, Beims U, Dieter H, Dietze G, Eikmann T, Grummt T, Hanisch H, Henseling H, Käß W, Kerndorff H, Leibundgut C, Müller-Wegener U, Rönnefahrt I, Scharenberg B, Schleyer R, Schloz W, Tilkes F (2001) Toxicological and ecotoxicological assessment of water tracers. Hydrogeology Journal 9: 321-325 DOI 10.1007/s100400100126

Beier RA, Hardy HH (1996) Fractals in reservoir engineering

Benischke R, Goldscheider N, Smart C (2007) Tracer techniques. In: Goldscheider N, Drew D (eds) Methods in Karst Hydrogeology, IAH international contributions to hydrogeology ; 26:147-170.

Berkaloff E (1966) Limite de validite des formules courantes de tarissement du debit BRGM (Bureau de Recherches Géologiques et Minières), Paris, pp. 22.

Berti A, Tardivo G, Chiaudani A, Rech F, Borin M (2014) Assessing reference evapotranspiration by the Hargreaves method in north-eastern Italy. Agric Water Manage 140: 20-25 DOI https://doi.org/10.1016/j.agwat.2014.03.015

Binet S, Joigneaux E, Pauwels H, Albéric P, Fléhoc C, Bruand A (2017) Water exchange, mixing and transient storage between a saturated karstic conduit and the surrounding aquifer:

Groundwater flow modeling and inputs from stable water isotopes. Journal of Hydrology 544: 278-289 DOI http://dx.doi.org/10.1016/j.jhydrol.2016.11.042
Bittner D, Narany TS, Kohl B, Disse M, Chiogna G (2018) Modeling the hydrological impact of land use change in a dolomite-dominated karst system. Journal of Hydrology 567: 267-279 DOI https://doi.org/10.1016/j.jhydrol.2018.10.017
Bonacci O (1993) Karst springs hydrographs as indicators of karst aquifers. Hydrological Sciences Journal 38: 51-62 DOI 10.1080/02626669309492639
Botha JF, Bakkes GN (1984) Modelling Ground-water Flow with the Global and Finite Elements Method. In: Laible JP, Brebbia CA, Gray W, Pinder G (eds) Finite Elements in Water Resources: Proceedings of the 5th International Conference, Burlington, USA, June 1984:175-186.
Box GEP, Jenkins GM (1976) Time series analysis forecasting and control, Revised edn Holden-Day, San Francisco ; London
Bunce C (2010) Poll Gonzo. Irish Speleology 19: 16-21
Bunce C, Drew D (2017) Water tracing in the Carron depression and River Fergus valley, Burren, Co Clare. Irish Groundwater Newsletter: 13-18
Burnett WC, Aggarwal PK, Aureli A, Bokuniewicz H, Cable JE, Charette MA, Kontar E, Krupa S, Kulkarni KM, Loveless A, Moore WS, Oberdorfer JA, Oliveira J, Ozyurt N, Povinec P, Privitera AMG, Rajar R, Ramessur RT, Scholten J, Stieglitz T, Taniguchi M, Turner JV (2006) Quantifying submarine groundwater discharge in the coastal zone via multiple methods. Science of The Total Environment 367: 498-543 DOI http://dx.doi.org/10.1016/j.scitotenv.2006.05.009
Busse J, Paillet FL, Hossack A, Bringemeier D, Scheuermann A, Li L (2016) Field performance of the heat pulse flow meter: Experiences and recommendations. Journal of Applied Geophysics 126: 158-171 DOI http://dx.doi.org/10.1016/j.jappgeo.2016.01.021
Carr MR, Winter TC (1980) An annotated bibliography of devices developed for direct measurement of seepageOpen-File Report.
Cave RR, Henry T (2009) Groundwater inputs to the coastal zone of South Galway and Clare, west coast of Ireland. Paper presented at the ASLO Aquatic Sciences Meeting 2009, Nice, France2009
Cave RR, Henry T (2011) Intertidal and submarine groundwater discharge on the west coast of Ireland. Estuarine, Coastal and Shelf Science 92: 415-423 DOI http://dx.doi.org/10.1016/j.ecss.2011.01.019
Chang Y, Wu J, Jiang G (2015) Modeling the hydrological behavior of a karst spring using a nonlinear reservoir-pipe model. Hydrogeology Journal 23: 901-914 DOI 10.1007/s10040-015-1241-6
Chapman T (1999) A comparison of algorithms for stream flow recession and baseflow separation. Hydrological Processes 13: 701-714
Chapman TG, Maxwell AI (1996) Baseflow separation—comparison of numerical methods with tracer experimentsHydrology and Water Resources Symposium 1996: Water and the Environment; Preprints of Papers Institution of Engineers Australia, Hobart, pp. 539-545.
Charlier J-B, Ladouche B, Maréchal J-C (2015) Identifying the impact of climate and anthropic pressures on karst aquifers using wavelet analysis. Journal of Hydrology 523: 610-623 DOI http://dx.doi.org/10.1016/j.jhydrol.2015.02.003
Chen Z, Auler AS, Bakalowicz M, Drew D, Griger F, Hartmann J, Jiang G, Moosdorf N, Richts A, Stevanovic Z, Veni G, Goldscheider N (2017) The World Karst Aquifer Mapping project: concept, mapping procedure and map of Europe. Hydrogeology Journal 25: 771-785 DOI 10.1007/s10040-016-1519-3
Chen Z, Goldscheider N (2014) Modeling spatially and temporally varied hydraulic behavior of a folded karst system with dominant conduit drainage at catchment scale, Hochifen–Gottesacker, Alps. Journal of Hydrology 514: 41-52 DOI http://dx.doi.org/10.1016/j.jhydrol.2014.04.005
Chiaudani A, Di Curzio D, Palmucci W, Pasculli A, Polemio M, Rusi S (2017) Statistical and Fractal Approaches on Long Time-Series to Surface-Water/Groundwater Relationship Assessment: A Central Italy Alluvial Plain Case Study. Water 9 DOI 10.3390/w9110850
Chinarro D, Cuchí J, L. Villarroel J (2010) Application of Wavelet Correlation Analysis to the Karst Spring of Fuenmayor. San Julian de Banzo, Huesca, Spain

Choquette P, Pray L (1970) Geologic Nomenclature and Classification of Porosity in Sedimentary Carbonates. The American Association of Petroleum Geologists Bulletin 54: 207-250
Colebrook C, White C (1937) The Reduction of Carrying Capacity of Pipes with Age. Journal of the Institution of Civil Engineers 7: 99-118 DOI 10.1680/ijoti.1937.14682
Collischonn W, Fan FM (2013) Defining parameters for Eckhardt's digital baseflow filter. Hydrological Processes 27: 2614-2622 DOI 10.1002/hyp.9391
Cooley JW, Tukey JW (1965) An Algorithm for the Machine Calculation of Complex Fourier Series. Mathematics of Computation 19: 297-301 DOI 10.2307/2003354
Corbett DR, Cable JE, Shinn EA, Reich CD, Hickey TD (2003) Seepage Meters and Advective Transport in Coastal Environments: Comments on "Seepage Meters and Bernoulli's Revenge" by E. A. Shinn, C. D. Reich, and T. D. Hickey. 2002. "Estuaries" 25:126-132. Estuaries 26: 1383-1387
Creamer R, Simo I, Reidy B, Carvalho J, Fealy R, Hallett S, Jones R, Holden A, Holden N, Hannam J, Massey P, Mayr T, McDonald E, O'Rourke S, Sills P, Truckell I, Zawadzka J, Schulte R (2014) Irish Soil Information System Synthesis Report Teagasc, Cranfield University, University College Dublin, Johnstown Castle, Ireland.
Dafny E, Burg A, Gvirtzman H (2010) Effects of Karst and geological structure on groundwater flow: The case of Yarqon-Taninim Aquifer, Israel. Journal of Hydrology 389: 260-275 DOI http://dx.doi.org/10.1016/j.jhydrol.2010.05.038
Daly D (1997) Epikarst : A 'New' Concept in Irish Hydrogeology. Irish Groundwater Newsletter: 4-6
Darcy H (1856) Les fontaines publiques la ville de Dijon, Paris, pp. 647.
Daubechies I (1992) Ten Lectures on Wavelets, CBMS-NSF Regional Conference Series in Applied Mathematics:341 p.
Davies SJ, Guion PD, Gutteridge P (2012) Carboniferous Sedimentation and Volcanism on the Laurussian Margin. Geological History of Britain and Ireland DOI doi:10.1002/9781118274064.ch1410.1002/9781118274064.ch14
Denić-Jukić V, Jukić D (2003) Composite transfer functions for karst aquifers. Journal of Hydrology 274: 80-94 DOI http://dx.doi.org/10.1016/S0022-1694(02)00393-1
DHI-WASY (2012) Feflow 6.1 - Finite Element Subsurface Flow and Transport Simulation System User Manual DHI-WASY GmbH, pp. 116 p.
DHI (2007) Mike She User Manual and Reference Guide Denmark Hydrology Institute (DHI), Denmark.
DiLorenzo J, Ram R, Huang P, Najarian T (1994) Pollution Susceptibility of Well-Mixed Tidal Basins. Journal of Waterway, Port, Coastal, and Ocean Engineering 120: 404-422 DOI 10.1061/(ASCE)0733-950X(1994)120:4(404)
Doummar J, Sauter M, Geyer T (2012) Simulation of flow processes in a large scale karst system with an integrated catchment model (Mike She) – Identification of relevant parameters influencing spring discharge. Journal of Hydrology 426–427: 112-123 DOI http://dx.doi.org/10.1016/j.jhydrol.2012.01.021
Drew D (1990) The Hydrology of the Burren, County Clare. Irish Geography 23: 69-89
Drew D (2003) The Hydrology of the Burren and of the Clare and Galway Lowlands. In: Mullan G (ed) Caves of County Clare and South Galway:31-43.
Drew D (2018) Karst of Ireland Geological Survey Ireland, Dublin, Ireland
Drew D, Burke AM, Daly D (1996) Assessing the extent and degree of karstification in Ireland. In: Rozkowski A, Kowalcyk A, Motyka J, Rubin K (eds) International Conference on Karst Fractured Aquifers – Vulnerability and Sustainability:37-47.
Drew DP (2008) Hydrogeology of lowland karst in Ireland. Quarterly Journal of Engineering Geology and Hydrogeology 41: 61-72
Dreybrodt W (2004) Dissolution: Carbonate rocks. In: Gunn J (ed) Encyclopedia of caves and karst science:608-615.
Drogue C (1972) Analyse statistique des hydrogrammes de decrues des sources karstiques statistical analysis of hydrographs of karstic springs. Journal of Hydrology 15: 49-68 DOI http://dx.doi.org/10.1016/0022-1694(72)90075-3
Dufoyer A, Lecoq N, Massei N, Maréchal J-C, Pennequin D, David PY (2018) Linking the Informative Content of Spring Flow Time Series to Physical Properties of Karst Aquifers. Paper presented at the American Geophysical Union Fall Meeting, Washington, D.C., USA, 10-14 December 2018 2018

Duran L (2015) Approches physique, conceptuelle et statistique du fonctionnement hydrologique d'un karst sous couverture. PhD, University of Rouen, France
Eckhardt K (2005) How to construct recursive digital filters for baseflow separation. Hydrological Processes 19: 507-515 DOI 10.1002/hyp.5675
Eckhardt K (2008) A comparison of baseflow indices, which were calculated with seven different baseflow separation methods. Journal of Hydrology 352: 168-173 DOI https://doi.org/10.1016/j.jhydrol.2008.01.005
Eijkelkamp (2016) Product Manual Diver, Giesbeek, The Netherlands, pp. 24.
Einsiedl F (2005) Flow system dynamics and water storage of a fissured-porous karst aquifer characterized by artificial and environmental tracers. Journal of Hydrology 312: 312-321 DOI http://dx.doi.org/10.1016/j.jhydrol.2005.03.031
El-Hakim M, Bakalowicz M (2007) Significance and origin of very large regulating power of some karst aquifers in the Middle East. Implication on karst aquifer classification. Journal of Hydrology 333: 329-339 DOI https://doi.org/10.1016/j.jhydrol.2006.09.003
Elachi C, Van Zyl J (2006) Introduction to the physics and techniques of remote sensing, 2nd edn Wiley-Interscience, Hoboken, N.J.
Engineers UACo (2010) HEC-HMS Users's Manual Version 3.5 Hydrologic Engineering Centre, Davis, CA, USA.
EPA (2004) Guidance on groundwater risk assessment sheet: GWDTERA2a - risk to turloughs from phosphateWFD Pressures and Impacts Assessment Methodology Guidance Document GW9, Working group on groundwater: sub-committee on turloughs
EPA (2006) Ireland Water Framewok Directive Monitoring Programme, 1.0 edn Environmental Protection Agency (EPA), Johnstown Castle, Co. Wexford, Ireland.
EPA (2011a) Site Information Ballindine Environmental Protection Agency, pp. 5.
EPA (2011b) Site Information ManorhamiltonWater Framework Directive Groundwater Monitoring Programme, pp. 5.
Epstein S, Mayeda T (1953) Variation of the 18O content of waters from natural sources. Geochimica et Cosmochimica Acta 4: 213-224
Field MS (2002) The Qtracer2 Program for Tracer-Breakthrough Curve Analysis for Tracer Tests in Karstic Aquifers and Other Hydrologic Systems US Environmental Protection Agency, Washington, DC pp. 179.
Fiorillo F (2011) Tank-reservoir drainage as a simulation of the recession limb of karst spring hydrographs. Hydrogeology Journal 19: 1009-1019 DOI 10.1007/s10040-011-0737-y
Fiorillo F (2014) The Recession of Spring Hydrographs, Focused on Karst Aquifers. Water Resources Management 28: 1781-1805 DOI 10.1007/s11269-014-0597-z
Fischer BMC, van Meerveld HJ, Seibert J (2017) Spatial variability in the isotopic composition of rainfall in a small headwater catchment and its effect on hydrograph separation. Journal of Hydrology 547: 755-769 DOI https://doi.org/10.1016/j.jhydrol.2017.01.045
Fitzsimons VP, Misstear BDR (2006) Estimating groundwater recharge through tills: a sensitivity analysis of soil moisture budgets and till properties in Ireland. Hydrogeology Journal 14: 548-561 DOI 10.1007/s10040-005-0450-9
Fleury P (2005) Sources sous-marines et aquifères côtiers méditerranéens. Fonctionnement et caractérisation. PhD, University of Paris, France
Fleury P, Bakalowicz M, de Marsily G (2007a) Submarine springs and coastal karst aquifers: A review. Journal of Hydrology 339: 79-92 DOI http://dx.doi.org/10.1016/j.jhydrol.2007.03.009
Fleury P, Plagnes V, Bakalowicz M (2007b) Modelling of the functioning of karst aquifers with a reservoir model: Application to Fontaine de Vaucluse (South of France). Journal of Hydrology 345: 38-49 DOI http://dx.doi.org/10.1016/j.jhydrol.2007.07.014
Flury M, Wai NN (2003) Dyes as tracers for vadose zone hydrology. Reviews of Geophysics 41 DOI 10.1029/2001RG000109
Flynn RM, Sinreich M (2010) Characterisation of virus transport and attenuation in epikarst using short pulse and prolonged injection multi-tracer testing. Water Research 44: 1138-1149 DOI http://dx.doi.org/10.1016/j.watres.2009.11.032
Ford D, Williams PW (2007) Karst Hydrogeology and Geomorphology John Wiley & Sons Ltd, West Sussex, England
Forkasiewicz J, Paloc H (1967) Régime de tarissement de la Foux-de-la-Vis (gard). Étude préliminaire. La Houille Blanche 1: 29-36

Fournillon A (2012) 3D geological modeling and hydrodynamic applied to karstic carbonate reservoirs: water resources of the Beausset Unit (SE France) characterization. PhD, Aix-Marseille Université, France [in French]
Freeze RA, Cherry JA (1979) Groundwater Prentice-Hall, Englewood Cliffs ; London [etc.]
Friederich H, Smart PL (1982) The classification of autogenic percolation waters in karst aquifers: a study in G.B. Cave, Mendip Hills, England. Proc Univ Bristol Spelaeol Soc 16: 143-159
Friedman I (1953) Deuterium content of natural waters and other substances. Geochimica et Cosmochimica Acta 4: 89-103 DOI https://doi.org/10.1016/0016-7037(53)90066-0
Fritz P, Cherry JA, Weyer M, Sklash M (1976) Storm runoff analysis using environmental isotopes and major ions. Paper presented at the Interpretation of Environmental Isotope and Hydrochemical Data in Groundwater Hydrology 1975, Vienna, 27-31 January 1975 1976
Gallagher SJ, MacDermot CV, Somerville ID, Pracht M, Sleeman AG (2006) Biostratigraphy, microfacies and depositional environments of upper Viséan limestones from the Burren region, County Clare, Ireland. Geological Journal 41: 61-91 DOI 10.1002/gj.1033
Gallegos JJ, Hu BX, Davis H (2013) Simulating flow in karst aquifers at laboratory and sub-regional scales using MODFLOW-CFP. Hydrogeology Journal 21: 1749-1760 DOI 10.1007/s10040-013-1046-4
Genereux D (1998) Quantifying uncertainty in tracer-based hydrograph separations. Water Resources Research 34: 915-919 DOI 10.1029/98WR00010
Geyer T, Birk S, Licha T, Liedl R, Sauter M (2007) Multitracer test approach to characterize reactive transport in karst aquifers. Ground Water 45: 36-45 DOI 10.1111/j.1745-6584.2006.00261.x
Geyer T, Birk S, Liedl R, Sauter M (2008a) Quantification of temporal distribution of recharge in karst systems from spring hydrographs. Journal of Hydrology 348: 452-463 DOI http://dx.doi.org/10.1016/j.jhydrol.2007.10.015
Geyer T, Birk S, Liedl R, Sauter M (2008b) Quantification of temporal distribution of recharge in karst systems from spring hydrographs. Journal of Hydrology 348: 452-463 DOI https://doi.org/10.1016/j.jhydrol.2007.10.015
Ghasemizadeh R, Hellweger F, Butscher C, Padilla I, Vesper D, Field M, Alshawabkeh A (2012) Review: Groundwater flow and transport modeling of karst aquifers, with particular reference to the North Coast Limestone aquifer system of Puerto Rico. Hydrogeology Journal 20: 1441-1461 DOI 10.1007/s10040-012-0897-4
Giese M, Reimann T, Bailly-Comte V, Maréchal JC, Sauter M, Geyer T (2018) Turbulent and Laminar Flow in Karst Conduits Under Unsteady Flow Conditions: Interpretation of Pumping Tests by Discrete Conduit-Continuum Modeling. Water Resources Research 54: 1918-1933 DOI 10.1002/2017WR020658
Gill LW (2010) Modelling a Network of Turloughs. PhD, Trinity College Dublin, Ireland
Gill LW, McCormack T, Johnston PM (2015) Use of stable isotopes to characterise the hydrogeology of a lowland karst aquifer. Paper presented at the International Conference on Groundwater in Karst, Birmingham, UK, 22-26 June 2015
Gill LW, Naughton O, Johnston PM (2013a) Modeling a network of turloughs in lowland karst. Water Resources Research 49: 3487-3503 DOI 10.1002/wrcr.20299
Gill LW, Naughton O, Johnston PM, Basu B, Ghosh B (2013b) Characterisation of hydrogeological connections in a lowland karst network using time series analysis of water levels in ephemeral groundwater-fed lakes (turloughs). Journal of Hydrology 499: 289-302 DOI https://doi.org/10.1016/j.jhydrol.2013.07.002
Gillespie PA, Walsh JJ, Watterson J, Bonson CG, Manzocchi T (2001) Scaling relationships of joint and vein arrays from The Burren, Co. Clare, Ireland. Journal of Structural Geology 23: 183-201 DOI http://dx.doi.org/10.1016/S0191-8141(00)00090-0
Goldscheider N (2010) Chapter 8 - Delineation of spring protection zones. In: Kresic N, Stevanovic Z (eds) Groundwater Hydrology of Springs:305-338.
Goldscheider N, Andreo B (2007) The geological and geomorphological framework. In: Goldscheider N, Drew D (eds) Methods in karst hydrogeology, IAH international contributions to hydrogeology; 26:264.
Goldscheider N, Drew D, Worthington S (2007) Introduction. In: Goldscheider N, Drew D (eds) Methods in karst hydrogeology, IAH international contributions to hydrogeology; 26:264.
Graham JR (2009) Variscan deformation and metamorphism. In: Holland CH, Sanders I (eds) The Geology of Ireland, 2nd edn:568.

Grasso DA, Jeannin P-Y (2002) A Global Experimental System Approach of Karst Springs1 Hydrographs and Chemographs. Ground Water 40: 608-618 DOI 10.1111/j.1745-6584.2002.tb02547.x
Grinsted A, Moore JC, Jevrejeva S (2004) Application of the cross wavelet transform and wavelet coherence to geophysical time series. Nonlin Processes Geophys 11: 561-566 DOI 10.5194/npg-11-561-2004
Gröning M, Lutz HO, Roller-Lutz Z, Kralik M, Gourcy L, Pöltenstein L (2012) A simple rain collector preventing water re-evaporation dedicated for δ18O and δ2H analysis of cumulative precipitation samples. Journal of Hydrology 448: 195-200 DOI https://doi.org/10.1016/j.jhydrol.2012.04.041
Groundwater Aquifers (2016) Geological Survey of Ireland, 2016
Gunn J (2004) Encyclopedia of caves and karst science Fitzroy Dearborn, New York, USA, pp. 1939.
Gupta HV, Kling H, Yilmaz KK, Martinez GF (2009) Decomposition of the mean squared error and NSE performance criteria: Implications for improving hydrological modelling. Journal of Hydrology 377: 80-91 DOI https://doi.org/10.1016/j.jhydrol.2009.08.003
Gustard A, Bullock A, Dixon JM (1992) Low flow estimation in the United Kingdom Institute of Hydrology, Wallingford, UK.
Hagemann R, Nief G, Roth E (1970) Absolute isotopic scale for deuterium analysis of natural waters. Absolute D/H ratio for SMOW1. Tellus 22: 712-715 DOI 10.1111/j.2153-3490.1970.tb00540.x
Hagen G (1839) Ueber die Bewegung des Wassers in engen cylindrischen Röhren. Annalen der Physik 122: 423-442 DOI 10.1002/andp.18391220304
Hall F (1968) Base-Flow Recessions—A Review. Water Resources Research 4: 973-983 DOI 10.1029/WR004i005p00973
Hao Y, Yeh T-CJ, Gao Z, Wang Y, Zhao Y (2006) A gray system model for studying the response to climatic change: The Liulin karst springs, China. Journal of Hydrology 328: 668-676 DOI http://dx.doi.org/10.1016/j.jhydrol.2006.01.022
Harbaugh AW (2005) MODFLOW-2005, The U.S. Geological Survey Modular Ground-Water Model—the Ground-Water Flow ProcessUS Geological Survey Techniques and Methods 6-A16 U.S. Geological Survey, Reston, Virginia.
Hargreaves G, H. (1994) Defining and Using Reference Evapotranspiration. Journal of Irrigation and Drainage Engineering 120: 1132-1139 DOI 10.1061/(ASCE)0733-9437(1994)120:6(1132)
Hartmann A, Goldscheider N, Wagener T, Lange J, Weiler M (2014a) Karst water resources in a changing world: Review of hydrological modeling approaches. Reviews of Geophysics 52: 218-242 DOI 10.1002/2013RG000443
Hartmann A, Mudarra M, Andreo B, Marín A, Wagener T, Lange J (2014b) Modeling spatiotemporal impacts of hydroclimatic extremes on groundwater recharge at a Mediterranean karst aquifer. Water Resources Research 50: 6507-6521 DOI 10.1002/2014WR015685
Hill ME, Stewart MT, Martin A (2010) Evaluation of the MODFLOW-2005 Conduit Flow Process. Ground Water 48: 549-559 DOI 10.1111/j.1745-6584.2009.00673.x
Hiscock KM (2014) Hydrogeology : principles and practice, Second edition. edn Wiley-Blackwell, Chichester
Holko L, Malík P, Michalko J, Dóša M, Zostka Z (2013) Combined hydrologic and isotopic assessment of the Vah catchment, Danube river basin, SlovakiaIsotopic Age and Composition of Streamflow as Indicators of Groundwater Sustainability - Results of a 2004-2009 Coordinated Research Project:189-204.
Hubbert MK (1940) The Theory of Ground-Water Motion. The Journal of Geology 48: 785-944
Hunter Williams NH, Misstear BDR, Daly D, Lee M (2013) Development of a national groundwater recharge map for the Republic of Ireland. Quarterly Journal of Engineering Geology and Hydrogeology 46: 493-506
Huntoon PW (1995) Is it appropriate to apply porous media groundwater circulation models to karstic aquifers? In: El-Kadi AI (ed) Groundwater models for resources analysis and management:384.
Hurst HE (1951) Long-term storage capacity of reservoirs. Transactions of the American Society of Civil Engineers 116: 770-799

Global Network of Isotopes in Precipitation. The GNIP Database. (2016), http://www.iaea.org/water2016
Indarto, Novita E, Wahyuningsih S (2016) Preliminary Study on Baseflow Separation at Watersheds in East Java Regions. Agriculture and Agricultural Science Procedia 9: 538-550 DOI https://doi.org/10.1016/j.aaspro.2016.02.174
Innovyze (2015) InfoWorks ICM Help Menu.
Ireson AM, Butler AP (2013) A critical assessment of simple recharge models: application to the UK Chalk. Hydrol Earth Syst Sci 17: 2083-2096 DOI 10.5194/hess-17-2083-2013
Ireson AM, Mathias SA, Wheater HS, Butler AP, Finch J (2009) A model for flow in the chalk unsaturated zone incorporating progressive weathering. Journal of Hydrology 365: 244-260 DOI https://doi.org/10.1016/j.jhydrol.2008.11.043
IUSS (2015) World Reference Base for Soil Resources 2014, update 2015. International soil classification system for naming soils and creating legends for soil maps World Reference Base for Soil Resources (WRB) of the Working Group of the International Union of Soil Sciences (IUSS), Rome, Italy.
Jeannin P-Y (2001) Modeling flow in phreatic and epiphreatic Karst conduits in the Hölloch Cave (Muotatal, Switzerland). Water Resources Research 37: 191-200 DOI 10.1029/2000WR900257
Jeannin P-Y, Maréchal J-C (1995) Lois de pertes de charge dans les conduits karstiques: base théorique et observations. Bulletin du Centre d'hydrogéologie de Neuchâtel 14: 149-176
Jemcov I, Petrič M (2010) Time series analysis, modelling and assessment of optimal exploitation of the Nemanja karst springs, Serbia. Acta Carsologica 39: 187–200
Johnson AG, Glenn CR, Burnett WC, Peterson RN, Lucey PG (2008) Aerial infrared imaging reveals large nutrient-rich groundwater inputs to the ocean. Geophysical Research Letters 35: 1-6 DOI 10.1029/2008GL034574
Jukić D, Denić-Jukić V (2009) Groundwater balance estimation in karst by using a conceptual rainfall–runoff model. Journal of Hydrology 373: 302-315 DOI http://dx.doi.org/10.1016/j.jhydrol.2009.04.035
Jukić D, Denić-Jukić V (2015) Investigating relationships between rainfall and karst-spring discharge by higher-order partial correlation functions. Journal of Hydrology 530: 24-36 DOI http://dx.doi.org/10.1016/j.jhydrol.2015.09.045
Kaess W (1998) Tracing Technique in Geohydrology CRC Press
Katz BG (2005) Demystifying Ground-water Flow and Contaminant Movement in Karst Systems Using Chemical and Isotopic Tracers. In: Kuniansky EL (ed) US Geological Survey Karst Interest Group U.S. Geological Survey, Tallahassee, FL, pp. 1014-1028.
Katz BG, Coplen TB, Bullen TD, Davis JH (1997) Use of Chemical and Isotopic Tracers to Characterize the Interactions Between Ground Water and Surface Water in Mantled Karst. Ground Water 35: 1014-1028 DOI 10.1111/j.1745-6584.1997.tb00174.x
Kazakis N, Chalikakis K, Mazzilli N, Ollivier C, Manakos A, Voudouris K (2018) Management and research strategies of karst aquifers in Greece: Literature overview and exemplification based on hydrodynamic modelling and vulnerability assessment of a strategic karst aquifer. Science of The Total Environment 643: 592-609 DOI https://doi.org/10.1016/j.scitotenv.2018.06.184
Kelly C, Hunter Williams T, Misstear B, Motherway K (2015) Irish aquifer properties - A reference manual and guide, Version 1 edn.
Kendall C, Doctor DH, Young MB (2014) 7.9 - Environmental Isotope Applications in Hydrologic Studies A2 - Holland, Heinrich D. In: Turekian KK (ed) Treatise on Geochemistry (Second Edition):273-327.
Kendall C, McDonnell JJ (1998) Isotope Tracers in Catchment Hydrology, 1st edn Elsevier Science, Amsterdam.
Kiraly L (1975) Rapport sur l'état actuel des connaissances dans le domaine des caractères physiques des roches karstiques. In: Burger A, Dubertret L (eds) Hydrogeology of karstic terrains (Hydrogéologie des terrains karstiques):53-67.
Kiraly L (1998) Modelling karst aquifers by the combined discrete channel and continuum approach. Bulletin du Centre d'hydrogéologie de Neuchâtel 16: 77-98
Kiraly L, Perrochet P, Rossier Y (1995) Effect of the epikarst on the hydrograph of karst springs : a numerical approach. Bulletin du Centre d'hydrogéologie de Neuchâtel: 199-220

Klaus J, McDonnell JJ (2013) Hydrograph separation using stable isotopes: Review and evaluation. Journal of Hydrology 505: 47-64 DOI https://doi.org/10.1016/j.jhydrol.2013.09.006
Knee KL, Crook ED, Hench JL, Leichter JJ, Paytan A (2016) Assessment of Submarine Groundwater Discharge (SGD) as a Source of Dissolved Radium and Nutrients to Moorea (French Polynesia) Coastal Waters. Estuaries and Coasts 39: 1651-1668 DOI 10.1007/s12237-016-0108-y
Koeniger P, Margane A, Abi-Rizk J, Himmelsbach T (2017) Stable isotope-based mean catchment altitudes of springs in the Lebanon Mountains. Hydrological Processes 31: 3708-3718 DOI 10.1002/hyp.11291
Kong-A-Siou L, Cros K, Johannet A, Borrell-Estupina V, Pistre S (2013) KnoX method, or Knowledge eXtraction from neural network model. Case study on the Lez karst aquifer (southern France). Journal of Hydrology 507: 19-32 DOI https://doi.org/10.1016/j.jhydrol.2013.10.011
Kovács A, Perrochet P (2008) A quantitative approach to spring hydrograph decomposition. Journal of Hydrology 352: 16-29 DOI http://dx.doi.org/10.1016/j.jhydrol.2007.12.009
Kovács A, Perrochet P, Darabos E, Lénárt L, Szűcs P (2015) Well hydrograph analysis for the characterisation of flow dynamics and conduit network geometry in a karst aquifer, Bükk Mountains, Hungary. Journal of Hydrology 530: 484-499 DOI http://dx.doi.org/10.1016/j.jhydrol.2015.09.058
Kovács A, Perrochet P, Király L, Jeannin P-Y (2005) A quantitative method for the characterisation of karst aquifers based on spring hydrograph analysis. Journal of Hydrology 303: 152-164 DOI http://dx.doi.org/10.1016/j.jhydrol.2004.08.023
Kovács A, Sauter M (2007) Modelling karst hydrodynamics. In: Goldscheider N, Drew D (eds) Methods in karst hydrogeology, IAH international contributions to hydrogeology; 26:264 p.
Kresic N (2007) Hydraulic methods. In: Goldscheider N, Drew D (eds) Methods in karst hydrogeology, IAH international contributions to hydrogeology; 26:264.
Kresic N (2009) Groundwater Resources: Sustainability, Management, and Restoration McGraw-Hill Professional, New York, London
Labat D, Ababou R, Mangin A (2000a) Rainfall–runoff relations for karstic springs. Part I: convolution and spectral analyses. Journal of Hydrology 238: 123-148 DOI http://dx.doi.org/10.1016/S0022-1694(00)00321-8
Labat D, Ababou R, Mangin A (2000b) Rainfall–runoff relations for karstic springs. Part II: continuous wavelet and discrete orthogonal multiresolution analyses. Journal of Hydrology 238: 149-178 DOI http://dx.doi.org/10.1016/S0022-1694(00)00322-X
Labat D, Ababou R, Mangin A (2001) Introduction of Wavelet Analyses to Rainfall/Runoffs Relationship for a Karstic Basin: The Case of Licq-Atherey Karstic System (France). Ground Water 39: 605--615 DOI 10.1111/j.1745-6584.2001.tb02348.x
Lakey B, Krothe NC (1996) Stable Isotopic Variation of Storm Discharge from a Perennial Karst Spring, Indiana. Water Resources Research 32: 721-731 DOI 10.1029/95WR01951
Larocque M, Mangin A, Razack M, Banton O (1998) Contribution of correlation and spectral analyses to the regional study of a large karst aquifer (Charente, France). Journal of Hydrology 205: 217-231 DOI http://dx.doi.org/10.1016/S0022-1694(97)00155-8
Lauber U, Goldscheider N (2014) Use of artificial and natural tracers to assess groundwater transit-time distribution and flow systems in a high-alpine karst system (Wetterstein Mountains, Germany). Hydrogeology Journal 22: 1807-1824 DOI 10.1007/s10040-014-1173-6
Laudon H, Slaymaker O (1997) Hydrograph separation using stable isotopes, silica and electrical conductivity: an alpine example. Journal of Hydrology 201: 82-101 DOI https://doi.org/10.1016/S0022-1694(97)00030-9
Lee CM, Jiao JJ, Luo X, Moore WS (2012) Estimation of submarine groundwater discharge and associated nutrient fluxes in Tolo Harbour, Hong Kong. Science of The Total Environment 433: 427-433 DOI http://dx.doi.org/10.1016/j.scitotenv.2012.06.073
Leibundgut C, Maloszewski P, Külls C (2009) Tracers in Hydrology John Wiley, Hoboken, N.J. Chichester
Lerner DN, Issar AS, Simmers I (1990) Groundwater recharge: A guide to understanding and estimating natural recharge Heise, Hannover, Germany

Long CB (2005) Geology of South Mayo : a geological description of South Mayo, to accompany the Bedrock geology 1:100,000 scale map series, sheet 11, South Mayo Geological Survey of Ireland.
Luhmann AJ, Covington MD, Alexander SC, Chai SY, Schwartz BF, Groten JT, Alexander Jr EC (2012) Comparing conservative and nonconservative tracers in karst and using them to estimate flow path geometry. Journal of Hydrology 448–449: 201-211 DOI http://dx.doi.org/10.1016/j.jhydrol.2012.04.044
Mac Sharry B (2006) The influence of fractures on topography and groundwater flow in the Burren and Gort lowlands, western Ireland. PhD, Trinity College Dublin
MacDermot CV (1996) Geology of Sligo-Leitrim : a geological description of Sligo, Leitrim, and adjoining parts of Cavan, Fermanagh, Mayo and Roscommon, to accompany the bedrock geology 1:100,000 scale map series; sheet 7, Sligo-Leitrim Geological Survey of Ireland, Dublin
MacDermot CV, McConnell B, Pracht M (2003) Bedrock Geology 1:100,000 Sacle Map Series, Sheet 14, Galway Bay Geological Survey of Ireland, Dublin.
Machiwal D, Jha M (2006) Time Series Analysis of Hydrologic Data for Water Resources Planning and Management: A Review. Journal of Hydrology and Hydromechanics 54: 237-257
Maillet E (1905) Essais d'hydraulique souterraine & fluviale A. Hermann, Paris
Majone B, Bellin A, Borsato A (2004) Runoff generation in karst catchments: multifractal analysis. Journal of Hydrology 294: 176-195 DOI https://doi.org/10.1016/j.jhydrol.2003.11.042
Mandelbrot BB, Wallis JR (1968) Noah, Joseph, and Operational Hydrology. Water Resources Research 4: 909-918 DOI 10.1029/WR004i005p00909
Mangin A (1975) Contribution à l'étude hydrodynamique des aquifères karstiques. PhD, University of Dijon, France [in French]
Mangin A (1984) Pour une meilleure connaissance des systèmes hydrologiques à partir des analyses corrélatoire et spectrale. Journal of Hydrology 67: 25-43
Margane A, Abi-Risk J (2011) Practice Guide for Tracer Tests - Special Report No. 3 Bundesanstalt fuer Geowissenschaften und Rohstoffe (BGR), Ballouneh, pp. 45.
Margane A, Makki I, Raad R, Schuler P, Abi-Risk J, Doummar J, Koeniger P, Hahne K, Stoeckl L (2018) Hydrogeology of the Jeita Groundwater Catchment in Lebanon. Geologisches Jahrbuch Reihe B Bundesanstalt fuer Geowissenschaften und Rohstoffe (BGR), Hannover, pp. 192.
Marsaud B (1997) Structure et fonctionnement de la zone noyée des karsts à partir des résultats expérimentaux BRGM, Orléans, France, pp. 301.
Massei N, Dupont JP, Mahler BJ, Laignel B, Fournier M, Valdes D, Ogier S (2006) Investigating transport properties and turbidity dynamics of a karst aquifer using correlation, spectral, and wavelet analyses. Journal of Hydrology 329: 244-257 DOI http://dx.doi.org/10.1016/j.jhydrol.2006.02.021
Massei N, Mahler BJ, Bakalowicz M, Fournier M, Dupont JP (2007) Quantitative Interpretation of Specific Conductance Frequency Distributions in Karst. Groundwater 45: 288-293 DOI 10.1111/j.1745-6584.2006.00291.x
Mathevet T, Lepiller MI, Mangin A (2004) Application of time-series analyses to the hydrological functioning of an Alpine karstic system: the case of Bange-L'Eau-Morte. Hydrol Earth Syst Sci 8: 1051-1064 DOI 10.5194/hess-8-1051-2004
Mathias SA, Butler AP, Jackson BM, Wheater HS (2006) Transient simulations of flow and transport in the Chalk unsaturated zone. Journal of Hydrology 330: 10-28 DOI https://doi.org/10.1016/j.jhydrol.2006.04.010
Maurice L (2009) Investigations of rapid groundwater flow and karst in the Chalk. PhD, University College London, UK
Maurice L, Atkinson TC, Williams AT, Barker JA, Farrant AR (2010) Catchment scale tracer testing from karstic features in a porous limestone. Journal of Hydrology 389: 31-41 DOI http://dx.doi.org/10.1016/j.jhydrol.2010.05.019
Maurice L, Barker JA, Atkinson TC, Williams AT, Smart PL (2011) A Tracer Methodology for Identifying Ambient Flows in Boreholes. Ground Water 49: 227-238 DOI 10.1111/j.1745-6584.2010.00708.x
Mayaud C (2014) Groundwater Modelling in Karst Terrains using Single-Continuum Models. PhD, University of Graz, Austria

Mayaud C, Wagner T, Benischke R, Birk S (2014) Single event time series analysis in a binary karst catchment evaluated using a groundwater model (Lurbach system, Austria). Journal of Hydrology 511: 628-639 DOI http://dx.doi.org/10.1016/j.jhydrol.2014.02.024
Mays LW (2011) Water Resources Engineering, 2nd edn Wiley John Wiley [distributor], Hoboken, N.J., Chichester
Mazzilli N, Bertin D (2018) KarstMod User Guide version 2.2 National Observing Service (INSU) & National Center for Scientific Research (CNRS), pp. 22.
Mazzilli N, Guinot V, Jourde H, Lecoq N, Labat D, Arfib B, Baudement C, Danquigny C, Dal Soglio L, Bertin D (2017) KarstMod: A modelling platform for rainfall - discharge analysis and modelling dedicated to karst systems. Environ Model Software DOI https://doi.org/10.1016/j.envsoft.2017.03.015
McCormack T (2014) Quantifying Nutrient Dynamics through a Lowland Karst Ketwork. PhD, Trinity College Dublin, Ireland
McCormack T, Gill LW, Naughton O, Johnston PM (2014) Quantification of submarine/intertidal groundwater discharge and nutrient loading from a lowland karst catchment. Journal of Hydrology 519, Part B: 2318-2330 DOI http://dx.doi.org/10.1016/j.jhydrol.2014.09.086
McCormack T, O'Connell Y, Daly E, Gill LW, Henry T, Perriquet M (2017) Characterisation of karst hydrogeology in Western Ireland using geophysical and hydraulic modelling techniques. Journal of Hydrology: Regional Studies 10: 1-17
McCuen RH, Johnson PA, Ragan RM (2002) Highway HydrologyHydraulic Design Series Number 2, 2nd edn, pp. 424.
McDonnell JJ, Bonell M, Stewart MK, Pearce AJ (1990) Deuterium variations in storm rainfall: Implications for stream hydrograph separation. Water Resources Research 26: 455-458 DOI 10.1029/WR026i003p00455
Meyer B, Kincaid T, Hazlett T (2008) Modeling Karstic Controls on Watershed-Scale Groundwater Flow in the Floridan Aquifer of North FloridaSinkholes and the Engineering and Environmental Impacts of Karst (2008):351-361.
Miljević N, Boreli-Zdravković DJ, Golobočanin D, Janković M, Ogrinc N, Holko L, Solomon DK (2013) Surface-water groundwater relationship in the Velika Morava catchment, SerbiaIsotopic Age and Composition of Streamflow as Indicators of Groundwater Sustainability - Results of a 2004-2009 Coordinated Research Project:169-187.
Misstear B, Brown L (2007) 2002-W-MS/16: Recharge and Groundwater Vulnerability Environmental Protection Agency, Johnstown Castle, Co.Wexford, Ireland
Moles NR, Moles RT (2002) Influence of geology, glacial processes and land use on soil composition and Quaternary landscape evolution in The Burren National Park, Ireland. CATENA 47: 291-321 DOI http://dx.doi.org/10.1016/S0341-8162(01)00190-4
Molz FJ, Boman GK, Young SC, Waldrop WR (1994) Borehole flowmeters: field application and data analysis. Journal of Hydrology 163: 347-371 DOI http://dx.doi.org/10.1016/0022-1694(94)90148-1
Molz FJ, Morin RH, Hess AE, Melville JG, Güven O (1989) The Impeller Meter for measuring aquifer permeability variations: Evaluation and comparison with other tests. Water Resources Research 25: 1677-1683 DOI 10.1029/WR025i007p01677
Mook WG, Groeneveld DJ (1974) Analysis of a run-off hydrograph by means of natural 18OIsotope Techniques in Groundwater Hydrology:145-156.
Moore GK (1992) Hydrograph Analysis in a Fractured Rock Terrane. Ground Water 30: 390-395 DOI 10.1111/j.1745-6584.1992.tb02007.x
Moore JP, Walsh JJ (2013) Analysis of fracture systems and their impact on flow pathways in Irish bedrock aquifers. Irish Groundwater Newsletter: 28-33
Moore WS (2006) Radium isotopes as tracers of submarine groundwater discharge in Sicily. Continental Shelf Research 26: 852-861 DOI http://dx.doi.org/10.1016/j.csr.2005.12.004
Morgan DT (2014) The influence of particle size on the nature and transport of sediments and associated pollutants in urban stormwater drainage. PhD, Trinity College Dublin, Ireland
Moriasi DN, Arnold JG, Van Liew MW, Bingner RL, Harmel RD, Veith TL (2007) Model evaluation guidelines for systematic quantification of accuracy in watershed simulations. Transactions of the ASABE 50: 885-900
Narasimhan TN, Witherspoon PA (1982) Overview of the Finite Element Method in Groundwater Hydrology. In: Holz KP, Meissner U, Zielke W, Brebbia CA, Pinder G, Gray W (eds) Finite

Elements in Water Resources: Proceedings of the 4th International Conference, Hannover, Germany, June 1982:29-44.
Nash JE, Sutcliffe JV (1970) River flow forecasting through conceptual models part I — A discussion of principles. Journal of Hydrology 10: 282-290 DOI https://doi.org/10.1016/0022-1694(70)90255-6
Naughton O, Johnston PM, Gill LW (2012) Groundwater flooding in Irish karst: The hydrological characterisation of ephemeral lakes (turloughs). Journal of Hydrology 470–471: 82-97 DOI http://dx.doi.org/10.1016/j.jhydrol.2012.08.012
Norbiato D, Borga M, Merz R, Blöschl G, Carton A (2009) Controls on event runoff coefficients in the eastern Italian Alps. Journal of Hydrology 375: 312-325 DOI https://doi.org/10.1016/j.jhydrol.2009.06.044
Null KA, Knee KL, Crook ED, de Sieyes NR, Rebolledo-Vieyra M, Hernández-Terrones L, Paytan A (2014) Composition and fluxes of submarine groundwater along the Caribbean coast of the Yucatan Peninsula. Continental Shelf Research 77: 38-50 DOI http://dx.doi.org/10.1016/j.csr.2014.01.011
O'Brien RJ, Misstear BD, Gill LW, Johnston PM, Flynn R (2014) Quantifying flows along hydrological pathways by applying a new filtering algorithm in conjunction with master recession curve analysis. Hydrological Processes 28: 6211-6221 DOI 10.1002/hyp.10105
O'Connell Y, Daly E, Duffy GP, Henry T (2012) Investigation of Submarine Groundwater Discharge and Preferential Groundwater Flow-paths in a Coastal Karst Area using towed Marine &Terrestrial Electrical Resistivity. Paper presented at the American Geophysical Union Conference, San Francisco2012
O'Connell Y, Daly E, Henry T, Brown C (2018) Terrestrial and marine electrical resistivity to identify groundwater pathways in coastal karst aquifers. Near Surface Geophysics 16: 1-12 DOI 10.3997/1873-0604.2017062
OTT (2009) Operating instructions - Groundwater datalogger OTT CTD OTT Hydromet GmbH, Kempten, Germany.
OTT (2013) OTT Acoustic Digital Current (ADC) Meter User Manual, 3 (North American Version) edn, pp. 48.
Padilla A, Pulido-Bosch A (1995) Study of hydrographs of karstic aquifers by means of correlation and cross-spectral analysis. Journal of Hydrology 168: 73-89 DOI http://dx.doi.org/10.1016/0022-1694(94)02648-U
Padilla A, Pulido-Bosch A, Mangin A (1994) Relative Importance of Baseflow and Quickflow from Hydrographs of Karst Spring. Ground Water 32: 267-277 DOI 10.1111/j.1745-6584.1994.tb00641.x
Paillet FL (2004) Borehole flowmeter applications in irregular and large-diameter boreholes. Journal of Applied Geophysics 55: 39-59 DOI http://dx.doi.org/10.1016/j.jappgeo.2003.06.004
Panagopoulos G, Lambrakis N (2006) The contribution of time series analysis to the study of the hydrodynamic characteristics of the karst systems: Application on two typical karst aquifers of Greece (Trifilia, Almyros Crete). Journal of Hydrology 329: 368-376 DOI https://doi.org/10.1016/j.jhydrol.2006.02.023
Panday S (2017) Fundamentals and Application of MODFLOW-USG, an Unstructured Grid Version of MOFFLOW GSI Environmental, Dublin.
Pellerin BA, Wollheim WM, Feng X, Vörösmarty CJ (2008) The application of electrical conductivity as a tracer for hydrograph separation in urban catchments. Hydrological Processes 22: 1810-1818 DOI 10.1002/hyp.6786
Percival DB, Walden AT (2000) Wavelet methods for time series analysis Cambridge University Press, Cambridge
Perrin J, Jeannin P-Y, Zwahlen F (2003) Epikarst storage in a karst aquifer: a conceptual model based on isotopic data, Milandre test site, Switzerland. Journal of Hydrology 279: 106-124 DOI http://dx.doi.org/10.1016/S0022-1694(03)00171-9
Perriquet M (2014) Characterization of the hydrodynamics and saltwater wedge variations in a coastal karst aquifer in response to tide and precipitation events (Bell Harbour catchment, Co. Clare, Ireland). PhD, National University of Galway, Ireland
Perriquet M, Henry T, Cave R, Leonardi V, Jourde H (2012) Hydrodynamics of a coastal karst aquifer affetced by saltwater intrusion under oceanic climatic influence, Co. Clare, Ireland. Paper presented at the 22nd Salt Water Intrusion Meeting, Búzios, Brazil2012

Perriquet M, Leonardi V, Henry T, Jourde H (2014) Saltwater wedge variation in a non-anthropogenic coastal karst aquifer influenced by a strong tidal range (Burren, Ireland). Journal of Hydrology 519: 2350-2365 DOI http://dx.doi.org/10.1016/j.jhydrol.2014.10.006
Peterson RN, Burnett WC, Taniguchi M, Chen J, Santos IR, Ishitobi T (2008) Radon and radium isotope assessment of submarine groundwater discharge in the Yellow River delta, China. Journal of Geophysical Research: Oceans 113: n/a-n/a DOI 10.1029/2008JC004776
Pettitt AN (1979) A Non-Parametric Approach to the Change-Point Problem. Journal of the Royal Statistical Society Series C (Applied Statistics) 28: 126-135 DOI 10.2307/2346729
Pinder GF, Jones JF (1969) Determination of the ground-water component of peak discharge from the chemistry of total runoff. Water Resources Research 5: 438-445 DOI 10.1029/WR005i002p00438
Poiseuille JLM (1846) Recherches expérimentales sur le mouvement des liquides dans les tubes de très petits diamètres, (Paris)
Powers JG, Shevenell L (2000) Transmissivity Estimates from Well Hydrographs in Karst and Fractured Aquifers. Ground Water 38: 361-369 DOI 10.1111/j.1745-6584.2000.tb00221.x
Pracht M, Lees A, Leake B, Feely M, Long B, Morris J, McConnell B (2004) Geology of Galway Bay : A geological description to accompany the Bedrock Geology 1:100,000 map series, Sheet 14, Galway Bay Geological Survey of Ireland, Dublin
Pracht M, Somerville ID, Wang Y (2015) A revised Mississippian lithostratigraphy of County Galway (western Ireland) with an analysis of carbonate lithofacies, biostratigraphy, depositional environments and palaeogeographic reconstructions utilising new borehole data. Journal of Palaeogeography 4: 1-26 DOI http://dx.doi.org/10.3724/SP.J.1261.2015.00065
Price H (1999) Strategies for source protection in karstic aquifers. MSc, Trinity College Dublin
Ramirez RW (1985) The FFT : fundamentals and concepts Prentice Hall, Englewood Cliffs, NJ ; London
Read T, Bour O, Selker JS, Bense VF, Borgne TL, Hochreutener R, Lavenant N (2014) Active-distributed temperature sensing to continuously quantify vertical flow in boreholes. Water Resources Research 50: 3706-3713 DOI 10.1002/2014WR015273
Reimann T, Rehrl C, Shoemaker WB, Geyer T, Birk S (2011) The significance of turbulent flow representation in single-continuum models. Water Resources Research 47: 1-15 DOI 10.1029/2010WR010133
Rihas G (2010) Wiener Wasser ("Water of Vienna")ORF Universum Film 2010 Magistratsabteilung 31 and ORF.
Rimmer A, Hartmann A (2014) Optimal hydrograph separation filter to evaluate transport routines of hydrological models. Journal of Hydrology 514: 249-257 DOI https://doi.org/10.1016/j.jhydrol.2014.04.033
Rimmer A, Salingar Y (2006) Modelling precipitation-streamflow processes in karst basin: The case of the Jordan River sources, Israel. Journal of Hydrology 331: 524-542 DOI https://doi.org/10.1016/j.jhydrol.2006.06.003
Rollmann P, Spindler K (2015) Explicit representation of the implicit Colebrook–White equation. Case Studies in Thermal Engineering 5: 41-47 DOI https://doi.org/10.1016/j.csite.2014.12.001
Rorabaugh MI (1964) Estimating changes in bank storage and ground-water contribution to streamflow: 432-441
Rubinato M, Shucksmith J, Saul AJ, Shepherd W (2013) Comparison between InfoWorks hydraulic results and a physical model of an urban drainage system. Water Sci Technol 68: 372-379 DOI 10.2166/wst.2013.254
Runkel RL (2015) On the use of rhodamine WT for the characterization of stream hydrodynamics and transient storage. Water Resources Research 51: 6125-6142 DOI 10.1002/2015WR017201
Rushton KR, Ward C (1979) The estimation of groundwater recharge. Journal of Hydrology 41: 345-361 DOI https://doi.org/10.1016/0022-1694(79)90070-2
Rushton KR, Wedderburn LA (1973) Starting Conditions for Aquifer Simulations. Ground Water 11: 37-42 DOI 10.1111/j.1745-6584.1973.tb02956.x
Rutledge AT (1998) Computer programs for describing the recession of ground-water discharge and for estimating mean ground-water recharge and discharge from streamflow records-updateWater-Resources Investigations Report, Supercedes WRI 93-4121 edn.

Santos IR, Niencheski F, Burnett W, Peterson R, Chanton J, Andrade CFF, Milani IB, Schmidt A, Knoeller K (2008) Tracing anthropogenically driven groundwater discharge into a coastal lagoon from southern Brazil. Journal of Hydrology 353: 275-293 DOI http://dx.doi.org/10.1016/j.jhydrol.2008.02.010
Sauter M, Geyer T, Kovács A, Teutsch G (2006) Modelling karst groundwater hydraulics – An overview. Grundwasser 11: 143-156 DOI 10.1007/s00767-006-0140-0
Schlumberger (n.k.) Groundwater Monitoring Solutions - Diver.
Schnegg P-A (2002) An inexpensive field fluorometer for hydrogeological tracer tests with three tracers and turbidity measurement. Paper presented at the Groundwater and Human Development, Mar del Plata, Argentina, 21-25 October 2002
Schroeder MR (1991) Fractals, chaos, power laws : minutes from an infinite paradise / Manfred Schroeder, pp. 0-0.
Schubert M, Scholten J, Schmidt A, Comanducci FJ, Pham KM, Mallast U, Knoeller K (2014) Submarine groundwater discharge at a single spot location: Evaluation of different detection approaches. Water 6 DOI 10.3390/w6030584
Schuler P, Duran L, Johnston PM, Gill L (2019a) Quantifying submarine and intertidal groundwater discharge and linearity of the coastal karst aquifer Bell Harbour. Irish Groundwater Newsletter: 22-26
Schuler P, Duran L, McCormack T, Gill L (2018a) Submarine and intertidal groundwater discharge through a complex multi-level karst conduit aquifer. Hydrogeology Journal 28: 2629-2647 DOI 10.1007/s10040-018-1821-3
Schuler P, Stoeckl L, Bunce C, Gill L (2018b) A method for tracing submarine groundwater discharge from a coastal karst aquifer. Paper presented at the Geoscience 2018, Dublin, Ireland, 6th of November 2018b
Schuler P, Stoeckl L, Schnegg P-A, Bunce C, Gill L (2019b) A combined-method approach to trace submarine groundwater discharge from a coastal karst aquifer in Ireland. Hydrogeology Journal DOI 10.1007/s10040-019-02082-0
Seametrics (2016a) INW CT2X Instructions, Kent, Washington, pp. 27.
Seametrics (2016b) INW PT2X Instructions, Kent, Washington, pp. 27.
Sekulic B, Vertacnik ACfMR, Ruder Boskovic Institute, POB 1016, 10001 Zagreb (Croatia)) (1996) Balance of average annual fresh water inflow into the Adriatic Seav. 12
Sevastopulo GD, Wyse Jackson PN (2009) Carboniferous: Mississippian (Tournaisian and Viséan). In: Holland CH, Sanders I (eds) The Geology of Ireland, 2nd edn:568.
Shevenell L (1996) Analysis of well hydrographs in a karst aquifer: estimates of specific yields and continuum transmissivities. Journal of Hydrology 174: 331-355 DOI http://dx.doi.org/10.1016/0022-1694(95)02761-0
Shoemaker WB, Kuniansky EL, Birk S, Bauer S, Swain ED (2008) Documentation of a Conduit Flow Process (CFP) for MODFLOW-2005Techniques and Methods, Book 6, Chapter A24 U.S. Geological Survey, Reston, Virginia, pp. 50.
Shuttleworth WJ (1993) Evaporation. In: Maidment DR (ed) Handbook of hydrology:4.1-4.53.
Siegel D (2008) Reductionist hydrogeology: ten fundamental principles. Hydrological Processes 22: 4967-4970 DOI 10.1002/hyp.7139
Simms MJ (2014) Karst and Paleokarst. Reference Module in Earth Systems and Environmental Sciences: 1-10 DOI http://dx.doi.org/10.1016/B978-0-12-409548-9.09370-2
Singleton RC (1979) Mixed Radix Fast Fourier TransformsPrograms for Digital Signal Processing.
Sinreich M, Flynn RM (2006) Comparative tracing experiments to investigate epikarst structural and compositional heterogeneity. In: Goldscheider N, Mudry J, Savoy L, Zwahlen F (eds) 8th Conference on Limestone Hydrogeology Presses universitaires de Franche-Comté, Neuchâtel (Switzerland), pp. 253-258.
Sloto RA, Crouse MY (1996) HYSEP: A Computer Program for Streamflow Hydrograph Separation and AnalysisWater-Resources Investigations Report.
Smart C, Simpson B (2002) Detection of fluorescent compounds in the environment using granular activated charcoal detectors. Environmental Geology 42: 538-545 DOI 10.1007/s00254-001-0517-4
Smith AJ, Nield SP (2003) Groundwater discharge from the superficial aquifer into Cockburn Sound Western Australia: Estimation by inshore water balance. Biogeochemistry 66: 125-144 DOI 10.1023/B:BIOG.0000006152.27470.a9
Solinst (2017) LTC Levelogger Edge - Model 3001 Data Sheet, Georgetown, Canada.

Solinst (2018) Levelogger Series - Model 3001 Data Sheet, Georgetown, Canada.
Spongberg ME (2000) Spectral analysis of base flow separation with digital filters. Water Resources Research 36: 745-752 DOI 10.1029/1999WR900303
Stowell J (2013) Optimizing the measurement of fluid flow in boreholes -a review of current hardware and applicationsSymposium on the Application of Geophysics to Engineering and Environmental Problems 2013, Symposium on the Application of Geophysics to Engineering and Environmental Problems:589-600.
Sutton DJ, Kabala ZJ, Francisco A, Vasudevan D (2001) Limitations and potential of commercially available rhodamine WT as a groundwater tracer. Water Resources Research 37: 1641-1656 DOI 10.1029/2000WR900295
Sutton JE, Screaton EJ, Martin JB (2015) Insights on surface-water/groundwater exchange in the upper Floridan aquifer, north-central Florida (USA), from streamflow data and numerical modeling. Hydrogeology Journal 23: 305-317 DOI 10.1007/s10040-014-1213-2
Tamborski JJ, Rogers AD, Bokuniewicz HJ, Cochran JK, Young CR (2015) Identification and quantification of diffuse fresh submarine groundwater discharge via airborne thermal infrared remote sensing. Remote Sensing of Environment 171: 202-217 DOI http://dx.doi.org/10.1016/j.rse.2015.10.010
Taniguchi M, Burnett WC, Cable JE, Turner JV (2002) Investigation of submarine groundwater discharge. Hydrological Processes 16: 2115-2129 DOI 10.1002/hyp.1145
Taniguchi M, Burnett WC, Cable JE, Turner JV (2003) Assessment methodologies for submarine groundwater dischargeLand and Marine Hydrogeology:1-23.
Taniguchi M, Fukuo Y (1996) An Effect of Seiche on Groundwater Seepage Rate into Lake Biwa, Japan. Water Resources Research 32: 333-338 DOI 10.1029/95WR03245
Taniguchi M, Ono M, Takahashi M (2015) Multi-scale evaluations of submarine groundwater discharge. Proc IAHS 365: 66-71 DOI 10.5194/piahs-365-66-2015
Teagasc, Cranfield-University (2014) Irish National Soils Map, 1:250,000k, V1b(2014) edn.
TeledyneISCO (2015) 6712 Portable Samplers - Installation and Operation Guide Teledyne Isco.
Teutsch G (1989) Groundwater models in karstified terrains: two practical examples from the Swabian Alb (S. Germany)Solving Ground Water Problems with Models International Ground Water Modeling Center, Indianapolis, Indiana, pp. 929–953.
Teutsch G, Sauter M (1991) Groundwater modeling in karst terranes: Scale effects, data acquisition and field validationThird Conference Hydrogeology, Ecology, Monitoring, and Management of Ground Water in Karst Terranes, Nashville, TN, pp. 17-35.
Thermo (2004) Konelab Reference Manual Thermo Electron Oy, Vantaa, Finland.
Thompson C, Smith L, Maji R (2007) Hydrogeological modeling of submarine groundwater discharge on the continental shelf of Louisiana. Journal of Geophysical Research: Oceans 112: 1-13 DOI 10.1029/2006JC003557
Thrailkill J (1974) Pipe Flow Models of a Kentucky Limestone Aquifer. Ground Water 12: 202-205 DOI 10.1111/j.1745-6584.1974.tb03023.x
Tooth AF, Fairchild IJ (2003) Soil and karst aquifer hydrological controls on the geochemical evolution of speleothem-forming drip waters, Crag Cave, southwest Ireland. Journal of Hydrology 273: 51-68 DOI http://dx.doi.org/10.1016/S0022-1694(02)00349-9
Torrence C, Compo GP (1998) A Practical Guide to Wavelet Analysis. Bulletin of the American Meteorological Society 79: 61-78 DOI 10.1175/1520-0477(1998)079<0061:APGTWA>2.0.CO;2
Torrence C, Webster PJ (1999) Interdecadal Changes in the ENSO–Monsoon System. J Clim 12: 2679-2690 DOI 10.1175/1520-0442(1999)012<2679:ICITEM>2.0.CO;2
TRADA Wood Species Database (2018) UK Timber Research and Development Association (TRADA), 2018
Trček B, Zojer H (2010) Chapter 3 - Recharge of springs. In: Kresic N, Stevanovic Z (eds) Groundwater Hydrology of Springs:87-127.
Trescott PC, Larson SP (1976) Documentation of finite-difference model for simulation of three-dimensional ground-water flowOpen-File Report, - edn.
Tritz S, Guinot V, Jourde H (2011) Modelling the behaviour of a karst system catchment using non-linear hysteretic conceptual model. Journal of Hydrology 397: 250-262 DOI http://dx.doi.org/10.1016/j.jhydrol.2010.12.001

Uhlenbrook S, Frey M, Leibundgut C, Maloszewski P (2002) Hydrograph separations in a mesoscale mountainous basin at event and seasonal timescales. Water Resources Research 38: 31-31-31-14 DOI 10.1029/2001WR000938
UNESCO/IAEA (2001a) Environmental Isotopes in the hydrological cycle. Principles and applicationsIHP-V Technical Documents in Hydrology, Nº 39 UNESCO – IAEA.
UNESCO/IAEA (2001b) Environmental Isotopes in the hydrological cycle. Principles and applicationsIHP-V Technical Documents in Hydrology, Nº 39 UNESCO – IAEA.
Valdes D, Dupont J-P, Massei N, Laignel Bt, Rodet J (2006) Investigation of karst hydrodynamics and organization using autocorrelations and T–ΔC curves. Journal of Hydrology 329: 432-443 DOI http://dx.doi.org/10.1016/j.jhydrol.2006.02.030
Valens C (1999) A really friendly guide to wavelets, pp. 19.
Van den Daele GFA, Barker JA, Connell LD, Atkinson TC, Darling WG, Cooper JD (2007) Unsaturated flow and solute transport through the Chalk: Tracer test and dual permeability modelling. Journal of Hydrology 342: 157-172 DOI https://doi.org/10.1016/j.jhydrol.2007.05.021
van Geldern R, Barth JAC (2012) Optimization of instrument setup and post-run corrections for oxygen and hydrogen stable isotope measurements of water by isotope ratio infrared spectroscopy (IRIS). Limnology and Oceanography: Methods 10: 1024-1036 DOI 10.4319/lom.2012.10.1024
Varian (1999) Liberty Series II Analytical Methods book.
Vasudevan D, Fimmen RL, Francisco AB (2001) Tracer-Grade Rhodamine WT: Structure of Constituent Isomers and Their Sorption Behavior. Environmental Science & Technology 35: 4089-4096 DOI 10.1021/es010880x
Venables WN, Ripley BD (2002) Modern Applied Statistics With S, 4 edn Springer
Wagner T, Mayaud C, Benischke R, Birk S (2013) A better understanding of the Lurbach karst system via a conceptional rainfall-runoff model. Grundwasser 18: 225-235 DOI 10.1007/s00767-013-0234-4
Walawender JP, Hajto MJ, Iwaniuk P (2012) A new ArcGIS toolset for automated mapping of land surface temperature with the use of LANDSAT satellite data2012 IEEE International Geoscience and Remote Sensing Symposium, pp. 4371-4374.
Walker JS (1999) A primer on wavelets and their scientific applications Chapman & Hall/CRC, Boca Raton, Florida. ; London
Wallingford (2006) Groundwater Infiltration Module Technical Note 2, Wallingford, Oxfordshire, U.K.
Walsh JJ, Moore JP, Bunce C, Hollis SP, Kelly J, Menuge JF (in review) The origin and nature of hydraulic fractures and veins within The Burren, County Clare, Ireland. Irish Journal of Earth Sciences
Wang HF (1995) Introduction to groundwater modeling : finite difference and finite element methods Academic Press, San Diego ; London
Wels C, Cornett RJ, Lazerte BD (1991) Hydrograph separation: A comparison of geochemical and isotopic tracers. Journal of Hydrology 122: 253-274 DOI https://doi.org/10.1016/0022-1694(91)90181-G
White WB (1988) Geomorphology and hydrology of Karst terrains Oxford University Press
White WB, White EL (2005) Ground water flux distribution between matrix, fractures, and conduits: constraints on modeling. Speleogenesis And Evolution Of Karst Aquifers 3: 1-6
Williams PW (2008) The role of the epikarst in karst and cave hydrogeology: a review. International Journal of Speleology 37: 1-10
Wilson J, Rocha C (2012) Regional scale assessment of submarine groundwater discharge in Ireland combining medium resolution satellite imagery and geochemical tracing techniques. Remote Sensing of Environment 119: 21-34 DOI http://dx.doi.org/10.1016/j.rse.2011.11.018
Winston WE, Criss RE (2004) Dynamic hydrologic and geochemical response in a perennial karst spring. Water Resources Research 40: 1-11 DOI 10.1029/2004WR003054
WMO (2008) Guide to Meteorological Instruments and Methods of Observation, 2008 edition edn World Meteorological Organization, Geneva, Switzerland.
Worthington S, Ford D, Beddows P (2000) Porosity and permeability enhancement in unconfined carbonate aquifers as a result of solution. In: Klimchouk AB, Ford DC, Palmer AN, Dreybrodt W (eds) Speleogenesis: evolution of karst aquifers:463-472.

Yevjevich V (1993) General Introduction to application of Stochastic Hydrology In: Marco JB, Harboe R, Salas JD (eds) Stochastic Hydrology and its Use in Water Resources Systems Simulation and Optimization, Proceedings of the NATO Advanced Study Institute:3-23.

Zektser IS, Dzhamalov RG, Everett LG (2007) Submarine Groundwater CRC/Taylor & Francis, Boca Raton, USA

Zeng Z, Grigg R (2006) A Criterion for Non-Darcy Flow in Porous Media. Transport in Porous Media 63: 57-69 DOI 10.1007/s11242-005-2720-3

Appendix A: Photos

Appendix A1: Photos Ballindine

Figure A.1: Upstream view on Ballindine spring with the EPA gauging station on the right side.

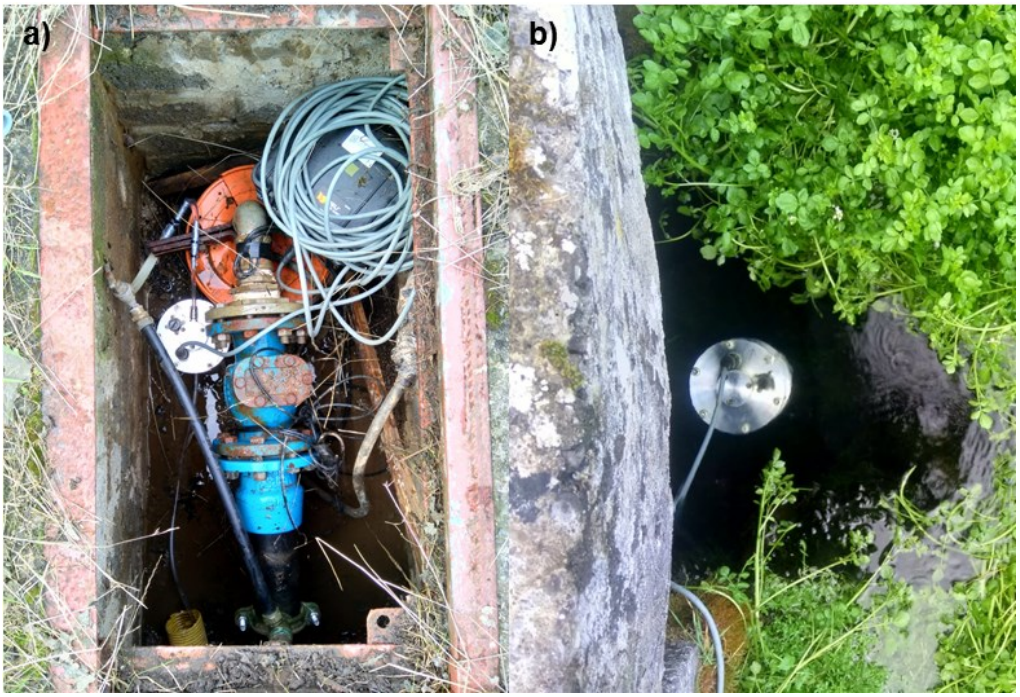

Figure A.2: Observation of tracer results at a) OS 2 and b) OS 1.

Figure A.3: Injection of tracers at a) IS-b, b) IS-a and c) IS-c.

Appendix A2: Photos Bell Harbour

Figure A.4: Discharge measurement taken in the Fergus River at Crossard Bridge.

Figure A.5: View over Carron depression in a) December 2015 and b) February 2016.

Figure A.6: Sampling sites of a) CAN and b) CAS.

Figure A.7: Weather station (C1) at the BOEC including rainfall sampler and rainfall collector (a) and rainfall collector at FN (b).

Figure A.8: Borehole BH1 during a single borehole dilution test (SBDT, a) and during automated sampling using an ISCO auto sampler (b) and borehole BH2 (c).

Figure A.9: Turlough Gortboyheen (T1).

Figure A.10: Waterfall in Poll Gonzo.

Figure A.11: Offshore buoy sampler before (a) and after (b) installation and monitoring of the inter-tidal spring Pouldoody (c).

Appendix A3: Photos Manorhamilton

Figure A.12: EPA gauging station Manorhamilton spring (MH3, a) and discharges at b) MH2 and c) MH1.

Figure A.13: Rainfall collection (left) and sampling (right) at MH3.

Figure A.14: Tracer injections at a) IS-a, b) IS-b and c) IS-c.

Appendix B: Hydrochemistry data

Appendix B1: Hydrochemistry Ballindine

Table B.1: Hydrochemistry data of Ballindine spring.

Date / time UTC	pH	alkalinity CaCO3 [mg/l]	Cl [mg/l]	NH4 [mg/l]	NO2 [mg/l]	TON [mg/l]	NO3 [mg/l]	SO4 [mg/l]	SiO2 [mg/l]	d18O VSMOW	sd	d2H VSMOW	sd	DE
20/07/2017 10:00		643.13	18.08	0.00	0.00	1.65	1.65			-6.35	0.01	-39.77	0.19	11.02
12/09/2017 18:20	6.86	337.38	19.71	0.00	0.00	1.87	1.87	10.27		-6.23	0.06	-38.97	0.15	10.89
14/09/2017 07:15	6.85	310.77	19.60	0.00	0.00	1.81	1.81	9.00		-6.20	0.06	-38.46	0.11	11.12
07/07/2017 10:15										-6.52	0.13	-40.10	0.50	12.06

Appendix B2: Hydrochemistry Bell Harbour

Table B.2: Hydrochemistry data of C1.

Date / time UTC	pH	alkalinity CaCO3 [mg/l]	Cl [mg/l]	NH4 [mg/l]	NO2 [mg/l]	TON [mg/l]	NO3 [mg/l]	SO4 [mg/l]	SiO2 [mg/l]	d18O VSMOW	sd	d2H VSMOW	sd	DE
30/03/2017			24.33					0.00		-3.81	0.08	-21.24	0.16	9.26
06/04/2017			25.37					0.00		-3.04	0.04	-20.60	0.26	3.76
20/04/2017			39.31					0.00		-1.24	0.02	-3.72	0.07	6.17
27/04/2017			46.20					0.23						
04/05/2017			32.49					0.00		-1.92	0.05	-6.37	0.12	9.02
18/05/2017			24.81					1.38		-4.86	0.06	-31.37	0.13	7.53
25/05/2017			25.06					0.00		-3.34	0.04	-20.31	0.17	6.41
17/06/2017										-2.06	0.05	-10.77	0.10	5.69
23/06/2017										-2.05	0.05	-12.13	0.04	4.31
25/06/2017										-2.22	0.07	-9.83	0.17	7.97
28/06/2017										-5.90	0.04	-39.96	0.21	7.28
06/07/2017										-3.56	0.05	-21.59	0.16	6.91
13/07/2017										-2.69	0.06	-17.13	0.03	4.43
16/07/2017										-1.11	0.05	-4.02	0.20	4.83
22/07/2017										-12.82	0.01	-93.42	0.21	9.15
28/07/2017										-4.12	0.07	-24.29	0.18	8.69
03/08/2017										-6.03	0.05	-42.16	0.17	6.10
10/08/2017										-4.18	0.06	-26.17	0.13	7.28
17/08/2017										-3.84	0.06	-23.43	0.12	7.26
24/08/2017										-4.76	0.02	-31.67	0.08	6.44
11/09/2017										-5.09	0.02	-33.26	0.11	7.48
21/09/2017										-5.87	0.03	-36.82	0.10	10.15
28/09/2017										-5.40	0.01	-34.80	0.10	8.37
06/10/2017										-3.10	0.03	-12.96	0.19	11.82
13/10/2017										-2.94	0.02	-15.71	0.10	7.83

26/10/2017	6.07	0.43	15.17	0.00	0.00	0.00	0.00	3.16	0.07	-5.74	0.02	-36.93	0.04	8.97
07/11/2017 08:15										-6.65	0.01	-34.56	0.07	18.62
10/11/2017 13:00										-2.75	0.03	-8.83	0.07	13.13
19/11/2017										-4.49	0.03	-24.50	0.10	11.42
24/11/2017										-8.39	0.02	-54.50	0.10	12.62
30/11/2017										-5.04	0.01	-23.20	0.10	17.12
07/12/2017										-5.32	0.07	-34.50	0.40	8.06
14/12/2017										-16.45	0.03	-119.50	0.40	12.10
02/01/2018										-7.18	0.04	-45.70	0.20	11.74
11/01/2018										-7.99	0.03	-48.80	0.20	15.12
18/01/2018										-7.37	0.03	-46.90	0.20	12.06
26/01/2018										-5.20	0.06	-31.10	0.30	10.50
01/02/2018										-5.51	0.05	-35.70	0.20	8.38
08/02/2018										-5.33	0.01	-28.20	0.10	14.44
15/02/2018										-6.52	0.05	-35.70	0.10	16.46
23/02/2018										-6.78	0.06	-34.80	0.30	19.44
16/03/2018										-9.21	0.09	-67.40	0.80	6.28
22/03/2018										-6.53	0.12	-45.20	0.20	7.04
01/04/2018										-7.27	0.19	-48.20	0.70	9.96

Table B.3: Hydrochemistry data of FN.

Date / time UTC	pH	alkalinity CaCO3 [mg/l]	Cl [mg/l]	NH4 [mg/l]	NO2 [mg/l]	TON [mg/l]	NO3 [mg/l]	SO4 [mg/l]	SiO2 [mg/l]	d18O VSMOW	sd	d2H VSMOW	sd	DE
04/11/2017 08:00	6.90	3.34	13.82	0.11	0.00	0.00	0.00	0.00	0.06	-5.55	0.02	-22.36	0.13	22.03
06/11/2017 13:00		1.04	24.93	0.11	0.00	0.00	0.00		0.06	-6.16	0.02	-25.87	0.09	23.39
07/11/2017 08:00										-9.67	0.01	-62.13	0.10	15.26
10/11/2017 11:15	7.05	0.96	18.67	0.00	0.00	0.00	0.00	1.52	0.05	-1.89	0.03	-3.44	0.21	11.68

Table B.4: Hydrochemistry data of NUIG.

Date / time UTC	pH	alkalinity CaCO3 [mg/l]	Cl [mg/l]	NH4 [mg/l]	NO2 [mg/l]	TON [mg/l]	NO3 [mg/l]	SO4 [mg/l]	SiO2 [mg/l]	d18O VSMOW	sd	d2H VSMOW	sd	DE
07/11/2017 07:30										-6.72	0.03	-37.57	0.31	16.17
10/11/2017 11:00										-3.91	0.03	-15.02	0.16	16.29

Table B.5: Hydrochemistry data of BH1.

Date / time UTC	pH	alkalinity CaCO3 [mg/l]	Cl [mg/l]	NH4 [mg/l]	NO2 [mg/l]	TON [mg/l]	NO3 [mg/l]	SO4 [mg/l]	SiO2 [mg/l]	d18O VSMOW	sd	d2H VSMOW	sd	DE
09/06/2017 14:15	7.51	322.05	9.03	0.00	0.00	1.55	1.55	11.43	0.00	-5.51	0.03	-34.45	0.11	9.61
25/06/2017 10:37		395.96	21.66	0.00	0.00	1.98	1.98	5.82		-5.54	0.09	-34.07	0.26	10.22
25/06/2017 11:10	7.17													
25/06/2017 11:30	7.22	350.27	20.07	0.00	0.00	1.66	1.66	5.44		-5.28	0.02	-32.88	0.29	9.33
25/06/2017 12:22	7.21													
25/06/2017 12:30		309.13	17.49	0.00	0.00	1.63	1.63	5.34		-5.10	0.08	-31.46	0.55	9.37
25/06/2017 13:25	6.70													
25/06/2017 13:30		298.22	17.36	0.00	0.00	1.18	1.18	5.18		-5.02	0.06	-31.25	0.22	8.92
25/06/2017 14:00	7.16													
25/06/2017 14:30		282.00	18.89	0.00	0.00	1.23	1.23	5.65		-5.02	0.06	-31.14	0.11	9.05
25/06/2017 15:25	6.82													
25/06/2017 15:30		289.57	19.66	0.00	0.00	1.61	1.61	5.42		-5.00	0.06	-30.96	0.09	9.06
25/06/2017 16:25	7.20													
25/06/2017 16:30		305.50	22.02	0.00	0.00	1.94	1.94	5.44		-5.03	0.09	-31.04	0.09	9.22
25/06/2017 17:00	6.80													
25/06/2017 17:30	7.24	305.49	20.71	0.00	0.00	1.66	1.66	5.21		-5.04	0.04	-30.95	0.24	9.39
12/07/2017 07:30	7.29	592.79	16.92	0.00	0.00	4.19	4.19			-6.00	0.02	-37.15	0.19	10.82
16/07/2017 14:30	7.27	572.16	19.71	0.00	0.00	4.25	4.25	2.63		-5.99	0.03	-36.75	0.14	11.16
26/10/2017 08:45	7.00	519.52	15.51	0.00	0.00	1.89	1.89	2.80	2.31	-4.94	0.01	-30.48	0.13	9.02
30/10/2017 16:30	7.12	283.92	15.38	0.00	0.00	3.81	3.81	7.33	2.48	-4.80	0.02	-30.33	0.09	8.08

30/10/2017 16:30	7.00	576.80	15.87	0.00	0.00	3.86	3.86	2.75	2.44	-4.82	0.03	-30.26	0.12	8.26
30/10/2017 23:00	7.69	287.57	16.30	0.00	0.00	3.83	3.83	7.27	2.47	-4.80	0.02	-30.03	0.15	8.39
30/10/2017 23:00	7.66	262.74	15.95	0.00	0.00	3.83	3.83	5.19	2.50	-4.84	0.02	-30.38	0.22	8.36
31/10/2017 07:00	7.60	271.34	16.50	0.00	0.00	3.79	3.79	4.68	2.47	-4.81	0.02	-30.13	0.06	8.35
31/10/2017 15:00	7.63	274.27	15.67	0.00	0.00	3.77	3.77	3.96	2.48	-4.83	0.02	-30.27	0.21	8.38
31/10/2017 23:00	7.54	252.66	14.69	0.00	0.00	3.90	3.90	3.88	2.42	-4.83	0.02	-30.27	0.07	8.39
01/11/2017 07:00	7.54	290.96	16.01	0.00	0.00	3.81	3.81	3.33	2.41	-4.83	0.03	-30.31	0.10	8.35
01/11/2017 15:00	7.61	281.29	16.89	0.00	0.00	3.89	3.89	3.43	2.43	-4.82	0.01	-30.28	0.20	8.25
01/11/2017 23:00	7.39	266.33	16.97	0.00	0.00	3.83	3.83	3.73	2.41	-4.84	0.01	-30.35	0.11	8.40
02/11/2017 07:00	7.31	269.89	17.07	0.00	0.00	3.78	3.78	2.33	2.36	-4.83	0.01	-30.21	0.07	8.42
02/11/2017 15:00	7.36	279.29	15.90	0.00	0.00	3.80	3.80	3.35	2.37	-4.86	0.03	-30.55	0.23	8.30
03/11/2017 00:00	7.26	270.45	15.13		0.00	3.81	3.81	2.44	2.34	-4.82	0.06	-31.24	0.42	7.33
03/11/2017 08:00	7.32	262.76	14.82	0.00	0.00	3.75	3.75	3.04	2.35	-4.77	0.05	-30.07	0.44	8.11
03/11/2017 16:00	7.34	274.57	14.99	0.00	0.00	3.98	3.98	2.52	2.38	-4.84	0.02	-30.35	0.19	8.35
03/11/2017 17:00	7.39	276.87	15.58	0.00	0.00	3.92	3.92	0.73	2.38	-4.82	0.03	-30.28	0.04	8.30
03/11/2017 18:00	7.41	269.94	16.47	0.00	0.00	3.88	3.88	1.62	2.38	-4.85	0.01	-30.57	0.17	8.21
03/11/2017 19:00	7.41	271.75	15.86	0.00	0.00	3.94	3.94	2.41	2.69	-4.79	0.02	-30.19	0.12	8.16
03/11/2017 20:00	7.39	265.82	14.89	0.00	0.00	4.09	4.09	1.31	2.36	-4.82	0.04	-30.30	0.16	8.28
03/11/2017 21:00	7.37	271.82	15.24	0.00	0.00	3.99	3.99	3.24	2.41	-4.85	0.01	-30.42	0.09	8.35
03/11/2017 22:00	7.35	275.01	16.42	0.00	0.00	3.99	3.99	1.64	2.64	-4.85	0.02	-30.57	0.08	8.25
03/11/2017 23:00	7.46	266.68	16.99	0.00	0.00	4.07	4.07	1.25	2.40	-4.83	0.02	-30.40	0.08	8.28
04/11/2017 01:00	7.40	264.85	16.04	0.00	0.00	4.15	4.15	1.83	2.40	-4.82	0.03	-30.25	0.09	8.27
04/11/2017 03:00	7.33	270.96	15.83	0.00	0.00	4.06	4.06	1.14	2.39	-4.84	0.02	-30.42	0.07	8.32
04/11/2017 05:00	7.19	271.35	15.44	0.00	0.00	4.06	4.06	1.00	2.38	-4.85	0.01	-30.36	0.12	8.40
04/11/2017 07:00	7.12	263.97	15.08	0.00	0.00	4.03	4.03	1.83	2.40	-4.81	0.01	-30.26	0.13	8.19
04/11/2017 09:00	7.09	277.67	15.78	0.00	0.00	4.04	4.04	1.46	2.41	-4.84	0.02	-30.48	0.19	8.20
06/11/2017 11:00	6.74	267.97	16.48	0.00	0.00	3.89	3.89	5.41	2.32	-4.84	0.04	-30.28	0.12	8.45
06/11/2017 18:00	6.69	273.63	17.49	0.00	0.00	4.29	4.29	5.33	2.35	-4.77	0.03	-30.05	0.05	8.09
06/11/2017 20:00	6.76	269.96	17.25	0.00	0.00	4.10	4.10	4.75	2.34	-4.83	0.04	-30.40	0.32	8.24
06/11/2017 21:00	6.93	269.22	17.40	0.00	0.00	4.13	4.13	4.48	2.34	-4.82	0.03	-30.17	0.15	8.42

06/11/2017 22:00	6.97	270.10	16.19	0.00	0.00	4.07	4.07	4.46	2.33	-4.83	0.06	-30.49	0.52	8.16
06/11/2017 23:00	7.05	273.55	16.02	0.00	0.00	4.16	4.16	5.26	2.34	-4.84	0.04	-30.20	0.31	8.48
07/11/2017 00:00	7.04	276.00	16.28	0.00	0.00	4.14	4.14	5.19	2.33	-4.83	0.02	-30.31	0.10	8.36
07/11/2017 01:00	7.14	281.08	12.63	0.00	0.00	1.77	1.77	3.54	2.20	-4.89	0.04	-30.52	0.20	8.59
07/11/2017 02:00	7.12	260.24	15.97	0.00	0.00	3.34	3.34	1.91	2.26	-4.98	0.07	-31.80	0.31	8.07
07/11/2017 03:00	7.04	268.65	11.79	0.00	0.00	1.75	1.75	3.56	2.16	-4.98	0.02	-31.64	0.21	8.23
07/11/2017 04:00	7.13	259.45	13.52	0.00	0.00	1.53	1.53	2.61	2.20	-5.01	0.03	-31.36	0.11	8.76
07/11/2017 05:00	6.84	241.91	14.63	0.00	0.00	1.37	1.37	2.69	2.16	-5.06	0.01	-30.98	0.17	9.48
07/11/2017 06:00	6.88	215.42	14.30	0.00	0.00	1.25	1.25	3.59	1.99	-5.06	0.03	-30.47	0.10	9.98
07/11/2017 07:00	6.91	205.12	14.08	0.00	0.00	1.23	1.23	1.13	1.86	-5.03	0.01	-30.19	0.14	10.05
07/11/2017 08:00	6.94	202.42	14.48	0.00	0.00	1.14	1.14	1.26	1.83	-5.02	0.01	-30.14	0.08	10.03
07/11/2017 11:00	7.13	383.95	14.20	0.00	0.00	1.19	1.19	1.06	1.71	-4.97	0.02	-29.45	0.14	10.27
07/11/2017 16:00	7.39	362.10	14.19	0.00	0.00	1.06	1.06	3.82	1.65	-4.89	0.02	-29.03	0.10	10.06
08/11/2017 00:00	7.43	272.99	14.96	0.00	0.00	0.60	0.60	3.53	1.35	-4.88	0.01	-28.00	0.08	11.04
08/11/2017 08:00	7.46	316.25	15.22	0.00	0.00	0.77	0.77	2.25	1.53	-4.89	0.02	-28.08	0.06	11.08
08/11/2017 16:00	7.50	377.90	15.71	0.00	0.00	1.00	1.00	2.62	1.72	-4.88	0.02	-28.46	0.18	10.56
09/11/2017 00:00	7.50	201.20	16.35	0.00	0.00	1.10	1.10	1.86	1.77	-4.88	0.02	-28.47	0.13	10.60
09/11/2017 08:00	7.47	207.21	16.91	0.00	0.00	1.45	1.45	2.27	1.88	-4.90	0.02	-29.21	0.07	9.99
09/11/2017 16:00	7.06	247.86	15.42	0.00	0.00	1.77	1.77	2.08	2.02	-4.87	0.01	-29.22	0.08	9.74
10/11/2017 00:00	7.04	254.29	15.86	0.00	0.00	1.74	1.74	1.54	2.10	-4.90	0.01	-29.58	0.15	9.58
10/11/2017 08:00	7.08	228.81	15.48	0.00	0.00	1.13	1.13	0.56	1.79	-4.91	0.01	-28.78	0.06	10.48
10/11/2017 12:00	7.08	193.44	15.57	0.00	0.00	1.18	1.18	1.64	1.78	-4.91	0.01	-28.83	0.03	10.47

Table B.6: Hydrochemistry data of CAN.

Date / time UTC	EC [µS/cm]	pH	alkalinity CaCO3 [mg/l]	Cl [mg/l]	NH4 [mg/l]	NO2 [mg/l]	TON [mg/l]	NO3 [mg/l]	SO4 [mg/l]	SiO2 [mg/l]	d18O VSMOW	sd	d2H VSMOW	sd	DE
16/07/2017 12:00	360.00	7.90	249.62	6.46	0.00	0.00	0.05	0.05	0.00		-4.26	0.08	-25.38	0.22	8.67
26/10/2017 10:45		7.18	237.16	14.35	0.00	0.00	0.00	0.00	0.52	1.04	-4.59	0.01	-25.67	0.12	11.07
03/11/2017 17:15		7.57	357.46	13.32	0.00	0.00	0.00	0.00	0.00	1.05	-4.65	0.06	-26.41	0.42	10.75

Table B.7: Hydrochemistry data of CAS.

Date / time UTC	EC [µS/cm]	pH	alkalinity CaCO3 [mg/l]	Cl [mg/l]	NH4 [mg/l]	NO2 [mg/l]	TON [mg/l]	NO3 [mg/l]	SO4 [mg/l]	SiO2 [mg/l]	d18O VSMOW	sd	d2H VSMOW	sd	DE
09/06/2017 09:30	355.00	8.11	204.57	4.39	0.01	0.00	0.02	0.02	4.56		-5.18	0.05	-32.06	0.14	9.36
25/06/2017 08:45	400.00	7.50	277.45	14.80	0.00	0.00	0.00	0.00	5.31		-4.48	0.04	-26.60	0.18	9.27
16/07/2017 11:30	413.00	7.91	314.19	8.87	0.00	0.00	0.00	0.00	0.00		-4.37	0.03	-26.29	0.24	8.68
26/10/2017 10:30		7.56	264.94	13.84	0.00	0.00	0.00	0.00	0.42	1.49	-4.66	0.03	-26.41	0.23	10.91

Table B.8: Hydrochemistry data of PG.

Date / time UTC	EC [µS/cm]	pH	alkalinity CaCO3 [mg/l]	Cl [mg/l]	NH4 [mg/l]	NO2 [mg/l]	TON [mg/l]	NO3 [mg/l]	SO4 [mg/l]	SiO2 [mg/l]	d18O VSMOW	sd	d2H VSMOW	sd	DE
12/07/2017 13:00	600.00	7.45	665.06	10.40	0.00	0.00	0.44	0.44	0.00		-5.38	0.09	-32.58	0.08	10.45

Table B.9: Hydrochemistry data of SiGD1.

Date / time UTC	EC [µS/cm]	pH	alkalinity CaCO3 [mg/l]	Cl [mg/l]	NH4 [mg/l]	NO2 [mg/l]	TON [mg/l]	NO3 [mg/l]	SO4 [mg/l]	SiO2 [mg/l]	d18O VSMOW	sd	d2H VSMOW	sd	DE
09/06/2017 11:30	39600.0	7.96	226.67	33.00	0.54	0.00	0.00	0.00	1368.96		-1.47	0.02	-8.59	0.15	3.16
16/07/2017 16:00	50000.0	8.53	192.05	0.00	0.54	0.00	0.00	0.00	59.38		-0.05	0.05	-0.27	0.04	0.12
26/10/2017 13:40		7.29	331.72	1968.23	0.00	0.00	0.00	0.00	428.45	2.10	-4.53	0.04	-27.38	0.14	8.85
03/11/2017 11:30		7.38	305.91	920.35	0.00	0.00	0.18	0.18	144.24	2.80	-5.07	0.03	-30.70	0.13	9.83

Appendix B3: Hydrochemistry Manorhamilton

Table B.10: Hydrochemistry data of rainfall at MH3.

Date / time UTC	pH	alkalinity CaCO3 [mg/l]	Cl [mg/l]	NH4 [mg/l]	NO2 [mg/l]	TON [mg/l]	NO3 [mg/l]	SO4 [mg/l]	SiO2 [mg/l]	d18O VSMOW	sd	d2H VSMOW	sd	DE
12/09/2017 15:00		2.09	3.75	0.16	0.00	0.00	0.00	4.14		-7.01	0.09	-41.93	0.12	14.17
12/09/2017 16:15										-8.30	0.04	-52.93	0.10	13.44
14/09/2017 09:30		1.33	8.36	0.00	0.00	0.00	0.00	4.16		-7.37	0.09	-46.67	0.18	12.29
21/09/2017 07:25			3.41							-7.21	0.04	-50.69	0.12	6.99

Table B.11: Hydrochemistry data of MH3.

Date / time UTC	pH	alkalinity CaCO3 [mg/l]	Cl [mg/l]	NH4 [mg/l]	NO2 [mg/l]	TON [mg/l]	NO3 [mg/l]	SO4 [mg/l]	SiO2 [mg/l]	d18O VSMOW	sd	d2H VSMOW	sd	DE
24/05/2017 16:15			20.30					7.91		-5.82	0.02	-34.79	0.22	11.75
13/08/2017 12:20			10.76							-5.52	0.04	-34.16	0.14	10.00
13/08/2017 16:42			9.26							-5.52	0.04	-34.20	0.11	9.92
12/09/2017 09:30	7.35	333.71	10.81	0.03	-0.04	0.19	0.19	4.23	1.78	-5.82	0.09	-36.29	0.25	10.25
12/09/2017 12:30	7.39	354.51	11.00	-0.08	-0.04	0.08	0.08	4.23	1.87	-5.79	0.16	-35.76	0.17	10.58
12/09/2017 15:30	7.34	371.05	11.42	-0.09	-0.04	0.09	0.09	3.96	1.93	-5.83	0.04	-35.87	0.09	10.81
12/09/2017 18:30	7.44	353.87	11.26	-0.07	-0.04	0.08	0.08	3.80	1.83	-5.88	0.03	-36.12	0.22	10.89
12/09/2017 21:30	7.41	247.25	11.13	-0.06	-0.04	0.34	0.34	3.91	1.66	-6.10	0.06	-37.56	0.25	11.28
13/09/2017 00:30	7.45	245.89	9.66	-0.09	-0.04	0.01	0.01	4.11	1.58	-6.22	0.05	-38.09	0.15	11.68
13/09/2017 03:30	7.55	284.56	10.03	-0.09	-0.04	0.03	0.03	4.49	1.59	-6.29	0.02	-38.64	0.09	11.66
14/09/2017 09:30	7.42	393.30	10.12	-0.10	-0.04	0.11	0.11	4.26	1.93	-6.32	0.08	-38.50	0.27	12.10
14/09/2017 15:30	8.08	192.87	10.81	-0.10	-0.04	0.06	0.06	5.29	1.94	-6.22	0.01	-38.39	0.24	11.36
14/09/2017 21:30	8.05	355.73	11.03	-0.10	-0.04	0.03	0.03	4.69	1.81	-6.30	0.10	-38.56	0.25	11.87
15/09/2017 03:30	8.00	385.33	10.98	-0.10	-0.04	0.02	0.02	4.67	1.79	-6.30	0.08	-38.54	0.24	11.86
15/09/2017 09:30	7.95	397.10	11.29	-0.10	-0.04	0.02	0.02	4.64	1.83	-6.10	0.05	-37.97	0.21	10.83
15/09/2017 15:30	7.89	207.04	11.47	-0.10	-0.04	0.03	0.03	4.28	1.89	-6.14	0.04	-37.58	0.13	11.53
15/09/2017 21:30	7.82	215.67	10.32	-0.09	-0.04	0.09	0.09	4.83	2.01	-6.14	0.03	-37.41	0.06	11.69

16/09/2017 03:30	7.77	214.72	9.53	-0.10	-0.04	0.12	0.12	4.69	2.09	-6.06	0.05	-37.29	0.10	11.22
16/09/2017 09:30	7.68	224.86	10.09	-0.09	-0.04	0.46	0.46	4.56	2.13	-6.08	0.02	-37.10	0.09	11.56
16/09/2017 17:30	7.61	225.63	10.46	-0.10	-0.04	0.14	0.14	4.42	2.21	-6.13	0.08	-36.99	0.24	12.03
21/09/2017 07:25	7.10	223.89	11.44	-0.10	-0.04	0.30	0.30	1.28		-5.99	0.04	-36.82	0.14	11.12
19/03/2018 12:00										-7.33	0.03	-42.81	0.15	15.81
30/05/2018 10:00										-6.88	0.03	-40.99	0.10	14.08
07/07/2018 12:00										-6.89	0.09	-40.20	0.20	14.92

Table B.12: Hydrochemistry data of MH2.

Date / time UTC	pH	alkalinity CaCO3 [mg/l]	Cl [mg/l]	NH4 [mg/l]	NO2 [mg/l]	TON [mg/l]	NO3 [mg/l]	SO4 [mg/l]	SiO2 [mg/l]	d18O VSMOW	sd	d2H VSMOW	sd	DE
24/05/2017 16:15			19.29					4.79		-5.74	0.03	-34.48	0.17	11.43
13/08/2017 12:15			9.94							-5.40	0.04	-33.57	0.23	9.62
13/08/2017 16:33			10.57							-5.37	0.03	-33.73	0.13	9.25
21/09/2017 07:15	6.78	224.02	11.76	0.00	0.00	0.30	0.30	1.25		-5.94	0.05	-36.92	0.11	10.63

Table B.13: Hydrochemistry data of MH1.

Date / time UTC	pH	alkalinity CaCO3 [mg/l]	Cl [mg/l]	NH4 [mg/l]	NO2 [mg/l]	TON [mg/l]	NO3 [mg/l]	SO4 [mg/l]	SiO2 [mg/l]	d18O VSMOW	sd	d2H VSMOW	sd	DE
24/05/2017 16:15			19.17					6.36		-5.79	0.02	-34.69	0.04	11.65
13/08/2017 12:07			10.19							-5.37	0.07	-33.70	0.25	9.25
13/08/2017 16:26			9.77							-5.39	0.05	-34.13	0.34	8.96
21/09/2017 07:05	6.89	223.32	10.53	0.00	0.00	0.29	0.29	1.33		-5.95	0.10	-36.92	0.36	10.70

Appendix C: SBDTs

Single borehole dilution test
Location: GAA pitch Bell Harbour
Date: **11-02-2017**
Injections: 1
Tracer: NaCl solution (125g/l)
Tracer quantity: 1,200 ml
Flushing solution: 850 ml tab water

Goals
1. Inject NaCl solution at the outlet point of the tube to identify vertical flow direction (upwards/downwards) and estimate the mean flow velocity and tracer recovery

Method
1. Establishing vertical CTD-background profile (a).
2. Installation of lower CTD sensor with a sampling rate of 30 s.
3. Installation of tubing system, incl. an attached CTD sensor on the bottom at -7 masl to measure time of tracer injection at outlet and concentration.
4. Installation of upper CTD sensor.
5. 1 injection was carried out:
   I. 2:43: injection at -7 masl following flushing using 850 ml tab water (b).

Problems
1. Upper sampler blocked the way and got tangled up with the tubing system and/or the weight attached to the bottom. Results of the upper diver not of use.

Results/Conclusions
1. Injection of tracer follows rapid disappearance of tracer at injection point.
2. Tracer cocktail does not arrive at the upper CTD sensor.
3. Tracer cocktail moves downwards passing by the lower sampler.
4. Time between release of tracer at tube outlet and arrival at the bottom sampler is ~30 s.
5. 100% tracer recovery.
6. Mean flow velocity estimated at 5.14 cm/s (185 m/h).

Tools
41 m tube Ø 6mm
Funnel
1,200 ml NaCl solution
850 ml tab water
Funnel
Schlumberger 86084 (tube outlet)
INW CT2X SN 21443061 (bottom)
INW CT2X SN 21443059 (top)

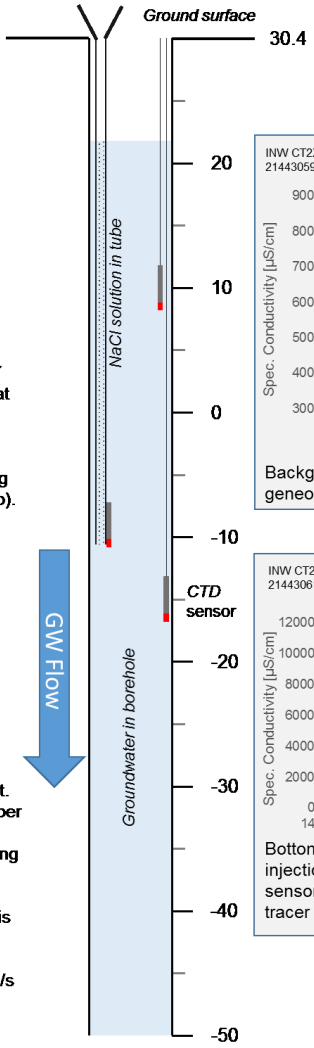

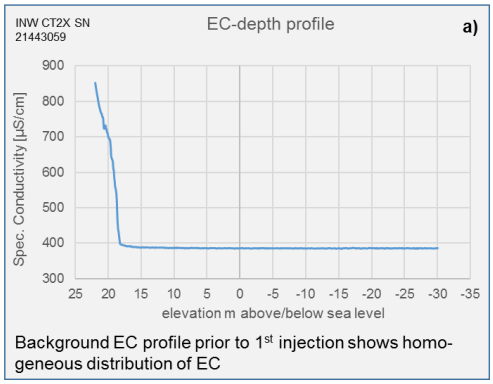

Background EC profile prior to 1st injection shows homogeneous distribution of EC

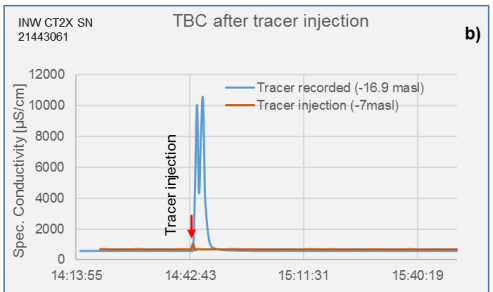

Bottom profile at 47.2 mbgl (-16.9 masl) during the tracer injection at 2:43:30 pm: EC readings of the bottom CTD sensor (10 m below tube bottom) show an arrival of the tracer within 30 s after injection

Figure C.1: SBDT conducted on 11 Feb 2017.

Single borehole dilution test

Location: GAA pitch Bell Harbour
Date: **26-02-2017**
Injections: 7
Tracer: NaCl solution (125g/l)
Tracer quantity: 500 ml
Flushing solution: 850 ml tab water

Goals

1. Inject NaCl solution at the outlet point of the tube to identify vertical flow direction (upwards/downwards), flow velocities and the tracer recovery.

Method

1. Establishing vertical CTD-background profile (a).
2. Installation of lower CTD sensor at -43.7 masl, sampling rate 1 s.
3. Installation of tubing system at -4.3 masl, incl. an attached CTD sensor with sampling rate 1 s on the bottom to measure time of tracer injection at outlet and concentration.
4. Installation of upper CTD sensor with sampling rate 1 s.
5. Carrying out 5 injections, with varying levels of observations on the bottom (b):
   I. 15:05: observation at -43.7 masl
   II. 15:30: observation at -37.8 masl
   III. 16:02: observation at -33.2 masl
   IV. 16:25: observation at -27.6 masl
   V. 16:48: observation at -21.9 masl
   VI. 17:40: observation at -45.2 masl
   VII. Observation at -45.2 masl
6. Mean vertical flow velocities following each tracer injection were calculated based on the time after which 50% of tracer-influenced readings occurs

Problems

1. Diver attached to tube running out of memory before the last injection 7, therefore, the injection time is unknown.

Results/Conclusions

1. Injection of tracer follows rapid disappearance of tracer at injection point.
2. Tracer does not arrive at the upper CTD sensor.
3. Tracer shows downwards movement passing by the lower sensor.
4. Mean vertical flow velocities range between 129 m/h and 242 m/h.
5. Flow velocities increase with depth, indicating groundwater inflow.
6. Tracer recovery:
   I. 46%
   II. 35%
   III. 50%
   IV. 45%
   V. 50%
   VI. 51%
7. Very consistent mean downwards flow velocities, total average of 4.57 cm/s (164 m/h)

Tools

41 m tube Ø 6mm
Funnel
1,200 ml NaCl solution
850 ml tab water
Funnel
Schlumberger 86084 (tube outlet)
INW CT2X SN 21443061 (bottom)
INW CT2X SN 21443059 (top)

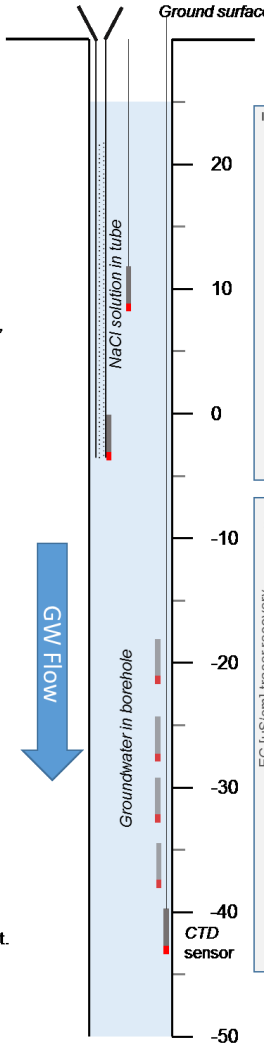

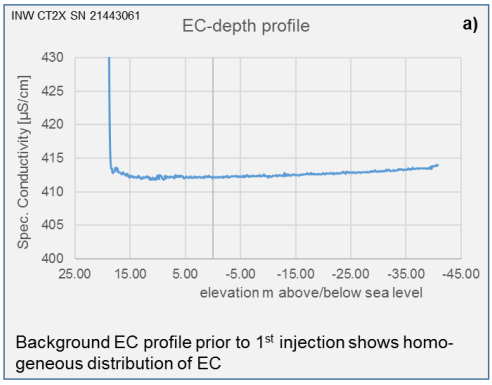

Background EC profile prior to 1st injection shows homogeneous distribution of EC

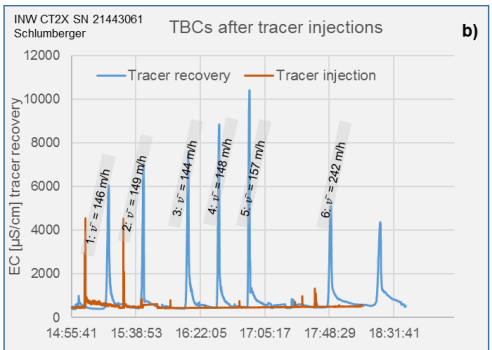

Tracer injections 1 to 6 at -4.3 masl and following TBCs at the bottom CTD sensor at 1.: -43.7 masl, 2.: -37.8 masl, 3.: -33.2 masl, 4.: -27.6 masl, 5.: -21.9 masl and 6: -45.2 masl. The mean flow velocities very little, yet an increase towards depth indicates groundwater inflow in this section

Figure C.2: SBDT conducted on 26 Feb 2017.

Single borehole dilution test

Location: GAA pitch Bell Harbour
Date: **04-03-2017**
Injections: 8
Tracer: NaCl solution (125g/l) and deionized water
Tracer quantity: 500 ml and 1,000 ml
Flushing solution: ~650 ml tab water

Goals

1. Inject NaCl solution at the outlet point of the tube to identify vertical flow direction (upwards/downwards) and identify if deionized tracer behaves different to NaCl solution. Further, estimate mean flow velocities, tracer recovery and evaluate the maximum level of recovered tracer.

Method

1. Establishing vertical CTD-background profile (a).
2. Installation of lower CTD sensor with a sampling rate 1 s.
3. Installation of tubing system, incl. an attached sensor on the bottom at 4.8 masl to measure time of tracer injection at outlet and concentration.
4. Installation of upper CTD sensor.
5. 8 injections were repeated using different tracer cocktails and observation was carried out at different levels:
   - I. 12:24: injection of 1,000 ml de-ion, observation at 12.8 masl
   - II. 15:00: injection of 500 ml de-ion, observation at 18.4 masl
   - III. 15:25: injection of ~500 ml low saline, observation at 18.5 masl (b)
   - IV. 15:45: injection of ~500 ml med saline, observation at 18.5 masl
   - V. 16:05: injection of 500 ml 100% NaCl, observation at 18.4 masl
   - VI. 16:37: injection of 500 ml 100% NaCl, observation at 23.4 masl
   - VII. 16:49: injection of 500 ml 100% NaCl, observation at 27.9 masl (b)
   - VIII. 16:59: injection of ~500 ml 100% NaCl, observation at 24.0 masl

Problems

1. Schlumberger sensor running out of memory

Results/Conclusions

1. Injection of tracer follows rapid disappearance of tracer at injection point.
2. No tracer arrives at the lower CTD sensor.
3. Tracer shows upwards movement, which was recorded up to 24 masl
4. Tracer recovery:
   - VI. 0.3%
   - VII. 0.1%
5. Upwards flow velocity of 7.3 cm/s (263 m/h).

Tools

25 m tube Ø 6mm
Funnel
NaCl solution, deionized water
tab water
Funnel
Schlumberger 86084 (tube outlet)
INW CT2X SN 21443061 (bottom)
INW CT2X SN 21443059 (top)

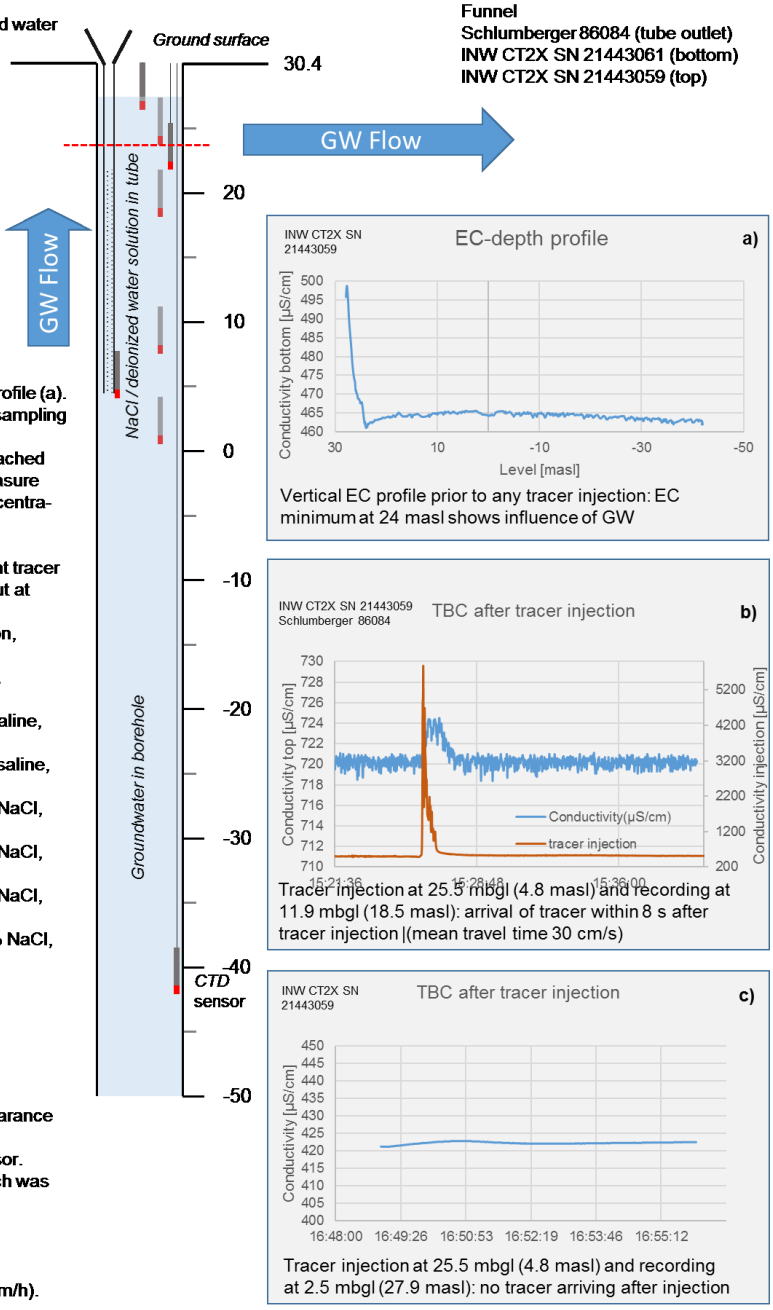

Figure C.3: SBDT conducted on 04 Mar 2017.

Single borehole dilution test

Location: GAA pitch Bell Harbour
Date: **23-03-2017**
Injections: 3
Tracer: NaCl solution (125g/l) and deionized water
Tracer quantity: 500 ml NaCl and 1,000 ml deionized water
Flushing solution: 850 ml turlough water

Goals

1. Inject NaCl solution at the outlet point of the tube to identify vertical flow direction (upwards/downwards), estimate mean flow velocities, tracer recovery and evaluate maximum level of recovered tracer.

Method

1. Installation of lower CTD sensor at -44.7 masl with a sampling rate of 1 s.
2. Installation of tubing system at 4.8 masl, incl. an attached CTD sensor with sampling rate 1 s on the bottom to measure time of tracer injection at outlet and concentration.
3. Installation of upper CTD sensor at 14.1 masl with sampling rate 1 s.
4. 3 injections were carried out using different tracer cocktails:
   I. 1255: injection of 500 ml NaCl, observation at -44.7 masl.
   II. 13:33: injection of 1,000 ml deionized water, observation at -18.8 masl.
5. A mean vertical flow velocity could only be estimated for injection 1 (following TBC was terminated by arrival of deionized water).

Problems

1. Very slow flow velocities: injection 1 arrived after 45 min. The following TBC was interrupted by injection 2 (deionized water). Injection 3 could not be fully recorded due to very long travel times.

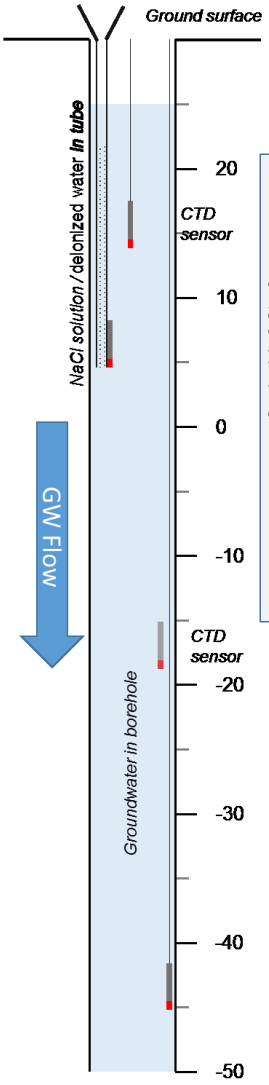

Tools

41 m tube Ø 6mm
Funnel
500 ml NaCl solution
1,000 ml deionized water
Turlough water
Funnel
Schlumberger 86084 (tube outlet)
INW CT2X SN 21443061 (bottom)
INW CT2X SN 21443059 (top)

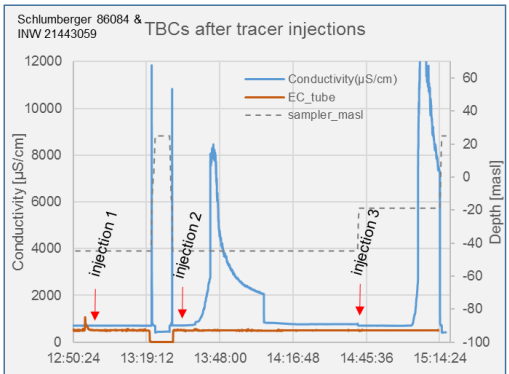

Tracer injections 1 to 3 at 4.8 masl and following tracer breakthrough curves at the bottom CTD sensor at 1.: -44.7 masl and 2.: -18.8 masl. A mean flow velocity was estimated for injection 1 reaching 54.7 m/h.

Results/Conclusions

1. No tracer arrives at the upper CTD sensor.
2. Tracer moves downwards passing by the lower sampler.
3. The TBC of the NaCl tracer of injection 1 suggests a tracer recovery of 89.8%.
4. Downwards flow velocity is estimated at 1.52 cm/s (54.7 m/h).
5. Downwards flow reaches beyond -44.7 masl.

Figure C.4: SBDT conducted on 23 Mar 2017.

Single borehole dilution test

Location: GAA pitch Bell Harbour
Date: **14-04-2017**
Injections: 2
Tracer: NaCl solution (125 g/l)
Tracer quantity: 500 ml
Flushing solution: ~650 ml tab water

Goals

1. Inject NaCl solution at the outlet point of the tube to identify vertical flow direction (upwards/downwards) and estimate the mean flow velocities, tracer recovery and evaluate the maximum level of recovered tracer.

Method

1. Installation of one lower CTD sensor at -80.4 masl with a sampling frequency of 30 s.
2. Installation of tubing system, incl. an attached sensor on the bottom at 5.0 masl to measure time of tracer injection at outlet.
3. 2 injections were carried out:
    1. 10:25: injection of 500 ml NaCl at 5 masl, observation at -80.4 masl (a) (*2 TBCs recorded. Following on, the CTD sensor was released to -128.9 masl*).
    2. 10:44: injection of 500 ml NaCl at 22.7 masl, observation at -128.9 masl (b) (*the resulting TBCs slightly overlaps with the TBC of injection 1*).

Problems

1. The TBCs of injection 1 and 2 slightly overlap.
2. The TBC of injection 2 is not fully completed.

Results/Conclusions

1. Both injected tracers travel downwards.
2. Tracer was successfully recovered up to -128.9 masl:
3. Because of the overlap of TBCs of injection 1 and 2, an average mean vertical flow velocity was estimated reaching 2.72 cm/s (97.9 m/h).
4. The combined tracer recovery was estimated at 20.0%.

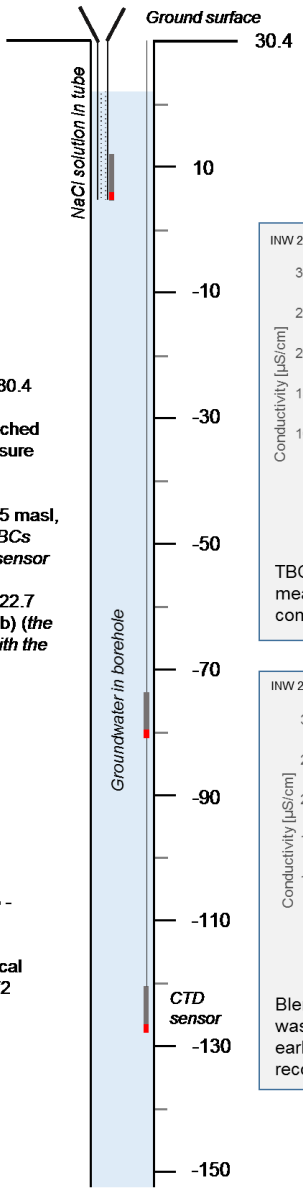

Tools

25 m tube Ø 6mm
Funnel
NaCl solution
tab water
Funnel
Schlumberger 86084 (tube outlet)
INW CT2X SN 21443059 (bottom)

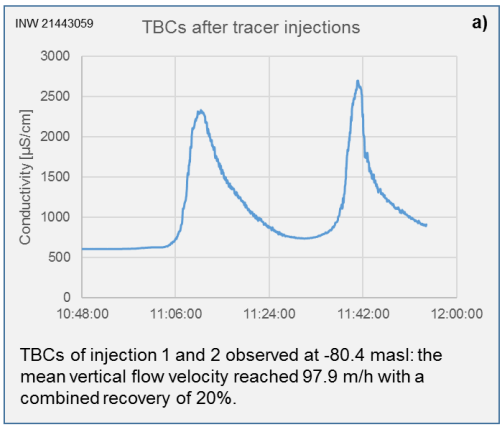

TBCs of injection 1 and 2 observed at -80.4 masl: the mean vertical flow velocity reached 97.9 m/h with a combined recovery of 20%.

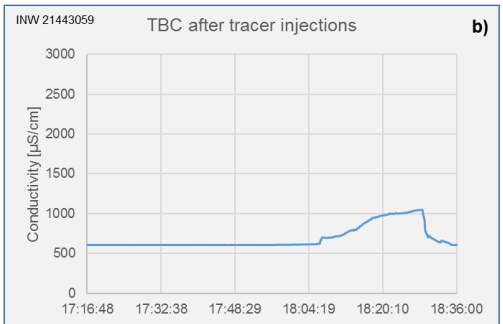

Blended TBC of injection 1 and 2 at -128.9 masl: the TBC was interrupted because of removing the CTD sensor too early. Therefore, no estimations on travel time and tracer recovery could be carried out.

Figure C.5: SBDT conducted on 14 Apr 2017.

Single borehole dilution test

Location: GAA pitch Bell Harbour
Date: **13-09-2017**
Injections: 3
Tracer: NaCl solution (62.5 g/l)
Tracer quantity: 500 ml
Flushing solution: ~650 ml tab water

Goals

1. Inject NaCl solution at the outlet point of the tube to identify vertical flow direction (upwards/downwards), estimate the mean flow velocity and tracer recovery and evaluate the maximum level of recorded tracer.

Method

1. Installation of two lower CTD sensor at -127.7 and -176 masl sampling at 30 s.
2. Installation of tubing system with the outlet at 4.8 masl.
3. 2 injections were carried out. The tracer was observed at -159.7 masl (a) and -176.0 masl (b):
   I. 11:20: injection of 500 ml NaCl (*injection unsuccessful*).
   II. 12:05: Injection of 500 ml NaCl (*injection potentially blended with injection 1*)
   III. 18:33: Injection of 500 ml NaCl

Problems

1. Injection 1 was not carried out successfully. It was concluded that injection 1 has blended together with injection 2, hence, only injection 3 was interpreted.

Results/Conclusions

1. All tracers travel downwards.
2. Tracer was successfully recovered up to -176.0 masl:
3. Mean vertical flow was estimated at 2.69 cm/s (97.0 m/h) for the upper sensor and 1.2 cm/s (43.0 m/h) for the lower sensor.
4. The tracer recovery was estimated at 25.6% for the upper sensor and 9.4% for the lower sensor.
5. Flow velocities decrease with increasing depth, presumably linked to groundwater outflow, which is also indicated by the lower tracer recovery at the bottom sensor.

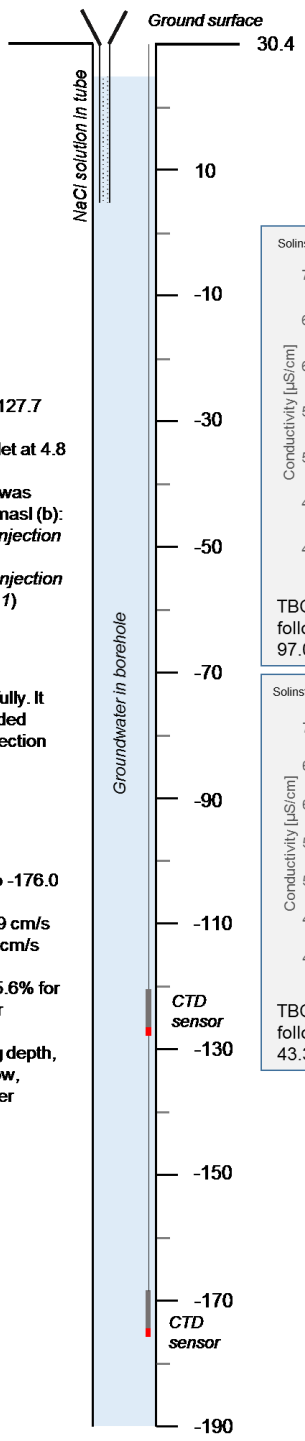

Tools

25 m tube Ø 6mm
Funnel
NaCl solution
tab water
Funnel
Solinst 3001 LTC M30 (top)
Solinst 3001 LTC M200 (bottom)

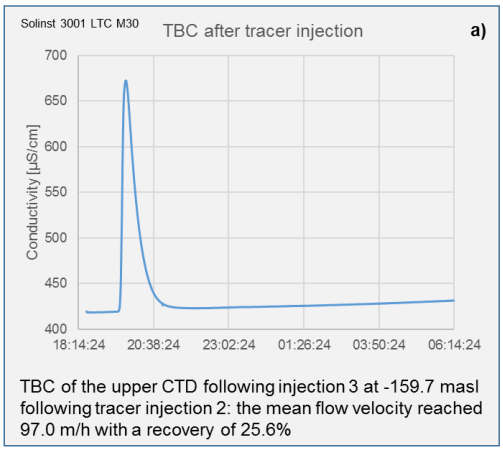

TBC of the upper CTD following injection 3 at -159.7 masl following tracer injection 2: the mean flow velocity reached 97.0 m/h with a recovery of 25.6%

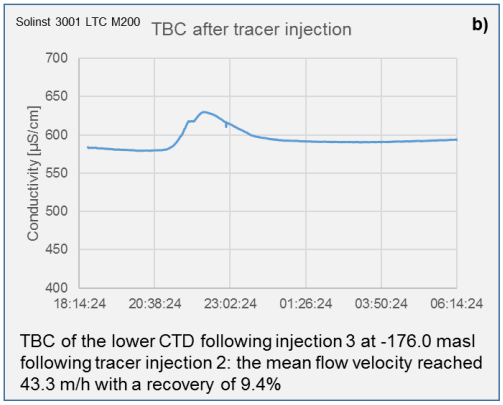

TBC of the lower CTD following injection 3 at -176.0 masl following tracer injection 2: the mean flow velocity reached 43.3 m/h with a recovery of 9.4%

Figure C.6: SBDT conducted on 13 Sep 2017.

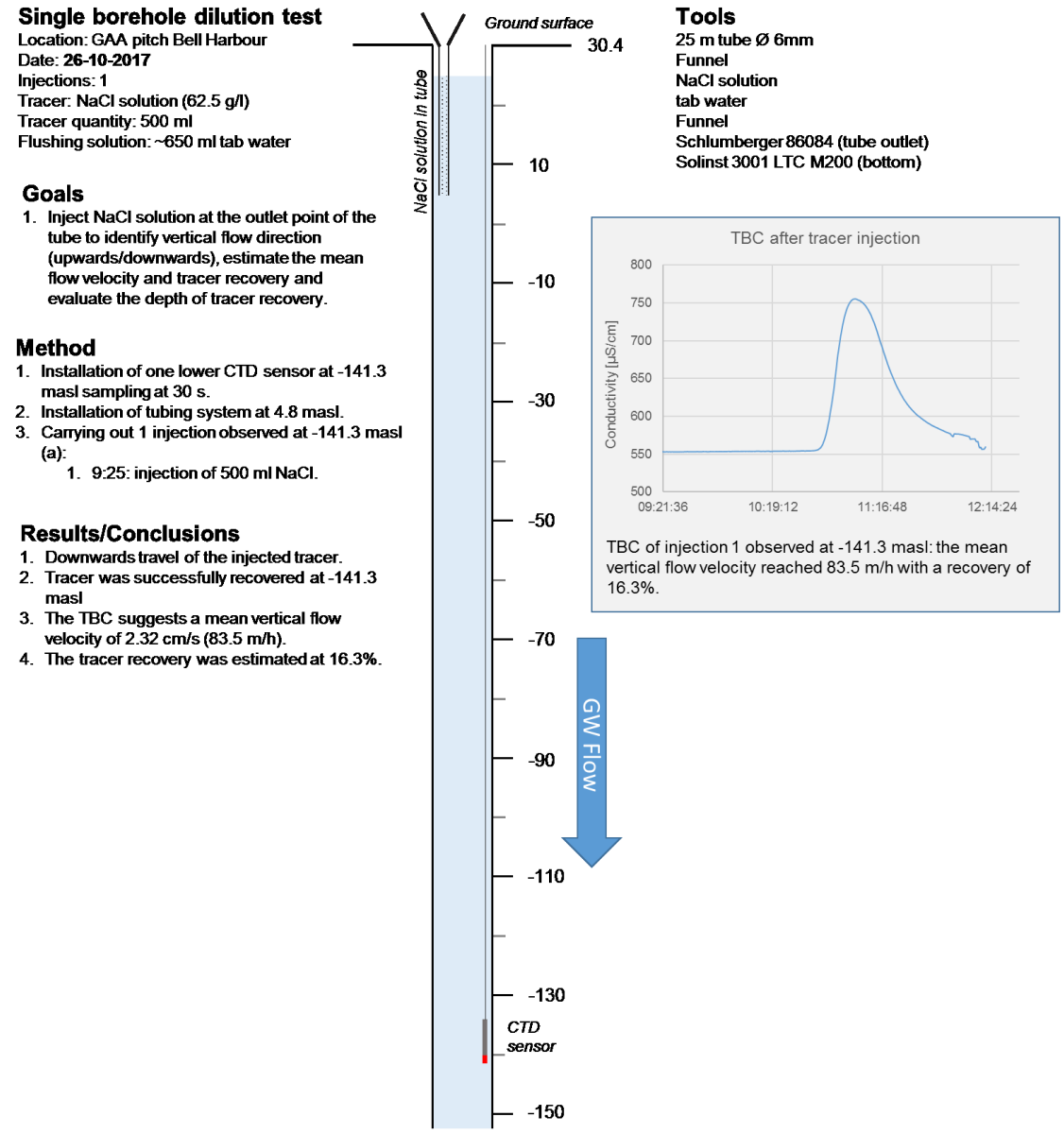

Figure C.7: SBDT conducted on 26 Oct 2017.